Complexity

Coevolving Spreading Dynamics of Complex Networks

Guest Editors: Wei Wang, Chenquan Gan, Jiaojiao Jiang, and Luxing Yang

Coevolving Spreading Dynamics of Complex Networks

Complexity

Coevolving Spreading Dynamics of Complex Networks

Guest Editors: Wei Wang, Chenquan Gan, Jiaojiao Jiang, and Luxing Yang

Contents

Contents

Hindawi
Complexity
Volume 2021, Article ID 6639632, 9 pages
https://doi.org/10.1155/2021/6639632

Research Article

Modeling and Analysis of the Spread of Malware with the Influence of User Awareness

Qingyi Zhu, Xuhang Luo, and Yuhang Liu

School of Cyber Security and Information Law, Chongqing University of Posts and Telecommunications, Chongqing 400065, China

Correspondence should be addressed to Qingyi Zhu; zhuqy@cqupt.edu.cn

Received 17 December 2020; Revised 19 May 2021; Accepted 13 October 2021; Published 1 November 2021

Academic Editor: Marcus Aguiar

By incorporating the security awareness of computer users into the susceptible-infected-susceptible (SIS) model, this study proposes a new malware propagation model, named the SID model, where D compartment denotes the group of nodes with user awareness. Through qualitative analysis, the basic reproductive number R_0 is given. Furthermore, it is proved that the virus-free equilibrium is globally asymptotically stable if R_0 is less than one, whereas the viral equilibrium is globally asymptotically stable if R_0 is greater than one. Then, some numerical examples are given to demonstrate the analytical results. Finally, we put forward some efficient control measures according to the theoretical and experimental analysis.

1. Introduction

Malware is the generic term used to designate any informatics program created deliberately to carry out an unauthorized activity that, in many cases, is harmful to the system in which it has been lodged [1]. There is an increasing trend in both the number and types of malware. According to the report in [2], there is an exponential growth in the number of viruses, and in 2017, there are 15,107,232 different malware files that we had never seen before, mainly because of the improvement of technology and the increasing Internet population. Hence, there are lots of researchers trying to develop effective methods and tools to detect malware from a microperspective [3–5].

Although the scientific approach to combating malware is mainly focused on the design of efficient methods to detect and remove malware [6], it is also worth modeling the propagation behaviors of malware and developing effective control strategies, furthermore, to prevent its outbreak. Most of these models are dynamical systems of ordinary differential equations [7]. They are compartmental, that is, the nodes are divided into different types, such as susceptible, exposed, infectious, recovered, and quarantined. Thus, a great number of models (SIS models [8, 9], SIR models [10, 11], SEIR models [12], and SIRQ models [13]) have been proposed.

In recent years, most malware propagation models are proposed by incorporating some new compartments into the existing models. In [14], by considering the protected nodes in cloud, Gan et al. proposed an SIP model for computer virus propagation. More specifically, the protected nodes in cloud can be not infected but might be converted into an S compartment in a certain probability. Similarly, considering the devices that can be infected by the malware but cannot be damaged, an SIRC model is built in [15], where C denotes the carrier device.

On the other hand, user's awareness also has gained a lot of attention from researchers. In [16], the authors pointed out that the missing of user awareness might cause some security issues. In [17], Furnell also claimed that phishing is a significant security threat, and the problem cannot be completely solved by technology alone; in this context, user awareness is highly required. It is no doubt that user awareness is essential for cybersecurity. Considering that user awareness also plays an important role in slowing down the propagation of malware, an improved model based on the SLIR model with user awareness has been put forward in [18]. In [18], the user whose computer is not infected or

exposed is probable to install antivirus programs, and the probability here is called user awareness.

In [1], the author raised the issue that the infection rate of computers may vary from computer to computer. For example, if users are worried about security issues, the infection rate should be reduced. In contrast, if users have dangerous behaviors, the infection rate should be higher. Inspired by this, this study aims to address the issue of different infection rates of computers with/without user awareness. Different from the work in [18], a new compartment (D compartment) is incorporated into the classical SIS model. Here, D compartment denotes the group of nodes with security awareness, whereas S represents the node with dangerous behaviors. Obviously, the infection rate of D nodes is less than S nodes. Besides, in [19, 20], the author proposed S and W compartments similar to S and D compartments in this article, where the conversion rate of the two is a constant. However, we noticed that the change in user awareness is related to the number of infections. The higher the number of infections, the higher the awareness of users. So, we consider that the rate of consciousness conversion is related to the number of infections.

The main contributions of this work are as follows:

(1) A new model describing computer virus propagation is built from the perspective of user awareness

(2) Two equilibrium of the model is obtained: the virus-free equilibrium point and the viral equilibrium, and furthermore, their local and global stabilities are proved, respectively.

(3) Through qualitative analysis and simulation experiments, effective control measures are proposed to prevent the outbreak and spread of malware

The remaining materials of this study are organized as follows: Section 2 formulates the proposed propagation model of malware. In Section 3, local stabilities of both the infection-free and viral equilibria are analyzed, respectively, while Section 4 deals with the global stabilities of the two equilibria. In Section 5, some numerical simulations are performed to illustrate the obtained theoretical results and efficient control measures. Finally, Section 6 summarizes this work and gives some shortcomings.

2. Mathematical Framework

The model proposed in this work is a compartmental model where the computers are divided into 3 classes: susceptible nodes (S) which can be infected by malware easily, nodes with user awareness (D) which can be infected by malware more difficult than S nodes, and infected nodes (I) which can infect other nodes. The transfer diagram is shown in Figure 1. The following notations and assumptions will be adopted in the sequel.

2.1. Notations

$S(t)$: the number of S nodes at time t

$D(t)$: the number of D nodes at time t

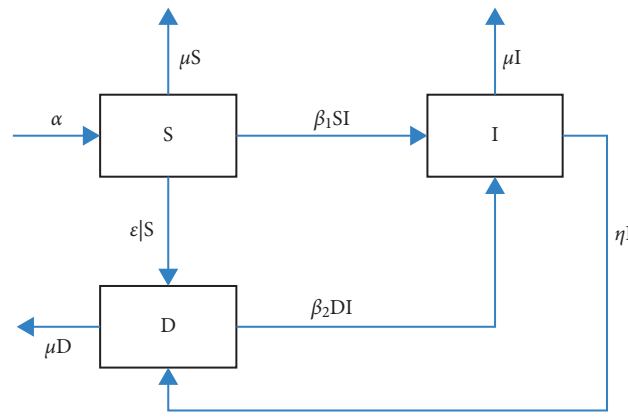

Figure 1: The transfer diagram of the model.

$I(t)$: the number of I nodes at time t

$N(t)$: the total number of nodes at time t

α: the rate at which the node connects to the network

μ: the rate at which the node disconnects to the network

β_1: the infection rate of S nodes caused by an I node

β_2: the infection rate of D nodes caused by an I node. Obviously, $\beta_2 < \beta_1$.

ϵ: the conversion rate from S nodes to D nodes caused by an I node

η: the recovery rates of I nodes due to the effect of antivirus software

2.2. Model Assumptions

(i) All newly accessed nodes are S nodes

(ii) At time t, the infection force from S to I is given by $\beta_1 S(t)I(t)$, and the infection force from D to I is given by $\beta_2 D(t)I(t)$.

(iii) Due to the spread of malware, users gradually become conscious. At time t, the conversion force from S to D is given by $\varepsilon S(t)I(t)$.

(iv) At time t, the users of the recovered nodes all have improved, and the recovered force of I nodes is $\eta I(t)$.

2.3. Model Formulation. Considering the above assumptions, the dynamics of the model is governed by the following system of ordinary differential equations:

$$\begin{cases} \dfrac{dS}{dt} = \alpha - \mu S - \beta_1 SI - \epsilon IS, \\ \dfrac{dD}{dt} = \epsilon IS + \eta I - \beta_2 DI - \mu D, \\ \dfrac{dI}{dt} = \beta_1 SI + \beta_2 DI - \eta I - \mu I. \end{cases} \tag{1}$$

According to $N(t) = S(t) + D(t) + I(t)$, we have $dN/dt = \alpha - \mu N$. Obviously, when $t \longrightarrow \infty$, $N \longrightarrow \alpha/\mu$.

Thus, system (1) can be reduced to the following limit system:

$$\begin{cases} \dfrac{\mathrm{d}S}{\mathrm{d}t} = \alpha - \mu S - \beta_1 SI - \epsilon IS, \\ \dfrac{\mathrm{d}I}{\mathrm{d}t} = \beta_1 SI + \beta_2\left(\dfrac{\alpha}{\mu} - S - I\right)I - \eta I - \mu I. \end{cases} \tag{2}$$

It is easy to verify that all feasible solutions of equation (2) are bounded and finally fall inside the region Ψ defined as

$$\Psi = \left\{(S, I):\ S \geq 0, I \geq 0, D + I \leq \frac{\alpha}{\mu}\right\}. \tag{3}$$

Obviously, system (2) has infection-free equilibrium $E_0 = (\alpha/\mu, 0)$.

The basic reproduction number R_0 is defined as the average number of computers infected by an infected device during the period from infection. R_0 often serves as a threshold parameter that predicts whether an infection will spread. For system (2), we have

$$R_0 = \frac{\beta_1 \alpha}{\mu(\mu + \eta)}. \tag{4}$$

If $R_0 > 1$, system (2) has a viral equilibrium $E^* = (S^*, I^*)$:

$$\begin{aligned} I^* &= \frac{\sqrt{b^2 - 4ac} - b}{2a}, \\ S^* &= \frac{\alpha}{\mu + \beta_1 I^* + \varepsilon I^*}, \end{aligned} \tag{5}$$

where

$$\begin{aligned} a &= \mu\beta_2(\beta_1 + \varepsilon), \\ b &= \mu^2(\beta_1 + \beta_2 + \varepsilon) + (\beta_1 + \varepsilon)(\mu\eta - \beta_2\alpha), \\ c &= \mu\left(\mu^2 + \mu\eta - \beta_1\alpha\right). \end{aligned} \tag{6}$$

3. Local Stability

In this section, we will analyze the two local stabilities of the equilibria of the system.

Theorem 1. *E_0 is locally asymptotically stable if $R_0 < 1$. Whereas, E_0 is unstable if $R_0 > 1$.*

Proof. By linearizing system (2) at E_0, we get the characteristic equation:

$$\begin{vmatrix} \lambda + \mu & \beta_1\dfrac{\alpha}{\mu} + \varepsilon \\ 0 & \lambda + \eta + \mu - \beta_1 N\dfrac{\alpha}{\mu} \end{vmatrix} = 0. \tag{7}$$

Thus,

$$(\lambda + \alpha)\left(\lambda + \eta + \mu - \beta_1 N\frac{\alpha}{\mu}\right) = 0, \tag{8}$$

$$\begin{aligned} \lambda_1 &= -\mu < 0, \\ \lambda_2 &= -\eta - \mu + \beta_1 N\frac{\alpha}{\mu}. \end{aligned} \tag{9}$$

On the one hand, all roots of equation (8) have negative real parts, and hence, E_0 is locally asymptotically stable if $R_0 < 1$. On the other hand, equation (8) has at least one root with positive real, and hence, E_0 is unstable if $R_0 > 1$. □

Theorem 2. *E^* is locally asymptotically stable if $R_0 > 1$.*

Proof. By linearizing system (2) at E^*, we get the characteristic equation:

$$\begin{vmatrix} \lambda + \mu + \beta_1 I^* + \varepsilon I^* & \beta_1 S^* + \varepsilon S^* \\ \beta_2 I^* - \beta_1 I^* & \lambda + \beta_2 S^* + 2\beta_1 I^* + \eta + \mu - \beta_1 S^* - \beta_2\dfrac{\alpha}{\mu} \end{vmatrix} = 0. \tag{10}$$

Thus,

$$\lambda^2 + k_1\lambda + k_2 = 0, \tag{11}$$

where

$$\begin{cases} k_1 = \beta_2 S^* + 3\beta_1 I^* + \eta + 2\mu + \varepsilon I^* - \beta_1 S^* - \beta_2 \dfrac{\alpha}{\mu}, \\ k_2 = (\mu + \beta_1 I^* + \varepsilon I^*)\left(\beta_2 S^* + 2\beta_1 I^* + \eta + \mu - \beta_1 S^* - \beta_2 \dfrac{\alpha}{\mu}\right) + I^* S^* (\beta_1 + \varepsilon)(\beta_1 - \beta_2). \end{cases} \tag{12}$$

The following inequality can be obtained from Section 2: $\beta_1 > \beta_2$. We can also obtain an equation from the second equation of system (2): $\beta_1 S^* + \beta_2(\alpha/\mu) = \beta_2 S^* + \beta_2 I^* + \eta + \mu$.

We have $k_1 = 2\beta_1 I^* + \mu + \varepsilon I^* + (\beta_1 - \beta_2) I^* > 0$ and $\beta_2 S^* + 2\beta_1 I^* + \eta + \mu - \beta_1 S^* - \beta_2(\alpha/\mu) = \beta_1 I^* > 0$, so $k_2 > 0$.

It follows from the Hurwitz [21] criterion that the two roots of (11) have negative real parts. Thus, the claimed result follows. □

4. Global Stability

Theorem 2 has revealed that the equilibrium E^* and E_0 in the system (2) are locally asymptotically stable, respectively. Then, we intend to analyze the global stability of the SID epidemic model in this section. A famous method is for determining a system whether having periodic orbits is the Bendixson–Dulac [22] criterion. The following lemma will be useful in the sequel before proving the global stability of equilibrium points.

Lemma 1. *The system has no periodic orbits in* Ψ *for system (2).*

Proof. Define

$$\begin{aligned} h_1(S, I) &= \alpha - \mu S - \beta_1 SI - \varepsilon IS, \\ h_2(S, I) &= \beta_1 SI + \beta_2 \frac{\alpha}{\mu} I - \beta_2 SI - \beta_2 I^2 - \eta I - \mu I. \end{aligned} \tag{13}$$

Constructing Dulac function [22],

$$F(D, I) = \frac{1}{SI}. \tag{14}$$

In the interior of Ψ, one can get

$$\frac{\partial(Fh_1)}{\partial S} + \frac{\partial(Fh_2)}{\partial I} = -\frac{\alpha}{S^2 I} - \frac{\beta_2}{S} < 0. \tag{15}$$

Therefore, it follows from the Bendixson–Dulac criterion [22] that the interior of Ψ for system (2) does not contain periodic orbit.

We should take into account the boundary of Ψ after considering the interior area. Assume that an arbitrary point $(\widetilde{S}, \widetilde{I})$ is on the edge of the Ψ. After that, the following three possibilities will be discussed, respectively:

(1) Case 1: when $0 < \widetilde{S} \le \alpha/\mu$ and $\widetilde{I} = 0$, then

$$\frac{\mathrm{d}}{I}\mathrm{d}t\Big|_{\widetilde{(S,I)}} = 0. \tag{16}$$

(2) Case 2: when $0 < \widetilde{I} \le \alpha/\mu$ and $\widetilde{S} = 0$, then

$$\frac{\mathrm{d}S}{\mathrm{d}t}\Big|_{\widetilde{(S,I)}} = \alpha > 0. \tag{17}$$

(3) Case 3: when $\widetilde{S} + \widetilde{I} = \alpha/\mu$, $\widetilde{S} \neq 0$, and $\widetilde{I} \neq 0$, then

$$\begin{aligned} \frac{\mathrm{d}(S+I)}{\mathrm{d}t}\Big|_{\widetilde{(S,I)}} &= \alpha + \beta_2 I\left(\frac{\alpha}{\mu} - I - S\right) - \mu(S+I) \\ &- \epsilon IS - \eta I = -\epsilon IS - \eta I < 0. \end{aligned} \tag{18}$$

Thus, it complies with the above three cases that there is no periodic orbit getting past $(\widetilde{S}, \widetilde{I})$ for system (2). In brief, there is no periodic orbit within $\widetilde{\Omega}$ for system (2). Now, the proof has been completed.

Then, we can set out to prove the equilibria E^* and E_0 of system (2) are global asymptotically stable in corresponding conditions, respectively. □

Theorem 3. *E_0 is globally asymptotically stable with respect to Ψ if $R_0 < 1$, whereas E^* is globally asymptotically stable with respect to Ψ if $R_0 > 1$.*

Proof. With the basis of Theorems 1 and 2 and Lemma 1, according to the Poincare–Bendixson theorem [22], one can get that the equilibrium E^* is globally asymptotically stable for system (2) with respect to Ψ if $R_0 > 1$, and E_0 is globally asymptotically stable with respect to Ψ if $R_0 < 1$. Now, we accomplish the proof. □

Remark 1. Theorems 1–3 have presented a phenomenon that the malware cannot be completely suppressed if $R_0 > 1$. But according to Theorem 1, some factors can also suppress the spread of malware. In another aspect, with these related parameters, the proportion of infected can be reduced. This also provides an effective direction to curb the spread of malware in computers.

5. Numerical Simulations

This section is to give some numerical simulations to verify our theoretical results.

Example 1. Consider system (1) with parameters $\alpha = 1, \mu = 0.1, \epsilon = 0.02$, $\beta_1 = 0.05$, $\beta_2 = 0.02$, and $\eta = 0.45$; then, $R_0 = 0.91 < 1$, and some initial values are given in Table 1.

In Figure 2, E_0 is globally stable if $R_0 < 1$. What is more, we can get a conclusion that the initial value has nothing to do with the global stability if $R_0 < 1$.

Example 2. Consider system (1) with parameters $\alpha = 1, \mu = 0.1, \epsilon = 0.02$, $\beta_1 = 0.1$, $\beta_2 = 0.05$, and $\eta = 0.45$;

Table 1: Simulation initial values.

Initial value	$S(0)$	$D(0)$	$I(0)$
Case 1	2	0	8
Case 2	4	0	6
Case 3	6	0	4
Case 4	2	3	5
Case 5	4	4	2

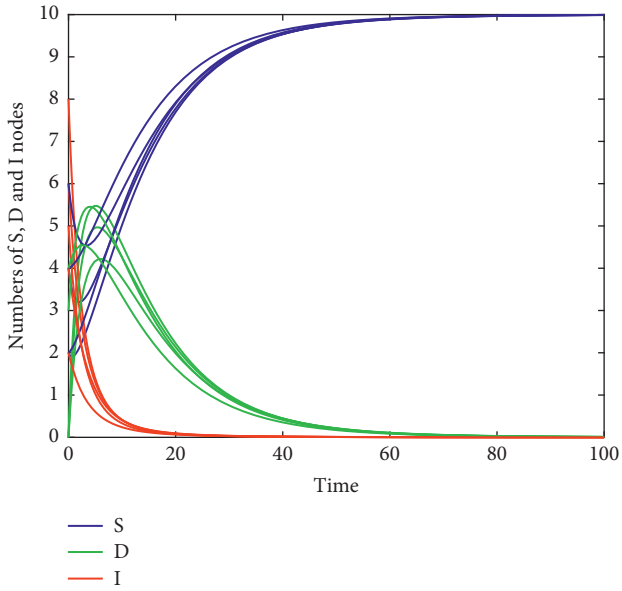

Figure 2: The time plot for the system given in Example 1.

then, $R_0 = 1.82 > 1$, and the initial values of the system are kept the same as given in Table 1.

In Figure 3, E^* is globally stable if $R_0 > 1$. We can also find that the initial value has no effect on the spread of malware if $R_0 > 1$. By comparing Figure 2 with Figure 3, keeping the basic reproduction number $R_0 < 1$ is an effective way to prevent the breakout of malware.

Example 3. We will illustrate the influence of different the awareness conversion rate $\epsilon = \{0.02, 0.08, 0.14, 0.20, 0.26\}$ on system (1). Consider system (1) with parameters $\alpha = 1, \mu = 0.1, \beta_1 = 0.1$, $\beta_2 = 0.02$, and $\eta = 0.1$ and with initial conditions $S(0) = 9$, $D(0) = 0$, and $I(0) = 1$.

Since user awareness plays an important role in malware propagation, Figure 4 shows time plots of the number of infected users with varied awareness conversion rates. We can find that the higher the awareness conversion rate, the smaller the number of infected users. So, raising user awareness can effectively control the number of infected users.

Example 4. Due to the importance of R_0, we will discuss how parameters affect the evolution of malware propagation over time. The parameters are given in Table 2.

We can find that R_0 and β_1 have a positive linear relationship as shown in Figure 5. Therefore, we can keep the contact rate β_1 at a low level to prevent the spread of malware

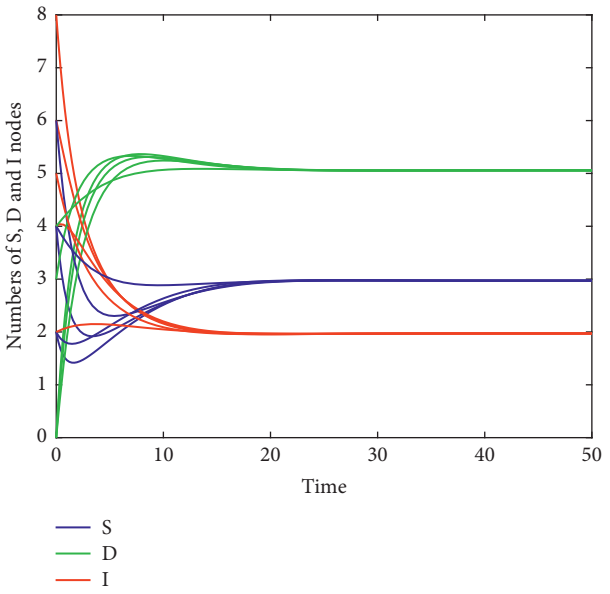

Figure 3: The time plots for the system given in Example 2.

in computers effectively. R_0 and α have a positive linear relationship in Figure 6. Figure 7 shows that R_0 decreases as μ increases. Thus, it is reasonable to reduce the online rate of the computer and increase the disconnect rate of computer

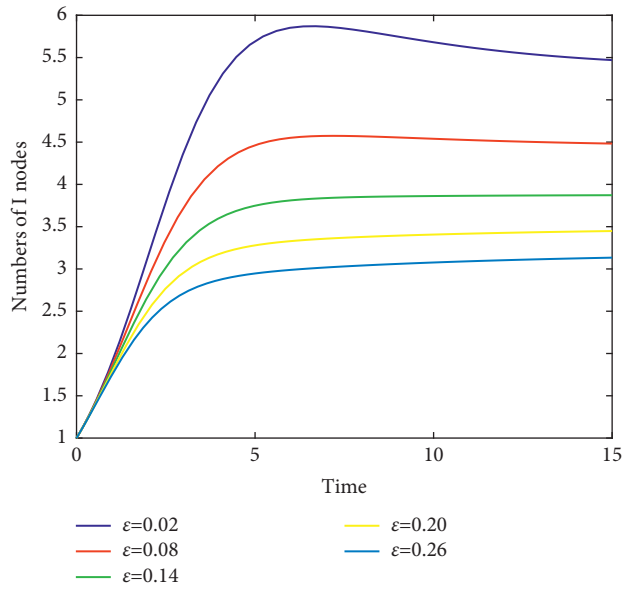

Figure 4: The time plots of number of infected nodes of the system with conditions given in Example 3.

Table 2: Simulation parameters.

Figures	β_1	α	μ	η
Figure 5	*	1	0.1	0.6
Figure 6	0.05	*	0.1	0.6
Figure 7	0.05	1	*	0.6
Figure 8	0.05	1	0.1	*

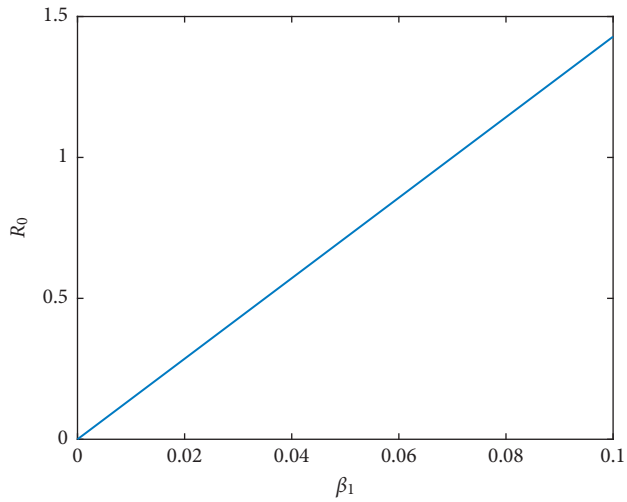

Figure 5: The effect of β_1 on R_0.

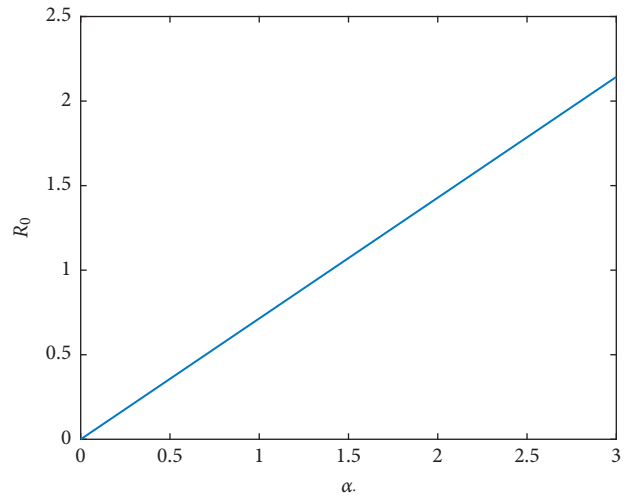

Figure 6: The effect of α on R_0.

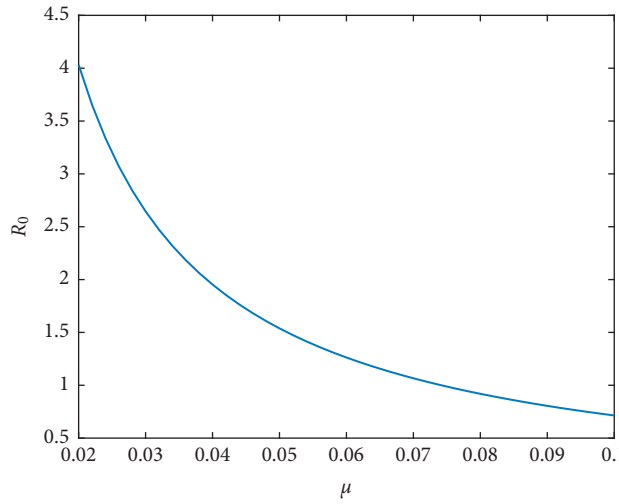

Figure 7: The effect of μ on R_0.

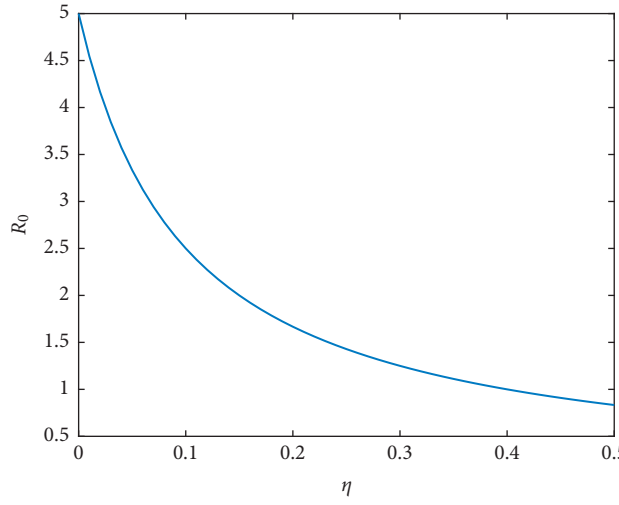

Figure 8: The effect of η on R_0.

Table 3: Simulation parameters.

Parameters	α	μ	β_1	β_2	η	ϵ	β	η_1
Case 1	1	0.1	0.1	0.05	0.2	0.04	0.1	0.2
Case 2	1	0.1	0.3	0.1	0.2	0.02	0.3	0.2
Case 3	1	0.1	0.5	0.2	0.2	0.04	0.5	0.2

when the malware spreads and breaks out. Figure 8 shows that R_0 will drop sharply if the recovery rate increased. So, installing the latest antimalware software on computers is another effective countermeasure to control the propagation of malware.

Example 5. Finally, we compare the SIS model with our proposed model through several sets of simulation experiments. The SIS model with the infection rate β and the recovery rate η_1 have been proposed in [23]. Here, $\beta = \beta_1$ and $\eta_1 = \eta$. The initial conditions are $S(0) = 6$, $D(0) = 0$, and $I(0) = 4$. The parameters are given in Table 3.

In Figure 9, we can clearly see that the final number of infected nodes in the SID model is always smaller than the corresponding number in the SIS model. So, it makes sense to improve the security awareness of users.

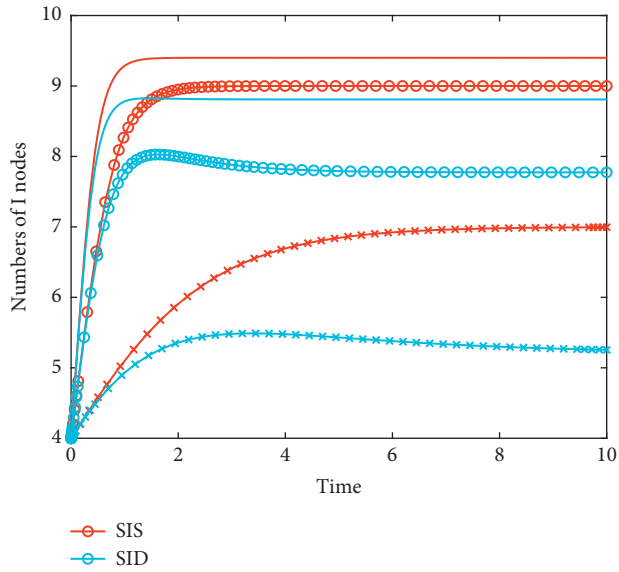

Figure 9: The time plots for the system given in Example 5.

6. Conclusion

Inspired that user awareness plays an important role in the spread of malware, a new model based on the SIS model is proposed. Through mathematical analysis and simulation experiments, the rationality of the model is verified, and it is proposed that if we improve user awareness before malware propagation, then preventing the spread of malware will be achieved. Moreover, biological and malware models have many similar behaviors. Hence, it makes sense to compare biological and malware models. The novel coronavirus infectious disease is commonly known as COVID-19 and has become the greatest challenge in this world [24]. To study the spread of the coronavirus, there are plenty of mathematical models about COVID-19 [25–27]. The model proposed in this article can also be used to describe the propagation of COVID-19. In this context, S node represents people who have not taken any measures against COVID-19, D node represents people who have taken measures against COVID-19, such as wearing a mask or staying at home, and I node represents people who have been infected and can infect others.

Data Availability

The data used to support the findings of this study are included within the article.

Conflicts of Interest

The authors declare that they have no conflicts of interest.

Acknowledgments

This work was supported by the National Natural Science Foundation of China (61903056 and 61702066) and the Chongqing Research Program of Basic Research and Frontier Technology (cstc2019jcyj-msxmX0681 and cstc2018jcyjAX0154).

References

[1] A. M. del Rey and M. Angel, "Mathematical modeling of the propagation of malware: a review," *Security and Communication Networks*, vol. 8, no. 15, pp. 2561–2579, 2015.

[2] Panda Security, *PandaLabs Annual Report*, Panda Security, Bilbao, Spain, 2017.

[3] Y. Dai, H. Li, Y. Qian, Y. Guo, R. Yang, and M. Zheng, "Using IRP and local alignment method to detect distributed malware," *Computers Security*, vol. 100, Article ID 102109, 2020.

[4] P. Vinod, A. Zemmari, and M. Conti, "A machine learning based approach to detect malicious android apps using discriminant system calls," *Future Generation Computer Systems*, vol. 94, pp. 333–350, 2019.

[5] F. Abri, S. Siami-Namini, M. A. Khanghah, F. M. Soltani, and A. S. Namin, "Can machine/deep learning classifiers detect zero-day malware with high accuracy?" in *Proceedings of the IEEE International Conference on Big Data (Big Data)*, pp. 3252–3259, IEEE, Los Angeles, CA, USA, December 2019.

[6] A. Damodaran, F. D. Troia, C. A. Visaggio, T. H. Austin, and M. Stamp, "A comparison of static, dynamic, and hybrid analysis for malware detection," *Journal of Computer Virology and Hacking Techniques*, vol. 13, no. 1, pp. 1–12, 2017.

[7] J. D. Hernández Guillén and A. Martín del Rey, "A mathematical model for malware spread on WSNs with population dynamics," *Physica A: Statistical Mechanics and Its Applications*, vol. 545, Article ID 123609, 2020.

[8] J. O. Kephart and S. R. White, "Directed-graph epidemiological models of computer viruses," in *Proceedings of the IEEE Computer Society Symposium on Research in Security and Privacy*, pp. 343–359, IEEE, Oakland, CA, USA, 1999.

[9] I. Tomovski, I. Trpevski, and L. Kocarev, "Topology independent SIS process: an engineering viewpoint," *Communications in Nonlinear Science and Numerical Simulation*, vol. 19, no. 3, pp. 627–637, 2014.

[10] J. C. Wierman and D. J. Marchette, "Modeling computer virus prevalence with a susceptible-infected-susceptible model with reintroduction," *Computational Statistics & Data Analysis*, vol. 45, no. 1, pp. 3–23, 2004.

[11] Q. Zhu, X. Yang, and J. Ren, "Modeling and analysis of the spread of computer virus," *Communications in Nonlinear Science and Numerical Simulation*, vol. 17, no. 12, pp. 5117–5124, 2012.

[12] B. K. Mishra and D. K. Saini, "SEIRS epidemic model with delay for transmission of malicious objects in computer network," *Applied Mathematics and Computation*, vol. 188, no. 2, pp. 1476–1482, 2007.

[13] C. Zou, W. Gong, and D. Towsley, "Code red worm propagation modeling and analysis," in *Proceedings of the 9th ACM Conference on Computer and Communications Security*, pp. 138–147, Washington, DC, USA, November 2002.

[14] C. Gan, Q. Feng, X. Zhang, Z. Zhang, and Q. Zhu, "Dynamical propagation model of malware for cloud computing security," *IEEE Access*, vol. 8, pp. 20325–20333, 2020.

[15] J. D. Hernández Guillén and A. Martín del Rey, "Modeling malware propagation using a carrier compartment," *Communications in Nonlinear Science and Numerical Simulation*, vol. 56, pp. 217–226, 2018.

[16] M. O'Neill, S. Ruoti, K. Seamons, and D. Zappala, "TLS proxies: friend or foe?" in *Proceedings of the 2016 Internet Measurement Conference*, pp. 551–557, Santa Monica, CA, USA, November 2016.

[17] S. Furnell, "Still on the hook: the persistent problem of phishing," *Computer Fraud & Security*, vol. 2013, no. 10, pp. 7–12, 2013.

[18] X. Zhang, S. Chen, H. Lu, and F. Zhang, "An improved computer multi-virus propagation model with user awareness," *Journal of Information and Computational Science*, vol. 8, no. 16, pp. 4301–4308, 2011.

[19] W. S. Bahashwan and S. M. Al-Tuwairqi, "Modeling the effect of external computers and removable devices on a computer network with heterogeneous immunity," *International Journal of Differential Equations*, vol. 2021, Article ID 6694098, 13 pages, 2021.

[20] S. M. Al-Tuwairqi and W. S. Bahashwan, "A dynamic model of viruses with the effect of removable media on a computer network with heterogeneous immunity," *Advances in Difference Equations*, vol. 2020, no. 1, pp. 1–20, 2020.

[21] E. A. Barbashin, *Introduction to the Theory of Stability*, Walters-Noordhoff, Groningen, Netherlands, 1970.

[22] R. C. Robinson, *An Introduction to Dynamical Systems: Continuous and Discrete*, Prentice-Hall, Upper Saddle River, NJ, USA, 2004.

[23] W. O. Kermack and A. G. Mckendrick, "Contributions to the mathematical theory of epidemics. II. the problem of endemicity," *Proceedings of the Royal Society of London. Series A*, vol. 138, no. 834, pp. 55–83, 1932.

[24] S. Ullah and M. A. Khan, "Modeling the impact of non-pharmaceutical interventions on the dynamics of novel coronavirus with optimal control analysis with a case study," *Chaos, Solitons, and Fractals*, vol. 139, Article ID 110075, 2020.

[25] M. A. Khan, A. Atangana, E. Alzahrani, and A. Fatmawati, "The dynamics of COVID-19 with quarantined and isolation," *Advances in Difference Equations*, vol. 2020, no. 1, p. 425, 2020.

[26] M. A. Khan and A. Atangana, "Modeling the dynamics of novel coronavirus (2019-nCov) with fractional derivative," *Alexandria Engineering Journal*, vol. 59, no. 4, pp. 2379–2389, 2020.

[27] M. S. Alqarni, M. Alghamdi, T. Muhammad, A. S. Alshomrani, and M. Altaf Khan, "Mathematical modeling for novel coronavirus (COVID-19) and control," *Numerical Methods for Partial Differential Equations*, 2020.

Hindawi
Complexity
Volume 2021, Article ID 6672630, 17 pages
https://doi.org/10.1155/2021/6672630

Research Article

Predicting Spread Probability of Learning-Effect Computer Virus

Wei-Chang Yeh,[1] **Edward Lin**,[2] **and Chia-Ling Huang**[3]

[1]*Department of Industrial Engineering and Engineering Management, National Tsing Hua University, Hsinchu 300, Taiwan*
[2]*Department of Electrical Engineering and Computer Sciences, University of California, Berkeley, CA 94720-1234, USA*
[3]*Department of International Logistics and Transportation Management, Kainan University, Taoyuan 33857, China*

Correspondence should be addressed to Wei-Chang Yeh; wcyeh@ie.nthu.edu.tw

Received 23 November 2020; Revised 4 February 2021; Accepted 7 June 2021; Published 12 July 2021

Academic Editor: Luxing Yang

With the rapid development of network technology, computer viruses have developed at a fast pace. The threat of computer viruses persists because of the constant demand for computers and networks. When a computer virus infects a facility, the virus seeks to invade other facilities in the network by exploiting the convenience of the network protocol and the high connectivity of the network. Hence, there is an increasing need for accurate calculation of the probability of computer-virus-infected areas for developing corresponding strategies, for example, based on the possible virus-infected areas, to interrupt the relevant connections between the uninfected and infected computers in time. The spread of the computer virus forms a scale-free network whose node degree follows the power rule. A novel algorithm based on the binary-addition tree algorithm (BAT) is proposed to effectively predict the spread of computer viruses. The proposed BAT utilizes the probability derived from PageRank from the scale-free network together with the consideration of state vectors with both the temporal and learning effects. The performance of the proposed algorithm was verified via numerous experiments.

1. Introduction

Almost all individuals and industries constantly rely on computer and network technology [1–16]. Thus, the types of computer viruses are becoming more diversified, and the intensity of the attacks is increasing. When a computer virus infects a facility, the virus seeks to invade other facilities in the network by exploiting the convenience of the network protocol and the high connectivity of the network. Hence, computer viruses cause serious damage to computer facilities. The terminology "computer virus" was introduced by von Neumann in 1966 [17], and it was extended from his lectures regarding self-reproducing computer programs given in 1949 [18]. Subsequently, scholars performed small-scale research on computer viruses, publishing conference papers from 1988 to 2000, and numerous computer virus-related research papers have been published in different journals. For example, Risak studied the functional virus in computer programs in 1972 [19], and Kraus researched self-reproducing computer programs and investigated the behavior of computer-language-like biological viruses in 1980 [20].

The evolution of terminologies on virus includes the worm, malware (trojan horse is the old term) that originated approximately in 1990, and advanced persistent threats (APT) that are newer developments on computer viruses in the past decade.

Researches on worm involve Shoutkov and Spesivtsev explored self-replication of worm [21], and Griffin and Brooks paid attention to the spread of worm in the computer network [22]. The computer viruses of malware are researched such as Witte explored the detection of malware [23] and Peng et al. focus on a survey of the propagation of malware [24]. Furthermore, the researches in APT including Li and Yang, improved the system of cloud memory under APT [25] and Tian et al. defended against APT in power grid [26].

In the past five years, research on computer viruses has focused on defense against viruses [27–29]. The research on computer viruses can be classified into the following major

research directions: the description of the computer virus, the detection of computer viruses, and protection against computer viruses:

1.1. The Description of the Computer Virus. Eichin and Rochlis described the computer virus via a detailed analysis in 1989 [30], and Spafford investigated how computer viruses are formed in 1994 [31].

1.2. The Detection of Computer Viruses. Davis investigated the detection of computer viruses to enhance the control of risk management in 1988 [32]. Okamoto and Masumoto adopted authentication for detecting computer viruses in 1990 [33]. Spinellis proved that the detection of computer viruses is NP-complete [34]. A detection mechanism for processing sign streams was adopted to evaluate viruses by Wang et al. in 2015 [35]. A model for the nonlinear vaccination probability was used to detect computer viruses by Gan et al. in 2004 [36].

1.3. Protection against Computer Viruses. Al-Dossary proposed a classification formula for defense against computer viruses in 1989 [37]. Yuan et al. established a virus model to optimize the performance of the infection mechanism in 2009 [38]. Youssef and Scoglio focused on reducing the dissemination of viruses by optimizing the weight function of the network structure in 2014 [39].

Understanding the development of computer viruses is important for understanding the historical defense strategies against viruses [27]. In addition, for the detection of the aforementioned computer viruses, the method of identifying the code mode of the virus can be used. If the virus has a self-replicating function whereby the code of the virus is copied to other files, the appropriate protection strategy for the self-replicating virus can be selected and executed immediately [34]. Therefore, the aforementioned three types of computer-virus research all involve protection against computer viruses.

The lifecycle of the virus includes dormant, propagation, triggering, and execution. The dormant phase indicates that the computer virus code is being created and finally born. The propagation phase shows that the files of computer viruses are placed in places that are easy to propagate. Once infected by the computer viruses, it will cause great harm. In addition, the triggering and execution indicate when all the conditions are formed; the computer viruses then begin to execute destructive actions.

Therefore, to prevent computer virus infection, protection in advance is important in the propagation phase. Computer viruses persist owing to the constant demand for computer networks. Hence, it is important to predict the probabilities of the virus spreading to different areas so as to interrupt the relevant connections between the uninfected and possibly infected computers in time to save the files in the computers. This was the major focus of this study.

With the strength of the advanced technology, the susceptible-infectious-recovered (SIR) model is adapted to predict the number of computer-virus spread areas in this study. In the SIR model, all susceptible nodes can be infected at most once. After the infected node is recovered by removing the computer virus, it is protected by using a virus detection and killer software such that it is impossible to be infected by the same computer virus.

Assume that a virus can propagate in a heterogeneous environment freely. Hosts like Linux, Windows, Mac, etc., and different operating systems can have different code bases and the same virus may not work for all OS.

The spread of computer viruses is a scale-free model formed by a scale-free network in which all node degrees follow a power-law distribution. The PageRank algorithm is the most popular among the different scale-free model-related algorithms for calculating the influence of nodes. Hence, the PageRank algorithm is used to provide the theoretical spread probability of the computer virus.

With the defense mechanism (antivirus protection) in the scale-free model to prevent or slow down virus propagation, the computer virus can be detected and killed more easily from time to time. The above defense mechanism is called the learning effect here. Hence, the learning effect can be the temporal learning-effect spread probability $p_{i,j,t}$ of the computer virus spread from nodes $i \in V$ to $j \in V(i)$ and is higher than $p_{i,j,\tau}$ if $\tau < t$ during the computer-virus propagation.

During the process of computer-virus propagation, consecutive timeslots in the time period when the infected node i can still spread out the computer virus are called valid timeslots. An infected node can affect any neighboring node at any valid timeslot; that is,

$$\sum_{t} \sum_{\forall i \in V} \sum_{k \in V(i)} p_{i,k,t} = 1 \text{ for any valid timeslot } t, \tag{1}$$

$$0 \le p_{i,k,t} \le 1, \tag{2}$$

for any node k in $V(i)$ and the validation timeslot t.

A novel computer-virus spread dynamic model based on the binary-addition tree (BAT) search algorithm with the learning effect is proposed for modeling the spread of computer viruses. The BAT proposed by Yeh [40] is a heuristic search method similar to the depth-first search (DFS), breadth-first search (BFS), and universal generating function methodology (UGFM). The BAT is more efficient than the DFS and more economical with regard to computer memory than the BFS and UGFM, both of which can crash the computer system because of computer memory overflow problems. Moreover, the BAT is easy to learn, convenient to code, and flexible (i.e., it can be made-to-fit).

The objective of this study was to theoretically predict the probabilities of a computer virus infection and the spread of the virus to different areas. The remainder of the paper is organized as follows. Section 2 provides acronyms and notations. Section 3 presents an overview of the infection model, the scale-free model, the PageRank algorithm, the BAT, and the learning effect, which form the basis of the proposed dynamic BAT. Section 4 introduces the novel temporal learning-effect spread probability and period, which are required data for using the proposed dynamic

BAT. Section 5 describes the proposed state vectors formed by the spread vector and the temporal that needed to be found in the proposed dynamic BAT before predicting the spread areas of computer viruses. Section 6 formally presents the proposed dynamic BAT, together with its computational complexity, a demonstration, and experimental results. Section 7 concludes the paper.

2. Acronyms and Notations

All required acronyms and notations are provided in Tables 1 and 2, respectively.

Table 1: Acronyms.

APT	Advanced persistent threats
SIR	Susceptible-Infectious-Recovered Model
BAT	Binary-Addition Tree
BFS	Breadth-First Search
DFS	Depth-First Search
UGFM	Universal Generating Function Methodology

3. Infection Model, Scale-Free, Page Rank, BAT, and Learning Effect

The proposed dynamic BAT, which is a scale-free model, is based on the BAT with a temporal learning effect to predict the areas infected by the computer virus and the areas to which the virus will spread. The infection model is adopted to describe the spread of computer viruses. The scale-free model and PageRank algorithm are used to simulate the computer-virus spread probability before the proposed dynamic BAT is used to predict the probability of the areas infected and spread from the computer virus and the learning effect, which is integrated into the proposed model to simulate the spread of the computer virus in a more practical manner.

Hence, before the proposed BAT is discussed, an overview of the infection model, the scale-free model, the PageRank algorithm, the traditional BAT, and the learning effect are described in this section.

3.1. Infection Model. In recent years, the theory of the spread of epidemics in complex networks has yielded considerable success. Individuals in the system have several basic states: the susceptible state S (healthy but may be infected); infected state I; and removal state R (infected after being cured and gaining immunity or dying after infection).

There are three mature epidemic infection models: the Susceptible–Infected (SI) model, Susceptible–Infected–Susceptible model, Susceptible–Infectious–Recovered (SIR) model, and Susceptible–Infectious–Recovered–Susceptible model.

In the SIR model, a susceptible node (S) has become infectious (I) and can recover (R) to obtain lifelong immunity after curing. The SIR model is the most popular mathematical model. The spread of computer viruses is similar to that of epidemics, and both propagations can be captured by a scale-free model. Hence, the SIR model was adopted to model the spread of the computer virus.

The SIR model acquires lifelong immunity after an illness as shown in Figure 1 [41]. Let $S(t)$, $I(t)$, and $R(t)$ be the proportions of susceptible, infectious, and recovered nodes, respectively, and $S(t) + I(t) + R(t) = 1$ in $G(V, E)$ [41, 42]. The differential equation describing the propagation mechanism of the SIR model is as follows [41, 42]:

$$\begin{aligned} \frac{\mathrm{d}S(t)}{\mathrm{d}t} &= -\beta \cdot S(t) \cdot I(t), \\ \frac{\mathrm{d}I(t)}{\mathrm{d}t} &= -\beta \cdot S(t) \cdot I(t) - \gamma(t), \\ \frac{\mathrm{d}R(t)}{\mathrm{d}t} &= \gamma(t), \end{aligned} \tag{3}$$

where β and γ represent the transmission and recovery rates, respectively.

3.2. Scale-Free and Page Rank Algorithm. The scale-free network is a special network, and its growth is independent of the number of nodes with the same underlying structure. The major difference between the scale-free network and other networks is that it has power-law (or scale-free) degree distributions. For example, the network in Figure 2 is generated from the Barabási–Albert model, which is the first scale-free model.

PageRank, which is used by Google search engines, was the first and the most popular among these famous algorithms for ranking nodes (web page, website, user, etc.) according to importance in the scale-free network. The PageRank value of a node (web page, website, user, etc.) $i \in V$ is the probability that users clicking on nodes randomly will arrive at i. The array PR can be calculated as follows:

$$\mathrm{PR} = \left[d \cdot M + \frac{(1-d)}{N_{\mathrm{node}}} \cdot I \right] \cdot \mathrm{PR}, \tag{4}$$

where PR (i) represents the i^{th} element in PR for all $i \in V$, N_{node} represents the number of nodes, d represents a damping factor between 0 and 1, M represents the normalized adjacency square matrix such that $\sum_{a=1}^{N_{\mathrm{node}}} M_{a,b} = 1$, $M_{a,b}$ represents the element in the a^{th} row and the b^{th} column in M, and I represents the identity matrix. The sizes of both matrices I and M are $\mathrm{N}_{\mathrm{node}} \times \mathrm{N}_{\mathrm{node}}$.

The pseudo code of the PageRank algorithm is described as follows (Algorithm 1).

STEP PR0 initializes PR (i) for all $i \in V$. STEP PR1 updates PR (i) for all $i \in V$ according to Equation (4), by adding part of PR (j) for all nodes $j \in V$ with $e_{j,i} \in V$. STEP PR2 adjusts the value of PR (i) by assuming that the search of users will continue even if it reaches a dead end for all $i \in V$. When PR (i) is updated and redistributed in STEPs PR1 and PR2 recursively, the value of PR (i) converges, and the process halts for all $i \in V$.

For example, in Figure 2, we need to have the adjacency matrix first and normalize the matrix by dividing the

Table 2: Notations.

$G(V, E)$	A scale-free network with sets of nodes V and arcs E
N_{node}	The number of nodes
$e_{i,\ j}\ e_{i,j} \in E$	Such that information can be transmitted directly from node i to j
$Deg(i)$	Degree of node i
$V(i)$	Subset of nodes that receive information from node i
t_i	Infected timeslot of node $i \in V$
$p_{i,j}$	Spread probability that the computer virus is spread out from an infected node $i \in V$ to a susceptible node $j \in V(i)$
$p_{i,j,t}$	Temporal learning-effect spread probability of the computer virus from nodes $i \in V$ to $j \in V(i)$ for any valid timeslot t
$S(t)$	Proportions of susceptible nodes
$I(t)$	Proportions of infectious nodes
$R(t)$	Proportions of recovered nodes
β	Transmission rates
γ	Recovery rates
PR	Probability that users clicking on nodes randomly will arrive at i
PR (i)	The i^{th} element in PR for all $i \in V$
d	A damping factor between 0 and 1
M	Normalized adjacency square matrix
$M_{a,b}$	Element in the a^{th} row and the b^{th} column in M
I	Identity matrix
X	State vector
$X(i)$	Value in the i^{th} coordinate of vector X
T	Timeslot vector
$T_{i,t}$	The t-lag temporal vector of node i
Y	Temporal vector
TARGET	The first infected node
N_t	The number of temporal state vector candidates for time lag t
n_t	The number of feasible temporal vectors for time lag t

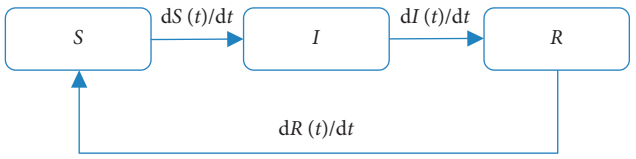

Figure 1: Example network.

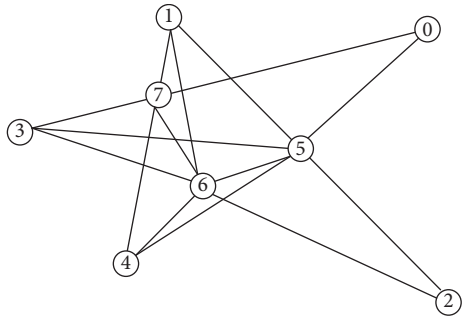

Figure 2: Example network.

element values in the adjacency matrix by their degrees, as shown in Tables 3 and 4, respectively.

Then, by simply following the pseudocode above, we obtain all the PR (i) values for all $i \in V$, as follows:

As shown in Table 5, a higher degree of the node corresponds to a higher probability to have a larger PR value. Hence, more important nodes have more links from other nodes in the PageRank algorithm, which is the "rich-gets-richer" phenomenon [41].

PR (i) is used to simulate the spread probability of the computer virus to node i in the proposed dynamic BAT to solve the spread of the computer-virus problem.

3.3. BAT. The BAT proposed by Yeh is a simple implicit enumeration method. Experiments revealed that the BAT is more efficient than the DFS and more economical with regard to computer memory than the BFS and UGFM. The DFS, BFS, and UGFMs are all well-known implicit enumeration methods.

By adding one to the zero vector repeatedly via binary addition, the BAT can generate all binary-state vectors whose coordinates are either 0 or 1. Let X be a binary-state vector with an n-tuple and X_i be the value of its i^{th} coordinate (Algorithm 2). The source code of the BAT is presented below [40]:

In STEP B0, the BAT begins to generate all vectors from the zero vector X. From STEPs B1 to B3, the state vector X is added to generate a new vector repeatedly. To reduce the runtime, the current coordinate is changed either from 0 to 1 or from 1 to 0. If it is changed from 1 to 0, we must go to the coordinate adjacent to the current coordinate to repeat the same procedure until it is changed from 0 to 1. After each new X is generated in STEP B4, its probability, cost, time, or any predefined function can be calculated. STEP B4 also tests whether the stopping criterion SUM $= n$ is satisfied, that is, whether X becomes a vector of which all the coordinates are 1.

For example, let $n = 5$ and $X = (0, 0, 0, 0, 0)$. To easily understand how BAT is based on the binary addition, each vector is rewritten to a binary number such that the i^{th} digit

(i) INPUT: A scale-free network $G(V, E)$.
(ii) OUTPUT: The PageRank value PR (i) for all $i \in V$.
(iii) STEP PR0. Let $t = 0$ and PR $(i) = 1/n$ for all $i \in V$.
(iv) STEP PR1. Let PR $= [d \cdot M + (1-d)/\mathrm{N_{node}} \cdot I] \cdot$PR.
(v) STEP PR2. Let PR (j) = PR(j) + $\sum_{i \in I \subseteq V}PR(i)/|V-I|$, where $I = \{i \in V \mid \mathrm{Deg_{out}}(i) = 0\}$ and for all $j \in (V-I)$.
(vi) STEP PR3. Halt if there is no change of PR (i) for all $i \in V$. Otherwise, let $t = t + 1$ and go to STEP PR1.

Algorithm 1: PageRank algorithm.

Table 3: The adjacency matrix.

i	0	1	2	3	4	5	6	7
0						1		1
1						1	1	1
2						1	1	
3						1	1	1
4						1	1	1
5	1	1	1	1	1		1	
6		1	1	1	1	1		1
7	1	1		1	1		1	
Deg (i)	2	3	2	3	3	6	6	5

Table 4: The normalized adjacency matrix based on each column.

i	0	1	2	3	4	5	6	7
0	0	0	0	0	0	1/6	0	1/5
1	0	0	0	0	0	1/6	1/6	1/5
2	0	0	0	0	0	1/6	1/6	0
3	0	0	0	0	0	1/6	1/6	1/5
4	0	0	0	0	0	1/6	1/6	1/5
5	1/2	1/3	1/2	1/3	1/3	0	1/6	0
6	0	1/3	1/2	1/3	1/3	1/6	0	1/5
7	1/2	1/3	0	1/3	1/3	0	1/6	0

of such a binary number is equal to the i^{th} coordinate of X, e.g., the binary number of $X = (0, 0, 0, 0, 0)$ is 00000. Note that there 32 different vectors in total because $2^5 = 32$.

Following the BAT code listed above, we have the first five new state vectors generated from zero in the sequence:

$$\begin{aligned} &00000 + 1 = 00001,\\ &00001 + 1 = 00010,\\ &00001 + 1 = 00011,\\ &00011 + 1 = 00100,\\ &00100 + 1 = 00101. \end{aligned} \tag{5}$$

In the same way, we have all state vectors from (0, 0, 0, 0, 0) to (1, 1, 1, 1, 1) obtained from the BAT without duplications as listed in Table 6.

From the above, the BAT is very simple to learn, easy to code, and flexible (can be made-to-fit). Hence, BAT is modified to solve the proposed problem.

3.4. Learning Effect. In economics, productivity increases and results in higher wages after suitable education, and this process is the learning effect. In realistic industrial processes, the operation time is reduced because the workers' skill or the flow process improves steadily, and this phenomenon is also called the learning effect. In many real-world applications [7, 28, 29, 40, 43–49], the learning effect is pragmatic. Hence, the learning effect is introduced in this work to study the proposed computer-virus spread area prediction problem and offers a defense mechanism (antivirus protection) in the scale-free model to prevent or slow down virus propagation.

Table 5: The Deg (i), $V(i)$, $C(i)$, and PR (i) values of node i.

i	Deg (i)	$V(i)$	PR (i)
0	2	{5, 7}	0.117460
1	3	{5, 6, 7}	0.119714
2	2	{6, 7}	0.117062
3	3	{5, 6, 7}	0.119714
4	3	{5, 6, 7}	0.119714
5	6	{0, 1, 2, 3, 4, 6}	0.138452
6	6	{1, 2, 3, 4, 5, 7}	0.135284
7	5	{0, 1, 3, 4, 6}	0.132599

Let $p_{i,j,t}$ be the probability that the computer virus spreads from node i to its j^{th} state at time t. If there is no learning effect, $p_{i,j,t}$ is a constant for all values of t. However, $p_{i,j,t}$ is reduced occasionally because users acknowledge the spread of the computer virus and learn how to prevent infection or propagation after the infection.

The values of $p_{i,j,t}$ are reduced gradually because of the learning effect, according to the following formula:

$$p_{i,j,t} = \frac{p_{i,j,t-1}}{(t+1)^{\alpha}}, \tag{6}$$

where α represents the learning rate and is set to 0.35, as in [39–41]. Owing to the learning effect, $\lim_{t \longrightarrow \infty} p_{i,j,t} = 0$ and $p_{i,j,t} < p^*_{i,j,t} \leq 1$ for all $t^* < t < \infty$ and $0 < p_{i,j,t}$, in accordance with Equation (6). Note that $0 \leq p_{i,j,t} = p^*_{i,j,t} \leq 1$ for all t^* and t if there is no learning effect.

4. Temporal Learning-Effect Spread Probability and Period

Before the proposed method is solved for calculating the probability of a specified number of infected computers conducted from a computer virus during a specific time period, we need to know both the temporal learning-effect spread probability and the length of the infected period. These two factors are discussed in this section.

4.1. Proposed Learning-Effect-SIR Model. The SIR model is adopted. As mentioned in Section 3.1, each node can be categorized into susceptible (S), infected (I), or removed (R) in the SIR model. Each node undergoes the transition of $S \longrightarrow I \longrightarrow R$, that is, from a susceptible node (S) to an infected node (I) and then to a removed node (R) after a certain infected period.

The spread probability $p_{i,j}$ is the probability that the computer virus is spread out from an infected node $i \in V$ to a susceptible node $j \in V\ (i)$. The temporal learning-effect spread probability Pr (node j infected from node i at time t only) = pi,j,t is a special spread probability at timeslot t only, and it varies with the timeslot because of the learning effect of which users know how to resist the computer virus to reduce the loss gradually.

The computer virus can spread to any susceptible node in $V\ (i)$ at timeslot t with probability $p_{i,j,t}$ if node $i \in V$ is infected. The computer virus cannot spread from node $i \in V$ to any neighboring node $j \in V\ (i)$, that is, $p_{i,j,t} = 0$, if i is a removed node. Moreover because of the learning effect, the computer virus can occasionally be detected and killed easily, such that the temporal learning-effect spread probability $p_{i,j,t}$ is decreased if t is increased.

4.2. Initial Spread Probability. $p_{i,j,0} = p_{i,j}$ represents the initial spread probability of node i infected at time 0, where no learning effect is considered, where for all infected node $i \in V$ and susceptible node $j \in V\ (i)$. Hence, the initial spread probability is simple to calculate, and it is derived here before we determine the temporal learning-effect spread probability.

The value of $p_{i,j}$ for all nodes $i \in V$ to $j \in V\ (i)$ is defined according to the PageRank algorithm. Details are presented in Section 3.2, as follows:

$$\Pr_{(ei,j)} = p_{i,j,0} = p_{i,j} == \frac{\mathrm{PR}(j)}{\sum_{k \in V(i)} \mathrm{PR}(k)}. \tag{7}$$

Equation (7) is based on the fundamental concept of the scale-free network: a larger PageRank number, that is, a higher node distribution probability, corresponds to a higher spread out probability, that is, $p_{i,j}$ is proportional to PR (j). For example, suppose that after node 0 is infected, we have $p_{0,5}$ and $p_{0,7}$ based on $V\ (0) = \{5, 7\}$ and equation (7):

$$p_{0,5} = \frac{0.138452}{0.138452 + 0.132599} = 0.510797, \tag{8}$$

$$p_{0,7} = \frac{0.132599}{0.138452 + 0.132599} = 0.489203. \tag{9}$$

According to equations (8) and (9), we have four possible situations: infected node 0 can spread the computer virus to susceptible node 5 only, node 7 only, both nodes 5 and 7, or nowhere with the following probabilities:

$$\begin{aligned} p_{0,5}p_{0,7} &= 0.249883, \\ p_{0,5}\left(1 - p_{0,7}\right) &= 0.249883, \\ \left(1 - p_{0,5}\right)p_{0,7} &= 0.239320, \\ \left(1 - p_{0,5}\right)\left(1 - p_{0,7}\right) &= 0.249883, \end{aligned} \tag{10}$$

respectively.

Without considering the learning effect, the initial spread probability of each infected node is provided below according to the adjacent matrix and PagePank values listed in Tables 3 and 5, respectively.

4.3. LAGS. The infected timeslot of node $i \in V$ is denoted as t_i if node i is infected at time t_i. Moreover, the infected timeslot of any node spread from node i can only be after or equal to t_i. If node i is infected at time t_i but only starts to spread to node j at time t_j, there is a lag of $\Delta t_{i,j} = t_i - t_j$. The value of $\Delta t_{i,j}$ can be any nonnegative integer, and it is called a no-lag infection if $\Delta t_{i,j} = 0$.

For example, in Figure 2, let the computer virus start spreading after infecting node 0 at time 0, that is, $t_0 = 0$. Assuming that susceptible node 5 is infected from node 0 and susceptible node 7 is infected from node 5, we have $t_0 = 0 \le t_5$ and $t_5 \le t_7$, for example, $t_5 = t_7 = \Delta t_{0,5} = \Delta t_{5,7} = 0$; $t_5 = \Delta t_{0,5} = 1$, $t_7 = 2$, and $\Delta t_{5,7} = 1$; $t_5 = \Delta t_{0,5} = 2$, $t_7 = 3$, and $\Delta t_{5,7} = 1$. Moreover, as shown in Table 6, the whole network is infected at timeslot 2 if node 0 spreads the computer virus out to all its neighboring nodes, that is, $V\ (0) = \{5, 7\}$ at timeslot 1, and the computer virus spreads from node 5 to all the nodes connected to node 5, that is, $V\ (5) = \{1, 2, 3, 4, 6\}$, at timeslot 2.

Suppose that all infections have 1-lag as shown in Table 7 and the computer virus is initialized at node 0. In the worst case, the computer virus is spread out in the order of the node labels, that is, 1, 2, . . ., $|V| - 1$, at time 1, 2, . . ., $|V| - 1$, respectively. Hence, we have the following property:

Property 1. The upper bound of the spread period is $|V| - 1$ if all infections are 1-lag infections.

4.4. Spread Probability with Learning Effect. As mentioned in Section 3.4, $p_{i,j,t}$ is reduced according to the learning effect modeled in the following equation:

$$p_{i,j,t} = \frac{p_{i,j,t-1}}{(t+1)^{\alpha}}, \tag{11}$$

For example, the values of $p_{i,j,1}$, $p_{i,j,2}$, and $p_{i,j,3}$ are presented in Tables 8–10 on the basis of the initial spread probability given in Table 11 and Equation (7).

If node i infected at timeslot t did not spread the computer virus at timeslots t, t+1, . . ., and t^*−1 and spread it to node j at timeslot t, the related probability is denoted as $P_{i,j,t}$ and calculated using Equation (12).

$$P_{i,j,t} = \prod_{\tau=0}^{t-1} \prod_{\forall k \in V(i)} \left(1 - p_{i,k,\tau}\right) \times p_{i,j,(t-1)}, \tag{12}$$

Here,

$$\prod_{\forall k \in V(i)} \left(1 - p_{i,k,\tau}\right), \tag{13}$$

and

(i) Input: The number of coordinates n.
(ii) Output: All n-tuple binary-state vectors X.
(iii) STEP B0. Let X be a zero vector, SUM = 0, and $i = 1$.
(iv) STEP B1. If $X_i = 1$, let $X_i = 0$, SUM = SUM −1, and go to STEP B4.
(v) STEP B2. Let $X_i = 1$ and SUM = SUM +1.
(vi) STEP B3. Let $i = i + 1$ and go back to STEP B1 if $i < n$.
(vii) STEP B4. If SUM = n, halt; otherwise, let $i = 1$ and go back to STEP B1.

Algorithm 2: Algorithm BAT.

Table 6: All state vectors generated from (0, 0, 0, 0, 0) using the Bat.

i	X
1	(0, 0, 0, 0, 0) = 00000
2	(0, 0, 0, 0, 1) = 00001
3	(0, 0, 0, 1, 0) = 00010
4	(0, 0, 0, 1, 1) = 00011
5	(0, 0, 1, 0, 0) = 00100
6	(0, 0, 1, 0, 1) = 00101
7	(0, 0, 1, 1, 0) = 00110
8	(0, 0, 1, 1, 1) = 00111
9	(0, 1, 0, 0, 0) = 01000
10	(0, 1, 0, 0, 1) = 01001
11	(0, 1, 0, 1, 0) = 01010
12	(0, 1, 0, 1, 1) = 01011
13	(0, 1, 1, 0, 0) = 01100
14	(0, 1, 1, 0, 1) = 01101
15	(0, 1, 1, 1, 0) = 01110
16	(0, 1, 1, 1, 1) = 01111
17	(1, 0, 0, 0, 0) = 10000
18	(1, 0, 0, 0, 1) = 10001
19	(1, 0, 0, 1, 0) = 10010
20	(1, 0, 0, 1, 1) = 10011
21	(1, 0, 1, 0, 0) = 10100
22	(1, 0, 1, 0, 1) = 10101
23	(1, 0, 1, 1, 0) = 10110
24	(1, 0, 1, 1, 1) = 10111
25	(1, 1, 0, 0, 0) = 11000
26	(1, 1, 0, 0, 1) = 11001
27	(1, 1, 0, 1, 0) = 11010
28	(1, 1, 0, 1, 1) = 11011
29	(1, 1, 1, 0, 0) = 11100
30	(1, 1, 1, 0, 1) = 11101
31	(1, 1, 1, 1, 0) = 11110
32	(1, 1, 1, 1, 1) = 11111

$$\prod_{\tau=0}^{t-1} \prod_{\forall k \in V(i)} \left(1 - p_{i,k,\tau}\right), \tag{14}$$

represent the probabilities that node i did not spread to any node during time τ and any time before t, respectively.

From equation (12), a larger $(t^* - t)$ corresponds to a lower probability of the computer virus spreading from node i regardless of whether there is a learning effect.

For example, node 0 is infected at the beginning in Figure 2. The temporal learning effect spread probabilities of nodes 5, 7, and ∅ are presented in the 2nd, 3rd, and 4th columns below. In addition, the probability that node i spreads the virus to nodes $j = 5$ and 7 are presented in the last two columns. The temporal learning-effect probability $p_{0,5,t}$ is reduced from 0.1610000 at $t = 0$ to 0.1263180, 0.1096058, ..., 0.0719161 at timeslots $t = 1, 2, \ldots, 9$, respectively, as indicated by Table 12. The probabilities that node 0, that is, $P_{0,5,t}$, start to spread to node 5 are 0.088903, 0.046458, 0.024074, ..., 0.000299 at timeslots $t = 1, 2, \ldots, 9$, respectively.

According to Equations (6) and (12), = 0 with the learning effect and $\lim_{t \longrightarrow \infty} P_{i,j,t} = 0$ regardless of whether there is a learning effect, respectively. Hence, the spread stops at a specific timeslot. The infected period is the total time in which either the whole network is infected or the computer virus is removed from the whole network. The node infected period of node i is defined as the time from the infection of the node to any of the following circumstances:

(1) Node i becomes a recovered node, that is, the computer virus-infected node i is killed;
(2) There are no susceptible nodes in $V(i)$, that is, all nodes are either infected nodes or recovered nodes in $V(i)$.

Because of the instantaneous infection, the smallest t such that $p_{i,j,t} = 0$ for all $j \in V(i)$ is called the infected period of node i. $P_{i,j,t} = 0$ if $p_{i,j,t} = 0$ for all $j \in V(i)$.

5. State Vectors

A state vector is a feasible vector to indicate where and when the computer virus spreads. This section proposes a dual-vector form to construct the state vector by integrating the spread vector and the temporal vector, where the former and the latter indicate where and when the computer virus spreads, respectively.

5.1. Spread Vectors. The spread vector is a $|V|$-tuple vector, and the k^{th} coordinate is the state of the node $(k-1)$ or node k if the first node is labeled 0 or 1, respectively. Moreover, in the spread vector, the first infected node is the node where the value of its related coordinate is equal to itself. Let both the first node and the first coordinate be labeled as 0. For example, in Figure 2, the spread vector $X_1 = (0, 5, 5, 5, 7, 0, 2, 0)$ indicates that node 0 is the first infected node and that the virus spreads to nodes 5 and 7; node 5 spreads the virus to nodes 1–3 after it is infected, because the values in coordinates 1–3 are all 5; nodes 4–7 are infected by nodes 7, 0, 2, and 0, respectively.

A spread vector must be feasible; i.e., the spread of the computer virus must be possible. Only nodes in $V(i)$ can spread the virus to or from node $i \in V$. Hence, we have the following important property and such property is implemented in the proposed BAT to have all spread vectors without needing to verify its feasibility to reduce the runtime.

Property 2. Let $X(i)$ be the value in the i^{th} coordinate represented by node i of vector X. A vector X is a feasible spread vector if $X(i) \in V(i)$ for all nodes $i \in V$.

For example, in Figure 2, $X = (0, 5, 5, 5, 7, 0, 7, 0)$ is an infeasible spread vector, because it is impossible for the computer virus to spread from node 7 to node 6; that is, $X(6) = 7 \in V(6)$.

To simplify the use of the proposed BAT, each spread vector is reconstructed and called the labeled spread vector such that.

(1) The value, i.e., j, at coordinate i is the j^{th} node in $V(i)$, of which all nodes are arranged in the increasing order of the node labels.

(2) The first infect node is in bold.

For example, $X_1 = (0, 5, 5, 5, 7, 0, 2, 0)$ discussed above is rewritten as $X^* = (\mathbf{0}, 0, 0, 0, 2, 0, 1, 0)$ because node 0 is the first infected node and must be written in bold, and nodes 5, 5, 5, 7, 0, 2, 0 at coordinates 1–7 are the nodes labeled 0, 0, 0, 2, 0, 1, and 0 in $V(1) = \{5, 7\}$, $V(2) = \{5, 6, 7\}$, $V(3) = \{5, 6\}$, $V(4) = \{5, 6, 7\}$, $V(5) = \{0, 1, 2, 3, 4, 6\}$, $V(6) = \{1, 2, 3, 4, 5, 7\}$, and $V(7) = \{0, 1, 2, 3, 4, 6\}$, respectively.

To clarify, the following list contains the first 10 spread vectors, labeled spread vectors, and their corresponding 1-lag temporal vectors, which are discussed in Section 5.2.

5.2. Basic Temporal Vectors and Instantaneous Infection. A temporal vector is a vector in which the coordinate value is the timeslot of the related node that has the infection. Similar to the labeled spread vector, the first infect node is in bold in the temporal vector. For example, $T = (\mathbf{0}, 2, 2, 2, 2, 1, 2, 1)$ is the timeslot vector with respect to that in Table 13. In T, nodes 0–7 are infected at timeslots 0, 2, 2, 2, 2, 1, 2, and 1, respectively. Moreover, from T, we observe that node 0 is the first infected node, because $T_0 = 0$ and all the infections have 1-lag, as the gap between two consecutive distinctive numbers in T is 1, e.g., 0 and 1; 1 and 2.

Let $T_{i,t}$ be the t-lag temporal vector of node i if all infections are t-lag, that is, $\Delta t_{j,k} = t$ for all $j \in V$ and $k \in V(j)$. Because all infections are t-lag, the following property holds.

Property 3. The t-lag timeslot vector is the upper-bound of any feasible timeslot that has at most t-lag.

We have the following important property that is implemented in the proposed BAT to serve as an upper-bound to help in searching for all possible feasible timeslot vectors.

Property 4. The t-lag timeslot vector $T_{i,t} = t \times T_{i,1}$ for all $i \in V$.

Each infected node can spread the computer virus only after it is infected and before it is cured. The maximal spread period can be infinity if the computer virus is not detected, as discussed in Section 4.1, theoretically. Hence, a new concept called instantaneous infection is provided for defensive pessimism.

In an instantaneous infection, the computer virus can spread without waiting for another timeslot, that is, $\Delta t_{i,j} = 0$ for all $i \in V$ and all j in $V(i)$ if the node is first infected. Note that a 0-lag timeslot $T_{i,0}$ corresponds to a zero vector and an instantaneous infection. Hence, we have the following property:

Property 5. The 1-lag basic temporal vector is the upper-bound of any feasible timeslot vector.

All temporal vectors can be generated according to Property 5 such that each of their coordinates is less than or equal to that of the related basic temporal vector. Moreover, owing to the characteristic of the instantaneous infection, we have the following important property in filtering out the feasible temporal vectors from all vectors generated according to Property 5.

Property 6. The temporal vector Y is feasible if and only if the following conditions are satisfied, where T represents the 1-lag basic temporal vector that generates Y; that is, $Y(i) \le T(i)$ for all node i in V.

(1) $Y(i) < Y(j)$ if $T(i) < T(j)$, where $i, j \in V$,

(2) $Y(i) \le Y(j)$ if $T(i) = T(j)$, where $i, j \in V$.

5.3. Basic State Vectors. The state vector is a dual vector formed by two vectors—a spread vector and a temporal vector—separated using the notation ";". For example, $X_1 = (0, 5, 5, 5, 7, 0, 2, 0; 0, 2, 2, 3, 2, 1, 5, 1)$ indicates the following:

(1) Node 0 is the first infected node at timeslot 0 because it is characterized by $X_1(0) = 0$

(2) Node 0 spreads the virus to nodes 5 and 7 at $t = 1$

(3) Node 5 spreads the virus to nodes 1 and 2 at $t = 2$ and to node 3 at $t = 3$

(4) Node 7 spreads the virus to node 4 at $t = 2$

(5) Node 2 spreads the virus to node 6 at $t = 5$

A state vector is a basic state vector if its temporal vector is basic. A state vector and/or a basic state vector are infeasible if it is impossible to spread the computer virus according to either its spread vector or the temporal vector, that is, $j_{i,t}$, and $j \notin V(i)$ or $t_j \le t_i$; otherwise, it is a feasible state vector. For example, X_1 discussed above is a feasible state vector, $X_2 = (0, 0, 5, 5, 7, 1, 5, 0; 0, 2, 2, 3, 2, 1, 5, 1)$ is infeasible because $1 \notin V(0)$ in its spread vector, and $X_3 = (0, 5, 5, 5, 7, 0, 2, 0; 0, 2, 0, 3, 2, 1, 5, 1)$ is infeasible because $T_2 = 0$ but $T_5 = 1$ and node 2 is infected from node 5.

For any state vector, the feasibility of its temporal vector depends on its spread vector. Moreover, from Property 5, all temporal vectors can be deduced from the 1-lag temporal vectors. Hence, in the proposed BAT, all the feasible spread vectors together with their 1-lag temporal vectors are found

Table 7: Spread period example with 1-Lag.

t	i	Susceptible nodes	Infectious nodes at $(t+1)$
0	0	{5, 7}	{0, 5, 7}
1	5	{1, 2, 3, 4, 6}	{0, 1, 2, 3, 4, 5, 6, 7}

first to reduce the computational burden of searching for all the state vectors.

The following property involves the relationship between the damping factor d and state vectors. According to this important property, we can simply find all the state vectors for a specific d (without finding all the state vectors for any d), which is very useful for improving the efficiency of the related algorithms.

Property 7. Regardless of the values of the damping factor d, a feasible state vector is always feasible for all d.

6. Proposed BAT

Similar to the DFS, BFS, and UGFM, the BAT is an implicit enumeration search method that can find all the feasible state vectors. However, the BAT is easier to code, more flexible to modify, and more efficient in execution than the other methods [40, 50, 51]. Hence, the BAT is adopted in this study and developed in this section formally to solve the proposed problem.

6.1. Basic Idea behind the Proposed BAT. Let the update procedure be started from the last coordinate to the first coordinate. The basic idea in the proposed BAT is redefined in terms of the fundamental concept in the traditional BAT update procedure by changing a binary vector to a multistate vector as follows:

(1) If it is possible to replace the value of the current coordinate with a larger feasible value, it is replaced, and the new vector is a new state vector. For example, in the traditional BAT, the last 0 in the binary-state vector $X_i = (0, 1, 1, 0)$ can be updated to 1, and $X_{i+1} = (0, 1, 1, 1)$ is a new binary-state vector.

(2) If it is impossible to replace the value of the current coordinate with a larger feasible value, the current value is reset to the smallest feasible value, the algorithm moves to the next coordinate, the foregoing procedure is repeated until the replacement is possible, and then the first step is performed. For the example used in the first step, $X_{i+1} = (0, 1, 1, 1)$ is updated to $X_{i+2} = (1, 0, 0, 0)$.

To deal with the temporal and learning effect properties in the proposed BAT, the details of the foregoing new idea are explained in the remainder of this section.

6.2. BAT-1 for Spread Vector and 1-LAG Temporal Vector. There are two BATs in the proposed BAT. The first one, which is called BAT-1, finds all the feasible spread vectors together with the related 1-lag temporal vectors. The second BAT, which is called BAT-2, finds all the feasible temporal vectors according to the found 1-lag temporal vectors.

BAT-1 is proposed here by changing the binary states to multistates to find all the feasible labeled spread vectors to fit the proposed problem, and its pseudocode is presented below (Algorithms 3 and 4):

The above procedure essentially follows the concepts proposed in Section 6.1. For example, according to the proposed BAT-1 algorithm, we have the first 10 spread states and the related temporal vectors, as shown in Table 11 listed in Section 5.1.

6.3. BAT-2 for All Temporal Vectors. From Property 5, all temporal vectors can be obtained from 1-lag temporal vectors. Hence, another BAT based on Properties 3–6 is implemented to find all temporal vectors for each 1-lag temporal vector as follows (Algorithm 5:

For example, there are 2591 1-lag temporal vector candidates generated from the basic 1-lag temporal vector $T = (0, 2, 2, 2, 2, 1, 3, 3)$ obtained according to the feasible labeled spread vector $X = (\mathbf{0}, 0, 0, 0, 0, 0, 0, 3)$, for which the spread vector is (0, 5, 5, 5, 5, 0, 1, 1) in Figure 2. In total, 479 of them are feasible, and the first 30 temporal vectors are presented in Table 14.

6.4. Pseudocode for the Proposed Algorithm. Assume that the computer virus starts to spread from node TARGET, and we wish to determine the probability that the whole network is infected within a t-lag. The pseudocode of the proposed method for solving the foregoing problem, according to the temporal spread probability with the learning effect derived in Section 4.4, the novel dual state vectors developed in Section 5.3, and the new BAT proposed in Sections 6.2 and 6.3, in estimating the infected probability of computer virus spread areas is presented below (Algorithm 6:

For example, let the damping factor be $d = 0.1$, the lag be one timeslot, and node 0 be the first infected node in Figure 2. Then, we can obtain the PageRank values of each node, the degree of each node, the initial spread probability of each directed arc, and the temporal learning-effect spread probability of each directed, as shown in Tables 5, 7, and 9, respectively.

Using the proposed BAT-1 and BAT-2 algorithms, the basic state vectors and state vectors are obtained. The first 10 basic state vectors and the first 30 1-lag temporal vectors generated from the basic 1-lag temporal vector $T = (0, 2, 2, 2, 2, 1, 3, 3)$ are presented in Table 14.

In the last step, that is, STEP 3, the probabilities of all the feasible state vectors are calculated and summed. The final probability of node 0, which is infected first and spreads the virus throughout the whole network within one timeslot, is 0.7038000, and there are 1268 feasible basic state vectors among the 9720 state vector candidates. In addition, the probability of the labeled spread vector $X = (\mathbf{0}, 0, 0, 0, 0, 0, 0,$ and 3), for which the basic 1-lag temporal vector is $T = (0, 2, 2, 2, 2, 1, 3, 3)$, is 1.00259E-08, with 479 feasible 1-lag temporal vectors filtered out from 2591 1-lag temporal vectors, and the probabilities of the first 30 1-lag temporal vectors are presented in Table 15.

Table 8: Spread probability of each infected node at timeslot 1.

	0	1	2	3	4	5	6	7
0						0.40076		0.38382
1						0.26733	0.26122	0.25603
2						0.39683	0.38775	
3						0.26733	0.26122	0.25603
4						0.26733	0.26122	0.25603
5	0.12642	0.12885	0.12600	0.12885	0.12885			
6		0.12569	0.12291	0.12569	0.12569	0.14537		
7	0.15061	0.15350		0.15350	0.15350		0.17347	

Table 9: Spread probability of each infected node at timeslot 2.

	0	1	2	3	4	5	6	7
0						0.27283		0.26130
1						0.18200	0.17783	0.17430
2						0.27016	0.26397	
3						0.18200	0.17783	0.17430
4						0.18200	0.17783	0.17430
5	0.08607	0.08772	0.08578	0.08772	0.08772		0.09913	
6		0.08557	0.08367	0.08557	0.08557	0.09896		0.09478
7	0.10253	0.10450		0.10450	0.10450		0.11809	

Table 10: Spread probability of each infected node at timeslot 3.

	0	1	2	3	4	5	6	7
0						0.16795		0.16085
1						0.11203	0.10947	0.10730
2						0.16630	0.16250	
3						0.11203	0.10947	0.10730
4						0.11203	0.10947	0.10730
5	0.05298	0.05400	0.05280	0.05400	0.05400		0.06102	
6		0.05267	0.05151	0.05267	0.05267	0.06092		0.05834
7	0.06312	0.06433		0.06433	0.06433		0.07269	

Table 11: Initial spread probability of each infected node.

	0	1	2	3	4	5	6	7
0						0.51080		0.48920
1						0.34073	0.33294	0.32633
2						0.50579	0.49421	
3						0.34073	0.33294	0.32633
4						0.34073	0.33294	0.32633
5	0.16114	0.16423	0.16059	0.16423	0.16423		0.18559	
6		0.16021	0.15666	0.16021	0.16021	0.18528		0.17745
7	0.19196	0.19565		0.19565	0.19565		0.22109	

From the above, the proposed BAT can search for complete state vectors that satisfy the requirements of the proposed problem using BAT-1 and BAT-2. Only with all the state vectors can the analytical probability of the proposed algorithm be calculated, as described by STEP 3.

6.5. Experimental Analysis. In a scale-free network, the node degree distribution follows the power law. Thus, the computational burden increases with the size of the free-scale network, according to the power law. To confirm the performance of the proposed BAT in calculating the probability of the entire network being infected by a computer-virus, the proposed algorithm was tested on the mid-size network shown in Figure 2, which datasets are shown on the adjacency matrix in Table 3, by letting each node be the infected node individually for the damping factors of $d = 0.1$, 0.3, 0.5, 0.7, and 0.9 under allowed time lags of $t = 0$, 1, and 2. Hence, there were $8 \times 5 \times 3 = 120$ tests in total.

Table 12: Related probabilities for node 0 in Figure 2.

t	$p_{0,5,t}$	$p_{0,7,t}$	$\prod_{\tau=0}^{t-1}[(1-p_{0,5,\tau})\cdot(1-p_{0,5,\tau})]$	$P_{0,5,t}$	$P_{0,7,t}$
0	0.1610000	0.1352000	0.7038000		
1	0.1263180	0.1060758	0.5402412	0.088903	0.074656
2	0.0859949	0.0722144	0.4547700	0.046458	0.039013
3	0.0529361	0.0444532	0.4104803	0.024074	0.020216
4	0.0301379	0.0253083	0.3877207	0.012371	0.010389
5	0.0160975	0.0135179	0.3762382	0.006241	0.005241
6	0.0081466	0.0068411	0.3705993	0.003065	0.002574
7	0.0039345	0.0033040	0.3679167	0.001458	0.001224
8	0.0018235	0.0015313	0.3666824	0.000671	0.000563
9	0.0008145	0.0006840	0.3661329	0.000299	0.000251

Table 13: Labeled spread vectors and 1-LAG temporal vectors.

	Spread vectors	Labeled spread vectors	1-Lag temporal vectors
1	(5, 5, 5, 5, 5, 0, 1, 1)	(**0**, 0, 0, 0, 0, 0, 0, 1)	(**0**, 2, 2, 2, 2, 1, 3, 3)
2	(5, 5, 5, 5, 5, 0, 1, 3)	(**0**, 0, 0, 0, 0, 0, 0, 2)	(**0**, 2, 2, 2, 2, 1, 3, 3)
3	(5, 5, 5, 5, 5, 0, 1, 4)	(**0**, 0, 0, 0, 0, 0, 0, 3)	(**0**, 2, 2, 2, 2, 1, 3, 3)
4	(5, 5, 5, 5, 5, 0, 1, 6)	(**0**, 0, 0, 0, 0, 0, 0, 4)	(**0**, 2, 2, 2, 2, 1, 3, 4)
5	(5, 5, 5, 5, 5, 0, 2, 0)	(**0**, 0, 0, 0, 0, 0, 1, 0)	(**0**, 2, 2, 2, 2, 1, 3, 1)
6	(5, 5, 5, 5, 5, 0, 2, 1)	(**0**, 0, 0, 0, 0, 0, 1, 1)	(**0**, 2, 2, 2, 2, 1, 3, 3)
7	(5, 5, 5, 5, 5, 0, 2, 3)	(**0**, 0, 0, 0, 0, 0, 1, 2)	(**0**, 2, 2, 2, 2, 1, 3, 3)
8	(5, 5, 5, 5, 5, 0, 2, 4)	(**0**, 0, 0, 0, 0, 0, 1, 3)	(**0**, 2, 2, 2, 2, 1, 3, 3)
9	(5, 5, 5, 5, 5, 0, 2, 6)	(**0**, 0, 0, 0, 0, 0, 1, 4)	(**0**, 2, 2, 2, 2, 1, 3, 4)
10	(5, 5, 5, 5, 5, 0, 3, 0)	(**0**, 0, 0, 0, 0, 0, 2, 0)	(**0**, 2, 2, 2, 2, 1, 3, 1)

(i) Input: A scale-free network $G(V, E)$ and the computer virus infects node TARGET first.
(ii) Output: All state vectors without duplications.
(iii) STEP S0. Let X be a zero vector with n coordinates represented the node states, vector index k = 1, istop = 1 if TARGET = 0, and istop = 0 if TARGET >0.
(iv) STEP S1. Let coordinate index $i = (n-1)$.
(v) STEP S2. If i = TARGET, let $i = (i-1)$ and go to STEP S3.
(vi) STEP S3. If $X(i) < (W_i - 1)$, let $X(i) = X(i) + 1$, and execute 1-lag_Temporal_Vector (X).
(vii) STEP S4. If X_k is feasible, let $k = k + 1$ and go STEP S1.
(viii) STEP S5. If $i = i_{\text{stop}}$, halt and $X_1, X_2, \ldots, X_k$ are all feasible spread vectors.
(xi) STEP S6. Let $X(i) = 0$, $i = (i-1)$, and go to STEP S2.

Algorithm 3: BAT1.

As the number of state vectors increased, the runtime increased exponentially. Hence, we only discuss t values up to 2.

Both BAT-1 and BAT-2 were coded in Python 3.7.7 and run on Spyder 4.1.3. The 160 tests were conducted on Windows 10 with an Intel Core i7-8650U CPU at 1.90 GHz and 2.11 GHz with 16 GB RAM. The experimental results are presented in Tables 16–18.

The numbers of basic state vector candidates N_s and basic feasible state vectors n_s were only related to the node degrees Deg (i) based on the characteristics of the scale-free network and were unrelated to the values of the damping factors (d) and the allowed time lags (t), for all $i \in V$. Hence, we have the same number of basic and feasible state vectors and probabilities if $V(i) = V(j)$, for all nodes i and j. Thus, we list the values of N_s and n_s in Table 14 and not in the other tables.

The foregoing observation is useful, and, accordingly, we must focus on the nodes without the same neighbors. For example, nodes 1, 3, and 4 all have the same neighbors, that is, $V(1) = V(3) = V(4) = \{5, 6, 7\}$, and we can search for the state vectors and calculate the probability for node 1 because nodes 3 and 4 are identical.

Moreover, a higher degree of the first infected node corresponds to a higher probability of having a smaller number of basic state vector candidates. This is because the total initial spread probabilities from one node to its neighbors are one, and the more neighbors have a higher probability of having a lower spread probability. In addition, the more the neighbors, the smaller the values after using multiplications in Equation (12).

For the same reason as in Table 16, the probabilities that the whole network was infected by node i and node j are equal if $V(i) = V(j)$ in Table 17, for all nodes i and j. For

(i) STEP L0. Let FLAG(V) = false for all V ∈ V, FLAG(TARGET) = true, $t = 1$, $L_0 = \{\text{TARGET}\}$, and $L_1 = \varnothing$.
(ii) STEP L1. Let $T_u = t$, FLAG(u) = true, and $L_t = L_t \cup \{u\}$, where for all $L(X_u) = \text{v}$, for all v ∈ L_{t-1}, and FLAG(u) = false.
(iii) STEP L2. If $L_t = \varnothing$, halt and return the information that X is infeasible.
(iv) STEP L3. If FLAG(v) = true for all v ∈ V, halt and return the information that X is feasible.
(v) STEP L4. Let $t = t + 1$, $L_t = \varnothing$, and go to STEP L1.

Algorithm 4: 1-lag_Temporal_Vector (X).

(i) Input: A 1-lag temporal vector T reordered to T^* in decreasing of the coordinate values.
(ii) Output: All feasible temporal vectors respective to T.
(iii) STEP T0. Let Y be a zero vector with n coordinates represented the node infected time, vector index $k = 1$, $i_{\text{stop}} = 1$ if TARGET = 0, and $i_{\text{stop}} = 0$ if TARGET >0.
(iv) STEP T1. Let coordinate index $i = (n - 1)$.
(v) STEP T2. If $Y(i) < T^*(i)$, let $Y(i) = Y(i) + 1$, and execute 1-lag_Temporal_Vector(X).
(vi) STEP T3. If $Y(u) < Y(\text{v})$ and $T^*(u) < T^*(\text{v})$ for all nodes u and v in V, Y is infeasible and go STEP S1. Otherwise, let $k = k + 1$ and go STEP S1.
(vii) STEP T4. If $i = i_{\text{stop}}$, halt and $Y_1, Y_2, \ldots, Y_k$ are all feasible temporal vectors generated from T.
(viii) STEP T5. Let $X(i) = 0$, $i = (i - 1)$, and go to STEP T2.

Algorithm 5: BAT-2.

Table 14: First 30 1-Lag temporal vectors generated from T = (0, 2, 2, 2, 2, 1, 3, 3).

i	T_i
1	(**0**, 0, 0, 0, 0, 0, 0, 1)
2	(**0**, 0, 0, 0, 0, 0, 0, 2)
3	(**0**, 0, 0, 0, 0, 0, 0, 3)
4	(**0**, 0, 0, 0, 0, 0, 1, 0)
5	(**0**, 0, 0, 0, 0, 0, 1, 1)
6	(**0**, 0, 0, 0, 0, 0, 1, 2)
7	(**0**, 0, 0, 0, 0, 0, 1, 3)
8	(**0**, 0, 0, 0, 0, 0, 2, 0)
9	(**0**, 0, 0, 0, 0, 0, 2, 1)
10	(**0**, 0, 0, 0, 0, 0, 2, 2)
11	(**0**, 0, 0, 0, 0, 0, 2, 3)
12	(**0**, 0, 0, 0, 0, 0, 3, 0)
13	(**0**, 0, 0, 0, 0, 0, 3, 1)
14	(**0**, 0, 0, 0, 0, 0, 3, 2)
15	(**0**, 0, 0, 0, 0, 0, 3, 3)
16	(**0**, 0, 0, 0, 1, 0, 1, 1)
17	(**0**, 0, 0, 0, 1, 0, 1, 2)
18	(**0**, 0, 0, 0, 1, 0, 1, 3)
19	(**0**, 0, 0, 0, 1, 0, 2, 1)
20	(**0**, 0, 0, 0, 1, 0, 2, 2)
21	(**0**, 0, 0, 0, 1, 0, 2, 3)
22	(**0**, 0, 0, 0, 1, 0, 3, 1)
23	(**0**, 0, 0, 0, 1, 0, 3, 2)
24	(**0**, 0, 0, 0, 1, 0, 3, 3)
25	(**0**, 0, 0, 0, 2, 0, 2, 2)
26	(**0**, 0, 0, 0, 2, 0, 2, 3)
27	(**0**, 0, 0, 0, 2, 0, 3, 2)
28	(**0**, 0, 0, 0, 2, 0, 3, 3)
29	(**0**, 0, 0, 1, 0, 0, 1, 1)
30	(**0**, 0, 0, 1, 0, 0, 1, 2)

example, $V(1) = V(3) = V(4) = \{5, 6, 7\}$ from Table 5; the probabilities that the whole network was infected by nodes 1, 3, and 4 were 1.78550E-05 for $d = 0.1$ and $t = 0$.

The increment in d reduced the obtained probability. For example, for $t = 0$ and $i = 0$, the related probability was 1.05186E-05 for $d = 0.1$, and it was higher than 7.55361E-06 for $d = 0.3$, as shown in Table 15. This is because a smaller d corresponded to a higher probability of exploring new areas.

A virus that spent a longer amount of time spreading had a higher probability of spreading to the entire network. Hence, the increment of t increased the obtained probability; for example, the probability was 1.05186E-05 for $t = 0$ and increased to 1.64706E-05 for $t = 1$, as shown in Table 17. However, the rate of the increment in the probability decreased as t increased. This is because a larger value of t corresponded to a smaller number of susceptible nodes remaining, which resulted in a lower spread probability. For example, 1.64706E-05/1.05186E-05 = 1.56585477 > 1.67060 E-05/1.64706E-05 = 1.014292133, where 1.05186E-05, 1.64706E-05, and 1.67060E-05 represent the spread probabilities of $t = 0$, 1, and 2 for $i = 0$ and $d = 0.10$, respectively.

Similar to the foregoing observations in Table 17, Table 18 shows that the increment of the allowed time lag t increased the number of temporal state vector candidates Nt and feasible temporal vectors nt; e.g., Nt was 11651837 for t = 1 and increased to 514419848 for t = 2.

Interestingly, the ratio of (the number of temporal state vector candidates)/(the number of temporal state vectors), that is, N_t/n_t in Table 18, increased with t. This confirms that a larger value of t corresponded to a larger N_t and n_t. In

(i) Input: A scale-free network G (V, E), the first infected node TARGET, the damping factor d, and the allowed timeslot lag t.
(ii) Output: The probability that the computer virus spreads throughout the whole network within time lag t.
(iii) STEP 0. Count the degree of each node, calculate the PageRank values of each node, calculate the initial spread probability of each directed arc using Equation (7), and compute the temporal spread probability with the learning effect for each arc using Equation (12).
(iv) STEP 1. Implement the proposed BAT-1 algorithm to search for all feasible basic state vectors constructed by the spread vectors and the 1-lag temporal vectors.
(v) STEP 2. Implement the proposed BAT-2 algorithm to find all the feasible t-lag temporal vectors according to the 1-lag temporal vectors.
(vi) STEP 3. Calculate and sum the probabilities of all the feasible state vectors using Equation (12).

Algorithm 6: Procedure New-BAT.

Table 15: Probabilities of the first 30 1-LAG temporal vectors based on Table 14.

i	Pr (T_i)
1	4.08805E – 09
2	4.72604E – 09
3	5.04121E – 09
4	6.38271E – 09
5	7.02752E – 09
6	7.33750E – 09
7	7.49064E – 09
8	8.14295E – 09
9	8.45649E – 09
10	8.60723E – 09
11	8.68169E – 09
12	9.00670E – 09
13	9.16292E – 09
14	9.23803E – 09
15	9.27513E – 09
16	9.33043E – 09
17	9.35702E – 09
18	9.37015E – 09
19	9.39705E – 09
20	9.40997E – 09
21	9.41636E – 09
22	9.42976E – 09
23	9.43620E – 09
24	9.43938E – 09
25	9.44145E – 09
26	9.44247E – 09
27	9.44349E – 09
28	9.44400E – 09
29	9.49931E – 09
30	9.52589E – 09

Table 16: The Deg (i), N_s, and n_s.

i	Deg (i)	N_s	n_s
0	2	9720	1268
1	3	6480	1269
2	4	9720	1269
3	3	6480	1269
4	3	6480	1269
5	6	3240	1268
6	6	3240	1269
7	5	3888	1269

∗ N_s and n_s represent the numbers of basic state vector candidates and basic feasible state vectors, respectively.

Table 17: Probability that whole network was infected by node i at $t = 0, 1, 2, 3$.

t	id	0.10	0.30	0.50	0.70	0.90
0	0	0.105186E – 04	0.0755361E – 04	0.0556822E – 04	0.0417601E – 04	0.0315968E – 04
	1	**0.178550E – 04**	**0.135186E – 04**	**0.107111E – 04**	**0.0879585E – 04**	**0.0743470E – 04**
	2	0.111024E – 04	0.0815902E – 04	0.0614844E – 04	0.0472119E – 04	0.0367313E – 04
	3	**0.178550E – 04**	**0.135186E – 04**	**0.107111E – 04**	**0.0879585E – 04**	**0.0743470E – 04**
	4	**0.178550E – 04**	**0.135186E – 04**	**0.107111E – 04**	**0.0879585E – 04**	**0.0743470E – 04**
	5	0.0471508E – 04	0.0332248E – 04	0.0250894E – 04	0.0199343E – 04	0.0164777E – 04
	6	0.0787540E – 04	0.0576780E – 04	0.0435602E – 04	0.0337804E – 04	0.0267799E – 04
	7	0.0807434E – 04	0.0626301E – 04	0.0503922E – 04	0.0417717E – 04	0.0354717E – 04
	SUM	**0.958508E – 04**	0.716219E – 04	0.557541E – 04	0.448334E – 04	0.370098E – 04
1	0	0.164706E – 04	0.117532E – 04	0.0859807E – 04	0.0639718E – 04	0.0480194E – 04
	1	**0.285183E – 04**	**0.216532E – 04**	**0.171670E – 04**	**0.140823E – 04**	**0.118742E – 04**
	2	0.182460E – 04	0.136883E – 04	0.104863E – 04	0.0815713E – 04	0.0640909E – 04
	3	**0.285183E – 04**	**0.216532E – 04**	**0.171670E – 04**	**0.140823E – 04**	**0.118742E – 04**
	4	**0.285183E – 04**	**0.216532E – 04**	**0.171670E – 04**	**0.140823E – 04**	**0.118742E – 04**
	5	0.0723298E – 04	0.0512550E – 04	0.0388383E – 04	0.0309452E – 04	0.0256476E – 04
	6	0.122174E – 04	0.0907971E – 04	0.0693560E – 04	0.0542159E – 04	0.0431858E – 04
	7	0.119262E – 04	0.0914769E – 04	0.0728086E – 04	0.0597267E – 04	0.0502157E – 04
	SUM	**1.51648E – 04**	1.13754E – 04	0.886856E – 04	0.712898E – 04	0.587384E – 04
2	0	0.167060E – 04	0.119286E – 04	0.0873134E – 04	0.0649922E – 04	0.0487995E – 04
	1	**0.292036E – 04**	**0.222009E – 04**	**0.176183E – 04**	**0.144634E – 04**	**0.122025E – 04**
	2	0.184794E – 04	0.138706E – 04	0.106310E – 04	0.0827304E – 04	0.0650205E – 04
	3	**0.292036E – 04**	**0.222009E – 04**	**0.176183E – 04**	**0.144634E – 04**	**0.122025E – 04**
	4	**0.292036E – 04**	**0.222009E – 04**	**0.176183E – 04**	**0.144634E – 04**	**0.122025E – 04**
	5	0.0734090E – 04	0.0520308E – 04	0.0394432E – 04	0.0314450E – 04	0.0260794E – 04
	6	0.124624E – 04	0.0928453E – 04	0.0710513E – 04	0.0556119E – 04	0.0443307E – 04
	7	0.121382E – 04	0.0932064E – 04	0.0742342E – 04	0.0609150E – 04	0.0512156E – 04
	SUM	**1.54738E – 04**	1.16210E – 04	0.906902E – 04	0.729597E – 04	0.6.01522E – 04

Table 18: Numbers of t-LAG temporal vector candidates N_t and feasible temporal vectors n_t.

it	1			2			3		
	N_t	n_t	N_t/n_t	N_t	n_t	N_t/n_t	N_t	n_t	N_t/n_t
0	11651837	891932	13.1	514419848	24700821	20.8	5886456765	232325951	25.3
1	9196660	761060	12.1	396940282	20584520	19.3	4504323732	191929448	23.5
2	11303860	874525	12.9	496287202	24131654	20.6	5666506068	226652525	25.0
3	9196660	761060	12.1	396940282	20584520	19.3	4504323732	191929448	23.5
4	9196660	761060	12.1	396940282	20584520	19.3	4504323732	191929448	23.5
5	3783941	461678	8.2	142973828	11344701	12.6	1538807781	101716441	15.1
6	4434892	507651	8.7	173501602	12759040	13.6	1894848780	115517012	16.4
7	5354260	597341	9.0	212317522	15380446	13.8	2328937092	140479310	16.6

addition, a larger N_t corresponded to a smaller portion of feasible temporal vectors because all the feasible temporal vectors were selected from the temporal state vector candidates.

Table 18 shows another interesting finding that is coincident with those in Tables 16 and 17: the values of N_t for nodes i and j are identical if $V(i) = V(j)$. For example, $N_t = 9196660$ for nodes 1, 3, and 4 because $V(1) = V(3) = V(4) = \{5, 6, 7\}$. Moreover, the values of n_t for nodes i and j are still the same if $V(i) = V(j)$. Hence, the probability that the entire network is infected, N_s, n_s, N_t, and n_t are fixed for nodes i and j if $V(i) = V(j)$.

Summarize the experimental results and present the following recommendations that we can learn from:

(1) The decrement in the damping factors of d helps to obtain a higher probability of exploring new areas.

(2) The increment in the allowed time lags of t increases the obtained probability.

(3) The increment in the allowed time lags of t increases the number of temporal state vector candidates N_t, feasible temporal vectors n_t, and the ratio of (the number of temporal state vector candidates)/(the number of temporal state vectors), that is, N_t/n_t.

7. Conclusions

The spread of computer viruses not only jeopardizes the security of computer and network systems but also hinders their normal operation. Because of the skepticism of both human and software customers in dealing to virus detection, after it was acknowledged that post-creation, a computer virus' spread is aided by the digital antidote and decreases over time. This is called the learning effect.

The spread of a computer virus can be modeled using a scale-free network in which the node degree distribution follows the power rule. A novel computer-virus spread dynamic model with the learning effect based on the scale-free model is proposed. A simple and straightforward method based on the BAT and a novel concept called the temporal learning-effect spread probability and the dual-vector combined with the spread vector and the temporal vector is proposed for modeling the spread of computer viruses and theoretically predicting the analytical probabilities of all the infected-computer scenarios.

The reliability and performance of the proposed BAT was confirmed on a simulated temporal deterioration-effect scale-free network generated using the Barabási–Albert model. The results encourage the extension of the proposed BAT, including the development of the Monte Carlo [7] to BAT to solve larger-size scale-free problems.

In the future, we will strive for opportunities to collaborate with government and private organizations on this research to further verify how well the model proposed in this study fits in real life. In addition, comparing the current model with a virus-resistant model, with defense mechanism, will be planned for future works.

Moreover, several extended topics will be considered in the future for advanced research. For example, how to adjust the parameters of the model for calculating the probability of spreading will be studied when there are firewall devices, IDS, IPS, and DMZ in the intranet. We will further incorporate the version of the operating system, the status of opening service port, the status of protocol service, and the executive time of facility, etc., in order to define how these factors are influencing the probability of virus spreading.

Also, we will carefully consider whether to check for existing problems to ensure that the optimal control problem is solvable before attempting to formulate a solution. The proposed algorithm results will be compared with other methods provided in the literature, and the simulation results will also be displayed in a graphical format. Indeed, stability is an important issue for all dynamic systems. However, this paper is more academic. In fact, this paper has already considered stability in the learning effect. Moreover, we will discuss stability separately in the future. Later studies will discuss the scalability of the model and use a large network of 3000 to 5000 routers to understand the proposed performance algorithm and to understand the possibility of when the infection is less likely to become endemic or when it is more likely to become endemic.

Data Availability

The datasets are shown on the adjacency matrix in Table 3.

Disclosure

This article was once submitted to arXiv as a temporary submission that was just for reference and did not provide the copyright.

Conflicts of Interest

The authors declare that they have no conflicts of interest.

Acknowledgments

This research was supported in part by the Ministry of Science and Technology, R.O.C. under grant MOST 102-2221-E-007-086-MY3 and MOST 104-2221-E-007-061-MY3.

References

[1] W. Zhang, D. Chen, H. Si, N. N. Xiong, and R. T. D. C. M., "RTDCM: A coding preemption collection system for key data prioritization with hierarchical probability exchange mechanism in mobile computing," *IEEE Access*, vol. 8, pp. 4629–4639, Dec. 2019.

[2] W. C. Yeh, "A greedy branch-and-bound inclusion-exclusion algorithm for calculating the exact multi-state network reliability," *IEEE Transactions on Reliability*, vol. 57, no. 1, pp. 88–93, Mar. 2008.

[3] X. Zhou, P. Wang, Z. Yang, L. Tong, Y. Wang, C. Yang et al., "A manifold learning two-tier beamforming scheme optimizes resource management in massive MIMO networks," *IEEE Access*, vol. 8, pp. 22976–22987, Jan. 2020.

[4] W. C. Yeh, "A new branch-and-bound approach for the n/2/ flowshop/αF+ βCmax flowshop scheduling problem," *Computers & operations researchComputers & Operations Research*, vol. 26, no. 13, pp. 1293–1310, 1999.

[5] W. C. Yeh, C. Bae, and C. L. Huang, "A new cut-based algorithm for the multi-state flow network reliability problem," *Reliability Engineering & System Safety*," vol. 136, pp. 1–7, Apr. 2015.

[6] M. Wu, L. Zhong, L. Tan, and N. Xiong, "The sequential fusion estimation algorithms based on gauss-Newton method over multi-agent networked systems," *The Sequential Fusion Estimation Algorithms Based on Gauss-Newton Method Over Multi-Agent Networked Systems IEEE Access*, vol. 8, pp. 114315–114329, Jun. 2020.

[7] W. C. Yeh, Y. C. Lin, and Y. Y. Chung, "Performance analysis of cellular automata Monte Carlo Simulation for estimating network reliability," *Expert Systems with Applications*, vol. 37, no. 5, pp. 3537–3544, May 2010.

[8] M. Huang, A. Liu, N. N. Xiong, T. Wang, and A. V. Vasilakos, "An effective service-oriented networking management architecture for 5G-enabled internet of things," *Computer Networks*, vol. 173, Article ID 107208, 2020.

[9] W. C. Yeh, "A simple algorithm to search for all MCs in networks," *European Journal of Operational Research*, vol. 174, no. 3, pp. 1694–1705, Nov. 2006.

[10] W. C. Yeh, "An improved sum-of-disjoint-products technique for symbolic multi-state flow network reliability," *IEEE*

Transactions on Reliability, vol. 64, no. 4, pp. 1185–1193, Sep. 2015.

[11] W. C. Yeh, "A simple universal generating function method to search for all minimal paths in networks," *IEEE Transactions on Systems, Man, and Cybernetics - Part A: Systems and Humans*, vol. 39, no. 6, pp. 1247–1254, Nov. 2009.

[12] W. C. Yeh, "A simple universal generating function method for estimating the reliability of general multi-state node networks," *IIE Transactions*, vol. 41, no. 1, pp. 3–11, Nov. 2008.

[13] H. W. Corley, J. Rosenberger, W. C. Yeh, and T. K. Sung, "The cosine simplex algorithm," *The International Journal of Advanced Manufacturing Technology*, vol. 27, no. 9-10, pp. 1047–1050, Apr. 2005.

[14] C. M. Lai, W. C. Yeh, and C. Y. Chang, "Gene selection using information gain and improved simplified swarm optimization," *Neurocomputing*, vol. 218, pp. 331–338, Dec. 2016.

[15] C. Wu, S. Guo, Y. Wu, J. Ai, and N. N. Xiong, "Networked fault detection of field equipment from monitoring system based on fusing of motion sensing and appearance information," *Networked Fault Detection of Field Equipment from Monitoring System Based on Fusing of Motion Sensing and Appearance Information Multimedia Tools and Applications*, vol. 79, no. 23-24, pp. 16319–16348, Jun. 2020.

[16] W. C. Yeh, "Search for MC in modified networks," *Computers & Operations ResearchComputers & Operations Research*, vol. 28, no. 2, pp. 177–184, Feb. 2001.

[17] J. von Neumann, "Theory of Self-Reproducing Automata," *Essays on Cellular Automata*, pp. 64–87, University of Illinois Press, Champaign, IL, USA, 1966.

[18] Wikipedia,https://en.wikipedia.org/wiki/Computer_virus#Historical_development.

[19] V. Risak, *Selbstreproduzierende Automaten mit minimaler Informationsübertragung*, Zeitschrift für Maschinenbau und Elektrotechnik, Vienna, Austria, 1972.

[20] J. Kraus, "Selbstreproduktion bei Programmen," Thesis, University of Dortmund, Dortmund, Germany, 1980.

[21] S. I. Shoutkov and A. V. Spesivtsev, "Computer viruses: ways of reproduction in MS-DOS," in *Proceedings of the . 25th Annual 1991 IEEE International Carnahan Conference Oon Security Technology*, Taipei, Taiwan, Oct. 1991.

[22] C. Griffin and R. Brooks, "A note on the spread of worms in scale-free networks," *IEEE Transactions on Systems, Man, and Cybernetics, Part B (Cybernetics)IEEE Transactions on Systems, Man, and Cybernetics, Part B (Cybernetics)*, vol. 36, no. 1, pp. 198–202, Feb. 2006.

[23] T. N. Witte, "Phantom malware: conceal malicious actions from malware detection techniques by imitating user activity," *IEEE Access*, vol. 8, pp. 164428–164452, Sep. 2020.

[24] S. Peng, S. Yu, and A. Yang, "Smartphone malware and its propagation modeling: a survey," *IEEE Communications Surveys & TutorialsIEEE Communications Surveys & Tutorials*, vol. 16, no. 2, pp. 925–941, 2014.

[25] P. Li and X. Yang, "On dynamic recovery of cloud storage system under advanced persistent threats," *IEEE Access*, vol. 7, pp. 103556–103569, Jul. 2019.

[26] W.W Tian, X. Ji, W. Liu, G. Liu, J. Zhai, Y. Dai et al., "Prospect theoretic study of honeypot defense against advanced persistent threats in power grid," *IEEE Access*, vol. 8, pp. 64075–64085, Apr. 2020.

[27] J. Singh, D. Kumar, Z. Hammouch, and A. Atangana, "A fractional epidemiological model for computer viruses pertaining to a new fractional derivative," *Applied Mathematics and Computation*, vol. 3161316, pp. 504–515, January 2018.

[28] X. Wang, W. Ni, K. Zheng, R. P.R.P. Liu, and X. Niu, "Virus propagation modeling and convergence analysis in large-scale networks," *IEEE Transactions on Information Forensics and Security*, vol. 11, no. 10, pp. 2241–2254, Oct. 2016.

[29] Y. Huang and Q. Zhu, "A differential game approach to decentralized virus-resistant weight Adaptation policy over complex networks," *IEEE Transactions on Control of Network Systems*, vol. 7, no. 2, pp. 944–955, June 2020.

[30] M. W. Eichin and J. A. Rochlis, "With microscope and tweezers: an analysis of the internet virus of November 1988," in *Proceedings of the IEEE Symposium on Security a and Privacy*, Oakland, CA, USA, November 1989.

[31] E. H. Spafford, "Computer viruses as artificial life," *Artificial Life*, vol. 1, no. 3, pp. 249–265, April 1994.

[32] R. Davis, "Exploring computer viruses," in *Proceedings of the in Fourth Aerospace Computer Security Applications*, Orlando, FL, USA, September 1988.

[33] E. Okamoto and H. Masumoto, "ID-based authentication system for computer virus detection," *Electronics Letters*, vol. 26, no. 15, pp. 1169-1170, July 1990.

[34] D. Spinellis, "Reliable identification of bounded-length viruses is NP-complete," *IEEE Transactions on Information Theory*, vol. 49, no. 1, pp. 280–284, Jan 2003.

[35] X. Wang, N. L. Or, Z. Lu, and D. Pao, "Hardware aAccelerator to dDetect mMulti-sSegment vVirus pPatterns," *The Computer Journal*, vol. 58, no. 10, pp. 2443–2460, Oct. 2015.

[36] C. Gan, X. Yang, W. Liu, and Q. Zhu, "A propagation model of computer virus with nonlinear vaccination probability," *Communications in Nonlinear Science and Numerical Simulation*, vol. 19, no. 1, pp. 92–100, January 2014.

[37] G. M. Al-Dossary, "Computer vvirus pprevention and ccontainment on mmainframes," in *Proceedings of the International Carnahan Conference Oon Security Technology*, Zurich, Switzerland, October 1989.

[38] H. Yuan, J. Wu, and G. Chen, "Infection functions for virus propagation in computer networks: aAn empirical study," *Tsinghua Science and Technology*, vol. 14, no. 5, pp. 669–676, Oct. 2009.

[39] M. Youssef and C. Scoglio, "Optimal nNetwork-bBased iIntervention in the pPresence of uUndetectable vViruses," *IEEE Communications Letters*, vol. 18, no. 8, pp. 1347–1350, Aug. 2014.

[40] W. C. Yeh, "Novel binary-addition tree algorithm (BAT) for binary-state network reliability problem," 2020, http://arxiv.org/abs/2004.08238.

[41] J. C. Lang, H.H. D. SterckDe Sterck, J. L. Kaiser, J. C. Miller, and J. Gleeson, "Analytic models for SIR disease spread on random spatial networks," *Journal of Complex Networks*, vol. 6, no. 6, pp. 948–970, Dec. 2018.

[42] K. Zhu and L. Ying, "Information source detection in the SIR model: a sample-path-based approach," *IEEE/ACM Transactions on Networking*, vol. 24, no. 1, pp. 408–421, Feb. 2016.

[43] V. P. Dubey, R. Kumar, and D. Kumar, "A hybrid analytical scheme for the numerical computation of time fractional computer virus propagation model and its stability analysis," *Chaos, Solitons & Fractals*, vol. 133, Article ID 109626, 2020.

[44] J. Ren and Y. Xu, "A compartmental model for computer virus propagation with kill signals," *Physica A: Statistical Mechanics and Iits Applications*, vol. 48615486, pp. 446–454, November 2017.

[45] Q. A. Dang and M. T. Hoang, "Positivity and global stability preserving NSFD schemes for a mixing propagation model of computer viruses," *Journal of Computational and Applied Mathematics*, vol. 37415, Article ID 112753, August 2020.

[46] W. C. Yeh, "Methodology for the reliability evaluation of the novel learning-effect multi-state flow network," *IISE Transactions*, vol. 49, no. 11, pp. 1078–1085, 2017.

[47] W. C. Yeh, P. J. Lai, and M. C. Chuang, "Parallel-machine scheduling to minimize makespan with fuzzy processing times and learning effects," *Information Sciences*, Information Sciences, vol. 269, pp. 142–158, 2014.

[48] W. C. Lee, M. C. Chuang, and W. C. Yeh, "Uniform parallel-machine scheduling to minimize makespan with position-based learning curves," *Computers & Industrial EngineeringComputers & Industrial Engineering*, vol. 63, no. 4, pp. 813–818, 2012.

[49] W. C. Yeh, "Simplified swarm optimization in disassembly sequencing problems with learning effects," *Computers & Operations Research Computers & Operations Research*, vol. 39, no. 9, pp. 2168–2177, 2012.

[50] Y. Z. Su and W. C. Yeh, "Binary-addition tree algorithm-based resilience assessment for binary-state network problems," *Binary-Addition Tree Algorithm-Based Resilience Assessment for Binary-State Network Problems Electronics*, vol. 9, no. 8, p. 1207, 2020.

[51] W. C. Yeh, "Predicting and modeling wildfire propagation areas with BAT and maximum-state pageRank," *Applied Sciences*, IEEE Access Reviewing Paper, vol. 10, 2020/07.

Hindawi
Complexity
Volume 2021, Article ID 6612451, 7 pages
https://doi.org/10.1155/2021/6612451

Research Article

A Virus Propagation Model and Optimal Control Strategy in the Point-to-Group Network to Information Security Investment

Liping Feng,[1] **Ruifeng Han**,[1] **Hongbin Wang**,[1] **Qingshan Zhao**,[1] **Chengli Fu**,[1] **and Qi Han**[2]

[1]*Computer Science Department, Xinzhou Teachers University, Xinzhou, Shanxi 034000, China*
[2]*School of Intelligent Technology and Engineering, Chongqing University of Science &Technology, Chongqing 401331, China*

Correspondence should be addressed to Qi Han; hanqicq@163.com

Received 7 December 2020; Revised 3 May 2021; Accepted 25 May 2021; Published 3 June 2021

Academic Editor: Luxing Yang

Epidemiological dynamics is a vital method in studying the spread of computer network viruses. In this paper, an optimal control measure is proposed based on the SEIR virus propagation model in point-to-group information networks. First, considering the need for antivirus measures in reality, an optimal control problem is introduced, and then a controlled computer virus spread model in point-to-group information networks is established. Second, the optimal control measure is formulated by making a tradeoff between control cost and network loss caused by virus intrusion. Third, optimal control strategies are theoretically investigated by Pontryagin's maximum principle and the Hamiltonian function. Finally, through numerical simulations, effective measures for controlling virus spread in point-to-group information networks are proposed.

1. Introduction

Given the situation that critical infrastructures and human daily activities are becoming more and more dependent on information networks, it is vital to understand their weaknesses and uncover potential risks to threaten their security. Network viruses are the main threat that leads to the cyber security. Observing the significant similarities between the propagation of biological epidemics and network viruses, Kephart and White devoted pioneering work research that uses epidemic models to investigate the propagation characteristics of worms and targeted countermeasures [1–3]. After that, some biological epidemic models, such as susceptible-infected-susceptible (SI/SIS) and susceptible-infected-recovered (SIR), have been adapted to capture behaviors of the network virus propagation [4–10]. Based on these classical models, lots of extent models, which have more state transitions among nodes, have also been proposed to investigate the dynamical characteristic of internet worms [11–15]. These previous studies contributed to reveal the dynamical phenomena of internet worms and provided the effective theoretical instructions for network managers to protect network security.

The optimal control theory has been widely applied to the control of the spread of the epidemic [16–20]; however, to our knowledge, research studies which combine the optimal control theory with models of network viruses are seldom. Zhu et al. [21] established a delayed computer virus model with control, and the existence and uniqueness of an optimal control strategy were proved. Liu et al. [22] proposed a malware dynamical model with the impact of users' security awareness and, furthermore, developed effective prevention strategies with human interventions by optimal control theory. Yang et al. [23] proposed the novel conflicting opinion propagation model based on the differential game theory, which is contributed to the misinformation restraint and competitive viral marketing. These previous studies demonstrate that optimal control strategies are effective to prevent the diffusion of network viruses.

The above existing models suppose that the infection of network viruses is "point to point," i.e., an infected node infects a susceptible node one time. In fact, there is a

situation that an infected node will infect a group of nodes in the information sharing network, such as the popular e-mail system and instant message software. To investigate the effect of optimal control strategies on virus prevalence in the information sharing network, in this paper, an epidemic model with optimal control measures is addressed, which is based on [24].

Our main contributions are as follows: (1) we present a virus propagation model with variable antivirus measures in the point-to-group information sharing network; (2) the optimal control function to adjust antivirus strength is constructed; (3) the existence of the optimized solution is proved theoretically.

This paper is organized as follows. Section 2 formulates the model and corresponding optimal control strategy. The optimal control strategy is studied in Section 3. Section 4 represents some numerical results. Finally, Section 5 concludes the paper.

2. The Model and Optimal Control Strategy

2.1. Model Formulation. An information sharing network is a complex communicating network including a great deal of nodes (computer, terminal, or entity, etc.), in which one node that received the information can send the information to other nodes in the network. We can represent the information sharing network by an undirected network, as shown in Figure 1.

Our model is based on the network virus epidemic model with the point-to-group (P2G) information propagation proposed by Hua Yuan and Guoqing Chen [24]. This model assumes that the individuals in an information network system have four states: susceptible (S), exposed (E), infected (I), and recovered (R). At any time, the node is in one of the four states. And the state of an individual can switch under the action of virus infection and antivirus measures. Consider the following two facts:

The hosts will undergo a latent period (E-state) during the transition from the S-state to the I-state because users do not open the link or e-mail immediately

Users may immunize their hosts with countermeasures in states S, E, and I

These countermeasures can be seen as the strategies of multistate antivirus and may result in the following state transition paths:

$S \longrightarrow R$, using countermeasures of real-time immunization

$E \longrightarrow R$, cleaning viruses after hosts are infected

$I \longrightarrow R$, cleaning viruses after hosts are infected

As a result, the model is formulated as the following ordinary differential equations:

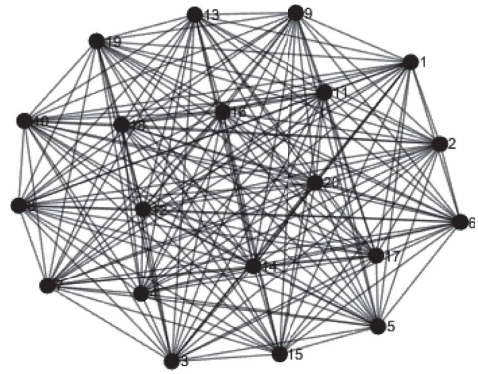

Figure 1: An information sharing network.

$$\begin{cases} \dfrac{dS(t)}{dt} = \mu N - \nu(t)S(t) - \rho_{SR}S(t) - \mu S(t), \\ \dfrac{dE(t)}{dt} = \nu(t)S(t) - \rho_{ER}E(t) - \alpha E(t) - \mu E(t), \\ \dfrac{dI(t)}{dt} = \alpha E(t) - (\delta + \mu)I(t), \\ \dfrac{dR(t)}{dt} = \rho_{SR}S(t) + \rho_{ER}E(t) + \delta I(t) - \mu R(t), \end{cases} \tag{1}$$

where μ is the replacement rate of old nodes, α is the transition rate from E to I, δ is the recovery rate from I to R, N is the total number of nodes in the network, ρ_{SR} describes the impact of implementing real-time immunization and ρ_{ER} describes the impact of cleaning the virus and immunizing the nodes in the latent period, $\nu(t)$ represents the transition rate from S to E, where $\nu(t) = (\alpha r/N)E(t)$, and r is the average number of neighbor nodes (with various states) that are directly connected with an infected node.

2.2. Optimal Control Strategy. In system (1), parameters ρ_{SR}, ρ_{ER}, and δ mean the strength of antivirus measures. In reality, they should be variable, so in this paper, we will induce a control function to adjust ρ_{SR}, ρ_{ER}, and δ. For our purpose, we want to find the control strategy which can obtain the minimum loss and cost when the accident of cyber security occurs. Let $\Theta = \{\varphi(t), 0 \le \varphi(t) \le \text{ƛ}, t \in [0, T]\}$ indicate an admissible control set. Consider the loss of finance caused by network viruses is relevant to the number of infected nodes. Assume that the average loss caused by a node per unit time is the constant χ. Then, the whole loss caused by all infected nodes in unit time is proportional to the number of infected nodes I, expressed as χI. Define $L_{\text{loss}}(I(t))$ as the loss function; then, during the time interval $[0, T]$, $L_{\text{loss}}(I(t))$ can be calculated as follows:

$$L_{\text{loss}}(I(t)) = \int_0^T \chi I(t)\mathrm{d}t. \tag{2}$$

In addition, countermeasures need the investment of enterprises, such as buying antivirus software and users' security education. The famous Gordon–Loeb model shows that the maximum security investment is not necessarily optimal from the view of economics [25]. So, the equilibrium is vital that the loss of the enterprise is the minimum in the condition of minimum investment in information security when a cyber security incident occurs. Let $L_{\cos t}(\varphi(t))$ be the cost of deploying security systems during the time interval $[0\ \ T]$. Define

$$L_{\cos t}(\varphi(t)) = \int_0^T \frac{\kappa\varphi^2(t)}{2}\mathrm{d}t, \tag{3}$$

subject to

$$\begin{cases} \dfrac{\mathrm{d}S(t)}{\mathrm{d}t} = \mu N - \nu(t)S(t) - \mu S(t) - \rho_{SR}\varphi(t)S(t), \\ \dfrac{\mathrm{d}E(t)}{\mathrm{d}t} = \nu(t)S(t) - \mu E(t) - \alpha E(t) - \rho_{ER}\varphi(t)E(t), \\ \dfrac{\mathrm{d}I(t)}{\mathrm{d}t} = \alpha E(t) - \mu I(t) - \delta\varphi(t)I(t), \\ \dfrac{\mathrm{d}R(t)}{\mathrm{d}t} = \rho_{\text{SR}}\varphi(t)S(t) + \rho_{\text{ER}}\varphi(t)E(t) + \delta\varphi(t)I(t) - \mu R(t), \end{cases} \tag{4}$$

where κ is a tradeoff coefficient. Equation (4) is the control system that we will concern. Aiming at equation (4), our aim is to find a control function $\varphi(t)$ to minimize the following objective function:

$$K(\varphi(t)) = \int_0^T \left[\chi I(t) + \frac{\kappa\varphi^2(t)}{2}\right]\mathrm{d}t, \tag{5}$$

where $K(\varphi)$ is the sum of loss and investment about cyber security.

For investigating the dynamics of control system (4), we can calculate the basic reproduction number and equilibria by the dynamical theory of differential equations [26]. From equation (4), it is easy to find that the fourth equation will not affect the dynamics of equation (4). So, without loss of generality, we can omit the fourth equation when discussing the dynamics of equation (4). It is easy to get the expression of the basic reproduction number, which is determined by

$$R_0 = \frac{r\mu\alpha}{(\mu + \rho_{\text{SR}}\varphi(t))(\rho_{\text{ER}}\varphi(t) + \alpha + \mu)}. \tag{6}$$

When $R_0 < 1$, equation (4) has the only equilibrium $Q_0 = (S^0, E^0, I^0) = ((\mu/\rho_{\text{SR}}\varphi(t) + \mu), 0, 0)$ which means the network virus will be eliminated completely with the evaluation of time. When $R_0 > 1$, equation (4) has the epidemic equilibrium Q_* besides Q_0, where Q_* is expressed by

$$Q_* = (S^*, E^*, I^*) = \left(\frac{\alpha + \mu + \rho_{\text{ER}}\varphi(t)}{r\alpha}N, \frac{\mu + \rho_{\text{SR}}\varphi(t)}{r\alpha}N(R_0 - 1), \frac{\alpha}{\delta\varphi(t) + \mu}E^*\right). \tag{7}$$

3. Solving the Optimal Control Strategies

For obtaining the optimal control solution, we need to define the Lagrangian and Hamiltonian function for optimal control problems (4) and (5). In fact, Lagrangian of the optimal problem can be given by

$$L(I, \varphi) = \chi I(t) + \frac{\kappa}{2}\varphi^2(t). \tag{8}$$

Next, we will seek an optimal function φ which satisfies that the integration of equation (8) is minimum. To do so, we define Hamiltonian H as follows:

$$H(S, E, I, \varphi, \lambda_1, \lambda_2, \lambda_3, \lambda_4, t) = L(I, \varphi) + \left[\lambda_1(t)\frac{\mathrm{d}S(t)}{\mathrm{d}t} + \lambda_2(t)\frac{\mathrm{d}E(t)}{\mathrm{d}t} + \lambda_3(t)\frac{\mathrm{d}I(t)}{\mathrm{d}t} + \lambda_4(t)\frac{\mathrm{d}R(t)}{\mathrm{d}t}\right]. \tag{9}$$

Theorem 1. *There exists an optimal control function φ^* such that $K(\varphi^*(t)) = \min_{\varphi\in\Theta} K(\varphi(t))$.*

Proof. According to the result of Kamien and Schwartz [27], it is easy to confirm the existence of an optimal control function to system (4).

First, the control set and corresponding state variables are not empty. The control set Θ is convex and closed. In the meanwhile, the right parts of the equations of system (4) are bounded and continuous and can be written a linear function of φ in the state variables. Besides, $L(I, \varphi)$ is convex on Θ, and there exist a constant $\rho > 1$ and two positive numbers ξ_1 and ξ_2 such that $L(I, \varphi) \geq \xi_1 + \xi_2(|\varphi|)^{(\rho/2)}$. Thus, we conclude that there exists an optimal control function.

Next, we will find the optimal solution by means of Pontryagin's maximum principle. □

Theorem 2. *Give an optimal control variable $\varphi^*(t)$ and the corresponding solution of system (4), $S^*(t)$, $E^*(t)$, $I^*(t)$, and $R^*(t)$, there exist adjoint variables $\lambda_i(i = 1, 2, 3)$ satisfying*

$$\begin{cases} \dfrac{d\lambda_1}{dt} = (\nu(t) + \mu)\lambda_1(t) + \rho_{SR}\varphi^*(t)\lambda_1(t) - \nu(t)\lambda_2(t) - \rho_{SR}\varphi^*(t)\lambda_4(t), \\ \dfrac{d\lambda_2}{dt} = (\mu + \alpha)\lambda_2(t) + \dfrac{r\alpha}{N}S^*(t) + \rho_{ER}\varphi^*(t)\lambda_2(t) - \alpha\lambda_3(t) - \rho_{ER}\varphi^*(t)\lambda_4(t), \\ \dfrac{d\lambda_3}{dt} = \mu\lambda_3(t) + \delta\varphi^*(t)\lambda_3(t) - \delta\varphi^*(t)\lambda_4(t), \\ \dfrac{d\lambda_4}{dt} = \mu\lambda_4(t), \end{cases} \tag{10}$$

with boundary conditions $\lambda_i(T) = 0$ $(i = 1, 2, 3)$.

Proof. By differentiating Hamiltonian (8) with respect to state variables S, E, I, and R, we obtain the adjoint system as follows:

$$\begin{cases} \dfrac{d\lambda_1}{dt} = -\dfrac{\partial H}{\partial S} = (\nu(t) + \mu)\lambda_1(t) + \rho_{SR}\varphi^*(t)\lambda_1(t) - \nu(t)\lambda_2(t) - \rho_{SR}\varphi^*(t)\lambda_4(t), \\ \dfrac{d\lambda_2}{dt} = -\dfrac{\partial H}{\partial S} = (\mu + \alpha)\lambda_2(t) + \dfrac{r\alpha}{N}S^*(t)\lambda_2(t) + \rho_{ER}\varphi^*(t)\lambda_2(t) - \alpha\lambda_3(t) - \rho_{ER}\varphi^*(t)\lambda_4(t), \\ \dfrac{d\lambda_3}{dt} = -\dfrac{\partial H}{\partial S} = \mu\lambda_3(t) + \delta\varphi^*(t)\lambda_3(t) - \delta\varphi^*(t)\lambda_4(t), \\ \dfrac{d\lambda_4}{dt} = -\dfrac{\partial H}{\partial S} = \mu\lambda_4(t). \end{cases} \tag{11}$$

By using optimality conditions, we have

$$\frac{\partial H}{\partial \varphi(t)}\Big|_{\varphi^*(t)} = \kappa\varphi^*(t) - \left[(\lambda_1 - \lambda_4)\rho_{SR}S^*(t) + (\lambda_2 - \lambda_4)\rho_{ER}E^*(t) + (\lambda_3 - \lambda_4)\delta I^*(t)\right] = 0. \tag{12}$$

It follows that

$$\varphi^*(t) = \frac{(\lambda_1 - \lambda_4)\rho_{SR}S^*(t) + (\lambda_2 - \lambda_4)\rho_{ER}E^*(t) + (\lambda_3 - \lambda_4)\delta I^*(t)}{\kappa}. \tag{13}$$

Considering the feature of the feasible region of Θ, we obtain

$$\begin{cases} \varphi^*(t) = 0, & \text{if } \dfrac{(\lambda_1-\lambda_4)\rho_{SR}S^*(t)+(\lambda_2-\lambda_4)\rho_{ER}E^*(t)+(\lambda_3-\lambda_4)\delta I^*(t)}{\kappa} \le 0, \\ \varphi^*(t) = \dfrac{(\lambda_1-\lambda_4)\rho_{SR}S^*(t)+(\lambda_2-\lambda_4)\rho_{ER}E^*(t)+(\lambda_3-\lambda_4)\delta I^*(t)}{\kappa}, & \text{if } \dfrac{(\lambda_1-\lambda_4)\rho_{SR}S^*(t)+(\lambda_2-\lambda_4)\rho_{ER}E^*(t)+(\lambda_3-\lambda_4)\delta I^*(t)}{\kappa} < D, \\ \varphi^*(t) = D, & \text{if } \dfrac{(\lambda_1-\lambda_4)\rho_{SR}S^*(t)+(\lambda_2-\lambda_4)\rho_{ER}E^*(t)+(\lambda_3-\lambda_4)\delta I^*(t)}{\kappa} > D. \end{cases} \tag{14}$$

Hence, we can have an optimal control function $\varphi^*(t)$ as follows:

$$\varphi^*(t) = \max\left\{\min\left\{\frac{(\lambda_1-\lambda_4)\rho_{SR}S^*(t)+(\lambda_2-\lambda_4)\rho_{ER}E^*(t)+(\lambda_3-\lambda_4)\delta I^*(t)}{\kappa}, D\right\}, 0\right\}. \tag{15}$$

So, we have the following optimal system:

$$\begin{cases} \dfrac{dS(t)}{dt} = \mu N - \nu(t)S(t) - \mu S(t) - \rho_{SR}\varphi(t)S(t), \\ \dfrac{dE(t)}{dt} = \nu(t)S(t) - \mu E(t) - \alpha E(t) - \rho_{ER}\varphi(t)E(t), \\ \dfrac{dI(t)}{dt} = \alpha E(t) - \mu I(t) - \delta\varphi(t)I(t), \\ \dfrac{dR(t)}{dt} = \rho_{SR}\varphi(t)S(t) + \rho_{ER}\varphi(t)E(t) + \delta\varphi(t)I(t) - \mu R(t), \\ \dfrac{d\lambda_1}{dt} = (\nu(t)+\mu)\lambda_1(t) + \rho_{SR}\varphi^*(t)\lambda_1(t) - \nu(t)\lambda_2(t) - \rho_{SR}\varphi^*(t)\lambda_4(t), \\ \dfrac{d\lambda_2}{dt} = (\mu+\alpha)\lambda_2(t) + \dfrac{r\alpha}{N}S^*(t)\lambda_2(t) + \rho_{ER}\varphi^*(t)\lambda_2(t) - \alpha\lambda_3(t) - \rho_{ER}\varphi^*(t)\lambda_4(t), \\ \dfrac{d\lambda_3}{dt} = \mu\lambda_3(t) + \delta\varphi^*(t)\lambda_3(t) - \delta\varphi^*(t)\lambda_4(t), \\ \dfrac{d\lambda_4}{dt} = \mu\lambda_4(t), \\ \varphi^*(t) = \max\left\{\min\left\{\dfrac{(\lambda_1-\lambda_4)\rho_{SR}S^*(t)+(\lambda_2-\lambda_4)\rho_{ER}E^*(t)+(\lambda_3-\lambda_4)\delta I^*(t)}{\kappa}, 1\right\}, 0\right\}. \end{cases} \tag{16}$$

□

4. Numerical Simulations

In this section, numerical simulations will be performed to compare system (1) without optimal control with system (16) with optimal control, and systems (1) and (16) will be solved with the Runge–Kutta fourth order. As shown in Table 1, the parameter values are taken. Furthermore, we assume that the initial states of the systems are

Table 1: Parameters used in experiments.

Parameter	Value
N	10,000
μ	1/4380
r	30
α	1/150
ρ_{SR}	1/200
ρ_{ER}	1/200
δ	$1/12-\mu$
κ	10

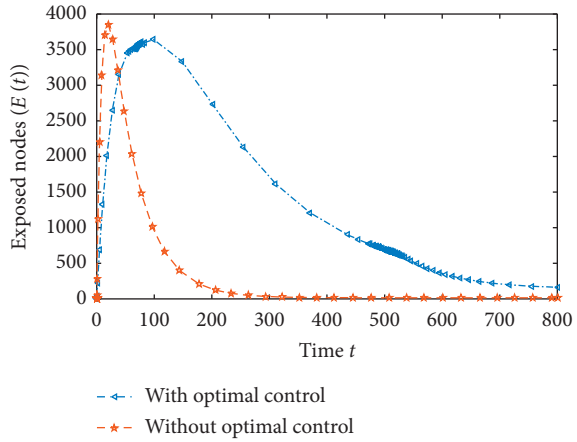

Figure 2: Evolution of the number of exposed nodes with or without control.

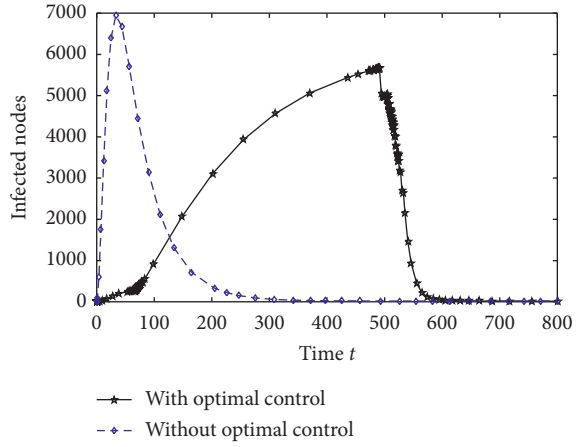

Figure 3: Evolution of the number of infected nodes with or without control.

$S(0) = 9999, E(0) = 1, I(0) = 0$, and $R(0) = 0$. Figures 2 and 3 depict the numerical results of $E(t)$ and $I(t)$, respectively.

Figure 2 shows that the growth rate of exposed nodes significantly decreased in the system with optimal control and that the evolution speed from exposed nodes to infected nodes slowed obviously. Hence, taking optimal control measures, network managers can have more time to protect information systems when viruses intrude.

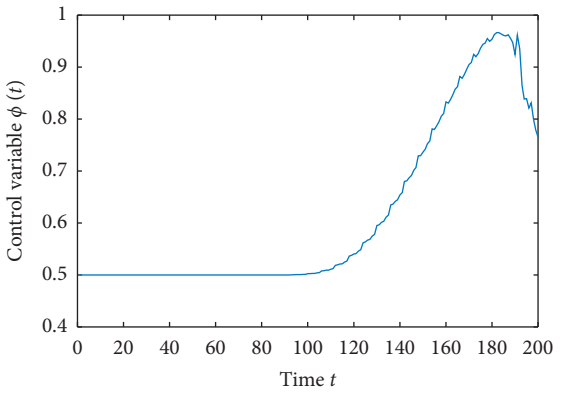

Figure 4: Optimal control function for system (16).

The same as Figure 2, Figure 3 shows that the growth rate of infected nodes with optimal control measures is much slower than that without optimal control measures. Moreover, the scale infected nodes also decreased in the network system with optimal control.

For surveying the evolution of the optimal control strategy with time, Figure 4 is depicted. From Figure 4, one can see that the control strategy keeps a stable state, and then the intensity of control increases with the increase of infected nodes. Subsequently, the intensity of control decreases with a reduction of virus spread.

5. Conclusion

The objective of this work is to model the virus prevalence in point-to-group information sharing networks and then find out certain optimal strategies of controlling the virus propagation. Taking into account the tradeoff of investment and income, the strength of network security defense measures should vary with the severity of the virus damage. So, based on the e-SEIR model [24], we consider the control parameters $\varphi(t)$ that change over time. First, we put forward the objective function and study the optimal control strategy toward the parameter $\varphi(t)$. Second, the existence and uniqueness of the optimal control strategy are proved. Finally, some numerical experiments are performed, which show that the scale and speed of virus prevalence will decrease greatly by taking optimal control strategies. In the future, we need more effort to trace the real data to test our results.

Data Availability

All the data used to support the findings of this study are available from the corresponding author upon request.

Conflicts of Interest

The authors declare that there are no conflicts of interest regarding the publication of this paper.

Acknowledgments

This work was supported by the Research Project supported by the Shanxi Scholarship Council of China (2020-139), Cultivate Scientific Research Excellence Programs of Higher Education Institutions in Shanxi (2020KJ025), Scientific and Technological Research Program of Chongqing Municipal Education Commission (Grant nos. KJZD-K201901504 and KJQN201901537), CAS "Light of West China" Program, Humanities and Social Sciences Research of Ministry of Education (19YJCZH047), and Xinzhou Teachers University Academic Leader Project.

References

[1] J. Kephart and S. White, "Directed-graph epidemiological models of computer viruses," in *Proceedings of the 1991 IEEE Symposium on Security and Privacy*, pp. 343–359, Oakland, CL, USA, May 1991.

[2] J. O. Kephart and S. R. White, "Measuring and modeling computer virus prevalence," in *Proceedings of the IEEE Computer Security Symposium on Research in Security and Privacy*, pp. 2–15, Oakland, CL, USA, May 1993.

[3] J. O. Kephart, S. R. White, and D. M. Chess, "Computers and epidemiology," *IEEE Spectrum*, vol. 30, no. 5, pp. 20–26, 1993.

[4] C. C. Zou, W. B. Gong, D. Towsley, and D. Towsley, "Code red worm propagation modeling and analysis," *Department of Health Care Services*, vol. 34, pp. 18–22, 2002.

[5] X. Han and Q. L. Tan, "Dynamical behavior of computer virus on Internet," *Applied Mathematics and Computation*, vol. 64, no. 7, pp. 1–7, 2010.

[6] S. Wang, Q. Liu, X. Yu, and Y. Ma, "Bifurcation analysis of a model for network worm propagation with time delay," *Mathematical and Computer Modelling*, vol. 52, no. 3-4, pp. 435–447, 2010.

[7] L. P. Feng, X. F. Liao, H. Q. Li, and Q. Han, "Hopf bifurcation analysis of a delayed viral infection model in computer networks," *Mathematical and Computer Modeling*, vol. 56, no. 7, pp. 167–179, 2012.

[8] L. Feng, L. Song, Q. Zhao, and H. Wang, "Modeling and stability analysis of worm propagation in wireless sensor network," *Mathematical Problems in Engineering*, vol. 2015, Article ID 129598, 8 pages, 2015.

[9] Q. Zhu and C. Cen, "A novel computer virus propagation model under security classification," *Discrete Dynamics in Nature and Society*, vol. 2017, Article ID 8609082, 11 pages, 2017.

[10] C. Gan, "Modeling and analysis of the effect of network eigenvalue on viral spread," *Nonlinear Dynamics*, vol. 84, no. 3, pp. 1727–1733, 2016.

[11] B. K. Mishra and D. K. Saini, "SEIRS epidemic model with delay for transmission of malicious objects in computer network," *Applied Mathematics and Computation*, vol. 188, no. 2, pp. 1476–1482, 2007.

[12] W. P. Liu, C. Liu, X. Y. Liu, S. G. Cui, and Y. Huang, "Modeling the spread of malware with the Influence of heterogeneous immunization," *Applied Mathematical Modelling*, vol. 40, pp. 269–276, 2016.

[13] Q. Liu, W. Cai, J. Shen, Z. Fu, X. Liu, and N. Linge, "A speculative approach to spatial-temporal efficiency with multi-objective optimization in a heterogeneous cloud environment," *Security and Communication Networks*, vol. 9, no. 17, pp. 4002–4012, 2016.

[14] T. Zhao and D. Bi, "Delay induced hopf bifurcation of an epidemic model with graded infection rates for internet worms," *Mathematical Problems in Engineering*, vol. 2017, Article ID 9563862, 10 pages, 2017.

[15] Y. Yao, Q. Fu, W. Yang, Y. Wang, and C. Sheng, "An epidemic model of computer worms with time delay and variable infection rate," *Security and Communication Networks*, vol. 2018, Article ID 9756982, 11 pages, 2018.

[16] A. Ali Lashari, "Optimal control of an SIR epidemic model with a saturated treatment," *Applied Mathematics & Information Sciences*, vol. 10, no. 1, pp. 185–191, 2016.

[17] L. Chen and J. Sun, "Optimal vaccination and treatment of an epidemic network model," *Physics Letters A*, vol. 378, no. 41, pp. 3028–3036, 2014.

[18] G. Zaman, Y. H. Kang, G. Cho, and I. H. Jung, "Optimal strategy of vaccination & treatment in an SIR epidemic model," *Mathematics and Computers in Simulation*, vol. 136, pp. 63–77, 2017.

[19] A. Jajarmi, A. Yusuf, D. Baleanu, and M. Inc, "A new fractional HRSV model and its optimal control: a non-singular operator approach," *Physica A: Statistical Mechanics and Its Applications*, vol. 547, Article ID 123860, 2020.

[20] I. Ahmad Nasidi, D. Nasidi, and D. Baleanu, "Optimal control model for the transmission of novel COVID-19," *Computers, Materials & Continuation*, vol. 66, no. 3, pp. 3089–3106, 2021.

[21] Q. Zhu, X. Yang, L.-X. Yang, and C. Zhang, "Optimal control of computer virus under a delayed model," *Applied Mathematics and Computation*, vol. 218, no. 23, pp. 11613–11619, 2012.

[22] W. Liu and S. Zhong, "Web malware spread modelling and optimal control strategies," *Scientific Reports*, vol. 7, no. 1, Article ID 42308, 2017.

[23] L.-X. Yang, P. Li, X. Yang, Y. Xiang, and Y. Y. Tang, "Simultaneous benefit maximization of conflicting opinions: modeling and analysisfit maximization of conflicting opinions: modeling and analysis," *IEEE Systems Journal*, vol. 14, no. 2, pp. 1623–1634, 2020.

[24] H. Yuan and G. Chen, "Network virus-epidemic model with the point-to-group information propagation," *Applied Mathematics and Computation*, vol. 206, no. 1, pp. 357–367, 2008.

[25] L. A. Gordon and M. P. Loeb, "The economics of information security investment," *ACM Transactions on Information and System Security*, vol. 5, no. 4, pp. 438–457, 2002.

[26] J. Hale and S. M. Verduyn Lunel, *Introduction to Functional Differential Equations*, Springer, Berlin, Germany, 1993.

[27] M. I. Kamien and N. L. Schwartz, *Dynamics Optimization: The Calculus of Variations and Optimal Control in Economics and Management*, Elsevier Science, Amsterdam, The Netherlands, 2000.

Hindawi
Complexity
Volume 2021, Article ID 6644292, 12 pages
https://doi.org/10.1155/2021/6644292

Research Article

Dynamic Analysis of a Competition-Cooperation Enterprise Cluster with Core-Satellite Structure and Time Delay

Wenjie Hu,[1] Tao Dong ,[2] and Hua Zhao[1]

[1]*School of Business Administration, Chongqing Technology and Business University, Chongqing 400067, China*
[2]*College of Electronics and Information Engineering, Southwest University, Chongqing 400715, China*

Correspondence should be addressed to Tao Dong; david_312@126.com

Received 2 November 2020; Revised 3 April 2021; Accepted 12 May 2021; Published 2 June 2021

Academic Editor: Jiaojiao Jiang

Core and satellite structure is one of the common structures in enterprise clusters. In core and satellite structure, there are one core enterprise and at least two satellite enterprises. There exist a competitive relationship between satellite enterprises and a cooperative relationship between satellite enterprise and core enterprise. However, the dynamic evolution of competition-cooperation enterprise clusters with core-satellite structure is not well understood. In this paper, a novel competition-cooperation enterprise cluster model with core-satellite structure is proposed. The boundedness of the positive equilibrium is investigated. It is found that there exists upper bound of both core enterprise output and satellite enterprise output and the upper bound of core enterprise not only depends on its own production capacity but also depends on the production capacity of two satellite enterprises. Then, by selecting the production period as bifurcating parameter, the conditions of local stability and Hopf bifurcation are obtained. Once the production period passes a critical value, the output of both core enterprise and satellite enterprise loses stability and displays periodic fluctuations. This may lead to the decline of efficiency of enterprise and resource mismatch. Furthermore, the fluctuation properties are studied. Finally, a numerical example is presented to show the effectiveness of theorem.

1. Introduction

Recently, enterprise cluster, as an effective form of industrial space organization, has gradually become a common phenomenon in the process of modern industry and internationalization [1–4]. The competition-cooperation relationship widely exists in the real enterprise clusters and has a major impact on the evolution of enterprise clusters [5–9]. To study the influence of competition and cooperation on the evolution of enterprise clusters, researchers propose a competition-cooperation enterprise cluster model [10] based on the ecology model [11–15], which is described as follows:

$$\begin{cases} \dot{x}_1(t) = r_1 x_1(t)\left(1 - \dfrac{x_1(t)}{K_1} - \dfrac{\alpha\left(x_2(t-\tau) - c_2\right)^2}{K_2}\right), \\ \dot{x}_2(t) = r_2 x_2(t)\left(1 - \dfrac{x_2(t)}{K_2} + \dfrac{\alpha\left(x_1(t-\tau) - c_1\right)^2}{K_1}\right), \end{cases} \tag{1}$$

where x_1, x_2 are the enterprise output; r_i is the intrinsic growth; $K_i\,(i = 1, 2)$ denotes the carrying capacity of market under nature unlimited conditions; $c_i\,(i = 1, 2)$ is the initial output of core enterprise; and τ is the production period. Let $a_1 = (r_1/K)$, $a_2 = (r_2/K), b_1 = (r_1\alpha/K), b_2 = (r_2\beta/K)$, and system (1) can be rewritten as follows:

$$\begin{cases} \dot{x}_1(t) = x_1(t)\left(r_1 - a_1 x_1(t) - b_1\left(x_2(t-\tau) - d\right)^2\right), \\ \dot{x}_2(t) = x_2(t)\left(r_2 - a_2 x_2(t) + b_2\left(x_1(t-\tau) - d\right)^2\right). \end{cases} \tag{2}$$

For this model, the dynamic behaviors including stability, Hopf bifurcation, and chaos have been widely studied [16–21].

In practical enterprise clusters, organization structure has a major impact on the production efficiency of enterprise clusters. The efficiency of overall operation is one of the important factors of enterprise's success. Thus, it is necessary to consider the structure in the enterprise cluster model. Among the many organization structures, core and satellite structure is one of the common structures in enterprise clusters, which is described in Figure 1. In core and satellite structure, there are one core enterprise and at least two satellite enterprises. There exist competitive relationship among satellite enterprises and cooperative relationship between satellite enterprise and core enterprise. For example, in automobile enterprise cluster, the core enterprise produces the motor vehicle and the satellite enterprise produces automobile parts for core enterprises. To reduce the cost and ensure the stability of supply chain, the core enterprise has at least two satellite enterprises for the same automobile part. It is easy to see that there exists competition between the two satellite enterprises and there exists cooperation between satellite enterprise and core enterprise. However, few works investigate the dynamic evolution of enterprise cluster model with core-satellite structure.

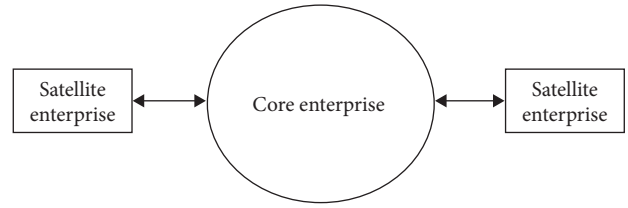

Figure 1: The enterprise cluster with one core enterprise and two satellite enterprises.

Inspired by the discussion, in this paper, a competition-cooperation enterprise cluster model composed of a core enterprise and two satellite enterprises is proposed, which is shown in Figure 1. In this enterprise cluster, there are one core enterprise and two satellite enterprises. There is a competitive relationship between two satellite enterprises. And there is a cooperative relationship between satellite enterprise and core enterprise. The model is described as follows:

$$\begin{cases} \dot{x}_1(t) = x_1(t)\left(r_1 - a_1 x_1(t) - b_1 x_2(t) - c_1\left(y(t-\tau) - d\right)^2\right), \\ \dot{x}_2(t) = x_2(t)\left(r_2 - a_2 x_2(t) - b_2 x_1(t) - c_1\left(y(t-\tau) - d\right)^2\right), \\ \dot{y}(t) = y(t)\left(r_3 - a_3 y(t) + c_2\left(\left(x_1(t-\tau) - d_1\right)^2 + \left(x_2(t-\tau) - d_2\right)^2\right)\right), \end{cases} \tag{3}$$

where $x_i(t)$ is the satellite enterprise output; $y(t)$ is the core enterprise output; a_i is the self-regulation of enterprise i; r_i is the intrinsic growth; b_i is the completion rate of satellite enterprise; c_1 is the completion rate between satellite enterprise and core enterprise; c_2 is the rate of conversion of commodity into the reproduction of enterprise; d is the initial output of core enterprise; d_1 is the initial output of satellite enterprisex_1; d_2 is the initial output of satellite enterprise x_2; and $\tau$is the production period. The main contributions of this paper are as follows:

(1) A competition-cooperation enterprise cluster model is composed of a core enterprise and two satellite enterprises. There is a competitive relationship between two satellite enterprises. And there is a cooperative relationship between satellite enterprise and core enterprise.

(2) The boundedness of positive equilibrium is investigated. And there exists a upper limit of output of enterprise cluster model.

(3) The production period plays a key role in dynamics of the proposed enterprise cluster. When it passes a critical value, the output of the enterprise cluster system loses its stability and displays a periodic fluctuation, which may cause a drop in productivity of the enterprise cluster system.

The remainder of this paper is organized as follows. In Section 2, the boundedness analysis of positive equilibrium is given. In Section 3, the conditions of Hopf bifurcation are discussed. In Section 4, the normal form of Hopf bifurcation is given. In Section 5, an example is given to verify the theoretical analysis. In Section 6, we give the economic meaning.

2. Boundedness of Positive Equilibrium

In this section, we investigate the boundedness of positive equilibrium. It can be seen that system (3) has more than three equilibria if any one of the enterprise output is zero. As it has no economic sense if one of the enterprise output is zero, we only study the property of positive equilibrium

where all enterprise outputs are positive. Let $E^* = (x_1^*, x_2^*, y^*)$ be the positive equilibrium of system (3), where

$$x_1^* = \frac{(a_2 r_1 - b_1 r_2) - (a_2 c_1 - b_1 c_2)(y^* - d)^2}{a_1 a_2 - b_1 b_2},$$
$$x_2^* = \frac{(b_2 r_1 - a_1 r_2) - (b_2 c_1 - a_1 c_2)(y^* - d)^2}{b_1 b_2 - a_1 a_2}, \quad (4)$$
$$y^* = \frac{r_3 + c_2\left((x_1^* - d_1)^2 + (x_2^* - d_2)^2\right)}{a_3}.$$

From the perspective of enterprise management, the output of enterprise cannot be negative. Thus, the initial condition of enterprise output must satisfy $x_1(\theta) \geq 0$, $x_2(\theta) \geq 0$, and $y(\theta) \geq 0$ for $\theta \in [-\tau, 0]$. In respect of the boundedness of $E^* = (x_1^*, x_2^*, y^*)$, we have the following lemma.

Lemma 1 (see [21]). *Let $c > 0, d > 0$.*

(1) If $(dx(t)/dt) \geq x(d - cx)$ is satisfied, then $\lim_{t\longrightarrow\infty} \inf x(t) \geq (d/c)$ for all $t \geq 0$ and $x(0) > 0$.

(2) If $(dx(t)/dt) \leq x(d - cx)$ is satisfied, then $\lim_{t\longrightarrow\infty} \sup x(t) \leq (d/c)$ for all $t \geq 0$ and $x(0) > 0$.

Theorem 1

(1) Suppose $x_i(\theta) \geq 0$, $(i = 1, 2), \theta \in [-\tau, 0]$ and $x_i(0) > 0$, $(i = 1, 2), t > 0$; there exists $\psi_i = \psi_i(x_i(\theta)) > 0$, $(i = 1, 2)$ such that $x_i(t) < \psi_i$, $(i = 1, 2)$, where $\psi_1 = \max\{\sup_{-\tau\leq\theta\leq 0} x \leq \theta \leq 0_1(\theta), (r_1/a_1)\}$, $\psi_2 = \max\{\sup_{-\tau\leq\theta\leq 0} x_2(\theta), (r_2/a_2)\}$.

(2) Suppose $y(\theta) \geq 0$, $\theta \in [-\tau, 0]$ and $y(0) > 0, t > 0$; there exists $\psi_3 = \psi_3(y(\theta)) > 0$, such that $y(t) < \psi_3$, where $\psi_3 = \max\{\sup_{-\tau\leq\theta\leq 0} y(\theta), \min\{r_1 - a_1\psi, r_2 - a_2\psi_2\}\}$.

Proof. First, we investigate the boundedness of $x_1(t)$ and $x_2(t)$. By (3), one can obtain $\dot{x}_1(t) \geq 0$ for all $t > T$. Then, we have

$$\frac{dx_1(t)}{dt} \leq x_1(t)(r_1 - a_1 x_1). \quad (5)$$

According to Lemma 1, one has

$$\lim_{t\longrightarrow\infty} \sup x_1 \leq \frac{r_1}{a_1}. \quad (6)$$

Similarly, one has

$$\lim_{t\longrightarrow\infty} \sup x_2 \leq \frac{r_2}{a_2}. \quad (7)$$

If there exists $\{t_n\}_{n=1}^{\infty}$ such that $\dot{x}_1(t_n) \geq 0$ is local max, where $x_1(t) < x_1(t_n) t \in (0, t_n)$, using the same method, one can obtain that $x_1(t)$ has upper limit at $t = t_n$. Thus, one has $\psi_1 = \max\{\sup_{-\tau\leq\theta\leq 0} x_1(\theta), (r_1/a_1)\}$. Similarly, we also can obtain $\psi_2 = \max\{\sup_{-\tau\leq\theta\leq 0} x_2(\theta), (r_2/a_2)\}$.

In this same way, it follows that there exists $\psi_3 > 0$, such that $y(0) < \psi_3$ for $t > 0$, where $\psi_3 = \max\{\sup_{-\tau\leq\theta\leq 0} y(\theta), \min\{r_1 - a_1\psi, r_2 - a_2\psi_2\}\}$. We complete the proof. □

Remark 1. From Theorem 1, one can see that there are upper bounds on the output of core enterprise and two satellite enterprises. Moreover, the upper bound of core enterprise not only depends on its own production capacity but also depends on the production capacity of two satellite enterprises.

3. Bifurcation Analysis

In this section, the conditions of Hopf bifurcation for (3) with $E^* = (x_1^*, x_2^*, y^*)$ are presented. By (3), one can obtain the Jacobian matrix for (3) with E^*:

$$\begin{pmatrix} -a_1 x_1^* & -b_1 x_1^* & -2c_1 x_1^*(y^* - d)e^{-\lambda\tau} \\ -b_2 x_2^* & -a_2 x_2^* & -2c_1 x_2^*(y^* - d)e^{-\lambda\tau} \\ -2c_2 y^*(x_1^* - d_1)e^{-\lambda\tau} & -2c_2 y^*(x_2^* - d_2)e^{-\lambda\tau} & -a_3 y^* \end{pmatrix}. \quad (8)$$

Then, we have

$$\lambda^3 + e_1\lambda^2 + e_2\lambda + e_3 + e^{-2\lambda\tau}(e_4\lambda + e_5) = 0, \quad (9)$$

where

$$\begin{aligned} e_1 &= a_1 x_1^* + a_2 x_2^* + a_3 x_3^*, \\ e_2 &= a_3 y^*(a_2 x_2^* + a_1 x_1^*) + x_1^* x_2^*(a_1 a_2 - b_1 b_2), \\ e_3 &= -4c_1 c_2 y^*(y^* - d_1)[x_1^*(x_1^* - d_1) - x_2^*(x_2^* - d_1)], \\ e_4 &= 4c_1 c_2 x_1^* x_2^* y^*(x_1^* - d_1)(y^* - d_1)(b_1 - a_1) + 4c_1 c_2 x_1^* x_2^* y^*(x_2^* - d_1)(y^* - d_1)(b_2 - a_1), \\ e_5 &= a_3 x_1^* x_2^* y^*(a_1 a_2 - b_1 b_2). \end{aligned} \quad (10)$$

If $i\omega(\omega>0)$ is a root of (9), one can obtain

$$-i\omega^3 - e_1\omega^2 + e_2 i\omega + e_3 i\omega e^{-2i\omega\tau} + e_4 e^{-2i\omega\tau} + e_5 = 0. \quad (11)$$

Separating the real and imaginary parts of (11), we have

$$e_3\omega \sin 2\omega\tau + e_4 \cos 2\omega\tau = e_1\omega^2 - e_5, \quad (12)$$

$$e_3\omega \cos 2\omega\tau - e_4 \sin 2\omega\tau = \omega^3 - e_2\omega. \quad (13)$$

By (12) and (13), one can obtain

$$\omega^6 + f_1\omega^4 + f_2\omega^2 + f_3 = 0, \quad (14)$$

where $f_1 = e_1^2 - 2e_2$, $f_2 = e_2 - 2e_1e_5 - e_3^2$, $f_3 = e_5^2 - e_4^2$.

Let $z=\omega^2$; then, (14) becomes

$$z^3 + f_1 z^2 + f_2 z + f_3 = 0. \quad (15)$$

Letting $z^* = (1/3)(-f_1 + \sqrt{f_1^2 - 3f_2})$, $h(z^*) = (z^*)^3 + f_1(z^*)^2 + f_2 z^* + f_3$, we get the following.

Lemma 2 (see [22–24]).

(i) If $f_3<0$, (15) has at least one positive root.

(ii) If $f_3\geq 0$ and $f_1^2 - fc_2 \leq 0$, (15) has no positive root.

(iii) If $f_3\geq 0$, $f_1^2 - 3f_2 > 0$, $z^*>0$, and $h(z^*)\leq 0$, (15) has positive roots.

Assume (14) has three positive roots $\omega_k = \sqrt{z_k}$, $k=1, 2, 3$. By (12) and (13), we have

$$\cos 2\omega\tau = \frac{e_3\omega^4 + e_1e_4\omega^2 - e_2e_3\omega^2 + e_4e_5}{e_3\omega^2 + e_4^2}. \quad (16)$$

Thus, denote

$$\tau_k^j = \frac{1}{2\omega_k} ar\cos\frac{e_3\omega^4 + e_1e_4\omega^2 - e_2e_3\omega^2 + e_4e_5}{e_3\omega^2 + e_4^2} + \frac{2j\pi}{2\omega_k}, \quad (17)$$

where $k=1, 2, 3$; $j=0, 2, \ldots$. Define $\tau_0 = \tau_{k_0}^0 = \min_{k=1,2,3}\left\{\tau_{k_0}^0\right\}$, $\omega_0 = \omega_{k_0}$.

Note that when $\tau = 0$, (9) becomes

$$\lambda^3 + e_1\lambda^2 + (e_2+e_3)\lambda + e_4 + e_5 = 0. \quad (18)$$

By using the Routh–Hurwitz criterion [16], one can obtain the condition that all roots of (18) have negative real parts.

$$(\mathrm{H1}) e_1(e_2+e_4) - (e_3+e_5) > 0. \quad (19)$$

Lemma 3 (see [25]). *Consider the exponential polynomial*

$$P\left(\lambda, e^{-\lambda\tau}, \ldots\ldots, e^{-\lambda\tau_m}\right) = \lambda^n + p_1^{(0)}\lambda^{n-1} + \ldots\ldots + p_{n-1}^{(0)}\lambda + p_n^{(0)} + \left[p_1^{(1)}\lambda^{n-1} + \ldots\ldots + p_{n-1}^{(1)}\lambda + p_n^{(1)}\right]e^{-\lambda\tau} + \ldots\ldots + \left[p_1^{(m)}\lambda^{n-1} + \ldots\ldots + p_{n-1}^{(m)}\lambda + p_n^{(m)}\right]e^{-\lambda\tau_m}, \quad (20)$$

where $\tau_i\geq 0 (i=1,2,\ldots,m)$ and $(p_j^{(i)} = (j=1,2,\ldots,m)$ are constants. As $(\tau_1,\tau_2,\ldots,\tau_m)$ vary, the sum of the order of the zeros of $P(\lambda, e^{-\lambda\tau},\ldots,e^{-\lambda\tau_m})$ on the open right half plane can change only if a zero appears on or crosses the imaginary axis.

Lemma 4. *If $h'(z_0)\neq 0$, then $\operatorname{sgn}\left\{\operatorname{Re}\left\{((d\lambda/d\tau))^{-1}\right\}\right\}\neq 0$ when $\tau=\tau_0$ and the sign of $h'(z_0)$ is same as the sign of $\operatorname{Re}\{((d\lambda/d\tau))\}|_{\tau=\tau_0}$.*

Proof. Differentiating (9) with respect to τ yields

$$\left\{3\lambda^2 + 2e_1\lambda + e_2 + [e_3 - 2\tau(e_3\lambda + e_4)]e^{-2\lambda\tau}\right\}\frac{d\lambda}{d\tau} = 2\lambda(e_3\lambda + e_4)e^{-2\lambda\tau}. \quad (21)$$

For convenience, we denote ω_0 and τ_0 by ω and τ; then, we have

$$\left(\frac{d\lambda}{d\tau}\right)^{-1} = \frac{(3\lambda^2 + 2e_1\lambda + e_2)e^{2\lambda\tau}}{2\lambda(e_3\lambda + e_4)} + \frac{e_3}{2\lambda(e_3\lambda + e_4)} - \frac{\tau}{\lambda}. \quad (22)$$

Then, we get

$$\begin{aligned}
&\operatorname{Re}\left\{\left(\frac{d\lambda}{d\tau}\right)^{-1}\right\}_{\tau=\tau_0} \\
&= \operatorname{Re}\left\{\frac{(3\lambda^2 + 2e_1\lambda + e_2)e^{2\lambda\tau}}{2\lambda(e_3\lambda + e_4)}\right\}_{\tau=\tau_0} + \operatorname{Re}\left\{\frac{e_3}{2\lambda(e_3\lambda + e_4)}\right\}_{\tau=0} \\
&= \frac{1}{A_k}\left[-2\omega_0(e_2 - 3\omega_0^2)(\omega_0^3 - e_2\omega_0) + 4e_1\omega_0^2(e_1\omega_0^2 - e_5) - 2e_3^2\omega_0^2\right] \\
&= \frac{1}{A_k}\left(6\omega_0^6 + 4f\omega_0^4 + 2f_2\omega_0^2\right) \\
&= \frac{2}{A_k}\left[z_0(3z_0^2 + 2f_1z_0 + f_2)\right] \\
&= \frac{2z_0}{A_k}h'(z_0),
\end{aligned} \quad (23)$$

where $A_k = 4e_3^2\omega_0^4 + 4e_4^2\omega_0^2 > 0$.

Then, if $h'(z_0)\neq 0$, we have $\operatorname{sgn}\left\{\operatorname{Re}\left\{((d\lambda/d\tau))^{-1}\right\}\right\}\neq 0$, and the sign of $h'(z_0)$ is the same as the sign of $\operatorname{Re}\{(d\lambda/d\tau)\}|_{\tau=\tau_0}$. We complete the proof.

Thus, from Lemmas 2, 3, and 4, one has the following. □

Theorem 2. *Suppose that (H1) holds, and we have*

(1) If $f_3 > 0$ and $f_1^2 - 3f_2 \le 0$, (3) is asymptotically stable at E^*.

(2) If either $f_3 < 0$ or $f_3 \ge 0$ and $f_1^2 - 3f_2 > 0$ $z^* > 0$, $h(z^*) \le 0$ holds, (3) is asymptotically stable at E^* for $\tau \in [0, \tau_0)$ and undergoes a Hopf bifurcation at E^* when $\tau = \tau_0$.

4. Direction of the Hopf Bifurcation

In this section, we study the properties of Hopf bifurcation by using the center manifold [23, 26–28]. Letting $x_1 = x_1 - x_1^*, x_2 = x_2 - x_2^*, x_3 = x_3 - x_3^*, \overline{x}_i(t) = x_i(\tau t), \tau = \tau_0 + \mu$, (3) can be transformed into a FDE as

$$\dot{x}(t) = L_\mu(x_t) + f(\mu, x_t), \tag{24}$$

with

$$L_\mu \phi = (\tau_0 + \mu)[B_1 \varphi(0) + B_2 \varphi(-1)], \tag{25}$$

where

$$B_1 = \begin{bmatrix} b_{11} & b_{12} & 0 \\ b_{21} & b_{22} & 0 \\ 0 & 0 & b_{33} \end{bmatrix}, \quad B_2 = \begin{bmatrix} 0 & 0 & b_{13} \\ 0 & 0 & b_{23} \\ b_{31} & b_{32} & 0 \end{bmatrix}, \tag{26}$$

$$f(\mu, \varphi) = (\tau_0 + \mu)\begin{pmatrix} f_1 \\ f_2 \\ f_3 \end{pmatrix}, \tag{27}$$

where

$$\begin{aligned}
f_1 &= b_{14}\varphi_1^2(0) + b_{15}\varphi_1(0)\varphi_2(0) + b_{16}\varphi_3^2(-1) + b_{17}\varphi_1(0)\varphi_3(-1) + b_{18}\varphi_1(0)\varphi_3^2(-1), \\
f_2 &= b_{24}\varphi_1(0)\varphi_2(0) + b_{25}\varphi_2^2(0) + b_{26}\varphi_3^2(-1) + b_{27}\varphi_2(0)\varphi_3(-1) + b_{28}\varphi_2(0)\varphi_3^2(-1), \\
f_3 &= b_{34}\varphi_1^2(-1) + b_{35}\varphi_2^2(-1) + b_{36}\varphi_3^2(0) + b_{37}\varphi_1(-1)\varphi_3(0) \\
&\quad + b_{38}\varphi_2(-1)\varphi_3(0) + b_{39}\varphi_1^2(-1)\varphi_3(0) + b_{39}\varphi_2^2(-1)\varphi_3(0), \\
b_{11} &= -a_1 x_1^*, \\
b_{12} &= -b_1 x_1^*, \\
b_{13} &= -2c_1 x_1^*(y^* - d), \\
b_{14} &= -a_1, \\
b_{15} &= -b_1, \\
b_{16} &= -c_1 x_1^*, \\
b_{17} &= -c_1, \\
b_{18} &= -2c_1 d_1 \\
b_{21} &= -b_2 x_2^*, \\
b_{22} &= -a_2 x_2^*, \\
b_{23} &= -2c_1 x_2^*(y^* - d), \\
b_{24} &= -b_2, \\
b_{25} &= -a_2, \\
b_{26} &= -c_1 x_2^*, \\
b_{27} &= -2c_1 d_1 \\
b_{28} &= -c_1 \\
b_{31} &= -2c_2 y^*(x_1^* - d_1), \\
b_{32} &= -2c_2 y^*(x_2^* - d_2), \\
b_{33} &= --a_3 y^*, \\
b_{34} &= c_2 y^*, \\
b_{35} &= c_2 y^*,
\end{aligned}$$

$$\begin{aligned} b_{36} &= -a_3, \\ b_{37} &= -2c_2d_1, \\ b_{38} &= -2c_2d_2, \\ b_{39} &= c_2. \end{aligned} \tag{28}$$

According to Riesz representation theorem, there exists a function $\eta(\theta,\mu)$ of bounded variation for $\theta \in [-1,0]$, such that

$$L_\mu\varphi = \int_{-1}^{0} \mathrm{d}\eta(\theta,\mu)\varphi(\theta), \quad \varphi \in C. \tag{29}$$

Let

$$\eta(\theta,\mu) = (\tau_0+\mu)\left[B_1\delta(\theta) + B_2\delta(\theta+1)\right], \tag{30}$$

where $\delta(\theta)$ is Dirac delta function.

By [21], we define

$$A(\mu)\varphi = \begin{cases} \dfrac{\mathrm{d}\varphi}{\mathrm{d}\theta}, & \theta \in [-1,0), \\ \displaystyle\int_{-1}^{0} \mathrm{d}\eta(\theta,\mu)\varphi(\theta), & \theta = 0, \end{cases} \tag{31}$$

$$R(\mu)\varphi = \begin{cases} 0, & \theta \in [-1,0], \\ f(\mu,\varphi), & \theta = 0. \end{cases} \tag{32}$$

Then, system (24) can be rewritten as

$$\dot{x}(t) = A(\mu)x_t + R(\mu)x_t, \tag{33}$$

where $x_t(\theta) = x(t+\theta)$.

The adjoint operator $A^*$of A is defined by

$$A^*(\mu)\psi = \begin{cases} -\dfrac{\mathrm{d}\psi(s)}{\mathrm{d}\theta}, & s \in (0,1], \\ \displaystyle\int_{-1}^{0} \mathrm{d}\eta^T(t,0)\psi(-t), & s = 0, \end{cases} \tag{34}$$

where η^T is the transpose of the matrix η.

For $\varphi \in C^1[-1,0]$ and $\psi \in C^1[0,1]$, we define

$$\langle\psi,\varphi\rangle = \overline{\psi}(0)\cdot\varphi(0) - \int_{\theta=-1}^{0}\int_{\xi=0}^{\theta} \overline{\psi}(\xi-\theta)\mathrm{d}\eta(\theta)\varphi(\xi)\mathrm{d}\xi, \tag{35}$$

where $\eta(\theta) = \eta(\theta,0)$. We know that $\pm i\tau_0\omega_0$ is an eigenvalue of $A(0)$, so $\pm i\tau_0\omega_0$ is also an eigenvalue of $A^*(0)$. We can get

$$q(\theta) = \begin{pmatrix} 1 \\ \alpha \\ \beta \end{pmatrix} e^{i\tau_0\omega_0\theta}, \quad -1 < \theta \le 0. \tag{36}$$

By [21], we have

$$Aq(0) = i\tau_0\omega_0 q(0). \tag{37}$$

Hence, one can obtain

$$\alpha = -\frac{b_{21}(i\omega_0 + b_{33}) + b_{31}e^{-2i\omega_0\tau_0}}{(i\omega_0 + b_{22})(i\omega_0 + b_{33}) + b_{32}b_{23}e^{-2i\omega_0\tau_0}}, \tag{38}$$

$$\beta = \frac{(b_{31}(i\omega_0 + b_{22}) - b_{21}b_{32})e^{-i\omega_0\tau_0}}{(i\omega_0 + b_{22})(i\omega_0 + b_{33}) + b_{32}b_{23}e^{-2i\omega_0\tau_0}}. \tag{39}$$

Assume that the eigenvector q^* of $A^*$is

$$q^*(s) = \begin{pmatrix} 1 \\ \alpha^* \\ \beta^* \end{pmatrix} e^{i\tau_0\omega_0 s}. \tag{40}$$

By [21], we have

$$A^*q(0) = -i\tau_0\omega_0 q^*(0). \tag{41}$$

Hence, we obtain

$$\begin{aligned} \alpha^* &= \frac{b_{13}b_{21} + b_{23}(i\omega_0 - b_{11})}{b_{12}b_{23}e^{-i\omega_0\tau_0} + b_{13}(i\omega_0 - b_{22})}, \\ \beta^* &= \frac{((i\omega_0 - b_{11})(i\omega_0 - b_{22}) - b_{12}b_{21})e^{i\omega_0\tau_0}}{(i\omega_0 - b_{22})(b_{13} + b_{21})}. \end{aligned} \tag{42}$$

Let

$$\langle q^*, q\rangle = 1. \tag{43}$$

Then, we can compute

$$\begin{aligned} \langle q^*, q\rangle &= q^*(0)\cdot q(0) - \int_{\theta=-1}^{0}\int_{\xi=0}^{\theta} -q^{*T}(\xi-\theta)\mathrm{d}\eta(\theta)q(\xi)\mathrm{d}\xi \\ &= \frac{1}{\overline{\rho}}\left(1 + \alpha\alpha^* + \beta\beta^*\right) - \int_{\theta=-1}^{0}\frac{\theta}{\overline{\rho}}\tau_0 e^{i\omega_0\tau_0\theta}\left[\left(b_{11} + b_{21}\overline{\alpha}^* + b_{12}\alpha + b_{22}\alpha\overline{\alpha}^* + b_{33}\beta\overline{\beta}^*\right)\delta(\theta)\right. \end{aligned}$$

$$+\left(b_{31}\overline{\beta}^{*}+b_{32}\alpha\overline{\beta}^{*}+b_{13}\beta+b_{23}\overline{\alpha}^{*}\beta\right)\delta(\theta+1)\Big]\mathrm{d}\theta\mathrm{d}\xi$$

$$=\frac{1}{\overline{\rho}}\left(1+\alpha\alpha^{*}+\beta\beta^{*}\right)+\frac{\tau_0}{\overline{\rho}}e^{-i\tau_0\omega_0}\left(b_{31}\overline{\beta}^{*}+b_{32}\alpha\overline{\beta}^{*}+b_{13}\beta+b_{23}\overline{\beta}^{*}\beta\right)$$

$$=1. \tag{44}$$

Hence, we obtain

$$\overline{\rho}=\left(1+\alpha\alpha^{*}+\beta\beta^{*}\right)+\tau_0 e^{-i\tau_0\omega_0}\left(b_{31}\overline{\beta}^{*}+b_{32}\alpha\overline{\beta}^{*}+b_{13}\beta+b_{23}\overline{\alpha}^{*}\beta\right). \tag{45}$$

Assume that x_t is a solution of (33) with $\mu=0$; we define

$$\begin{aligned} z(t)&=\langle q^{*},x_t\rangle,\\ W(t,\theta)&=x_t-2\mathrm{Re}\{z(t)q(\theta)\}. \end{aligned} \tag{46}$$

On C_0, one has

$$W(t,\theta)=W(z,\overline{z},t), \tag{47}$$

where

$$W(z,\overline{z},t)=W_{20}(\theta)\frac{z^2}{2}+W_{11}(\theta)\frac{z\overline{z}}{2}+W_{02}(\theta)\frac{\overline{z}^2}{2}+\cdots. \tag{48}$$

In fact, z and $\overline{z}$ are local coordinates for C_0 in q and q^{*}. As $\mu=0$, we have

$$\begin{aligned} \dot{z}(t)&=\langle q^{*},\dot{x}_t\rangle=\langle q^{*},A(\mu)x_t+R(\mu)x_t\rangle=\langle q^{*},Ax_t\rangle+\langle q^{*},Rx_t\rangle\\ &=i\tau_0w_0z+\overline{q}^{*}(0)\cdot f(0,W(t,0)+2\mathrm{Re}[z(t)q(0)]). \end{aligned} \tag{49}$$

Rewrite (39) as

$$\dot{z}(t)=i\tau_0\omega_0z+g(z,\overline{z}), \tag{50}$$

where

$$g(z,\overline{z})=g_{20}\frac{z^2}{2}+g_{11}z\overline{z}+g_{02}\frac{\overline{z}^2}{2}+g_{21}\frac{z^2\overline{z}}{2}+\cdots. \tag{51}$$

By (37) and (40), one has

$$\dot{W}=\dot{x}_t-\dot{z}q-\dot{\overline{z}}\overline{q}=\begin{cases} AW-2\mathrm{Re}\left[\overline{q}^{*}(0)\cdot f(z,\overline{z})q(\theta)\right], & \theta\in[-2\tau,0),\\ AW-2\mathrm{Re}\left[\overline{q}^{*}(0)\cdot f(z,\overline{z})q(\theta)\right]+f_0(z,\overline{z}), & \theta=0. \end{cases} \tag{52}$$

Let

$$\dot{W}=AW+H(z,\overline{z},\theta), \tag{53}$$

where

$$H(z,\overline{z},\theta)=H_{20}(\theta)\frac{z^2}{2}+H_{11}(\theta)\frac{z\overline{z}}{2}+H_{02}(\theta)\frac{\overline{z}^2}{2}+\cdots. \tag{54}$$

Following the method in [18–21], one can obtain

$$\begin{aligned} (A-2i\omega_0)W_{20}(\theta)&=-H_{20}(\theta),\\ AW_{11}(\theta)&=-H_{11}(\theta),\\ (A+2i\omega_0)W_{02}(\theta)&=-H_{02}(\theta). \end{aligned} \tag{55}$$

Since $x_t=x(t+\theta)=W(z,\overline{z},\theta)+zq+\overline{z}\cdot\overline{q}$, one has

$$x_t=\begin{pmatrix} W^{(1)}(z,\overline{z},\theta)\\ W^{(2)}(z,\overline{z},\theta)\\ W^{(3)}(z,\overline{z},\theta)\end{pmatrix}+z\begin{pmatrix}1\\ q_1\\ q_2\end{pmatrix}e^{i\omega_0\theta}+\overline{z}\begin{pmatrix}1\\ \overline{q}_1\\ \overline{q}_2\end{pmatrix}e^{-i\omega_0\theta}. \tag{56}$$

Thus, one can obtain

$$\begin{aligned} \varphi_1(0)&=z+\overline{z}+W_{20}^{(1)}(0)\frac{z^2}{2}+W_{11}^{(1)}(0)z\overline{z}+W_{02}^{(1)}(0)\frac{\overline{z}^2}{2},\\ \varphi_2(0)&=zq_1+\overline{z}\overline{q}_1^{*}+W_{20}^{(1)}(0)\frac{z^2}{2}+W_{11}^{(1)}(0)z\overline{z}+W_{02}^{(1)}(0)\frac{\overline{z}^2}{2}. \end{aligned} \tag{57}$$

So,

$$\varphi_1(0)\varphi_2(0) = q_1 z^2 + \overline{q}_1 \overline{z}^2 + (q_1 + q_2) z\overline{z} + \left(W_{11}^{(2)} + \frac{1}{2} W_{20}^{(2)} + W_{11}^{(1)} q_1 + \frac{1}{2} W_{20}^{(1)} \overline{q} \right) z^2 \overline{z}. \tag{58}$$

By (27) and (43), one can obtain

$$f(\varphi, \mu) = \begin{pmatrix} K_{11} z^2 + K_{12} z\overline{z} + K_{13} \overline{z}^2 \\ K_{21} z^2 + K_{22} z\overline{z} + K_{23} \overline{z}^2 \\ K_{31} z^2 + K_{32} z\overline{z} + K_{33} \overline{z}^2 \end{pmatrix}, \tag{59}$$

where

$$\begin{aligned}
K_{11} &= b_{14} + \alpha b_{15} + b_{16} \beta^2 e^{-2i\omega_0 \tau_0}, \\
K_{12} &= 2b_{14} + b_{15}\alpha + b_{15}\overline{\alpha} + b_{17}\beta e^{-i\omega_0\tau_0} + 2\beta\overline{\beta} b_{16} + \overline{\beta} b_{17} e^{i\omega_0\tau_0}, \\
K_{13} &= b_{14} + \overline{\alpha} b_{15} + b_{16}\overline{\beta}^2 e^{2i\omega_0\tau_0} + b_{17}\overline{\beta} e^{i\omega_0\tau_0}, \\
K_{14} &= 2b_{14} W_{11}^{(1)}(0) + b_{15} W_{11}^{(2)}(0) + b_{14} W_{20}^{(1)}(0) + \frac{1}{2} b_{15} W_{20}^{(2)}(0) + b_{17} W_{11}^{(3)}(-1) \\
&\quad + \frac{1}{2} b_{17} W_{20}^{(3)}(-1) + \beta^2 b_{18} e^{-2i\omega_0\tau_0} + 2\beta\overline{\beta} b_{18} + b_{15}\alpha W_{11}^{(1)}(0) + b_{17}\beta W_{11}^{(1)}(0) \\
&\quad + 2\beta b_{16} e^{-i\omega_0\tau_0} W_{11}^{(3)}(-1) + \frac{1}{2}\overline{\beta} b_{17} W_{20}^{(1)}(0) e^{i\omega_0\tau_0} + \overline{\beta} b_{16} W_{20}^{(3)}(-1) e^{i\omega_0\tau_0}, \\
K_{21} &= b_{25}\alpha^2 + b_{27}\beta\alpha e^{-i\omega_0\tau_0} + b_{24}\alpha + b_{26}\beta^2 e^{-2i\omega_0\tau_0}, \\
K_{22} &= 2b_{25}\alpha\overline{\alpha} + b_{27}\alpha\overline{\beta} e^{i\omega_0\tau_0} + b_{24}\alpha + b_{27}\overline{\alpha}\beta e^{-i\omega_0\tau_0} + b_{24}\overline{\alpha} + 2b_{26}\beta\overline{\beta}, \\
K_{23} &= b_{25}\overline{\alpha}^2 + b_{27} e^{i\omega_0\tau_0}\overline{\alpha}\overline{\beta} + b_{24}\overline{\alpha} + b_{26}\overline{\beta}^2 e^{2i\omega_0\tau_0}, \\
K_{24} &= 2b_{28}\alpha\beta\overline{\beta} + 2b_5\alpha W_{11}^{(2)}(0) + b_{27}\alpha W_{11}^{(3)}(-1) + b_{24} W_{11}^{(1)}(0)\alpha + b_{28}\overline{\alpha}\beta^2 e^{-2i\omega_0\tau_0} \\
&\quad + b_{25}\overline{\alpha} W_{20}^{(2)}(0) + \frac{1}{2} b_{27}\overline{\alpha} W_{20}^{(3)}(-1) + \frac{1}{2} b_{24}\overline{\alpha} W_{20}^{(1)}(0) + 2b_{26} e^{-i\omega_0\tau_0} W_{11}^{(3)}(-1) \\
&\quad + \frac{1}{2} b_{27} e^{i\omega_0\tau_0}\overline{\beta} W_{20}^{(2)}(0) + b_{26}\overline{\beta} W_{20}^{(3)}(-1) e^{-i\omega_0\tau_0} + b_{24} W_{11}^{(2)}(0) + \frac{1}{2} b_{24} W_{20}^{(2)}(0), \\
K_{31} &= b_{35} e^{-2iw_0\tau_0}\alpha^2 + b_{38} e^{-iw_0\tau_0}\alpha\beta + b_{36}\beta^2 + b_{37} e^{-iw_0\tau_0}\beta + b_{34} e^{-2iw_0\tau_0}, \\
K_{32} &= 2b_{35}\alpha\overline{\alpha} + b_{38}\alpha\overline{\beta} e^{-iw_0\tau_0} + b_{38}\overline{\alpha}\beta e^{iw_0\tau_0} + 2b_{36}\beta\overline{\beta} + b_{37}\beta e^{iw_0\tau_0} + 2b_{34}, \\
K_{33} &= b_{35}\overline{\alpha}^2 e^{iw_0\tau_0} + b_{38}\overline{\alpha}\overline{\beta} e^{iw_0\tau_0} + b_{36}\overline{\beta}^2 + b_{37}\overline{\beta} e^{iw_0\tau_0} + b_{34} e^{2iw_0\tau_0}, \\
K_{34} &= b_{39}\alpha^2\beta e^{-2iw_0\tau_0} + 2b_{39}\alpha\overline{\alpha}\beta + b_{38}\alpha W_{02}^{(2)}(-1) e^{-iw_0\tau_0} + 2b_{35} e^{-iw_0\tau_0}\alpha W_{11}^{(2)}(-1) \\
&\quad + b_{35}\alpha W_{20}^{(2)}(-1) e^{iw_0\tau_0} + 2b_{36}\beta W_{11}^{(3)}(0) + b_{37}\beta W_{11}^{(1)}(-1) + b_{38}\beta W_{11}^{(2)}(-1) \\
&\quad + 2b_{39}\beta + b_{39}\overline{\beta} e^{-2iw_0\tau_0} + b_{37} W_{11}^{(3)}(0) e^{-iw_0\tau_0} + \frac{1}{2} b_{37} W_{20}^{(3)} e^{iw_0\tau_0} \\
&\quad + +2b_{34} W_{11}^{(1)}(-1) e^{-iw_0\tau_0} + b_{34} W_{20}^{(1)}(-1) e^{iw_0\tau_0}.
\end{aligned} \tag{60}$$

As $q^*(0) = (1/\rho)(1, \overline{q}_1^*, \overline{q}_2^*)^T$, one has

$$g(z,\overline{z}) = \frac{1}{\rho}(1,\overline{q}_1^*,\overline{q}_2^*)\begin{pmatrix} K_{11}z^2 + K_{12}z\overline{z} + K_{13}\overline{z}^2 \\ K_{21}z^2 + K_{22}z\overline{z} + K_{23}\overline{z}^2 \\ K_{31}z^2 + K_{32}z\overline{z} + K_{33}\overline{z}^2 \end{pmatrix}. \quad (61)$$

Then, we have

$$\begin{aligned} g_{20} &= \frac{2}{\rho}\left(K_{11} + \overline{\alpha}^* K_{21} + \overline{\beta}^* K_{31}\right), \\ g_{11} &= \frac{1}{\rho}\left(K_{12} + \overline{\alpha}^* K_{22} + \overline{\beta}^* K_{32}\right), \\ g_{02} &= \frac{2}{\rho}\left(K_{13} + \overline{\alpha}^* K_{23} + \overline{\beta}^* K_{33}\right). \end{aligned} \quad (62)$$

Next, we compute $W_{20}(\theta)$ and $W_{11}(\theta)$. According to the expression of g_{21}, we have $H(z,\overline{z},\theta) = -2\mathrm{Re}[\overline{q}^*(0)\cdot f(z,\overline{z})q(\theta)]$.

$$= -\left(g_{20}\frac{z^2}{2} + g_{11}z\overline{z} + g_{02}\frac{\overline{z}^2}{2} + \ldots\right)q(\theta) - \left(\overline{g}_{20}\frac{\overline{z}^2}{2} + \overline{g}_{11}z\overline{z} + \overline{g}_{02}\frac{z^2}{2} + \ldots\right)q(\theta), \quad (63)$$

Comparing the coefficients of (63), one has

$$H_{20}(\theta) = -g_{20}q(\theta) - \overline{g}_{02}\overline{q}(\theta), \quad \theta \in [-1,0), \quad (64)$$

$$H_{11}(\theta) = -g_{11}q(\theta) - \overline{g}_{11}\overline{q}(\theta), \quad \theta \in [-1,0). \quad (65)$$

Substituting (64) and (65) into (55), one can obtain

$$\begin{cases} \dot{W}_{20}(\theta) = 2i\tau_0\omega_0 W_{20}(\theta) + g_{20}q(\theta) + \overline{g}_{20}\overline{q}(\theta), \\ \dot{W}_{11}(\theta) = +g_{11}q(\theta) + \overline{g}_{11}\overline{q}(\theta). \end{cases} \quad (66)$$

So,

$$\begin{cases} W_{20}(\theta) = \dfrac{ig_{20}}{\tau_0\omega_0}q(0)e^{i\tau_0\omega_0\theta} - \dfrac{\overline{g}_{02}}{3i\tau_0\omega_0}\overline{q}(0)e^{-i\tau_0\omega_0\theta} + E_1 e^{2i\tau_0\omega_0\theta}, \\ W_{11}(\theta) = \dfrac{g_{11}}{i\tau_0\omega_0}q(0)e^{i\tau_0\omega_0\theta} - \dfrac{\overline{g}_{11}}{i\tau_0\omega_0}\overline{q}(0)e^{-i\tau_0\omega_0\theta} + E_2. \end{cases} \quad (67)$$

Now, we compute E_1 and E_2. From the definition of A in (31), one can obtain

$$\int_{-1}^{0} d\eta(\theta)W_{20}(\theta) = 2i\tau_0\omega_0 W_{20}(0) - H_{20}(0), \quad (68)$$

$$\int_{-1}^{0} d\eta(\theta)W_{11}(\theta) = -H_{11}(0). \quad (69)$$

From (50), (68), and (69), we have

$$\begin{aligned} H_{20}(\theta) &= -g_{20}q(\theta) - \overline{g}_{02}\overline{q}(\theta) + (K_{11}, K_{21}, 0)^T, \\ H_{11}(\theta) &= -g_{11}q(\theta) - \overline{g}_{11}\overline{q}(\theta) + (K_{12}, K_{22}, 0)^T. \end{aligned} \quad (70)$$

Following the method in [18–21], we have

$$\begin{aligned} \left(i\omega_0 I - \int_{-1}^{0} e^{i\omega_0\theta}d\eta(\theta)\right)q(0) &= 0 \\ \left(-i\omega_0 I - \int_{-1}^{0} e^{-i\omega_0\theta}d\eta(\theta)\right)\overline{q}(0) &= 0. \end{aligned} \quad (71)$$

Then, we can obtain

$$\left(2i\omega_0 I - \int_{-1}^{0} e^{2i\tau_0\omega_0\theta}d\eta(\theta)\right)E_1 = (K_{11}\ \ K_{21}\ \ 0)^T, \quad (72)$$

which leads to

$$\begin{pmatrix} 2i\omega_0 + b_{11} & b_{12} & b_{13}e^{-i\omega_0\tau_0} \\ b_{21} & 2i\omega_0 + b_{22} & b_{23}e^{-i\omega_0\tau_0} \\ -b_{31}e^{-i\omega_0\tau_0} & -b_{32}e^{-i\omega_0\tau_0} & 2i\omega_0 + b_{33} \end{pmatrix}E_1 = \begin{pmatrix} K_{11} \\ K_{21} \\ K_{31} \end{pmatrix}, \quad (73)$$

and

$$\begin{pmatrix} -b_{11} & -b_{12} & -b_{13} \\ -b_{21} & -b_{22} & -b_{23} \\ b_{31} & b_{32} & -b_{33} \end{pmatrix}E_2 = \begin{pmatrix} K_{12} \\ K_{22} \\ K_{32} \end{pmatrix}. \quad (74)$$

Then, by (72) and (74), we can obtain the following properties of Hopf bifurcation:

$$\begin{aligned} \mu_2 &= -\frac{\mathrm{Re}C_1(0)}{\mathrm{Re}\lambda'(\tau_0)}, \\ T_2 &= -\frac{\mathrm{Im}C_1(0) + \mu_2\mathrm{Im}\lambda'(0)}{\omega_0}, \\ \beta_2 &= -2\mathrm{Re}C_1(0). \end{aligned} \quad (75)$$

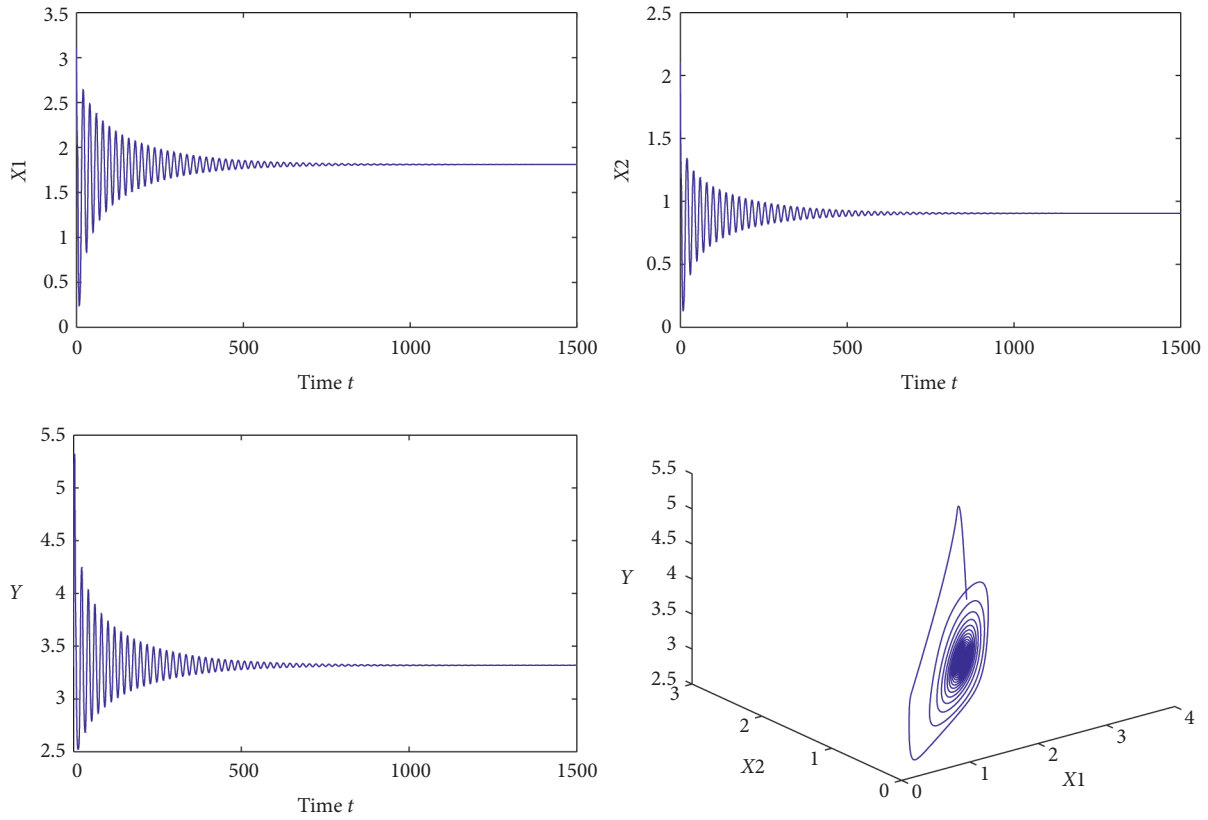

Figure 2: $\tau = 4.05 < \tau_0$. The positive equilibrium of system (3) is asymptotically stable.

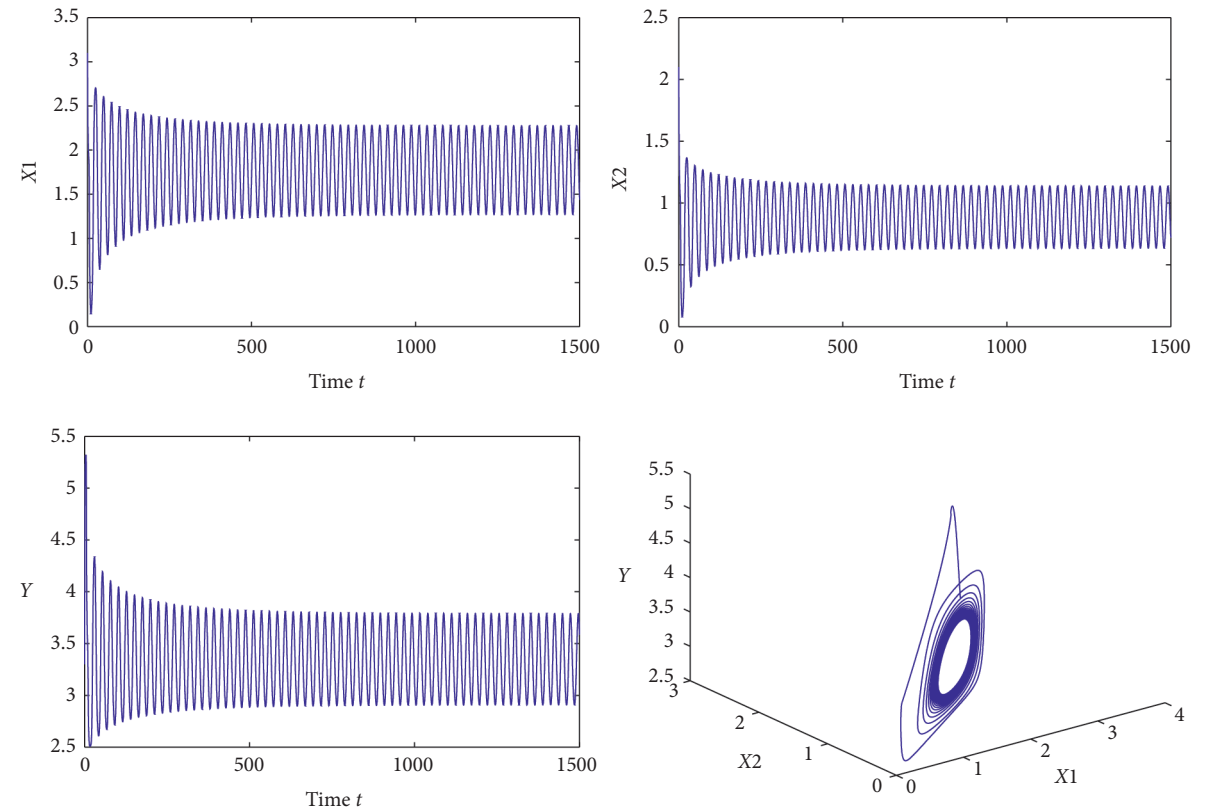

Figure 3: $\tau = 4.25 > \tau_0$. The bifurcation periodic solution is stable.

Theorem 3. *From (75), one has*

(1) The directions of the Hopf bifurcation is determined by $sign(\mu_2)$*: if* $\mu_2 > 0\,(\mu_2 < 0)$*, then the Hopf bifurcation is forward (backward) and the bifurcating periodic solutions exist for* $\tau > \tau_0\,(\tau < \tau_0)$.

(2) The stability of the bifurcating periodic solutions is determined by $sign(\beta_2)$*: the bifurcating periodic solutions are stable (unstable) if* $\beta_2 < 0\,(\beta_2 > 0)$.

(3) The period of the bifurcating periodic solutions is determined by $sign(T_2)$*: the period increases (decreases) if* $T_2 > 0\,(T_2 < 0)$.

5. Numerical Examples

In this section, a numerical example is presented to support our obtained results. Consider system (3) with the following parameters: $r_1 = r_2 = r_3 = 1$, $c_1 = 0.05$, $c_2 = 0.081$, $d_1 = d_2 = d = 0.01$, $a_1 = 0.2$, $a_2 = 0.3$, $a_3 = 0.4$, $b_1 = 0.1$, and $b_2 = 0.1$. The positive equilibrium of (3) is $(1.8155,\ 0.9077,\ 3.3149)$. By (17), we can obtain $\tau_0 = 4.15$.

First, we choose $\tau = 4.1 < \tau_0$, and the outputs of three enterprises are shown in Figure 2. It is easy to see that output of enterprise is asymptotically stable.

Finally, we choose $\tau = 4.25 > \tau_0$, and the outputs of three enterprises are shown in Figure 3; it is easy to see that the output of the enterprise displays a periodic fluctuation.

6. Economic Meaning

In this paper, a novel competition-cooperation enterprise cluster model with core-satellite structure is proposed. The boundedness of the positive equilibrium is investigated. It is found that there exists upper bound of both core enterprise output and satellite enterprise output and the upper bound of core enterprise not only depends on its own production capacity but also depends on the production capacity of two satellite enterprises. Moreover, it is found that the production period plays a key role on the evolution of enterprise cluster. From simulation, we can obtain that the critical value of the production period is $\tau_0 = 4.15$. When the production period passes $\tau_0 = 4.15$, the output of the enterprise cluster system loses its stability and displays a periodic fluctuation, which means too long production cycle will lead to capacity fluctuations. From the viewpoint of enterprise management, output fluctuation may affect the stable development of enterprises, worker employment, and production efficiency. Thus, it is important for enterprise cluster to control the production period in a suitable region.

Data Availability

The data used to support the findings of this study are available from the corresponding author upon request.

Conflicts of Interest

The authors declare that they have no conflicts of interest.

Acknowledgments

This study was supported in part by the Chongqing Social Science Planning Project under grant no. 2019BS053, in part by the Science and the Technology Research Program of Chongqing Municipal Education Commission under grant no. KJQN201900816, in part by the Social Science Research Program of Chongqing Municipal Education Commission under grant no. 20SKJD072 in part by the Research Funds of Chongqing Technology and Business University under grant no. 1955028, and in part by the Chongqing Basic and Frontier Research Project under grant nos. cstc2019jcyj-msxmX0470 and cstc2020jcyj-msxmX0139.

References

[1] W. Souza, G. Scur, and W. Hilsdorf, "Eco-innovation practices in the brazilian ceramic tile industry: the case of the Santa Gertrudes and Criciúma clusters," *Journal of Cleaner Production*, vol. 199, pp. 1007–1019, 2018.

[2] G. Buenstorf and C. Costa, "Drivers of spin-off performance in industry clusters: embodied knowledge or embedded firms?" *Research Policy*, vol. 47, no. 3, pp. 663–673, 2018.

[3] S. W. Ximenes, S. Roberts, T. S. Lee, H.-S. Shin, B. Foing, and C. Duarte, "LEAP2 and LCATS industry clusters: a framework for lunar site technology development using global, space-STEM education and global space-industry development networks," *Acta Astronautica*, vol. 157, pp. 61–72, 2019.

[4] N. L. Duc and J. Lindeque, "Proximity and multinational enterprise co-location in clusters: a multiple case study of Dutch science," *Industry & Innovation*, vol. 25, no. 3, pp. 282–307, 2018.

[5] R. Zhou, "Empirical Analysis of the Impact Which the Shared Resources Have on the Competitive Advantages of the Logistics Enterprise in Logistics Industry Clusters," *Geo-Informatics in Resource Management and Sustainable Ecosystem*, pp. 60–69, 2017.

[6] D. Janasová, V. Bobáňová, and S. Strelcová, "Networking of small and medium enterprises into clusters in the Slovak republic," *Procedia Engineering*, vol. 192, pp. 370–375, 2017.

[7] L. Chen, Y. Zhou, D. Zhou, and L. Xue, "Clustering enterprises into eco-industrial parks: can interfirm alliances help small and medium-sized enterprises?" *Journal of Cleaner Production*, vol. 168, pp. 1070–1079, 2017.

[8] J. Zhao, C. Luo, and Y. Zheng, "Evolutionary dynamics of the cooperation clusters on interdependent networks," *Physica A: Statistical Mechanics and Its Applications*, vol. 517, pp. 132–140, 2019.

[9] L. Trujillo, J. Campos, and I. Pérez, "Competition vs. cooperation between neighbouring ports: a case study in Chile," *Research in Transportation Business & Management*, vol. 26, pp. 100–108, 2018.

[10] C. Xu, "Periodic behavior of competition and corporation dynamical model of two enterprises on time scales," *Journal of Quantitative Economics*, vol. 29, no. 2, pp. 1–4, 2012.

[11] D. Jana, P. Dolai, A. K. Pal, and G. P. Samanta, "On the stability and Hopf-bifurcation of a multi-delayed competitive population system affected by toxic substances with imprecise biological parameters," *Modeling Earth Systems and Environment*, vol. 2, pp. 110–127, 2016.

[12] G. P. Samanta, "A two-species competitive system under the influence of toxic substances," *Applied Mathematics and Computation*, vol. 216, no. 1, pp. 291–299, 2010.

[13] A. K. Pal, P. Dolai, and G. P. Samanta, "Dynamics of a delayed competitive system affected by toxic substances with imprecise biological parameters," *FILOMAT*, vol. 31, no. 16, pp. 5271–5293, 2017.

[14] X. Yang, Z. Zhu, H. Yu, Y. Zhao, and L. Guo, "Evolutionary Game Dynamics of the Competitive Information Propagation on Social Networks," *Complexity*, vol. 2019, Article ID 8385426, 11 pages, 2019.

[15] Z. Liu, Y. Liu, and H. Li, "A Coordination Mechanism of Supply Chain with a Retailer and Two Competitive Suppliers," *Complexity*, vol. 2020, Article ID 2128497, 14 pages, 2020.

[16] H. Zhou, "Enterprises cluster co-existence model and stability analysis," *Systems Engineering*, vol. 21, no. 4, pp. 32–37, 2003.

[17] Q. Guo, "Competitive strategies in an enterprise: an ecological model," *Geological Technoeconomic Management*, vol. 27, no. 2, pp. 49–52, 2005.

[18] Z. Wang and R. Pan, "Analysis to the equilibrium of industrial clusters based on ecological model," *Statistical Thinktank*, vol. 8, pp. 32–35, 2008.

[19] M. Liao, C. Xu, and X. Tang, "Dynamical behaviors for a competition and cooperation model of enterprises with two delays," *Nonlinear Dynamics*, vol. 75, no. 1-2, pp. 257–266, 2014.

[20] M. Liao, C. Xu, and X. Tang, "Stability and Hopf bifurcation for a competition and cooperation model of two enterprises with delay," *Communications in Nonlinear Science and Numerical Simulation*, vol. 19, no. 10, pp. 3845–3856, 2014.

[21] Y. Li and T. Zhang, "Global asymptotical stability of a unique almost periodic solution for enterprise clusters based on ecology theory with time-varying delays and feedback controls," *Communications in Nonlinear Science and Numerical Simulation*, vol. 17, no. 2, pp. 904–913, 2012.

[22] W. Hu, H. Zhao, and T. Dong, "Dynamic analysis for a kaldor-kalecki model of business cycle with time delay and diffusion effect," *Complexity*, vol. 2018, Article ID 1263602, 11 pages, 2018.

[23] T. Dong and Q. Zhang, "Stability and oscillation analysis of a gene regulatory network with multiple time delays and diffusion rate," *IEEE Transactions on NanoBioscience*, vol. 19, no. 2, pp. 285–298, 2020.

[24] T. Dong and L. Xia, "Spatial temporal dynamic of a coupled reaction-diffusion neural network with time delay," *Cognitive Computation*, vol. 11, no. 2, pp. 212–226, 2019.

[25] S. Ruan and J. Wei, "On the zeros of transcendental functions with applications to stability of delay differential equations with two delays," *Dynamics.of Continous Discrete Impulsive Systems Series. Applications and Algorithms.*vol. 10, pp. 863–873, 2003.

[26] B. Hassard, N. Kazarinoff, and Y. Wan, *Theory and Applications of Hopf Bifurcation*, Cambridge University Press, Cambridge, UK, 1981.

[27] X. Zhang and Z. Liu, "Hopf bifurcation analysis in a predator-prey model with predator-age structure and predator-prey reaction time delay," *Applied Mathematical Modelling*, vol. 91, pp. 530–548, 2021.

[28] X. Zhang and Z. Liu, "Periodic oscillations in HIV transmission model with intracellular time delay and infection-age structure," *Communications in Nonlinear Science and Numerical Simulation*, vol. 91, Article ID 105463, 2020.

Hindawi
Complexity
Volume 2021, Article ID 5515549, 13 pages
https://doi.org/10.1155/2021/5515549

Research Article

Coevolving Dynamics between Epidemic and Information Spreading considering the Dependence between Vigilance and Awareness Prevalence

Yixiao Zhang,[1] Xing Lu,[1] Ni Cui,[1] Jingtai Tang,[2] and Xiyun Zhang[1]

[1]*Department of Physics, Jinan University, Guangzhou, Guangdong 510632, China*
[2]*School of Journalism and Communication, Jinan University, Guangzhou, Guangdong 510632, China*

Correspondence should be addressed to Ni Cui; cuinicn@outlook.com, Jingtai Tang; tangjingtai@jnu.edu.cn, and Xiyun Zhang; zxy_822@126.com

Received 24 February 2021; Accepted 11 May 2021; Published 24 May 2021

Academic Editor: Chenquan Gan

It has been demonstrated that the propagation of information and awareness regarding a disease can assist in containing the outbreak of epidemics. Previous models for this coevolving usually introduced the dependence between these two processes by setting a lower but time-independent infection rate for individuals with awareness. However, a realistic scenario can be more complicated, as individual vigilance and the adopted protective measures may depend on the extent of the discussion on the disease, whereas individuals may be irrational or lack relevant knowledge, leading to improper measures being taken. These can introduce a time-varying dependence between epidemic dynamics and awareness prevalence and may weaken the effect of spreading awareness in containing a pandemic. To better understand this effect, we introduce a nonlinear dependence of the epidemic infection rate on awareness prevalence, focusing on the effect of different forms of dependence on the coevolving dynamics. We demonstrate that a positive correlation between vigilance and awareness prevalence can enhance the effect of information spreading in suppressing epidemics. However, this enhancement can be weakened if some individuals are irrational. Our results demonstrate the importance of rational behavior in the strategy of containing epidemics by propagation of disease information.

1. Introduction

Fighting a pandemic is a major challenge. Therefore, understanding the dynamics of epidemic spreading and determining an efficient strategy to contain a pandemic have attracted considerable attention in complex networks [1]. Various factors and effects have been discussed, from the network topology and competition between viruses to human behavior and robustness of the health system [2–12]. With the rapid development of modern techniques, the pattern of epidemic spreading has also changed. For instance, the development of modern airline transportation facilitates long-distance travel; however, it also promotes the spread of pathogens, such as the epidemic of SARS [13–15] and the novel influenza A (H_1N_1) [16–18]. High-speed trains are the best choice for intermediate-distance travel in several countries; however, the high passenger density on these trains can also accelerate the spread of viruses [19]. Cold chain logistics has become one of the most important techniques to ensure food supply. Recently, during the COVID-19 pandemic, it was found that this food transport technique can also carry pathogens and cause local epidemic events [20]. Therefore, there is an increasing demand for more realistic models to better understand epidemic spreading.

One of the characteristics of modern living is the omnipresence of information. Reading news, browsing webpages, and participating in online social networks have become important parts of our daily lives. Messages received through these activities can influence our decision making, can change our behaviors, and, as a result, may also impact the pattern of epidemic spreading [21–24]. Therefore,

understanding the effect of information propagation on the spread of a disease has attracted considerable attention. Models have been proposed to investigate the suppressive effect of spreading awareness on epidemic propagation, focusing on different mechanisms, such as nonlinear coupling [22, 23, 25–29] and competition [30–33].

Recent studies on the coevolution dynamics between information and disease spreading usually assume that the response of individuals to messages is independent of time, and the response to information is manifested by a relatively lower infection rate for individuals with awareness. However, a realistic situation can be more complicated: an individual may not immediately take the highest level of protective measures when he/she receives information regarding the epidemic. The level of protective measures is usually upgraded when individuals become more vigilant or frightened. Recently, it has been demonstrated that this vigilance (or fear) is related to the prevalence of public discussion on epidemics [34–36]. Therefore, it is possible that individuals become more vigilant and upgrade their protective measures when they receive more information regarding the pandemic. That is, there could be a positive correlation between the prevalence of the spreading of awareness of a disease and the protective measures taken by individuals. To better illustrate this, we collected data on COVID-19 in China [37] and the corresponding online discussion on *Sina Weibo*, the largest microblogging system in China. Figure 1 shows a plot of the number of existing cases of COVID-19 (red line), representing the prevalence of the epidemic, and the number of discussions on the epidemic on *Sina Weibo* (green line). As *disinfection* is one of the main protective measures taken by individuals to prevent the spread of epidemics, the prevalence of discussions on disinfection can thus reflect the level of vigilance or fear of the pandemic. Thus, we also indicate the prevalence of discussions on disinfection on *Sina Weibo* (blue line). As shown in Figure 1, the heat of the discussion changes with the prevalence of the epidemic in general; that is, the heat of the discussion increases quickly when the epidemic starts and gradually decreases after the epidemic is contained. However, the short-term fluctuation does not exactly reflect the trend of the epidemic. For instance, there is a peak in the heat of the discussion on *Sina Weibo* around the beginning of April 2020, when the number of existing infected cases continuously decreased. This peak was due to the Qingming day, the traditional tomb-sweeping day in China. A memorial service was held this day; thus, an increase in the discussion on *Sina Weibo* appeared. Nevertheless, the discussion on *disinfection*, which can represent the level of vigilance of individuals, follows the heat of the discussion on the epidemic. This indicates that the vigilance of individuals does not always follow the development of the epidemic but the heat of the discussion. Therefore, the effect of the dependence between individual vigilance and the prevalence of the discussion on the coevolving dynamics of information and epidemic spreading is worth investigating.

Previous studies on the coevolving dynamics of information and epidemic spreading usually assume that individuals are rational and can take proper protective measures. However, during a pandemic, not all individuals are rational. Irrational behaviors, such as irrational beliefs [38], irrational antimicrobial prescribing [39], and panic buying [40], cannot protect individuals from the epidemic. On the contrary, these irrational behaviors may facilitate the spread of the epidemic by inducing individuals to take improper protective measures. Therefore, the spread of awareness of the disease can suppress the epidemic when individuals can take proper protective measures. However, it may also facilitate the spread of the disease if individuals are irrational and take inadequate measures. This leads to a negative correlation between the efficiency of individual protective measures and the prevalence of the discussion for irrational individuals.

In this study, based on the framework of the coevolving dynamics of information and disease spreading in two-layer networks, we consider the effect of dependence between individual vigilance and the prevalence of the discussion. Using brief analytics and numerical simulations, we demonstrate that a positive dependence can assist in containing the spread of the epidemic. In some cases, strong individual vigilance can suppress the size of the final outbreak even without increasing the awareness of the population. However, irrational individuals can weaken this suppressive effect. In some extreme cases, when most individuals are irrational, the spreading of information can no longer suppress epidemics.

The remainder of this paper is organized as follows. In Section 2, we introduce the dynamic model. In Section 3, we briefly provide a theoretical analysis. The results for various scenarios are presented in Section 4. The conclusions are presented in Section 5.

2. Model

The model contains two components, as shown in Figure 2. The unaware-aware-unaware (UAU) dynamics describe information spreading. An individual can become aware when (i) he/she is infected by the disease or (ii) through communication with aware neighbors (with probability λ). At each step, each individual becomes unaware with probability δ. In the contagion network, a susceptible-infected-susceptible (SIS) model is used to describe the spread of the disease. The infection rates are β^U and β^A for individuals with and without awareness, respectively. As an individual will take protective measures when he/she becomes aware of the disease, we assume that $\beta^A = \gamma\beta^U$, where $0 \le \gamma \le 1$ is related to individual vigilance. The recovery rate for the SIS model is μ.

To incorporate the dependence between individual vigilance and the prevalence of awareness of the disease, we now investigate two specific forms of dependence, where ρ_A is the ratio of the population with awareness:

$$\text{Dependence 1: } \gamma = (1-\rho_A)^x, \text{ with } x > 0$$

$$\text{Dependence 2: } \gamma = x^{-\rho_A}, \text{ with } x > 1$$

Notably, the dynamics of the model are similar to those of the model in [30]. The difference is that we introduce a dependence between the protective efficiency of individuals

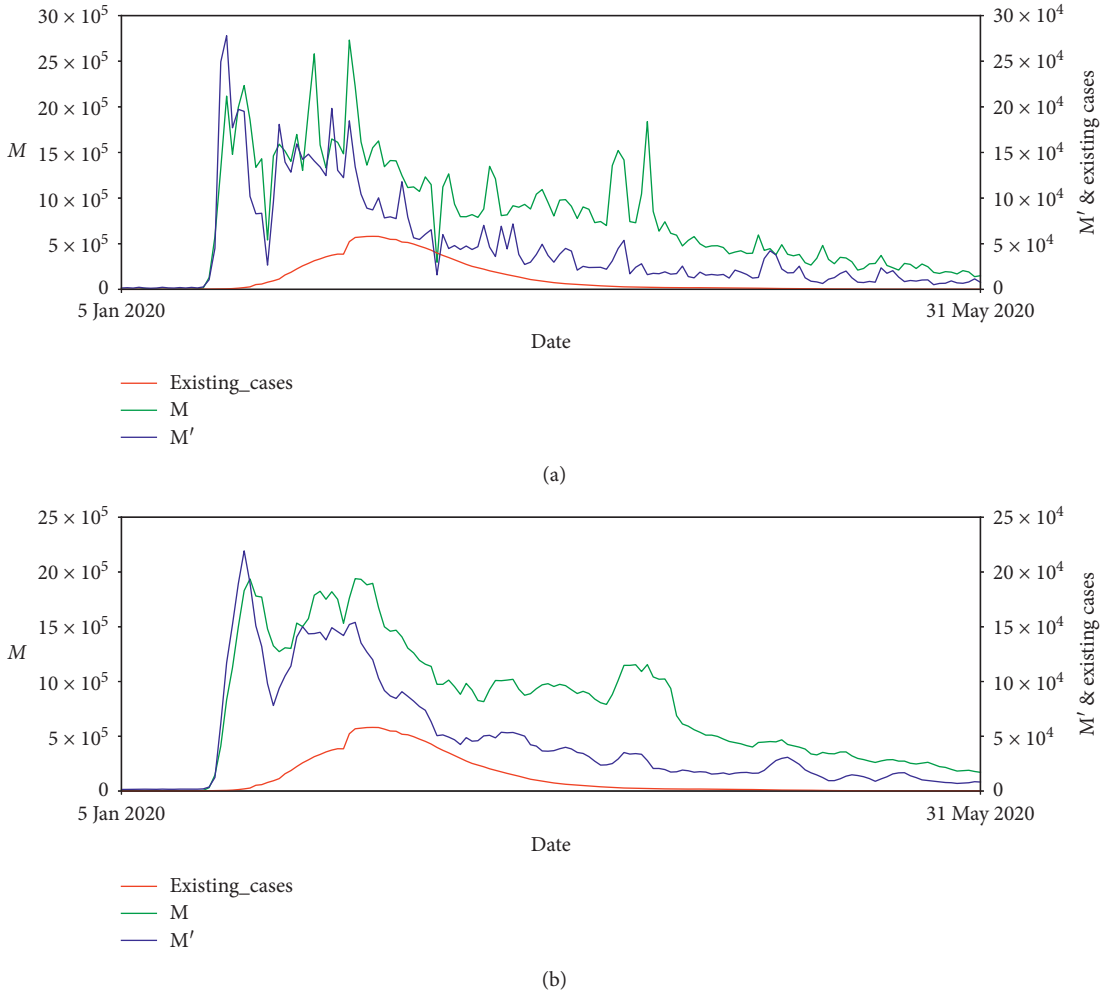

Figure 1: (a) Number of existing cases of COVID-19 in China (red line), number of discussions about COVID-19 (M) (green line), and disinfection on *Sina Weibo* (M', blue line). (b) Smoothed curves in (a) using nonoverlapping windows, $w = 5$.

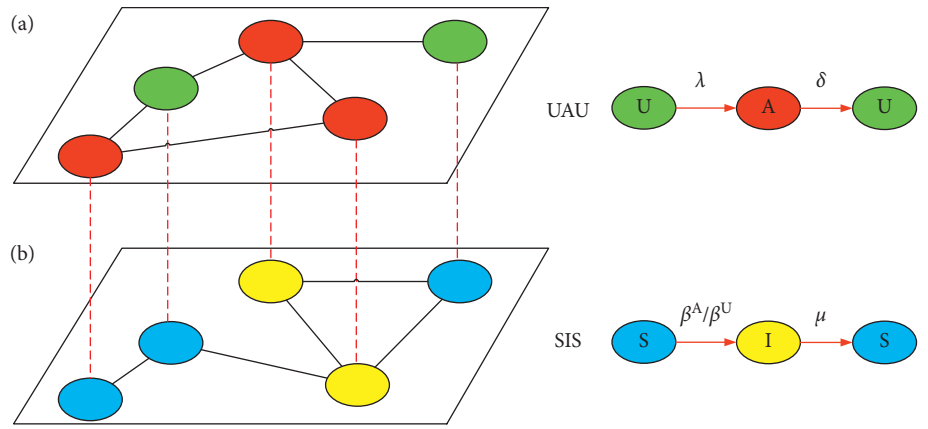

Figure 2: Schematic of the model. The dynamics of information spreading are described using the UAU model in the information network. The epidemic spreading process is described by the SIS model in the contagion network.

and the prevalence of awareness. Therefore, parameter γ is not constant, but it changes with the spreading of awareness.

3. Model Analysis

In the model, each individual can be unaware (U) or aware (A) and susceptible (S) or infected (I). According to the dynamics, three states are possible in the system: US, AS, and AI. We note that the UI state is erroneous because an individual will become aware of the disease immediately when he/she is infected. Here, we only include the correlation between ρ_A and γ; the transition trees for the possible states in our model are the same as those in [30], as shown in Figure 3. Therefore, we can also apply the microscopic Markov chain approach (MMCA) to analyze the coevolution dynamics between information spreading and disease spreading [30, 41–43].

We denote by a_{ij} and b_{ij} the adjacency matrices of the information- and disease-spreading networks, respectively. The probability that node i is in one of the three states at time t is denoted by $p_i^{AI}(t)$, $p_i^{AS}(t)$, and $p_i^{US}(t)$. The transition probability for node i from unaware to aware is $r_i(t)$. The probabilities for the transition from susceptible to infected are $q_i^A(t)$ and $q_i^U(t)$ for nodes with and without awareness, respectively. These probabilities can be estimated as

$$r_i(t) = \prod_j \left[1 - a_{ij} p_j^A(t)\lambda\right], \tag{1}$$

$$q_i^A(t) = \prod_j \left[1 - b_{ij} p_j^{AI}(t)\beta^A\right], \tag{2}$$

$$q_i^U(t) = \prod_j \left[1 - b_{ij} p_j^{AI}(t)\beta^U\right], \tag{3}$$

where $p_j^A(t) = p_j^{AI}(t) + p_j^{AS}(t)$. Therefore, according to the transition trees shown in Figure 3 and the transition probabilities calculated using equations (1)–(3), the microscopic Markov chains for the dynamics of each node can be obtained as

$$\begin{aligned}
p_i^{US}(t+1) &= p_i^{AI}(t)\delta\mu + p_i^{US}(t) r_i(t) q_i^U(t) + p_i^{AS}(t)\delta q_i^U(t),\\
p_i^{AS}(t+1) &= p_i^{AI}(t)(1-\delta)\mu + p_i^{US}(t)\left(1 - r_i(t)\right) q_i^A(t) + p_i^{AS}(t)(1-\delta) q_i^A(t),\\
p_i^{AI}(t+1) &= p_i^{AI}(t)(1-\mu) + p_i^{US}(t)\left\{\left[1 - r_i(t)\right]\left[1 - q_i^A(t)\right] + r_i(t)\left[1 - q_i^U(t)\right]\right\}\\
&\quad + p_i^{AS}(t)\left\{\delta\left[1 - q_i^U(t)\right] + (1-\delta)\left[1 - q_i^A(t)\right]\right\}.
\end{aligned} \tag{4}$$

The stationary state of the system can be estimated by the stationary state in equation (4). The populations of infected nodes and nodes with awareness are defined as $\rho_I = (1/N)\sum_i p_i^I$ and $\rho_A = (1/N)\sum_i p_i^A$, respectively.

4. Results

To quantitatively study the effect of different forms of dependence between individual vigilance and the prevalence of the discussion on the spread of the epidemic, we now focus on the two functional forms by comparing the results of a simulation with the theoretical estimation from equation (4). The simulation results were obtained by averaging the results from 30 independent realizations, based on Erdös–Rényi (ER) random networks, with $N = 1000$ nodes, and average degree $\langle k\rangle = 12$ for the information network and $\langle k\rangle = 10$ for the disease network. The recovery rates were set to $\delta = 0.6$ and $\mu = 0.4$. The theoretical estimation was obtained by iterating equation (4) until a stationary state was reached. For simplicity, we define $\beta^U = \beta$. The reproduction rate $R_0 = (\beta\langle k_b\rangle/\mu)$ is the key factor that determines the spread of the disease. Thus, we focus on the spreading pattern for different R_0.

As described in the model, individuals with awareness will take protective measures, leading to a reduced infection rate $\beta^A = \gamma\beta^U$ with $\gamma \le 1$. Therefore, the reproduction rate R_0 for individuals with awareness is also reduced. As individual vigilance can change with the prevalence of the discussion about the epidemic, we introduce a function for the dependence between γ and ρ_A. Figure 4(a) shows a plot of the first function $\gamma = (1 - \rho_A)^x$. As x increases, ρ_A decreases faster with an increase in ρ_A, indicating a faster increase in individual vigilance. As a result, a larger x results in a lower ratio of infected nodes, as well as a lower ratio of nodes with awareness, as shown in Figures 4(b)–4(d). Notably, for large R_0, ρ_A saturates and does not increase; however, a larger x can suppress the spread of the epidemic owing to the increase in the individual vigilance. Figures 4(e) and 4(f) show the dependence of the critical infection rate R_{0c} on x and λ. As in [30], increasing the information propagation rate λ holds back the outbreak of the epidemic. In addition, a smaller x can also significantly delay the outbreak of the epidemic, indicating that a positive correlation between individual vigilance and the prevalence of discussion can indeed suppress the outbreak of the epidemic.

Regarding the second form of $\gamma = x^{-\rho_A}$, Figure 5(a) shows that the level of vigilance also increases with x, as is the case with the first form in Figure 4. Thus, a larger x also leads to a lower ratio of infected population (Figures 5(b)–5(d)) and a larger critical infection rate R_{0c} (Figures 5(e) and 5(f)). Combining the results of the different forms of dependence between γ and ρ_A (Figures 4 and 5), we can conclude that a positive correlation between individual vigilance and the prevalence of discussion can significantly assist in containing the epidemic. In addition, when ρ_A saturates for large β, increasing individual vigilance can further suppress the epidemic.

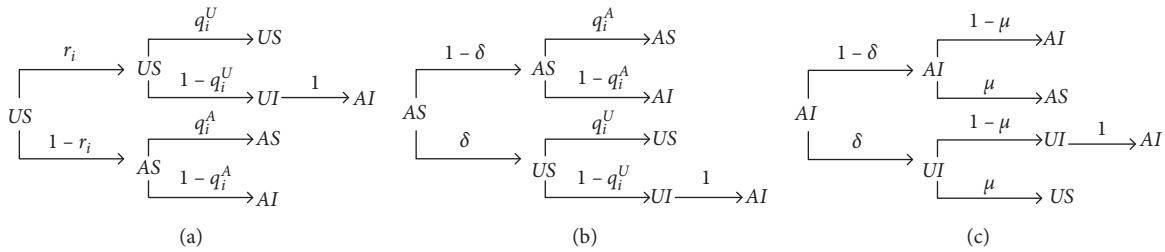

Figure 3: Probability trees for the transition for the possible states at each time step for the model. The four possible states are aware-infected (AI), aware-susceptible (AS), unaware-infected (UI), and unaware-susceptible (US). The transition probabilities are r_i from U to A, q_i^A from S to I if node i is aware, q_i^U from S to I if node i is unaware, δ from A to U, and μ from I to S.

Figures 4 and 5 show an intersection of ρ_A in the middle range of R_0. For small R_0, the population with awareness ρ_A for high vigilance (larger x in Figures 4 and 5) is lower than that for low vigilance, and it reverses when R_0 becomes large. This implies that high vigilance has a stronger suppressive effect on the spread of the epidemic but does not always result in a lower ratio of ρ_A owing to the containment of the epidemic. For small R_0, high vigilance can suppress the spread of both epidemic and information, whereas, for large R_0, high vigilance can suppress the epidemic but can slightly facilitate the spread of information. This can be understood from the first equation in equation (4). The stationary state $p_i^{US}(t+1) = p_i^{US}(t)$ yields $p_i^{US} = ((p_i^{AI}\delta\mu + p_i^{AS}\delta q_i^U)/(1 - r_i q_i^U))$. In the case of a low infection rate, the infected population is small ($\rho_I \ll 1$), and $p_i^{AI} \ll p_i^{AS}$ leads to $p_i^{US} \approx ((p_i^{AS}\delta q_i^U)/(1 - r_i q_i^U))$. The term $r_i q_i^U$ in the denominator is a high-order small quantity compared with the numerator, and the fluctuation of p_i^{US} primarily depends on the fluctuation of p_i^{AS} and q_i^U. When vigilance increases, ρ_I tends to decrease, leading to higher p_i^{AS} and q_i^U (estimated from equation (3)). Therefore, a higher vigilance level can lead to a higher p_i^{US}, resulting in a decrease in ρ_A because of the relation $\rho_A = 1 - \sum_i p_i^{US}$. In the case of a high infection rate, $p_i^{AI} \gg p_i^{AS}$ and thus $p_i^{US} = (p_i^{AI}\delta\mu/(1 - r_i q_i^U))$, where the fluctuation of p_i^{US} primarily depends on the fluctuation of p_i^{AI}. For a higher vigilance level, p_i^{AI} tends to decrease, resulting in a decrease in p_i^{US} and, thus, an increase in ρ_A. These different behaviors for small and large R_0 underlie the observed intersection of ρ_A for different vigilance levels in the intermediate range of the infection rate.

We have demonstrated that the dependence of γ on ρ_A can assist in suppressing the spread of the epidemic, assuming that all individuals are rational—higher prevalence of the discussion about the disease leads to a higher level of vigilance. However, in reality, not all individuals are rational. Irrational behaviors, such as irrational beliefs [39], irrational antimicrobial prescribing [39], and panic buying [40], may facilitate the spread of the epidemic by inducing individuals to take improper protective measures. Therefore, we now consider cases in which a part of the population is irrational. As irrational behavior can lead to the opposite effects of those by rational behavior, in our model, these two types of individuals are defined as follows:

Dependence 1: $\gamma = (1 - \rho_A)^x$ for rational individuals, and $\gamma = (1 + \rho_A)^x$ for irrational individuals

Dependence 2: $\gamma = x^{-\rho_A}$ for rational individuals, and $\gamma = x^{\rho_A}$ for irrational individuals

Accordingly, disease awareness can reduce the infection rate for rational individuals but increase the infection rate for irrational individuals.

Figure 6 shows the effect of irrational individuals on the spread of the epidemic for the first form of dependence. As the irrational population increases, the final infected population increases, whereas the critical infection rate decreases. This indicates that irrational individuals can facilitate the spread of the epidemic by introducing a negative correlation between vigilance and awareness prevalence. In extreme cases in which irrational individuals become the majority of the system, the spread of information can no longer suppress the epidemic. As shown in Figures 6(d) and 6(f), if most individuals are irrational and take improper measures, a larger population with awareness leads to more serious outbreaks of the epidemic. A similar conclusion can also be obtained for the second form of dependence, as shown in Figure 7. Heterogeneity is an important characteristic of real contagion networks, and different spatial distributions may impact the effect of irrational individuals. Thus, we also performed numerical simulations on BA networks. Figure 8 shows the result of the first form of dependence for three different infection rates: $R_0 = 1.25$, 2.5, and 3.75. The irrational individuals are distributed on nodes with the highest degree, nodes with the lowest degree, and randomly chosen nodes. It can be concluded that, in the second case, the epidemic is not significantly worsened by a small fraction of irrational individuals. When the irrational individuals are randomly distributed or placed on nodes with a high degree, the final infected population increases. This effect of irrational individuals is more pronounced for smaller values of R_0. Figure 8(d) shows the dependence of the critical infection rate on the ratio of irrational individuals for various scenarios. Again, we observe that an increased ratio of irrational individuals can facilitate the spread of the epidemic. A similar effect is observed for the second form of independence in Figure 9.

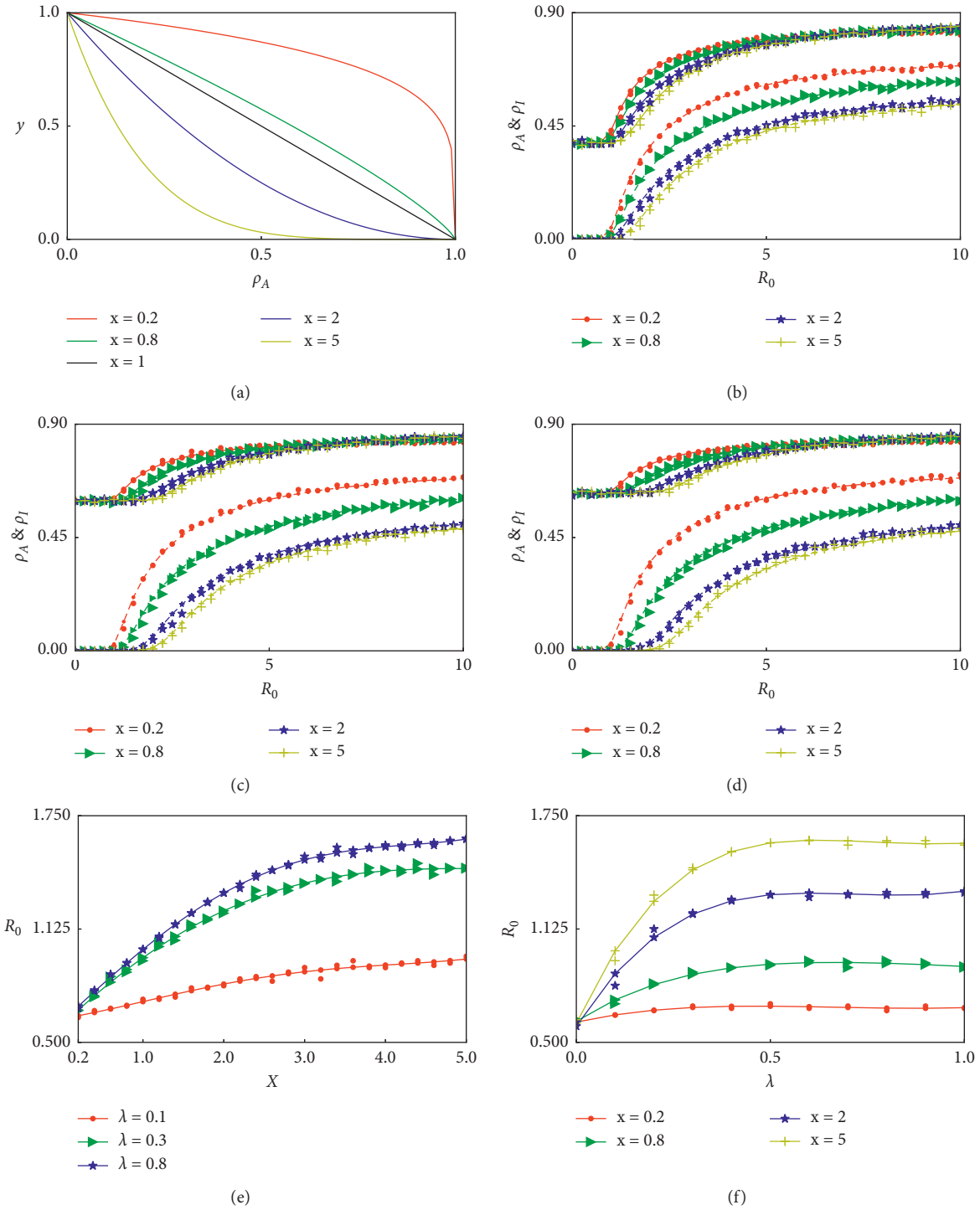

FIGURE 4: (a) Plots of the function $\gamma = (1 - \rho_A)^x$ for different x values. The dependence of prevalence ρ_A and ρ_I on the infection rate R_0 is shown in (b) for $\lambda = 0.1$, (c) for $\lambda = 0.3$, and (d) for $\lambda = 0.8$. Solid lines represent the ratio of awareness nodes ρ_A and dashed lines represent the ratio of infected nodes. Symbols represent the simulation results and different colors correspond to different x values. (e) Dependence of the critical infection rate R_{0c} for the epidemic outbreak on parameter x. (f) Dependence of R_{0c} on λ, with $\delta = 0.6$ and $\mu = 0.4$.

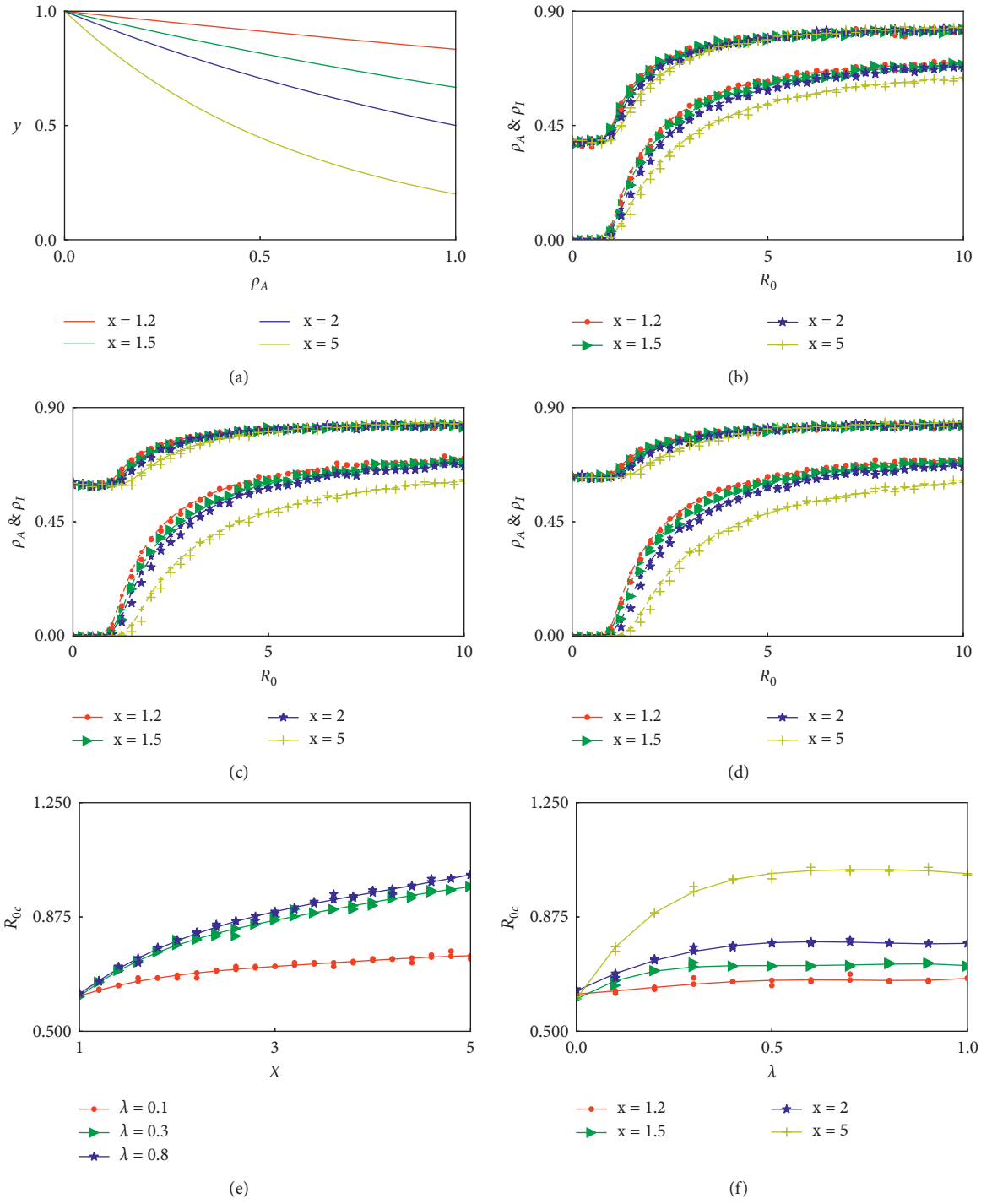

FIGURE 5: (a) Plots of the function $y = x^{-\rho_A}$ for different x values. The dependence of prevalence ρ_A and prevalence ρ_I on the infection rate R_0 is shown in (b) for $\lambda = 0.1$, (c) for $\lambda = 0.3$, and (d) for $\lambda = 0.8$. Solid lines represent the ratio of awareness nodes ρ_A and dashed lines represent the ratio of infected nodes. Symbols represent the simulation results and different colors correspond to different x values. (e) Dependence of the critical infection rate R_{0c} for the epidemic outbreak on parameter x. (f) Dependence of R_{0c} on λ, with $\delta = 0.6$ and $\mu = 0.4$.

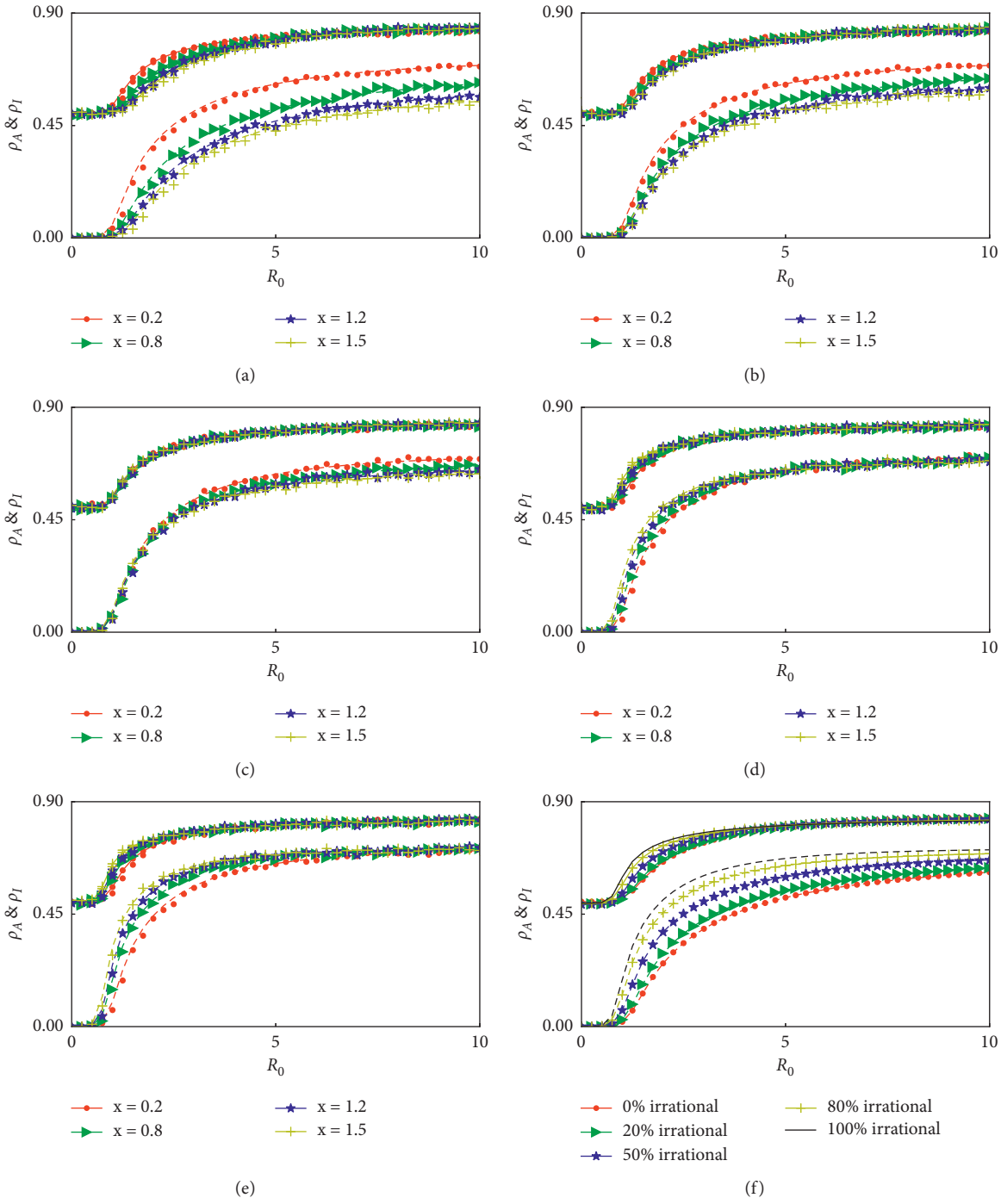

FIGURE 6: For the first form of dependence, where $\gamma = (1 - \rho_A)^x$ for rational individuals and $\gamma = (1 + \rho_A)^x$ for irrational individuals, the dependence of prevalence ρ_A and prevalence ρ_I on the infection rate R_0 is calculated for (a) 0%, (b) 20%, (c) 50%, (d) 80%, and (e) 100% irrational individuals. Solid lines represent the ratio of awareness nodes ρ_A and dashed lines represent the ratio of infected nodes. Symbols represent the simulation results and different colors correspond to different x values. (f) Comparison between cases of different ratios of irrational individuals, with $x = 0.8$. All calculations are based on $\delta = 0.6$ and $\mu = 0.4$.

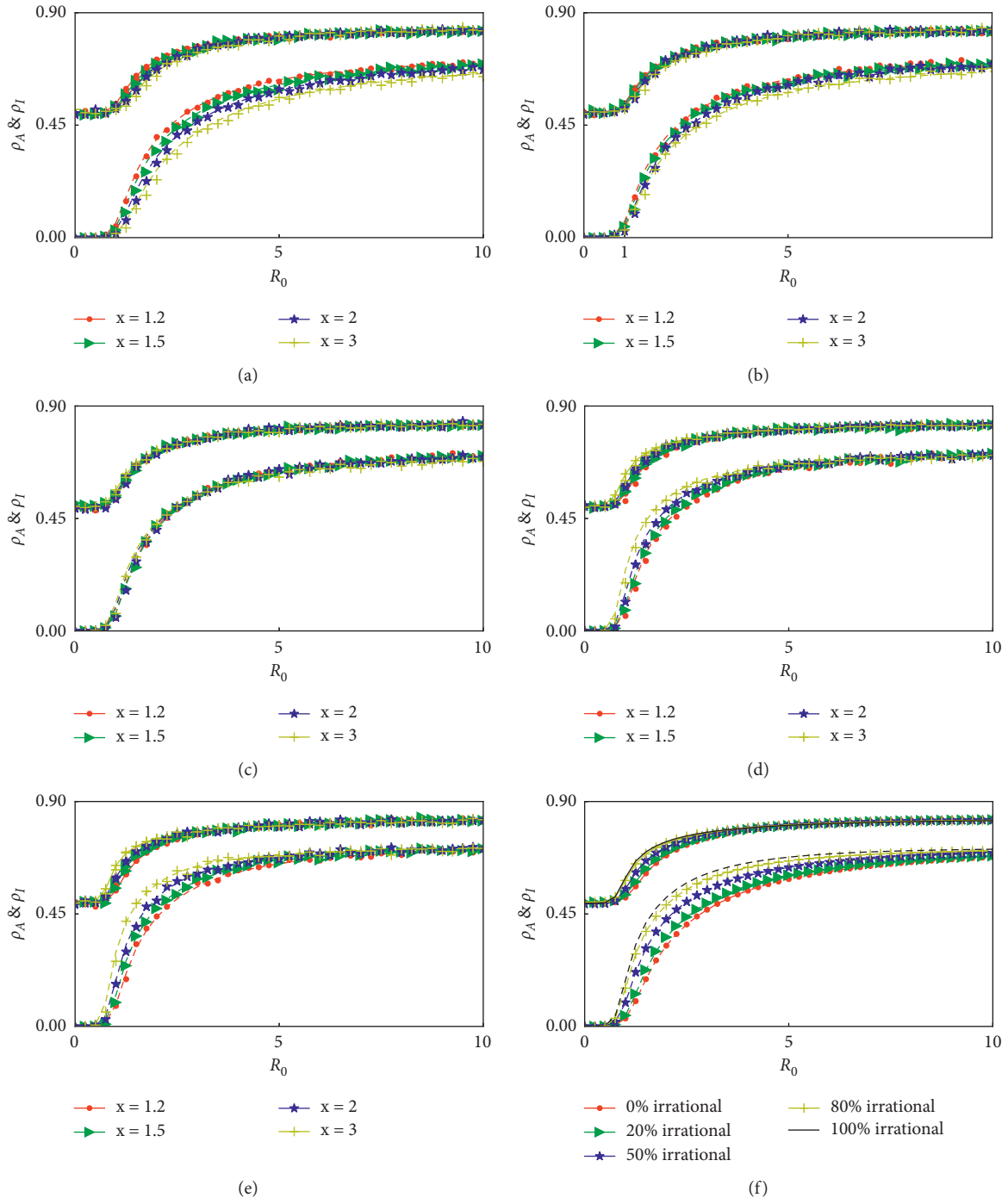

FIGURE 7: For the second form of dependence, where $\gamma = x^{-\rho_A}$ for rational individuals and $\gamma = x^{\rho_A}$ for irrational individuals, the dependence of prevalence ρ_A and prevalence ρ_I on the infection rate R_0 is calculated for (a) 0%, (b) 20%, (c) 50%, (d) 80%, and (e) 100% irrational individuals, respectively. Solid lines represent the ratio of awareness nodes ρ_A and dashed lines represent the ratio of infected nodes. Symbols represent the simulation results and different colors correspond to different x values. (f) Comparison between cases of different ratios of irrational individuals, with $x = 2$. All calculations are based on $\delta = 0.6$ and $\mu = 0.4$.

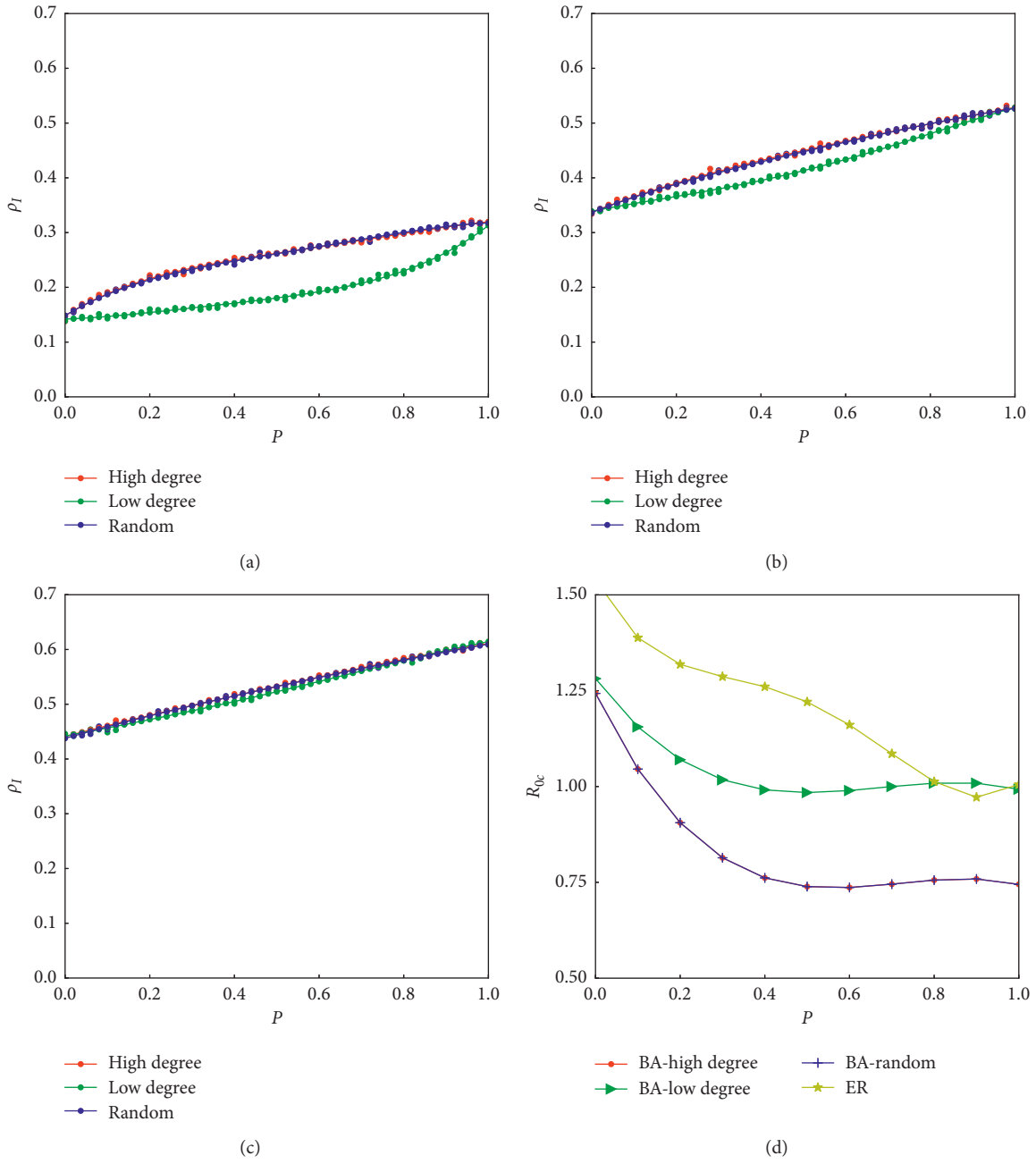

Figure 8: For the first form of dependence, where $\gamma = (1 - \rho_A)^x$ for rational individuals and $\gamma = (1 + \rho_A)^x$ for irrational individuals, the dependence of epidemic prevalence ρ_I on the ratio of irrational individuals on the BA scale-free network for (a) $R_0 = 1.25$, (b) $R_0 = 2.5$, and (c) $R_0 = 3.75$. Irrational individuals are distributed according to three different strategies: on nodes with the highest degree (red line), on nodes with the lowest degree (green line), and randomly distributed (blue line). (d) The critical infection rate R_{0c} for epidemic outbreak in different situations. The parameters are the same as those in Figures 4 and 6.

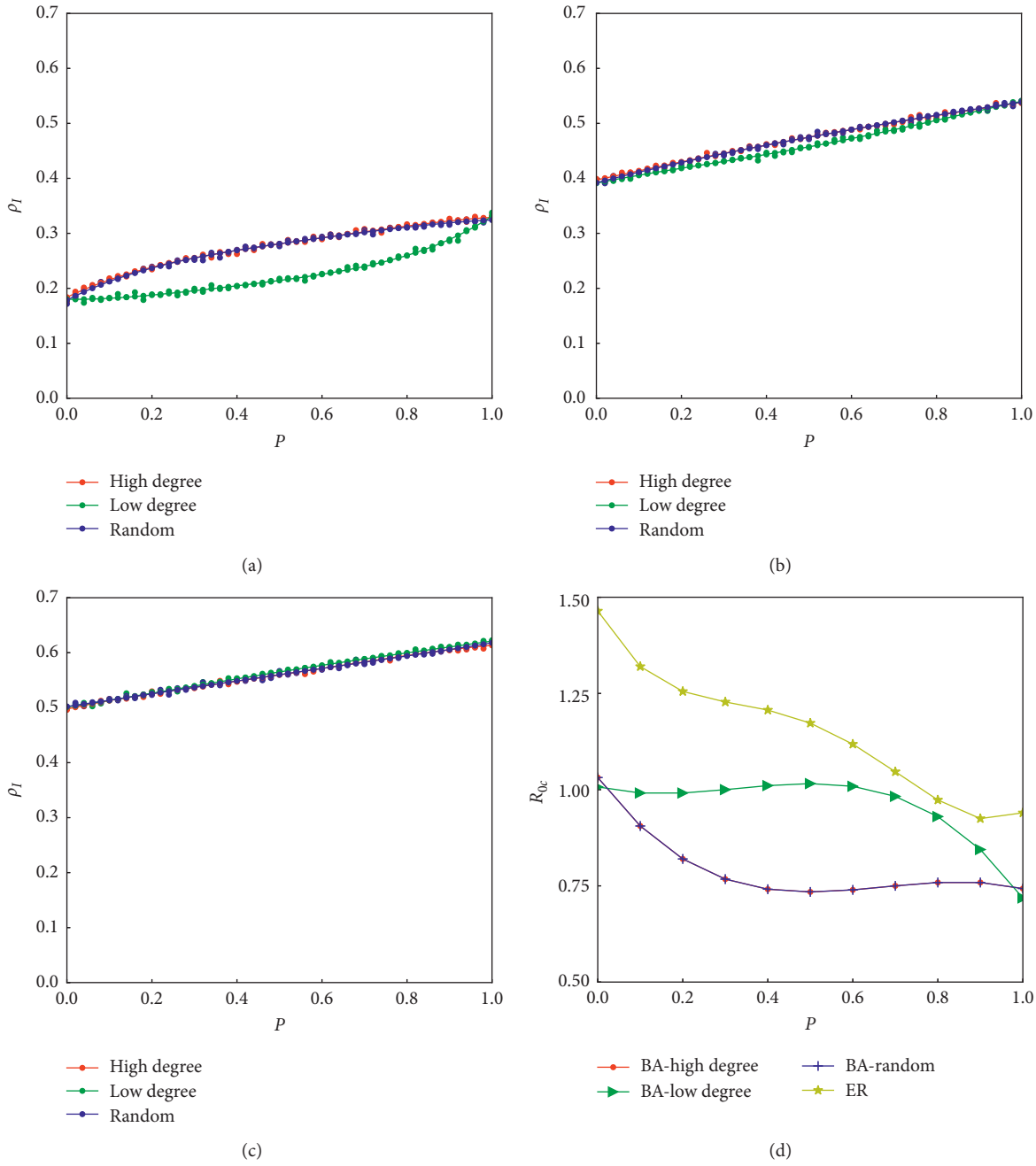

FIGURE 9: For the first form of dependence, where $\gamma = x^{-\rho_A}$ for rational individuals and $\gamma = x^{\rho_A}$ for irrational individuals, the dependence of epidemic prevalence ρ_I on the ratio of irrational individuals in the BA scale-free network for (a) $R_0 = 1.25$, (b) $R_0 = 2.5$, and (c) $R_0 = 3.75$. Irrational individuals are distributed according to three different strategies: on nodes with the highest degree (red line), on nodes with the lowest degree (green line), and randomly distributed (blue line). (d) The critical infection rate R_{0c} for epidemic outbreak in different situations. The parameters are the same as those in Figures 4 and 6.

These results demonstrate the importance of maintaining rationality in containing epidemics, as the efficiency of the strategy of inducing individuals to become aware of the disease and take protective measures depends on the ratio of individuals who can take proper measures. If most individuals cannot take proper protective measures, the spread of awareness cannot assist in containing the epidemic. Thus, irrational population is also a factor that may affect the spread of the pandemic.

5. Conclusion

In modern society, online communication and social media have become important sources of information. Accordingly, relevant information can be spread faster during a pandemic. Individuals can become vigilant about the spread of the disease and take protective measures. Therefore, the process of information propagation can suppress epidemics to a certain extent. In a more realistic scenario, the vigilance of individuals who are aware of the disease is not constant. The level of vigilance and protective measures may change with awareness prevalence. Therefore, investigating the effect of the dependence of individual vigilance on awareness prevalence may lead to a deeper understanding of the coevolution dynamics between epidemic spreading and information spreading.

In this study, we investigated the effect of various forms of dependence between individual vigilance and the spread of awareness of a disease. For rational individuals, vigilance and the level of protective measures increase with the prevalence of discussion. We demonstrated that this positive dependence can enhance the effect of information spreading in suppressing epidemics, as shown in Figures 4 and 5. However, individuals may not be rational and may not take proper protective measures. These irrational behaviors may weaken the effect of information spreading in the containment of the epidemic. In extreme cases where most individuals are irrational, information propagation may even facilitate the spread of the disease, as shown in Figures 6–9. Thus, our results demonstrate the importance of rational behaviors in containing epidemics. Information propagation can efficiently suppress epidemics only when most individuals remain rational and can take proper protective measures.

Data Availability

The data that support the findings of this study are available from the corresponding author upon reasonable request.

Conflicts of Interest

The authors declare that there are no conflicts of interest regarding the publication of this paper.

Acknowledgments

This study was supported by the National Social Science Foundation of China, "Risk Communication and Effectiveness Evaluation in Public Crises" (20AXW008).

References

[1] C. Castellano, P. Van Mieghem, and A. Vespignani, "Epidemic processes in complex networks," *Reviews of Modern Physics*, vol. 87, no. 3, pp. 925–979, 2015.

[2] U. Harush and B. Barzel, "Dynamic patterns of information flow in complex networks," *Nature Communications*, vol. 8, Article ID 2181, 2017.

[3] C. Hens, U. Harush, S. Haber, R. Cohen, and B. Barzel, "Spatiotemporal signal propagation in complex networks," *Nature Physics*, vol. 15, no. 4, pp. 403–412, 2019.

[4] Q. Liu, W. Wang, M. Tang, T. Zhou, and Y. Lai, "Explosive spreading on complex networks: the role of synergy," *Physical Review E*, vol. 95, Article ID 042320, 2017.

[5] J. Wu, M. Zheng, K. Xu, and C. Gu, "Effects of two channels on explosive information spreading," *Nonlinear Dynamics*, vol. 99, no. 3, pp. 2387–2397, 2020.

[6] L. Hébert-Dufresne, S. V. Scarpino, and J.-G. Young, "Macroscopic patterns of interacting contagions are indistinguishable from social reinforcement," *Nature Physics*, vol. 16, no. 4, pp. 426–431, 2020.

[7] T. Gross, C. J. D. Lima, and B. Blasius, "Epidemic dynamics on an adaptive network," *Physical Review Letters*, vol. 96, Article ID 208701, 2006.

[8] L. Böttcher, O. Woolley-Meza, E. Goles, D. Helbing, and H. J. Herrmann, "Connectivity disruption sparks explosive epidemic spreading," *Physical Review E*, vol. 93, Article ID 042315, 2016.

[9] X. Zhang, Z. Ruan, M. Zheng, B. Barzel, and S. Boccaletti, "Epidemic spreading under infection-reduced-recovery," *Chaos, Solitons & Fractals*, vol. 140, Article ID 110130, 2020.

[10] L. Pan, W. Wang, L. Tian, and Y. C. Lai, "Optimal networks for dynamical spreading," *Physical Review E*, vol. 103, Article ID 012302, 2021.

[11] L. Pan, W. Wang, S. Cai, and T. Zhou, "Optimal interlayer structure for promoting spreading of the susceptible-infected-susceptible model in two-layer networks," *Physical Review E*, vol. 100, Article ID 022316, 2019.

[12] L. Pan, D. Yang, W. Wang, S. Cai, T. Zhou, and Y. C. Lai, "Phase diagrams of interacting spreading dynamics in complex networks," *Physical Review Research*, vol. 2, Article ID 023233, 2020.

[13] V. Colizza, A. Barrat, M. Barthélemy, and A. Vespignani, "The role of the airline transportation network in the prediction and predictability of global epidemics," *Proceedings of the National Academy of Sciences of the USA*, vol. 103, Article ID 2015, 2005.

[14] V. Colizza, A. Barrat, M. Barthélemy, and A. Vespignani, "Epidemic predictions and predictability in complex environments," *Biophysical Reviews and Letters*, vol. 03, no. 01n02, pp. 217–226, 2008.

[15] C. Dye and N. Gay, "EPIDEMIOLOGY: modeling the SARS epidemic," *Science*, vol. 300, no. 5627, pp. 1884-1885, 2003.

[16] K. Khan, J. Arino, W. Hu et al., "Spread of a novel influenza A (H1N1) virus via global airline transportation," *New England Journal of Medicine*, vol. 361, no. 2, pp. 212–214, 2009.

[17] P. Mukherjee, P. L. Lim, A. Chow et al., "Epidemiology of travel-associated pandemic (H_1N_1) 2009 infection in 116 patients, Singapore," *Emerging Infectious Diseases*, vol. 16, no. 1, pp. 21–26, 2010.

[18] P. Bajardi, C. Poletto, J. J. Ramasco, M. Tizzoni, V. Colizza, and A. Vespignani, "Human mobility networks, travel restrictions, and the global spread of 2009 H_1N_1 pandemic," *PLoS One*, vol. 6, Article ID e16591, 2011.

[19] Z. Ruan, M. Tang, and Z. Liu, "How the contagion at links influences epidemic spreading," *The European Physical Journal B*, vol. 86, p. 149, 2013.

[20] X. Pang, L. Ren, S. Wu et al., "COVID-19 field response group, COVID-19 laboratory testing group, "cold-chain food contamination as the possible origin of COVID-19 resurgence in Beijing," *National Science Review*, vol. 7, no. 12, pp. 1861–1864, 2020.

[21] P. Manfredi and A. D'Onofrio, *Modeling the Interplay between Human Behavior and the Spread of Infectious Diseases*, Springer-Verlag, Berlin, Germany, 2013.

[22] S. Funk, M. Salathé, and V. A. A. Jansen, "Modelling the influence of human behaviour on the spread of infectious diseases: a review," *Journal of the Royal Society Interface*, vol. 7, Article ID 1257, 2010.

[23] S. Funk, E. Gilad, and V. A. A. Jansen, "Endemic disease, awareness, and local behavioural response," *Journal of Theoretical Biology*, vol. 264, no. 2, pp. 501–509, 2010.

[24] Z. Ruan, M. Tang, and Z. Liu, "Epidemic spreading with information-driven vaccination," *Physical Review E*, vol. 86, Article ID 036117, 2012.

[25] S. Funk, E. Gilad, C. Watkins, and V. A. A. Jansen, "The spread of awareness and its impact on epidemic outbreaks," *Proceedings of the National Academy of Sciences*, vol. 106, no. 16, pp. 6872–6877, 2009.

[26] S. Funk and V. A. A. Jansen, "Interacting epidemics on overlay networks," *Physical Review E*, vol. 81, Article ID 036118, 2010.

[27] X.-X. Zhan, C. Liu, G.-Q. Sun, and Z.-K. Zhang, "Epidemic dynamics on information-driven adaptive networks," *Chaos, Solitons & Fractals*, vol. 108, pp. 196–204, 2018.

[28] Q. Wu, X. Fu, M. Small, and X. Xu, "The impact of awareness on epidemic spreading in networks," *Chaos*, vol. 22, Article ID 013101, 2012.

[29] X.-X. Zhan, C. Liu, G. Zhou et al., "Coupling dynamics of epidemic spreading and information diffusion on complex networks," *Applied Mathematics and Computation*, vol. 332, pp. 437–448, 2018.

[30] C. Granell, S. Gómez, and A. Arenas, "Dynamical interplay between awareness and epidemic spreading in multiplex networks," *Physical Review Letters*, vol. 111, Article ID 128701, 2013.

[31] C. Granell, S. Gómez, and A. Arenas, "Competing spreading processes on multiplex networks: awareness and epidemics," *Physical Review E*, vol. 90, Article ID 012808, 2014.

[32] W. Wang, M. Tang, H. Yang, Y. Do, Y. Lai, and G. Lee, "Asymmetrically interacting spreading dynamics on complex layered networks," *Scientific Reports*, vol. 4, p. 5097, 2014.

[33] W. Wang, Q. Liu, S. Cai, M. Tang, L. A. Braunstein, and H. E. Stanley, "Suppressing disease spreading by using information diffusion on multiplex networks," *Scientific Reports*, vol. 6, Article ID 29259, 2016.

[34] C. Xu, X. Zhang, and Y. Wang, "Mapping of health literacy and social panic via web search data during the COVID-19 public health emergency: infodemiological study," *Journal of Medical Internet Research*, vol. 22, Article ID e18831, 2020.

[35] A. Depoux, S. Martin, E. Karafillakis, R. Preet, A. Wilder-Smith, and H. Larson, "The pandemic of social media panic travels faster than the COVID-19 outbreak," *Journal of Travel Medicine*, vol. 27, no. 3, Article ID taaa031, 2020.

[36] A. R. Ahmad and H. R. Murad, "The impact of social media on panic during the COVID-19 pandemic in Iraqi Kurdistan: online questionnaire study," *Journal of Medical Internet Research*, vol. 22, Article ID e19556, 2020.

[37] E. Dong, H. Du, and L. Gardner, "An interactive web-based dashboard to track COVID-19 in real time Modeling and forecasting of epidemic spreading: the case of COVID-19 and beyond," *Lancet Infect Disease*, vol. 3099, pp. 19-20, 2020.

[38] P. Teovanović, P. Lukić, Z. Zupan, A. Lazić, M. Ninković, and I. Žeželj, "Irrational beliefs differentially predict adherence to guidelines and pseudoscientific practices during the COVID-19 pandemic," *Applied Cognitive Psychology*, vol. 35, pp. 486–496, 2020.

[39] M. Parveen, M. Yeasmin, and M. A. Molla, "Antimicrobial resistance, evidences on irrational anti-microbial prescribing and consumption during COVID-19 pandemic and possible mitigation strategies: a Bangladesh perspective," *Bangladesh Journal of Infectious Diseases*, vol. 7, pp. S3–SX7, 2020.

[40] S. M. Y. Arafat, S. K. Kar, V. Menon et al., "Panic buying: an insight from the content analysis of media reports during COVID-19 pandemic," *Neurology, Psychiatry and Brain Research*, vol. 37, pp. 100–103, 2020.

[41] D. Chakrabarti, Y. Wang, C. Wang, J. Leskovec, and C. Faloutsos, "Epidemic thresholds in real networks," *ACM Transactions on Information and System Security*, vol. 10, no. 4, pp. 1–26, 2008.

[42] S. Gómez, A. Arenas, J. Borge-Holthoefer, S. Meloni, and Y. Moreno, "Discrete-time Markov chain approach to contact-based disease spreading in complex networks," *EPL (Europhysics Letters)*, vol. 89, no. 3, Article ID 38009, 2010.

[43] S. Gómez, J. Gómez-Gardenës, Y. Moreno, and A. Arenas, "Nonperturbative heterogeneous mean-field approach to epidemic spreading in complex networks," *Physical Review E*, vol. 84, Article ID 036105, 2011.

Hindawi
Complexity
Volume 2021, Article ID 5554322, 8 pages
https://doi.org/10.1155/2021/5554322

Research Article

Information Entropy Based on Propagation Feature of Node for Identifying the Influential Nodes

Linfeng Zhong,[1] **Yu Bai**,[1] **Yan Tian**,[2] **Chen Luo**,[1] **Jin Huang**,[1] **and Weijun Pan**[1]

[1]*Civil Aviation Flight University of China, Guanghan 618307, China*
[2]*School of Science, Southwest Petroleum University, Chengdu 610500, China*

Correspondence should be addressed to Weijun Pan; wjpan@cafuc.edu.cn

Received 24 February 2021; Accepted 9 May 2021; Published 20 May 2021

Academic Editor: Chenquan Gan

For understanding and controlling spreading in complex networks, identifying the most influential nodes, which can be applied to disease control, viral marketing, air traffic control, and many other fields, is of great importance. By taking the effect of the spreading rate on information entropy into account, we proposed an improved information entropy (IIE) method. Compared to the benchmark methods in the six different empirical networks, the IIE method has been found with a better performance on Kendall's Tau and imprecision function under the Susceptible Infected Recovered (SIR) model. Especially in the Facebook network, Kendall's Tau can grow by 120% as compared with the original IE method. And, there is also an equally good performance in the comparative analysis of imprecise functions. The imprecise functions' value of the IIE method is smaller than the benchmark methods in six networks.

1. Introduction

The phenomena of spreading can be seen everywhere in nature [1–7]. Many activities can be described as spreading in nature [8–13]. In recent years, many research studies focused on the spreading process due to its theoretical meaning and practical value [14, 15], including rumor controlling [16–18], information diffusion [19–22], air traffic controlling [23–25], and viral marketing [26–28]. Among them, research on identification of the influential nodes in complex networks is a hotspot. Understanding the influence of the node has revealed new insight into applications such as mining the key nodes [29–34] and designing effective strategies to prevent epidemic from spreading or accelerate information diffusion.

The identification of influential nodes is of great significance in fields of epidemic and rumor control, targeted advertising, and air traffic planning [35, 36]. Recently, many researchers have put forward a variety of centrality methods to deal with the problem in a more efficient way to identifying these nodes. Degree centrality can be regarded as a typical method to deal with the former problem in consideration for the local information [37, 38]. In view of this idea, Chen et al. proposed the Local Rank method by considering the 4th order neighbors of the node [39]. By taking into account the location information of nodes in the network, through the K-shell decomposition method, Kitsak et al. [40] discovered a fact that the most influential nodes are located at the heart of the network. Then, a lot of improved methods based on the K-shell decomposition [41–43] have been proposed to identify the influential nodes. Closeness centrality [44] and betweenness centrality [45] are two path-based methods. In consideration of the neighbors' influence, Ren et al. [46] came up with the IRA method. Based on the IRA method, Zhong et al. [47] proposed the IIRA method by taking the propagation feature into account. Information entropy is also used as an important centrality to evaluate the influence of nodes [48, 49].

Most of the previous methods assume that the node's influence depends on its own importance. But there is another key factor that cannot be neglected, namely, the neighbors' importance. On the basis of this idea, Guo et al. [50] put forward a method of information entropy (IE) by considering the neighbors' information quantity.

Nevertheless, the performance of the IE method is also affected by the propagation feature. In the example network that is presented in Figure 1, the influence of nodes 1 and 6 cannot be accurately identified by the IE method. In this case, we think that the neighbors' number and spreading rate are likely to have a positive effect on the target node. Based on this idea, we proposed an improved information entropy (IIE) method in which the target node's information entropy may be affected by the propagation feature. Compared with the benchmark methods in six real networks, the IIE method has been found with a better performance on Kendall's Tau and imprecision function under the Susceptible Infected Recovered (SIR) model [51, 52].

2. IIE Method

The original IE method assumes that the influence of the node should be obtained through the information entropy of its neighbors. In the IIE method, we argue that the spreading rate and the number of neighbors could adjust the initial information entropy. We can fulfill the identification of the influential nodes by using the final information entropy, namely, the IIE method. The details of the IIE method can be interpreted below.

In general, an undirected network $G = (N, E)$ can be described by an adjacent matrix $A = \{a_{ij}\} \in R^{n,n}$, where N represents the number of nodes and E represents the number of edges. If node i is connected to node j, $a_{ij} = 1$; if not, $a_{ij} = 0$. And, we think that the spreading rate and the number of neighbors could adjust the target node's information entropy. Thus, the IIE value of any node j can be calculated by

$$\begin{aligned} \mathrm{IIE}_j &= \sum_{i \in \Gamma(j)} \psi_j H_{ij}, \\ &= \sum_{i \in \Gamma(j)} \psi_j \left(-p_{ij} \log\, p_{ij}\right), \end{aligned} \tag{1}$$

where H_{ij} is the information quantity provided from i to j, ψ_j represents the influence of the propagation feature, the spreading rate is β, and k_j represents the number of neighbors for node j, also the expression of k_j is

$$k_j = \sum_{i \in G} a_{ij}. \tag{2}$$

Equation (1) can be written as

$$\mathrm{IIE}_j = \sum_{i \in \Gamma(j)} \left[1 - (1 - \beta)^{k_j}\right] \left(-p_{ij} \log\, p_{ij}\right), \tag{3}$$

where $p_{ij} = (k_i / \sum_{m \in \Gamma_{L-j}} k_m)$ and Γ_{L-j} indicates node j's Lth order neighbors. If $L = 1$, it indicates node j's direct neighbors.

To describe the IIE method in more detail, we set $L = 1$ and $\beta = 0.2$ by taking into account the example network in Figure 2. For the black nodes (node 1), the improved information entropy (IIE) of node 1 is then calculated by $\mathrm{IIE}_1 = (1 - 0.8^4) \times (H_{21} + H_{31} + H_{41} + H_{51}) = 0.7734$.

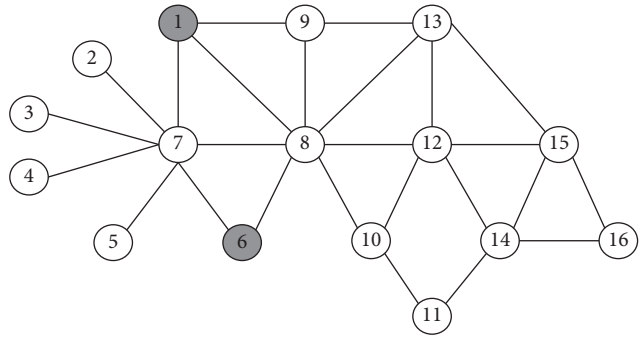

Figure 1: (Color online) The sample network in the figure has 16 nodes as well as 25 edges. The SIR model can be used to simulate the nodes' real spreading influence, that is, the amount of the infected nodes can be considered as spreading influence. We set $\beta = 0.2$ and $\mu = 1$, and the number of simulations are 10^3. Therefore, we can get results of 2.405 and 2.101, respectively, for the spreading influence of nodes 1 and 6. With the IE method, the influence of nodes 1 and 6 should be 1.875 and 2.023, respectively.

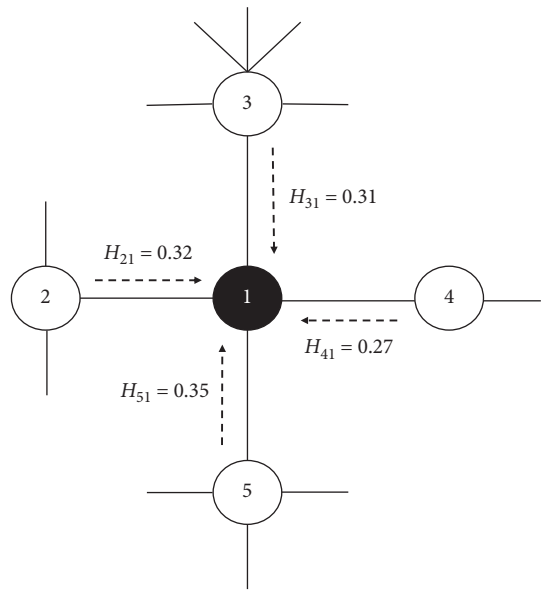

Figure 2: (Color online) The figure shows how to calculate the IIE. There are four neighbors for node 1. H is the information quantity. For example, H_{21} represents the information quantity provided from node 2 to node 1. We set $L = 1$ and $\beta = 0.2$. Each data point is calculated from the average of 10^3 experiments.

3. Results

3.1. Data Description. There are six empirical networks used to evaluate the performance of the IIE method. The US air network [53] is an integral part of the US air traffic networks. The Polblogs network works as a network of political blogs in the United States with political relationship. The datasets are available on the web.

The e-mail network [54] refers to an electronic mail network of a university in Spain. The Soc-hamsterster network is a social network where the edges between nodes indicate the friendship or family ties. The Facebook network was derived from the Facebook online social platform, and

its edges indicate the interpersonal relationship. The LastFM network [55] was derived from an FM broadcast platform for the Asian users where the edges represent that there exist friendships between nodes. The statistical attributes of the six networks are listed above in Table 1.

3.2. Measurement. For this paper, the node spreading influence is simulated with the SIR model [52]. There are three components to this system, namely, susceptible individuals (S), infected individuals (I), and recovered individuals (R). In each time step of the SIR model, the susceptible neighbor nodes of each infected node will be infected randomly with a certain probability β. During this time, each infected node would recover with a certain probability μ and will no longer be infected. The spreading influence of a node is the range of infected nodes X which refers to the number of nodes infected by the initial infected node in the whole network. The range of infected nodes X was calculated from an average of 10^3 experiments.

Kendall's Tau [56] and the imprecision function can be used to evaluate the superiority of the IIE methods. The value of Kendall's Tau is between [−1, 1], and this function can be used to evaluate whether there is a correlation between two ranking lists. The higher the value of Kendall's Tau, the stronger the correlation between the two ranking lists. Kendall's Tau τ can be expressed as

$$\tau = \frac{2}{N(N-1)} \sum_{i<j} \operatorname{sgn}\left[\left(x_i - x_j\right)\left(y_i - y_j\right)\right]. \quad (4)$$

$\operatorname{sgn}(x)$ works as a sign function; if $x > 0$, the figure of $\operatorname{sgn}(x)$ equals to 1; if $x < 0$, the figure of $\operatorname{sgn}(x)$ equals to −1; and, if $x = 0$, the figure of $\operatorname{sgn}(x)$ equals to 0. N represents the number of nodes in the lists, that is, in the network. Calculated by the centrality method, x_i and x_j are the order values in the ranking list for the nodes i and j. And, y_i and y_j are the order values in the ranking list for the nodes i and j which are generated by the real spreading influence. If $(x_i - x_j)(y_i - y_j) > 0$, it means that there is a large correlation coefficient between the two different ranking lists.

The imprecision function $\varepsilon_\vartheta(p)$ evaluates the performance of the centrality method by calculating the average propagation ability of the top key nodes in the ranking list obtained by the centrality method. $\varepsilon_\vartheta(p)$ should be expressed as

$$\varepsilon_\vartheta(p) 1 - \frac{M_\vartheta(p)}{M_{eff}(p)}, \quad (5)$$

where p is a proportion of the nodes to be selected, $p \in [0, 1]$, N represents the number of nodes, $M_\vartheta(p)$ represents the average spreading influence of the top pN nodes in the ranking list obtained by the centrality method, and $M_{eff}(p)$ can be illustrated as the mean spreading influence of top pN nodes in the ranking list calculated by the SIR model. If $M_\vartheta(p)$ is closer to $M_{eff}(p)$, $\varepsilon_\vartheta(p)$ is smaller. It means that the spreading influence for the top pN nodes calculated by the centrality method is closer to the spreading influence of the top pN nodes with the real ability of spreading. This also indicates that the accuracy of the centrality method is higher.

Table 1: There are six fundamental statistical attributes in the six networks, such as N, E, $\langle k \rangle$, β_{thd}, r, and C. N and E, respectively, represent the number of nodes and edges. $\langle k \rangle$, β_{thd}, r, and C, respectively, represent the average degree, epidemic threshold, degree assortativity, and clustering coefficient.

Network	N	E	$\langle k \rangle$	β_{thd}	r	C
US air	332	2126	12.8	0.024	−0.208	0.625
Polblogs	643	16097	7.09	0.052	−0.217	0.232
E-mail	1133	5451	9.62	0.055	0.078	0.22
Soc-hamsterster	2426	16630	13.71	0.023	0.047	0.537
Facebook	4039	88234	43.69	0.009	0.063	0.605
LastFM	7624	27806	7	0.037	0.017	0.219

Site[1].

3.3. Simulation Results. For this paper, we selected six real networks to test the IIE method. According to different networks, we set $\beta \in [0.1, 0.2]$ and $\mu = 1$ in the SIR model.

At first, we test the influence of different values of L on the performance of the IIE method. L represents the distance between nodes. If $L = 1$, the direct neighbors' information quantity will be provided to the target node. And, if $L = 2$, the target node's information quantity will be provided by its 2nd order neighbors. The influence of parameter L on the IIE method in six networks is shown in Figure 3, $L \in [1, 4]$.

From Figure 3, we can figure out that the effect of L on Kendall's Tau τ calculated by the IIE method in different networks. Obviously, when we set the distance $L = 2$, Kendall's Tau τ can get the maximum in the US air, Polblogs, e-mail, and LastFM networks. It demonstrates that the IIE method is more accurate than the ones generated by the other values of L in the four networks. However, there are different phenomena in the Soc-hamsterster and Facebook networks. When $L = 3$ or $L = 4$, the value of Kendall's Tau is the largest, while the computation time of the IIE method increases dramatically. In addition, we know from the TDI theory [57] that individuals affect only a relatively small range of neighbors. Therefore, we set $L = 2$ in later experiments.

To check the efficiency of the IIE method, the K-shell, degree centrality, closeness centrality, betweenness centrality, and IE method are selected as benchmark methods to compare with the IIE method in six networks. We set $\beta \in [0.1, 0.2]$, $\mu = 1$, and the distance $L = 2$. As can be seen from Figure 4, in the six networks, Kendall's Tau τ obtained by the IIE method is much bigger than the ones obtained by the benchmark methods. This indicates that the IIE method is superior to the benchmark method. It can also be seen from Figure 4 that, in the US air and LastFM networks, the value of Kendall's Tau τ obtained by the IIE method gradually increases along with the spreading rate β. On the contrary, in the Soc-hamsterster and Facebook networks, the value of Kendall's Tau τ obtained by the IIE method decreases with growth of spreading rate β. However, divergent phenomena exist in the Polblogs and e-mail networks. As the spreading rate β increases, the value of Kendall's Tau τ,

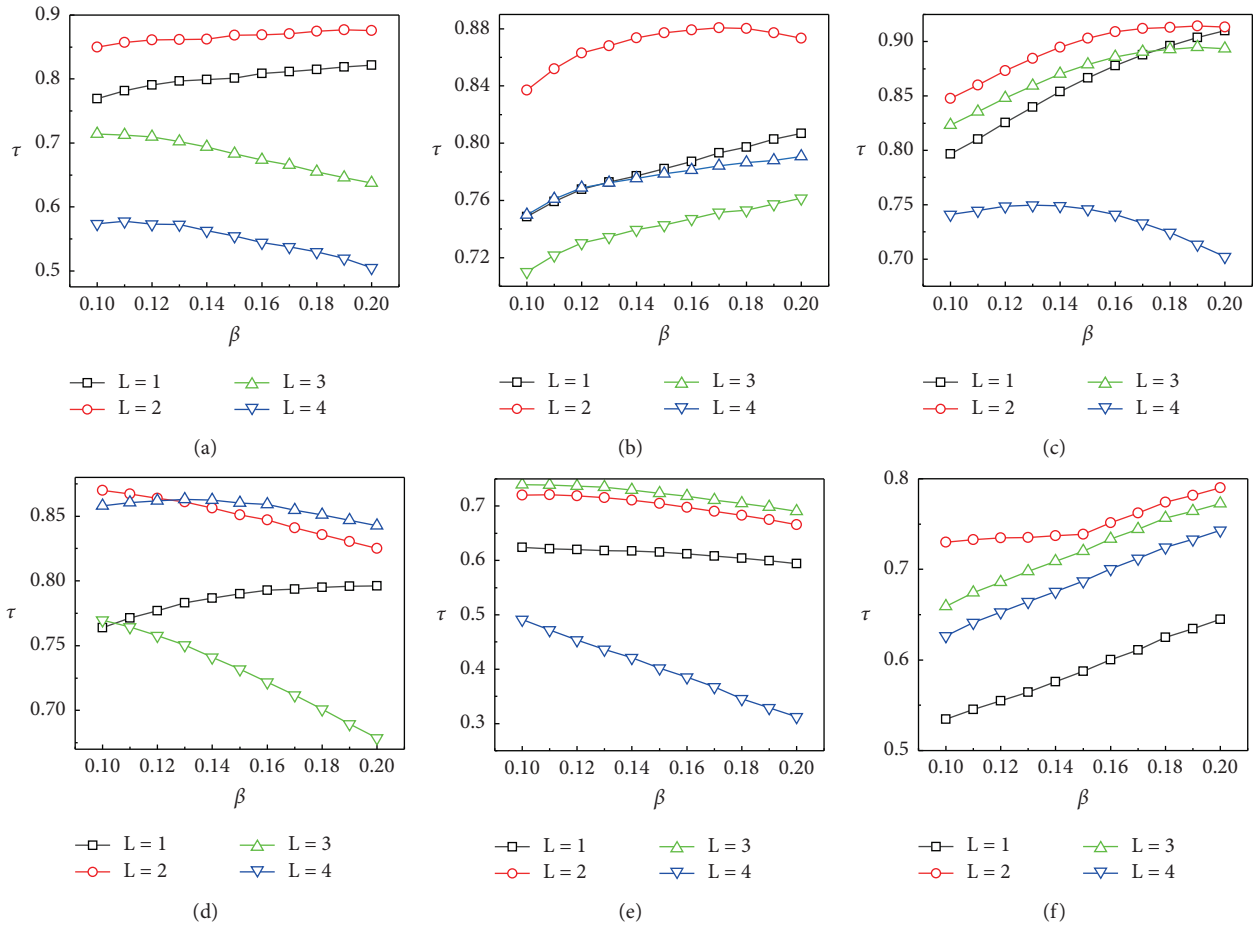

FIGURE 3: (Color online) The figure shows the effect of parameter L on Kendall's Tau τ calculated by the IIE method in six networks. The larger value of Kendall's Tau indicates that the IIE method performs best along with the parameter L. We set $\beta \in [0.1, 0.2]$ and $\mu = 1$. Each data point is calculated from the average of 10^3 experiments. (a) US air. (b) Polblogs. (c) E-mail. (d) Soc-hamsterster. (e) Facebook. (f) LastFM.

which is calculated obtained by the IIE method, will increase first and then decrease.

Figure 5 illustrates the improvement of ratio η for Kendall's Tau as making a comparison between the IIE method and the benchmark methods. We define η as

$$\eta = \frac{\tau^{\mathrm{IIE}} - \tau^0}{\tau^0}, \tag{6}$$

where τ^{IIE} represents Kendall's Tau which is obtained by the IIE method. τ^0 represents Kendall's Tau τ calculated by the different benchmark methods. Obviously, if $\eta > 0$, which means the performance of the IIE method is much better. Figure 5 clearly shows that, when the IIE method compared with the benchmark methods, Kendall's Tau τ increases considerably. That is, in the six networks, the IIE method is more accurate than the other benchmark methods on identifying the influential nodes. We can also find that, compared with the IE method, the maximum value of η can grow by 80%. Similarly, Kendall's Tau τ shows a significant increase when the IIE method is compared with the other benchmark methods in the US air network. This means that the IIE method is superior to the benchmark methods. The same phenomenon occurs in other different networks. In particular, in the Facebook network, compared with the IE method, the maximum value of η can grow by 120% when $\beta = 0.12$.

As can be seen from Figure 6, the imprecision functions $\varepsilon_\vartheta(p)$ of each method are presented and impressive results have been achieved by the IIE method in the six networks. In small networks such as US air and e-mail, the results of the IIE method are remarkably superior to those of other benchmark methods. For instance, $\varepsilon_{\mathrm{IIE}}(p)$ is much lower than the benchmark methods, which means that the outcome of spreading predicted by the IIE method is more reliable than that predicated by the benchmark method. In the large LastFM network, $\varepsilon_{\mathrm{IIE}}(p)$ is much lower than $\varepsilon_{\mathrm{IE}}(p)$. This result reveals that the IIE method performs more accurately than the original IE method in identifying the most influential nodes. It is worth noticing that when p is small, the IIE method shows much better performance than the other benchmark methods. These phenomena show the rationality of the IIE method considering the propagation feature of the target node.

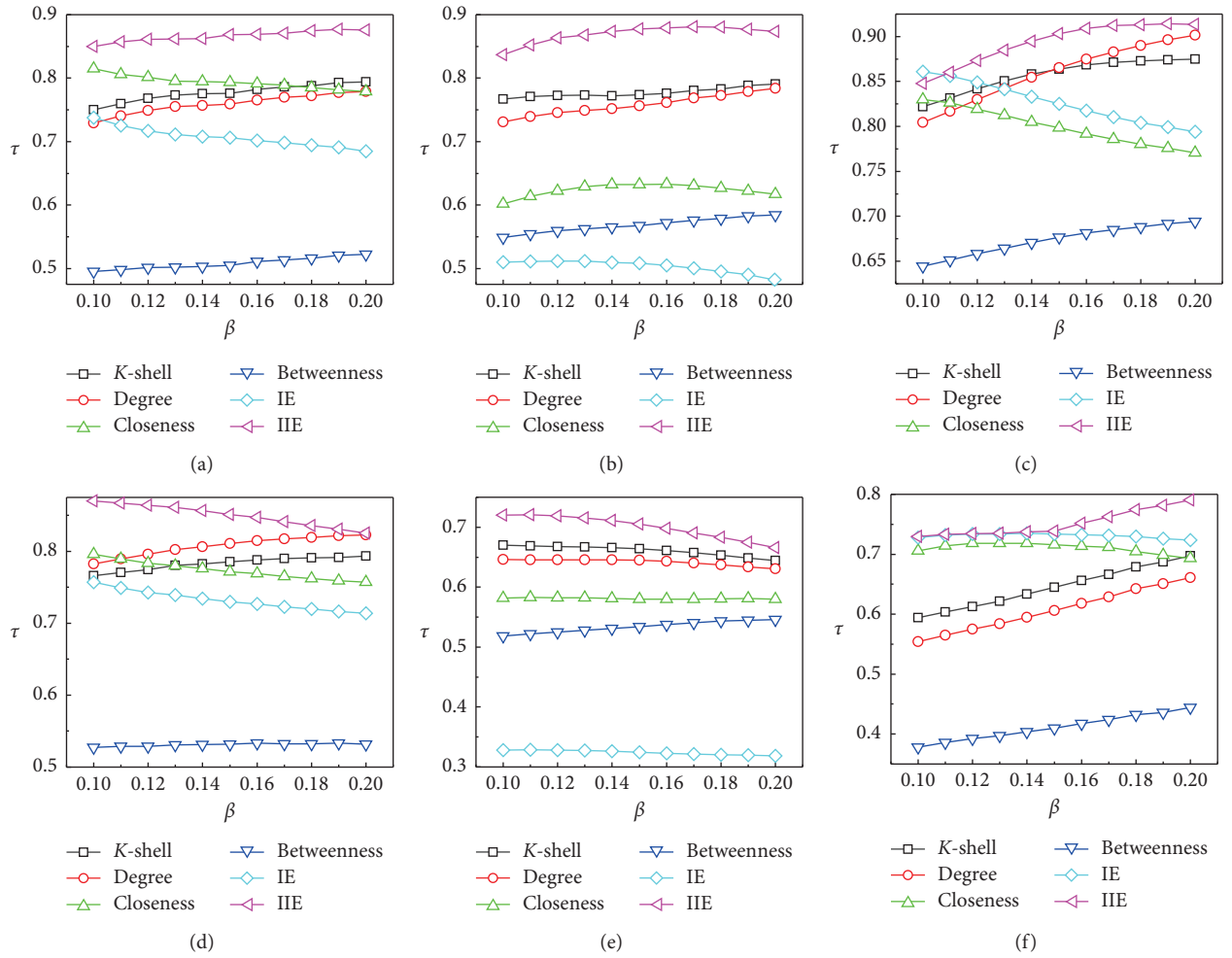

FIGURE 4: (Color online) The figure shows a comparison between the ranking list produced by the SIR model, and the ranking lists produced by the K-shell, degree centrality, closeness centrality, betweenness centrality, IE method, and IIE method lead to Kendall's Tau τ. We set $\beta \in [0.1, 0.2]$ and $\mu = 1$. Each data point is calculated from the average of 10^3 experiments. (a) US air. (b) Polblogs. (c) E-mail. (d) Soc-hamsterster. (e) Facebook. (f) LastFM.

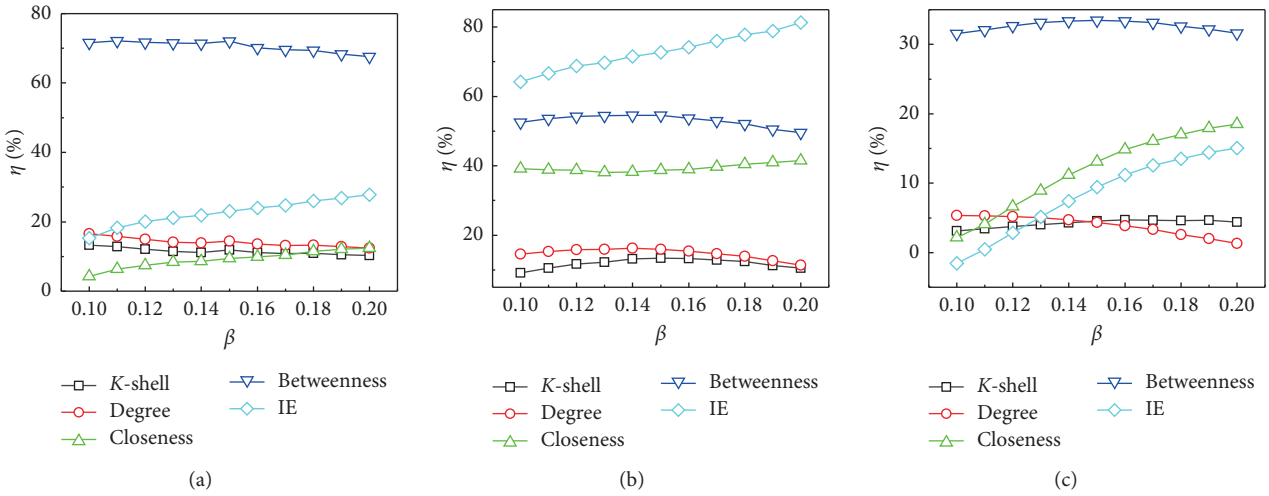

FIGURE 5: Continued.

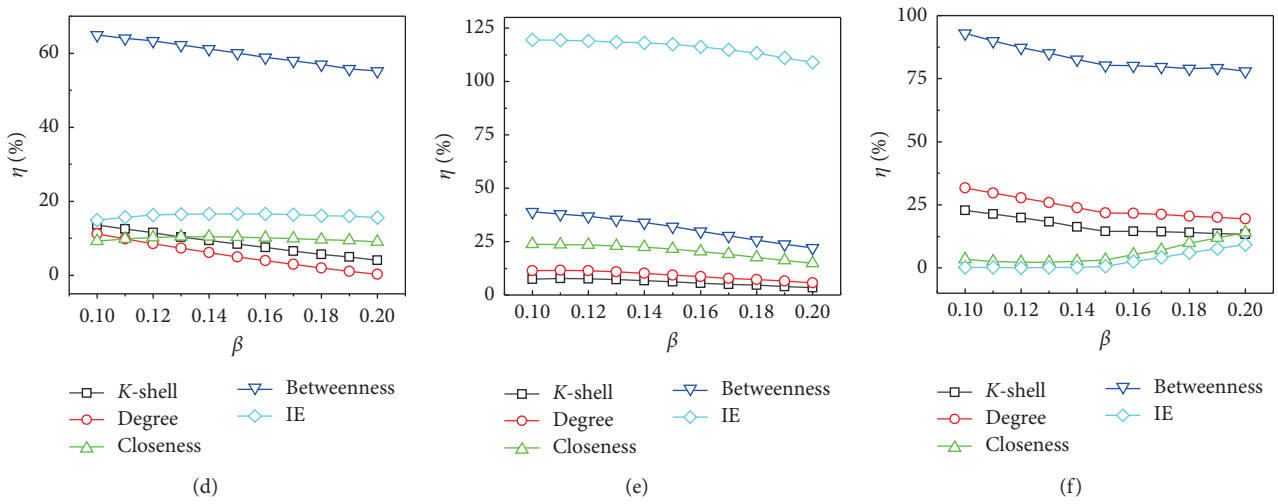

FIGURE 5: (Color online) The figure shows the improvement of ratio η for Kendall's Tau as making a comparison between the IIE method and the benchmark methods in six networks. We set $\beta \in [0.1, 0.2]$ and $\mu = 1$. (a) US air. (b) Polblogs. (c) E-mail. (d) Soc-hamsterster. (e) Facebook. (f) LastFM.

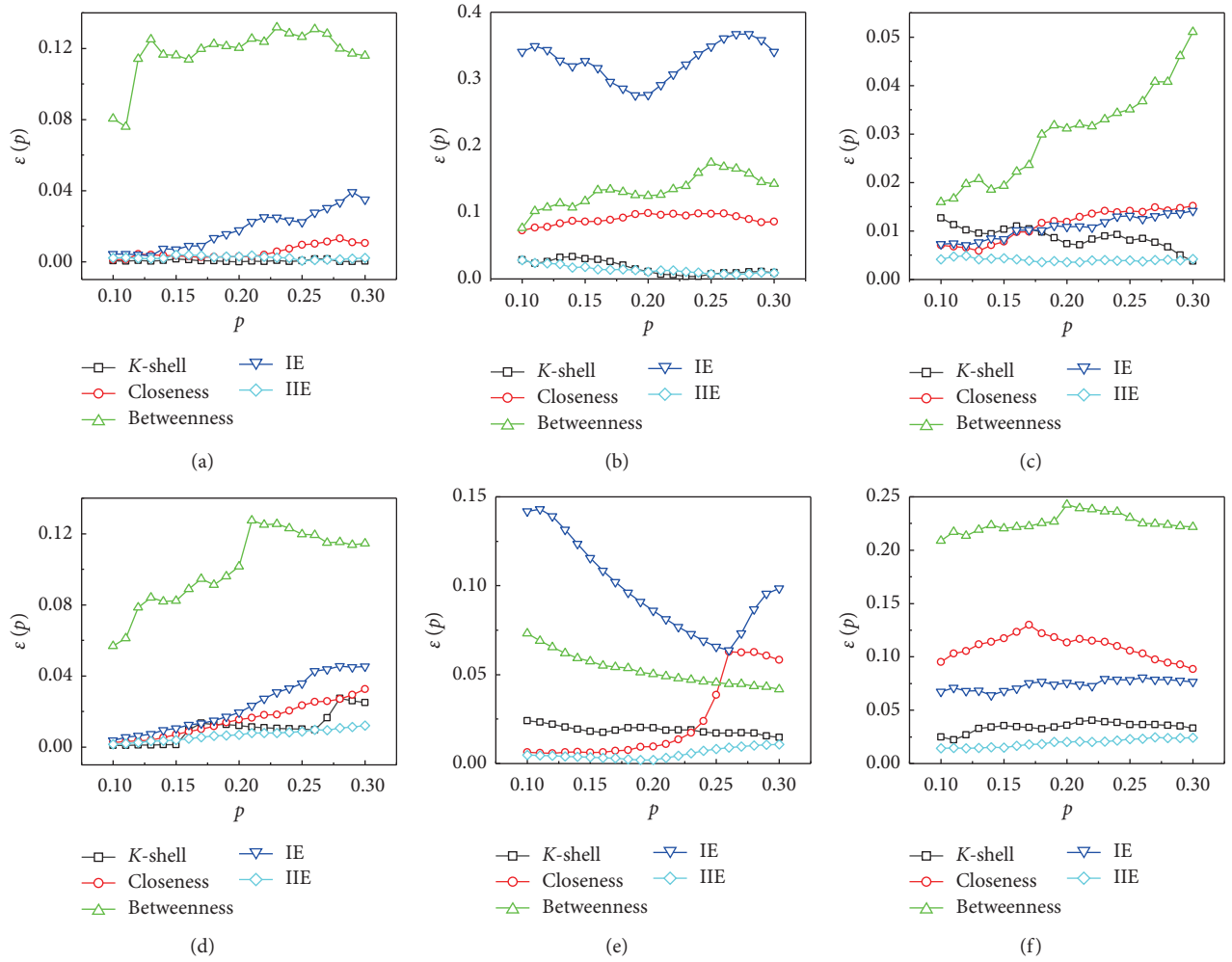

FIGURE 6: (Color online) This experiment compares different methods by using the imprecision functions $\varepsilon_9(p)$ in the six networks. p is the proportion of selected nodes, $p \in [0, 1]$. We set $\beta = 0.2$ and $\mu = 1$. The results were calculated from an average of 10^3 experiments. (a) US air. (b) Polblogs. (c) E-mail. (d) Soc-hamsterster. (e) Facebook. (f) LastFM.

4. Conclusions

For controlling the spreading process, one of the basic tasks is to estimate the spreading influence and identify the influential nodes. By considering the information entropy and spreading rate of the target nodes, we proposed an improved information entropy (IIE) method. The IIE method takes the spreading rate and the number of the target node's neighbors into account. And, those information dominate the new information entropy. According to the simulation results, the IIE method achieves a better performance than the IE method, and the IIE method ($O(N)$) does not add any parameters or increase computational complexity. In the six networks, the IIE method performs much better than the other benchmark methods, such as K-shell ($O(N)$), degree centrality ($O(N)$), closeness centrality ($O(N^3)$), betweenness centrality ($O(N^3)$), and IE method. Especially, in the Facebook network, comparing with the IE method, the maximum improved ratio η goes up to 120%. And, there also exists an equally good performance in the comparative analysis of imprecise functions. In the six networks, $\varepsilon_{\mathrm{IIE}}(p)$ is much lower than the benchmark methods. These results demonstrate that the IIE method is sure to identify the influential nodes more precisely than the benchmark methods. And, the key component of the IIE method can be utilized by other centralities. For example, the information entropy of the IIE method can be also obtained by the neighbors' K-shell values.

Compared to the benchmark methods of the six networks, accuracy of the IIE method can be more satisfactory on identifying the influential nodes, while it poses some inevitable challenges. One of the challenges is that the IIE method merely takes the influence of the spreading rate for the target node into consideration and neglects the impact from target node's neighbors. The distance L of the neighbors' should be paid more attention, for its value affects the performance of the IIE method. We should find out what factors affect the value of L. The temporal network has been paid more and more attention, which requires us to design an advanced information entropy method. And, it remains an interesting and open-ended problem.

Data Availability

The datasets used in the present study are available from the first author upon reasonable request (googlezlf@163.com).

Conflicts of Interest

The authors declare that they have no conflicts of interest.

Acknowledgments

This work was supported by the National Natural Science Foundation of China (no. U1733203), Safety Foundation of CAAC (no. AQ20200019), and Foundation of CAFUC (no. J2020-084).

References

[1] J. Ginsberg, M. H. Mohebbi, R. S. Patel, L. Brammer, M. S. Smolinski, and L. Brilliant, "Detecting influenza epidemics using search engine query data," *Nature*, vol. 457, no. 7232, pp. 1012–1014, 2009.

[2] C. Castellano, S. Fortunato, and V. Loreto, "Statistical physics of social dynamics," *Reviews of Modern Physics*, vol. 81, no. 2, pp. 591–646, 2009.

[3] D. Centola, "The spread of behavior in an online social network experiment," *Science*, vol. 329, no. 5996, pp. 1194–1197, 2010.

[4] R. Pastor-Satorras, C. Castellano, P. Van Mieghem, and A. Vespignani, "Epidemic processes in complex networks," *Reviews of Modern Physics*, vol. 87, no. 3, pp. 925–979, 2015.

[5] J. Wang and J. Wang, "Cross-correlation complexity and synchronization of the financial time series on potts dynamics," *Physica A: Statistical Mechanics and Its Applications*, vol. 541, Article ID 123286, 2020.

[6] J. Wang and J. Wang, "Measuring the correlation complexity between return series by multiscale complex analysis on potts dynamics," *Nonlinear Dynamics*, vol. 89, no. 4, pp. 2703–2721, 2017.

[7] J. Wang, J. Wang, and H. E. Stanley, "Multiscale multifractal dcca and complexity behaviors of return intervals for potts price model," *Physica A: Statistical Mechanics and Its Applications*, vol. 492, pp. 889–902, 2018.

[8] S. Boccaletti, G. Bianconi, R. Criado et al., "The structure and dynamics of multilayer networks," *Physics Reports*, vol. 544, no. 1, pp. 1–122, 2014.

[9] W. Wang, M. Tang, H.-F. Zhang, H. Gao, Y. Do, and Z.-H. Liu, "Epidemic spreading on complex networks with general degree and weight distributions," *Physical Review E*, vol. 90, no. 4, Article ID 042803, 2014.

[10] Z.-K. Zhang, C. Liu, X.-X. Zhan, X. Lu, C.-X. Zhang, and Y.-C. Zhang, "Dynamics of information diffusion and its applications on complex networks," *Physics Reports*, vol. 651, pp. 1–34, 2016.

[11] W. Wang, Q.-H. Liu, J. Liang, Y. Hu, and T. Zhou, "Coevolution spreading in complex networks," *Physics Reports*, vol. 820, pp. 1–51, 2019.

[12] Y. Lin, X. Wang, F. Hao et al., "Dynamic control of fraud information spreading in mobile social networks," *IEEE Transactions on Systems, Man, and Cybernetics: Systems*, vol. 2014, 14 pages, 2014.

[13] W. Wang, M. Tang, H.-F. Zhang, and Y.-C. Lai, "Dynamics of social contagions with memory of nonredundant information," *Physical review e*, vol. 92, no. 1, Article ID 012820, 2015.

[14] R. Albert and A.-L. Barabási, "Statistical mechanics of complex networks," *Reviews of Modern Physics*, vol. 74, no. 1, pp. 47–97, 2002.

[15] M. J. Keeling and P. Rohani, *Modeling Infectious Diseases in Humans and Animals*, Princeton university press, 2011.

[16] R. Pastor-Satorras and A. Vespignani, "Epidemic spreading in scale-free networks," *Physical Review Letters*, vol. 86, no. 14, Article ID 3200, 2001.

[17] R. Pastor-Satorras and A. Vespignani, "Epidemic dynamics and endemic states in complex networks," *Physical Review E*, vol. 63, no. 6, Article ID 066117, 2001.

[18] B. Gross and S. Havlin, "Epidemic spreading and control strategies in spatial modular network," *Applied Network Science*, vol. 5, no. 1, pp. 1–14, 2020.

[19] C. Liu and Z.-K. Zhang, "Information spreading on dynamic social networks," *Communications in Nonlinear Science and Numerical Simulation*, vol. 19, no. 4, pp. 896–904, 2014.

[20] K. M. A. Kabir, K. Kuga, and J. Tanimoto, "Analysis of SIR epidemic model with information spreading of awareness," *Chaos, Solitons & Fractals*, vol. 119, pp. 118–125, 2019.

[21] G. Miritello, E. Moro, and R. Lara, "Dynamical strength of social ties in information spreading," *Physical Review E*, vol. 83, no. 4, Article ID 045102, 2011.

[22] L. Pan, W. Wang, L. Tian, and Y.-C. Lai, "Optimal networks for dynamical spreading," *Physical Review E*, vol. 103, no. 1, Article ID 012302, 2021.

[23] D. Bertsimas and S. S. Patterson, "The traffic flow management rerouting problem in air traffic control: a dynamic network flow approach," *Transportation Science*, vol. 34, no. 3, pp. 239–255, 2000.

[24] K.-C. Pien, K. Han, W. Shang, A. Majumdar, and W. Ochieng, "Robustness analysis of the european air traffic network," *Transportmetrica A: Transport Science*, vol. 11, no. 9, pp. 772–792, 2015.

[25] K. Gopalakrishnan and H. Balakrishnan, "Control and optimization of air traffic networks," *Annual Review of Control, Robotics, and Autonomous Systems*, vol. 4, 2021.

[26] J. Leskovec, L. A. Adamic, and B. A. Huberman, "The dynamics of viral marketing," *ACM Transactions on the Web*, vol. 1, no. 1, p. 5, 2007.

[27] M. Kimura, K. Saito, R. Nakano, and H. Motoda, "Extracting influential nodes on a social network for information diffusion," *Data Mining and Knowledge Discovery*, vol. 20, no. 1, pp. 70–97, 2010.

[28] S. Gao, H. Wang, X. Yuan, and L. Lin, "Cooperative mechanism of sme growth in the mesoscopic structure with strategic and nonstrategic partners," *IEEE Intelligent Systems*, vol. 35, no. 3, pp. 7–18, 2019.

[29] S. Aral and D. Walker, "Identifying influential and susceptible members of social networks," *Science*, vol. 337, no. 6092, pp. 337–341, 2012.

[30] L.-F. Zhong, Q.-H. Liu, W. Wang, and S.-M. Cai, "Comprehensive influence of local and global characteristics on identifying the influential nodes," *Physica A: Statistical Mechanics and Its Applications*, vol. 511, pp. 78–84, 2018.

[31] S. Iyer, T. Killingback, B. Sundaram, and Z. Wang, "Attack robustness and centrality of complex networks," *PloS One*, vol. 8, no. 4, Article ID e59613, 2013.

[32] M. Bellingeri, D. Cassi, and S. Vincenzi, "Efficiency of attack strategies on complex model and real-world networks," *Physica A: Statistical Mechanics and Its Applications*, vol. 414, pp. 174–180, 2014.

[33] Z. Qiu, T. Fan, M. Li, and L. Lü, "Identifying vital nodes by achlioptas process," *New Journal of Physics*, vol. 23, no. 3, p. 033036, 2021.

[34] S. Wang, W. Lv, J. Zhang, S. Luan, C. Chen, and X. Gu, "Method of power network critical nodes identification and robustness enhancement based on a cooperative framework," *Reliability Engineering & System Safety*, vol. 207, Article ID 107313, 2021.

[35] Y.-Y. Liu and A.-L. Barabási, "Control principles of complex systems," *Reviews of Modern Physics*, vol. 88, no. 3, Article ID 035006, 2016.

[36] J. You, J. Leskovec, K. He, and S. Xie, "Graph structure of neural networks," in *Proceedings of the International Conference on Machine Learning*, pp. 10881–10891, PMLR, Shenzhen, China, February 2020.

[37] M. G. Everett and S. P. Borgatti, "Extending centrality," *Models and Methods in Social Network Analysis*, vol. 35, no. 1, pp. 57–76, 2005.

[38] L. Lü, T. Lü, Q. M. Zhang, and H. E. Stanley, "The h-index of a network node and its relation to degree and coreness," *Nature Communications*, vol. 7, no. 1, pp. 1–7, 2016.

[39] D. Chen, L. Lü, L. Lü, Y.-C. Zhang, and T. Zhou, "Identifying influential nodes in complex networks," *Physica a: Statistical Mechanics and Its Applications*, vol. 391, no. 4, pp. 1777–1787, 2012.

[40] M. Kitsak, L. K. Gallos, S. Havlin et al., "Identification of influential spreaders in complex networks," *Nature Physics*, vol. 6, no. 11, pp. 888–893, 2010.

[41] A. Zeng and C.-J. Zhang, "Ranking spreaders by decomposing complex networks," *Physics Letters A*, vol. 377, no. 14, pp. 1031–1035, 2013.

[42] Y. Liu, M. Tang, T. Zhou, and Y. Do, "Core-like groups result in invalidation of identifying super-spreader by k-shell decomposition," *Scientific Reports*, vol. 5, no. 1, pp. 1–8, 2015.

[43] Y. Liu, M. Tang, T. Zhou, and Y. Do, "Improving the accuracy of the k-shell method by removing redundant links: from a perspective of spreading dynamics," *Scientific Reports*, vol. 5, no. 1, pp. 1–11, 2015.

[44] G. Sabidussi, "The centrality index of a graph," *Psychometrika*, vol. 31, no. 4, pp. 581–603, 1966.

[45] L. C. Freeman, "A set of measures of centrality based on betweenness," *Sociometry*, vol. 40, no. 1, pp. 35–41, 1977.

[46] Z.-M. Ren, A. Zeng, D.-B. Chen, H. Liao, and J.-G. Liu, "Iterative resource allocation for ranking spreaders in complex networks," *EPL (Europhysics Letters)*, vol. 106, no. 4, Article ID 48005, 2014.

[47] L.-F. Zhong, J.-G. Liu, and M.-S. Shang, "Iterative resource allocation based on propagation feature of node for identifying the influential nodes," *Physics Letters A*, vol. 379, no. 38, pp. 2272–2276, 2015.

[48] T. Nie, Z. Guo, K. Zhao, and Z.-M. Lu, "Using mapping entropy to identify node centrality in complex networks," *Physica A: Statistical Mechanics and Its Applications*, vol. 453, pp. 290–297, 2016.

[49] X. Ai, "Node importance ranking of complex networks with entropy variation," *Entropy*, vol. 19, no. 7, p. 303, 2017.

[50] C. Guo, L. Yang, X. Chen, D. Chen, H. Gao, and J. Ma, "Influential nodes identification in complex networks via information entropy," *Entropy*, vol. 22, no. 2, p. 242, 2020.

[51] A. Barrat, M. Barthelemy, and A. Vespignani, *Dynamical Processes on Complex Networks*, Cambridge University Press, Cambridge, UK, 2008.

[52] M. E. Newman, "Spread of epidemic disease on networks," *Physical Review E*, vol. 66, no. 1, Article ID 016128, 2002.

[53] V. Batagelj and A. Mrvar, "Pajek-program for large network analysis," *Connections*, vol. 21, no. 2, pp. 47–57, 1998.

[54] J.-G. Liu, Z.-M. Ren, and Q. Guo, "Ranking the spreading influence in complex networks," *Physica A: Statistical Mechanics and Its Applications*, vol. 392, no. 18, pp. 4154–4159, 2013.

[55] B. Rozemberczki and R. Sarkar, "Characteristic functions on graphs: birds of a feather, from statistical descriptors to parametric models," in *Proceedings of the 29th ACM International Conference on Information & Knowledge Management*, pp. 1325–1334, New York. NY. USA, October 2020.

[56] M. G. Kendall, "A new measure of rank correlation," *Biometrika*, vol. 30, no. 1/2, pp. 81–93, 1938.

[57] N. A. Christakis and J. H. Fowler, "The spread of obesity in a large social network over 32 years," *New England Journal of Medicine*, vol. 357, no. 4, pp. 370–379, 2007.

Hindawi
Complexity
Volume 2021, Article ID 9923837, 9 pages
https://doi.org/10.1155/2021/9923837

Research Article

Competing Complex Information Spreading in Multiplex Social Network

Xiang Li and Bocheng Hou

Yellow River Conservancy Technical Institute, Kaifeng, Henan Province 475004, China

Correspondence should be addressed to Bocheng Hou; houbocheng@yrcti.edu.cn

Received 5 March 2021; Accepted 28 April 2021; Published 11 May 2021

Academic Editor: Wei Wang

Coevolution spreading dynamics on complex networks is a hot topic, which attracts much attention in network science. This paper proposes a mathematical model to describe the two competing complex information spreading dynamics on multiplex networks. An individual can only accept one of the two pieces of information. A heterogeneous mean-field theory is developed to describe the spreading dynamics. We reveal different regions through Monte Carlo simulations of the competing complex information spreading dynamics: no global information, one information dominant, and two information coexistence. We finally find that the heterogeneity of the multiplex networks' degree distributions does not qualitatively affect the results.

1. Introduction

Social networks, e.g., WeChat, Twitter, and Facebook, are the convenient way to express and share information with friends [1–5]. Students may retransmit an article to support or oppose the opinions of the authors. To describe the interaction of two types of information spreading dynamics on social networks, researchers used the framework of coevolution spreading dynamics on complex networks [6]. Generally speaking, scholars used complex networks to describe the social network, in which the nodes represent the individuals and edges stand for the relationships among individuals. Extensive empirical analyses revealed that social network exhibits degree heterogeneity, high clustering, multilayer, and temporality [7–18]. Including some of those characteristics, many research studies have been designed (see some important reviews in this field, e.g., reference [19–21]).

Based on the shared information's content, we can classify the information spreading dynamics into simple and complex information [22–24]. The simple information means that a single contact between the informed and susceptible individuals can trigger the infection transmission and widely used to describe epidemic spreading and simple news diffusion. In contrast, single contact cannot eliminate some complex information's legality and reliability (e.g., political networks). Therefore, social reinforcement is included in the dynamics of complex information spreading. In the following content, we present the progress for simple and complex information spreading detailedly.

The study about the simple information spreading on complex networks independently is the most widely investigated and revealed some critical results. For instance, simple information can always spread in the social network regardless of the values of information transmission probability when the heterogeneity of degree distribution is extremely strong [25–27]. Besides, the high clustering promotes the breakout of the information while suppresses the spreading size for large transmission probability [28]. Once several information are transmitted simultaneously, scholars revealed more novel phenomena. When two pieces of information are spreading on networks consecutively, the second information's outbreak threshold is larger than the threshold of the first information [29]. Karrer and Newman [30] further considered two competing spreading dynamics on the single network simultaneously. By using the competing percolation theory, they found that two epidemic cannot coexist in the thermodynamic limit (i.e., when the

network size is extremely large). Sahneh and Scoglio [31] investigated two competing information on multiplex networks and computed the absolute-dominance and coexistence regions. When two information collaborate, i.e., if the acceptance probability for another information is enlarged when an individual accepts one information, the system exhibits a discontinuous phase transition [32–34]. Scholars considered another situation, asymmetric interacting, i.e., one spreading dynamic promotes the other. In contrast, the other one suppresses the spreading and reveals that the global epidemic will be greatly suppressed once the information spreading is included [35–37].

To include the social reinforcement in the dynamics of complex information spreading, the linear threshold model is the most widely used, in which an individual accepts the information only when the received information is larger than a threshold [22, 38–40]. Setting the final spreading size as the order parameter, researchers revealed the discontinuous phase transition in the system. More detailedly, the final spreading size versus the transmission probability exhibits a discontinuous growth. Liu et al. [41] investigated two complex information spreading consecutively on single complex network and revealed a transition for continuous and discontinuous phase transitions. Furthermore, Liu et al. [42] studied two complex synergetic information spreading dynamics on multiplex networks and revealed that the synergetic induced the discontinuous phase transition. To the best of our knowledge, there is still lacking a mathematical model to investigate two competing complex information spreading dynamics on multiplex networks. We will propose a mathematical model in section 2 and then develop a heterogeneous mean-field theory in section 3. We further study the complex competing information spreading model by using Monte Carlo simulation in section 4. Finally, we conclude in section 5.

2. Competing Complex Information Spreading Model

This section proposes the competing information spreading model on social network to describe different opinions evolving in the campus.

2.1. Network Description. Students usually discuss the events happened and diffuse the information or opinions through social platforms. We here use a multiplex network $G = (N_A, N_B, E_A, E_B)$ to describe the multiplex social network with two layers A and B, where N_A and N_B, respectively, represent the sizes of networks A and B and E_A and E_B, respectively, stand for the number of edges in of networks A and B. Nodes stand for the student users, and edges mean the relationships among those users. If two students i and j communicate with each other in network A (B), an edge exists between them.

We assume there are $n = |N_A| = |N_B|$ students in the social network and $e_A = |E_A|$ and $e_B = |E_B|$ connections among them. Therefore, the average degrees of the social network are $\widetilde{k_A} = (2e_A/n)$ and $\widetilde{k_B} = (2e_B/n)$, respectively. The two networks' degree distribution is denoted as $P_A(k_A)$ and $P_B(k_B)$, respectively. Nodes with large degrees mean that they have more communication with friends and always act as hubs. A node in two networks represents that it communicates with others through two platforms. To build the multiplex network, we first generate the intralayer edges using the uncorrelated configuration model proposed in reference [43] according the degree distributions $P_A(k_A)$ and $P_B(k_B)$. Then, we build the interlayer edges randomly, that is to say, we randomly match two nodes in the two subnetworks.

2.2. Competing Spreading Dynamics. In social networks, students always express different opinions on the same event, and as a result, additional information is competing with each other. In reality, adopting an idea is risky. Therefore, social reinforcement is included. Social reinforcement means that the adoption of the information requires multiple verifications from friends. We here adopt a generalized susceptible-informed-recovered model to describe the two information spreading dynamics. The susceptible node means that it does not know the information and can adopt the information. An informed node stands for that adopted the information and willing to transmit it to friends. A node in the recovered state means that it has lost interest in the information.

The two competing information spreading dynamics are denoted as ℓ_A and ℓ_B. We assume information ℓ_A and ℓ_B, respectively, spread on networks A and B simultaneously. The competing between two dynamics means that a node cannot adopt two information simultaneously. The two competing spreading dynamics evolve as follows. Initially, we randomly select a node infected by ℓ_A and ℓ_B in two subnetworks. At every time step, every node informed by information ℓ_h ($h \in \{A, B\}$) will transmit the information to its neighboring nodes in network h with probability λ. To eliminate the information's credibility, we include the social reinforcement and assume a node adopting information ℓ_h must receive $T > 1$ pieces. A susceptible node i, respectively, obtains $m_A \geq T$ and $m_B \geq T$ pieces of ℓ_A and ℓ_B information at time step t, and it adopts information ℓ_A with probability $m_A/(m_A + m_B)$ and adopts information ℓ_B with probability $m_B/(m_A + m_B)$. The informed nodes are recovered with probability γ. The two competing spreading dynamics evolve until there are no nodes in the informed state. The pseudocode of the competing spreading dynamics as shown in Algorithm 1. At each time step, the time complexity of the algorithm is $\mathcal{O}(E)$, where E is the number of edges in the network. The space complexity is $\mathcal{O}(N)$.

3. Theoretical Analysis

Mathematically, the competing information spreading dynamics on social networks can be described by using the heterogeneous mean-field approach [25, 26, 44], which is widely used in investigating the dynamics on networks. There are some basic assumptions behind the heterogeneous mean-field approach as follows:

(1) Input: network G, and dynamical parameters λ, T, γ, w;
(2) Output: spreading sizes of information ℓ_A and ℓ_B and denoted as R_A and R_B;
(3) $t \leftarrow 0$;
(4) Randomly a seed for information ℓ_A and ℓ_B, and put them into queue Q_A;
(5) **while** Q_A is not empty **do**
(6) $m_A \leftarrow 0$;
(7) $m_B \leftarrow 0$;
(8) Initialize Q_B to be empty;
(9) $\delta t \leftarrow 1/\text{length}(Q_A)$;
(10) **for** $i = 1$ to length(Q_A) **do**
(11) **if** Node i adopt the information ℓ_A **then** Node i transmits the information to every susceptible neighbor j in subnetwork A with probability λ;
(12) **if** Node j received the information ℓ_A successfully **then**
(13) $m_A \leftarrow m_A + 1$;
(14) **end if**
(15) **end if**
(16) **if** Node i adopt the information ℓ_B **then**
(17) Node i transmits the information to every susceptible neighbor in subnetwork B with probability λ;
(18) **if** Node j received the information ℓ_A successfully **then**
(19) $m_A \leftarrow m_A + 1$;
(20) **end if**
(21) **end if**
(22) **if** $m_A \geq T$ and $m_B \geq T$ **then**
(23) Node j adopts information ℓ_A with probability $m_A/(m_A + m_B)$;
(24) **if** Node j adopts information ℓ_A **then**
(25) Adding node j into queue Q_B;
(26) **end if**
(27) Node j adopts information ℓ_B with probability $m_B/(m_A + m_B)$;
(28) **if** Node j adopts information ℓ_B **then**
(29) Adding node j into queue Q_B;
(30) **end if**
(31) **end if**
(32) **if** $m_A \geq T$ and $m_B < T$ **then**
(33) Node j adopts information ℓ_A with probability 1;
(34) Adding node j into queue Q_B;
(35) **end if**
(36) **if** $m_A < T$ and $m_B \geq T$ **then**
(37) Node j adopts information ℓ_B with probability 1;
(38) Adding node j into queue Q_B;
(39) **end if**
(40) **end for**
(41) **for** $i = 1$ to length(Q_A) **do**
(42) Recovering node i with probability γ;
(43) **if** Node i recovers **then**
(44) Delete node i from queue Q_A;
(45) **end if**
(46) **end for**
(47) **for** $i = 1$ to length(Q_B) **do**
(48) Adding node i to queue Q_A;
(49) Deleting node i from queue Q_B;
(50) **end for**
(51) $t \leftarrow t + \delta t$
(52) **end while**

Algorithm 1: Competing spreading dynamics.

(i) The network size is large enough.

(ii) There are no degree-degree correlations in the network.

(iii) The infection probability of informed nodes is independent, i.e., there are no dynamical correlations among nodes. Based on the above assumptions, we derive the evolution equations for competing information spreading dynamics.

To describe the evolution equations, we use the following mathematical notations $s_{k_A}^{\ell_A}(t)$, $\rho_{k_A}^{\ell_A}(t)$, and $r_{k_A}^{\ell_A}(t)$ to represent the probability that a node with degree k_A in subnetwork A is in the susceptible, informed, and recovered state for information ℓ_A at time t. Similarly, we use $s_{k_B}^{\ell_B}(t)$, $\rho_{k_B}^{\ell_B}(t)$, and $r_{k_B}^{\ell_B}(t)$ to represent the probability that a node with degree k_B in subnetwork B is in the susceptible, informed, and recovered state for information ℓ_B at time t. Since the symmetry of the two spreading dynamics, we only describe the evolution equations for one of them. At time step t, the fraction of nodes in susceptible, informed, and recovered for information ℓ_h $(h \in \{A, B\})$ is $S^{\ell_h}(t) = \sum P_h(k_h) s_{k_h}^{\ell_h}(t)$, $\rho^{\ell_h}(t) = \sum P_h(k_h)\rho_{k_h}^{\ell_h}(t)$, and $R^{\ell_h}(t) = \sum P_h(k_h) r_k^{\ell_h}(t)$, respectively. In the following, we derive the evolutions of $s_{k_h}^{\ell_h}(t)$, $\rho_{k_h}^{\ell_h}(t)$, and $r_{k_h}^{\ell_h}(t)$.

The fraction of $s_{k_h}^{\ell_h}(t)$ decreases once node i with degree kk_h in subnetwork h becomes informed. On the one hand, node i must receive $m_{\ell_h} \geq T$ pieces of information ℓ_h in subnetwork h at time t. In uncorrelated network, the probability of node i connecting to an informed node j with degree k_h' is $k_h' P_h(k_h)/\langle k_h \rangle$. Therefore, the probability of node j transmits the information to node i successfully which is $\lambda k_h' P_h(k_h)/\langle k_h \rangle \rho_{k_h}^{\ell_h}(t)$. The pieces of information ℓ_h that node i received at time t are

$$m_{\ell_h} = k_h \lambda \frac{1}{\langle k_h \rangle} \sum_{k_h'} k_h' P_h(k_h) \rho_{k_h}^{\ell_h}(t). \tag{1}$$

According to descriptions of the model, we know node i adopts information ℓ_h with probability

$$\xi_{\ell_h} = \frac{m_{\ell_h} \delta_{m_{\ell_h} \geq T}}{m_{\ell_h} \delta_{m_{\ell_h} \geq T} + m_{\ell_g} \delta_{m_{\ell_g} \geq T}}, \tag{2}$$

where $\delta_{m_{\ell_h} \geq T} = 1$ if $m_{\ell_h} \geq T$; otherwise, $m_{\ell_h} \geq T = 0$. Note that ℓ_g is the other type of information. Based the above discussions, we know the evolution of $s_k^{\ell_h}(t)$ as

$$\frac{\mathrm{d}s_{k_h}^{\ell_h}(t)}{\mathrm{d}t} = -s_{k_h}^{\ell_h}(t) s_{k_h}^{\ell_g}(t) \xi_{\ell_h}. \tag{3}$$

With a similar discussion, we know the evolutions of $\rho_{k_h}^{\ell_h}(t)$ and $r_{k_h}^{\ell_h}(t)$ as

$$\begin{aligned} \frac{\mathrm{d}\rho_{k_h}^{\ell_h}(t)}{\mathrm{d}t} &= -\gamma \rho_{k_h}^{\ell_h}(t) + s_{k_h}^{\ell_h}(t) s_{k_h}^{\ell_g}(t) \xi_{\ell_h}, \\ \frac{\mathrm{d}\rho_{k_h}^{\ell_h}(t)}{\mathrm{d}t} &= \gamma \rho_{k_h}^{\ell_h}(t), \end{aligned} \tag{4}$$

respectively.

4. Results Analysis

In this section, we numerically study the competing information spreading on multiplex networks detailedly. We study the competing information spreading on two types of multiplex networks. The first one is ER-ER multiplex network, i.e., networks A and B are Erdös–Rényi (ER), in which the degree distribution follows a Poisson distribution. That is to say, the degree distribution of subnetwork $h \in \{A, B\}$ is $P_h(k_h) = (\langle k_h \rangle^{k_h}/k_h!) e^{-\langle k_h \rangle}$, where $\langle k_h \rangle$ is the average degree of subnetwork h. We assume there is no interlayer degree-degree correlations, and thus the joint degree distribution is $P(k_A, k_B) = (\langle k_A \rangle^{k_A}/\ k_A!) e^{-\langle k_A \rangle} (\langle k_B \rangle^{k_B}/\ k_B!) e^{-\langle k_B \rangle}$. For ER-ER multiplex networks, the degree distribution is homogeneous. In reality, many real-data revealed that the degree distribution is heterogeneous. We therefore use the SF-SF multiplex networks, in which the two subnetworks are both scale-free networks. The degree distribution of subnetwork $h \in \{A, B\}$ is $P_h(k_h) = (1/\varepsilon_h) k_h^{-\gamma_h}$, where $\varepsilon_h = \sum k_h k_h^{-\gamma_h}$. Similar with ER-ER multiplex networks, we assume there is no interlayer degree-degree correlations, and the joint degree distribution is $P(k_A, k_B) = (1/\varepsilon_A \varepsilon_B) k_A^{-\gamma_A} k_B^{-\gamma_B}$. In numerical simulations, we set the network size $n = N_A = N_B = 2 \times 10^4$ and $\langle k_A \rangle = \langle k_B \rangle = 10$. The results presented in the paper are averaged over at least 1000 times.

4.1. ER-ER Multiplex Networks. Because the social reinforcement is included in the information spreading dynamics, we first study the effects of initial seed size in Figure 1. To study the fraction of new informed nodes by each information, we investigate $R_A - \rho_0$ and $R_B - \rho_0$ versus λ_A for different values of λ_B and ρ_0. For small values of λ_B, e.g., $\lambda_B = 0.2$, the fraction of new informed nodes by the seeds depends on the fraction of seeds shown in Figure 1(a). When the seed is small (e.g., $\rho_0 = 0.01$), any values of information transmission probability λ_A cannot trigger the global outbreak for information ℓ_A. Since the social reinforcement is included, a small fraction of seeds cannot further adopt the information. With the increase in ρ_0, the global outbreak of ℓ_A becomes possible when λ_A is above the threshold point λ_A^c. Note that λ_A^c can be numerically determined by studying the variability χ of $R_A - \rho_0$, and at the threshold point, χ exhibits a peak. We do not show χ in this paper. Note that the global information of ℓ_B cannot outbreak when $\lambda_B = 0.2$, as shown in Figure 1(b). For larger values of λ_B, such as $\lambda_B = 0.5$ and 0.8, we find that a small fraction of seeds cannot trigger the global outbreak for the two types of information (see Figures 1(c)–1(f)). For larger values of $\rho_0 = 0.05$ and 0.1, $R_A - \rho_0$ increases with λ_A, meanwhile $R_B - \rho_0$ decreases with λ_A. We note that two types of information may coexist, and the coexistence conditions are discussed detailedly in Figure 2.

In Figure 2, we investigate the fractions of new informed nodes by the two types of information triggered by the initial seeds on a plane (λ_A, λ_B). As shown in Figure 2(a), the global information can not trigger small values λ_A. Previous studies

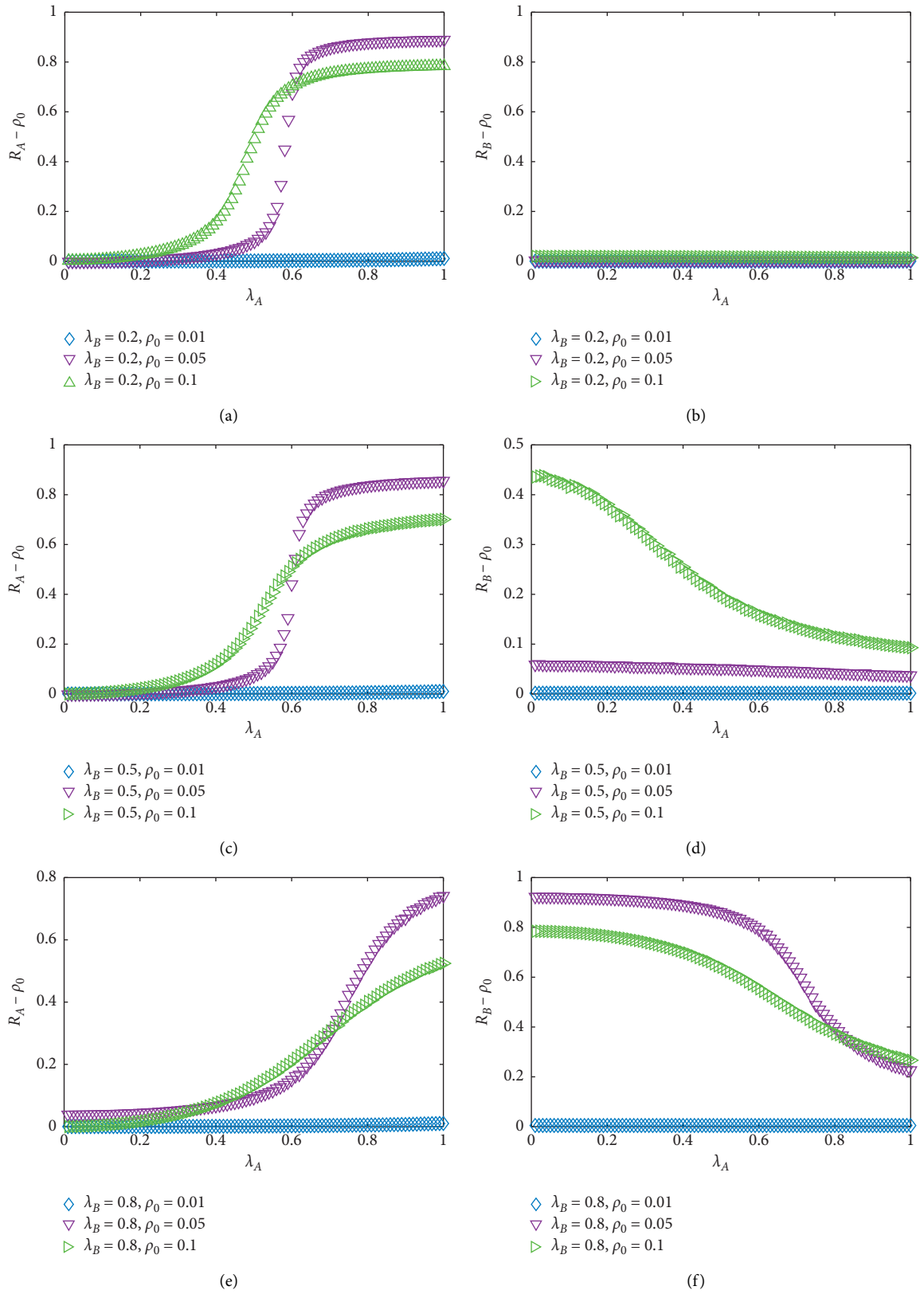

FIGURE 1: Competing information spreading on ER-ER multiplex networks: (a) The new informed information spreading size $R_A - \rho_0$ of information ℓ_A; (b) new informed information spreading size $R_B - \rho_0$ of information ℓ_B as a function of λ_A with $\lambda_B = 0.2$; (c)$R_A - \rho_0$; (d)$R_B - \rho_0 \lambda_A$ with $\lambda_B = 0.5$; (e)$R_A - \rho_0$; (f)$R_B - \rho_0 \lambda_A$ with $\lambda_B = 0.8$. We set the threshold $T = 2$, the average degrees of the two networks are $\langle k_A \rangle = \langle k_B \rangle = 10$, and we set the recovery probability $\gamma = 0.5$.

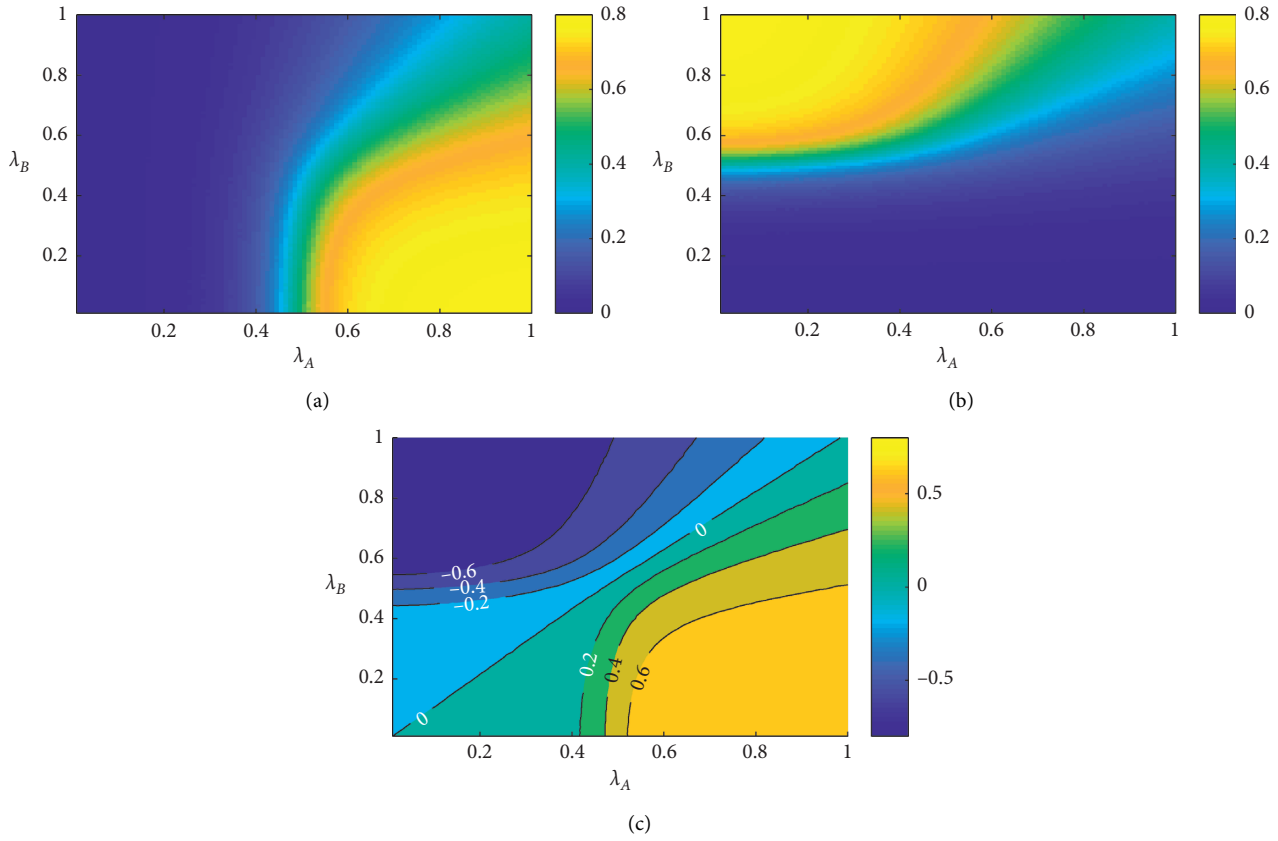

FIGURE 2: Competing information spreading on ER-ER multiplex networks versus information transmission probability: (a) the new informed information spreading size $R_A - \rho_0$ of information ℓ_A; (b) new informed information spreading size $R_B - \rho_0$ of information ℓ_B; (c)$R_A - R_A$ as a function of (λ_A, λ_B). We set the threshold $T = 2$, the average degrees of the two networks are $\langle k_A \rangle = \langle k_B \rangle = 10$, and we set the initial fraction seed of the two types of information as $\rho_0 = 0.1$ and $\gamma = 0.5$.

indicated that the global information outbreak threshold of information ℓ_A is $\lambda_A^0 = 1/\langle k_A \rangle = 0.1$ when there is only information ℓ_A spreading on network A. However, when the two competing information spreads on multiplex networks simultaneously, the global information cannot break when λ_A slightly is more extensive than λ_A^0. We know that the competing information suppresses the spreading dynamics, and the global information outbreak threshold λ_A^c is much larger than λ_A^0. With the two information spreading dynamics' symmetry mechanisms, we find the similar phenomena of $R_B - \rho_0$ in Figure 2(b).

One important question is the domination and coexistence of regions. Domination means that one information spreads to most nodes, while the other only transmits to a few nodes. Coexistence stands for the two types of information spread to a large fraction of nodes. To this end, we study $R_A - R_B$ in Figure 2(c). For the case of $R_A - R_B > 0$, we know information ℓ_A dominates. When $R_A < R_B$, the information ℓ_B dominates. When $R_A \approx R_B$, the two types of information compete for the nodes. Combing Figures 2(a)–2(c), we speculate information ℓ_A dominates when $\lambda_A > \lambda_A^0$ and $\lambda_A \gg \lambda_B$. Similarly, ℓ_B dominates when $\lambda_B > \lambda_B^0 = 1/\langle k \rangle$ and $\lambda_B \gg \lambda_A$. The two types of information are competing with the nodes and can coexist when $\lambda_A \approx \lambda_B$, $\lambda_A > \lambda_A^0$, and $\lambda_B > \lambda_B^0$.

In Figure 3, we further study the effects of the average degrees on the competing information spreading dynamics when $\lambda_A = \lambda_B$. When the two types of information spreading on the two networks with the same average degree, i.e., $\langle k_A \rangle = \langle k_B \rangle = 10$, we find that $R_A - \rho_0$ and $R_B - \rho_0$ exhibit the similar behavior, that is to say, $R_A - \rho_0$ and $R_B - \rho_0$ increase monotonously with the increase in $\lambda_A = \lambda_B$. However, $R_A - \rho_0$ first increases with $\lambda_A = \lambda_B$ and then decreases when $\langle k_A \rangle > \langle k_B \rangle$, e.g., $\langle k_A \rangle = 15$ and $\langle k_A \rangle = 10$. That is to say, there exists a peak at which $R_A - \rho_0$ reaches its maximum. Meanwhile, $R_B - \rho_0$ always increases with $\lambda_A = \lambda_B$ regardless the values of $\langle k_A \rangle$ and $\langle k_B \rangle$.

4.2. SF-SF Multiplex Networks. Finally, we study the two competing information spreading on SF-SF multiplex networks in Figure 4 and investigate the effects of degree heterogeneity of the two networks on the spreading dynamics. Compared with the ER-ER networks, the SF-SF networks promote the spreading dynamics since the existence of some nodes with large degrees. In addition, we find that the degree heterogeneity does not qualitatively affect the phenomena presented in Figure 2. That is to say, the domination and coexistence regions are the same. The domination region of information ℓ_A is $\lambda_A > \lambda_A^0$ and $\lambda_A \gg \lambda_B$. Similarly, information

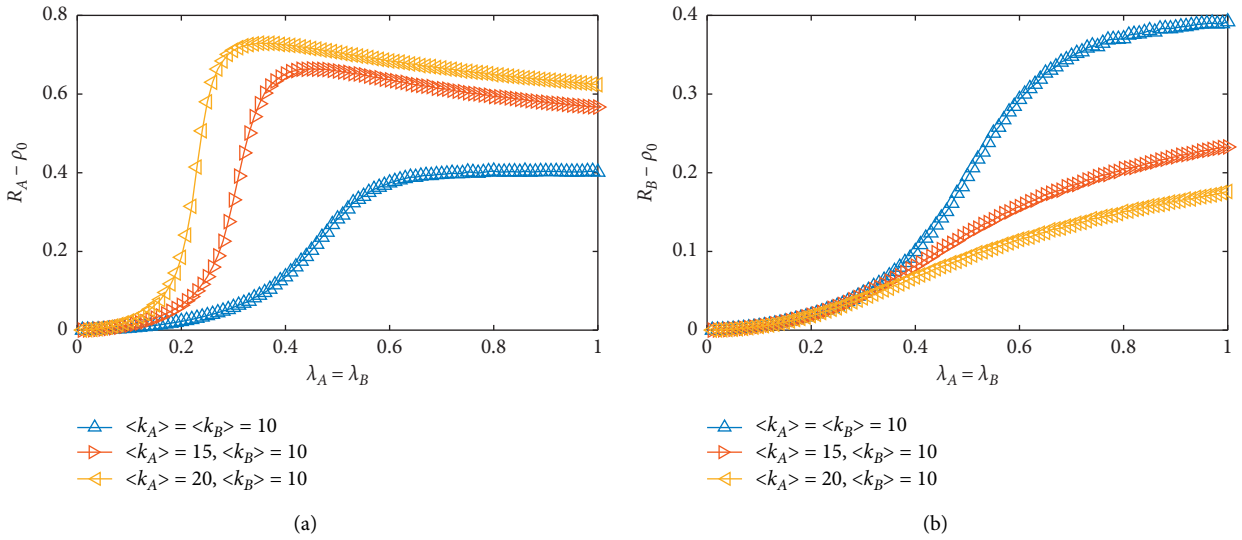

FIGURE 3: Competing information spreading on ER-ER multiplex networks: (a) the new informed information spreading size $R_A - \rho_0$ of information ℓ_A; (b) new informed information spreading size $R_B - \rho_0$ of information ℓ_B function of $\lambda_A = \lambda_B$. We set the threshold $T = 2$ and the initial fraction seed of the two types of information as $\rho_0 = 0.1$ and $\gamma = 0.5$.

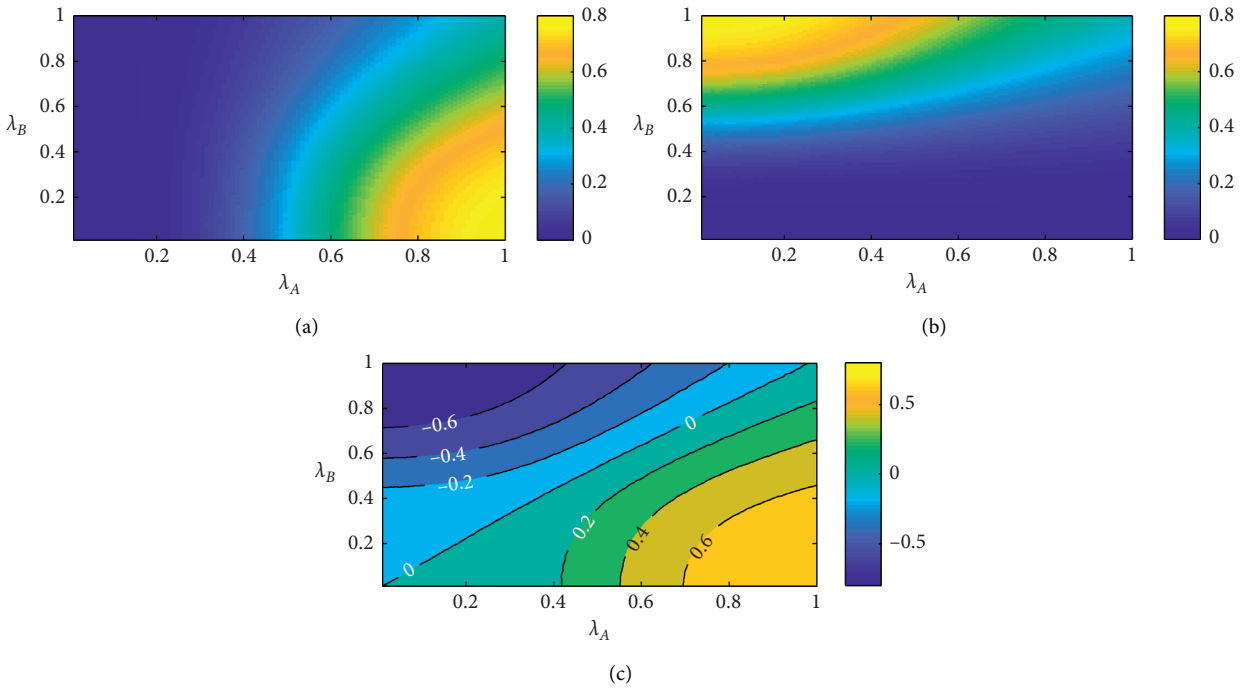

FIGURE 4: Competing information spreading on SF-SF multiplex networks versus information transmission probability: (a) the new informed information spreading size $R_A - \rho_0$ of information ℓ_A; (b) new informed information spreading size $R_B - \rho_0$ of information ℓ_B; (c)$R_A - R_A$ as a function of (λ_A, λ_B). We set the threshold $T = 2$, the average degrees of the two networks are $\langle k_A \rangle = \langle k_B \rangle = 10$, the degree exponents are $\gamma_A = \gamma_B = 3.0$, and we set the initial fraction seed of the two types of information as $\rho_0 = 0.1$ and $\gamma = 0.5$.

ℓ_B domination region is $\lambda_B > \lambda_B^0 = 1/\langle k \rangle$ and $\lambda_B \gg \lambda_A$. The coexistence region is $\lambda_A \approx \lambda_B$, $\lambda_A > \lambda_A^0$, and $\lambda_B > \lambda_B^0$.

5. Discussion

Coevolution spreading dynamics aims at describing interacting dynamics and revealing the phenomena induced by distinct interacting mechanisms. In this paper, we proposed a competing complex information model to describe two types of information diffusion on multiplex networks. A heterogeneous mean-field theory is developed to describe the model. Through extensive numerical simulations, we revealed the conditions of different regions. Specifically, no global information outbreak region is $\lambda_A \leq \lambda_A^0$ and $\lambda_B \leq \lambda_B^0$;

information ℓ_A dominant is $\lambda_A > \lambda_A^0$ and $\lambda_A \gg \lambda_B$; information ℓ_B dominant is $\lambda_B > \lambda_B^0$ and $\lambda_B \gg \lambda_A$; and two information coexistence region is $\lambda_A \approx \lambda_B$, $\lambda_A > \lambda_A^0$, and $\lambda_B > \lambda_B^0$. When the two competing complex information spread on a multiplex with heterogeneous degree distribution, the phenomena do not qualitatively be affected. The results presented in this paper may shed some light into further investigating the competing spreading, such as design of effective strategy to make one spreading always win regardless of the other spreading dynamics and network structures.

Data Availability

The data used to support the findings of this study are available from the corresponding author upon request.

Conflicts of Interest

The authors declare that they have no conflicts of interest.

Acknowledgments

This work was partially supported by the Ministry of Education Science and Technology Development Center University Research Innovation Fund: "Qingtai Digital Intelligence Integration" Collaborative Innovation, no. 2020QT20.

References

[1] D. Knoke and S. Yang, *Social Network Analysis*, Sage Publications, Thousand Oaks, CF, USA, 2019.

[2] G. Kossinets and D. J. Watts, "Empirical analysis of an evolving social network," *Science*, vol. 311, no. 5757, pp. 88–90, 2006.

[3] P. J. Carrington, J. Scott, and S. Wasserman, *Models and Methods in Social Network Analysis*, Vol. 28, Cambridge University Press, Cambridge, UK, 2005.

[4] Y. Amichai-Hamburger and G. Vinitzky, "Social network use and personality," *Computers in Human Behavior*, vol. 26, no. 6, pp. 1289–1295, 2010.

[5] M. Burke, C. Marlow, and T. Lento, "Social network activity and social well-being," in *Proceedings of the SIGCHI Conference on Human Factors in Computing Systems*, pp. 1909–1912, Atlanta, GO, USA, April 2010.

[6] W. Wang, Q.-H. Liu, J. Liang, Y. Hu, and T. Zhou, "Coevolution spreading in complex networks," *Physics Reports*, vol. 820, pp. 1–51, 2019.

[7] M. Newman, *Networks*, Oxford University Press, Oxford, UK, 2018.

[8] A.-L. Barabási, "The new science of networks," *Physics Today*, vol. 6, no. 5, 2003.

[9] A.-L. Barabási and R. Albert, "Emergence of scaling in random networks," *Science*, vol. 286, no. 5439, pp. 509–512, 1999.

[10] F. Papadopoulos, M. Kitsak, M. Á. Serrano, M. Boguñá, and D. Krioukov, "Popularity versus similarity in growing networks," *Nature*, vol. 489, no. 7417, pp. 537–540, 2012.

[11] P. Holme, "Rare and everywhere: perspectives on scale-free networks," *Nature Communications*, vol. 10, p. 1016, 2019.

[12] A. Clauset, C. R. Shalizi, and M. E. J. Newman, "Power-law distributions in empirical data," *SIAM Review*, vol. 51, no. 4, pp. 661–703, 2009.

[13] M. Kivelä, A. Arenas, M. Barthelemy, J. P. Gleeson, Y. Moreno, and M. A. Porter, "Multilayer networks," *Journal of Complex Networks*, vol. 2, no. 3, pp. 203–271, 2014.

[14] M. De Domenico, A. Solé-Ribalta, E. Cozzo et al., "Mathematical formulation of multilayer networks," *Physical Review X*, vol. 3, p. 041022, 2013.

[15] M. De Domenico, V. Nicosia, A. Arenas, and V. Latora, "Structural reducibility of multilayer networks," *Nature Communications*, vol. 6, p. 6864, 2015.

[16] P. Holme, "Modern temporal network theory: a colloquium," *The European Physical Journal B*, vol. 88, p. 234, 2015.

[17] P. Holme and J. Saramäki, *Temporal Network Theory*, Vol. 2, Springer, Berlin, Germany, 2019.

[18] X. Xue, L. Pan, M. Zheng, and W. Wang, "Network temporality can promote and suppress information spreading," *Chaos: An Interdisciplinary Journal of Nonlinear Science*, vol. 30, no. 11, p. 113136, 2020.

[19] Z.-K. Zhang, C. Liu, X.-X. Zhan, X. Lu, C.-X. Zhang, and Y.-C. Zhang, "Dynamics of information diffusion and its applications on complex networks," *Physics Reports*, vol. 651, pp. 1–34, 2016.

[20] C. Castellano, S. Fortunato, and V. Loreto, "Statistical physics of social dynamics," *Reviews of Modern Physics*, vol. 81, no. 2, pp. 591–646, 2009.

[21] M. De Domenico, C. Granell, M. A. Porter, and A. Arenas, "The physics of spreading processes in multilayer networks," *Nature Physics*, vol. 12, no. 10, pp. 901–906, 2016.

[22] D. J. Watts, "A simple model of global cascades on random networks," *Proceedings of the National Academy of Sciences*, vol. 99, no. 9, pp. 5766–5771, 2002.

[23] D. J. Watts and P. S. Dodds, "Influentials, networks, and public opinion formation," *Journal of Consumer Research*, vol. 34, no. 4, pp. 441–458, 2007.

[24] E. Bakshy, J. M. Hofman, W. A. Mason, and D. J. Watts, "Everyone's an influencer: quantifying influence on twitter," in *Proceedings of the Fourth ACM International Conference on Web Search and Data Mining*, pp. 65–74, Hong Kong, China, February 2011.

[25] R. Pastor-Satorras and A. Vespignani, "Epidemic dynamics and endemic states in complex networks," *Physical Review E*, vol. 63, p. 066117, 2001.

[26] R. Pastor-Satorras and A. Vespignani, "Epidemic dynamics in finite size scale-free networks," *Physical Review E*, vol. 65, p. 035108, 2002.

[27] S. Gómez, A. Arenas, J. Borge-Holthoefer, S. Meloni, and Y. Moreno, "Discrete-time Markov chain approach to contact-based disease spreading in complex networks," *EPL (Europhysics Letters)*, vol. 89, no. 3, p. 38009, 2010.

[28] M. E. Newman, "Random graphs with clustering," *Physical Review Letters*, vol. 103, p. 058701, 2009.

[29] M. E. Newman, "Threshold effects for two pathogens spreading on a network," *Physical Review Letters*, vol. 95, p. 108701, 2005.

[30] B. Karrer and M. E. Newman, "Competing epidemics on complex networks," *Physical Review E*, vol. 84, p. 036106, 2011.

[31] F. D. Sahneh and C. Scoglio, "Competitive epidemic spreading over arbitrary multilayer networks," *Physical Review E*, vol. 89, p. 062817, 2014.

[32] L. Chen, "Persistent spatial patterns of interacting contagions," *Physical Review E*, vol. 99, p. 022308, 2019.

[33] L. Chen, F. Ghanbarnejad, and D. Brockmann, "Fundamental properties of cooperative contagion processes," *New Journal of Physics*, vol. 19, no. 10, p. 103041, 2017.
[34] W. Cai, L. Chen, F. Ghanbarnejad, and P. Grassberger, "Avalanche outbreaks emerging in cooperative contagions," *Nature Physics*, vol. 11, no. 11, pp. 936–940, 2015.
[35] W. Wang, M. Tang, H. Yang, Y. Do, Y.-C. Lai, and G. Lee, "Asymmetrically interacting spreading dynamics on complex layered networks," *Scientific Reports*, vol. 4, p. 5097, 2014.
[36] C. Granell, S. Gómez, and A. Arenas, "Dynamical interplay between awareness and epidemic spreading in multiplex networks," *Physical Review Letters*, vol. 111, p. 128701, 2013.
[37] W. Wang, Q.-H. Liu, S.-M. Cai, M. Tang, L. A. Braunstein, and H. E. Stanley, "Suppressing disease spreading by using information diffusion on multiplex networks," *Scientific Reports*, vol. 6, p. 29259, 2016.
[38] M. S. Granovetter, "The strength of weak ties," *American Journal of Sociology*, vol. 78, no. 6, pp. 1360–1380, 1973.
[39] J. P. Gleeson and D. J. Cahalane, "Seed size strongly affects cascades on random networks," *Physical Review E*, vol. 75, p. 056103, 2007.
[40] W. Wang, M. Tang, H.-F. Zhang, and Y.-C. Lai, "Dynamics of social contagions with memory of nonredundant information," *Physical Review E*, vol. 92, p. 012820, 2015.
[41] Q.-H. Liu, L.-F. Zhong, W. Wang, T. Zhou, and H. Eugene Stanley, "Interactive social contagions and co-infections on complex networks," *Chaos*, vol. 28, p. 013120, 2018.
[42] Q.-H. Liu, W. Wang, S.-M. Cai, M. Tang, and Y.-C. Lai, "Synergistic interactions promote behavior spreading and alter phase transitions on multiplex networks," *Physical Review E*, vol. 97, p. 022311, 2018.
[43] M. Catanzaro, M. Boguná, and R. Pastor-Satorras, "Diffusion-annihilation processes in complex networks," *Physical Review E*, vol. 71, p. 027103, 2005.
[44] W. Wang, M. Tang, H. E. Stanley, and L. A. Braunstein, "Unification of theoretical approaches for epidemic spreading on complex networks," *Reports on Progress in Physics*, vol. 80, p. 036603, 2017.

Hindawi
Complexity
Volume 2021, Article ID 6655469, 12 pages
https://doi.org/10.1155/2021/6655469

Research Article

Symbiosis Evolution of Science Communication Ecosystem Based on Social Media: A Lotka–Volterra Model-Based Simulation

Ming Xia,[1] **Xiangwu He**,[2] **and Yubin Zhou**[1]

[1]*School of Economics and Management, Tongji University, Shanghai 200092, China*
[2]*Business School, Jiaxing University, Jiaxing 314001, China*

Correspondence should be addressed to Yubin Zhou; dazhou@tongji.edu.cn

Received 15 December 2020; Revised 27 February 2021; Accepted 1 April 2021; Published 15 April 2021

Academic Editor: Jiaojiao Jiang

Social media has become an important way for science communication. Some scholars have examined how to help scientists engage with social media from operational training, policy guidance, and social media services improving. The main contribution of this study is to construct a symbiosis evolution model of science communication ecosystem (SCE) between scientists and social media platforms based on the symbiosis theory and the Lotka–Volterra model to discuss the evolution of their symbiotic patterns and population size under different symbiosis coefficients. The results indicate that (1) the size of the symbiosis coefficients determines the equilibrium outcome of the symbiosis evolution of scientists and social media platforms; (2) scientists and social media platforms can promote each other's population size under the mutualism pattern, which can achieve sustainable science communication; (3) "$1 + 1 > 2$" effect can only be achieved under the symmetric mutualism pattern and the growth of scientists and social media platforms is more stable and sufficient than that of other patterns. The findings will provide additional perspectives for promoting the sustainable development of science communication based on social media.

1. Introduction

The communication between scientists and the public is changing as we enter the information age. It is a fact of mass communication effect research that exposure is a necessary condition for media effect and that communication activities often fail due to insufficient exposure [1]. The rapid development of new media, such as social media, has brought tremendous changes to the technological environment of science communication [2]. It has become one of the most influential factors in science communication, and the study of media as an environmental factor has become a research hotspot [3].

Social media has dramatically changed the ecological environment of science communication. The traditional form of media essentially disseminates information from a single point to the target audience [4]. The emergence of social media has created a domain-based electronic community that facilitates information interaction [5, 6]. In addition to changing the way information is disseminated, shortening the temporal and spatial distance between the public and the scientific community, and creating conditions for public participation in scientific research, changes in the technological environment have more importantly enriched the vector of dissemination of scientific information. Since the publication of Robert Hook's micrographs, images have been placed at the center of the modern science communication process [7]. In the era of digital communication, technological advances have enriched the transmission medium of science and technology information. The development of video images, virtual reality, augmented reality, and mixed reality technology has created a visual information-intensive environment for science communication and greatly expanded the dimension of interaction between experts and the public [8].

In recent years, recognizing the enormous potential of the changing technological environment at the level of knowledge exchange and knowledge diffusion, the academic community has begun to experiment with the use of social media as a way to communicate their academic ideas to the

public [9]. Through the use of social media in the process of academic research, social media has become structurally embedded in the scholarly communication system [10]. Scholars have confirmed the possibility of using social media for scientific research [11, 12]. Previous research has established that researchers can build connections and conduct academic exchanges through social media and obtain new research ideas from them, and there is evidence of a positive trend in this kind of use [13–15]. However, statistics show that most scientists have yet to use social media such as Facebook, Twitter, WeChat, and Weibo in their professional or academic work [16]. Collins et al. (2012) surveyed a large number of scholars from the US and UK on the use of social media and found that 3% of them are highly active on Twitter [17]. These data are far from the 23% of American adult users owned by Twitter and 71% of American adult users owned by Facebook. This gap also shows that the habit of using social media in academic workplaces has not yet been developed [18].

Therefore, what prevents scientists from using social media to engage in science communication? Most scholars believe that scientists are supposed to be dedicated to their research, not to the promotion of their findings on social media, and that the dissemination of science through the media results in the undermining of scientists' authority [19]. "Sagan Effect" has been used to describe scientists who "risk the contempt of serious scientists by becoming science communicators." The bias can be roughly summed up as scientists who are diligent in science communication are second-rate scientists [20]. After the gradual development of science communication, more scientists have emerged to participate in science communication, but the "Sagan Effect" still influences scientists' choices. Besides, it has been shown that some scientists are fearful of using social media due to a lack of knowledge about the usage of social media, privacy, and other considerations, which leads to knowledge barriers at the level of ability to use social media [21]. "Lack of time" is another important influencing factor, time wastage has been identified as an important barrier to scientists' outreach [22], in the field of science communication, the use of social media is considered a waste of time by some researchers [23, 24], as well as the lack of general clarity on the benefits of participating in social media, and the fact that social media themselves are at odds with scientific rigor make social media unattractive to scientists [25].

Further, how to help scientists use social media? Collins et al. (2016) advocate guiding scientists to engage with social media by conducting professional development training workshops or a more explicit departmental social media use policy [26]. Training usually includes helping scientists find and clarify their message, learning to work with media professionals, and preparing for the use of social media [27–29]. The science communication training program has developed rapidly in recent years; it emphasizes technical communication skills and guides scientists to find their communication opportunities. Exemplars of programs include Alan Alda Center for Communicating Science, the Center for Public Engagement with Science and Technology at the American Association for the Advancement of Science, COMPASS, and the Portal to the Public Network [30, 31]. From the perspective of social media platforms, some scholars have studied the service upgrades made by social media platforms to attract scientists and other content creators [32]. To be an attractive platform for users (especially content creators), social media offers a variety of features, such as allowing users to create their channels, postcontent that can be immediately shared with a wide audience, choose to become friends with others, or subscribe to other channels, and then comment on or choose the content what you like [33]. Features provide an incentive for content creators, including scientists. Also, content creators can share revenue generated by user donations through the platform, which supports social media to ensure its innovation and long-term viability [34]. The scale effect of social media can attract more content creators to participate in science communication [35]. Similarly, as a major force of science communication, the increase in the number of groups of scientists is indicative of a strong user demand that can lead to more niche social media-based science communication platforms [36, 37]. There is a symbiosis relationship between scientists and social media platforms, and the population numbers between scientists and social media platforms influence each other.

In summary, scholars have researched the current situation of scientists' participation in social media, the reasons for the lack of participation vitality, and the measures that should be taken and have achieved relatively rich results. A review of the literature reveals that existing research mainly focuses on the individual level of scientists and social media platforms. Scholars hope to achieve compatibility between scientists and social media on individual changes, thereby enhancing the vitality of scientists to participate in social media. From an ecological point of view, scientists and social media platforms, as two symbiotic units in the science communication ecosystem (SCE), are symbiosis relationship, and a change in the population size of one will have an impact on the population size of the other inevitably. In this study, we discuss the population symbiosis between scientists and social media platforms from an ecological perspective, establish a Lotka–Volterra population competition model between scientists and social media platforms, and investigate the symbiosis evolution between them with different symbiosis coefficients under a certain environmental carrying capacity, to complement the research about scientists' use of social media for sustainable science communication.

The remainder of this study is mainly divided into the following sections. Section 2 is preliminary. Section 3 introduces the symbiosis evolution model of the SCE based on the Lotka–Volterra model. Sections 4 and 5 are simulation analyses and conclusions, respectively.

2. Preliminary

2.1. Symbiosis Theory. The concept "symbiosis" is of Greek origin and was first introduced by the German mycologist Anto de Bary in 1879 to refer to the concept of different genera living together in an extended material relationship

[38]. Symbiosis is a self-organizing phenomenon and the need for survival between living organisms is inevitably interdependent and interactive in some way, forming a symbiosis relationship of coexistence and synergistic evolution [39]. However, the concept of symbiosis has not yet been harmonized due to the influence of different disciplinary contexts. Symbiosis in the narrower sense is considered as a reciprocal, mutually beneficial cooperative relationship between species. The German scientist Buchner considered symbiosis to be an intimate, enduring union between two dissimilar organisms and tended to limit it to a mutually beneficial union [40]. Dale Weis defines symbiosis as a stable, enduring, and intimate combined relationship between several pairs of cooperators [41]. In a broad sense, symbiosis is the existence of power relationships between species such as metabolism and energy conversion. Margulis, an American biologist, pointed out from an ecological point of view that "symbiosis is the union of important parts of the life cycles of individuals of different species" [39]. Goff (1982) pointed out that symbiosis includes various degrees of parasitism, commensalism, and mutualism [38].

Based on the symbiosis theory, Yuan (1998) discussed the three elements: symbiotic units, symbiotic patterns, and symbiotic environment [42]. The symbiotic units are the basic units of energy production and exchange that constitute the symbiosis relationship, which is the basis for the existence of the symbiosis relationship; the symbiotic pattern, also known as the symbiosis relationship, is the form of interaction or combination of symbiotic units, which reflects not only the pattern of action between the symbiotic units but also the intensity of action, which reflects the exchange of material information between the symbiotic units, as well as the exchange of energy between the symbiotic units; the symbiotic environment refers to the exogenous conditions for the development of the existence of the symbiotic pattern, and the sum of all factors other than the symbiotic units constitute the symbiotic environment, which is the guarantee for the survival of the symbiotic units. Three elements are indispensable as shown in Figure 1.

2.2. Structure of SCE. SCE based on social media is a complex system composed of multiple individual users gathered on a certain type of social media platform and formed by the interconnection and influence of its external network environment and the real social environment. Similar to the natural ecosystem, the SCE has a continuous evolutionary process from creation, expansion, maintenance to decline. The structure is an important indicator of the balance and sustainability of an ecosystem [43, 44]. The structure of the SCE refers to the combination of the relatively stable interaction patterns of various components and the internal manifestations of their temporal and spatial relationships. This study focuses on the analysis of the symbiosis relationship between scientists and social media platforms in terms of the ecological chain structure of the SCE and the flow of information resources.

The ecological chain structure of the ecosystem mainly refers to the network structure formed by the chain network between biological components [45]. Take natural ecosystems as an example. Although natural ecosystems vary greatly in appearance, structure, and feature, each natural ecosystem has three main elements, producers, consumers, and decomposers, and realizes the smooth flow of matter and energy through the above three main elements [46, 47]. The SCE belongs to the category of the social ecosystem, but it still has the relevant elements of the natural ecosystem. These similarities are manifested in the similar ecological chain structure of the natural ecosystem and the science ecosystem, but they are still different, as shown in Figure 2.

The natural ecological chain is composed of producers, multilevel consumers, and decomposers. Producers and primary consumers, primary consumers, and secondary consumers form an ecological sequence through the preying relationship. Producers and consumers involved in each link of energy flow are decomposed and released into the environment again to form a closed loop of energy flow.

The difference between the science communication ecological chain and the natural ecological chain is mainly reflected in the changes in the relationship between producers and consumers. The relationship between producers and consumers in the natural ecological chain is predation. Energy flow is a one-way flow from producers to consumers [48]. However, there is no traditional "predation" relationship between scientists and the public in the science communication ecological chain, or the meaning of "predation" has been transformed into a two-way symbiosis relationship between scientists' access to public attention and the public's access to knowledge from scientists. Scientists and social media platforms, social media platforms, and the public form a symbiosis relationship through the flow of information, and because of the addition of a two-way adjustment mechanism with feedback, the way of information flow has also changed from one-way to two-way, and the positive direction of information flow represents the process of scientific communication, and reverse flow represents the process of information consultation and feedback.

3. Methodology

This section will introduce the background and development status of the Lotka–Volterra model at first and then build a model of the symbiosis evolution of SCE based on the Lotka–Volterra model considering the specific context of the issue. Finally, we will discuss the different symbiosis relationships under different symbiosis coefficients and the stable conditions at this time.

3.1. Lotka–Volterra Model. In this paper, the authors attempt to explore the symbiosis and evolution of scientists and social media platforms in the SCE with computer simulation methods. The SCE based on social media is an ecosystem composed of scientific communities, social media platforms, users, and so on. This study draws on the ecological evolution method to explore the number, structure, and overall evolution of its internal population. From an

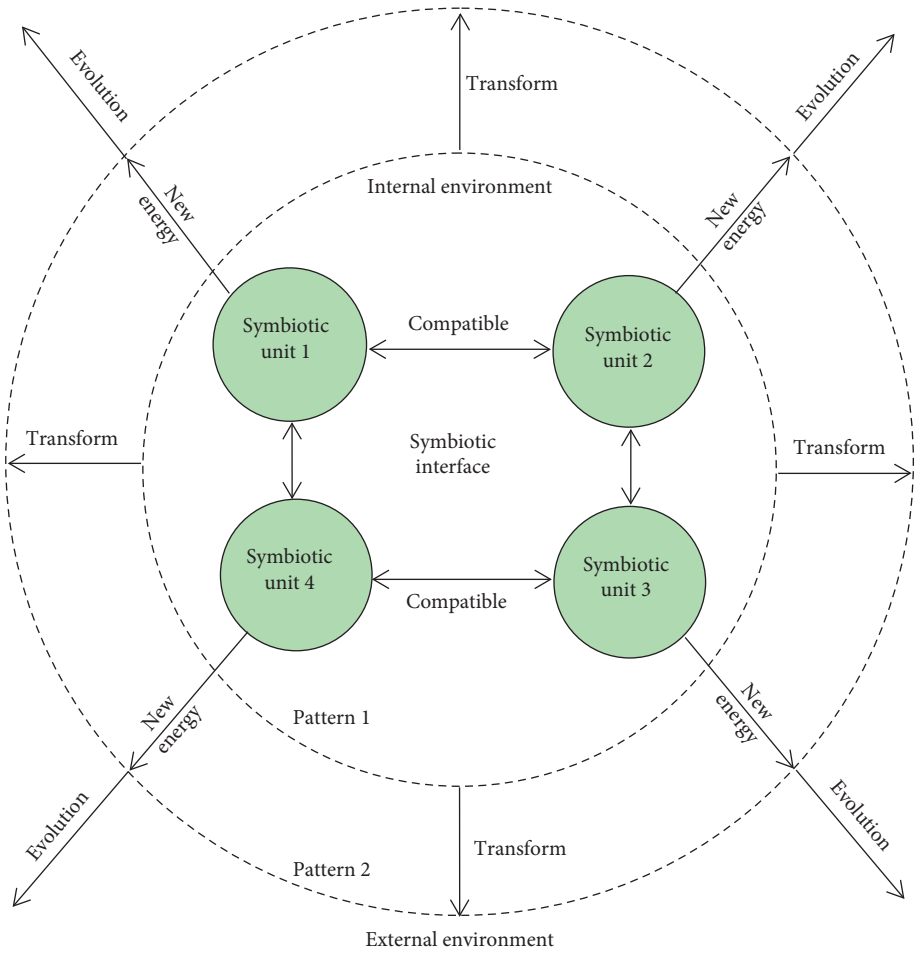

Figure 1: Symbiosis evolution of symbiotic units. The symbiotic units exchange energy and information through quality parameters on the symbiotic interface, and the new energy generated changes the symbiosis pattern and gradually realizes the symbiosis evolution.

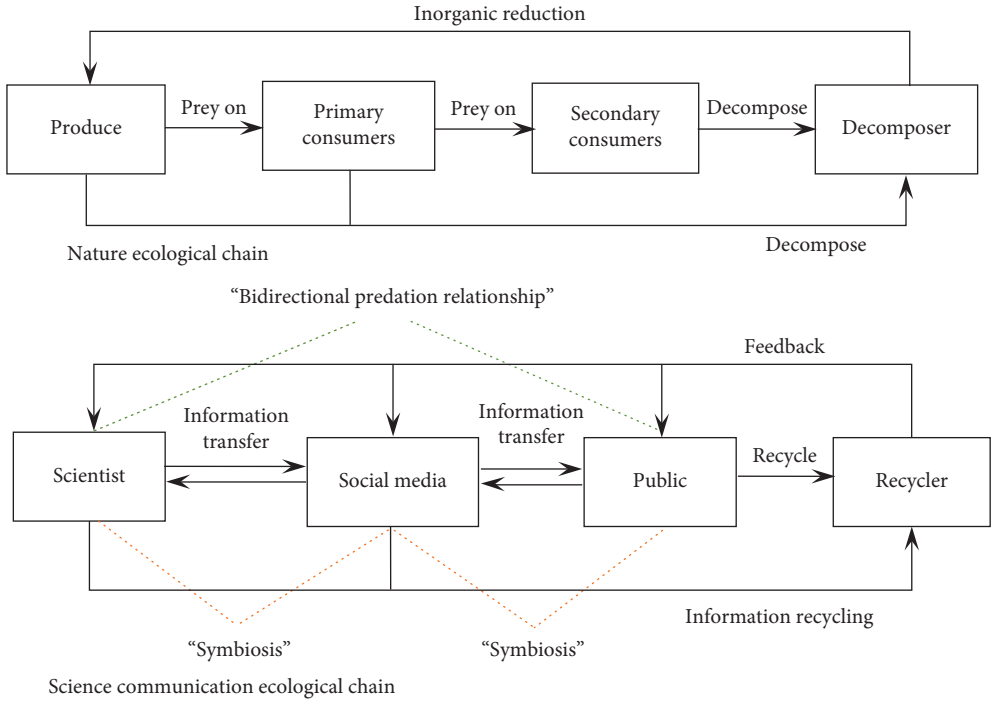

Figure 2: Comparison between nature ecological chain and science communication ecological chain. The direction of the arrow indicates the direction of information or energy flow, and the dashed line indicates the relationship between the two sides.

ecological point of view, the growth and change law of biological populations is as follows: in a short period, generally follow the Malthus model growth law; that is, the population size grows exponentially; with the growth of time, the population size gradually increases, the influence of density constraints is increasing and showing the logistic growth law, and the growth rate of population size becomes slower and gradually reaches saturation. The differential equation expression is shown in model

$$\frac{dN(t)}{dt} = \alpha N(t)\left(1 - \frac{N(t)}{N^*}\right). \tag{1}$$

In model (1), suppose that there is one population in the ecosystem under a certain natural growth rate α. The population size $N(t)$ will gradually change over time and reach the maximum population size N^*in a specific environment eventually. The logistic model was first applied to the estimation of population, and then it was widely used in population ecology and sociology [49].

The Lotka–Volterra model is proposed by Lotka and Volterra based on a single species logistic model, which considers the dynamic growth of two or more populations in the ecosystem at the same time [50], as shown in model

$$\frac{dN_1(t)}{dt} = \alpha_1 N_1(t)\left(1 - \frac{N_1(t)}{N_1^*} - \delta\frac{N_2(t)}{N_2^*}\right). \tag{2}$$

In model (2), suppose that there are two populations in the ecosystem under a certain natural growth rate α_1. The population size of each species is affected not only by the size of its population but also by the size of another population. The population size $N_1(t)$ will gradually change over time and reach the maximum population size N_1^* in a specific environment eventually.

Lotka–Volterra model has good data fitting and prediction performance and is widely used in research in various fields such as economics, business, urbanization, and sociology. In economic research, Bernardo and D'Alessandro (2016) studied a macroeconomic framework based on the Lotka–Volterra model to assess the social and economic consequences of investing in low-carbon options [51]. In business research, Khan et al. (2018) studied the impact of low-cost airlines on Korean full-service companies and tourism based on the Lotka–Volterra model [52]. In the urbanization research, Assumma et al. (2019) discussed how to use the system dynamics model and the Lotka–Volterra model to assess regional elasticity [53]. In sociological research, Marasco and Romano (2018) used Lotka–Volterra to study the intergenerational conflicts in the American aging society from 1974 to 2014 [54]. Ditzen (2018) studied the multinational convergence of the Lotka–Volterra model [55]. Christodoulakis (2016) used the dynamic Lotka–Volterra model to quantitatively analyze the armed confrontation that occurred in Greece from 1946 to 1949 and explained the dynamics and costs of the conflict in the Greek Civil War [56].

3.2. Analysis of the Symbiosis Evolution

3.2.1. Hypothesis

Hypothesis 1. There is a certain number of scientists and social media platforms in the SCE. The population of scientists and social media platforms is affected by factors such as policy, economy, society, infrastructure, technology, scientific research environment, and science communication industry environment.

Hypothesis 2. Changes in the scale of scientists and social media platforms in the social media ecology reflect their respective growth conditions. The positive change in the population size indicates the use of various science resources in the SCE. The higher the degree, the greater the gains obtained during the evolution of the symbiosis relationship and the better the growth; the reverse change of the population size indicates that the population has a low degree of utilization of various scientific resources in the SCE in the context of science communication, and the symbiosis relationship is evolving. The income obtained is low, and the growth of the population is poor. When the utilization rate of a population for popular science resources is 0, it indicates that the population is extinct.

Hypothesis 3. The growth process of the group of scientists and social media platforms obeys the logistic growth law. Due to the limitation of the capacity of the ecosystem, the population growth rate when each participant grows alone will gradually decrease as the population density increases.

Hypothesis 4. When the marginal output of the population of scientists or social media platforms equals the marginal input, the population growth rate tends to 0, and the population reaches its maximum size.

3.2.2. Symbiosis Evolution Model. Assume that the two groups grow independently and do not affect each other. We suppose that the population numbers of scientists and social media platforms are N_1 and N_2 and the natural growth rates are α_1 and α_2, respectively. N_1^* and N_2^* are here used to refer to the maximum size of the two types of the population under the given resource elements. The dynamic evolution equations of the two types of symbiotic units in the SCE can be expressed as equation group

$$\begin{cases} \dfrac{dN_1(t)}{dt} = \alpha_1 N_1(t)\left[1 - \dfrac{N_1(t)}{N_1^*}\right], \\ N_1(0) = N_{10}, \\ \dfrac{dN_2(t)}{dt} = \alpha_2 N_2(t)\left[1 - \dfrac{N_2(t)}{N_2^*}\right], \\ N_2(0) = N_{20}. \end{cases} \tag{3}$$

In the equation group (3), the initial size of the population of scientists and social media organizations in social media networks is N_{10} and N_{20}, respectively. $\alpha_1 N_1(t)$ and $\alpha_2 N_2(t)$ are used here to refer to reflect the number of scientists participating in social media and the development trend of the population of social media platforms; $1-(N_1(t)/N_1^*)$ and $1-(N_2(t)/N_2^*)$ are the logistic coefficient, which is used here to refer to the hindrance of the growth of their scale due to the consumption of limited resources by the two types of participants, respectively.

Considering the interaction between populations and according to the symbiosis theory, the two types of symbiotic units will undergo a transition from one symbiosis pattern to another during the development process, embodying different symbiosis effects and forming different symbiosis relationships [57]. When two types of symbiotic units interact in the SCE, the growth of each type of symbiotic unit is not only affected by its population size but also related to the population size of the other type of symbiotic units. According to the Lotka–Volterra model, the symbiosis coefficient δ is here introduced to reflect the size of the symbiosis effect. Based on this, the dynamic model of the interaction and evolution of the population of social media scientists and social media organizations can be expressed as equation group

$$\begin{cases} \dfrac{\mathrm{d}N_1(t)}{\mathrm{d}t} = \alpha_1 N_1(t)\left[1-\dfrac{N_1(t)}{N_1^*}-\delta_{21}\dfrac{N_2(t)}{N_2^*}\right], \\ N_1(t_0) = N_{10}, \\ \dfrac{\mathrm{d}N_2(t)}{\mathrm{d}t} = \alpha_2 N_2(t)\left[1-\dfrac{N_2(t)}{N_2^*}-\delta_{12}\dfrac{N_1(t)}{N_1^*}\right], \\ N_2(t_0) = N_{20}. \end{cases} \tag{4}$$

In equation group (4), δ_{12} and δ_{21} are symbiosis coefficient, which is used here to indicate the symbiosis effect of scientists participating in social media on the population size of social media organizations and social media organizations on the population size of scientists participating in social media. That is, the changes of the quality parameter of the other party caused by the interaction between the quality parameters $N_1(t)$ and $N_2(t)$, $\delta_{21}(N_2(t)/N_2^*)$ and $\delta_{12}(N_1(t)/N_1^*)$ indicate the degree of influence caused by both parties, and the values of δ_{12} and δ_{21} reflect the symbiotic pattern of the two types of symbiosis units in the SCE.

3.2.3. Model Analysis. According to the different value ranges of $\delta_{12}$and δ_{21}, the Lotka–Volterra model of the interaction of the two types of symbiotic units and their symbiosis relationship is discussed in Table 1.

It can be seen that the result of the symbiosis evolution between the group of scientists and social media organizations in the SCE depends on the value of the symbiosis coefficient. To study the symbiosis evolution relationship between scientists and social media organizations, it is necessary to analyze the equilibrium point and stability conditions of the dynamic evolution equation and analyze the symbiosis evolution results of the two types of symbiotic units. When $(\mathrm{d}N_1(t)/\mathrm{d}t)=0$ and $(\mathrm{d}N_2(t)/\mathrm{d}t)=0$, the four local equilibrium points of the symbiosis evolution of different symbiosis units in the social media ecological network can be obtained, namely, $E_1(0,0)$, $E_2(N_1^*,0)$, $E_3(0,N_2^*)$, and $E_4((N_1^*(1-\delta_{21})/1-\delta_{21}\delta_{12}),(N_2^*(1-\delta_{12})/1-\delta_{12}))$. For the SCE described by a system of differential equations to participate in the evolution of the subject, the stability of its equilibrium point can be obtained by analyzing the local stability of the Jacobian matrix. Taking the partial derivatives of $N_1$and $N_2$for the differential equations, in turn, the Jacobian matrix of the symbiosis evolution between scientists and social media organizations in the SCE can be obtained as equation (5):

$$J = \begin{pmatrix} \alpha_1\left(1-2\dfrac{N_1(t)}{N_1^*}-\delta_{21}\dfrac{N_2(t)}{N_2^*}\right) & -\alpha_1\delta_{21}\dfrac{N_1(t)}{N_2^*} \\ -\alpha_2\delta_{12}\dfrac{N_2(t)}{N_1^*} & \alpha_2\left(1-2\dfrac{N_2(t)}{N_2^*}-\delta_{12}\dfrac{N_1(t)}{N_1^*}\right) \end{pmatrix}. \tag{5}$$

The method of using the Jacobian matrix to judge whether the equilibrium point is locally asymptotically stable is as follows: when the system equilibrium point makes $\det(J)>0$ and $\mathrm{tr}(J)<0$, then it is a stable equilibrium point. At this time, the equilibrium point is in a locally progressive and stable state. Therefore, in the SCE, the conditions for the symbiosis evolution between the group of scientists and social media organizations are $\det(J)>0$ and $\mathrm{tr}(J)<0$. The specific analysis results are shown in Table 2.

4. Results and Discussion

4.1. Simulation Analysis. The two types of symbiotic units, scientists and social media platforms, adopt a division of labor and cooperation to create new value, generate newly available resources, promote the evolution of symbiosis relationships, expand the scale of the SCE through the reuse of resources, and improve the operational efficiency of the SCE. This study uses MATLAB2019a to simulate the

Table 1: The value range of the symbiosis coefficient and its corresponding symbiosis pattern. δ_{21} represents the influence coefficient of the scale change of population 2 on the growth of population 1.

Value range	Symbiosis pattern	Feature
$\delta_{12} = 0, \delta_{21} = 0$	Not symbiosis	Two symbiotic units developed independently
$\delta_{12} > 0, \delta_{21} > 0$	Not symbiosis	Two symbiotic units compete maliciously
$\delta_{12} < 0, \delta_{21} > 0$ or $\delta_{12} > 0, \delta_{21} < 0$	Parasitic	Two types of symbiotic units, one reduced ($\delta > 0$) and the other benefited ($\delta < 0$)
$\delta_{12} < 0, \delta_{21} = 0$ or $\delta_{12} = 0, \delta_{21} < 0$	Commensalism	Two types of symbiotic units, one that benefits ($\delta < 0$) and the other that does not affect ($\delta = 0$)
$\delta_{12} < 0, \delta_{21} < 0$	Mutualism	Asymmetric mutualism between two types of symbiotic units ($\delta_{12} \neq \delta_{21}$); symmetric mutualism between two types of symbiotic units ($\delta_{12} = \delta_{21}$)

Table 2: Equilibrium and stability condition of SCE.

Equilibrium	det(J)	tr(J)	Stability condition
$E_1(0,0)$	$\alpha_1\alpha_2$	$\alpha_1 + \alpha_2$	Unstable
$E_2(N_1^*, 0)$	$-\alpha_1\alpha_2(1-\delta_{12})$	$-\alpha_1 + \alpha_2(1-\delta_{12})$	$\delta_{12} > 1$
$E_3(0, N_2^*)$	$-\alpha_1\alpha_2(1-\delta_{21})$	$-\alpha_2 + \alpha_1(1-\delta_{21})$	$\delta_{21} > 1$
$E_4((N_1^*(1-\delta_{21})/1-\delta_{21}\delta_{12}), (N_2^*(1-\delta_{12})/1-\delta_{12}))$	$(\alpha_1\alpha_2(\delta_{21}-1)(\delta_{12}-1)/1-\delta_{21}\delta_{12})$	$(\alpha_1(\delta_{21}-1)+\alpha_2(\delta_{12}-1)/1-\delta_{21}\delta_{12})$	$\delta_{21} < 1, \delta_{12} < 1$

differential equations (3) to explore how the community of scientists and social media platforms interact and evolve symbiosis under different values of δ_{12} and δ_{21} as shown in

$$\begin{bmatrix} \frac{dN_1(t)}{dt} \\ \frac{dN_2(t)}{dt} \end{bmatrix} = \begin{bmatrix} \alpha_1 N_1(t)\left(1 - \frac{N_1(t)}{N_1^*} - \delta_{21}\frac{N_2(t)}{N_2^*}\right) \\ \alpha_2 N_2(t)\left(1 - \frac{N_2(t)}{N_2^*} - \delta_{12}\frac{N_1(t)}{N_1^*}\right) \end{bmatrix}, \quad (6)$$

$$\begin{bmatrix} N_{10} \\ N_{20} \end{bmatrix} = \begin{bmatrix} 100 \\ 100 \end{bmatrix}.$$

This paper uses the fourth-fifth-order Runge–Kutta algorithm to solve the numerical problem. It is assumed that the natural growth rates of the population of scientists participating in social media and the social media platforms are $\alpha_1 = 0.02$ and $\alpha_2 = 0.01$, respectively, the maximum growth scale of the two types of symbiosis units is $N_1^* = N_2^* = 100$, when resources and environment allow, the iteration period is set to 1000, and the simulation results are shown in Figures 3–8 .

(1) Independent coexistence. Figure 3 shows the simulation results of the two types of symbiotic units in the SCE under the independent coexistence pattern. At this time, there is no symbiosis relationship between them, and the symbiosis coefficient between the scientist and the social media platform is 0. In this pattern, the growth rate of the two types of symbiotic units does not affect each other, and the growing scale is only affected by its growth rate. In the independent coexistence pattern, the stable equilibrium point is (N_1^*, N_2^*); that is, when the two types of symbiotic units are in equilibrium, their growth scale reaches the upper limit. This pattern generally exists in the early stage of the formation of the SCE. Science communication activities not only are related to startups but also involve various entities in the system. Therefore, this pattern is very rare, short-lived, and unstable.

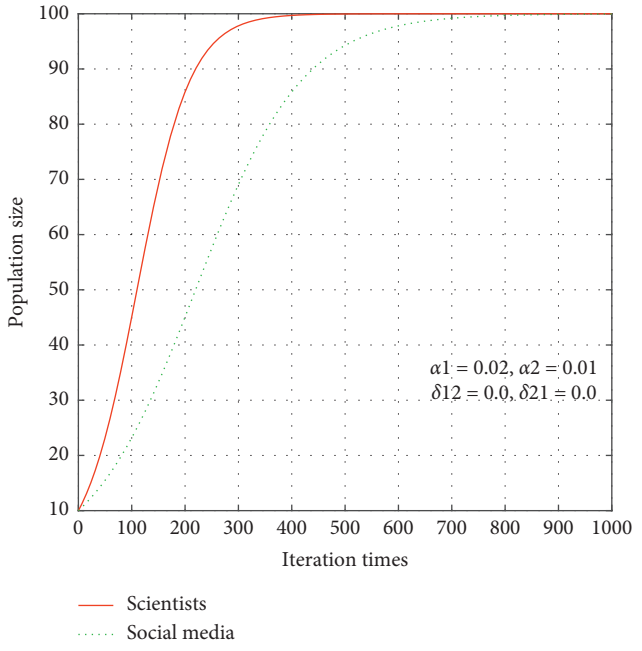

Figure 3: Independent coexistence pattern. Changes in the size of the two populations after 1000 iterations ($\alpha_1 = 0.02$, $\alpha_2 = 0.01$, $\delta_{12} = 0$, and $\delta_{21} = 0$).

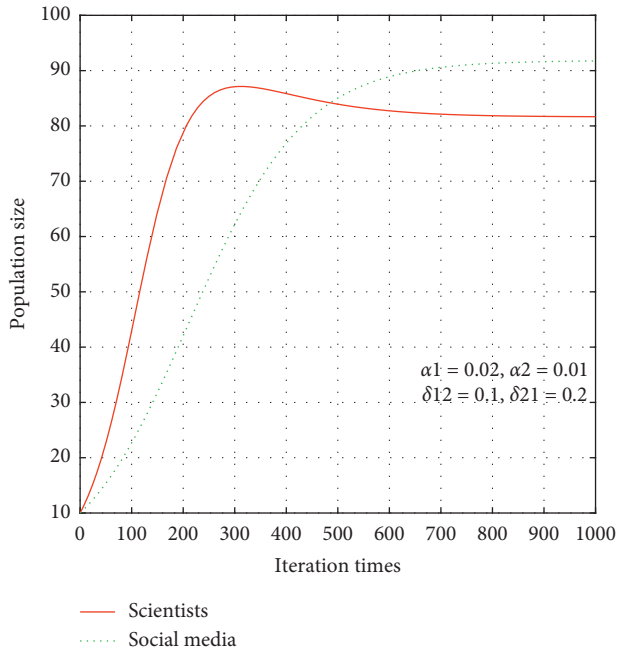

Figure 4: Competitive coexistence pattern. Changes in the size of the two populations after 1000 iterations ($\alpha_1 = 0.02$, $\alpha_2 = 0.01$, $\delta_{12} = 0.1$, and $\delta_{21} = 0.2$).

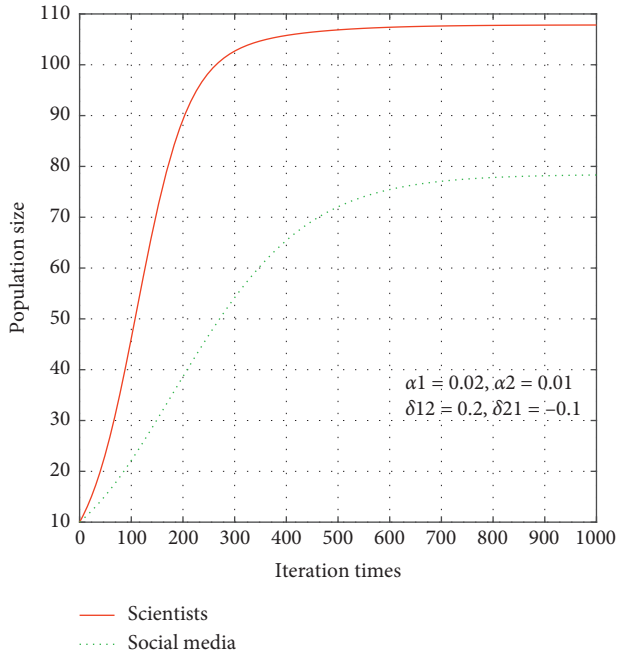

Figure 5: Parasitic coexistence pattern. Changes in the size of the two populations after 1000 iterations ($\alpha_1 = 0.02$, $\alpha_2 = 0.01$ $\delta_{12} = 0.2$, and $\delta_{21} = -0.1$).

(2) Competitive coexistence. In the evolution of the SCE, another pattern that does not exist in symbiosis is competition and coexistence. As shown in Figure 4, the symbiosis coefficient between the scientist group and the social media platform at this time is greater than 0, the symbiosis coefficient of the participating social media scientists on the social media platform is greater than 1, and the stable equilibrium point is $(N_1^*, 0)$. This pattern may exist when scientists have better resources and technology from other channels. Social media platforms tend to decline due to the consumption of a large number of resources, and the group of scientists has survived. However, due to mutual competition, the group of scientists has also suffered losses, and it is difficult to exceed the maximum scale under its constraints N_1^*.

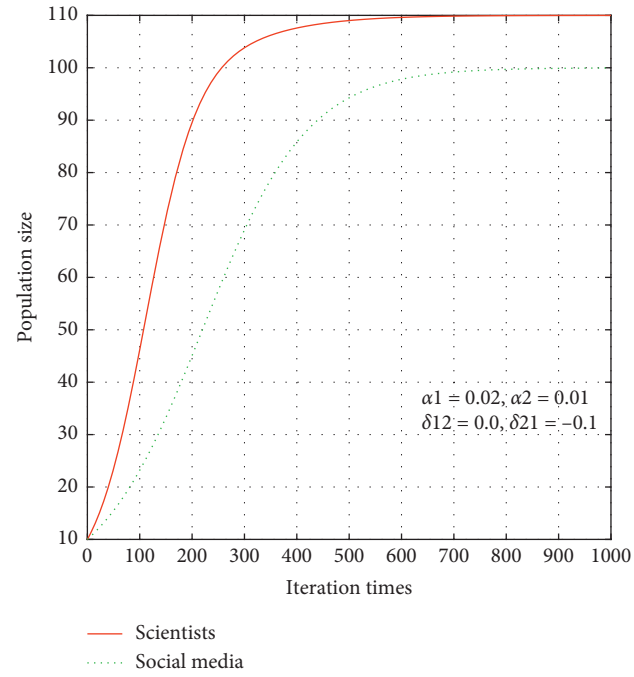

Figure 6: Commensalism pattern. Changes in the size of the two populations after 1000 iterations ($\alpha_1 = 0.02$, $\alpha_2 = 0.01$, $\delta_{12} = 0$, and $\delta_{21} = -0.1$).

(3) Parasitic coexistence. Figure 5 shows the simulation results of the parasitic symbiosis pattern of two types of symbiotic units in the SCE. In this pattern, the social media platforms have a positive symbiosis effect on the group of scientists participating in it, while the group of scientists cannot give equal returns to the social media platforms and cause a negative symbiosis effect on it. $0 < \delta_{12} < 1$ and $\delta_{21} < 0$; the stable equilibrium point at this time is $((N_1^*(1-\delta_{21})/1-\delta_{21}\delta_{12}), (N_2^*(1-\delta_{12})/1-\delta_{12}))$. It can be seen that the upper limit of the growth scale of the scientist population under equilibrium conditions exceeds its maximum growth scale N_1^*. The social media platform has declined due to the consumption of the resources of the scientists participating in social media, and the growth scale is far below the maximum scale N_2^*. At the same time, with the advancement of science communication activities, the scale of the group of scientists participating in social media has gradually expanded. Although the parasitic behavior of the group of scientists has

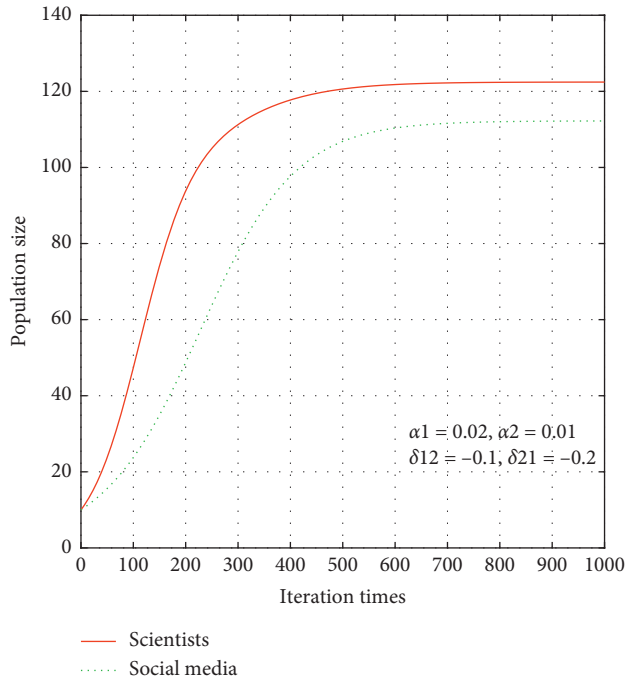

Figure 7: Asymmetric mutualism pattern. Changes in the size of the two populations after 1000 iterations ($\alpha_1 = 0.02$, $\alpha_2 = 0.01$, $\delta_{12} = -0.1$, and $\delta_{21} = -0.2$).

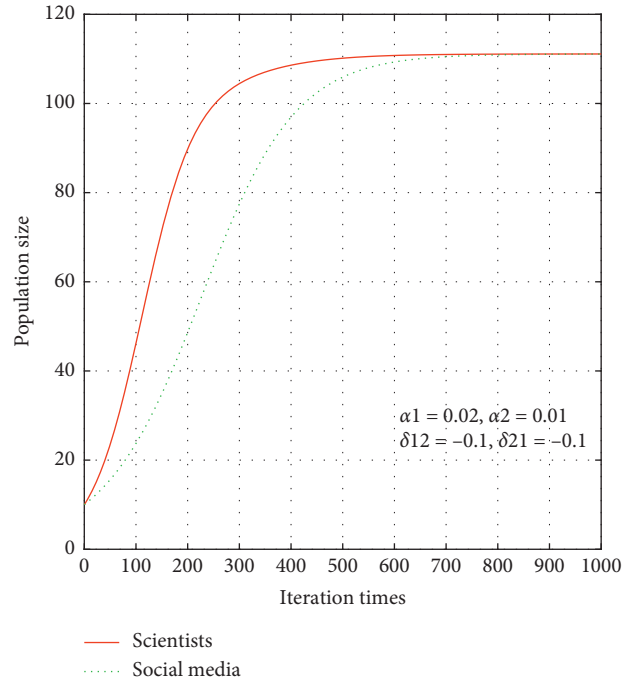

Figure 8: Symmetric mutualism pattern. Changes in the size of the two populations after 1000 iterations ($\alpha_1 = 0.02$, $\alpha_2 = 0.01$, $\delta_{12} = -0.1$, and $\delta_{21} = -0.1$).

hindered the development of social media platforms, it has not formed a fatal threat, and the growth of social media platforms has been stable at a certain value below its maximum growth scale. At this time, the benefits of "1 + 1 > 2" have not been realized between symbiotic units, and both of them need more resource interaction and value sharing to promote symbiosis evolution.

(4) Commensalism. As shown in Figure 6, in this pattern, one of the symbiosis coefficients between the social media platform and the participating scientists is less than zero, and the other is equal to zero. The stable equilibrium point at this time is $(N_1^*(1-\delta_{21}), N_2^*)$. The benefits brought by the symbiosis relationship made up for the damage that the social media platform suffered in the parasitic symbiosis pattern, and its growth scale returned to the maximum quality parameter N_2^* of independent growth. The group of scientists participating in social media continues to benefit through symbiosis relationships, beyond the maximum growth scale N_1^* when growing up independently. Under the commensalism pattern, the group of scientists continued to obtain technical, capital, and equipment support from the social media platform and gradually returned profits, talents, services, and content to compensate for the prerequisite investment of the social media platforms. The two types of symbiotic units get through the most difficult period for science communication and transit into the growth phase.

(5) Asymmetric mutualism. Figure 7 shows the simulation results of the asymmetric mutualism between scientists participating in social media and social media platforms. The symbiosis coefficients of the two types of symbiosis units are both less than 0, but not equal. The stable equilibrium point at this time is $((N_1^*(1-\delta_{21})/1-\delta_{21}\delta_{12}), (N_2^*(1-\delta_{12})/1-\delta_{12}))$. The growth scale of the two types of symbiotic units exceeds the maximum scale of independent development under the constraints of their respective resources and environments. The upper limit of the size of each symbiotic unit is related to the symbiosis coefficient. The greater the absolute value of the symbiosis coefficient, the higher the upper limit of its growth scale. At the same time, with the withdrawal of funds and technologies from social media platforms, there are more options to choose from, and the growth momentum is accelerating. At this time, the evolution of the SCE has gradually entered a mature stage, and the symbiosis relationship between scientists participating in social media and social media platforms has begun to enter a win-win pattern.

(6) Symmetric mutualism. Symmetric mutualism is the highest level pursued in the process of symbiosis evolution. As shown in Figure 8, the symbiosis coefficients of the two types of symbiotic units are both less than zero and equal. The growth scale of the two types of symbiotic units not only exceeds the maximum quality parameter of independent development but also tends to be consistent. In the mutualism pattern, scientists involved in social

media have close cooperation, mutual promotion, and mutual dependence on social media platforms. They have a good coordination mechanism and a resource sharing mechanism and ultimately achieve "1 + 1 > 2" economic benefits.

From the above analysis, it can be concluded that the SCE based on social media is a complex system formed by the symbiosis and evolution of scientists and social media platforms. The coefficient of symbiosis between scientists participating in social media and social media platforms determines the result of the evolution of the system; different symbiosis relationships will eventually lead to different evolution directions and eventually reach an equilibrium state. The two types of symbiosis units under the mutually beneficial symbiosis pattern have the largest growth rate, which is the best direction for the evolution of social media ecological symbiosis.

5. Conclusions

This study summarized the concept of the SCE based on the actual situation, discussed the symbiosis evolution relationship between scientists and social media platforms in the SCE based on the Lotka–Volterra model within the theoretical framework of symbiosis theory, and calculated the equilibrium point and stability conditions of the symbiosis evolution with the Jacobian matrix. Comparing the symbiosis evolution pattern under different coefficients, we got some important conclusions as follows.

(1) The SCE in the context of science communication is composed of symbiotic units including scientists and social media platforms and interacts through different symbiosis patterns under the influence of economic, policy, and cultural symbiosis environments. Eventually, a self-organizing, adaptive coordination system is formed. The process of system integration is bound to go through stages of formation, growth, and maturity. The symbiosis relationship between the group of scientists and social media platforms will directly affect the development of the SCE. (2) The symbiosis coefficient between scientists and social media determines the equilibrium result of the symbiosis and evolution of the SCE. Independent coexistence, competitive coexistence, parasitic coexistence, and commensalism cannot promote the virtuous circle of the SCE, only if under the mutualism pattern, scientists and social media platforms promote each other's population size, which can achieve sustainable science communication. (3) The SCE based on social media can only produce economic benefits of "1 + 1 > 2" under the symmetric mutualism pattern. The growth of scientists and social media organizations under the symmetric mutualism pattern is more stable and abundant than that of other patterns.

Generally, subsequent research can be carried out from the following aspects: (1) Introduce the research results of this study into specific practical situations for analysis. For example, we could conduct an empirical analysis of the number of scientists participating in social media for scientific communication and the number of social media platforms during a period, to make a useful supplement to the simulation results. (2) Explore the evolution of the SCE under the symbiosis organization mode, and discuss how it evolves from point symbiosis, intermittent symbiosis, and continuous symbiosis to integrated symbiosis. (3) Refer to the existing research on complex systems, explore the competition and cooperation mechanism and metabolism mechanism in the SCE, and provide corresponding suggestions for more effectively promoting the virtuous circle of science communication.

Data Availability

The data used to support the findings of this study are included within the article.

Conflicts of Interest

The authors declare that there are no conflicts of interest regarding the publication of this paper.

Acknowledgments

This study was supported by the National Natural Science Foundation of China (no. 71972148).

References

[1] F. El Kihal, I. Abouelkheir, M. Rachik, and I. Elmouki, "Role of media and effects of infodemics and escapes in the spatial spread of epidemics: a stochastic multi-region model with optimal control approach," *Mathematics*, vol. 7, 2019.

[2] A. Orben, "Teenagers, screens and social media: a narrative review of reviews and key studies," *Social Psychiatry and Psychiatric Epidemiology*, vol. 55, no. 4, pp. 407–414, 2020.

[3] J. Maier and B. Rittberger, "Shifting europe's boundaries," *European Union Politics*, vol. 9, no. 2, pp. 243–267, 2008.

[4] C. Puschmann, "Analyzing political communication with digital trace data: the role of twitter messages in social science research," *Information, Communication & Society*, vol. 19, no. 12, pp. 1691-1692, 2015.

[5] D. Sgroi, "Social network theory, broadband and the future of the World Wide Web," *Telecommunications Policy*, vol. 32, no. 1, pp. 62–84, 2008.

[6] A. I. Cristea, D. Katsaros, and Y. Manolopoulos, "Introduction to the special issue of the world wide web journal on "social media preservation and applications"," *World Wide Web*, vol. 17, no. 4, pp. 691–693, 2014.

[7] C. Leppanen, D. M. Frank, J. J. Lockyer et al., "Media representation of hemlock woolly adelgid management risks: a case study of science communication and invasive species control," *Biological Invasions*, vol. 21, no. 2, pp. 615–624, 2018.

[8] P. Hunter, "The growth of social media in science," *EMBO Reports*, p. 21, 2020.

[9] V. Cheplygina, F. Hermans, C. Albers, N. Bielczyk, and I. Smeets, "Ten simple rules for getting started on Twitter as a scientist," *Plos Comput Biol*, vol. 16, Article ID e1007513, 2020.

[10] C. R. Sugimoto, S. Work, V. Larivière, and S. Haustein, "Scholarly use of social media and altmetrics: a review of the literature," *Journal of the Association for Information Science and Technology*, vol. 68, no. 9, pp. 2037–2062, 2017.

[11] X. Lu, C. W. Phang, and J. Yu, "Encouraging participation in virtual communities through usability and sociability development," *ACM SIGMIS Database: The DATABASE for Advances in Information Systems*, vol. 42, no. 3, pp. 96–114, 2011.

[12] S. Choi, H. Lee, and Y. Yoo, "The impact of information technology and transactive memory systems on knowledge sharing, application, and team performance: a field study," *Mis Quarterly*, vol. 34, no. 4, pp. 855–870, 2010.

[13] A. Gruzd, K. Staves, and A. Wilk, "Connected scholars: examining the role of social media in research practices of faculty using the UTAUT model," *Computers in Human Behavior*, vol. 28, no. 6, pp. 2340–2350, 2012.

[14] R. B. Lee, R. Baring, M. S. Maria, and S. Reysen, "Attitude towards technology, social media usage and grade-point average as predictors of global citizenship identification in Filipino University Students," *International Journal of Psychology*, vol. 52, no. 3, pp. 213–219, 2017.

[15] C. Tenopir, R. Volentine, and D. W. King, "Social media and scholarly reading," *Online Information Review*, vol. 37, no. 2, pp. 193–216, 2013.

[16] E. C. M. Parsons, D. S. Shiffman, E. S. Darling, N. Spillman, and A. J. Wright, "How Twitter literacy can benefit conservation scientists," *Conservation Biology*, vol. 28, no. 2, pp. 299–301, 2014.

[17] K. Collins, D. Shiffman, and J. Rock, "How are scientists using social media in the workplace?" *PLoS One*, vol. 11, Article ID e0162680, 2016.

[18] J. Juenger and B. Faehnrich, "Does really no one care? analyzing the public engagement of communication scientists on Twitter," *New Media & Society*, vol. 22, pp. 387–408, 2019.

[19] B. Faehnrich and C. Luthje, "Roles of social scientists in crisis media reporting-the case of the German populist radical right movement PEGIDA," *Science Communication*, vol. 39, pp. 415–442, 2017.

[20] X. Liang, L. Y.-F. Su, S. K. Yeo et al., "Building buzz," *Journalism & Mass Communication Quarterly*, vol. 91, no. 4, pp. 772–791, 2014.

[21] J. M. Heemstra, "A scientist's guide to social media," *ACS Central Science*, vol. 6, no. 1, pp. 1–5, 2020.

[22] I. Rowlands, D. Nicholas, B. Russell, N. Canty, and A. Watkinson, "Social media use in the research workflow," *Learned Publishing*, vol. 24, no. 3, pp. 183–195, 2011.

[23] B. Beck-Winchatz, "Involvement of scientists in the NASA Office of Space Science education and public outreach program," *Nuclear Physics B - Proceedings Supplements*, vol. 138, pp. 451–453, 2005.

[24] C. Stylinski and A. Johnson, "Impacts of a comprehensive public engagement training and support program," *International Journal of Science Education*, vol. 4, no. 8, pp. 340–354, 2018.

[25] A. T. Taylor and S. M. Sammons, "Bridging the gap between scientists and anglers: the black bass conservation committee's social media outreach efforts," *Fisheries*, vol. 44, no. 1, pp. 37–41, 2019.

[26] J. T. H. Wang, C. J. Power, C. M. Kahler et al., "Communication ambassadors-an Australian social media initiative to develop communication skills in early career scientists," *Journal of Microbiology & Biology Education*, vol. 19, 2018.

[27] B. Smith, N. Baron, C. English et al., "COMPASS: navigating the rules of scientific engagement," *PLoS Biology*, vol. 11, Article ID e1001552, 2013.

[28] K. D. Heath, E. Bagley, A. J. M. Berkey et al., "Amplify the signal: graduate training in broader impacts of scientific research," *BioScience*, vol. 64, no. 6, pp. 517–523, 2014.

[29] A. Baram-Tsabari and B. V. Lewenstein, "Science communication training: what are we trying to teach?" *International Journal of Science Education, Part B*, vol. 7, no. 3, pp. 285–300, 2017.

[30] C. Stylinski, M. Storksdieck, N. Canzoneri, E. Klein, and A. Johnson, "Impacts of a comprehensive public engagement training and support program on scientists' outreach attitudes and practices," *International Journal of Science Education, Part B*, vol. 8, no. 4, pp. 340–354, 2018.

[31] E. Salas, S. I. Tannenbaum, K. Kraiger, and K. A. Smith-Jentsch, "The science of training and development in organizations," *Psychological Science in the Public Interest*, vol. 13, no. 2, pp. 74–101, 2012.

[32] J. Wan, Y. Lu, B. Wang, and L. Zhao, "How attachment influences users' willingness to donate to content creators in social media: a socio-technical systems perspective," *Information & Management*, vol. 54, no. 7, pp. 837–850, 2017.

[33] A. Susarla, J.-H. Oh, and Y. Tan, "Social networks and the diffusion of user-generated content: evidence from YouTube," *Information Systems Research*, vol. 23, no. 1, pp. 23–41, 2012.

[34] S. Krishnamurthy and A. K. Tripathi, "Monetary donations to an open source software platform," *Research Policy*, vol. 38, no. 2, pp. 404–414, 2009.

[35] Q. K. Mahmood, S. R. Jafree, and M. M. Sohail, "Pakistani youth and social media addiction: the validation of bergen Facebook addiction scale (BFAS)," *International Journal of Mental Health and Addiction*, 2020.

[36] M. Kaakinen, A. Sirola, I. Savolainen, and A. Oksanen, "Shared identity and shared information in social media: development and validation of the identity bubble reinforcement scale," *Media Psychology*, vol. 23, no. 1, pp. 25–51, 2018.

[37] B. B. Dedeoğlu, B. Taheri, F. Okumus, and M. Gannon, "Understanding the importance that consumers attach to social media sharing (ISMS): scale development and validation," *Tourism Management*, p. 76, 2020.

[38] L. J. GOFF, "Symbiosis and parasitism: another viewpoint," *BioScience*, vol. 32, no. 4, pp. 255-256, 1982.

[39] D. Leidner, "Review and theory symbiosis: an introspective retrospective," *Journal of the Association for Information Systems*, vol. 19, no. 06, pp. 552–567, 2018.

[40] L. Vančurová, V. Kalníková, O. Peksa et al., "Symbiosis between river and dry lands: phycobiont dynamics on river gravel bars," *Algal Research*, p. 51, 2020.

[41] P. Kerdlap, J. S. C. Low, and S. Ramakrishna, "Life cycle environmental and economic assessment of industrial symbiosis networks: a review of the past decade of models and computational methods through a multi-level analysis lens," *The International Journal of Life Cycle Assessment*, vol. 25, no. 9, pp. 1660–1679, 2020.

[42] J. Zhang and W. L. Chen, "The study on integration of supply chain based on the symbiosis theory," *Applied Mechanics and Materials*, vol. 275-277, pp. 2706–2709, 2013.

[43] G. Fontaine, M.-A. Maheu-Cadotte, A. Lavallée et al., "Communicating science in the digital and social media ecosystem: scoping review and typology of strategies used by health scientists," *JMIR Public Health and Surveillance*, vol. 5, no. 3, p. e14447, 2019.

[44] K. M. Meyer, A. M. Hopple, A. M. Klein, A. H. Morris, S. D. Bridgham, and B. J. M. Bohannan, "Community structure - ecosystem function relationships in the Congo Basin methane cycle depend on the physiological scale of function," *Molecular Ecology*, vol. 29, no. 10, pp. 1806–1819, 2020.

[45] M. Loreau, "Coexistence of multiple food chains in a heterogeneous environment: interactions among community structure, ecosystem functioning, and nutrient dynamics," *Mathematical Biosciences*, vol. 134, no. 2, pp. 153–188, 1996.
[46] X. Tan, W. Qin, G. Tang, C. Xiang, and X. Liu, "Models to assess the effects of nonsmooth control and stochastic perturbation on pest control: a pest-natural-enemy ecosystem," *Complexity*, vol. 2019, 14 pages, 2019.
[47] P. Wang, W. Qin, and G. Tang, "Modelling and analysis of a host-parasitoid impulsive ecosystem under resource limitation," *Complexity*, vol. 2019, 12 pages, 2019.
[48] J.-L. Usó-Doménech, J.-A. Nescolarde-Selva, M. Lloret-Climent, H. Gash, and K. Alonso-Stenberg, "Indirect effects, biotic inferential interactions and time functions in H-semiotic systems: ecosystems case," *Mathematics*, vol. 7, 2019.
[49] A. Voroshilova and J. Wafubwa, "Discrete competitive lotka–volterra model with controllable phase volume," *Systems*, vol. 8, 2020.
[50] S. Guo and S. Yan, "Hopf bifurcation in a diffusive Lotka-Volterra type system with nonlocal delay effect," *Journal of Differential Equations*, vol. 260, no. 1, pp. 781–817, 2016.
[51] G. Bernardo and S. D'Alessandro, "Systems-dynamic analysis of employment and inequality impacts of low-carbon investments," *Environmental Innovation and Societal Transitions*, vol. 21, pp. 123–144, 2016.
[52] N. T. Khan, Y. H. Kim, and Y. B. Kim, "The dynamic impact of low-cost carriers on full-service carriers and the tourism industry of South Korea: a competitive analysis using the Lotka-Volterra model," *Asia Pacific Journal of Tourism Research*, vol. 23, no. 7, pp. 656–666, 2018.
[53] V. Assumma, M. Bottero, G. Datola, E. De Angelis, and R. Monaco, "Dynamic models for exploring the resilience in territorial scenarios," *Sustainability*, vol. 12, 2019.
[54] A. Marasco and A. Romano, "Deterministic modeling in scenario forecasting: estimating the effects of two public policies on intergenerational conflict," *Quality & Quantity*, vol. 52, no. 5, pp. 2345–2371, 2017.
[55] J. Ditzen, "Cross-country convergence in a general Lotka-Volterra model," *Spatial Economic Analysis*, vol. 13, no. 2, pp. 191–211, 2017.
[56] N. Christodoulakis, "Conflict dynamics and costs in the Greek Civil war 1946-1949," *Defence and Peace Economics*, vol. 27, no. 5, pp. 688–717, 2015.
[57] G. Faye and M. Holzer, "Asymptotic stability of the critical pulled front in a Lotka-Volterra competition model," *Journal of Differential Equations*, vol. 269, no. 9, pp. 6559–6601, 2020.

Hindawi
Complexity
Volume 2021, Article ID 6664530, 10 pages
https://doi.org/10.1155/2021/6664530

Research Article

Time-Frequency Analysis and Target Recognition of HRRP Based on CN-LSGAN, STFT, and CNN

Jianghua Nie,[1] **Yongsheng Xiao**,[1,2] **Lizhen Huang**,[1] **and Feng Lv**[3]

[1]*Key Laboratory of Jiangxi Province for Image Processing and Pattern Recognition, School of Information Engineering, Nanchang Hangkong University, Nanchang 330063, China*
[2]*National Engineering Laboratory for Video Technology, School of Electronics Engineering and Computer Science, Peking University, Beijing 100871, China*
[3]*Henan Aerospace Hydraulic Pneumatic Technology Company Limited, China Aerospace Science and Industry Corporation Limited, Zhengzhou 451191, China*

Correspondence should be addressed to Yongsheng Xiao; xysfly@nuaa.edu.cn

Received 18 December 2020; Revised 15 March 2021; Accepted 26 March 2021; Published 13 April 2021

Academic Editor: Chenquan Gan

Aiming at the problem of radar target recognition of High-Resolution Range Profile (HRRP) under low signal-to-noise ratio conditions, a recognition method based on the Constrained Naive Least-Squares Generative Adversarial Network (CN-LSGAN), Short-time Fourier Transform (STFT), and Convolutional Neural Network (CNN) is proposed. Combining the Least-Squares Generative Adversarial Network (LSGAN) with the Wasserstein Generative Adversarial Network with Gradient Penalty (WGAN-GP), the CN-LSGAN is presented and applied to the HRRP denoise. The frequency domain and phase features of HRRP are gained by STFT in order to facilitate feature learning and also match the input data format of the CNN. These experimental results show that the CN-LSGAN has better data augmentation performance and can effectively avoid the model collapse compared to the generative adversarial network (GAN) and LSGAN. Also, the method has better recognition performance than the one-dimensional CNN method and the Long Short-Term Memory (LSTM) network method.

1. Introduction

HRRP is the vector sum of all scatters electromagnetic echoes, which can reflect the geometric structure, scatters point distribution, and other characteristics of the target. Also, it is easy to be obtained and processed, so the radar target recognition of HRRP has become a research hotspot that has attracted much attention in the academic community [1–11]. In recent years, with the large-scale rise of deep neural networks, deep learning provides new ideas for the research of radar automatic target recognition (RATR) of HRRP. Compared to the traditional recognition method, the HRRP target recognition method of deep learning can avoid the excessive use of manual rules to extract the target features and acquire high-order features. The recognition rate of the Deep Belief Network (DBN) reached 92.8% [12]; the CNN was also applied to RATR [13, 14], and the recognition rate was greatly improved; the Recurrent Neural Network (RNN) [15] and LSTM [16] had both achieved good recognition rates. However, in these actual application scenarios, HRRP acquired contain noise, which affects the amplitude of HRRP. When the signal-to-noise ratio of the data is low, the amplitude of these data differs greatly from the amplitude of the real data, and when the features are extracted, the extracted features also differ greatly from the features of the real data, thus interfering with the recognition results. So, HRRP needs to be enhanced in order to improve the signal-to-noise ratio. The GAN is a deep-learning model widely applied to data augmentation, and it was used for image blind denoising [17] and speech augmentation [18, 19]. But, it has not been applied to HRRP augmentation. HRRP is denoised only by an Auto Encoder (AE) [20].

To solve the problem of radar target recognition of HRRP under low signal-to-noise ratio circumstances, we proposed a new kind of generative model, called the

CN-LSGAN. The CN-LSGAN can generate data similar to the real data with low signal-to-noise data as input, thus improving the signal-to-noise ratio of the data. In addition, in order to simulate the noisy HRRP data in actual application scenarios, we added different degrees of Gaussian white noise to the real data and then used the CN-LSGAN to enhance the data to improve the SNR. Then, we used the obtained data for target recognition. In order to improve the recognition effect as much as possible, time-frequency analysis is performed on the data before the recognition, and the data are converted from one-dimensional data to two-dimensional data. The obtained time-frequency data contain more features. In the target recognition task, the more the data features, the better the recognition effect is generally. Finally, the obtained time-frequency data are recognized by the CNN, and the recognition result is obtained. In this paper, the following contributions have been achieved:

(1) Improve the LSGAN to solve the model collapse problem

(2) Improve the signal-to-noise ratio of HRRP data by the CN-LSGAN

(3) Use the combination of STFT time-frequency analysis and shallow network CNN architecture to test the recognition rate of the enhanced data by CN-LSGAN

The rest of this paper is organized as follows: The second part introduces the proposed method in detail, mainly including the illustration of the CN-LSGAN, STFT, and CNN; the third part chiefly focuses on the experimental results and analysis; and the fourth part concludes the paper.

2. Time-Frequency Analysis and Target Recognition of HRRP Based on the CN-LSGAN, STFT, and CNN

2.1. Design of the CN-LSGAN. The GAN is a generative model designed by Goodfellow [21]. The model consists of a generator (G) and a discriminator (D), as shown in Figure 1.

The input of D is real data or $G(z)$, and the output of D is 1 or 0. The adversarial training is carried out between D and G, so that $G(z)$ approaches the real data. When D cannot determine the source of the input after continuous adversarial training and iterative optimization, it is considered that G has learned the real data distribution.

The loss function of the GAN is

$$\min_G \max_D V(D,G) = E_{x\sim P_{\text{data}}(x)}[\log D(x)] + E_{z\sim P_z(z)}[\log 1 - D(G(z))], \tag{1}$$

where E is the expectation of the distribution function, P_{data} is the real data distribution, and P_z is the noise distribution.

The real data are the clean HRRP, and the input of G is the noisy HRRP, as is shown in Figure 2. Through the adversarial training, the data generated by G are similar to the clean HRRP, and then, the denoise purpose is achieved.

The LSGAN [22] is used instead of the GAN in this paper, and the loss function of the LSGAN is shown as follows:

$$\begin{cases} \min_D V(D,G) = E_{x\sim P_{\text{data}}(x)}\left[(D(x)-1)^2\right] + E_{z\sim P_z(z)}\left[(D(G(z)))^2\right], \\ \min_G V(D,G) = E_{z\sim P_z(z)}\left[(D(G(z))-1)^2\right]. \end{cases} \tag{2}$$

Compared to the GAN, the LSGAN uses least-squares loss in place of cross-entropy loss, which effectively solves the gradient disappearance problem during the model training stage. However, the LSGAN also has shortcomings; the LSGAN has a large output freedom degree and is prone to model collapse. These problems will lead to poor quality and low diversity of generated samples. In terms of these problems, a constraint item is, respectively, added to the loss function of the LSGAN's D and G, and the two constraint items are shown as follows:

$$\xi(D) = E_{\hat{x}\sim P_{\hat{x}}}\left[\left(\left\|\nabla_{\hat{x}} D(\hat{x})\right\|_2 - 1\right)^2\right], \tag{3}$$

$$\xi(G) = E_{z-p_z(z)}\left[(G(z)-x)^2\right]. \tag{4}$$

Through the improvement of the LSGAN, formula (2) can be rewritten as follows:

$$\begin{cases} \min_D V(D,G) = E_{x\sim P_{\text{data}}(x)}\left[(D(x)-1)^2\right] + E_{z\sim P_z(z)}\left[(D(G(z)))^2\right] + \lambda_1 E_{\hat{x}\sim P_{\hat{x}}}\left[\left(\left\|\nabla_{\hat{x}} D(\hat{x})\right\|_2 - 1\right)^2\right], \\ \min_G V(D,G) = E_{z\sim P_z(z)}\left[(D(G(z))-1)^2\right] + \lambda_2 E_{z\sim P_z(z), x\sim P_{\text{data}}(x)}\left[(G(z)-x)^2\right]. \end{cases} \tag{5}$$

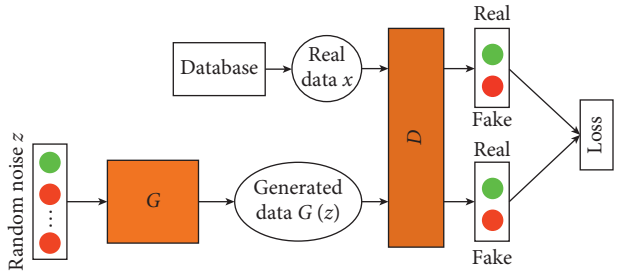

Figure 1: Schematic diagram of the GAN.

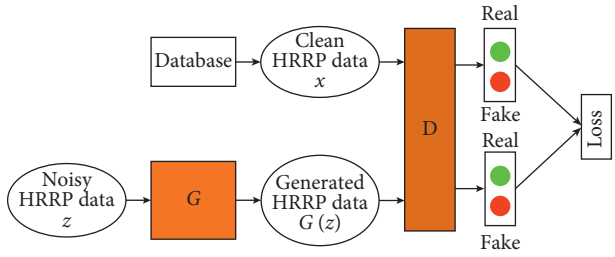

Figure 2: Schematic diagram of the GAN used for HRRP denoise.

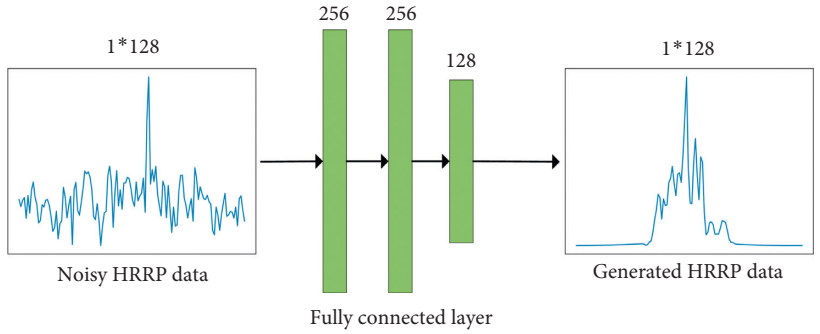

Figure 3: Schematic diagram of G.

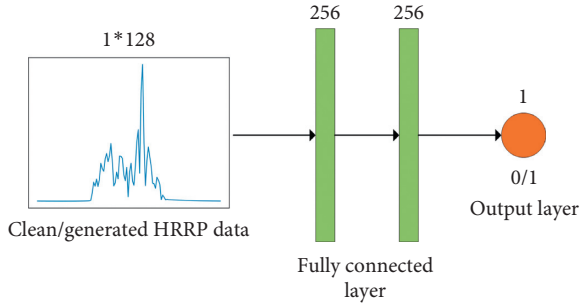

Figure 4: Schematic diagram of D.

In formula (5), λ_1 and λ_2 represent the adjustment weights, which adjust $\xi(D)$ and $\xi(G)$, respectively. $\xi(D)$ can solve the model collapse, and $\xi(G)$ can reduce the output freedom degree of G. The LSGAN with the abovementioned constraint items is called the CN-LSGAN.

Both G and D of the CN-LSGAN adopt the fully connected network structure, as shown in Figures 3 and 4 .

2.2. Time-Frequency Analysis Based on STFT. Time-domain analysis of HRRP only characterizes the amplitude of the signal, which only provides limited information for feature learning. In contrast, the spectral feature is a two-dimensional (time and frequency) representation of HRRP, which includes the frequency-domain characteristics of the target and reflects the phase information. STFT is used for the

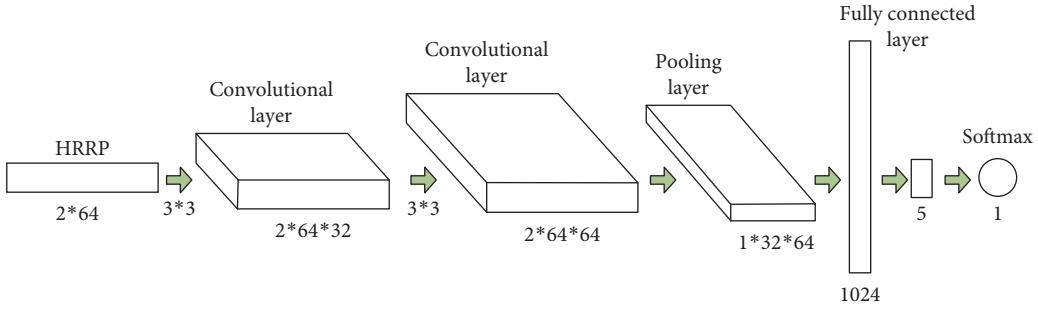

Figure 5: Schematic diagram of the CNN.

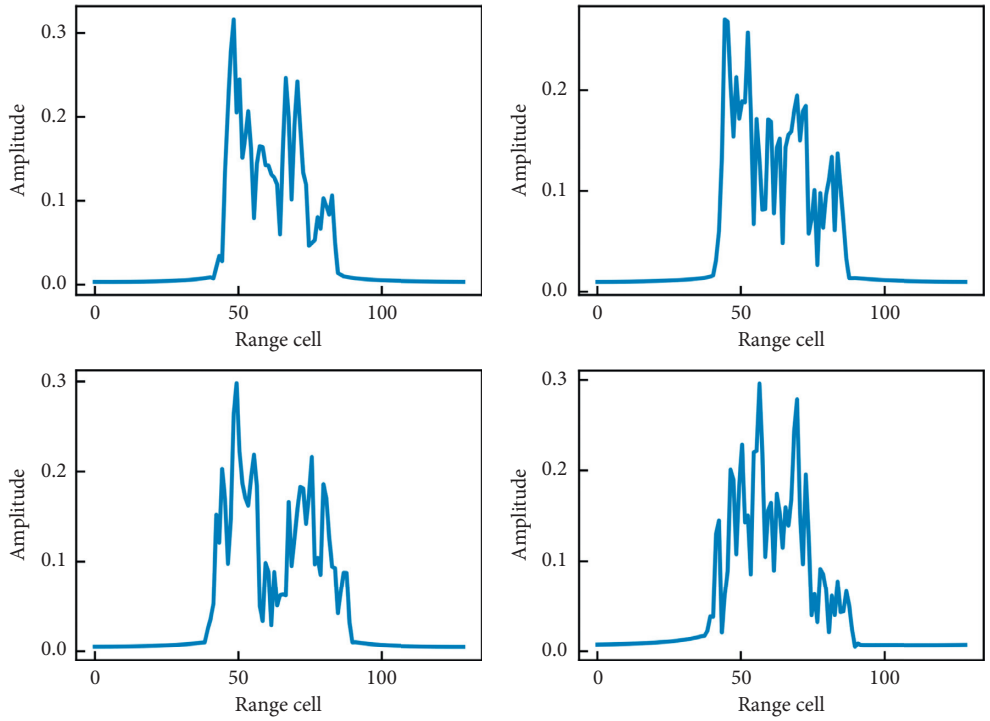

Figure 6: Four different data samples in dataset A.

time-frequency analysis of HRRP, and the window function is Hanning window. The width of the window affects the relative resolution of the time domain and frequency domain. In order to make a trade-off between the time-domain resolution and the frequency-domain resolution, the adjacent signal segments are superimposed on each other. According to the HRRP characteristics, the overlapping length between adjacent signal segments is selected to be half of the length of each segment, and Hanning windows with window lengths of 32, 16, 8, and 4 are used for STFT.

2.3. Design of the CNN. The dimension of the time-frequency data obtained by the time-frequency analysis for HRRP is (2, 64), and the CNN is designed according to the dimension. The model consists of two convolutional layers, a pooling layer, two fully connected layers, and a SoftMax classifier, and the sizes of the convolutional kernel of two convolutional layers are 3∗3, as shown in Figure 5.

3. Experimental Results and Analysis

3.1. Experimental Data. The clean HRRP are gained by the electromagnetic simulation technology, which has simulated five kinds of aircraft (Su27, F16, M2000, J8II, and J6). There are 18,000 samples for each aircraft, so there are a total of 90,000 samples. In order to verify the effectiveness of the denoise method based on the CN-LSGAN, Gaussian white noise is added to the clean HRRP, and six kinds of noisy HRRP data with signal-to-noise ratios of 0 dB, 5 dB, 10 dB, 15 dB, 20 dB, and 25 dB are obtained, where, the clean HRRP is called dataset A, the noisy HRRP is called dataset B, and the HRRP generated by the generative model is called dataset C; these three datasets are divided into a training set and test set at a ratio of 9:1.

3.2. HRRP Denoise. Figure 6 shows four samples of dataset A, and Figure 7 shows four samples of dataset B with a signal-to-noise ratio of 10 dB.

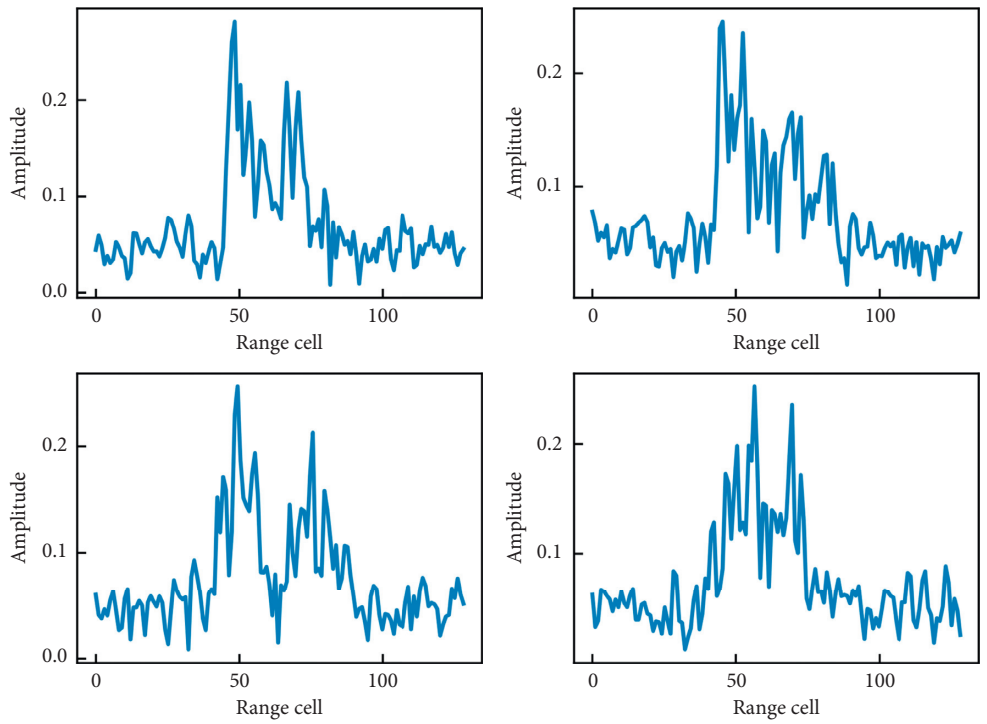

Figure 7: Four different data samples in dataset B with a signal-to-noise ratio of 10db.

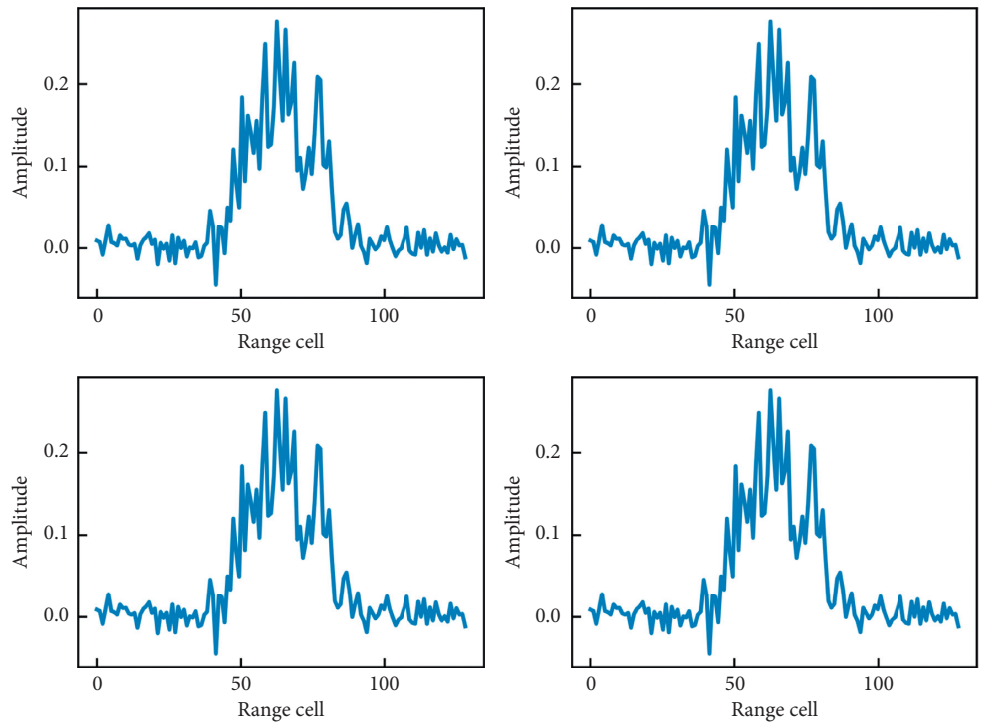

Figure 8: Four data samples in dataset (C), and dataset C is generated by the GAN.

Dataset B with a signal-to-noise ratio of 10 dB is input to the GAN, LSGAN, and CN-LSGAN, respectively. Three kinds of data are generated, and they are shown in Figures 8–10 .

Cosine similarity and Mean Square Error (MSE) among these data samples are technical indexes which indicate the probability of model collapse. They are calculated, respectively, for three kinds of data generated by the GAN,

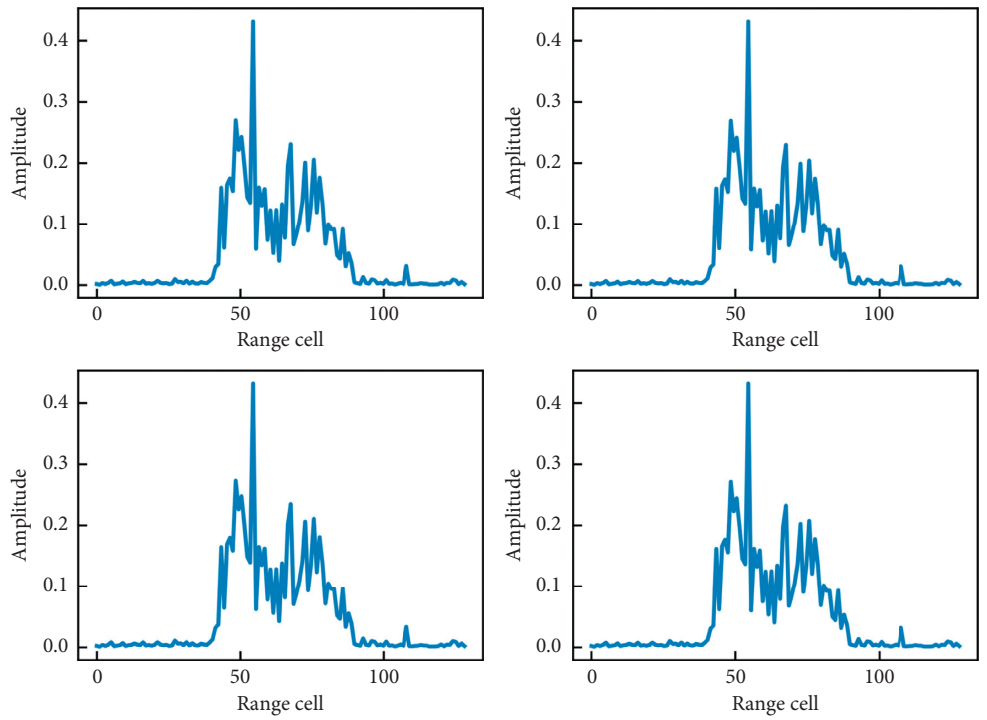

Figure 9: Four data samples in dataset (C), and dataset C is generated by the LSGAN.

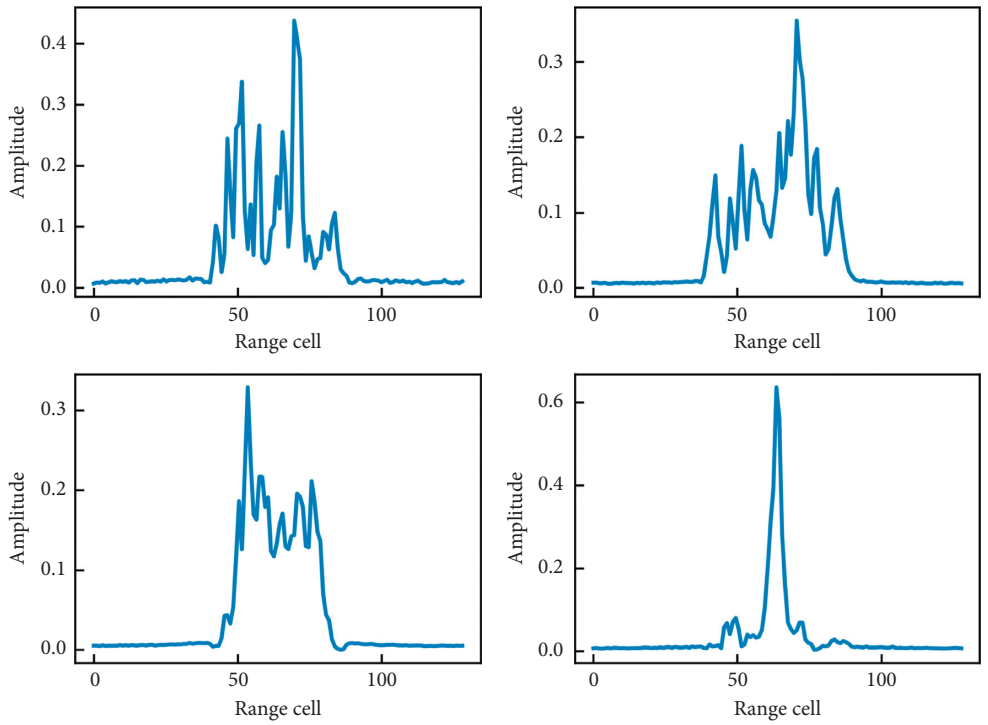

Figure 10: Four data samples in dataset (C), and dataset C is generated by the CN-LSGAN.

LSGAN, and CN-LSGAN. The calculated data are shown in Table 1.

When cosine similarity is equal to 1 or the MSE is equal to 0, it means that the data samples in a certain dataset are very similar, which means that model collapse has occurred. From Table 1, it can be seen that the cosine similarity of the data generated by the GAN and LSGAN is both 1.0 and the MSE is equal to or very close to 0, which means that the data

Table 1: Sample correlation.

Model	Cosine similarity	MSE
GAN	1.0	0
LSGAN	1.0	1.7984e-6
CN-LSGAN	0.8457	1.9800e-3

Table 2: Quality evaluation.

Model	GRA	PCC
Noisy HRRP data	0.8056	0.6935
GAN	0.8491	0.7749
LSGAN	0.8668	0.8086
CN-LSGAN	0.9443	0.8061

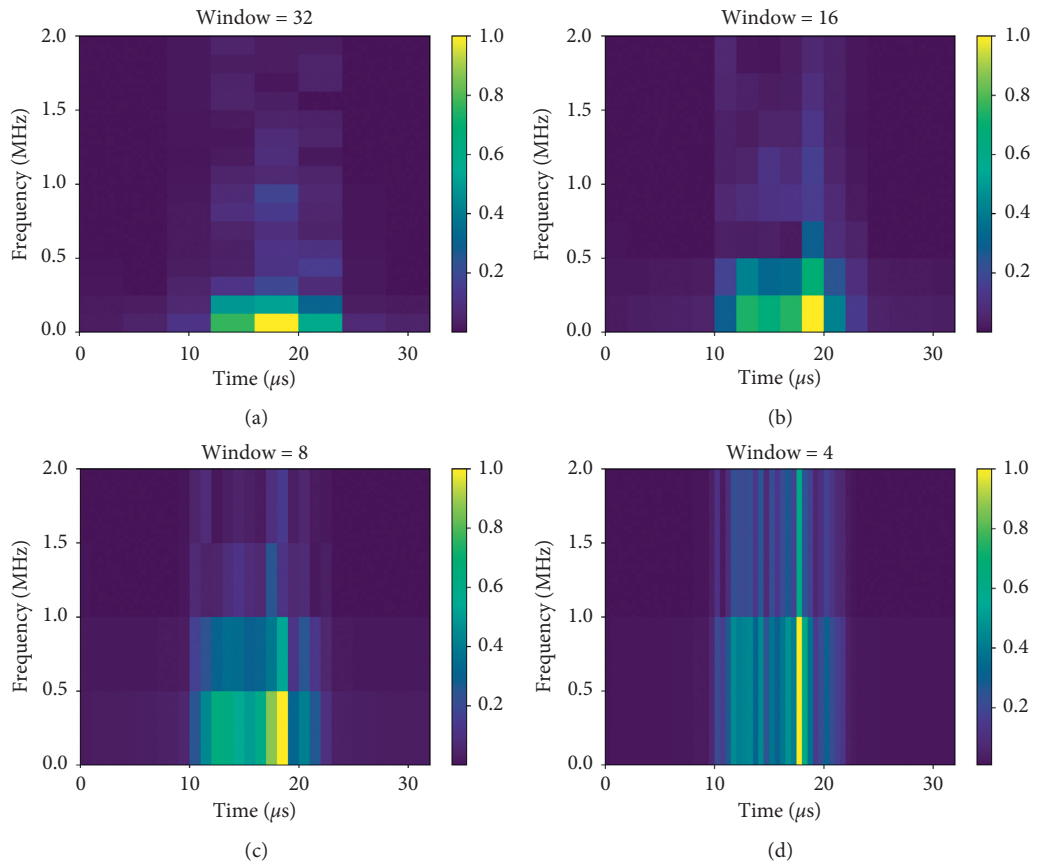

Figure 11: Time-frequency analysis diagrams under four different window lengths. (a) Time-frequency analysis diagram with a window length of 32. (b) Time-frequency analysis diagram with a window length of 16. (c) Time-frequency analysis diagram with a window length of 8. (d) Time-frequency analysis diagram with a window length of 4.

generated by the GAN and LSGAN are very similar and model collapse has occurred.

Pearson Correlation Coefficient (PCC) and Grey Relational Analysis (GRA) are used to evaluate the quality of generated data and denoise performance of different generation models. The measured data are shown between four kinds of data and the clean HRRP, as shown in Table 2.

When the PCC is equal to 1 or the GRA is equal to 1, the generated data are the same as the clean data, which means that the quality of the generated data and the denoise performance are great. The PCC value of the CN-LSGAN is slightly lower than the PCC value of the LSGAN, but is higher than the PCC value of the GAN. Also, the GRA value of the CN-LSGAN is much larger than that of the other two networks. From Tables 1 and 2, it can be seen that the

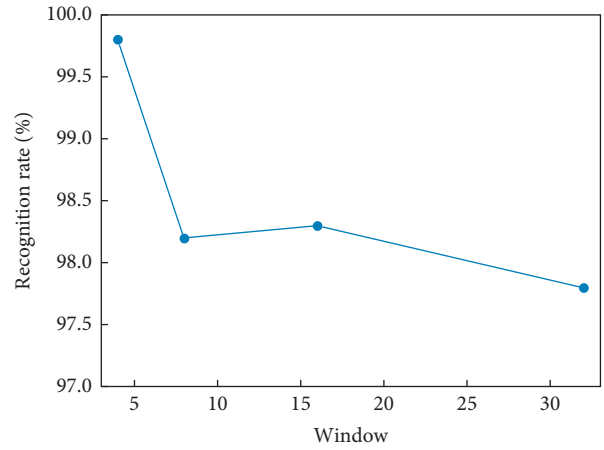

Figure 12: Recognition rate of time-frequency analysis results with different window lengths.

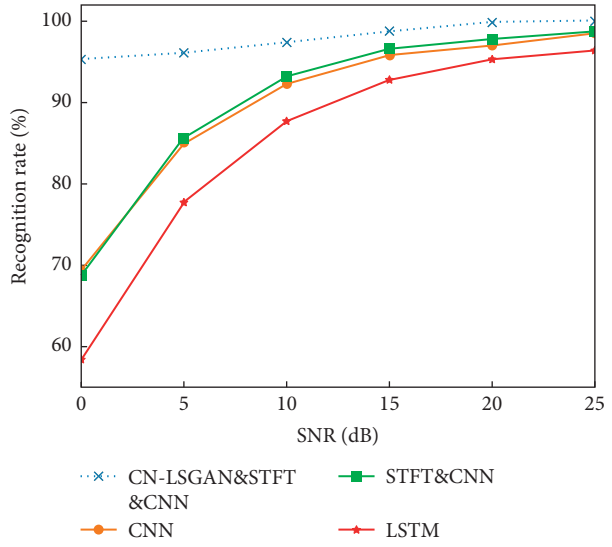

Figure 13: Recognition rate curves of four different recognition methods. The recognition rate curves showed the change trend of the recognition rate with the data signal-to-noise ratio.

CN-LSGAN not only effectively solved the model collapse problem but also generated higher data quality and better denoise performance than the GAN and LSGAN.

3.3. Time-Frequency Analysis. STFT is used for the HRRP time-frequency analysis. When the window length is large, the time resolution is poor and the frequency resolution is high. The situation is the opposite when the window length is narrow. According to the sample characteristics, the Hanning windows with window lengths of 32, 16, and 4 are used, and the obtained time-frequency data are shown in Figure 11.

Data set A performed STFT under the Hanning windows of four window lengths, and the obtained time-frequency data are recognized by the CNN; the result is shown in Figure 12.

When the window length of the window function is 4, the recognition rate of the obtained time-frequency analysis results can reach 99.8%, so the optimal STFT window function length is 4.

3.4. Target Recognition. The enhanced data by the CN-LSGAN are transformed into two-dimensional data by STFT and then recognized by the CNN. A variety of methods are used to recognize the noisy HRRP data (dataset B), and these recognition rates are shown in Figure 13.

These recognition rates of three methods are compared to the proposed method. The first method is the one-dimensional CNN method, the second method is the LSTM method, and the third method is the STFT-CNN method, that is, STFT is combined with the two-dimensional CNN. It can be seen that the proposed method based on the CN-LSGAN, STFT, and CNN has a better recognition performance than the other three recognition methods. Also, the other three recognition methods are greatly affected by the signal-to-noise ratio, and when the

data signal-to-noise ratio is low, these recognition rates are low. By comparing the recognition rate curve of the first method to the curve of the third method, the recognition rate of the third method is slightly lower than that of the first method when the signal-to-noise ratio is 0 dB, while under other signal-to-noise ratios, the recognition rates are higher than the those of the first method. It shows that the third method can improve the recognition performance by combining STFT with the two-dimensional CNN.

4. Conclusions

This paper described an HRRP target recognition method based on the CN-LSGAN, STFT, and CNN, which effectively solves the recognition problem under low signal-to-noise ratio conditions. Among them, the CN-LSGAN is obtained through adding a constraint item to D and G of the LSGAN, respectively. The CN-LSGAN not only solves the problems of excessive freedom degrees of GAN output, poor quality of generated data, and insignificant denoise performance but also solves the model collapse problem of the GAN and LSGAN. By the means of STFT which analyzes the time-frequency characteristics of HRRP, the frequency-domain features and phase features of the target are introduced, and more features are helpful in the feature extraction and target recognition for the CNN. These experimental results show that the method based on STFT and the CNN has better recognition performance compared to the method of one-dimensional CNN and the method of LSTM.

The proposed target recognition method has achieved a high recognition performance based on low signal-to-noise ratio HRRP, but there are still some problems. For example, CN-LSGAN training is unstable, and it is difficult to achieve the trade-off between the time resolution and the frequency resolution by STFT. In future research, the network structure and parameter adjustment of the CN-LSGAN will be further optimized and the Deep Convolution Generative Adversarial Network (DCGAN) will be tried to be combined with the CN-LSGAN. Also, other time-frequency analysis methods such as wavelet transform will be utilized for HRRP.

Data Availability

Experimental data are provided in supplementary materials.

Conflicts of Interest

The authors state that there are no conflicts of interest in the publication of this article.

Acknowledgments

This work was supported by the National Natural Science Foundation (61661035), Jiangxi Natural Science Foundation (20192BAB207001), and Aviation Science Foundation (201920056001).

Supplementary Materials

See Figures 1–13 in the supplementary materials for comprehensive image analysis. For datasets A, B, and C, see text clean, 10db, and generate in the supplementary materials. In addition, for data file description, see text document description in the supplementary materials. (*Supplementary Materials*)

References

[1] L. Du, P. Wang, H. Liu, M. Pan, F. Chen, and Z. Bao, "Bayesian spatiotemporal multitask learning for radar HRRP target recognition," *IEEE Transactions on Signal Processing*, vol. 59, no. 7, pp. 3182–3196, 2011.

[2] J. Lundén and V. Koivunen, "Deep learning for HRRP-based target recognition in multistatic radar systems," in *Proceedings of the 2016 IEEE Radar Conference (RadarConf)*, pp. 1–6, Philadelphia, PA, USA, May 2016.

[3] K. Liao, J. Si, F. Zhu, and X. He, "Radar HRRP target recognition based on concatenated deep neural networks," *IEEE Access*, vol. 6, pp. 29211–29218, 2018.

[4] X. Peng, X. Gao, and X. Li, "An infinite classification RBM model for radar HRRP recognition," in *Proceedings of the 2017 International Joint Conference on Neural Networks (IJCNN)*, pp. 1442–1448, Anchorage, Alaska, USA, May 2017.

[5] L. Shi, P. Wang, H. Liu et al., "Radar HRRP statistical recognition with local factor analysis by automatic Bayesian Ying-Yang harmony learning," *IEEE Transactions on Signal Processing*, vol. 59, no. 2, pp. 610–617, 2010.

[6] S. Luo and S. Li, "Automatic target recognition of radar HRRP based on high order central moments features," *Journal of Electronics (China)*, vol. 26, no. 2, pp. 184–190, 2009.

[7] B. Feng, B. Chen, and H. Liu, "Radar HRRP target recognition with deep networks," *Pattern Recognition*, vol. 61, pp. 379–393, 2017.

[8] D. Zhou, "Radar target HRRP recognition based on reconstructive and discriminative dictionary learning," *Signal Processing*, vol. 126, pp. 52–64, 2016.

[9] C. Guo, Y. He, H. Wang, T. Jian, and S. Sun, "Radar HRRP target recognition based on deep one-dimensional residual-inception network," *IEEE Access*, vol. 7, pp. 9191–9204, 2019.

[10] H. Zhang, D. Ding, Z. Fan et al., "Adaptive neighborhood-preserving discriminant projection method for HRRP-based radar target recognition," *IEEE Antennas and Wireless Propagation Letters*, vol. 14, pp. 650–653, 2014.

[11] L. Du, H. Liu, Z. Bao et al., "A two-distribution compounded statistical model for radar HRRP target recognition," *IEEE Transactions on Signal Processing*, vol. 54, no. 6, pp. 2226–2238, 2006.

[12] M. Pan, J. Jiang, Q. Kong, J. Shi, Q. Sheng, and T. Zhou, "Radar HRRP target recognition based on t-SNE segmentation and discriminant deep Belief network," *IEEE Geoscience and Remote Sensing Letters*, vol. 14, no. 9, pp. 1609–1613, 2017.

[13] J. Li, S. Li, Q. Liu et al., "A novel algorithm for HRRP target recognition based on CNN," in *Proceedings of the International Conference on Internet of Things as a Service*, pp. 397–404, Springer, Diego, CA, USA, June 2019.

[14] J. Song, Y. Wang, W. Chen, Y. Li, and J. Wang, "Radar HRRP recognition based on CNN," *The Journal of Engineering*, vol. 2019, no. 21, 7769 pages, 2019.

[15] B. Xu, B. Chen, J. Wan, H. Liu, and L. Jin, "Target-aware recurrent attentional network for radar HRRP target recognition," *Signal Processing*, vol. 155, pp. 268–280, 2019.

[16] V. Jithesh, M. J. Sagayaraj, and K. G. Srinivasa, "LSTM recurrent neural networks for high resolution range profile based radar target classification," in *Proceedings of the 2017 3rd International Conference on Computational Intelligence &*

Communication Technology (CICT), pp. 1–6, IEEE, Athens, Greece, July 2017.

[17] D. Li, S. Gong, S. Niu, Z. Wang, D. Zhou, and H. Lu, "Image blind denoising using a generative adversarial network for LED chip visual localization," *IEEE Sensors Journal*, vol. 20, no. 12, pp. 6582–6595, 2020.

[18] T. Kaneko, H. Kameoka, N. Hojo et al., "Generative adversarial network-based postfilter for statistical parametric speech synthesis," in *Proceedings of the 2017 IEEE International Conference on Acoustics, Speech and Signal Processing (ICASSP)*, pp. 4910–4914, IEEE, Orleans, LA, USA, March 2017.

[19] S. Pascual, A. Bonafonte, and J. Serrà, "SEGAN: speech enhancement generative adversarial network," in *Proceedings of the Annual Conference of the International*, Austin, Texas, Janurary 2017.

[20] C. Zhao, X. He, J. Liang, T. Wang, and C. Huang, "Radar HRRP target recognition via semi-supervised multi-task deep network," *IEEE Access*, vol. 7, pp. 114788–114794, 2019.

[21] I. Goodfellow, J. Pouget-Abadie, M. Mirza et al., "Generative adversarial network," *Communications of the ACM*, vol. 63, no. 11, pp. 139–144, 2014.

[22] X. Mao, Q. Li, H. Xie et al., "Least squares generative adversarial networks," in *Proceedings of the IEEE International Conference on Computer Vision*, pp. 2794–2802, Venice, Italy, October 2017.

Hindawi
Complexity
Volume 2021, Article ID 6614545, 11 pages
https://doi.org/10.1155/2021/6614545

Research Article

Identifying the Influential Latent Edges for Promoting the Co-SIR Model

Dan Yang,[1] **Liming Pan**,[2] **Zhidan Zhao**,[3,4] **and Tao Zhou**[1]

[1]*Web Sciences Center, School of Computer Science and Engineering, University of Electronic Science and Technology of China, Chengdu 611731, China*
[2]*School of Computer and Electronic Information, Nanjing Normal University, Nanjing, Jiangs, 210023, China*
[3]*Department of Computer Science, School of Engineering, Shantou University, Shantou 515063, China*
[4]*Key Laboratory of Intelligent Manufacturing Technology (Ministry of Education), Shantou University, Shantou 515063, China*

Correspondence should be addressed to Liming Pan; panlm99@gmail.com

Received 14 December 2020; Revised 13 January 2021; Accepted 15 March 2021; Published 24 March 2021

Academic Editor: Chenquan Gan

The network-based cooperative information spreading is a widely existing phenomenon in the real world. For instance, the spreading of disease outbreak news and disease prevention information often coexist and interact with each other on the Internet. Promoting the cooperative spreading of information in network-based systems is a subject of great importance in both theoretical and practical perspectives. However, very limited attention has been paid to this specific research area so far. In this study, we propose an effective approach for identifying the influential latent edges (that is, the edges that do not originally exist) which, if added to the original network, can promote the cooperative susceptible-infected-recovered (co-SIR) dynamics. To be specific, we first obtain the probabilities of each nodes being in different node states by the message-passing approach. Then, based on the state probabilities of nodes obtained, we come up with an indicator, which incorporates both the information of network topology and the co-SIR dynamics, to measure the influence of each latent edge in promoting the co-SIR dynamics. Thus, the most influential latent edges can be located after ranking all the latent edges according to their quantified influence. We verify the rationality and superiority of the proposed indicator in identifying the influential latent edges of both synthetic and real-world networks by extensive numerical simulations. This study provides an effective approach to identify the influential latent edges for promoting the network-based co-SIR information spreading model and offers inspirations for further research on intervening the cooperative spreading dynamics from the perspective of performing network structural perturbations.

1. Introduction

The influence of information spreading on human society is increasingly profound. Promoting the spreading of some typical information, for instance, the vaccination guidance, technological innovation, commercials, and political propaganda can benefit all the aspects of socio-economic systems [1–5]. Therefore, researchers from multiple fronts, including statistical physics and network science, have been paying substantial attention to the specific subject of modeling and promoting the information spreading [6–10].

The complex network theory plays an important role in the study of information spreading. Under the framework of complex networks, a large amount of studies on information spreading dynamics have been gained. For instance, various network-based information spreading models such as the susceptible-informed-susceptible (SIS) model [11, 12], susceptible-informed-recovered (SIR) model [13, 14], threshold model [15–19], and many of their extensions [20–24] have been proposed to describe the various spreading dynamics of a single piece of information. The theoretical study of network-based spreading dynamics with a single-information has a long and successful history. However, cooperative information spreading widely exists in the real world [25, 26]. For example, the transmission of epidemic outbreak news may promote the spreading of epidemic prevention

information. Recently, considering the fact that the spreading phenomena in the real world are often influenced by cooperativity effects, researchers go further to study on the cooperative spreading dynamics. Many efforts have been made to uncover and understand the interaction mechanisms [27], evolution patterns [28, 29], phase transition [30], and critical dynamics [31] of the cooperative spreading dynamics [32].

In addition to understanding and modeling of the cooperative spreading dynamics, the problem of how to effectively intervene the cooperative dynamics evolution is also of great importance in both theoretical and practical perspectives. In the study of intervening a single dynamics, researchers have developed numerous strategies from the perspective of designing effective transmission strategies [33–38], identifying vital nodes [39–46] and performing network structural perturbations [3, 47–49]. However, the study of intervening cooperative spreading started to attract attention only recently. Min et al. [50] adopted the message-passing approach to find the influential spreaders by predicting the probability that an extensive coinfection outbreak initiated by two singly infected seed nodes.

Given the limited number of studies so far, no attention has been paid in intervening the cooperative information spreading from the perspective of performing network structural perturbations, to the best of our knowledge. To raise the interest of researchers to fill up this research blankness, in this study, we propose an effective approach to identify the influential latent edges which can promote the cooperative susceptible-infected-recovered (co-SIR) dynamics [50] if added to the original networks. The co-SIR model is first proposed to study the cooperative epidemic spreading. In this study, we extend it to describe cooperative information spreading. Specifically, we first employ the message-passing approach to predict the probabilities of each node being in different node states. Next, based on the obtained state probabilities of nodes, we come up with an indicator for measuring the influence of each latent edge in promoting the cooperative dynamics. Finally, the influential latent edges can be identified by ranking all the latent edges according to their quantified influence. Note that, the indicator we proposed in this study incorporates both the network topology information and dynamics information in the network-based co-SIR dynamical system. This study will verify the rationality and superiority of the proposed indicator in identifying the influential latent edges.

This paper is organized as follows. Firstly, Section 2 will give a detailed description of the co-SIR model. Secondly, Section 3 will show how to identify the influential latent edges in the network-based co-SIR dynamical system. Further, Section 4 will present the extensive numerical simulations to verify the effectiveness of our approach in identifying the influential latent edges. Finally, Section 5 will give a conclusion about this study.

2. Model Description

We consider a discrete-time cooperative co-SIR information spreading model [50] in this study. The co-SIR dynamics runs on a complex network G of N nodes and M edges. Denote the adjacency matrix of network G as H; thus, when there is an edge between node i and j, we have $H_{ij} = 1$; otherwise, $H_{ij} = 0$. To be specific, the co-SIR model merges two classic SIR dynamics, that is, a and b. Each node of the network G can be in three distinct states with respect to each one of the two dynamics. For instance, when dynamics A alone is considered, a node i can be in susceptible (S^a), informed and able to transmit the information (I^a), or removed (R^a) state. Therefore, when we take both dynamics a and b into consideration, there should be overall nine possible node states, that is, S^aS^b, S^aI^b, S^aR^b, I^aS^b, I^aI^b, IS^aR^b, R^aS^b, R^aI^b, and R^aR^b.

Besides, the cooperativity between dynamics a and b is defined as follows: for a node informed with both dynamics, the probability to transmit the information by a single contact increases. Recently, Min and Castellano [50] introduced this kind of cooperative mechanism to describe the cooperativity of epidemics, considering the biological rationale that an infection with a pathogen may cause an individual to pass from the latent state to a fully infective one with respect to another pathogen. Similarly, when it comes to the spreading of information, being informed with message a may encourage an individual to be more active in transmitting another message b. For instance, when an individual is informed of an epidemic outbreak, he/she may be more willing to transmit the information about epidemic prevention.

To be specific, the dynamic process is as follows. Initially, all the nodes of network G are set to be in the S^aS^b state. Next, we selected a small fraction of nodes to be the spreading seeds with respect to dynamics a and b, respectively. At the beginning of each discrete-time step, for each node i and each one of its neighbor j, if i is informed with dynamics a (or b) alone and susceptible with respect to the other, then i will transmit the information a (or b) to j with probability λ_a(or λ_b). That is to say, in this case, the state of node j will be updated according to the following transition rules:

$$\begin{cases} I^aS^b + S^aS^b \xrightarrow{\lambda_a} I^aS^b + I^aS^b, \\ I^aS^b + S^aI^b \xrightarrow{\lambda_a} I^aS^b + I^aI^b, \\ I^aS^b + S^aR^b \xrightarrow{\lambda_a} I^aS^b + I^aR^b, \\ S^aI^b + S^aS^b \xrightarrow{\lambda_b} S^aI^b + S^aI^b, \\ S^aI^b + I^aS^b \xrightarrow{\lambda_b} S^aI^b + I^aI^b, \\ S^aI^b + R^aS^b \xrightarrow{\lambda_b} S^aI^b + R^aI^b. \end{cases} \tag{1}$$

Otherwise, if i is in the recovered state with respect to the other dynamics, the transmission probability will be $\lambda_a^\dagger$(or $\lambda_b^\dagger$). Accordingly, the updating rules of the state of node j are as follows:

$$\begin{cases} I^aR^b + S^aS^b \xrightarrow{\lambda_a^\dagger} I^aR^b + I^aS^b, \\ I^aR^b + S^aI^b \xrightarrow{\lambda_a^\dagger} I^aR^b + I^aI^b, \\ I^aR^b + S^aR^b \xrightarrow{\lambda_a^\dagger} I^aR^b + I^aR^b, \\ R^aI^b + S^aS^b \xrightarrow{\lambda_b^\dagger} R^aI^b + S^aI^b, \\ R^aI^b + I^aS^b \xrightarrow{\lambda_b^\dagger} R^aI^b + I^aI^b, \\ R^aI^b + R^aS^b \xrightarrow{\lambda_b^\dagger} R^aI^b + R^aI^b. \end{cases} \tag{2}$$

Similarly, when i is in the informed state and j is not susceptible (i.e., j is in the informed or recovered state) with respect to the other dynamics, the transmission probability should be $\lambda_a^\dagger$ (or $\lambda_b^\dagger$) as well. The corresponding updating rules are shown as follows:

$$\begin{cases} I^aI^b + S^aI^b \xrightarrow{\lambda_a^\dagger} I^aI^b + I^aI^b, \\ I^aI^b + S^aR^b \xrightarrow{\lambda_a^\dagger} I^aI^b + I^aR^b, \\ I^aI^b + I^aS^b \xrightarrow{\lambda_b^\dagger} I^aI^b + I^aI^b, \\ I^aI^b + R^aS^b \xrightarrow{\lambda_b^\dagger} I^aI^b + R^aI^b. \end{cases} \tag{3}$$

Note that when the state of node i and j is I^aI^b and S^aS^b, respectively, node i may transmit information a (or b) with probability λ_a(or λ_b) first and then transmit information b (or a) with probability $\lambda_b^\dagger$ (or $\lambda_a^\dagger$) during the same time step. Specifically, the state of the susceptible node j is updated according to the following transition rules:

$$\begin{cases} I^aI^b + S^aS^b \xrightarrow{\frac{1}{2}} (\lambda_a\lambda_b^\dagger + \lambda_a^\dagger\lambda_b)\, I^aI^b + I^aI^b, \\ I^aI^b + S^aS^b \xrightarrow{\frac{1}{2}} \lambda_a(1-\lambda_b^\dagger)\, I^aI^b + I^aS^b, \\ I^aI^b + S^aS^b \xrightarrow{\frac{1}{2}} \lambda_b(1-\lambda_a^\dagger)\, I^aI^b + S^aI^b. \end{cases} \tag{4}$$

After the transmission process, all the informed nodes recover with probability γ_a (or γ_b) with respect to dynamic a (or b); and the time step is over. The recovery rules are as follows:

$$\begin{cases} I^aS^b \xrightarrow{\gamma_a} R^aS^b, \\ I^aI^b \xrightarrow{\gamma_a} \gamma_b\, R^aR^b, \\ I^aI^b \xrightarrow{\gamma_a} (1-\gamma_b)\, R^aI^b, \\ I^aI^b \xrightarrow{(} 1-\gamma_a)\gamma_b\, I^aR^b, \\ I^aR^b \xrightarrow{\gamma_a} R^aR^b, \\ S^aI^b \xrightarrow{\gamma_b} S^aR^b, \\ R^aI^b \xrightarrow{\gamma_b} R^aR^b. \end{cases} \tag{5}$$

Finally, the spreading dynamics will be terminated once there is no node that can further transmit information.

In the rest of the paper, we consider only the symmetric case, where $\lambda_a = \lambda_b = \lambda$ and $\lambda_a^\dagger = \lambda_b^\dagger = \lambda^\dagger$, and leave the nonsymmetric case open for future work. Besides, for the sake of simplicity, we assume the recovery probability $\gamma_a = \gamma_b = 1$.

3. Identifying Influential Latent Edges

Now, we turn to the identification of the influential latent edges of network G, which can promote the spreading of the co-SIR model. For convenience, we call the nodes that are informed with both dynamics as the co-informed nodes. Denote the cooperative spreading prevalence of information a and b (that is, the fraction of co-informed nodes) as ρ_{ab}. Specifically, we are interested in finding the influential latent edges, which, if added to the original network G, can maximize the cooperative spreading prevalence ρ_{ab}.

To identify the influential latent edges, we need an indicator to measure the influence of each latent edge in promoting the cooperative spreading prevalence ρ_{ab}. A direct indicator for measuring the influence of latent edge (i, j) is the expected incremental number of co-informed nodes observed after adding an edge between node i and j. However, this indicator expects a large analytical and computational cost. Inspired by the recent references [7, 51], we narrow our focus to the node set U_{ij}, which is composed of node i, j, and their neighbors. It will be much more convenient to calculate the expected incremental number of co-informed nodes in the node set U_{ij}. Denote the probability of node i being in the $\epsilon_i = X^aY^b$ state after the termination of dynamics as p_i^{XY}. Note that we should have $p_i^{XY} = p_i^{YX}$ in the symmetric case. After adding an edge between node i and j, consider the information is transmitted from node i to j; then, according to the transmission rules in Section 2, node j becomes a new co-informed node with probability:

$$p_{i\longrightarrow j} = \lambda\lambda^\dagger p_i^{RR} p_j^{SS} + 2\lambda^\dagger p_i^{RR} p_j^{RS} + 2\lambda p_i^{RS} p_j^{RS}. \tag{6}$$

The first term on the r.h.s accounts for the case when the final states of node i and j are R^aR^b and S^aS^b, respectively; the second term takes into account the case when the final

state of node i is R^aR^b and the final state of node j is R^aS^b or S^aR^b; and the third term accounts for the case when $\epsilon_i = S^aR^b$ and $\epsilon_j = R^aS^b$ or $\epsilon_i = R^aS^b$ and $\epsilon_j = S^aR^b$. Next, the co-informed node j may transmit both information a and b to its neighbors. Therefore, we can approximately get the expected incremental number of co-informed nodes generated through this way of transmission initiated at node i as

$$\delta_{i\longrightarrow j} = p_{i\longrightarrow j}\left[1 + \sum_{r=1}^{N} H_{jr}\left(\lambda\lambda^{\dagger} p_r^{SS} + 2\lambda p_r^{RS}\right)\right]. \tag{7}$$

Similarly, we can get the expected incremental number $\delta_{j\longrightarrow i}$ by symmetry. Take both cases of $\delta_{i\longrightarrow j}$ and $\delta_{j\longrightarrow i}$ into consideration; therefore, we can define an indicator $\overline{\delta}$ to measure the influence of latent edge (i, j) as

$$\overline{\delta}_{ij} = \delta_{i\longrightarrow j} + \delta_{j\longrightarrow i}. \tag{8}$$

Hereafter, the problem reduces to solving Equation (8), i.e., finding the probabilities of nodes being in different states after the termination of dynamics.

According to Section 2, the steady state behavior of the co-SIR model considered in this study can be predicted analytically by a message-passing approach [50]. Denote σ_{ij}^a as the probability that node i has not been informed by node j with respect to information a. In the symmetric case, we have $\sigma_{ij}^a = \sigma_{ij}^b = \sigma_{ij}$, and the message-passing equations for these quantities are

$$\begin{aligned} 1 - \sigma_{ij} = {} & \frac{1}{2}\left(\lambda + \lambda^{\dagger}\right)\left(1 - \prod_{r\in\partial j\backslash i}\sigma_{jr}\right)\left(1 - \prod_{r\in\partial j}\sigma_{jr}\right) \\ & + \lambda\left(1 - \prod_{r\in\partial j\backslash i}\sigma_{jr}\right)\prod_{r\in\partial j}\sigma_{jr}, \end{aligned} \tag{9}$$

where ∂j is the set of neighbor of node j and $\partial j\backslash i$ represents the set of neighboring nodes of node j excluding i. The first term on the r.h.s. takes into account the case that node i is informed with one piece of the information by node j that is in the co-informed state at the end of the dynamics. Meanwhile, the second term accounts for the case that node i is informed with one piece of the information by node j that is informed with only one piece of information.

Solving Equation (9) by iteration, we can get the probability that node i being informed with both information a and b at the end of the dynamics as follows:

$$p_i^{RR} = \left(1 - \prod_{j\in\partial i}\sigma_{ij}\right)^2. \tag{10}$$

Similarly, the probability that node i being informed only with one piece of the dynamics at the end is

$$p_i^{SR} = \left(1 - \prod_{j\in\partial i}\sigma_{ij}\right)\prod_{j\in\partial i}\sigma_{ij}. \tag{11}$$

Besides, the fraction of co-informed nodes after the termination of the dynamics is

$$\rho_{ab} = \frac{1}{N}\sum_{r=1}^{N}\left(1 - \prod_{j\in\partial i}\sigma_{ij}\right)^2. \tag{12}$$

Combining Equations (10) and (11), we can calculate the influence $\overline{\delta}_{ij}$ of each latent edge (i, j) according to Equation (8) and then identify the influential latent edges for promoting the spreading of the co-SIR model by ranking all the latent edges with respect to the corresponding values of $\overline{\delta}$.

4. Simulation Results

This section will show the results of extensive numerical simulations on both synthetic and real-world networks to verify the effectiveness of our approach in identifying the influential latent edges. The detailed structural information of the networks employed in this section can be found from Table 1. Note that the message-passing approach [50] mentioned in Section 3 can accurately predict the Monte Carlo simulations; thus, to avoid large computational cost, we obtain the numerical value of cooperative spreading prevalence ρ_{ab} by solving Equation (12) instead of using the Monte Carlo simulation approach.

In our approach, we identify the influential latent edges by ranking the values of $\overline{\delta}$, which incorporates the information of both network structure (i.e., the adjacency matrices H) and spreading dynamics (i.e., λ and $\lambda^{\dagger}$). For comparison, we also test two additional approaches that only rely on network topology. On the one hand, we consider the approach to rank all the latent edges by θ^d which denotes the product of the degree centrality of nodes connected by the given latent edge. On the other hand, we employ the strategy to rank all the latent edges by θ^b, which is the product of betweenness centrality of nodes connected by the given latent edge. With the help of numerical simulations, now we are going to show the effectiveness and advantage of our approach in identifying the influential latent edges step by step.

Firstly, to verify the rationality and superiority of employing indicator $\overline{\delta}$ to rank the influence of latent edges in promoting the spreading of co-SIR dynamics, we investigate the correlations between $\overline{\delta}$ and the incremental cooperative spreading prevalence $\widehat{\rho}_{ab}$. The dynamics runs on a scale-free (SF) network G_s with degree distribution $p(k)\,k^{-\alpha}$, where $\alpha = 2.3$ denotes the degree exponent. More detailed information about the network G_s can be found in Table 1. Figures 1(a)–1(c) show $\overline{\delta}$ versus $\widehat{\rho}_{ab}$ when the cooperativity parameters $\beta = \lambda^{\dagger}/\lambda$ are equal to 1, 1.5, and 2, respectively. Note that the transmission probabilities are set to be $\lambda = 0.4$ in all the numerical simulations of Figures 1(a)–1(c). As can be seen, the values of $\overline{\delta}$ and $\widehat{\rho}_{ab}$ are almost linearly correlated in all the cases studied; thus, it is rational to use the indicator $\overline{\delta}$ in ranking all the latent edges. Next, we go further to investigate the correlations between $\overline{\delta}$ and $\widehat{\rho}_{ab}$ for all the parameter regions by calculating the Spearman rank correlation coefficient [52, 53] between them. The Spearman rank correlation coefficient is defined as follows:

Table 1: Network statistics.

Name	N	M	$\langle k\rangle$	$\langle k^2\rangle$	$k_{\max}$	λ_c
SF	200	1000	10	129.5	28	0.084
Physicians	117	465	7.95	79.162	26	0.114
Inf-USAir97	332	2126	12.807	568.163	139	0.025
Jazz musicians	198	2742	27.697	1070.242	100	0.026

N: the node number; M: the edge number; $\langle k\rangle$: the average degree; $\langle k^2\rangle$: the second moment of the degree distribution; $k_{\max}$: the maximum degree; λ_c: the threshold value.

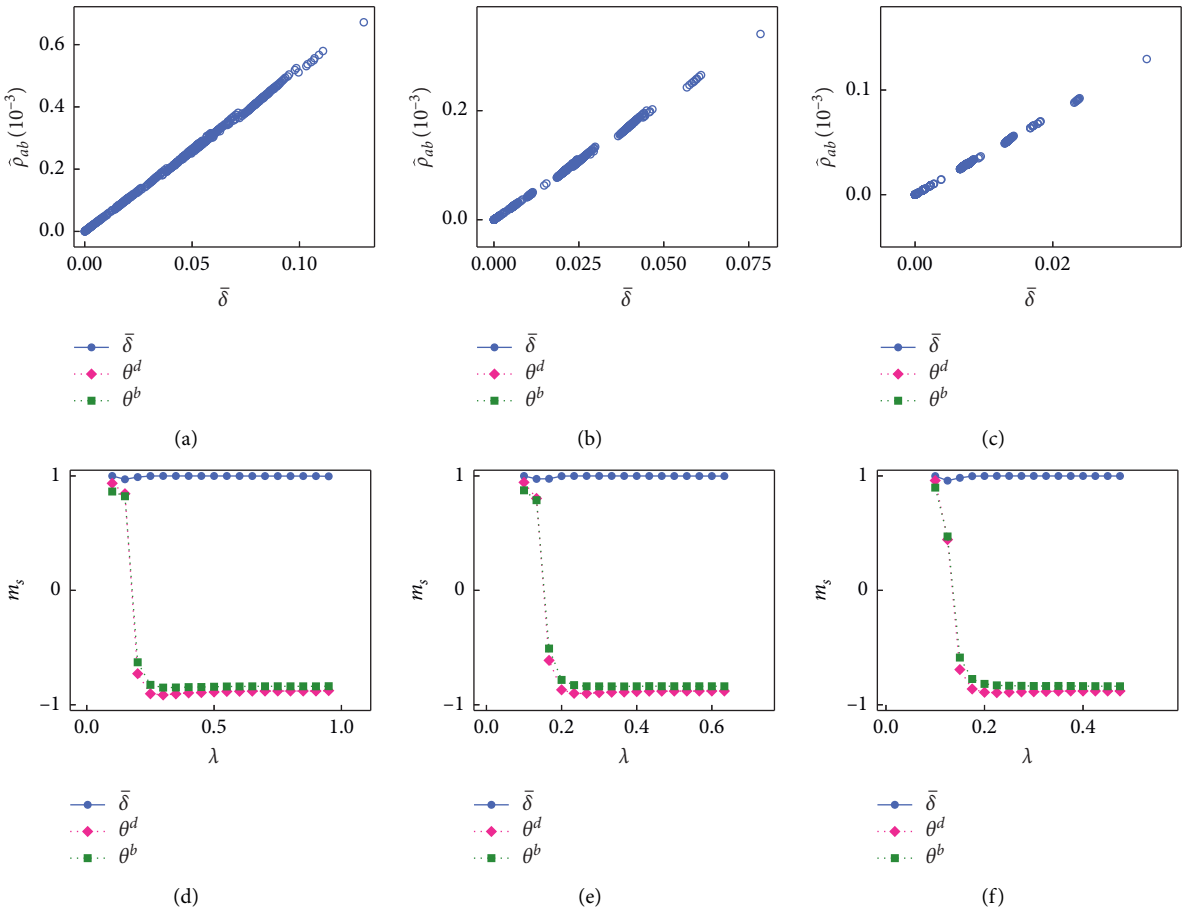

Figure 1: The correlation between influence indicator $\overline{\delta}$ and incremental cooperative spreading prevalence $\widehat{\rho}_{ab}$ on the SF network. $\widehat{\rho}_{ab}$ versus $\overline{\delta}$ when the cooperativity parameter (a) $\beta = 1$, (b) $\beta = 1.5$, and (c) $\beta = 2$. The Spearman rank correlation m_s between $\widehat{\rho}_{ab}$ and $\overline{\delta}$ (blue circles), product θ^d (pink diamonds), or θ^b (green squares) versus λ when (d) $\beta = 1$, (e) $\beta = 1.5$, and (f) $\beta = 2$.

$$m_s = 1 - 6\frac{\sum_{l=1}^{M_u}\left(\phi_l - \hat{\phi}_l\right)^2}{M_u\left(M_u - 1\right)^2}, \tag{13}$$

where $\overline{\phi}_l$ and $\widehat{\phi}_l$ are the ranks of latent edge l scored by $\overline{\delta}$ and $\widehat{\rho}_{ab}$, respectively, and $M_u = (1/2)N(N-1) - M$ is the total number of latent edges. For convenience, we refer to the latent edge rank scored by $\widehat{\rho}_{ab}$ as numerical rank $\widehat{\phi}$. Figures 1(d)–1(f) show the correlation m_s versus transmission probability λ when $\beta = 1$, $\beta = 1.5$, and $\beta = 2$, respectively. Note that we only consider the situation when $\lambda > \lambda_c$, where λ_c is the threshold value of the dynamics; since in the case when $\lambda < \lambda_c$, the cooperative spreading prevalence ρ_{ab} should be theoretically equal to 0. The theoretical values of λ_c are given by the inverse of the principal eigenvalue Λ of the nonbacktracking matrix B [50], where B is a $2M * 2M$ matrix with elements:

$$B_{i\longrightarrow j,l\longrightarrow k} = \delta_{jl}\left(1 - \delta_{ik}\right). \tag{14}$$

The specific values of λ_c of the networks can be found in Table 1. We can observe that the values of m_s stay close to 1 (that is to say, the latent edge ranks scored by $\overline{\delta}$ and $\widehat{\rho}_{ab}$ are strongly correlated) in all the parameter regions. For comparison, we also calculate the Spearman rank correlations between the latent edge ranks scored by degree centrality product θ^d or betweenness centrality product θ^b and $\widehat{\rho}_{ab}$. As shown in Figures 1(d)–1(f), the latent edge ranks

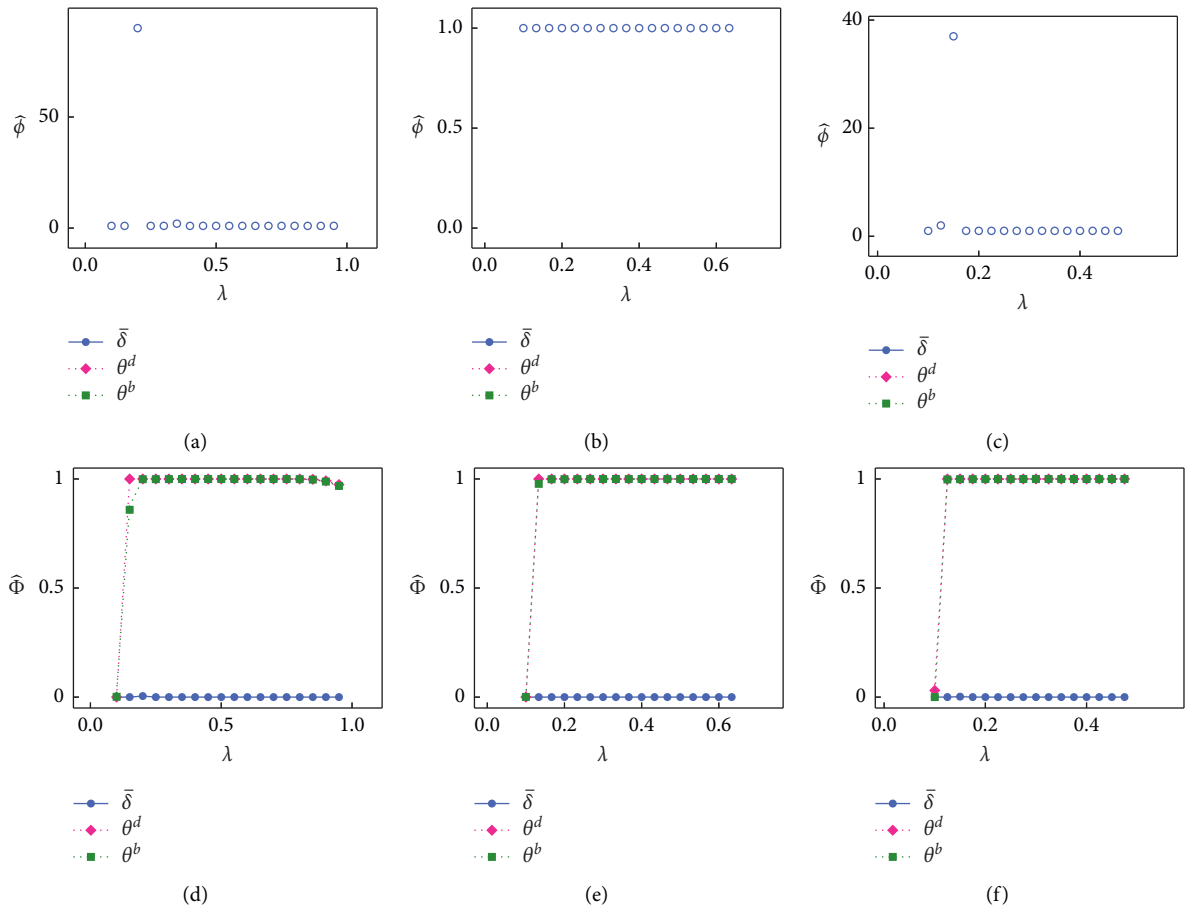

FIGURE 2: The numerical ranks of optimal latent edges on the SF network. The numerical rank of the optimal latent edge scored by $\bar{\delta}$ versus λ when (a) $\beta = 1$, (b) $\beta = 1.5$, and (c) $\beta = 2$. The normalized numerical rank $\widehat{\Phi}$ of the optimal latent edge scored by $\bar{\delta}$ (blue circles), product θ^d (pink diamonds), or θ^b (green squares) versus λ when (d) $\beta = 1$, (e) $\beta = 1.5$, and (f) $\beta = 2$.

scored by θ^d or θ^b are positively correlated with the numerical rank $\widehat{\phi}$ only when λ is small. However, when λ becomes large, the underlined correlations become negative. To sum up, Figures 1(a)-1(f) demonstrate that using the proposed indicator $\bar{\delta}$ to identify the influential latent edges is more rational than using the centrality product θ^d or θ^b.

Secondly, considering the problem of identifying the influential latent edges, we are particularly interested in finding the optimal latent edge which can maximize the cooperative spreading prevalence; thus, we are going to show that the indicator $\bar{\delta}$ proposed in this study performs well in identifying the optimal latent edge. Denote L, L^d, and L^b as the optimal latent edges selected according to indicators $\bar{\delta}$, θ^d, and θ^b, respectively. Let us continue with the co-SIR dynamics on the SF network G_s. Figures 2(a)–2(c) present the numerical rank $\widehat{\phi}_L$ of the optimal latent edge L versus transmission probability λ when $\beta = 1$, $\beta = 1.5$, and $\beta = 2$, respectively. It can be seen that $\widehat{\phi}_L = 1$ for most values of λ regardless of the values of cooperative parameter β. That is to say, the indicator $\bar{\delta}$ can well predict the optimal edge which can maximize the cooperative spreading prevalence $\widehat{\rho}_{ab}$. Denote $\widehat{\Phi} = \widehat{\phi}/M_u$ as the normalized numerical rank, where smaller $\widehat{\Phi}$ indicates higher rank. Figures 2(d)–2(f) further show the normalized ranks of optimal latent edges L, L^d, and L^b versus λ when $\beta = 1$, $\beta = 1.5$, and $\beta = 2$, respectively. Visually, L, L^d, and L^b all rank high when λ is slight above the threshold value, but once λ becomes large, the ranks of L^d and L^b fall quickly. Therefore, we can draw a conclusion that the strategy of using the indicator $\bar{\delta}$ which incorporates both information of network topology and dynamics is better than using those structural indicators (i.e., θ^d and θ^b) in finding the optimal latent edge.

Thirdly, to better understand the specific influence of the optimal latent edges L, L^d, and L^b in promoting the co-SIR dynamics, we calculated the corresponding incremental cooperative spreading prevalence $\widehat{\rho}_{ab}$ after adding those optimal latent edges to the original networks. For network G_s, Figures 3(a)–3(c) show the incremental cooperative spreading prevalence $\widehat{\rho}_{ab}$ versus λ when $\beta = 1$, $\beta = 1.5$, and $\beta = 2$, respectively. The results demonstrate that adding the optimal latent edge L selected according to the proposed indicator $\bar{\delta}$ can effectively promote the cooperative spreading prevalence ρ_{ab} for most of the values of λ. However, adding the optimal L^d or L^b to G_s has little influence in promoting ρ_{ab} for almost all the cases studied. Note that, on the network G_s, when λ is small, the cooperative spreading prevalence $\rho_{ab} \longrightarrow 0$; thus, the incremental spreading prevalence $\widehat{\rho}_{ab} \longrightarrow 0$ after adding any

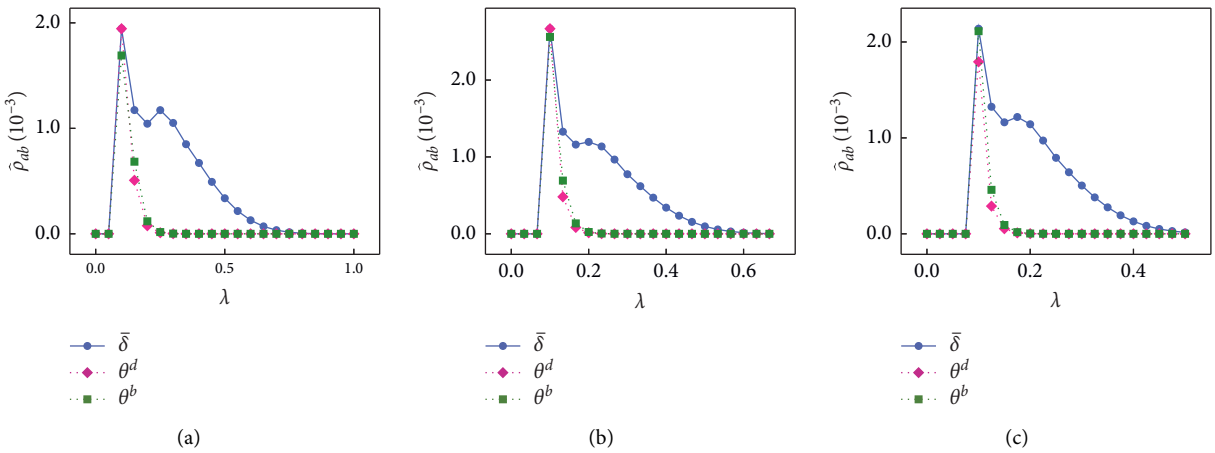

FIGURE 3: Incremental cooperative spreading prevalence $\widehat{\rho}_{ab}$ after adding the optimal latent edge to the SF network. The incremental cooperative spreading prevalence $\widehat{\rho}_{ab}$ after adding the optimal latent edge scored by $\overline{\delta}$ (blue circles), product θ^d (pink diamonds), or θ^b (green squares) versus λ when (a) $\beta = 1$, (b) $\beta = 1.5$, and (c) $\beta = 2$.

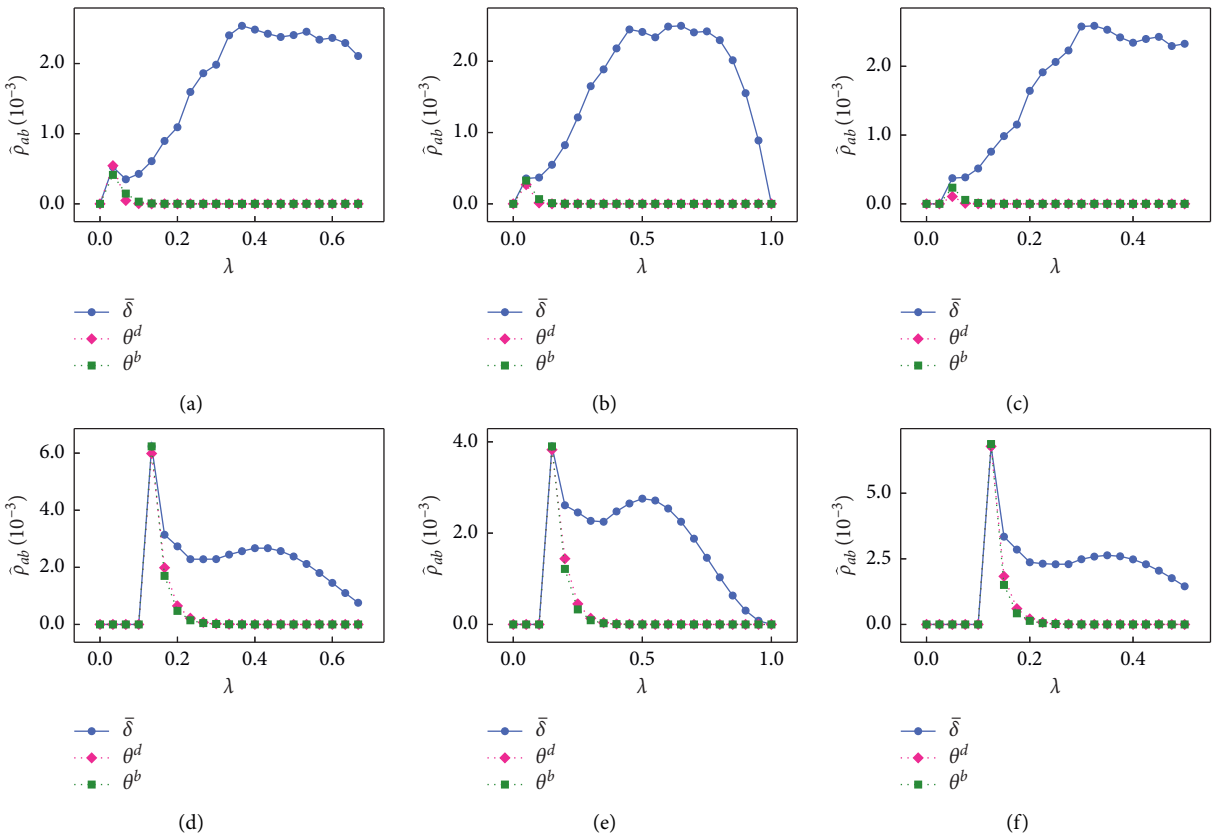

FIGURE 4: Continued.

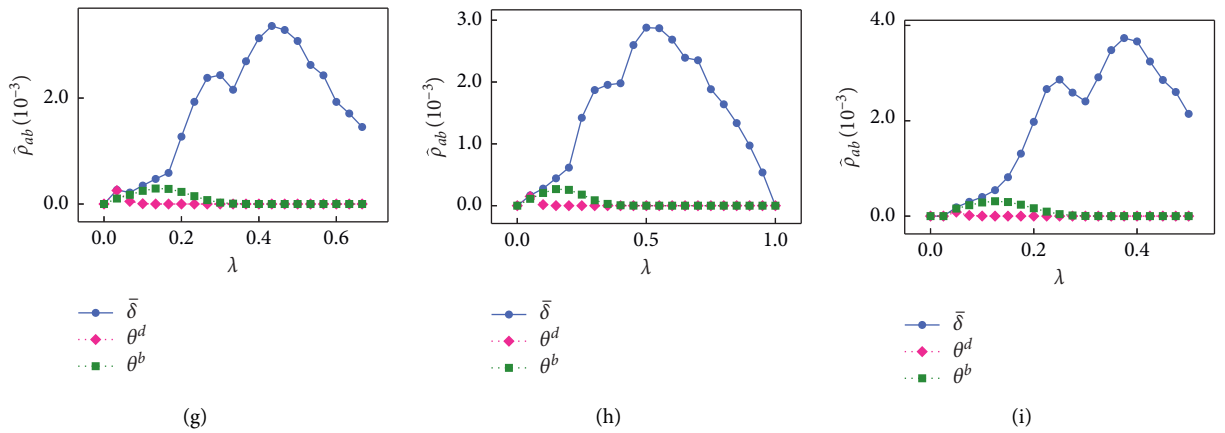

Figure 4: Incremental cooperative spreading prevalence $\widehat{\rho}_{ab}$ after adding the optimal latent edge to the real-world networks. The incremental cooperative spreading prevalence $\widehat{\rho}_{ab}$ after adding the optimal latent edge scored by $\overline{\delta}$ (blue circles), product θ^d (pink diamonds), or θ^b (green squares) to the real-world network Jazz musicians [54] when (a) $\beta = 1$, (b) $\beta = 1.5$, and (c) $\beta = 2$. The corresponding results of real-world network physicians [54] and inf-USAir97 [55] are shown in (d) $\beta = 1$, (e) $\beta = 1.5$, and (f) $\beta = 2$ and (g) $\beta = 1$, (h) $\beta = 1.5$, and (i) $\beta = 2$, respectively.

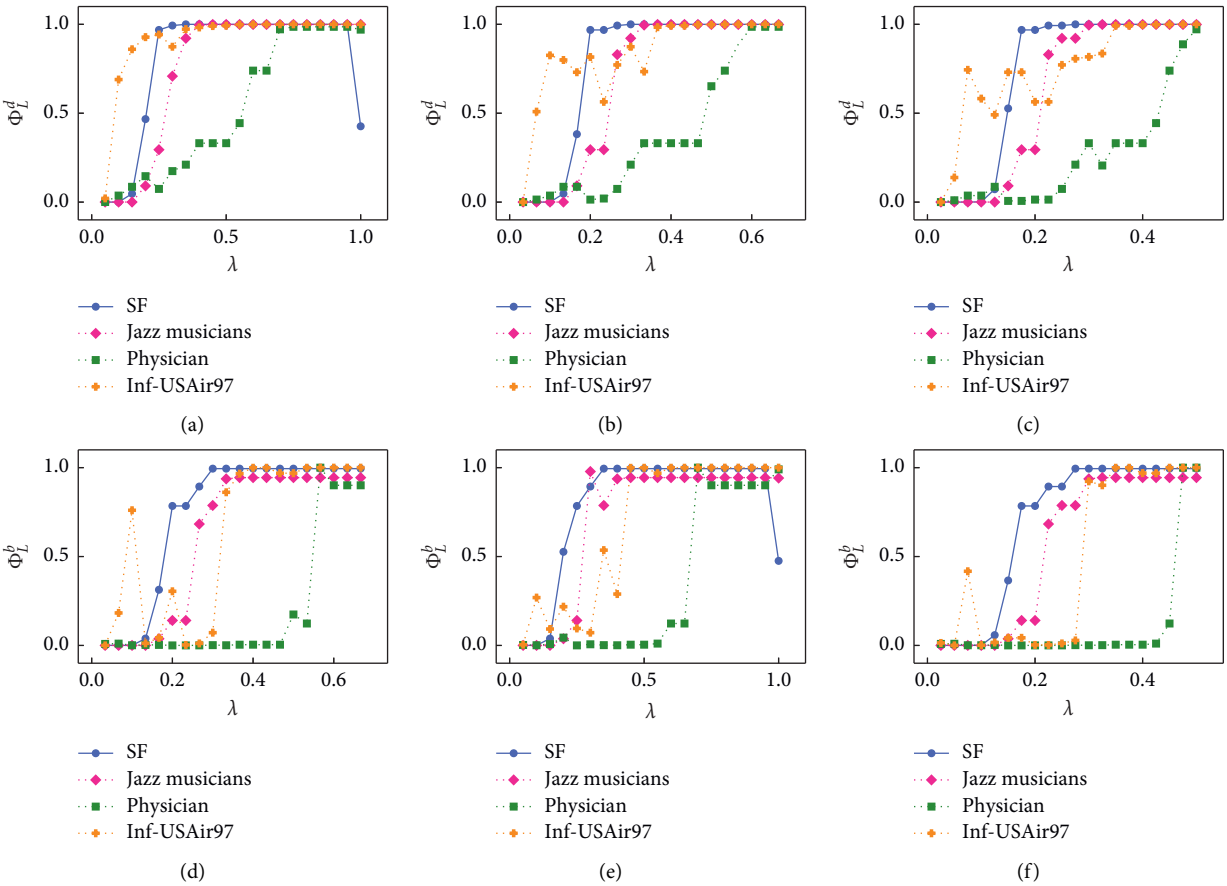

Figure 5: Continued.

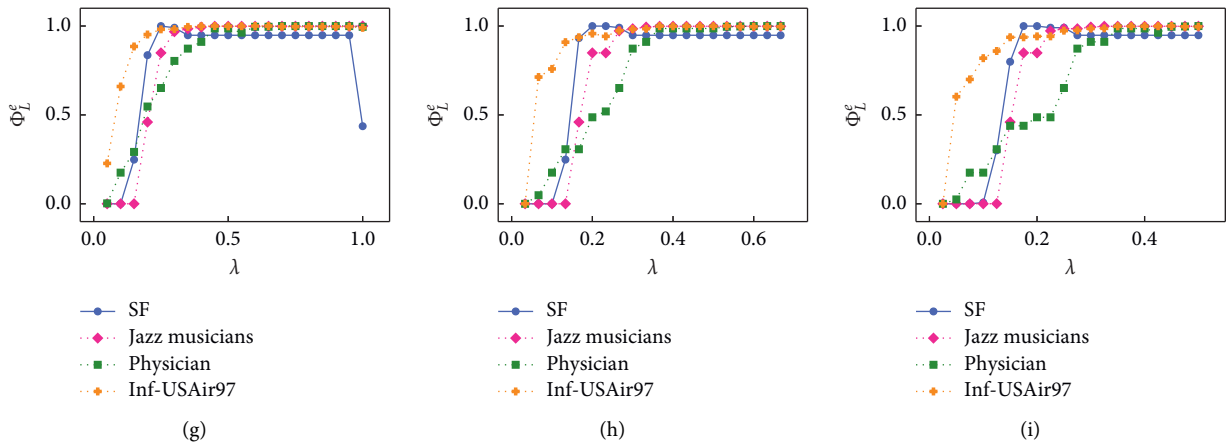

FIGURE 5: Structural properties of the optimal latent edge L scored by influence indicator $\overline{\delta}$. The normalized latent edge rank Φ^d scored by the degree centrality product θ^d of the optimal latent edge L on network SF (blue circles), Jazz musicians (pink diamonds), physician (green squares), and inf-USAir97 (orange plus) when the cooperativity parameter (a) $\beta = 1$, (b) $\beta = 1.5$, and (c) $\beta = 1.5$. The corresponding results of the normalized latent edge rank Φ^b scored by the betweenness centrality product θ^b and normalized latent edge rank Φ^e scored by the eigenvector centrality product θ^e are shown in (d) $\beta = 1$, (e) $\beta = 1.5$, and (f) $\beta = 1.5$ and (g) $\beta = 1$, (h) $\beta = 1.5$, and (i) $\beta = 1.5$, respectively.

single edge to the network. Similarly, when λ becomes too large, $\rho_{ab} \longrightarrow 1$; thus, $\widehat{\rho}_{ab} \longrightarrow 0$ as well. We also test the effectiveness of optimal latent edges L, L^d, and L^b in promoting the spreading dynamics on three real-world networks: (a) Jazz musicians [54]; (b) physicians [54]; and (c) inf-USAir97 [55]. Some structural information of these real-world networks can be found in Table 1. Figure 4 shows the incremental cooperative spreading prevalence $\widehat{\rho}_{ab}$ versus λ on the three real-world networks with different cooperativity parameter β. The results are consistent with those of the SF network G_s, i.e., using the proposed indicator $\overline{\delta}$ in this study can effectively identify the influential latent edge to promote the co-SIR dynamics.

Finally, we investigate how the structural properties (i.e., degree, betweenness, and eigenvector centrality) of optimal latent edge L change with λ. Denote Φ^d, Φ^b, and Φ^e as the normalized latent edge rank scored by the degree centrality product θ^d, betweenness centrality product θ^b, and eigenvector centrality product θ^e, respectively. Figures 5(a)–5(c) show the normalized rank Φ_L^d of the optimal latent edge L versus λ on different networks when $\beta = 1$, $\beta = 1.5$, and $\beta = 2$, respectively. Similarly, the corresponding results about normalized rank Φ_L^b and Φ_L^e are shown in Figures 5(d)–5(f) and Figures 5(g)–5(i), respectively. As can be demonstrated from Figure 5, when λ is small, the centrality ranks of the optimal latent edge L are high for most of the cases. In other words, adding connection between nodes with high centrality can effectively promote the spreading of co-SIR dynamics when the transmission probability is small. This can be understood by the fact that when λ is near, the threshold ρ_{ab} should be small, and adding an edge between nodes with high centrality can help to keep the cluster of co-informed nodes, thus, promoting the co-SIR spreading dynamics. However, when λ becomes large, the centrality ranks of L fall quickly in most of the cases studied. This is because nodes with high centrality ranks will have a higher probability to be co-informed when λ is large; thus, it is unnecessary to add connection between them. The results in Figure 5 give an intuitive explanation for the failure of indicator θ^d and θ^b in identifying influential latent edges when λ is large.

5. Conclusions

Cooperative information spreading on networked systems is a common phenomenon in the real world. The study of promoting the network-based cooperative spreading dynamics is of both theoretical and practical importance. In this study, we proposed an effective approach to identify the influential latent edges for promoting the spreading of the co-SIR model on complex networks.

To be specific, we first employ the message-passing approach to obtain the probabilities of each nodes being in different node states. Next, given the obtained state probabilities of nodes, we proposed the indicator $\overline{\delta}$ to measure the influence of each latent edge in promoting the spreading of the co-SIR model. Then, we can rank all the latent edges by the indicator $\overline{\delta}$ to identify the influential latent edges for promoting the co-SIR dynamics on the complex networks. Note that the indicator $\overline{\delta}$ incorporates both the information of network structure and the co-SIR dynamics; and the numerical simulations verified that the indicator $\overline{\delta}$ outperforms those structural indicators (i.e., the degree centrality product θ^d and betweenness centrality product θ^b) in identifying the influential latent edges on both synthetic and real-world networks. Finally, we investigated how the structure properties of the optimal latent edges change with the transmission probability λ. It is surprising that the centrality ranks of the optimal latent edges fall quickly when λ becomes large in most of the cases studied. This finding gives an intuitive explanation for the failure of those structural indicators in identifying the influential latent edges when λ is large.

This study provides an effective approach for identifying the influential latent edges for promoting the network-based co-SIR information spreading dynamics. The research findings offer inspirations for further studies on intervening the cooperative spreading dynamics from the perspective of performing network structural perturbations.

Data Availability

The network data used to support the findings of this study have been deposited in the KONECT: the Koblenz Network Collection repository (10.1145/2487788.2488173) and the Network Data Repository with Interactive Graph Analytics and Visualization (http://networkrepository.com).

Conflicts of Interest

The authors declare that they have no conflicts of interest regarding the publication of this paper.

Acknowledgments

This work was supported in part by the National Natural Science Foundation of China under Grant 11975071 and 62006122, in part by the Scientific Research Foundation of Shantou University under Grant NTF19015, and in part by the 2020 Li Ka Shing Foundation Cross-Disciplinary Research under Grant 2020LKSFG09D.

References

[1] Z. Wang, C. T. Bauch, S Bhattacharyya et al., "Statistical physics of vaccination," *Physics Reports*, vol. 664, pp. 1–113, 2016.

[2] M. Gong, J. Yan, B. Shen, L. Ma, and Q. Cai, "Influence maximization in social networks based on discrete particle swarm optimization," *Information Sciences*, vol. 367, pp. 600–614, 2016.

[3] G. Del Ferraro, A. Moreno, B. Min et al., "Finding influential nodes for integration in brain networks using optimal percolation theory," *Nature Communications*, vol. 9, p. 2274, 2018.

[4] Y. Hu, S. Ji, Y. Jin, L. Feng, H. E. Stanley, and S. Havlin, "Local structure can identify and quantify influential global spreaders in large scale social networks," *Proceedings of the National Academy of Sciences*, vol. 115, pp. 7468–7472, 2018.

[5] A. Y. Lokhov and D. Saad, "Optimal deployment of resources for maximizing impact in spreading processes," *Proceedings of the National Academy of Sciences*, vol. 114, pp. E8138–E8146, 2017.

[6] F. Morone and H. A. Makse, "Influence maximization in complex networks through optimal percolation," *Nature*, vol. 524, pp. 65–68, 2015.

[7] D. Yang, J. Xian, L. Pan, W. Wang, and T. Zhou, "Effective edge-based approach for promoting the spreading of information," *IEEE Access*, vol. 8, pp. 83745–83753, 2020.

[8] L. Pan, W. Wang, S. Cai, and T. Zhou, "Optimal interlayer structure for promoting spreading of the susceptible-infected-susceptible model in two-layer networks," *Physical Review E*, vol. 100, Article ID 022316, 2019.

[9] T. Wu, L. Chen, X. Xian, and Y. Guo, "Evolution prediction of multi-scale information diffusion dynamics," *Knowledge-Based Systems*, vol. 113, pp. 186–198, 2016, http://www.sciencedirect.com/science/article/pii/S0950705116303574.

[10] L. Pan, W. Wang, S. Cai, and T. Zhou, "Chaos optimizing spreading dynamics in interconnected networks," *Chaos: An Interdisciplinary Journal of Nonlinear Science*, vol. 29, no. 10, Article ID 103106, 2019.

[11] X. Fu, M. Small, D. M. Walker, and H. Zhang, "Epidemic dynamics on scale-free networks with piecewise linear infectivity and immunization," *Physical Review E*, vol. 77, Article ID 036113, 2008.

[12] J. Xian, D. Yang, L. Pan, and W. Wang, "The optimal edge for containing the spreading of SIS model," *Journal of Statistical Mechanics: Theory and Experiment*, vol. 2020, no. 4, Article ID 043501, 2020.

[13] D J Daley and D G Kendall, "Epidemics and Rumours," *Nature*, vol. 204, no. 4963, 1118 pages, 1964.

[14] D. J. Daley and D. G. Kendall, "Stochastic Rumours," *Journal of Applied Mathematics*, vol. 1, pp. 42–55, 1965.

[15] S. Aral and C. Nicolaides, "Exercise contagion in a global social network," *Nature Communications*, vol. 8, p. 14753, 2017.

[16] D. M. Romero, B. Meeder, and J. Kleinberg, "Differences in the mechanics of information diffusion across topics: idioms, political hashtags, and complex contagion on twitter," in *Proceedings of the 20th International Conference on World Wide Web*, pp. 695–704, ACM, Hyderabad, India, March 2011.

[17] D. Centola and M. Macy, "Complex contagions and the weakness of long ties," *American journal of sociology*, vol. 113, pp. 702–734, 2007.

[18] D. J. Watts, "A simple model of global cascades on random networks," in *Proceedings of the National Academy of Sciences*, vol. 99, pp. 5766–5771, 2002.

[19] L. Lü, D. B. Chen, and T. Zhou, "The small world yields the most effective information spreading," *New Journal of Physics*, vol. 13, no. 12, Article ID 123005, 2011.

[20] Z. Wang, H. Zhang, and Z. Wang, "Multiple effects of self-protection on the spreading of epidemics," *Chaos, Solitons & Fractals*, vol. 61, pp. 1–7, 2014.

[21] G. Q. Sun, M. Jusup, Z. Jin, Y. Wang, and Z. Wang, "Pattern transitions in spatial epidemics: Mechanisms and emergent properties," *Physics of Life Reviews*, vol. 19, pp. 43–73, 2016.

[22] L. A. Zuzek, H. Stanley, and L. Braunstein, "Epidemic Model with Isolation in Multilayer Networks," *Scientific Reports*, vol. 5, Article ID 12151, 2015.

[23] Z. Wang, Q. Guo, S. Sun, and C. Xia, "The impact of awareness diffusion on SIR-like epidemics in multiplex networks," *Applied Mathematics and Computation*, vol. 349, pp. 134–147, 2019.

[24] C. Xia, Z. Wang, C. Zheng, Q. Guo, and Y. Shi, "A new coupled disease-awareness spreading model with mass media on multiplex networks," *Information Sciences*, vol. 471, pp. 185–200.

[25] X. Chen, K. Gong, R. Wang, S. Cai, and W. Wang, "Effects of heterogeneous self-protection awareness on resource-epidemic coevolution dynamics," *Applied Mathematics and Computation*, vol. 385, Article ID 125428, 2020.

[26] X. Chen, R. Wang, D. Yang, J. Xian, and Q. Li, "Metal Roof Fault Diagnosis Method Based on RBF-SVM," *Complexity*, vol. 2020, Article ID 9645817, 12 pages, 2020.

[27] M. E. J. Newman, "Eigen model of randomness in species evolution," *Acta Physica Sinica*, vol. 95, no. 10, Article ID 108701, 2005.

[28] W. Cai, L. Chen, F. Ghanbarnejad, and P. Grassberger, "Avalanche outbreaks emerging in cooperative contagions," *Nature Physics*, vol. 11, pp. 936–940, 2015.
[29] X. Chen, Q. Liu, R. Wang, Q. Li, and W. Wang, "Life Cycle Assessment of Environmental Impact of Steelmaking Process," *Complexity*, vol. 2020, Article ID 8863941, 9 pages, 2020.
[30] L. Hébert-Dufresne and B. M. Althouse, "Complex dynamics of synergistic coinfections on realistically clustered networks," *Proceedings of the National Academy of Sciences*, vol. 112pp. 10551–10556, 2015, https://www.pnas.org/content/112/33/10551.full.pdf.
[31] J. D. Noh and H. Park, "Complex dynamics of synergistic coinfections on realistically clustered networks," *Proceedings of the National Academy of Sciences*, vol. 94, no. 14, Article ID 145702, 2005.
[32] W. Wang, Q. H. Liu, J. Liang, Y. Hu, and T. Zhou, "Editorial Board," *Physics Reports*, vol. 820, pp. 1–51, 2019.
[33] R. Yang, T. Zhou, Y. B. Xie, Y. C. Lai, and B. H. Wang, "Optimal contact process on complex networks," *Physical Review E*, vol. 78, Article ID 066109, 2008.
[34] L. Gao, W. Wang, L. Pan, M. Tang, and H. F. Zhang, "Effective information spreading based on local information in correlated networks," *Scientific Reports*, vol. 6, Article ID 38220, 2016.
[35] R. Yang, L. Huang, and Y. C. Lai, "Selectivity-based spreading dynamics on complex networks," *Physical Review E*, vol. 78, Article ID 026111, 2008.
[36] F. Roshani and Y. Naimi, "Effects of degree-biased transmission rate and nonlinear infectivity on rumor spreading in complex social networks," *Physical Review E*, vol. 85, Article ID 036109, 2012.
[37] L. Gao, W. Wang, P. Shu, H. Gao, and L. Braunstein, "Promoting information spreading by using contact memory," *Europhysics Letters*, vol. 118, Article ID 18001, 2017.
[38] P. B. Cui, W. Wang, S. M. Cai, T. Zhou, Y. C. Lai et al., "Close and ordinary social contacts: How important are they in promoting large-scale contagion?" *Physical Review E*, vol. 98, Article ID 052311, 2018.
[39] L. Lü, D. Chen, X. L. Ren, Q. M. Zhang, Y. C. Zhang, and T. Zhou, "Vital nodes identification in complex networks," *Physics Reports*, vol. 650, pp. 1–63, 2016.
[40] H. Liao, M. S. Mariani, M. Medo, Y. C. Zhang, and M. Y. Zhou, "Ranking in evolving complex networks," *Physics Reports*, vol. 689, pp. 1–54, 2017.
[41] Y. Xin, C. Gao, Z. Wang, X. Zhen, and X. Li, "Discerning Influential Spreaders in Complex Networks by Accounting the Spreading Heterogeneity of the Nodes," *IEEE Access*, vol. 7, pp. 92070–92078, 2019.
[42] W. Chen, C. Wang, and Y. Wang, "Scalable influence maximization for prevalent viral marketing in large-scale social networks," in *Proceedings of the 16th ACM SIGKDD International Conference on Knowledge Discovery and Data Mining*, pp. 1029–1038, Washington, DC, USA, July 2010.
[43] F. Riquelme and P. González-Cantergiani, "Measuring user influence on Twitter: A survey," *Information Processing & Management*, vol. 52, pp. 949–975, 2016.
[44] M. Kitsak, L. K. Gallos, S Havlin et al., "Identification of influential spreaders in complex networks Nature Physics," vol. 6, pp. 888–893, 2010.
[45] L. Lü, T. Zhou, Q. M. Zhang, and H. E. Stanley, "The H-index of a network node and its relation to degree and coreness," *Nature Communications*, vol. 7, Article ID 10168, 2016.
[46] W. Chen, Y. Wang, and S. Yang, "Efficient influence maximization in social networks," in *Proceedings of the 15th ACM SIGKDD International Conference on Knowledge Discovery and Data Mining*, pp. 199–208, Paris, France, July 2009.
[47] J. Aguirre, D. Papo, and J. M. Buldú, "Successful strategies for competing networks," *Nature Physics*, vol. 9, pp. 230–234, 2013.
[48] A. Milanese, J. Sun, and T. Nishikawa, "Approximating spectral impact of structural perturbations in large networks," *Physical Review*, vol. E 81, Article ID 046112, 2010.
[49] P. Van Mieghem, H. Wang, X. Ge, S. Tang, and F. A. Kuipers, "Influence of assortativity and degree-preserving rewiring on the spectra of networks," *The European Physical Journal*, vol. B 76, pp. 643–652, 2010.
[50] B. Min and C. Castellano, "Chaos: Message-passing theory for cooperative epidemics," *An Interdisciplinary Journal of Nonlinear Science*, vol. 30, Article ID 023131, 2020.
[51] J. T. Matamalas, A. Arenas, and S. Gómez, "Effective approach to epidemic containment using link equations in complex networks," *Science Advances*, vol. 4, Article ID Eaau4212, 2018.
[52] K. M. Lee, J. Y. Kim, W. k Cho, K. I. Goh, and I. Kim, "Correlated multiplexity and connectivity of multiplex random networks," *New Journal of Physics*, vol. 14, Article ID 033027, 2012.
[53] W. k Cho, K. I. Goh, and I. M. Kim, arXiv preprint arXiv: 1010.4971, 2010.
[54] J. Kunegis, "Konect: the koblenz network collection," in *Proceedings of the 22nd International Conference on World Wide Web WWW '13 Companion*, pp. 1343–1350, Association for Computing Machinery, New York, NY, USA, 2013.
[55] R. A. Rossi and N. K. Ahmed, The network data repository with interactive graph analytics and visualization AAAI, 2015.

Hindawi
Complexity
Volume 2021, Article ID 6694383, 11 pages
https://doi.org/10.1155/2021/6694383

Research Article

Impact of Defending Strategy Decision on DDoS Attack

Chunming Zhang

School of Information Engineering, Guangdong Medical University, Dongguan 523808, China

Correspondence should be addressed to Chunming Zhang; chunfei2002@163.com

Received 14 October 2020; Revised 15 November 2020; Accepted 4 March 2021; Published 16 March 2021

Academic Editor: Wei Wang

Distributed denial-of-service (DDoS) attack is a serious threat to cybersecurity. Many strategies used to defend against DDoS attacks have been proposed recently. To study the impact of defense strategy selection on DDoS attack behavior, the current study uses logistic function as basis to propose a dynamic model of DDoS attacks with defending strategy decisions. Thereafter, the attacked threshold of this model is calculated. The existence and stability of attack-free and attacked equilibria are proved. Lastly, some effective strategies to mitigate DDoS attacks are suggested through parameter analysis.

1. Introduction

A distributed denial-of-service (DDoS) attack is a cyber-attack in which hackers attempt to make a website or computer unavailable by flooding or crashing the website with too much traffic [1, 2]. Given the rapid development of cloud computing, big data, and artificial intelligence, distributed denial-of-service (DDoS) attacks have become one among the most critical threats to network security [3, 4]; for example, in February 2018, the official website of the PyeongChang Winter Olympics Organizing Committee was forced to shut down during the Winter Olympic Games due to a DDoS attack [5]; in March 2018, GitHub suffered a DDoS attack with the maximum peak traffic reaching 1.7 TBPS [6]; in October 2019, Amazon Web Services was attached by DDoS for several hours, resulting in an outage affecting many websites [7]. Therefore, it is an important issue to study the dynamic behavior of DDoS attacks and propose defense strategies on this basis. Numerous models of DDoS attacks have been proposed in recent years. Haldar et al. [8] proposed a DDoS attack model based on the compartment model and obtained threshold conditions that determine the success or failure of such attacks. Kumar et al. [9] presented a dynamic model of DDoS attack in a computer network and studied the dynamic behavior of this model through numerical simulation. Hou et al. [10] investigated a DDoS attack model with a saturated contact infection rate and proved the stability of this model. Mishra et al. [11] considered the characteristics of DDoS attacks on the Internet of Things (IoT) and proposed a DDoS attack model on IoT, given the conditions for a successful attack. Furthermore, some effective defense strategies, such as installing defense software and upgrading firewalls, have been widely used to mitigate DDoS attacks [12, 13]. Several DDoS attack dynamic models with defending strategies have been proposed recently to study the impact of defending strategies on DDoS attacks. Zhang et al. [13] studied a differential dynamics model for DDoS attacks with four states, namely, weak-defensive, attacked, strong-defensive, and compromised nodes. The global stability conditions of the model are given, and some defending strategies are proposed to mitigate the DDoS attack. Zhang et al. [14] used mean-field theory as basis to develop a DDoS attack model on arbitrary networks. Some reasonable strategies for defending against DDoS attacks have been provided based on theoretical analysis. Rao et al. [15] proposed a DDoS attack model with quarantine strategy; mathematical analysis demonstrated that quarantining infected computers can effectively block DDoS attacks. Zhang et al. [16] constructed an optimal control model for DDoS attacks on the Internet of Things and obtained its optimal defense strategy. Huang et al. [17] proposed a new low-cost DDoS attack architecture and got three optimal attack strategies based on variational method. Li et al. [18] established a low-rate DDoS attack model based on cloud computing environment and proposed a strategy to mitigate low-rate DDoS attacks.

However, the existing dynamic models have assumed that defenders will adopt a defending strategy with a fixed probability. On the one hand, adopting defending strategies in the real world will benefit from mitigating DDoS attacks. On the other hand, defenders may choose not to adopt defense strategies owing to defensive costs, which can be considered a dilemma. As rational persons, defenders will compare the benefits and costs caused by DDoS attacks. If the benefits outweigh the costs, then defenders will be likely to adopt a defending strategy; otherwise, they will be less likely to adopt such a strategy. That is, defenders decide the probability of adopting a defending strategy based on a cost-benefit analysis. In addition, none of the existing defense strategy recommendations has analyzed the cost-benefit, so the defense strategies obtained are not feasible solutions.

To overcome the above shortcomings, this study uses the preceding discussions as bases to first propose a game theory-based DDoS attack model with defending strategy decisions. Our main contributions are summarized as follows:

(a) In order to study the impact of defense strategy decisions on the dynamic behavior of DDoS attacks, according to the above cost-benefit analysis, this research first constructs two smooth logistic functions, which can describe the defense strategy choices of the defender under different cost-benefit conditions. Based on the above logistic function and compartmental model theory, this paper first proposed a game-theoretic DDoS attack dynamics model with a cost-benefit function.

(b) The current study obtains the attack threshold of the above model, which is the condition for successful attack, and then the local stability of the attacked equilibrium and the attack-free equilibrium is proved, using the theory of differential stability. In addition, this study uses the analysis of the impact of parameters on model behavior as basis to propose some effective defending strategies to mitigate DDoS attacks. Some numerical experiments are also presented to verify the effectiveness of defending strategies.

The remainder of this paper is organized as follows. Section 2 proposes a novel DDoS attack model. Section 3 presents the mathematical properties of the proposed model. Section 4 provides some suggestions for the defense of DDoS attacks by analyzing the effects of parameters on model behavior. Section 5 concludes this study.

2. Model Descriptions and Cost-Benefit Analysis

This section proposes a dynamic model with defending strategy decision based on a cost-benefit analysis.

2.1. Differential Dynamic Model. A typical computer network system mainly consists of numerous client and server computers. Clients and servers often have different levels of cybervulnerabilities. Clients are considered to be relatively vulnerable to malware and flooding attacks. Servers are often equipped with firewalls. Although they are considerably resilient to malware, servers could still be vulnerable to flooding attacks.

A typical DDoS attack and defense is carried out in the following three-phase procedure, which is depicted in Figure 1.

2.1.1. Spreading Malware. Attackers attempt to spread malware to infect normal clients on networks by using fake emails or web links. Once normal clients have been affected by malware, they are controlled by attackers to become zombie clients capable of infecting other clients.

2.1.2. Launching Attacks. Attackers manipulate zombie clients to launch flooding attacks targeting at least one target server. Such attacks will compromise the target servers, thereby losing their abilities to provide services to the external environment.

2.1.3. Recovering. Defenders adopt some defense strategies, such as antivirus software or firewalls, to recover the attacked computers, including zombie clients and compromised servers.

The following reasonable assumptions can be obtained on bases of the preceding facts:

($H1$) Computers on the Internet can be divided into two parts: client and server parts. The total numbers of computers on the client and server parts are N_W and N_S, respectively [7].

($H2$) Computers on the client part can be classified into three classes: normal clients (W nodes), infected clients (I nodes), and recovered clients (R nodes) [19, 20]. Let $W(t)$, $I(t)$, and $R(t)$ represent the proportion of the W, I, and R nodes, respectively, in the total number of computers on the client part at time t. The total number is constantly equal to N_W:

$$W(t) + I(t) + R(t) \equiv 1. \tag{1}$$

($H3$) Computers on the server part can also be classified into three classes: normal servers (S nodes), compromised servers (C nodes), and recovered servers (D nodes). Let $S(t)$, $C(t)$, and $D(t)$ represent the proportion of the S, C, and D nodes, respectively, in the total number of computers on the server part at time t. The total number is constantly equal to NS:

$$S(t) + C(t) + D(t) \equiv 1. \tag{2}$$

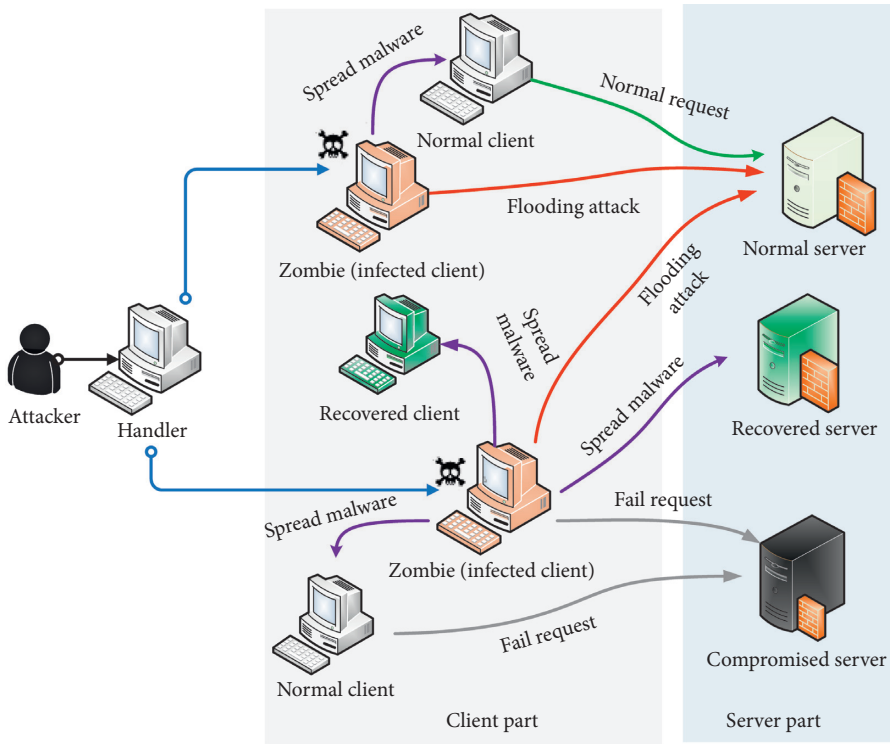

Figure 1: Schematic of a DDoS attack.

(*H*4) Owing the implementation of some dangerous operations, such as browsing phishing sites, a W node will be infected with a probability of β.

(*H*5) Owing to the execution of some positive measures, such as running antivirus software, an I node will recover with a probability of τ.

(*H*6) Owing to the reinstallation of an operation system, an R node becomes a W node with probability γ.

(*H*7) Owing to DDoS attacks, a S node will compromise with probability α.

(*H*8) Owing to the implementation of some positive measures, such as running firewall software, a C node becomes a D node with probability η.

(*H*9) Owing to the reinstallation of an operating system, a D node becomes a S node with probability δ.

(*H*10) Owing to the adoption of some defensive strategies, such as installing antivirus software, a W node becomes a R node with probability f [21, 22].

(*H*11) Owing to the implementation of some defensive strategies, such as upgrading firewall software, a S node becomes a D node with probability g. Probabilities f and g are determined by the cost-benefit analysis of defenders, which we will discuss in part B of this section.

Given the preceding assumptions, the following DDoS attack model can be obtained (see Figure 2):

$$\begin{cases} \dfrac{dW(t)}{dt} = -\beta W(t)I(t) + \gamma R(t) - fW(t), \\ \dfrac{dI(t)}{dt} = \beta W(t)I(t) - \tau I(t), \\ \dfrac{dR(t)}{dt} = \tau I(t) - \gamma R(t) + fW(t), \\ \dfrac{dS(t)}{dt} = -\alpha S(t)I(t) + \delta\, D(t) - gS(t), \\ \dfrac{dC(t)}{dt} = \alpha S(t)I(t) - \eta C(t), \\ \dfrac{dD(t)}{dt} = \eta C(t) + gS(t) - \delta\, D(t), \end{cases} \tag{3}$$

where $0 \le W(t), I(t), R(t), S(t), C(t), D(t) \le 1$, and $0 \le \alpha, \beta, \gamma, \eta, \tau, \delta \le 1$.

2.2. Cost-Benefit Analysis. Although defensive strategies may bring benefits, there are costs to adopting these defensive strategies, which is considered a dilemma for defenders. Logistic function can be used to describe the rational decision problem of whether to adopt defensive

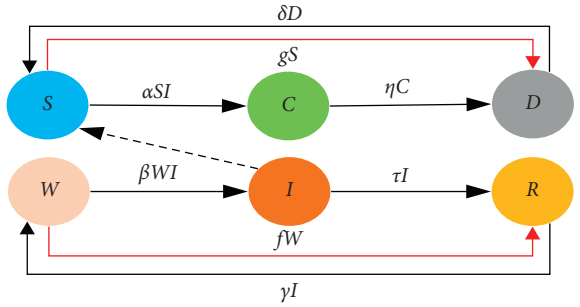

Figure 2: State transition diagram of the proposed model (dashed lines on the graph represent DDoS attacks, and red lines represent defense strategies).

strategies. When the cost of adopting a defending strategy is greater than the benefit, defenders will not adopt such a strategy. Otherwise, defenders will adopt this strategy. For the client part, the benefit is directly proportional to the loss of not adopting this strategy L_W, the number of computers infected $N_W I(t)$, and the probability of infection β. The cost of adopting this strategy is C_W. Thus, the total payoff of adopting this strategy for the client part is $\Delta\omega_W = \beta N_W L_W I(t) - C_W$. For the server part, let L_S represent the cost of not adopting a defending strategy and C_W represents the cost of adopting a defending strategy. The total payoff of adopting this strategy for the server part is $\Delta\omega_S = \alpha N_S L_S I(t) - C_S$.

To describe the strategic decision problem, we define the following two logistic functions. Figure 3 depicts the logistic equation [23–25].

$$f = \frac{\phi}{1 + e^{\Delta\omega_W}} = \frac{\phi}{1 + e^{\mu\left(N_W\beta L_W I(t) - C_W\right)}} = \frac{\phi e^{\mu C_W}}{e^{\mu C_W} + e^{\mu N_W \beta L_W I(t)}}, \tag{4}$$

$$g = \frac{\varphi}{1 + e^{\Delta\omega_S}} = \frac{\varphi}{1 + e^{\nu\left(N_S\alpha L_S I(t) - C_S\right)}} = \frac{\varphi e^{\nu C_S}}{e^{\nu C_S} + e^{\nu N_S \alpha L_S I(t)}}, \tag{5}$$

where μ and ν represent the smooth exponents of functions f and g, respectively, and ϕ and φ represent the maximum value of functions f and g, respectively. $0 \le \phi$ and $\varphi \le 1$.

3. Theoretical Analysis

This section investigates some mathematical properties of the proposed model, including equilibrium, attacked threshold, and stability of system (3).

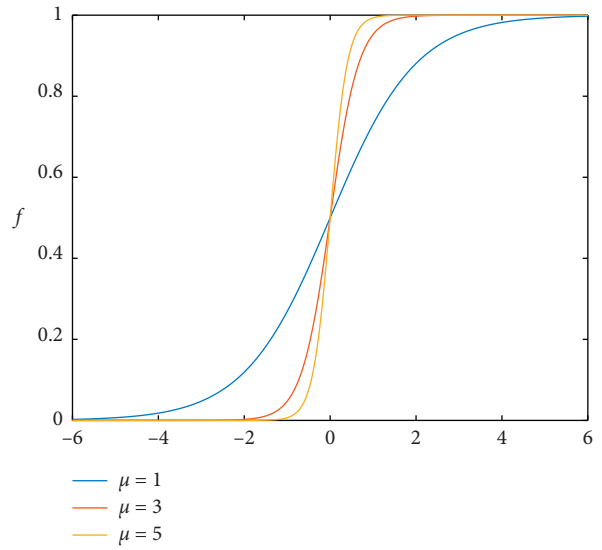

Figure 3: Logistic function.

Given that $W(t) + I(t) + R(t) \equiv 1$ and $S(t) + C(t) + D(t) \equiv 1$, we use a simple calculation to obtain $W(t) \equiv 1 - I(t) - R(t)$ and $S(t) \equiv 1 - C(t) - D(t)$. Hence, the first and fourth equations in system (3) can be represented by the other four equations in this system. Therefore, system (3) can be simplified to the following system:

$$\begin{cases} \dfrac{dI(t)}{dt} = \beta(1 - I(t) - R(t))I(t) - \tau I(t), \\ \dfrac{dR(t)}{dt} = \tau I(t) - \gamma R(t) + f(1 - I(t) - R(t)), \\ \dfrac{dC(t)}{dt} = \alpha(1 - C(t) - D(t))I(t) - \eta C(t), \\ \dfrac{dD(t)}{dt} = \eta C(t) + g(1 - C(t) - D(t)) - \delta D(t), \end{cases} \tag{6}$$

where $f = \phi e^{\mu C_W}/e^{\mu C_W} + e^{\mu N_W \beta L_W I(t)}$ and $g = \varphi e^{\nu C_S}/e^{\nu C_S} + e^{\nu N_S \alpha L_S I(t)}$. The parameter range of system (6) is as follows:

$$\Theta = \left\{(\alpha, \beta, \gamma, \eta, \tau, \phi, \varphi, \mu, \nu, L_W, L_S, C_W, C_S, N_W, N_S) \in R_+^{15}: 0 \le \alpha, \beta, \gamma, \eta, \tau, \phi, \varphi \le 1\right\}. \tag{7}$$

Evidently, the domain of system (6) is as follows:

$$\Omega = (I(t), R(t), C(t), D(t)) \in R_+^4: 0 \le I(t), R(t), C(t), D(t) \le 1. \tag{8}$$

Given that systems (3) and (6) are equivalent, the remainder of this paper mainly focuses on the properties of system (6).

3.1. Attack-Free Equilibrium

Theorem 1. *A unique attack-free equilibrium* $E_0 = (I_0, R_0, C_0, D_0) = (0, f_0/\gamma + f_0, 0, g_0/\delta + g_0)$ *is present in system (6), where* $f_0 = \phi e^{\mu C_W}/1 + e^{\mu C_W}$ *and* $g_0 = \varphi e^{\nu C_S}/1 + e^{\nu C_S}$.

Proof. By solving the following equations,

$$\begin{cases} \beta(1 - I(t) - R(t))I(t) - \tau I(t) = 0, \\ \tau I(t) - \gamma R(t) + f(1 - I(t) - R(t)) = 0, \\ \alpha(1 - C(t) - D(t))I(t) - \eta C(t) = 0, \\ \eta C(t) + g(1 - C(t) - D(t)) - \delta\ D(t) = 0. \end{cases} \tag{9}$$

E_0 is evidently a solution to equation (7). Thus, E_0 is constantly an attack-free equilibrium of system (6). □

Remark 1. An equilibrium represents a possible final state of DDoS attacks. Thereafter, attack-free equilibrium represents the possible final state of DDoS attack extinction.

The attacked threshold is a crucial parameter that determines whether computers on a network will experience DDoS attacks. This section calculates the attacked threshold by using the **FV** method proposed in [26, 27].

Let $y = (I(t), C(t))^{\mathrm{T}}$ and $y_0 = (I_0, C_0)^{\mathrm{T}}$. Accordingly, the following functions can be obtained:

$$\begin{aligned} F(y) &= \big(F_1(y), F_2(y)\big)^T \\ &= (\beta(1 - I(t) - R(t))I(t), \\ &\quad \alpha\big(1 - C(t) - D(t)\big)I(t))^T, \end{aligned} \tag{10}$$

$$V(y) = \big(V_1(y), V_2(y)\big)^T = (\tau I(t), \eta C(t))^T. \tag{11}$$

By considering the partial derivative of I and C at E_0, we obtain as follows:

$$\mathbf{F} = \begin{pmatrix} \dfrac{\partial F_1(y_0)}{\partial I} & \dfrac{\partial F_1(y_0)}{\partial C} \\ \dfrac{\partial F_2(y_0)}{\partial I} & \dfrac{\partial F_2(y_0)}{\partial C} \end{pmatrix} = \begin{pmatrix} \beta(1 - R_0) & 0 \\ \alpha(1 - D_0) & 0 \end{pmatrix}, \tag{12}$$

$$\mathbf{V} = \begin{pmatrix} \dfrac{\partial V_1(y_0)}{\partial A} & \dfrac{\partial V_1(y_0)}{\partial C} \\ \dfrac{\partial V_2(y_0)}{\partial A} & \dfrac{\partial V_2(y_0)}{\partial C} \end{pmatrix} = \begin{pmatrix} \tau & 0 \\ 0 & \eta \end{pmatrix}. \tag{13}$$

By calculation, we obtain as follows:

$$\mathbf{FV}^{-1} = \begin{pmatrix} \beta(1 - R_0) & 0 \\ \alpha(1 - D_0) & 0 \end{pmatrix} \begin{pmatrix} \dfrac{1}{\tau} & 0 \\ 0 & \dfrac{1}{\eta} \end{pmatrix} = \begin{pmatrix} \dfrac{\beta}{\tau}(1 - R_0) & 0 \\ \dfrac{\alpha}{\tau}(1 - D_0) & 0 \end{pmatrix}. \tag{14}$$

The attacked threshold can be obtained by calculating the eigenvalue of $\mathbf{FV}^{-1}$. Lastly, the two eigenvalues of $\mathbf{FV}^{-1}$ are calculated as $\rho(\mathbf{FV}^{-1}) = 0$ and $\rho(\mathbf{FV}^{-1}) = \beta/\tau(1 - R_0)$, while the eigenvalue $\rho(\mathbf{FV}^{-1}) = 0$ is disregarded. Hence, the attacked threshold can be obtained as follows:

$$T_0 = \frac{\beta}{\tau}(1 - R_0) = \frac{\beta\gamma\big(1 + e^{\mu C_W}\big)}{\tau\big(\gamma + (\gamma + \phi)e^{\mu C_W}\big)}. \tag{15}$$

Theorem 2. *When system (6) is considered,* E_0 *is locally asymptotically stable if* $T_0 < 1$.

Proof. When system (6) is considered, the Jacobian matrix at E_0 is as follows:

$$\begin{bmatrix} \beta - \tau - \dfrac{\beta f_0}{\gamma + f_0} & 0 & 0 & 0 \\ \tau + f_0'\left(1 - \dfrac{\beta f_0}{\gamma + f_0}\right) - f_0 & -\gamma - f_0 & 0 & 0 \\ \alpha\left(1 - \dfrac{g_0}{\delta + g_0}\right) & 0 & -\eta & 0 \\ \left(1 - \dfrac{g_0}{\delta + g_0}\right)g_0' & 0 & \eta - g_0 - \delta & -g_0 \end{bmatrix}. \tag{16}$$

The corresponding characteristic equation can be deduced as follows:

$$\begin{bmatrix} \beta - \tau - \dfrac{\beta f_0}{\gamma + f_0} - \lambda & 0 & 0 & 0 \\ \tau + f_0'\left(1 - \dfrac{\beta f_0}{\gamma + f_0}\right) - f_0 & -\gamma - f_0 - \lambda & 0 & 0 \\ \alpha\left(1 - \dfrac{g_0}{\delta + g_0}\right) & 0 & -\eta - \lambda & 0 \\ \left(1 - \dfrac{g_0}{\delta + g_0}\right)g_0' & 0 & \eta - g_0 - \delta & -g_0 - \lambda \end{bmatrix},$$

$$= (-\eta - \lambda)(-g_0 - \lambda)(-\gamma - f_0 - \lambda)\left(\beta - \tau - \frac{\beta f_0}{\gamma + f_0} - \lambda\right). \tag{17}$$

Equation (17) has three negative roots $\lambda_1 = -\eta < 0$, $\lambda_2 = -g_0 < 0$, and $\lambda_3 = -f_0 - \gamma < 0$. The remaining root is determined by the following equation:

$$\beta - \tau - \frac{\beta f_0}{\gamma + f_0} - \lambda = 0. \tag{18}$$

As $T_0 = \beta/\tau(1 - R_0) = \beta/\tau(1 - f_0/\gamma + f_0) < 1$, by calculation, we obtain as follows:

$$\lambda_4 = \beta - \tau - \frac{\beta f_0}{\gamma + f_0} < 0. \tag{19}$$

All roots of the characteristic equation (17) are negative. Thus, E_0 is locally asymptotically stable if $T_0 < 1$. □

Remark 2. Theorem 2 shows that DDoS attacks would die out if $T_0 < 1$.

Example 1. Consider system (6) with $\alpha = 0.02$, $\beta = 0.01$, $\gamma = 0.1$, $\delta = 0.1$, $\eta = 0.02$, $\tau = 0.005$, $\delta = 0.03$, $\phi = 0.6$, $\varphi = 0.5$, $\mu = 1$, $\nu = 1$, $N_W = 1000$, $N_S = 1000$, $L_W = 1$, $L_S = 1$, $C_W = 1$, and $C_S = 2$. By calculation, $E_0 = (0,\ 0.814,\ 0,\ 0.936)^T$ and $T_0 = 0.371 < 1$ satisfies the condition of Theorem 2. Hence, the system is locally asymptotically stable at E_0 (see Figure 4).

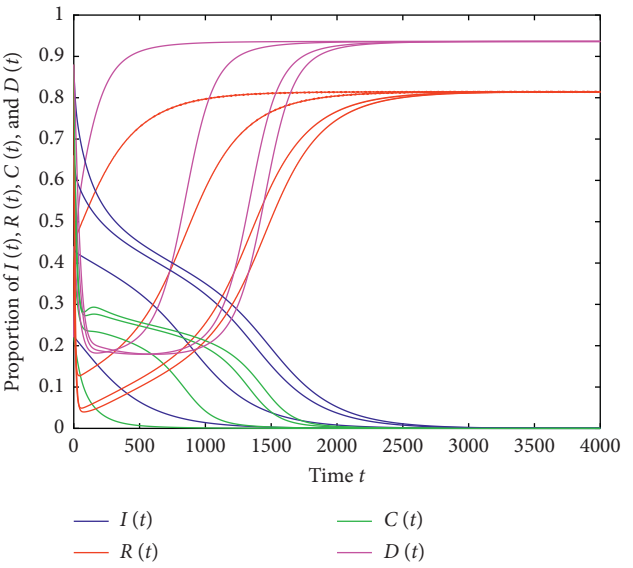

FIGURE 4: Stability of the attack-free solution E_0.

3.2. Attacked Equilibrium

Theorem 3. *Consider system (6) on domain Ω. If $T_0 > 1$, then system (6) has an attacked equilibrium:*

$$E_1 = (I_1, R_1, C_1, D_1)^T, \tag{20}$$

$$I_1 = \frac{x}{\mu N_W \beta L_W}, \tag{21}$$

$$R_1 = 1 - I_1 - \frac{\tau}{\beta}, \tag{22}$$

$$C_1 = \frac{\delta \alpha I_1}{\alpha I_1 (\eta + \delta) + \eta (g_1 + \delta)}, \tag{23}$$

$$D_1 = 1 - C_1 - \frac{\eta C_1}{\alpha I_1}, \tag{24}$$

where $g_1 = \varphi e^{\nu C_S}/e^{\nu C_S} + e^{\nu N_S \alpha L_S I_1}$ and x is a positive solution of the transcendental equation as follows:

$$(\tau + \gamma) x e^x + \left(\frac{\tau}{\beta}\gamma - \gamma\right)\mu N_W \beta L_W e^x + (\tau + \gamma)x + \mu N_W \beta L_W e^{\mu C_W}\left(\frac{\tau}{\beta}\gamma - \gamma + \frac{\tau}{\beta}\phi\right) = 0. \tag{25}$$

Proof. By solving equation (9), we can obtain $R = 1 - I - \tau/\beta$, $C = \delta\alpha I/\alpha I(\eta + \delta) + \eta(g_1 + \delta)$, $D = 1 - C - \eta C/\alpha I$, and $I = x/\mu N_W \beta L_W$ x $(0 \le x \le \mu N_W \beta L_W)$ is the root of equation (24).

Thereafter, we examine the existence of the solution of equation (24).

Equation (24) can be organized as follows:

$$(\tau + \gamma)x + \mu N_W \beta L_W \left(\frac{\gamma\tau}{\beta} - \gamma\right) = -\frac{\mu\tau\phi e^{\mu C_W}}{e^{\mu C_W} + e^x} N_W L_W. \tag{26}$$

Let

$$G_1(x) = (\tau + \gamma)x + \mu N_W \beta L_W \left(\frac{\gamma\tau}{\beta} - \gamma\right), \tag{27}$$

$$G_2(x) = -\frac{\phi e^{\mu C_W}}{e^{\mu C_W} + e^x}\frac{\tau}{\beta}\mu N_W \beta L_W. \tag{28}$$

As $G_1'(x) = \tau + \gamma > 0$, function G_1 is an increasing function. As $G_2'(x) = \phi e^{\mu C_W} e^x/(e^{\mu C_W} + e^x)^2 \tau/\beta\mu N_W \beta L_W > 0$, function G_2 is also an increasing function.

As $G_1(0) = \mu N_W \beta L_W(\gamma\tau/\beta - t\gamma)$ and $G_2(0) = -\phi e^{\mu C_W}/e^{\mu C_W} + 1\tau/\beta\mu N_W \beta L_W$, according to $T_0 = \beta\gamma(1 + e^{\mu C_W})/\tau(\gamma + (\gamma + \phi)e^{\mu C_W}) > 1$, we have $G_2(0) > G_1(0)$. As $G_1(\mu N_W \beta L_W) = \mu N_W \beta L_W(\tau + \gamma\tau/\beta) > 0$ and $G_2(\mu N_W \beta L_W) = -\phi e^{\mu C_W}/e^{\mu C_W} + e^{\mu N_W \beta L_W}\tau/\beta\mu N_W \beta L_W < 0$, $G_1(\mu N_W \beta L_W) > G_2(\mu N_W \beta L_W)$. Therefore, transcendental equation (24) has at least one solution x $(0 \le x \le \mu N_W \beta L_W)$.

The proof is complete. □

Remark 3. The attacked equilibrium represents the possible final state of DDoS attacks.

Theorem 4. *Consider system (6). If $-(a_{11} + a_{22}) > 0$, $a_{11}a_{22} - a_{12}a_{21} > 0$, $-(b_{11} + b_{22}) > 0$, and $b_{11}b_{22} - b_{12}b_{21} > 0$, then E_1 is locally asymptotically stable:*

$$a_{11} = \beta(1 - 2I_1 - R_1) - \tau, \tag{28}$$

$$a_{12} = -\beta I_1, \tag{29}$$

$$a_{21} = \tau - f_1 + (1 - I_1 - R_1) f_1', \tag{30}$$

$$a_{22} = -\gamma - f_1, \tag{31}$$

$$b_{11} = -\alpha I_1 - \eta, \tag{32}$$

$$b_{12} = -\alpha I_1, \tag{33}$$

$$b_{21} = \eta - g_1, \tag{34}$$

$$b_{22} = -g_1 - \delta, \tag{35}$$

$$f_1 = \frac{\phi e^{\mu C_W}}{e^{\mu C_W} + e^{\mu N_W \beta L_W I_1}}, \tag{36}$$

$$g_1 = \frac{\varphi e^{\nu C_S}}{e^{\nu C_S} + e^{\nu N_S \alpha L_S I_1}}, \tag{37}$$

$$f_1' = \frac{\mu N_W \beta L_W \phi e^{\mu C_W} e^{\mu N_W \beta L_W I_1}}{\left(e^{\mu C_W} + e^{\mu N_W \beta L_W I_1}\right)^2}, \tag{38}$$

$$g_1' = \frac{\nu N_S \alpha L_S \varphi e^{\nu C_S} e^{\nu N_S \alpha L_S I_1}}{\left(e^{\nu C_S} + e^{\nu N_S \alpha L_S I_1}\right)^2}. \tag{39}$$

Proof. For system (6), the Jacobian matrix at E_1 is

$$\begin{pmatrix} \beta(1 - 2I_1 - R_1) - \tau & -\beta I_1 & 0 & 0 \\ \tau - f_1 + (1 - I_1 - R_1) f_1' & -\gamma - f_1 & 0 & 0 \\ \alpha(1 - C_1 - D_1) & 0 & -\alpha I_1 - \eta & -\alpha I_1 \\ (1 - C_1 - D_1) g_1' & 0 & \eta - g_1 & -g_1 - \delta \end{pmatrix}. \tag{40}$$

The corresponding characteristic equation of the Jacobian matrix (40) can be deduced as follows:

$$\begin{pmatrix} \beta(1 - 2I_1 - R_1) - \tau - \lambda & -\beta I_1 & 0 & 0 \\ \tau - f_1 + (1 - I_1 - R_1) f_1' & -\gamma - f_1 - \lambda & 0 & 0 \\ \alpha(1 - C_1 - D_1) & 0 & -\alpha I_1 - \eta - \lambda & -\alpha I_1 \\ (1 - C_1 - D_1) g_1' & 0 & \eta - g_1 & -g_1 - \delta - \lambda \end{pmatrix} = \begin{pmatrix} a_{11} - \lambda & a_{12} \\ a_{21} & a_{22} - \lambda \end{pmatrix} \begin{pmatrix} b_{11} - \lambda & b_{12} \\ b_{21} & b_{22} - \lambda \end{pmatrix} = 0, \tag{41}$$

where

$$a_{11} = \beta(1 - 2I_1 - R_1) - \tau, a_{12} = -\beta I_1, a_{21} = \tau - f_1 + (1 - I_1 - R_1) f_1', a_{22} = -\gamma - f_1, b_{11} = -\alpha I_1 - \eta,$$

$$b_{12} = -\alpha I_1, b_{21} = \eta - g_1, b_{22} = -g_1 - \delta, g_1 = \frac{\varphi e^{\nu C_S}}{e^{\nu C_S} + e^{\nu N_S \alpha L_S I_1}}, f_1 = \frac{\phi e^{\mu C_W}}{e^{\mu C_W} + e^{\mu N_W \beta L_W I_1}}, f_1' = \frac{\mu N_W \beta L_W \phi e^{\mu C_W} e^{\mu N_W \beta L_W I_1}}{\left(e^{\mu C_W} + e^{\mu N_W \beta L_W I_1}\right)^2}, \tag{42}$$

$$g_1' = \frac{\nu N_S \alpha L_S \varphi e^{\nu C_S} e^{\nu N_S \alpha L_S I_1}}{\left(e^{\nu C_S} + e^{\nu N_S \alpha L_S I_1}\right)^2}.$$

By calculation, the roots of the characteristic equation (41) are determined by the following two equations:

$$\begin{aligned} \lambda^2 - (a_{11} + a_{22})\lambda + a_{11}a_{22} - a_{12}a_{21} = 0, \\ \lambda^2 - (b_{11} + b_{22})\lambda + b_{11}b_{22} - b_{12}b_{21} = 0. \end{aligned} \tag{43}$$

The Hurwitz criterion [28, 29] indicates sufficient conditions for all roots of the characteristic equation (30) to be negative are $-(a_{11} + a_{22}) > 0$, $a_{11}a_{22} - a_{12}a_{21} > 0$, $-(b_{11} + b_{22}) > 0$, and $b_{11}b_{22} - b_{12}b_{21} > 0$.

The proof is complete. □

Remark 4. Theorems 3 and 4 imply that DDoS attacks would persist if conditions in theorems are satisfied.

Example 2. Consider system (6) with $\alpha = 0.02$, $\beta = 0.05$, $\gamma = 0.1$, $\delta = 0.1$, $\eta = 0.02$, $\tau = 0.004$, $\delta = 0.03$, $\phi = 0.6$, $\varphi = 0.5$, $\mu = 1$, $\nu = 1$, $N_W = 1000$, $N_S = 1000$, $L_W = 1$, $L_S = 1$, $C_W = 1$, and $C_S = 2$. By calculation, $E_1 = (0.885, 0.035, 0.358, 0.238)^T$, $T_0 = 2.321 > 1$, $-(a_{11} + a_{22}) = 0.144 > 0$, $a_{11}a_{22} - a_{12}a_{21} = 0.0046 > 0$, $-(b_{11} + b_{22}) = 0.068 > 0$, and $b_{11}b_{22} - b_{12}b_{21} = 0.0015 > 0$ satisfy the condition of Theorem 4. Hence, the system is locally asymptotically stable at E_1 (see Figure 5).

4. Further Discussion

This section investigates the impact of some parameters on the dynamic behavior of the proposed model.

From Theorem 2, T_0 is an important parameter that determines whether DDoS attacks are successful. If $T_0 < 1$, then the attacks will not succeed. Hence, we need to take some measures to make T_0 considerably below one.

Given that $T_0 = \beta\gamma(1 + e^{\mu C_W})/\tau(\gamma + (\gamma + \phi)e^{\mu C_W})$, taking the derivative with respect to β, γ, τ, ϕ, μ, and C_W, we obtain the following:

$$\begin{cases} \dfrac{\partial T_0}{\partial \beta} = \dfrac{\gamma\left(1+e^{\mu C_W}\right)}{\tau\left(\gamma+(\gamma+\phi)e^{\mu C_W}\right)} > 0, \\ \dfrac{\partial T_0}{\partial \gamma} = \dfrac{\beta\phi}{\tau\gamma^2}\dfrac{e^{\mu C_W}\left(1+e^{\mu C_W}\right)}{\left[1+(1+(\phi/\gamma))e^{\mu C_W}\right]^2} > 0, \\ \dfrac{\partial T_0}{\partial \phi} = -\dfrac{\beta\gamma\left(1+e^{\mu C_W}\right)e^{\mu C_W}}{\tau\left[\gamma+(\gamma+\phi)e^{\mu C_W}\right]^2} < 0, \\ \dfrac{\partial T_0}{\partial \tau} = -\dfrac{1}{\tau^2}\dfrac{\beta\gamma\left(1+e^{\mu C_W}\right)}{\left(\gamma+(\gamma+\phi)e^{\mu C_W}\right)} < 0, \\ \dfrac{\partial T_0}{\partial \mu} = -\dfrac{\beta\phi\gamma}{\tau}\dfrac{C_W e^{\mu C_W}}{\left[\gamma+(\gamma+\phi)e^{\mu C_W}\right]^2} < 0, \\ \dfrac{\partial T_0}{\partial C_W} = -\dfrac{\beta\phi\gamma}{\tau}\dfrac{\mu e^{\mu C_W}}{\left[\gamma+(\gamma+\phi)e^{\mu C_W}\right]^2} < 0. \end{cases} \tag{44}$$

T_0 is strictly increasing with parameters β and γ (see Figures 6 and 7) and strictly decreasing with ϕ, τ, μ, and C_W (see Figures 8–11).

Some reasonable suggestions for computers on the client prat to mitigate the DDoS attack are provided as follows based on the preceding calculation:

(1) Adopting some defensive strategies (e.g., installing firewalls) on the client part, the infected probability β can be remarkably reduced.

(2) Keeping defensive software updates in time on the client part, γ can be maintained low.

(3) Upgrading antivirus software, τ will be enhanced.

(4) Strengthening defense strength on the client part will enhance ϕ.

(5) Decreasing the cost of the defending strategy will reduce C_W.

Accordingly, controlling the preceding parameters will be conducive to the mitigation of DDoS attacks on the client part. Thereafter, we focus on the defensive strategies for computers on the server part.

As $C_1 = \delta\alpha I_1/\alpha I_1(\eta+\delta)+\eta(g_1+\delta)$, where $g_1 = \varphi e^{\nu C_S}/e^{\nu C_S}+e^{\nu N_S \alpha L_S I_1}$, parameters δ, α, ν, φ, η, N_S, C_S, and L_S are independent of I_1. Thus, we investigate the effects of these parameters on C_1:

$$\frac{\partial C_1}{\partial \delta} = \frac{\alpha I_1(\alpha I_1\eta+\eta g_1)}{\left[\alpha I_1(\eta+\delta)+\eta(g_1+\delta)\right]^2} > 0. \tag{45}$$

C_1 is strictly increasing with parameter δ:

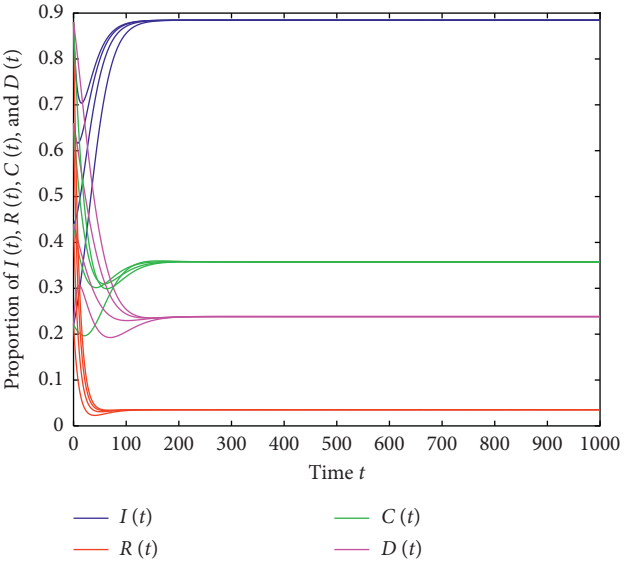

Figure 5: Stability of the attacked solution E_1.

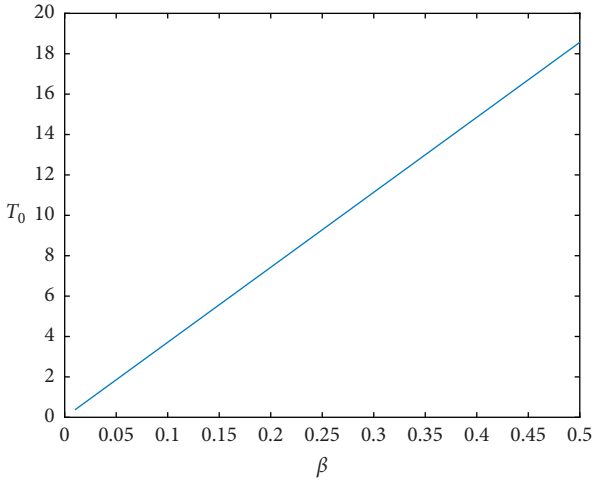

Figure 6: T_0 versus β in the case where $\gamma = 0.1$, $\phi = 0.6$, $\tau = 0.005$, $\mu = 1$, and $C_W = 1$.

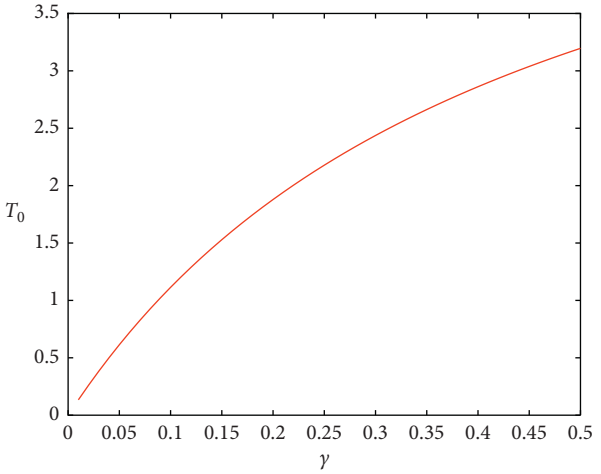

Figure 7: T_0 versus γ in the case where $\beta = 0.03$, $\phi = 0.6$, $\tau = 0.005$, $\mu = 1$, and $C_W = 1$.

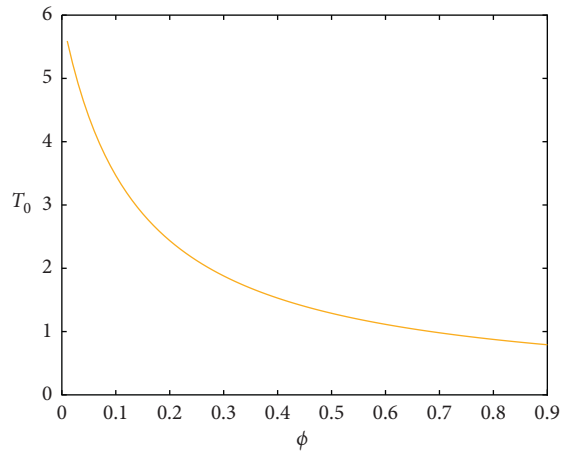

FIGURE 8: T_0 versus ϕ in the case where $\beta = 0.03$, $\gamma = 0.1$, $\tau = 0.005$, $\mu = 1$, and $C_W = 1$.

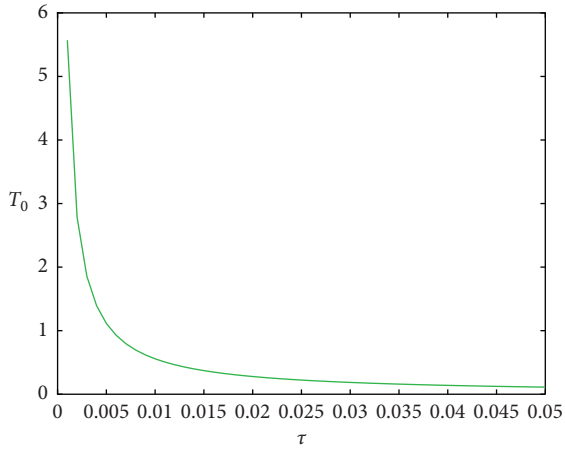

FIGURE 9: T_0 versus τ in the case where $\beta = 0.03$, $\gamma = 0.1$, $\phi = 0.6$, $\mu = 1$, and $C_W = 1$.

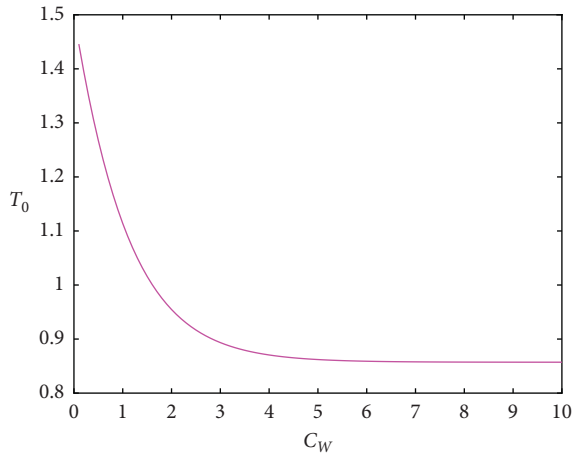

FIGURE 10: T_0 versus C_W in the case where $\beta = 0.03$, $\gamma = 0.1$, $\phi = 0.6$, $\mu = 1$, and $\tau = 0.005$.

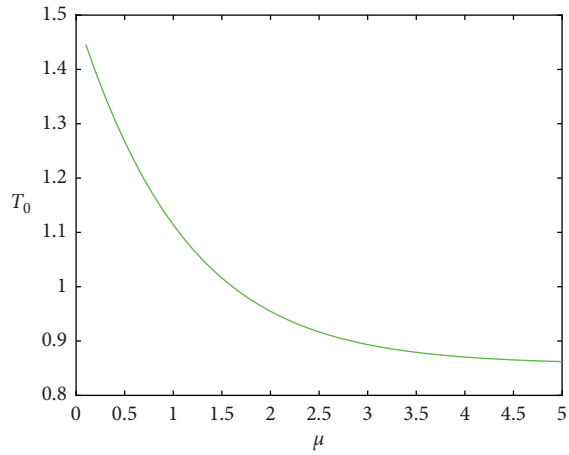

FIGURE 11: T_0 versus μ in the case where $\beta = 0.03$, $\gamma = 0.1$, $\phi = 0.6$, $C_W = 1$, and $\tau = 0.005$.

$$C_1 = \frac{\delta I_1}{I_1(\eta + \delta) + \eta 1/\alpha\left(\left(\varphi e^{\nu C_S}/e^{\nu C_S} + e^{\nu N_S \alpha L_S I_1}\right) + \delta\right)}. \quad (46)$$

From the preceding form of C_1, we can see that C_1 increases with an increase in α.

$$C_1 = \frac{\delta \alpha I_1}{\alpha I_1(\eta + \delta) + \eta\left(\left(\varphi/1 + e^{\nu\left(N_S \alpha L_S I_1 - C_S\right)}\right) + \delta\right)}. \quad (47)$$

From the form of C_1, we can see that C_1 increases with an increase in ν, N_S, and L_S, and C_1 decreases with an increase in φ, η, and C_S.

The following defense strategies are proposed for computers on the server part to deduce DDoS attacks:

(1) Detecting possible security holes may facilitate the reduction in α.

(2) Restarting computers on the server part will significantly increase η.

(3) Upgrading defensive software of DDoS attack, δ will decrease.

(4) Strengthening defense strength on the server part will enhance φ.

(5) Decreasing the cost of the defending strategy will reduce C_S.

(6) Increasing the number of computers on the server part facilitates the enhancement of N_S.

Controlling these parameters is conducive to the mitigation of DDoS attacks on the server part.

5. Conclusion

This paper studies the decision-making problem of DDoS attack defense strategy. In order to mitigate DDoS risk with minimum defending loss and cost, based on game theory, this paper establishes a dynamic differential system with the defense cost and loss function. We perform analytical analysis to show that the attack model has two equilibria, i.e., an attack-free equilibrium E_0 and an attacked equilibrium

E_1. The attacked threshold T_0 is an important parameter that determines whether DDoS attacks are successful or failed. Some beneficial recommendations to mitigate DDoS attacks are provided after conducting some numerical experiments of the proposed model with different parameters. These suggestions for effective defense against DDoS attacks include installing firewalls, upgrading antivirus software, reducing defense costs, and detecting possible security holes. This research not only has strong theoretical value but can also be widely used in the following fields: (1) advanced persistent threats: study the dynamic behavior of DDoS attack and defense with advanced persistent threat characteristics [30, 31]; (2) Honeynet defense: study the influence of honeynet defense on the dynamic behavior of DDoS attacks [32]; (3) smart grid: study the dynamic behavior of DDoS attack and defense on the smart grid [16].

Data Availability

The data used to support the findings of this study are included within the article.

Conflicts of Interest

The author declares that there are no conflicts of interest.

References

[1] J. Mirkovic and P. Reiher, "A taxonomy of DDoS attack and DDoS defense mechanisms," *ACM Special Interest Group on Data Communication*, vol. 34, no. 2, pp. 39–53, 2004.

[2] S. T. Zargar, J. Joshi, and D. Tipper, "A survey of defense mechanisms against distributed denial of service (DDoS) flooding attacks," *IEEE Communications Surveys & Tutorials*, vol. 15, no. 4, pp. 2046–2069, 2013.

[3] P. Passeri, "Cyber attacks statistics," 2016.

[4] P. Passeri, "Symantec internet security threat report," 2019.

[5] S. Sharwood, "Winter olympics website downed by cyber attack," 2020.

[6] S. Ranger, "GitHub hit with the largest DDoS attack ever seen," 2020.

[7] N. Arboleda, "AWS hit by DDoS attack dragging half of web down," 2020.

[8] K. Haldar and B. K. Mishra, "A mathematical model for a distributed attack on targeted resources in a computer network," *Communications in Nonlinear Science and Numerical Simulation*, vol. 19, no. 9, pp. 3149–3160, Sep. 2014.

[9] U. Kumar and S. K. Pandey, "Dynamic model on DDoS attack in computer network," 2016.

[10] W. T. Hou and H. Wang, "Study of a mathematical model for a distributed attack on targeted resources in a computer network," *Journal of Natural Science of Heilongjiang University*, vol. 3, pp. 315–321, 2016.

[11] B. K. Mishra, A. K. Keshri, D. K. Mallick, and B. K. Mishra, "Mathematical model on distributed denial of service attack through Internet of things in a network," *Nonlinear Engineering*, vol. 8, no. 1, pp. 486–495, 2018.

[12] C. Zhang and J. Xiao, "Stability analysis of an advanced persistent distributed denial-of-service attack dynamical model," *Security and Communication Networks*, vol. 2018, pp. 1–10, 2018.

[13] C. M. Zhang, J. B. Peng, and J. W. Xiao, "Advanced persistent distributed denial of service attack model on scale-free networks," 2018.

[14] C. M. Zhang, J. B. Peng, and J. W. Xiao, "An advanced persistent distributed denial-of-service attacked dynamical model on networks," *Discrete Dynamics in Nature and Society*, vol. 2019, 2019.

[15] Y. S. Rao, A. K Keshri, B. K. Mishra, and T. C. Pand, "Distributed denial of service attack on targeted resources in a computer network for critical infrastructure: a differential e-epidemic model," *Physica A: Statistical Mechanics and Its Applications*, vol. 2019, 2019.

[16] C. Zhang, F. Luo, M. Sun, and G. Ranzi, "Modeling and defending advanced metering infrastructure subjected to distributed denial-of-service attacks," *IEEE Transactions on Network Science and Engineering*, vol. 99, p. 1, 2020.

[17] K. Huang, L. X. Yang, X. Yang, Y. Xiang, and Y. Y. Tang, "A low-cost distributed denial-of-service attack architecture," *IEEE Access*, vol. 99, pp. 1–9, 2020.

[18] Z. Li, H. Jin, D. Zou, and B. Yuan, "Exploring new opportunities to defeat low-rate DDoS attack in container-based cloud environment," *IEEE Transactions on Parallel and Distributed Systems*, vol. 31, no. 3, pp. 695–706, 2020.

[19] X. Zhong, F. Deng, and H. Ouyang, "Sharp threshold for the dynamics of a SIRS epidemic model with general awareness-induced incidence and four independent brownian motions," *IEEE Access*, vol. 8, pp. 29648–29657, 2020.

[20] E. González and M. J. Villena, "On the spatial dynamics of vaccination: a spatial SIRS-V model," *Computers & Mathematics with Applications*, vol. 80, no. 5, pp. 733–743, 2020.

[21] H. Zhang, F. Fu, W. Zhang, and B. Wang, "Rational behavior is a 'double-edged sword' when considering voluntary vaccination," *Physica A: Statistical Mechanics and Its Applications*, vol. 391, no. 20, pp. 4807–4815, 2012.

[22] G. Liu, S. Peng, H. Qiu, B. Shi, and Y. W. Chen, "Voluntary vaccination through perceiving epidemic severity in social networks," *Complexity*, vol. 2019, 2019.

[23] J. Yang, M. Martcheva, and Y. Chen, "Imitation dynamics of vaccine decision-making behaviours based on the game theory," *Journal of Biological Dynamics*, vol. 10, no. 1, pp. 31–58, 2016.

[24] F. Xu and C. Ross, "Disease control through voluntary vaccination decisions based on the smoothed best response," *Computational and Mathematical Methods in Medicine*, vol. 2014, 2014.

[25] J. S. Cramer, *Logit Models from Economics and Other Fields*, Cambridge University Press, Cambridge, UK, 2003.

[26] X. Zhou and J. Cui, "Analysis of stability and bifurcation for an SEIV epidemic model with vaccination and nonlinear incidence rate," *Nonlinear Dynamics*, vol. 63, no. 4, pp. 639–653, 2011.

[27] C. Gan, X. Yang, W. Liu, and Q. Zhu, "A propagation model of computer virus with nonlinear vaccination probability," *Communications in Nonlinear Science and Numerical Simulation*, vol. 19, no. 1, pp. 92–100, 2014.

[28] R. C. Robinson, "An introduction to dynamical systems: continuous and discrete," *American Mathematical Society*, vol. 2012, 2012.

[29] L. X. Yang, M. Draief, and X. Yang, "Heterogeneous virus propagation in networks: a theoretical study," *Mathematical Methods in the Applied Sciences*, vol. 40, no. 5, 2017.

[30] L.-X. Yang, P. Li, Y. Zhang, X. Yang, Y. Xiang, and W. Zhou, "Effective repair strategy against advanced persistent threat: a

differential game approach," *IEEE Transactions on Information Forensics and Security*, vol. 14, no. 7, pp. 1713–1728, 2019.

[31] L.-X. Yang, P. Li, X. Yang, Y. Xiang, F. Jiang, and W. Zhou, "Effective quarantine and recovery scheme against advanced persistent threat," *IEEE Transactions on Systems, Man, and Cybernetics: Systems*, vol. 1, 2020.

[32] J. Ren, C. Zhang, and Q. Hao, "A theoretical method to evaluate honeynet potency," *Future Generation Computer Systems*, vol. 116, pp. 76–85, 2021.

Hindawi
Complexity
Volume 2021, Article ID 6635202, 11 pages
https://doi.org/10.1155/2021/6635202

Research Article

Research on Hybrid Collaborative Filtering Recommendation Algorithm Based on the Time Effect and Sentiment Analysis

Xibin Wang[1,2] **Zhenyu Dai**[3] **Hui Li**[3] **and Jianfeng Yang**[1,2]

[1]*School of Data Science, Guizhou Institute of Technology, Guiyang 550003, Guizhou, China*
[2]*Special Key Laboratory of Artificial Intelligence and Intelligent Control of Guizhou Province, Guiyang 550003, Guizhou, China*
[3]*College of Computer Science & Technology, Guizhou University, Guiyang 550025, Guizhou, China*

Correspondence should be addressed to Hui Li; cse.huili@gzu.edu.cn

Received 14 December 2020; Revised 19 February 2021; Accepted 22 February 2021; Published 8 March 2021

Academic Editor: Wei Wang

In this study, we focus on the problem of information expiration when using the traditional collaborative filtering algorithm and propose a new collaborative filtering algorithm by integrating the time factor (ITWCF). This algorithm considers information influence attenuation over time, introduces an information retention period based on the information half-value period, and proposes a time-weighted function, which is applied to the nearest neighbor selection and score prediction to assign different time weights to the scores. In addition, to further improve the quality of the nearest neighbor selection and alleviate the problem of data sparsity, a method of calculating users' sentiment tendency by analysis of user review features is proposed to mine users' attitudes about the reviewed items, which expands the score matrix. The time factor and sentiment tendency are then integrated into the *K*-means clustering algorithm to select the nearest neighbor. A hybrid collaborative filtering model (TWCHR) based on the improved *K*-means clustering algorithm is then proposed, by combining item-based and user-based collaborative filtering. Finally, the experimental results show that the proposed algorithm can address the time effect and sentiment analysis in recommendations and improve the predictive performance of the model.

1. Introduction

E-commerce has gradually developed into social commerce with the rapid development of the Internet. Users can publish through and obtain information from an increasing number of channels. Recommendation technology, based on the notion of collaborative filtering, helps users better utilize information [1]. Both practically and theoretically, collaborative filtering recommendation algorithms based on users or items have achieved good results. However, problems such as data sparsity, cold start, and information expiration still occur [2, 3]. Researchers have thus proposed various improvements to achieve higher quality predictions and recommendations.

The most common method for addressing the problem of data sparsity is to use dimension reduction techniques to compress the original data [4]. In terms of the cold start problem, Guo et al. [5] noted that, in early stages, neighbors can be found according to user or item features. To address the problem of information expiration, the nonlinear forgetting function was introduced, which considers the loss of information influence over time, and a series of recommendation algorithms incorporating this function have been proposed [3, 6–9].

Most e-commerce websites feature online reviews representing users' specific feedback on products, but the issue of data sparsity is still a major challenge. Researchers have found that mining the users' sentiment tendencies from review information will improve user preference models and recommendation accuracy [10–12]. Thus, the mining of reviews to establish users' interest preferences, combined with user scores to improve the traditional collaborative filtering algorithm, has recently become a topic of great interest. Ganu et al. [13] proposed a multilabel text classifier based on the support vector machine (SVM) to classify reviews and to generate text scores and recommendations

based on them. However, this method requires the topic category and sentiment classification of 3400 sentences to be manually annotated. McAuley and Leskovec [14] proposed the hidden factors as topics (HFT) model by combining the latent-factor model with the document topic generation model (Latent Dirichlet allocation, LDA). The LDA method is used to obtain the product review topic distribution, which is then combined with the latent-factor model to establish the relationship between the review topic and the score. This method regards the review topic distribution as consistent with the potential score dimension and thus establishes the transformation. Dehkordi et al. [15] added user reviews and users with similar preferences as implicit feedback into the collaborative filtering algorithm to improve the accuracy of the recommendation results.

The abovementioned improved algorithms are to some extent able to solve the problems faced by traditional collaborative filtering algorithms, but the recommendation quality could still be further improved by effectively solving the problems of information expiration and sparsity. In this study, we address information expiration by first introducing an improved time-weighted collaborative filtering algorithm (ITWCF), which assumes that although the influence of information is nonlinearly attenuated with the passage of time, it will not change significantly within a specific period. The time window in which the information remains unchanged is integrated into the attenuation function. By applying the information half-value period [7] and the proposed concept of a period of information retention, an improved time-weighted function is generated in this study and introduced into the traditional similarity calculation to improve its accuracy, with the aim of achieving better recommendation results. In addition, to make better use of user review information and alleviate the problem of data sparsity, a sentiment tendency calculation method based on review features' analysis is proposed and applied to clustering analysis, which improves the quality of the nearest neighbor selection. Thus, a hybrid recommendation model is proposed by combining item-based and user-based collaborative filtering. The experimental results show that the proposed method can effectively account for the time factor and user sentiment tendency, thus improving the performance of the recommendation model.

2. Related Work

2.1. User-Based Collaborative Filtering. In user-based collaborative filtering, it is assumed that the target user will like items that are similar to his or her interests and preferences. This similarity is calculated based on the score set of users' items, and those that are more similar to the target user make a greater contribution to the predicted score. Currently, the most common similarity calculation methods include cosine similarity, the Pearson correlation coefficient, and the adjusted cosine [16].

(1) Cosine similarity regards each user's historical score as an n-dimensional vector, where the vectors u and v represent the historical scores of users u and v, respectively. Here, the ith element of the vector is the user's score for the ith item, and an unrated item is represented by 0. The cosine similarity of users u and v can be expressed by the cosine of the angle between the two vectors, that is,

$$\mathrm{sim}(u,v) = \cos(u,v) = \frac{\vec{u}\cdot\vec{v}}{\|\vec{u}\|\cdot\|\vec{v}\|} = \frac{\sum_{i\in I_{uv}} r_{ui}\cdot r_{vi}}{\sqrt{\sum_{i\in I_u} r_{ui}^2}\cdot\sqrt{\sum_{i\in I_v} r_{vi}^2}}, \tag{1}$$

where r_{ui} is the score of user u for item i and I_{uv} is the set of items rated by users u and v.

(2) Pearson similarity describes the degree of consistency between two users' rating trends on several items in user-based collaborative filtering. The calculation method is as follows:

$$\mathrm{sim}(u,v) = \frac{\sum_{i\in I_{uv}}\left(r_{ui}-\bar{r_u}\right)\cdot\left(r_{vi}-\bar{r_v}\right)}{\sqrt{\sum_{i\in I_{uv}}\left(r_{ui}-\overline{R_u}\right)^2}\cdot\sqrt{\sum_{i\in I_{uv}}\left(r_{vi}-\overline{r_v}\right)^2}}, \tag{2}$$

where $\overline{r_u}$ is the average score of user u on the items.

(3) In modified cosine similarity, all users have different rating preferences. To correct the deviation of different users' rating scales, the user's average score is subtracted. The modified cosine similarity calculation method is as follows:

$$\mathrm{sim}(u,v) = \frac{\sum_{i\in I_{uv}}\left(r_{ui}-\bar{r_u}\right)\cdot\left(r_{vi}-\bar{r_v}\right)}{\sqrt{\sum_{i\in I_u}\left(r_{ui}-\overline{r_u}\right)^2}\cdot\sqrt{\sum_{i\in I_v}\left(r_{vi}-\overline{r_v}\right)^2}}. \tag{3}$$

(4) Prediction score and recommendation calculates the similarity of users, where the nearest neighbor set $N_{(u)}$ of target user u is obtained according to the Top-N algorithm, and then, the prediction score of user u for the unrated item i is

$$P(r_{ui}) = \overline{r_u} + \frac{\sum_{v\in N_{(u)}}\mathrm{sim}(u,v)\left(r_{v,i}-\bar{r_v}\right)}{\sum_{v\in N_{(u)}}\mathrm{sim}(u,v)}. \tag{4}$$

All unrated items of target user u are predicted based on the above method, and the Top-N items with the highest predicted scores are selected and recommended to target user u.

2.2. Item-Based Collaborative Filtering. The unrated item I_i of user u can be taken as an example. First, the similarity between the target item I_i and other items in set I is calculated. The k items with the highest similarity are then removed to form the nearest neighbor set $N_{(i)} = \{I_1, I_2, \ldots, I_k\}$ of item I_i. Similarity can be calculated using various methods, and the most basic of which are

cosine similarity, Pearson correlation similarity, and modified cosine similarity [16].

(1) The cosine similarity method is similar to the angle between two score vectors. The smaller the angle, the higher the similarity (see formula (5)). If the score in the matrix r is null, it takes the value of 0:

$$\mathrm{sim}(i,j) = \cos(i,j) = \frac{\vec{i}\cdot\vec{j}}{\|\vec{i}\|\cdot\|\vec{j}\|} = \frac{\sum_{u\in U_{ij}} r_{ui}\cdot r_{uj}}{\sqrt{\sum_{u\in U_i} r_{ui}^2}\cdot\sqrt{\sum_{u\in U_j} r_{uj}^2}}, \tag{5}$$

where r is the vector space, $\vec{i}$ and $\vec{j}$ are the score vectors of all users on items i and j, respectively, and U_{ij} is the set of users who have rated items i and j.

(2) Pearson similarity is used to measure the linear correlation between two score vectors and is calculated as follows:

$$\mathrm{sim}(i,j) = \frac{\sum_{u\in U_{ij}}\left(r_{ui}-\bar{r}_i\right)\cdot\left(r_{uj}-\bar{r}_j\right)}{\sqrt{\sum_{u\in U_{ij}}\left(r_{ui}-\overline{R_i}\right)^2}\cdot\sqrt{\sum_{u\in U_{ij}}\left(r_{uj}-\overline{r_j}\right)^2}}, \tag{6}$$

where $\overline{r_i}$ and $\overline{r_j}$ are the average scores of all users for items i and j, respectively.

(3) Modified cosine similarity addresses a major shortcoming of using the basic cosine method to measure similarity. Specifically, the basic cosine method ignores the differences among users in their understanding of the rating criteria. To address this, the modified cosine similarity is calculated after subtracting the average score of the corresponding user from each score. The details are as follows:

$$\mathrm{sim}(i,j) = \frac{\sum_{u\in U_{ij}}\left(r_{ui}-\bar{r}_u\right)\cdot\left(r_{uj}-\bar{r}_u\right)}{\sqrt{\sum_{u\in U_{ij}}\left(r_{ui}-\overline{r_u}\right)^2}\cdot\sqrt{\sum_{u\in U_{ij}}\left(r_{uj}-\overline{r_u}\right)^2}}. \tag{7}$$

(4) In prediction score and recommendation, after obtaining the nearest neighbor set $N_{(i)}$ of item I_i, the score of user u on I_i can be predicted based on the score of target user u for the items in $N_{(i)}$:

$$P\left(r_{ui}\right) = \bar{r}_i + \frac{\sum_{j\in N_{(i)}}\mathrm{sim}(i,j)\left(r_{uj}-\bar{r}_j\right)}{\sum_{j\in N_{(i)}}|\mathrm{sim}(i,j)|}. \tag{8}$$

All unrated items of target user u are predicted according to the above method, and the Top-N items with the highest predicted scores are selected and recommended to target user u.

3. Collaborative Filtering Based on Time Effect

3.1. Time Effect Analysis of Item Score. The traditional collaborative filtering recommendation algorithm does not consider changes over time. In reality, however, the contribution of item scores to recommendations does vary over time, so the time effect should be considered in the recommendation [17]. In general, users are more interested in the most recently selected item than those selected earlier. However, when calculating the neighbor set, the traditional algorithm treats the item scores of different time periods equally, which means that the neighbor set of the target user may not include the nearest neighbor in a true sense, thus reducing the recommendation accuracy.

Calculating the set of neighbors based on user item scores in the same or a similar time period is more accurate. An example illustrating this is presented in Table 1, in which the score records of 4 users (*User*, denoted by u) correspond to 3 time periods for 5 items.

Assume that $User_1$ is the target user, there are only three neighbor users, and it is necessary to predict $User_1$'s score on $Item_3$. The time difference between t_1 and t_2 is relatively small, but the difference from t_4 is relatively large. According to the traditional similarity calculation method, the nearest neighbors of $User_1$ are $sim\ (u_1, u_2) > sim(u_1, u_3) > sim\ (u_1, u_4)$. If the time effect is considered, then the weight of the recommended contribution should be increased for the more recent time periods. In this case, the nearest neighbors of $User_1$ are $sim\ (u_1, u_2) > sim(u_1, u_4) > sim\ (u_1, u_3)$. Thus, the traditional method is unable to appropriately judge the nearest neighbor of $User_1$.

3.2. Improved Time-Weighted Function. In reference [3], the nonlinear exponential forgetting function is used to describe the attenuation degree of information, and the time-weighted function T value (t) is proposed, which reflects the different contributions of the scores at different times toward the recommendation. To describe the process of information from release to decay and finally its disappearance, the concept of the information half-value period is proposed in [7].

The definition of this information half-value period T_s is the time it takes for the information released to halve its influence, that is, after time T_s, the influence of the information is halved. Thus, it can be described as follows:

$$\mathrm{Tvalue}\left(T_s\right) = 0.5\times\mathrm{Tvalue}(0). \tag{9}$$

From the above formula, after time T_s, the time-weighted function becomes 0.5, that is, the reference value of the user's score becomes half of the original. We then define the attenuation factor γ as follows:

$$\gamma = \frac{(\ln 0.5)}{T_s}. \tag{10}$$

The time-weighted function T value (t) can thus be calculated as follows:

$$\mathrm{Tvalue}(t) = e^{\gamma\cdot t}, \tag{11}$$

where $t = t_{\mathrm{now}} - t_{ui}$, t_{ui} is the rating time of the item i by user u, and the value of T value (t) is the time-weighted value, that is, the degree of attenuation of the information. The value of

Table 1: User-item scores in different time periods.

Item	$Item_1$	$Item_2$	$Item_3$	$Item_4$	$Item_5$
$User_1$ (t_1)	5	4	?	3	4
$User_2$ (t_4)	4	3	4	3	4
$User_3$ (t_3)	3	4	3	4	3
$User_4$ (t_1)	2	4	5	2	2

this function is kept in (0, 1], and it decreases with the increase of time $t_{u,i}$, which indicates that the user's recent rating records have more predictive value.

The influence of information generally shows a nonlinear decline, but within a certain period, it does not change significantly. Thus, we introduce the concept of an information retention period.

The definition of information retention period T^p is the time period in which the influence of information remains constant.

Introducing the information retention period gives an improved time-weighted function F value (t):

$$\mathrm{Fvalue}(t) = e^{\gamma \cdot T^p \cdot \lceil t/T^p \rceil}, \tag{12}$$

where $\gamma = (\ln 0.5)/T_s$, $t = t_{\mathrm{now}} - t_{ui}$, and t_{ui} is the rating time of the item i by user u.

Adding the concept of the information retention period to the improved time-weighted function is equivalent to introducing a time window, in which the information remains basically unchanged, into the original weighted function. This leads to a gradient of exponential attenuation of the information, which is more in line with reality.

3.3. Improved Similarity Calculation Methods. In traditional cosine similarity calculations, the improved time-weighted function is introduced to assign a time weight to each score.

(1) The improved calculation method of item-based similarity measurement is as follows:

$$\mathrm{Tsim}(i, j) = \frac{\sum_{u \in U_{ij}} r_{ui} \cdot \mathrm{Fvalue}(\Delta t_{ui}) \cdot r_{uj} \cdot \mathrm{Fvalue}(\Delta t_{uj})}{\sqrt{\left(\sum_{u \in U_{ij}} r_{ui} \cdot \mathrm{Fvalue}(\Delta t_{ui})\right)^2} \times \sqrt{\left(\sum_{u \in U_{ij}} r_{uj} \cdot \mathrm{Fvalue}(\Delta t_{uj})\right)^2}}, \tag{13}$$

where $Tsim$ (i, j) is the similarity of items i and j, r_{ui} and r_{uj} are user u's scores on items i and j, respectively, Fvalue ($\Delta t_{u,i}$) is the time-weighted function, and $\Delta t_{ui} = t_{now}$-t_{ui} is the interval between the rating time of item i and the current time.

(2) The improved user-based similarity measurement calculation method is as follows:

$$\mathrm{Tsim}(u, v) = \frac{\sum_{i \in I_{uv}} r_{ui} \cdot \mathrm{Fvalue}(\Delta t_{ui}) \cdot r_{vi} \cdot \mathrm{Fvalue}(\Delta t_{vi})}{\sqrt{\sum_{i \in I_u} (r_{ui} \cdot \mathrm{Fvalue}(\Delta t_{ui}))^2} \cdot \sqrt{\sum_{i \in I_v} (r_{vi} \cdot \mathrm{Fvalue}(\Delta t_{vi}))^2}}, \tag{14}$$

where $Tsim$ (u, v) is the similarity between users u and v.

(3) The improved user-based score prediction is as follows:

$$P_{\mathrm{user}}(r_{ui}) = \bar{r_u} + \frac{\sum_{v \in N_{(u)}} \mathrm{Tsim}(u, v) \cdot \mathrm{Fvalue}(\Delta t_{vi})(r_{vi} - \bar{r_v})}{\sum_{v \in N_{(u)}} |\mathrm{Tsim}(u, v)| \cdot F(\Delta t_{vi})}, \tag{15}$$

where P (r_{ui}) is user u's predicted score for item i, $N_{(u)}$ is the set of nearest neighbors of user u, and $\overline{r_u}$ and $\overline{r_v}$ are the average scores of users u and v in the entire item set.

(4) The improved item-based score prediction is as follows:

$$P_{\mathrm{item}}(r_{ui}) = \overline{r_i} + \frac{\sum_{j \in N_{(i)}} \mathrm{Tsim}(i, j) \cdot \mathrm{Fvalue}(\Delta t_{uj})(r_{ui} - \bar{r_j})}{\sum_{j \in N_{(i)}} |\mathrm{Tsim}(i, j)| \cdot \mathrm{Fvalue}(\Delta t_{uj})}, \tag{16}$$

where $P(r_{ui})$ is user u's predicted score for item i, $N_{(i)}$ is the set of nearest neighbors of item i, and $\overline{r_i}$ and $\overline{r_j}$ are the average scores of items i and j in the entire user set.

3.4. Collaborative Filtering Algorithm Integrating the Time Effect. Based on the improvements of the similarity calculation method and the score prediction method, an improved time-weighted collaborative filtering (ITWCF) algorithm is proposed (Algorithm 1).

4. Sentiment Analysis of Review Information

The sentiment tendency analysis conducted in this study is aimed at expanding the score matrix, so quantitative analysis results are required. In our analysis, using neutral sentiment as the reference, we assess the sentiment deviation tendency (deviation intensity) of reviews, which establishes the polarity intensity and enables the results to be quantified. A score matrix is finally constructed according to the calculated sentiment values, which can enable score prediction.

4.1. Review Data Preprocessing. A review sentence is generally composed of subjective and objective clauses. Objective clauses are not useful for analyzing sentiment tendency, so they must be deleted. A method based on [18] is used to analyze the type of clause and retain the subjective clauses. The word segmentation tool ICTCLAS is used to segment and label each review sentence. To make the analysis more effective, any information that is inconsistent in terms of the review topic is also manually labeled in advance, and a UTF-8 stop words' table is used to remove the stop words.

4.2. Feature Extraction and Sentiment Analysis of Review Information. Assume that the set of reviews is Review_D, and all feature words in the reviews are $F = \{f_1, f_2, \ldots, f_n\}$.

Step 1. Utilize the Chinese word segmentation tool ICTCLAS to output all adjectives and adverbs: $F_{AA} = \{f_1, f_2, \ldots, f_{AA}\}$.

Step 2. Adopt the IKAnalyzer to segment each review, and calculate the corpus frequency-inverse document frequency (CF-IDF) value w of all feature words. The calculation method is shown as formula (17), and feature words $F_{\text{CF-IDF}} = \{f_1, f_2, \ldots, f_{\text{CF-IDF}}\}$ are selected:

$$\text{CF} - \text{IDF}_i = \text{CF}_i \times \text{IDF}_i = \frac{f_i}{\sum_{i=1}^{n} f_i} \times \log \frac{\left|\text{Review}_D\right|}{\left|\left\{j | t_i \in d_j\right\}\right|}, \tag{17}$$

where f_i is the word frequency of the ith word in the entire corpus, $|\text{Review}_D|$ is the number of review texts in corpus Review_D, and $|\{j|t_i \in d_j\}|$ is the number of review texts containing the ith word in the corpus.

Step 3. Obtain the sentiment words in the reviews, including adjectives, adverbs, verbs, and nouns:

$$F = F_{AA} \cup F_{\text{CF-IDF}} = \{f_1, f_2, \ldots, f_n\}. \tag{18}$$

Step 4. Merge the features. Different words are often used to describe the same feature f in reviews, and thus, if the features are not merged, major deviations may occur in the analysis. We use the sentiment lexicon based on HowNet [19] and the point mutual information (PMI) method [20] to determine the semantic similarity between sentiment feature words (the calculation formula is (19)). When similarity reaches the set threshold, the features are merged:

$$\text{Sim}\left(f_i, f_j\right) = \log_2\left(\frac{P\left(f_i, f_j\right)}{P\left(f_i\right)P\left(f_j\right)}\right), \tag{19}$$

where $\text{Sim}(f_i, f_j)$ is the similarity of the features f_i and f_j, $P(f_i, f_j)$ is the probability that the features f_i and f_j appear together, $P(f_i)$ is the probability that the feature f_i is included in the review, and $P(f_j)$ is the probability that the feature f_j is included.

Step 5. Calculate the sentiment tendency of the feature words. For the feature word f_i, based on formula (19), the details are as follows:

$$\text{Tendency}\left(f_i\right) = \sum_{\text{Pword} \in \text{PosWords}} \text{Sim}\left(f_i, \text{Pword}\right) - \sum_{\text{Nword} \in \text{NegWords}} \text{Sim}\left(f_i, \text{Nword}\right), \tag{20}$$

where *PosWords* and *NegWords* are the sets of HowNet positive and negative sentiment words, respectively.

If $\text{Tendency}(f_i) > 0$, the feature f_i is a positive sentiment word and is denoted as positive once.

If $\text{Tendency}(f_i) < 0$, the feature f_i is a negative sentiment word and is denoted as negative once.

If $\text{Tendency}(f_i) = 0$, the feature f_i is a neutral sentiment word.

Input. Target user u; information half-value period T_s; information retention period T^p.
Output. A list of n items recommended for target user u.
Step 1. Set the items that target user u has not rated as the target item set I_{ua}.
Step 2. Use formula (12) to calculate the time-weighted values of scores in r to obtain the score-weighted matrix.
Step 3. Use formula (13) to calculate the similarity between target item $i \in I_{ua}$ and other items, and select the most similar k items to form the nearest neighbor set of target item i. Use formula (14) to calculate the similarity between target user u and other users, and based on this similarity, the most similar k users are selected to form the nearest neighbor set of target user u.
Step 4. Use formulas (15) and (16) to predict the scores $P_{user}(r_{ui})$ and $P_{item}(r_{ui})$ of target user u for item i, respectively.
Step 5. Repeat *Steps 3* and *4* for all items in I_{ua} to predict the scores of all unrated items. Then, calculate the weighted scores. Finally, recommend the top n items with the highest predicted $P(r_{ui})$ values for target user u.

Algorithm 1: The ITWCF algorithm.

Input. User rating matrix r; set i of n items; m users U; sentiment tendency value Pol of users toward items; the number of clusters K; and, the similarity threshold η.
Output. Clustering number K and K cluster centers.
Step 1. Select the input data. Extract set I of n items and set U of m users from r.
Step 2. Calculate the time-weighted scores, and integrate the sentiment tendency. Set the half-value period T_s and the retention period T^p, and use formula (12) to calculate the time-weighted value F value (Δt_{ui}) of each score r_{ui} to form a time-weighted score, as shown in the following: $r'_{ui} = r_{ui} \times \text{Fvalue}(\Delta t_{ui}) \times \text{Pol}$.
Step 3. Randomly select cluster centers. Randomly select the time-weighted scores of K items as the initial cluster centers, denoted as $C = \{C_u^1, C_u^2, \ldots, C_u^k\}$. Here, each cluster center $C_u^j \in C$ corresponds to a cluster, denoted as C^j.
Step 4. Calculate the similarity between the item and the cluster center. Use formula (22) to calculate the similarity between each item $i \in I$ and the cluster center $C_u^j \in C$, and the first s items that are greater than the similarity threshold η are put into cluster C^p corresponding to the most similar cluster center C_u^p. $\text{sim}(i, C_u^j) = (\sum_{u \in U_i} r'_{u,i} \times r_{uC_u^j} / \sqrt{(\sum_{u \in U_i} r'^2_{ui})} \times \sqrt{(\sum_{u \in U_i} r^2_{uC_u^j})})$.
Step 5. Update the cluster centers. Calculate the new center for each cluster, that is, update the cluster center vector after adding new items in one iteration.
Step 6. The algorithm is terminated, and the result is output. Repeat *Step 4* and *Step 5* until the cluster centers no longer change and convergence is reached. The clustering number K and cluster centers are thus obtained.

Algorithm 2: A K-means clustering algorithm based on time effect and sentiment analysis.

Step 6. Calculate the sentiment tendency value of the review sentence. Extract the feature words of each review sentence and the corresponding number of favorable reviews, and then, calculate the sentiment tendency value of the whole review sentence. The calculation method is shown in the following formula:

$$\text{Pol} = \frac{\sum_{i=1}^{N} \text{Tendency}(f_i)}{N}, \tag{21}$$

where N is the total number of features in the review sentence and $\text{Tendency}(f_i)$ is the sentiment tendency of the feature f_i.

5. Clustering Algorithm Based on Time Effect and Sentiment Analysis

As mentioned, the influence of information will decay over time. In this study, the improved time-weighted function F value (t) is applied to the item clustering. In addition, because the sentiment attitude of the user review item is a direct expression of the user's behavior, making full use of the sentiment tendencies of users can lead to improved adaptation to their personalized needs. Thus, the ITWCF algorithm can be optimized by clustering analysis, and therefore, an item clustering algorithm combining sentiment analysis and time-weighted function is proposed (Algorithm 2).

6. Hybrid Collaborative Filtering Model

To ensure that the recommendation algorithm has the features of item-based and user-based collaborative filtering, a hybrid collaborative filtering model based on both is proposed, which effectively improves the recommendation accuracy after clustering by the K-means algorithm.

6.1. Hybrid Model Construction

Step 1. Use n-fold cross-validation to predict and generate the training data for *Step 2*. R is defined as the user's original score matrix, and the whole original score set is randomly divided into n equal parts. The sth part is denoted as R_s (training set), and $\overline{R_s}$ (test set) is used to denote other rating data except R_s in the score matrix. P_{user} is the user-based score prediction function, and P_{item} the item-based score prediction function. Utilize formula (22) to construct the training data of *Step 2*:

Input. User score matrix r; set I of n items; m users U; clustering number K; and, similarity threshold η.
Output. A list of n items recommended for target user u.
Step 1. Substitute the half-value period T_s and retention period T^p in formula (12) to obtain the time-weighted values of each item's score.
Step 2. Utilize Algorithm 2 to cluster the score matrix and obtain the K clusters, namely, the nearest neighbor set.
Step 3. Use the hybrid collaborative filtering model to calculate score $P(r_{ui})$.
Step 4. Predict the scores of all items in the set I, sort them according to the score level, and then recommend the top n items to target user u.

Algorithm 3: TWCHR algorithm.

$$P_{\text{next}}(r_{ui}) = \{P^s_{\text{user}}(r_{ui}), P^s_{\text{item}}(r_{ui}), (r_{ui}) | r_{ui} \in R_s, s = 1, 2, \ldots, n\}, \tag{22}$$

where $P_{\text{next}}(r_{ui})$ is the predicted value, $P^s_{\text{user}}(r_{ui})$ is the predicted value of r_{ui} based on the user's prediction score function, and $P^s_{\text{item}}(r_{ui})$ is the predicted value of r_{ui} based on the score prediction function of the item.

Step 2. Conduct a weighted fusion of item-based and user-based prediction functions based on the training data generated in *Step 1*, and formula (23) is the fused prediction model:

$$P(r_{ui}) = \beta_1 \times P_{\text{user}}(r_{ui}) + \beta_2 \times P_{\text{item}}(r_{ui}), \tag{23}$$

where $P(r_{ui})$ is the predicted score after weighted fusion and β_1 and β_2 are the weights of item-based and user-based predicted values, respectively.

6.2. Hybrid Model Solution. The above problem is transformed into a quadratic optimization problem with constraints, referred to as an objective function, and the details are as follows:

$$\min_{\beta} \frac{1}{2} \sum_{j=1}^{|\text{next}|} \left(\beta^T x_k - r_k\right)^2, \tag{24}$$

$$\text{s.t.} \quad \beta_1 \geq 0, \beta_2 \geq 0,$$

where β is the parameter of the model, $\beta = (\beta_1, \beta_2)^T$, $|\text{next}|$ is the size of the training set, (x_k, r_k) is the kth training sample, and $x_k = (P_{\text{user}}(r_k), P_{\text{item}}(r_k))^T$.

Use the Lagrangian multiplier and the KT condition to solve the optimization problem. Set $J(\beta) = (1/2) \sum_{j=1}^{|\text{next}|} (\beta^T x_k - r_k)^2$, and the derivative of β can be obtained:

$$\begin{cases} \beta_1 = \dfrac{gp - fh}{g^2 - ef} \\ \\ \beta_2 = \dfrac{gh - eg}{g^2 - ef} \end{cases}, \quad \text{s.t. } \beta_1, \beta_2 \geq 0, \tag{25}$$

where $e = \sum_j P^2_{\text{user}}(r_j)$, $f = \sum_j P^2_{\text{item}}(r_j)$, $g = \sum_j P_{\text{user}}(r_j) P_{\text{item}}(r_j)$, $h = \sum_j r_j P_{\text{user}}(r_j)$, and $p = \sum_j r_j P_{\text{item}}(r_j)$.

6.3. Hybrid Recommendation Model Based on Time Effect and Sentiment Analysis. We apply a clustering algorithm that integrates time effect and sentiment analysis into the ITWCF algorithm and propose a hybrid recommendation algorithm based on time-weighted and sentiment tendency clustering (TWCHR). The details are as follows (Algorithm 3):

7. Experimental Verification and Results Analysis

7.1. Datasets

7.1.1. MovieLens Dataset. The MovieLens dataset contains 100,000 rating records for 1,682 movies from 943 users, where each user has rated at least 20 movies using a score of 1–5 to represent his or her preference. This dataset is used to verify the influence of the time effect on the recommendation results. In the experiment, 5 groups of data are randomly selected from MovieLens, each of which contains 180 random users' rating information on all items, and the scores of each user in each group of data are sorted by time from most recent to longest ago. The first 70% is used as the training set and the remaining 30% as the test set, and the algorithm is verified using the cross-validation method (Algorithm 3).

7.1.2. Book Dataset. Using a crawler algorithm written in *Python*, more than 20,000 book purchase records, 20,000 scores, and 100 book-related introductions were crawled from the popular e-commerce website jd.com, including book name, book classification, book introduction, user name, user ID, price, purchase time, review information, score, and review time. This dataset is used to verify the influence of the time factor and the sentiment tendency of the review information on users' purchasing behavior.

The dataset is divided into a training set and a test set, according to the ratio of 4 : 1. The training set is used to build the recommendation model, and the test set is used to evaluate the recommendation results. The evaluation indexes include accuracy rate, recall rate, and $F1$ value.

7.2. Evaluation Indexes

7.2.1. Mean Absolute Error (MAE). This evaluates the degree of deviation between the item scores predicted by the recommendation algorithm and the actual scores given by users. The calculation formula is as follows:

$$\mathrm{MAE} = \frac{\sum_{u,i}\left|P\left(r_{ui}\right) - r_{ui}\right|}{n}, \tag{26}$$

where $P(r_{ui})$ is the predicted value, r_{ui} is the actual score, and n is the number of predicted items.

7.2.2. Accuracy, Recall, and F1 Values. Recommend n items for user u, denoted as $R(u)$. Let user u's favorite item set on the test set be $T(u)$, then the accuracy and recall rates are defined as follows:

$$\begin{aligned}\mathrm{accuracy} &= \frac{\sum_u |R(u) \cap T(u)|}{\sum_u |T(u)|},\\ \mathrm{recall} &= \frac{\sum_u |R(u) \cap T(u)|}{\sum_u |R(u)|}.\end{aligned} \tag{27}$$

The accuracy rate and the recall rate are a pair of mutually exclusive indicators, which are usually combined. The $F1$ value is then used to measure the quality of recommendations, as follows:

$$F1 = \frac{2 \times \mathrm{accuracy} \times \mathrm{recall}}{\mathrm{accuracy} + \mathrm{recall}}. \tag{28}$$

7.3. Experimental Design and Results Analysis. Two experiments are designed to verify the effectiveness and feasibility of the method proposed in this paper. The first uses the MovieLens dataset to analyze the influence of parameters on the performance of the algorithm, including the information half-value period, information retention period, number of nearest neighbors, clustering number, and similarity threshold. Based on this, a comparative experiment is designed to compare and analyze the advantages and disadvantages of the proposed method and other methods under the same parameters. The second experiment uses the book dataset to verify the advantages of the proposed method when using the time factor and sentiment tendency.

7.3.1. Personalized Movie Recommendation Results and Analysis. (1) Analyze the Influence of Parameters on the Recommendation Effect.

(1) The influence of information half-value period T_s on the performance of the ITWCF algorithm

In this experiment, we set the information retention period $T^p = 3$ and the nearest neighbor number $cln = 25$, then observe the MAE values of the ITWCF algorithm under different half-value periods. We compare these values with those of the time-weighted collaborative filtering algorithm that does not introduce the time retention period (the TWCF algorithm), as shown in Figure 1.

Figure 1 shows that, in the case including the information retention period $T^p = 3$, the MAE of the ITWCF algorithm is the smallest, and the recommended accuracy is the highest under the information half-value period of 25. Compared with the TWCF algorithm, the ITWCF algorithm has a smaller MAE and higher recommended accuracy under the same half-value period and the same number of nearest neighbors.

(2) The influence of the information retention period T^p on the performance of the ITWCF algorithm

We set the information half-value period T_s as 15 days, 25 days, and 50 days, respectively, and the number of neighbors as $cln = 25$. Then, we observe the trend of the MAE value of the ITWCF algorithm as a function of the information retention period T^p, as shown in Figure 2.

Figure 2 shows that the smaller the value of T_s, the more sensitive the algorithm is to the changes of the value of T^p. That is, when the information retention period changes, the MAE value of the algorithm will change more significantly at smaller T_s. T^p also influences the recommendation results of the ITWCF algorithm, and the optimal values of the information retention period corresponding to different half-value periods are also different. However, the algorithm gives the best accuracy overall when T^p is 2–3 days.

(3) The influence of clustering number K and the target item similarity threshold η on the performance of the TWCHR algorithm

According to the above analysis of T_s and T^p, we set $T_s = 25$ and $T^p = 2$ and the similarity threshold to $\eta = 0.2$, 0.3, and 0.4, respectively. Then, we observe the MAE changes of the TWCHR algorithm under different clustering numbers of K, as shown in Figure 3.

Figure 3 shows that no matter how large the value of η is, when the clustering number is in the range of 6–9, the MAE of the algorithm is relatively low and the prediction accuracy is relatively high. However, when the clustering number is large, the number of items in each cluster is therefore small, and some true neighbor items will be excluded from the nearest neighbor set, leading to inaccurate recommendation results. Meanwhile, when the clustering number is too small, the MAE value will again increase because there are fewer items whose similarity to the cluster center can reach η, resulting in some items not achieving accurate prediction scores. That is, when there are too few clusters, the nearest neighbor candidate set becomes too large and some items that are nonnearest neighbors may be clustered together, which degrades the recommendation results.

(2) Comparative Analysis of Different Algorithms. This is based on the above analysis of the effects of various parameters. In this experiment, we set $T^p = 2$, $T_s = 25$, $K = 6$, and the similarity threshold between the cluster center and the target item as $\eta = 0.3$. The MAE values of the item-based collaborative filtering algorithm (ItemCF), the user-based collaborative filtering algorithm (UserCF), the ITWCF algorithm, the traditional clustering-based TWCHR (TR-TWCHR), and the TWCHR algorithm are, respectively, compared in the case of different numbers of neighbors, and the results are shown in Figure 4.

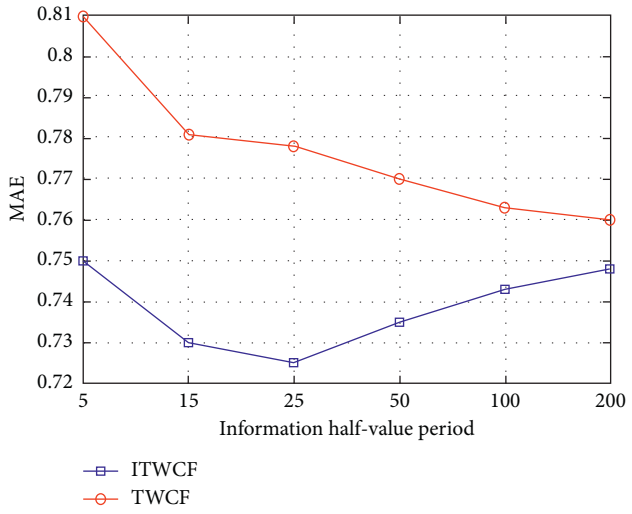

Figure 1: The influence of the information half-value period on the recommendation algorithm.

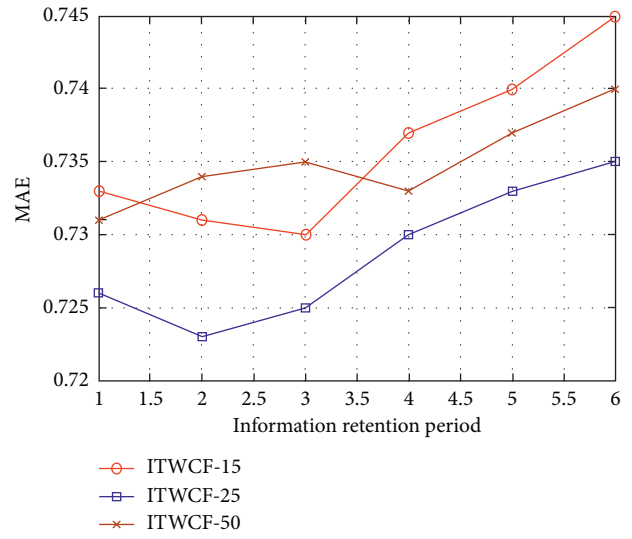

Figure 2: The influence of the information retention period on the recommendation algorithm.

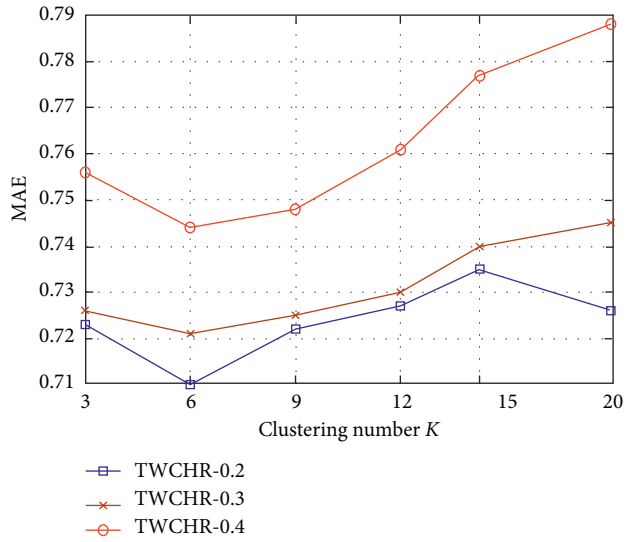

Figure 3: The influence of the clustering number on the recommendation algorithm.

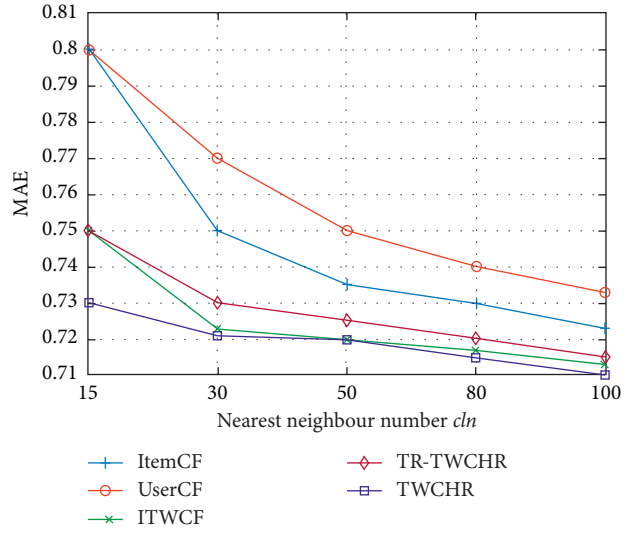

Figure 4: Performance comparison of five algorithms under different nearest neighbors.

The experimental results show that the MAEs of the ItemCF, UserCF, ITWCF, TR-TWCHR, and TWCHR algorithms all show a decreasing trend when the number of nearest neighbors increases. Thus, the selection of the nearest neighbor number is the key factor influencing the performance of the collaborative filtering algorithms. Given the same nearest neighbor number, the MAEs of the ITWCF and the TWCHR algorithms are basically equivalent, except when the number of nearest neighbors is most appropriate, in which case TWCHR outperforms ITWCF. In addition, the ITWCF, TR-TWCHR, and TWCHR algorithms, which all include the time factor, outperform ItemCF and UserCF. In conclusion, the TWCHR algorithm has the smallest MAE and is therefore superior to the others in terms of accuracy.

Through the above experiments, we find that the time factor and the clustering number have an obvious influence on personalized movie recommendations, and the method proposed in this paper using the time-weighted factor to improve the recommendation effect is feasible.

7.3.2. Personalized Book Recommendation and Results Analysis

(1) The Influence of User Review Sentiment Analysis on Recommendation. To verify the effect of the user review sentiment analysis in personalized book recommendations, in this experiment, we compare and analyze the

Table 2: The influence of sentiment analysis on recommendation results under different clustering numbers.

Recommendation algorithm	Clustering number K	Correctly recommended quantity	Recommended quantity	Accuracy (%)	Recall (%)	$F1$ value (%)
TR-TWCHR	10	1171	1852	63.23	29.28	40.02
	20	1435	2208	64.99	35.88	46.23
	30	1526	2096	72.81	38.15	50.07
	50	1470	2137	68.79	36.75	47.91
	100	1187	1839	64.55	29.68	40.66
TWCHR	10	1292	1965	65.75	32.30	43.32
	20	1584	2324	68.16	39.60	50.09
	30	1636	2158	75.81	40.90	53.13
	50	1615	2251	71.75	40.38	51.67
	100	1355	1981	68.40	33.88	45.31

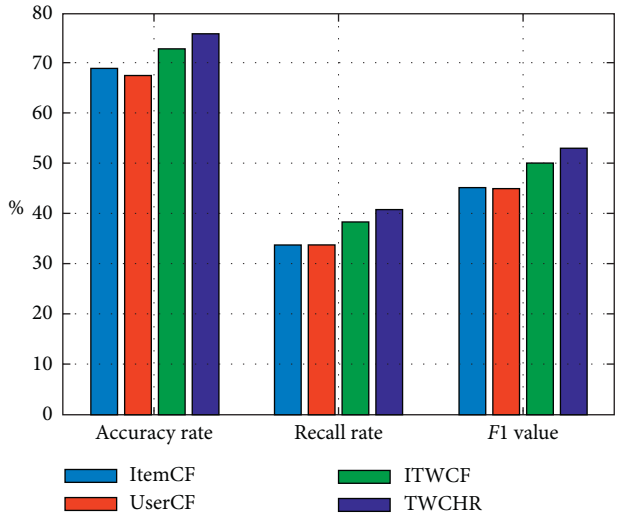

Figure 5: Performance comparison of four algorithms.

recommendation accuracy, recall rate, and $F1$ value of the TR-TWCHR and TWCHR algorithms under the different clustering numbers. The different values of cluster center K in the recommendation algorithm, based on review sentiment analysis, have different effects, so it is necessary to experiment using different K values and observe the influence of the recommendation results, which are shown in Table 2.

Table 2 shows that the recommendation algorithm based on review sentiment analysis (TWCHR) has different recommendation results under different K values. However, in general, the accuracy, recall rate, and $F1$ value of recommendations with the integrated review sentiment analysis are slightly higher than those of the recommendation algorithm without the integrated review sentiment analysis (TR-TWCHR). Thus, the performance of the recommendation model can be improved by integrating review sentiment analysis.

(2) Comparative Analysis of Different Algorithms. To verify the effectiveness of the algorithm proposed in this paper, the ItemCF, UserCF, ITWCF, and TWCHR algorithms (where $K = 30$) are compared in terms of classification accuracy rate, recall rate, and $F1$ value, and the results are shown in Figure 5.

Figure 5 shows that the TWCHR algorithm outperforms the ITWCF, which may be related to the improved method of selecting the nearest neighbors. For the TWCHR, a clustering algorithm combining the time factor with review analysis is used to select the nearest neighbors, whereas for the ITWCF, only the time factor is considered in the selection of the nearest neighbors. This indicates that the sentiment analysis of user reviews has a direct impact on the recommendation accuracy. In addition, the performance of the TWCHR algorithm is significantly better than those of ItemCF and UserCF, which may be related to both the selection method of nearest neighbors and to data sparsity. This indicates that the fusion of the time factor and sentiment analysis is very effective in improving the recommendation accuracy. In addition, the results demonstrate that the hybrid recommendation algorithm effectively combines the advantages of ItemCF and UserCF. Therefore, the algorithm proposed in this paper is reasonable and practical.

8. Conclusions

To solve the problems of information expiration and the use of review information, we first examine collaborative filtering algorithms that integrate the time factor and sentiment analysis. Second, we introduce the concept of an information retention period to improve the time-weighted function, leading to the newly proposed ITWCF algorithm. We then propose a calculation method for the sentiment tendency of review item features and a new clustering algorithm that integrates the time factor and sentiment tendency analysis to optimize the ITWCF algorithm. Third, to take advantage of item-based and user-based collaborative filtering, a hybrid recommendation model is proposed. Finally, two experiments are conducted to verify the proposed algorithm, and the results show that our algorithm can fully account for the time factor and the sentiment tendency and thus improve predictive performance.

Data Availability

The data used to support the findings of the personalized movie recommendation are available from https://grouplens.org/datasets/movielens/, and the original data

of precise book review records cannot be released in order to preserve the privacy of individuals.

Conflicts of Interest

The authors declare that they have no conflicts of interest.

Acknowledgments

This work was partially supported by the Technology Foundation of Guizhou Province (Grant no. QianKeHe-JiChu[2020]1Y269), New Academic Seedling Cultivation and Exploration Innovation Project (Grant no. QianKeHe Platform Talents[2017]5789–21), Program for Innovative Talent of Guizhou Province (Grant no. QianCaiJiao[2018] 190), National Natural Science Foundation of China (Grant nos. 71901078 and 71964009), High-Level Talent Project of Guizhou Institute of Technology (Grant no. XJGC20190929), and Special Key Laboratory of Artificial Intelligence and Intelligent Control of Guizhou Province (Grant no. KY[2020]001).

References

[1] X. Du, X. He, F. Yuan, J. Tang, Z. Qin, and T.-S. Chua, "Modeling embedding dimension correlations via convolutional neural collaborative filtering," *ACM Transactions on Information Systems*, vol. 37, no. 4, pp. 1–22, 2019.

[2] C. Feng, J. Liang, P. Song, and Z. Wang, "A fusion collaborative filtering method for sparse data in recommender systems," *Information Sciences*, vol. 521, pp. 365–379, 2020.

[3] Y. Ding and X. Li, "Time weight collaborative filtering," in *Proceedings of the 14th ACM International Conference on Information And Knowledge Management*, pp. 485–492, Bremen, Germany, November 2005.

[4] H. Zhu, L.-Z. Liao, and M. K. Ng, "Multi-instance dimensionality reduction via sparsity and orthogonality," *Neural Computation*, vol. 30, no. 12, pp. 3281–3308, 2018.

[5] G. Guo, J. Zhang, and N. Yorke-Smith, "A novel recommendation model regularized with user trust and item ratings," *IEEE Transactions on Knowledge and Data Engineering*, vol. 28, no. 7, pp. 1607–1620, 2016.

[6] C. Xing, F. Gao, S. Zhan, and L. Zhou, "A collaborative filtering recommendation algorithm incorporated with user interest change," *Journal of Computer Research and Development*, vol. 44, no. 2, pp. 296–301, 2007.

[7] S. Wu, Z. Xiaonan, and D. Yannan, "A collaborative filtering recommender system integrated with interest drift based on forgetting function," *International Journal of U- and E-Service, Science and Technology*, vol. 8, no. 4, pp. 247–264, 2015.

[8] C. Chao, S. Qu, and T. Du, "Research of collaborative filtering recommendation algorithm for short text," *Journal of Computer and Communications*, vol. 2, no. 14, pp. 59–66, 2014.

[9] J. Chen, C. Wang, and J. Wang, "Modeling the interest-forgetting curve for music recommendation," in *Proceedings of the 22nd ACM International Conference on Multimedia, ACM*, pp. 921–924, Orlando, Florida, USA, November 2014.

[10] J. Wang and T. Liu, "Improving sentiment rating of movie review comments for recommendation," in *Proceedings of the 2017 IEEE International Conference On Consumer Electronics, IEEE*, Taiwan, China, June 2017.

[11] L. Chen, G. Chen, and F. Wang, "Recommender systems based on user reviews: the state of the art," *User Modeling and User-Adapted Interaction*, vol. 25, no. 2, pp. 99–154, 2015.

[12] Q. Lin, G. Sheng, W. Cheng, and J. Guo, "Aspect-based latent factor model by integrating ratings and reviews for recommender system," *Knowledge-Based Systems*, vol. 110, pp. 233–243, 2016.

[13] G. Ganu, Y. Kakodkar, and A. Marian, "Improving the quality of predictions using textual information in online user reviews," *Information Systems*, vol. 38, no. 1, pp. 1–15, 2013.

[14] J. McAuley and J. Leskovec, "Hidden factors and hidden topics: understanding rating dimensions with review text," in *Proceedings of the 7th ACM Conference On Recommender System, ACM*, pp. 165–172, New York, NY, USA, October 2013.

[15] Y. Dehkordi, A. Thomo, and S. Ganti, "Incorporating user reviews as implicit feedback for improving recommender systems," in *Proceedings of the IEEE Fourth International Conference On Big Data & Cloud Computing, IEEE*, Sydney, Australia, December 2015.

[16] R. Latha and R. Nadarajan, "Analysing exposure diversity in collaborative recommender systems-entropy fusion approach," *Physica A: Statistical Mechanics and Its Applications*, vol. 533, p. 122052, 2019.

[17] J. Liu and G. Deng, "Link prediction in a user-object network based on time-weighted resource allocation," *Physica A: Statistical Mechanics and Its Applications*, vol. 388, no. 17, pp. 3643–3650, 2009.

[18] H. Song, Y. Fan, X. Liu, and D. Tao, "Extracting product features from online reviews for sentimental analysis," in *Proceedings Of the 2011 6th International Conference On Computer Sciences And Convergence Information Technology (ICCIT), IEEE*, Seogwipo, South Korea, December 2011.

[19] Z. Dong and Q. Dong, *HowNet and the Computation of Meaning*, World Scientific Press, New York, NY, USA, 2006.

[20] L. Yao, C. Mao, and Y. Luo, "Graph convolutional networks for text classification," *Proceedings of the AAAI Conference on Artificial Intelligence*, vol. 33, pp. 7370–7377, 2019.

Hindawi
Complexity
Volume 2021, Article ID 6624612, 9 pages
https://doi.org/10.1155/2021/6624612

Research Article

Virus-Information Coevolution Spreading Dynamics on Multiplex Networks

Jian Wang,[1,2,3] **Xiaolin Qin**,[2] **and Hongying Fang**[4]

[1]*School of Computer Science and Technology, University of Chinese Academy of Sciences, Beijing 100049, China*
[2]*Chengdu Institute of Computer Applications, Chinese Academy of Sciences, Chengdu 610041, China*
[3]*College of Computer Science and Technology, Chongqing University of Posts and Telecommunications, Chongqing 400065, China*
[4]*College of Mathematics and Statistics, Chongqing Jiaotong University, Chongqing 400074, China*

Correspondence should be addressed to Hongying Fang; 284199018@qq.com

Received 10 December 2020; Revised 22 December 2020; Accepted 10 February 2021; Published 5 March 2021

Academic Editor: Ning Cai

Virus and information spreading dynamics widely exist in complex systems. However, systematic study still lacks for the interacting spreading dynamics between the two types of dynamics. This paper proposes a mathematical model on multiplex networks, which considers the heterogeneous susceptibility and infectivity in two subnetworks. By using a heterogeneous mean-field theory, we studied the dynamic process and outbreak threshold of the system. Through extensive numerical simulations on artificial networks, we find that the virus's spreading dynamics can be suppressed by increasing the information spreading probability, decreasing the protection power, or decreasing the susceptibility and infectivity.

1. Introduction

Coevolution spreading dynamics, ranging from cyberspace security to epidemic contagions, widely exist in the natural systems, in which there are at least two spreading dynamics evolving and interacting simultaneously [1, 2]. For instance, the virus's information is always spreading on the social network when a computer virus spreads on the Internet. The users whose computers are not infected by the virus will install antivirus software and patches to protect their computers from being infected by the virus [3–6]. In this way, computer viruses can be prevented from spreading widely. Another example is the spreading of the epidemic in society. When a global pandemic was spreading, various kinds of information about the pandemic, such as protecting healthy individuals from infection, spreading on social networks will suppress the pandemic [7–9].

Researchers from the field of computer science and network science have developed some successful mathematical models to model such coevolution spreading dynamics. The state of the art in this field is reviewed in a recent paper by Wang et al. [1]. Historically, Newman [10] studied two viruses spreading on the same computer network in succession, where the two viruses follow the susceptible-infected-recovered model, and the second virus can only infect the remaining susceptible nodes. Using a bond percolation theory, he revealed that a global outbreak of the second virus is possible only if the susceptible nodes form a large cluster of connections and the outbreak threshold of the second virus is much higher than the threshold of the first. Newman and Ferrario [11] further discussed a different situation, i.e., the second virus can only spread on those infected nodes by the first virus. They found that the second virus's outbreak size can be suppressed by decreasing the spreading probability of the first virus. In reality, the spreading dynamics are always simultaneous. Karrer and Newman [12] proposed a model to include this factor and studied the phase transition by using a competing percolation theory.

The two spreading dynamics always evolve on different networks; that is to say, we should use multiplex or multilayer networks to describe the network topology of the coevolution spreading [13–18]. Previous studies have revealed that the topology of multilayer networks markedly affect the dynamics,

such as cascading failures [19–21], virus spreading [22, 23], controllability [24], and synchronization [25–27]. For virus-information spreading on multiplex networks, Granell and her colleagues [8] used an unaware-aware-unaware-susceptible-infected-susceptible (UAU-SIS) model. They revealed a metacritical critical point, above which the global virus will break out by using a generalized Markovian approach. Based on the research framework in Reference [8], researchers studied the global information [8], network topology [28, 29], and different interacting mechanisms [30, 31] on the virus spreading. Wang et al. revealed the asymmetric interaction between the virus and information spreading dynamics. They used a susceptible-informed-recovered-susceptible-infected-recovered-vaccination (SIR-SIRV) model. They found that the information can suppress the virus spreading greatly, especially when there is a positive correlation between layers.

Many real-world data analyses proved that the spreading dynamics on the network are heterogeneous. There are three aspects. On the one hand, the network topology is heterogeneous, e.g., heterogeneous degree distribution. Scholars revealed that heterogeneous degree distribution could decrease the virus's outbreak threshold spreading [32–34]. An important result is that Pastor-Satorras and Vespignani [32] used a heterogeneous mean-field theory to describe the computer virus spreading on the Internet and revealed that the existence of some hubs may make the outbreak threshold vanish. On the other hand, infectivity and susceptibility are heterogeneous since different computers have distinct circumstances. Miller [35] revealed that the global virus is more likely to break out for homogeneous infectivity when the average transmissibility is fixed. In addition, he found that the attack rate was highest when the susceptibility was homogeneous and lowest when the variance was maximum. Lastly, the virus and information always transmit through different networks. Generally, the virus spreads on the computer network and the information transmits on the social network. Therefore, the virus-information dynamics spreading on two-layered multiplex networks are more realistic. Previous paragraphs have stated the state-of-the-art progresses for virus-information spreading on multiplex networks. To our best knowledge, systematic study still lacks for the interacting spreading dynamics including the above three aspects. In the paper, we first describe the mathematical model in Section 2. In Section 3, we develop a heterogeneous mean-field theory to describe the spreading dynamics. In Section 4, we perform extensive numerical simulations. Finally, we conclude the paper in Section 5.

2. Model Descriptions

In this section, we propose the virus-information coevolution spreading model on computer-social network M. We first introduce the computer-social network and then present the virus-information spreading model.

2.1. Computer-Social Network. We denote the two subnetworks as L_1 and L_2, respectively. The computer virus spreads on subnetwork L_1, and the information spreads on subnetwork L_2. In subnetwork L_1 (L_2), nodes represent the computers (users), and the edges stand for the relationships among computers (users). To build the two-layered complex networks, we use the following steps: (i) assigning the subnetwork sizes $N_1 = N_2 = N$; (ii) building subnetworks L_1 and L_2 by using the uncorrelated configuration model [36] (the degree distributions of subnetworks L_1 and L_2 are $P_1(k_1)$ and $P_2(k_2)$, respectively); and (iii) randomly matching nodes in two subnetworks. Specifically, we build an interlayer connection e for node i_1 and i_2, which means that the user i_2 uses computer i_1. By using the above methods, there are node inter- and intradegree correlations. As shown in Figure 1, we illustrate the computer-social network.

Mathematically, the computer-social network M can be represented by a adjacency matrix $U = \begin{pmatrix} A^1 & A^{12} \\ A^{21} & A^2 \end{pmatrix}$, where A^1 and A^2, respectively, stand for the adjacency matrixes of subnetworks L_1 and L_2. An element $A^x_{ij} = 1$ of subnetwork $x \in \{1, 2\}$ means that nodes i_x and j_x are connected. The matrixes A^{12} and A^{21} are the adjacency matrixes of interlayer network, where $A^{12}_{i_1 i_2} = 1$ means that node i_1 uses computer i_2. Note that $A^{12}_{i_1 i_2} = A^{21}_{i_2 i_1}$ for any values of i_1 and i_2. The average degrees of the two subnetworks can be denoted as $\langle k_1 \rangle = \sum_{i,j} A^1_{ij} = \sum_{k_1} k_1 P_1(k_1)$ and $\langle k_2 \rangle = \sum_{i,j} A^2_{ij} = \sum_{k_2} k \ {}_2P_2(k_2)$, respectively.

2.2. Virus-Information Spreading Model. We here adopt a susceptible-infected-recovered (SIR) model to describe the virus spreading on subnetwork L_1. A node in the susceptible state means that it does not get infected by the computer virus. An infected node represents that it is infected by the virus and can transmit it to one of its neighbors. A node in the recovered state means that it has recovered and does not change its state.

For the information spread on subnetwork L_2, we consider using the irreversible susceptible-informed-recovered (SIR) model [37]. A susceptible node means that it does not obtain information about the virus. An informed node indicates that it knows information about the virus and is willing to share it with its neighbors. A node in the recovered state means that it loses interest in the information and will not transmit it to its neighbors. In this paper, we denote the virus-information coevolution spreading as a SIR-SIR model.

The virus-information coevolution spreading dynamic evolves as follows. Initially, we randomly select a node i_1 in subnetwork L_1, that is to say, the computer virus infects node i_1. The corresponding node i_2, i.e., the user of computer i_1, is also set to be the infected state, since the user can release the information of his infection to his neighbors. At every time step t, each infected node v_1 in subnetwork L_1 tries to transmit the computer virus to one of its neighbors u_1, since every infected node usually communicates with one neighbor at a short time interval. In reality, the infection transmission depends on the "source" and "target" nodes [35]. That is to say, the infectivity and susceptibility of the system are distinct for different nodes. To include this factor,

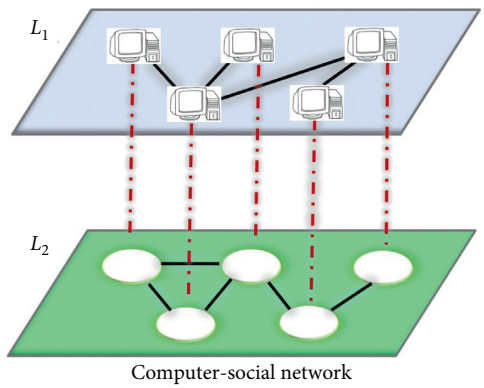

FIGURE 1: Illustration of computer-social networks. Subnetwork L_1 represents the computer network, and subnetwork L_2 stands for the social network.

we assume that nodes' infectivity and susceptibility depend on the degree of nodes. More specifically, the infectivity of node v_1 with degree k_1 is

$$\omega_{k_1}^1 = 1 - \left(1 - \alpha_1\right)^{k_1}, \tag{1}$$

where α_1 is the unit infectivity for a node with degree 1. Similarly, the susceptibility of node u_1 with degree k_1' is

$$\varpi_{k_1'}^1 = 1 - \left(1 - \alpha_1'\right)^{k_{1'}}, \tag{2}$$

where α_1' is the unit susceptibility for node with degree 1. Varying the values of α_1 and α_1', we get different infectivities and susceptibilities of the system. If node u_1 is susceptible, two different situations should be considered. (i) If the user u_2 of computer u_1 is in the susceptible state, the computer u_1 infects the virus with probability λ_1. Meanwhile, node u_2 obtains the information. Otherwise, u_2 is in the infected or recovered state, and nothing happens. (ii) If the user u_2 has already obtained the information before, the computer u_1 is infected by the virus with probability $q\lambda_1$, where $0 \le q \le 1$. We here use the parameter q to describe the degree of protection when a user knows the virus's spreading. The smaller the value of q, the stronger the protection against computer viruses. Every infected node recovers with probability γ_1.

The information about the virus spread on the subnetwork L_2 is as follows. At each time step t, every informed node v_2 transmits the information to one of its neighbor u_2 in subnetwork L_2 depending on the infectivity of v_2 and the susceptibility of u_2. The infectivity of v_2 with degree k_2 is

$$\omega_{k_2}^2 = 1 - \left(1 - \alpha_2\right)^{k_2}, \tag{3}$$

where α_2 is the unit infectivity. The susceptibility of u_2 with degree k_2' is

$$\varpi_{k_2'}^2 = 1 - \left(1 - \alpha_2'\right)^{k_{2'}}, \tag{4}$$

where α_2' is the unit susceptibility. The infection probability is λ_2. Finally, every informed node loses interest in transmitting the information with probability γ_2. The spreading ends when there are no nodes in the infected or informed state. In Table 1, we present the definitions of parameters and abbreviations.

3. Heterogeneous Mean-Field Theory

In this section, we develop a heterogeneous mean-field approach to describe the evolution of the virus-information spreading dynamics. In theory, we assume that nodes with same degrees have the same infection probability in statistical [32, 33, 38, 39]. In other words, the probability of nodes with the degree k is the same as each other.

We use the following parameters to describe the coevolution process. Denote $s_{k_1}^1(t)$, $\rho_{k_1}^1(t)$, and $r_{k_1}^1(t)$ as the probability that a node with degree k_1 is in the susceptible, infected, and recovered states at time t in subnetwork L_1, respectively. Similarly, we denote $s_{k_2}^2(t)$, $\rho_{k_2}^2(t)$, and $r_{k_2}^2(t)$ as the probability of node with degree k_2 in the susceptible, informed, and recovered states at time t in subnetwork L_2, respectively. Considering the degree distributions of subnetworks L_1 and L_2, we know the fraction of nodes in each state. For instance, the fraction of nodes in the susceptible state at time t is $S_1(t) = \sum_{k_1} P_1(k_1) s_{k_1}^1(t)$. In the final state, i.e., $t \longrightarrow \infty$, the fraction of nodes in the susceptible state is $S_1(\infty) \equiv S_1$.

Now we derive the expressions of the probability of nodes in each state. We know that $s_{k_1}^1(t)$ decreases with time t when nodes are infected by the virus. A susceptible computer u_1 with degree k_1 infected by the virus has two situations. (1) The corresponding node (i.e., the user) u_2 of node u_1 is in the susceptible state. In this situation, the infection transmitted to node u_1 should fulfill two necessary conditions.

(i) An infected neighbor v_1 of node u_1 contacts node u_1. In uncorrelated complex networks, the probability of node u_1 connecting to an infected neighbor v_1 with degree is k_1' is $((k_1' - 1)/\sum_{k_1} k_1 P_1(k_1))$, where k_1' is the degree of node v_1. Considering the degree distribution of subnetwork L_1, the average probability that a node connects to an infected neighbor through an edge is

$$\Theta_1(t) = \frac{1}{\langle k_1 \rangle} \sum_{k_1'} \omega_{k_1'}^1 (k_1' - 1) P_1(k_1') \rho_{k_1'}^1(t). \tag{5}$$

(ii) The infection is transmitted successfully with probability λ_1. According to the description of the model, for a node u_1 in the susceptible state, its corresponding node must also be in the susceptible state. However, the opposite situation does not always exist. Combining conditions (i) and (ii), we know situation (1) happens with probability $\lambda_1 k_1 \varpi_{k_1}^1 s_{k_1}^1(t) \Theta_1(t)$. Situation (2) indicates that node u_2 of node u_1 is in the informed state. Using a similar discussion with situation (1), we obtain the probability of situation (2) as follows: $q\lambda_1 k_1 \varpi_{k_1}^1 s_{k_1}^1(t) \Theta_1(t) [\sum_{k_2} P_2(k_2) \lambda_2 k_2 \varpi_{k_2}^2 \Theta_2(t)]$, where $\sum_{k_2} P_2(k_2) \lambda_2 k_2 \varpi_{k_2}^2 \Theta_2(t)$ is the probability that the corresponding node u_2 of u_1 is informed by neighbors in subnetwork L_2 at time t. $\Theta_2(t)$ will be defined later. The rate equation of $s_{k_1}^1(t)$ is

Table 1: Definitions of parameters and abbreviations.

Parameter	Definition
N_1	Subnetwork size of computer network L_1
N_2	Subnetwork size of social network L_2
$P_1(k_1)$	Degree distribution of computer network L_1
$P_2(k_2)$	Degree distribution of social network L_2
$\langle k_1 \rangle$	Average degree of computer network L_1
$\langle k_2 \rangle$	Average degree of social network L_2
$\omega_{k_1}^1$	Infectivity of node v_1 with degree k_1 in subnetwork L_1
$\omega_{k_2}^2$	Infectivity of node v_2 with degree k_2 in subnetwork L_2
$\varpi_{k_1'}^1$	Susceptibility of u_1 with degree k_1' in subnetwork L_1
$\varpi_{k_2'}^2$	Susceptibility of u_2 with degree k_2' in subnetwork L_2
α_1	Unit infectivity in subnetwork L_1
α_2	Unit infectivity in subnetwork L_2
α_1'	Unit susceptibility in subnetwork L_1
α_2'	Unit susceptibility in subnetwork L_2
q	Protection power
λ_1	Computer virus transmission probability
λ_2	Information transmission probability
γ_1	Computer virus recovery probability
γ_2	Information recovery probability
$s_{k_1}^1(t)$	Probability of node with degree k_1 in the susceptible state at time t in subnetwork L_1
$\rho_{k_1}^1(t)$	Probability of node with degree k_1 in the infected state at time t in subnetwork L_1
$r_{k_1}^1(t)$	Probability of node with degree k_1 in the recovered state at time t in subnetwork L_1
$s_{k_2}^2(t)$	Probability of node with degree k_2 in the susceptible state at time t in subnetwork L_2
$\rho_{k_2}^2(t)$	Probability of node with degree k_2 in the infected state at time t in subnetwork L_2
$r_{k_2}^2(t)$	Probability of node with degree k_2 in the recovered state at time t in subnetwork L_2
$\Theta_1(t)$	Average probability that a node connects to an infected neighbor through an edge in subnetwork L_1
$\Theta_2(t)$	Average probability that a node connects to an informed neighbor through an edge in subnetwork L_2

$$\frac{\mathrm{d}s_{k_1}^1(t)}{\mathrm{d}t} = -\lambda_1 k_1 \varpi_{k_1}^1 \Theta_1(t)\left[s_{k_1}^1(t) + q\sum_{k_2} P_2(k_2)\lambda_2 k_2 \varpi_{k_2}^2 \Theta_2(t)\right]. \tag{6}$$

The evolution of $\rho_{k_1}^1(t)$ is

$$\frac{\mathrm{d}\rho_{k_1}^1(t)}{\mathrm{d}t} = \lambda_1 k_1 \varpi_{k_1}^1 \Theta_1(t)\left[s_{k_1}^1(t) + q\sum_{k_2} P_2(k_2)\lambda_2 k_2 \varpi_{k_2}^2 \Theta_2(t)\right] - \gamma_1 \rho_{k_1}^1(t), \tag{7}$$

where $\gamma_1 \rho_{k_1}^1(t)$ is the fraction of nodes recovered at time t. Finally, the evolution of $r_{k_1}^1(t)$ is

$$\frac{\mathrm{d}r_{k_1}^1(t)}{\mathrm{d}t} = \gamma_1 \rho_{k_1}^1(t). \tag{8}$$

According to equations (6)–(8), we obtain the evolution of computer virus spreading on subnetwork L_1.

Now, we study the rate equations of the information about the virus spreading on social network L_2. There are two different situations for the reduction of $s_{k_2}^2(t)$. For the first situation, the susceptible node u_2 with degree k_2 is infected by its informed neighbor v_2. The infection probability is $\lambda_2 k_2 \varpi_{k_2}^2 s_{k_2}^2(t)\Theta_2(t)$, where $\Theta_2(t)$ denotes the probability of an edge connecting to an informed neighbor in subnetwork L_2. The expression of $\Theta_2(t)$ can be expressed as

$$\Theta_2(t) = \frac{1}{\langle k_2 \rangle}\sum_{k_2'} \omega_{k_2'}^2 (k_2' - 1) P_2(k_2') \rho_{k_2'}^2(t). \tag{9}$$

The second situation of node u_2 obtaining the information is that the corresponding node u_1 of u_2 is infected by the computer virus through an edge of u_1 with probability $\lambda_1 k_1 \varpi_{k_1}^1 s_{k_2}^2(t)\Theta_1(t)$. Since u_2 and u_1 are randomly coupled, the averaged infection probability of u_1 is $\lambda_1 \langle k_1 \rangle \langle \varpi_{k_1}^1 \rangle s_{k_2}^2(t)\Theta_1(t)$, where $\langle \varpi_{k_1}^1 \rangle = \sum_{k_1} P_1(k_1)\varpi_{k_1}^1$. Combining the two situations, we obtain the rate equation of $s^2 k_2(t)$ as

$$\frac{\mathrm{d}s_{k_2}^2(t)}{\mathrm{d}t} = -s_{k_2}^2(t)\left[\lambda_2 k_2 \varpi_{k_2}^2 \Theta_2(t) + \lambda_1 \langle k_1 \rangle \langle \varpi_{k_1}^1 \rangle \Theta_1(t)\right]. \tag{10}$$

With the similar discussion about the virus spreading on subnetwork L_1, we have

$$\frac{\mathrm{d}\rho_{k_2}^2(t)}{\mathrm{d}t} = s_{k_2}^2(t)\left[\lambda_2 k_2 \varpi_{k_2}^2 \Theta_2(t) + \lambda_1 \langle k_1\rangle \langle \varpi_{k_1}^1\rangle \Theta_1(t)\right] - \gamma_2 \rho_{k_2}^1(t), \tag{11}$$

$$\frac{\mathrm{d}r_{k_2}^2(t)}{\mathrm{d}t} = \gamma_2 \rho_{k_2}^2(t). \tag{12}$$

With the above equations, we know the fraction of nodes in each state at subnetworks L_1 and L_2.

In the following, we study the global outbreak conditions of the computer virus and information spreading. For global information outbreak condition, we can linearize equations (7) and (11) around the initial conditions, i.e., $s_{k_1}^1 \approx 1$, $s_{k_2}^2 \approx 1$. We know that $s_{k_1}^1 = 1$, $s_{k_2}^2 = 1$, $\rho_{k_1}^1 = 0$, and $\rho_{k_2}^2 = 0$ are trivial solutions. Denote a vector $\overrightarrow{\rho} = (\overrightarrow{\rho_1}, \overrightarrow{\rho_2})^T$, where $\overrightarrow{\rho_1} = (\rho_{k_1=1}^1, \ldots, \rho_{k_{1,\max}}^1)$, $\overrightarrow{\rho_2} = \rho_{k_2=1}^2, \ldots, \rho_{k_{2,\max}}^2$, and $k_{1,\max}^1$ and $k_{2,\max}^2$ represent the maximal degrees of subnetworks L_1 and L_2, respectively. We perform a Taylor expansion for equations (7) and (11) at $s_{k_1}^1 = 1$, $s_{k_2}^2 = 1$, $\rho_{k_1}^1 = 0$, and $\rho_{k_2}^2 = 0$ and neglect the high order of $\overrightarrow{\rho}$. We have

$$\frac{\mathrm{d}\overrightarrow{\rho}}{\mathrm{d}t} = \mathbf{J}\overrightarrow{\rho}, \tag{13}$$

where $\mathbf{J}$ is the Jacobian matrix. The expression of $\mathbf{J}$ is

$$\mathbf{J} = \begin{pmatrix} \frac{\partial\rho_1^1}{\partial\rho_1^1} & \frac{\partial\rho_1^1}{\partial\rho_2^1} & \cdots & \frac{\partial\rho_1^1}{\partial\rho_{1,\max}^1} & \frac{\partial\rho_1^1}{\partial\rho_1^2} & \frac{\partial\rho_1^1}{\partial\rho_2^2} & \cdots & \frac{\partial\rho_1^1}{\partial\rho_{2,\max}^2} \\ \frac{\partial\rho_2^1}{\partial\rho_1^1} & \frac{\partial\rho_2^1}{\partial\rho_2^1} & \cdots & \frac{\partial\rho_2^1}{\partial\rho_{1,\max}^1} & \frac{\partial\rho_2^1}{\partial\rho_1^2} & \frac{\partial\rho_2^1}{\partial\rho_2^2} & \cdots & \frac{\partial\rho_2^1}{\partial\rho_{2,\max}^2} \\ \vdots & \vdots & \vdots & \vdots & \vdots & \vdots & \vdots & \vdots \\ \frac{\partial\rho_{1,\max}^1}{\partial\rho_1^1} & \frac{\partial\rho_{1,\max}^1}{\partial\rho_2^1} & \cdots & \frac{\partial\rho_{1,\max}^1}{\partial\rho_{1,\max}^1} & \frac{\partial\rho_{1,\max}^1}{\partial\rho_1^2} & \frac{\partial\rho_{1,\max}^1}{\partial\rho_2^2} & \cdots & \frac{\partial\rho_{1,\max}^1}{\partial\rho_{2,\max}^2} \\ \frac{\partial\rho_1^2}{\partial\rho_1^1} & \frac{\partial\rho_1^2}{\partial\rho_2^1} & \cdots & \frac{\partial\rho_1^2}{\partial\rho_{1,\max}^1} & \frac{\partial\rho_1^2}{\partial\rho_1^2} & \frac{\partial\rho_1^2}{\partial\rho_2^2} & \cdots & \frac{\partial\rho_1^2}{\partial\rho_{2,\max}^2} \\ \frac{\partial\rho_2^2}{\partial\rho_1^1} & \frac{\partial\rho_2^2}{\partial\rho_2^1} & \cdots & \frac{\partial\rho_2^2}{\partial\rho_{1,\max}^1} & \frac{\partial\rho_2^2}{\partial\rho_1^2} & \frac{\partial\rho_2^2}{\partial\rho_2^2} & \cdots & \frac{\partial\rho_2^2}{\partial\rho_{2,\max}^2} \\ \vdots & \vdots & \vdots & \vdots & \vdots & \vdots & \vdots & \vdots \\ \frac{\partial\rho_{1,\max}^2}{\partial\rho_1^1} & \frac{\partial\rho_{1,\max}^2}{\partial\rho_2^1} & \cdots & \frac{\partial\rho_{1,\max}^2}{\partial\rho_{1,\max}^1} & \frac{\partial\rho_{1,\max}^2}{\partial\rho_1^2} & \frac{\partial\rho_{1,\max}^2}{\partial\rho_2^2} & \cdots & \frac{\partial\rho_{1,\max}^2}{\partial\rho_{2,\max}^2} \end{pmatrix}. \tag{14}$$

The Jacobian matrix $\mathbf{J}$ can be further expressed as block matrix as

$$\mathbf{J} = \begin{pmatrix} C^1 & D^2 \\ D^1 & C^2 \end{pmatrix}, \tag{15}$$

where dimensions of C^1, C^2, D^1, and D^2 are $k_{1,\max} \times k_{1,\max}$, $k_{2,\max} \times k_{2,\max}$, $k_{2,\max} \times k_{1,\max}$, and $k_{1,\max} \times k_{2,\max}$, respectively. When the global information on subnetwork L_2 breaks out, the largest eigenvalue of $\mathbf{J}$ is larger than zero. The global information outbreak condition is

$$\Lambda_1(\mathbf{J}) = 0, \tag{16}$$

where $\Lambda_1(\mathbf{J})$ is the largest eigenvalue of $\mathbf{J}$. For the virus outbreak condition, we cannot solve it directly. When the network is extensive, we can use the competing percolation theory [40]. That is to say, we can process the information spreading on subnetwork L_2 first and then the virus spreading on subnetwork L_1.

4. Simulation Results

In this section, we perform numerical simulations to study the virus-information spreading dynamics on computer-social network. To build the computer-social network, we use the uncorrelated configuration model [36]. We set the degree distributions of subnetworks L_1 and L_2 as $P_1(k_1) \sim k^{-\chi_1}$ and $P_2(k_2) \sim k^{-\chi_2}$, respectively, where χ_1 and χ_2, respectively, represent the degree exponents. There is no inter- and intralayer degree-degree correlations. In numerical simulations, we set the average degrees of the two subnetworks as $\langle k_1\rangle = \langle k_2\rangle = 8$, the network sizes as $N_1 = N_2 = 10^4$, and the degree exponent as $\chi_1 = \chi_2 = 3.0$. We set $\alpha_1 = \alpha_1'$ and $\alpha_2 = \alpha_2'$. Initially, we randomly select 5 seeds in subnetwork L_1. All results presented in this paper are averaged over at least 2000 times.

We first study the virus and information spreading sizes, respectively, denoted as $R_1 = 1 - S_1$ and $R_2 = 1 - S_2$, versus virus transmission probability λ_1 as shown in Figure 2. We find that R_1 increases with $\alpha_1 = \alpha_2$, i.e., the virus is more likely to spread when the infectivity and susceptibility are large. Specifically, we note that the virus cannot spread for any values of λ_1 when $\alpha_1 = \alpha_2$ are small, e.g., $\alpha_1 = \alpha_2 = 0.0$ and 0.2. When $\alpha_1 = \alpha_2$ are large enough, enlarging their values cannot promote the virus spreading. When comparing the effects of information spreading on virus spreading, i.e., increasing λ_2, the virus spreading can be suppressed, as shown in Figures 2(a)–2(d). That is to say, to contain the virus spreading, we can transmit more information about the virus on the social network. For the information spreading on subnetwork L_2, i.e., the social network, we find that R_2 increases with λ_1, λ_2, and $\alpha_1 = \alpha_2$, since the users have more chances to obtain the information.

In Figure 3, we further investigate the effects of protection power q on the virus-information spreading for different values of $\alpha_1 = \alpha_2$ and λ_2. Generally speaking, we find similar results with that discussed in Figure 2. When the protection power is large, we find that the virus spreading size is relatively smaller, i.e., $R_1(q = 0.8) \geq R_1(q = 0.5)$, since the susceptible nodes are less likely to be infected by neighbors. We also note that R_2 (q =

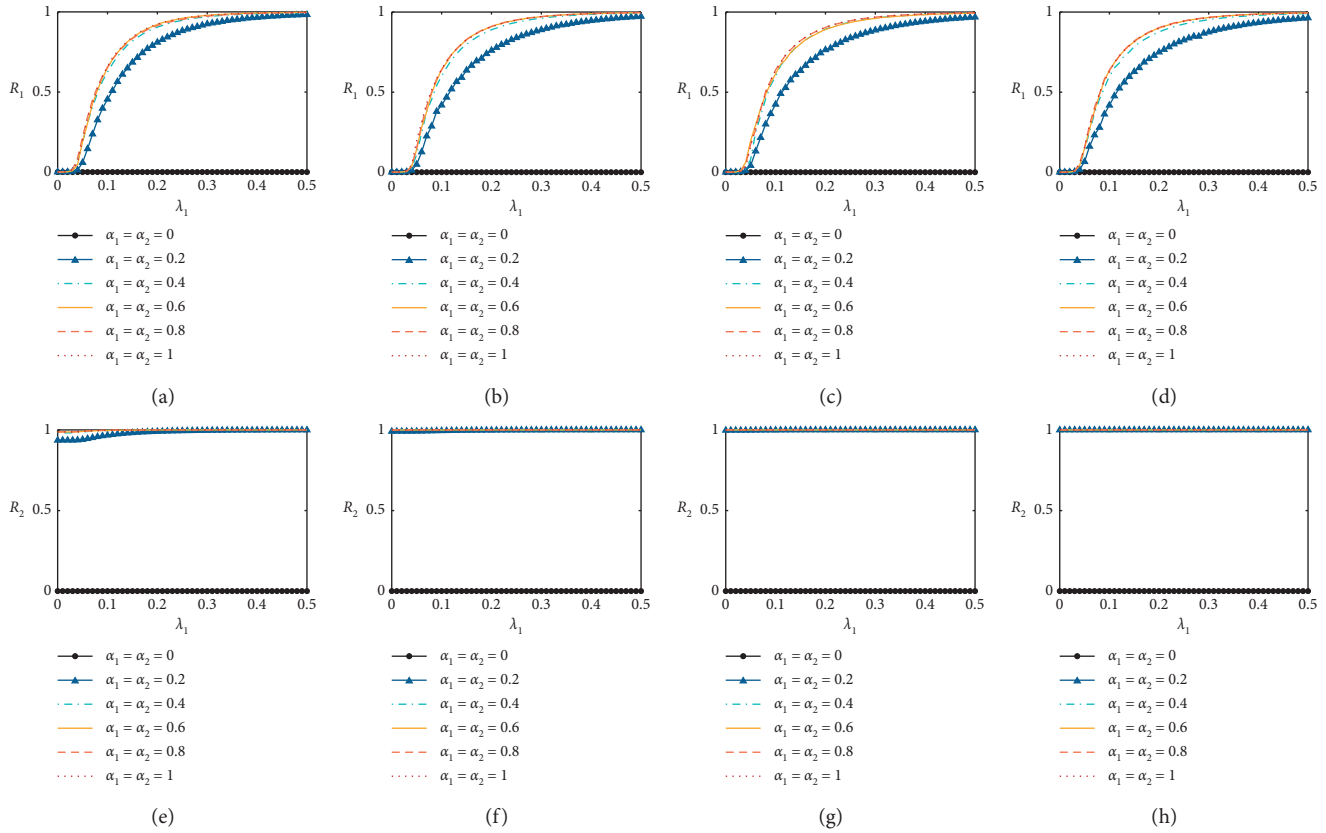

FIGURE 2: Virus spreading size R_1 and information spreading size R_2 versus computer virus transmission probability λ_1 with $q = 0.5$. R_1 versus λ_1 with (a) $\lambda_2 = 0.2$, (b) $\lambda_2 = 0.4$, (c) $\lambda_2 = 0.6$, and (d) $\lambda_2 = 0.8$. R_2 versus λ_1 with (e) $\lambda_2 = 0.2$, (f) $\lambda_2 = 0.4$, (g) $\lambda_2 = 0.6$, and (h) $\lambda_2 = 0.8$. Other parameters are set to be $\gamma_1 = \gamma_2 = 0.2$ and $\lambda_2 = 0.8$.

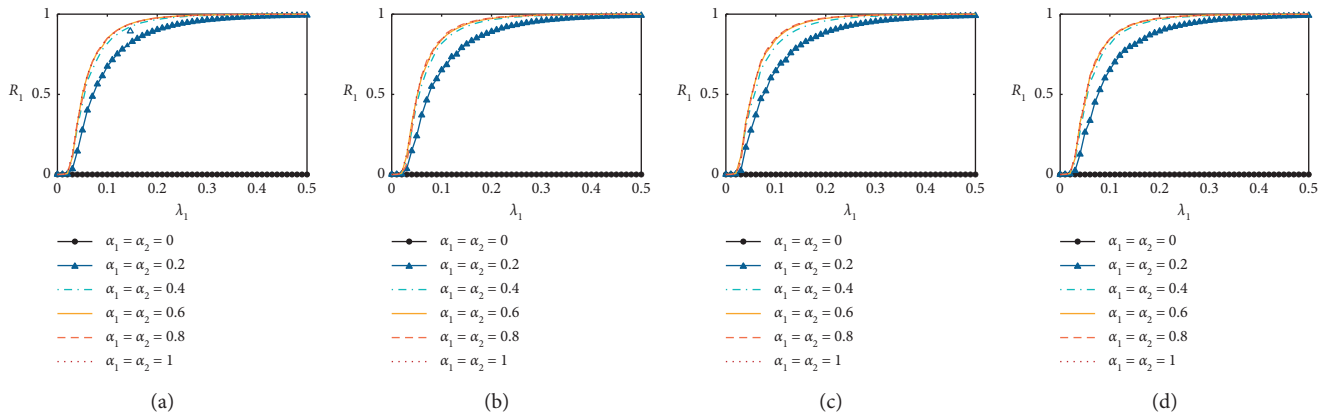

FIGURE 3: Continued.

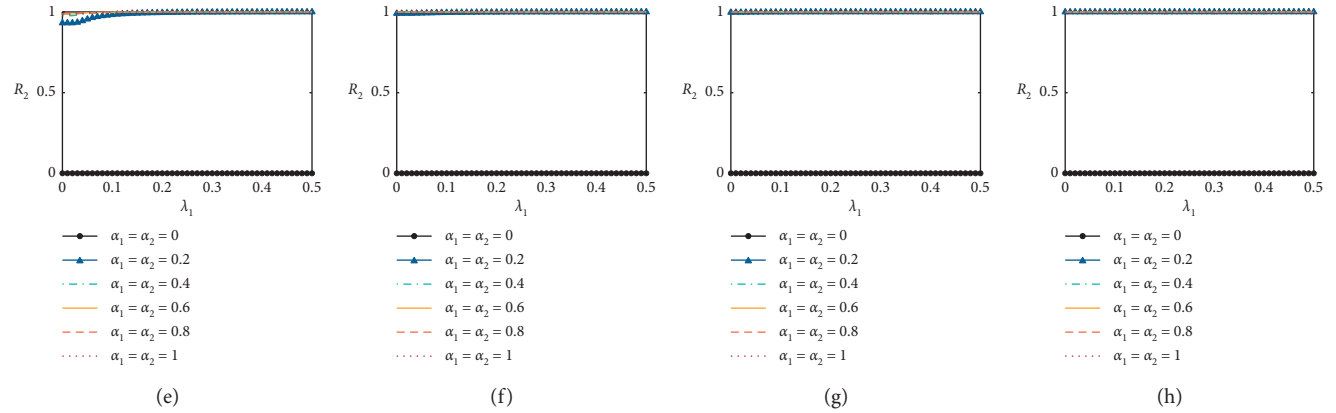

FIGURE 3: Virus spreading size R_1 and information spreading size R_2 versus computer virus transmission probability λ_1 with $q = 0.8$. R_1 versus λ_1 with (a) $\lambda_2 = 0.2$, (b) $\lambda_2 = 0.4$, (c) $\lambda_2 = 0.6$, and (d) $\lambda_2 = 0.8$. R_2 versus λ_1 with (e) $\lambda_2 = 0.2$, (f) $\lambda_2 = 0.4$, (g) $\lambda_2 = 0.6$, and (h) $\lambda_2 = 0.8$. Other parameters are set to be $\gamma_1 = \gamma_2 = 0.2$ and $\lambda_2 = 0.8$.

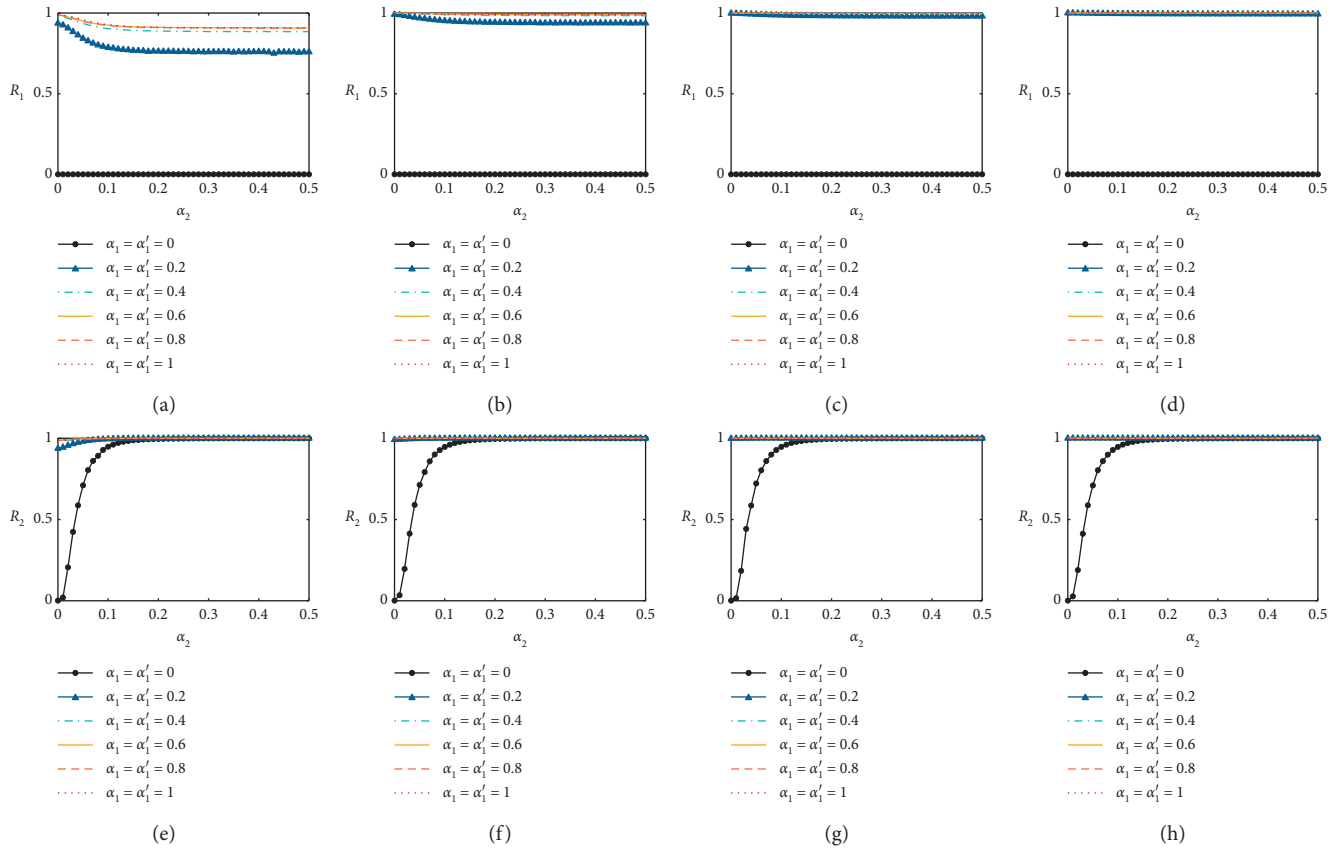

FIGURE 4: Virus spreading size R_1 and information spreading size R_2 versus computer virus transmission probability λ_1 with $q = 0.5$. R_1 versus α_2 with (a) $\lambda_1 = 0.2$, (b) $\lambda_1 = 0.4$, (c) $\lambda_1 = 0.6$, and (d) $\lambda_1 = 0.8$. R_2 versus α_2 with (e) $\lambda_1 = 0.2$, (f) $\lambda_1 = 0.4$, (g) $\lambda_1 = 0.6$, and (h) $\lambda_1 = 0.8$. Other parameters are set to be $\gamma_1 = \gamma_2 = 0.2$ and $\lambda_2 = 0.5$.

$0.8) \geq R_2\,(q = 0.5)$ since the promotion of virus spreading on information spreading is decreased.

In Figure 4, we study the effects of susceptibility and infectivity in detail. We find that R_1 decreases with the increase of susceptibility and infectivity of L_2. That is to say, the virus spreading can be suppressed by increasing the susceptibility and infectivity. We can explain the results as follows. Increasing susceptibility and infectivity, the information will be widely spread on social network (see Figures 4(e)–4(g)), and more susceptible nodes in subnetwork L_1 will take measures to protect themselves from being infected. As a result, R_1 decreases with α_2.

Finally, we studied the virus-information spreading as a function of α_2 when the protection power is lower with $q = 0.8$ in Figure 5. We reveal similar phenomena as shown in Figure 4.

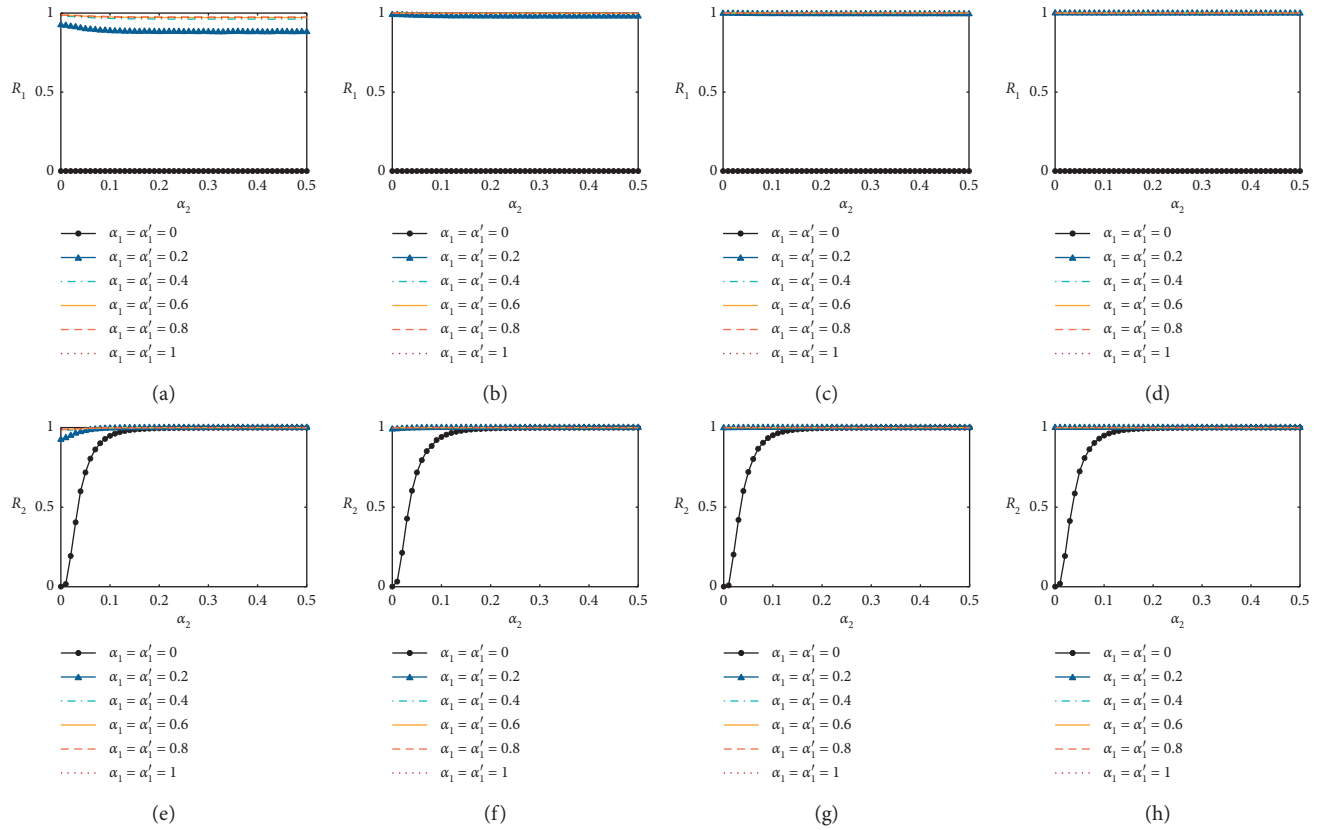

FIGURE 5: Virus spreading size R_1 and information spreading size R_2 versus computer virus transmission probability λ_1 with $q = 0.8$. R_1 versus α_2 with (a) $\lambda_1 = 0.2$, (b) $\lambda_1 = 0.4$, (c) $\lambda_1 = 0.6$, and (d) $\lambda_1 = 0.8$. R_2 versus α_2 with (e) $\lambda_1 = 0.2$, (f) $\lambda_1 = 0.4$, (g) $\lambda_1 = 0.6$, and (h) $\lambda_1 = 0.8$. Other parameters are set to be $\gamma_1 = \gamma_2 = 0.2$ and $\lambda_2 = 0.5$.

We note that $R_1(q = 0.5) \geq R_1(q = 0.8)$ and $R_2(q = 0.5) \geq R_2(q = 0.8)$ since the protection power is decreased.

5. Discussion

In this paper, we studied the virus-information spreading dynamics on computer-social multiplex networks. We first proposed a mathematical model to describe the co-evolution spreading dynamics. In this model, we assumed that nodes' susceptibility and infectivity are heterogeneous and positively correlated with the node's degree. To describe the spreading dynamics, we adopt a generalized heterogeneous mean-field approach. Using extensive numerical simulations, we revealed that the virus spreading dynamics can be significantly suppressed by promoting the information spreading on the computer network or decreasing the susceptibility and infectivity of nodes. Our results provide some insight into containing the virus spreading.

Data Availability

The data used to support the findings of this study are available from the corresponding author upon request.

Conflicts of Interest

The authors declare that there are no conflicts of interest regarding the publication of this paper.

Acknowledgments

This study was partially supported by the Sichuan Science and Technology Program (2020YFG0010).

References

[1] W. Wang, Q.-H. Liu, J. Liang, Y. Hu, and T. Zhou, "Co-evolution spreading in complex networks," *Physics Reports*, vol. 820, p. 1, 2019.

[2] S. Lehmann and Y.-Y. Ahn, *Complex Spreading Phenomena in Social Systems*, Springer, Berlin, Germany, 2018.

[3] P. Szor, *The Art of Computer Virus Research and Defense: Art Comp Virus Res Defense _p1*, Pearson Education, London, UK, 2005.

[4] L.-X. Yang, X. Yang, L. Wen, and J. Liu, "A novel computer virus propagation model and its dynamics," *International Journal of Computer Mathematics*, vol. 89, no. 17, p. 2307, 2012.

[5] F. D. Sahneh and C. Scoglio, "Competitive epidemic spreading over arbitrary multilayer networks," *Physical Review E*, vol. 89, Article ID 062817, 2014.

[6] L.-X. Yang, X. Yang, and Y. Y. Tang, "An effective rumor-containing strategy," *IEEE Transactions on Network Science and Engineering*, vol. 5, p. 2, 2017.
[7] C. Granell, S. Gómez, and A. Arenas, "Dynamical interplay between awareness and epidemic spreading in multiplex networks," *Physical Review Letters*, vol. 111, Article ID 128701, 2013.
[8] C. Granell, S. Gómez, and A. Arenas, "Competing spreading processes on multiplex networks: awareness and epidemics," *Physical Review E*, vol. 90, Article ID 012808, 2014.
[9] P. C. Ventura, Y. Moreno, and F. A. Rodrigues, "The role of time scale in the spreading of asymmetrically interacting diseases," 2020, http://arxiv.org/abs/2007.02774.
[10] M. E. Newman, "Threshold effects for two pathogens spreading on a network," *Physical Review Letters*, vol. 95, Article ID 108701, 2005.
[11] M. E. Newman and C. R. Ferrario, "Interacting epidemics and coinfection on contact networks," *PLoS One*, vol. 8, Article ID e71321, 2013.
[12] B. Karrer and M. E. Newman, "Competing epidemics on complex networks," *Physical Review E*, vol. 84, Article ID 036106, 2011.
[13] M. Kivelä, A. Arenas, M. Barthelemy, J. P. Gleeson, Y. Moreno, and M. A. Porter, "Multilayer networks," *Journal of Complex Networks*, vol. 2, no. 3, p. 203, 2014.
[14] M. De Domenico, A. Solé-Ribalta, E. Cozzo et al., "Mathematical formulation of multilayer networks," *Physical Review X*, vol. 3, Article ID 041022, 2013.
[15] M. De Domenico, V. Nicosia, A. Arenas, and V. Latora, "Structural reducibility of multilayer networks," *Nature Communications*, vol. 6, p. 1, 2015.
[16] G. Bianconi, *Multilayer Networks: Structure and Function*, Oxford University Press, Oxford, UK, 2018.
[17] Z. Wang, L. Wang, A. Szolnoki, and M. Perc, "Evolutionary games on multilayer networks: a colloquium," *The European Physical Journal B*, vol. 88, p. 1, 2015.
[18] X. Zhang, S. Boccaletti, S. Guan, and Z. Liu, "Explosive synchronization in adaptive and multilayer networks," *Physical Review Letters*, vol. 114, Article ID 038701, 2015.
[19] J. Gao, S. V. Buldyrev, H. E. Stanley, and S. Havlin, "Networks formed from interdependent networks," *Nature Physics*, vol. 8, no. 1, p. 40, 2012.
[20] D. Zhou, J. Gao, H. E. Stanley, and S. Havlin, "Percolation of partially interdependent scale-free networks," *Physical Review E*, vol. 87, Article ID 052812, 2013.
[21] F. Radicchi and A. Arenas, "Abrupt transition in the structural formation of interconnected networks," *Nature Physics*, vol. 9, no. 11, p. 717, 2013.
[22] S. Gomez, A. Diaz-Guilera, J. Gomez-Gardenes, C. J. Perez-Vicente, Y. Moreno, and A. Arenas, "Diffusion dynamics on multiplex networks," *Physical Review Letters*, vol. 110, Article ID 028701, 2013.
[23] M. Dickison, S. Havlin, and H. E. Stanley, "Epidemics on interconnected networks," *Physical Review E*, vol. 85, Article ID 066109, 2012.
[24] M. Pósfai, J. Gao, S. P. Cornelius, A.-L. Barabási, and R. M. D'Souza, "Controllability of multiplex, multi-timescale networks," *Physical Review E*, vol. 94, Article ID 032316, 2016.
[25] L. V. Gambuzza, M. Frasca, and J. Gómez-Gardeñes, "Intra-layer synchronization in multiplex networks," *EPL (Europhysics Letters)*, vol. 110, no. 2, Article ID 20010, 2015.
[26] L. Tang, X. Wu, J. Lü, J.-a. Lu, and R. M. D'Souza, "Master stability functions for complete, intralayer," *Physical Review E*, vol. 99, Article ID 012304, 2019.
[27] S. Jalan, V. Rathore, A. D. Kachhvah, and A. Yadav, "Inhibition-induced explosive synchronization in multiplex networks," *Physical Review E*, vol. 99, Article ID 062305, 2019.
[28] Z. Wang, Q. Guo, S. Sun, and C. Xia, "The impact of awareness diffusion on SIR-like epidemics in multiplex networks," *Applied Mathematics and Computation*, vol. 349, p. 134, 2019.
[29] C. Zheng, C. Xia, Q. Guo, and M. Dehmer, "Interplay between SIR-based disease spreading and awareness diffusion on multiplex networks," *Journal of Parallel and Distributed Computing*, vol. 115, p. 20, 2018.
[30] J.-Q. Kan and H.-F. Zhang, "Effects of awareness diffusion and self-initiated awareness behavior on epidemic spreading-an approach based on multiplex networks," *Communications in Nonlinear Science and Numerical Simulation*, vol. 44, p. 193, 2017.
[31] E. Massaro and F. Bagnoli, "Epidemic spreading and risk perception in multiplex," *Physical Review E*, vol. 90, Article ID 052817, 2014.
[32] R. Pastor-Satorras and A. Vespignani, "Epidemic dynamics and endemic states in complex networks," *Physical Review E*, vol. 63, Article ID 066117, 2001.
[33] R. Pastor-Satorras and A. Vespignani, "Epidemic dynamics in finite size scale-free networks," *Physical Review E*, vol. 65, Article ID 035108, 2002.
[34] R. Pastor-Satorras, C. Castellano, P. Van Mieghem, and A. Vespignani, "Epidemic processes in complex networks," *Reviews of Modern Physics*, vol. 87, no. 3, p. 925, 2015.
[35] J. C. Miller, "Natural visions: the power of images in american environmental reform," *Physical Review E*, vol. 76, Article ID 010101, 2007.
[36] M. Catanzaro, M. Boguñá, and R. Pastor-Satorras, "Diffusion-annihilation processes in complex networks," *Physical Review E*, vol. 71, Article ID 027103, 2005.
[37] Z.-K. Zhang, C. Liu, X.-X. Zhan, X. Lu, C.-X. Zhang, and Y.-C. Zhang, "Dynamics of information diffusion and its applications on complex networks," *Physics Reports*, vol. 651, p. 1, 2016.
[38] W. Wang, M. Tang, H. E. Stanley, and L. A. Braunstein, "Unification of theoretical approaches for epidemic spreading on complex networks," *Reports on Progress in Physics*, vol. 80, Article ID 036603, 2017.
[39] Y. Moreno, R. Pastor-Satorras, and A. Vespignani, "Epidemic outbreaks in complex heterogeneous networks," *The European Physical Journal B*, vol. 26, no. 4, p. 521, 2002.
[40] B. Karrer and M. E. J. Newman, "Random graphs containing arbitrary distributions of subgraphs," *Physical Review E*, vol. 82, Article ID 016101, 2010.

Hindawi
Complexity
Volume 2021, Article ID 6656797, 11 pages
https://doi.org/10.1155/2021/6656797

Research Article

Dual Generative Network with Discriminative Information for Generalized Zero-Shot Learning

Tingting Xu, Ye Zhao, and Xueliang Liu

School of Computer and Information, Hefei University of Technology, Hefei 230000, China

Correspondence should be addressed to Ye Zhao; zhaoye@hfut.edu.cn

Received 17 December 2020; Revised 15 January 2021; Accepted 20 February 2021; Published 28 February 2021

Academic Editor: Chenquan Gan

Zero-shot learning is dedicated to solving the classification problem of unseen categories, while generalized zero-shot learning aims to classify the samples selected from both seen classes and unseen classes, in which "seen" and "unseen" classes indicate whether they can be used in the training process, and if so, they indicate seen classes, and vice versa. Nowadays, with the promotion of deep learning technology, the performance of zero-shot learning has been greatly improved. Generalized zero-shot learning is a challenging topic that has promising prospects in many realistic scenarios. Although the zero-shot learning task has made gratifying progress, there is still a strong deviation between seen classes and unseen classes in the existing methods. Recent methods focus on learning a unified semantic-aligned visual representation to transfer knowledge between two domains, while ignoring the intrinsic characteristics of visual features which are discriminative enough to be classified by itself. To solve the above problems, we propose a novel model that uses the discriminative information of visual features to optimize the generative module, in which the generative module is a dual generation network framework composed of conditional VAE and improved WGAN. Specifically, the model uses the discrimination information of visual features, according to the relevant semantic embedding, synthesizes the visual features of unseen categories by using the learned generator, and then trains the final softmax classifier by using the generated visual features, thus realizing the recognition of unseen categories. In addition, this paper also analyzes the effect of the additional classifiers with different structures on the transmission of discriminative information. We have conducted a lot of experiments on six commonly used benchmark datasets (AWA1, AWA2, APY, FLO, SUN, and CUB). The experimental results show that our model outperforms several state-of-the-art methods for both traditional as well as generalized zero-shot learning.

1. Introduction

In recent years, deep learning [1–4] has achieved great success in a wide range of computer vision and machine learning tasks [5], including face recognition, emotion classification, and visual question answering. In most cases, these deep learning models are more effective than human beings in many aspects, because they can observe potential information that may be ignored by human eyes in pictures. However, as the inventor of neural network, human beings are better at identifying objects they have never seen before through some prior semantic knowledge about these novel objects. In this respect, the effect of deep learning is not as good as that of humans. It precisely is because deep learning tasks for image recognition rely heavily on fully-supervised training, so they need a very large amount of labeled data. However, some object classes are difficult to obtain, such as the image data of endangered species and newly produced commodities. Moreover, even if they get the labeled data of related classes, they will still face the problem of unbalanced data. It is very difficult to obtain images of these objects, let alone a large number of labeled samples. Therefore, training models with a large number of labeled data are unrealistic. In this background, the concept of zero-shot learning has been put forward, which has attracted wide attention in the field of computer vision and has been greatly developed.

As there are too many classes in the real world, it is impossible to collect enough labeled data for each class. In this case, the task of zero-shot learning is desirable, but it is

challenging. In the literature [6–10], zero-shot learning is usually realized by using the marked samples of seen categories and category-related semantic embedding which is regarded as auxiliary information. The semantic embedding, which encodes the interclass relationships, is usually attribute, word vector, or sentence embedding. Therefore, seen classes and unseen classes are shared in semantic embedding space. In traditional zero-shot learning settings [11, 12], the goal is to train an image classifier on the seen classes and then test the trained classifier on unseen classes, where the seen classes and unseen classes are disjoint. However, the traditional zero-shot learning setting is not realistic, and it is not always applicable in the real world, because in reality, the test images can come from the seen classes. Therefore, there is such a trend that we hope the trained classifier can not only identify unseen classes but also seen classes, which is called generalized zero-shot learning [13, 14]. In the following articles, we uniformly express the traditional zero-shot learning as ZSL and the generalized zero-shot learning as GZSL. The main difference between ZSL and GZSL is whether the label space contains seen classes during the test period. In this work, we have conducted comparative experiments to study both ZSL and GZSL by synthesizing visual features of unseen classes with using the potential and valuable discriminative information.

In this paper, we point out the existing problems of ZSL and GZSL works reported recently, and we analyze the effectiveness of the dual generative network proposed in this paper as well as the discriminative information of visual feature representation. In the early days, as is illustrated in Figure 1(a), most methods [7, 11, 15–18] mapped image visual features to the semantic space to solve ZSL tasks based on class attribute embeddings or other side knowledge. However, using semantic space as the mapping space will suffer from the hubness problem pointed out in [19–21]. It is because projecting high-dimensional visual features to low-dimensional semantic space will greatly reduce the diversity of features that some points from different classes may become more clustered as a hub, as shown in Figure 2. In order to alleviate the hubness problem, some works [19–21] proposed to map semantic features into the visual space as illustrated in Figure 1(b). However, this will lead to another problem called domain shift. For example, the tail of a pig and the tail of a horse are similar in semantic space, but they are quite different in visual space, as shown in Figure 3. Then, the concept of a shared latent space was put forward. People mapped visual features and semantic attributes into a latent space at the same time, as shown in Figure 1(c), and performed nearest neighbor search to calculate the average per-class top-1 accuracy. This shared latent space was considered to alleviate the hubness and shifting problems, but the generalization ability of this method is poor. When using mapping methods for GZSL, the performance will be significantly degraded. Our dual generation model combines the advantages of improved WGAN and conditional VAE, which can alleviate hubness and shifting problems, thus effectively achieving the goal of zero-shot learning and generalized zero-shot learning.

In contrast, most recent ZSL and GZSL approaches [8, 22–25] are based on generative adversarial network [26], which aims at directly optimizing the divergence between real and generated data distributions. The work of Xian et al. [8] learns a GAN by using the seen class visual features and the corresponding semantic embedding that are manually annotated attributes or word vector [27] representations. Fake visual features of the unseen categories are synthesized using the trained generator and then used together with the real visual features of seen classes to train ZSL classifiers in a fully-supervised setting. But GANs are often suffering from mode collapse and unstable training issues. Inspired by the idea of generative adversarial networks, our proposed dual generative framework combines the advantages of conditional variational auto encoder network and improved WGAN, with the discriminative information by using an additional classifier trained on the seen classes to increase the diversity and distinguishability of samples that are generated by the generator. Among them, the improved WGAN can overcome the mode collapse problem, and VAE can alleviate the unstable problem of GAN training, so that our model can stably and quickly generate visual features corresponding to categories according to semantic embedding.

As described above, we combine the advantages of improved WGAN and conditional VAE together with intrinsic characteristics of visual feature representation itself by using an additional classifier to propose a new model called dual generative network with discriminative information (DGDI). Compared with the previous generative methods for ZSL whose models suffer from mode collapse problems [28, 29], our model is more stable by using conditional VAE to assist GAN in generating visual features. In this work, our main task is to obtain a robust generator to synthesis visual features of the unlabeled classes. In particular, if the generator learns discriminative visual feature data with sufficient variation, the generated data should be useful for implementing supervised learning. Moreover, we consider our dual generative framework that was composed by improved WGAN and conditional VAE can learn the complementary information of semantic space, so we believe that our model can produce higher quality visual features from semantic embeddings.

Our main contributions are summarized as follows: (1) we propose a novel generative model named DGDI with combining the advantages of improved WGAN and conditional VAE, which can learn complementary information from semantic embeddings. (2) In contrast to previous zero-shot learning works, we add an additional classifier loss to train the generator by using the intrinsic characteristics of visual feature representation, which makes the synthesized visual features more diverse and distinguishable. (3) We conduct extensive experiments that demonstrate the effectiveness of our proposed model and the results maintain high accuracy for both ZSL and GZSL on six widely used benchmark datasets. In addition, in order to make better use of the discriminative information expressed by visual features, we also analyze the effects of classifiers with different structures. (4) We also conduct visual experiments on synthetic visual features from unseen classes by t-SNE [30], which intuitively proves the effective generation ability of our model.

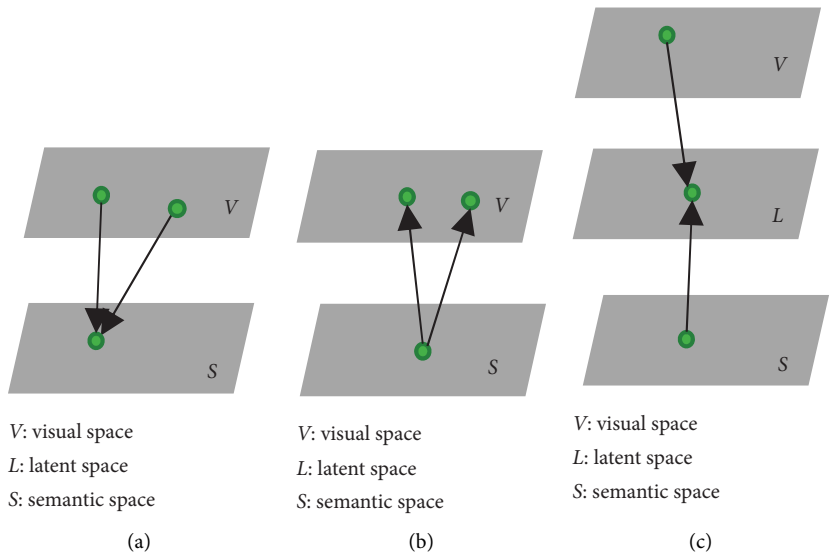

Figure 1: Three mapping methods commonly used in zero-shot learning. (a) Mapping from the visual space to the semantic space. (b) Mapping from the semantic space to its visual space. (c) Mapping both semantic features and visual features to a shared latent space.

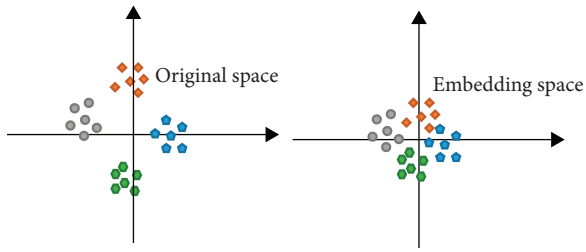

Figure 2: Visual explanation of hubness phenomenon. When a sample point is projected from the original space to the embedding space, the discriminative information in the original space is very likely to be lost, so the sample points belonging to the same class will be closer to other classes, which is especially obvious when mapping from high-dimensional space to low-dimensional space.

2. Related Work

In this section, we will discuss some relevant works on (generalized) zero-shot learning as well as generative models.

We are interested in both ZSL and GZSL tasks, in which the former aims at predicting the labels of unseen classes, while the latter tries to predict labels of both seen and unseen classes. Visual feature representation itself has strong distinguishability, but this is often ignored by previous researchers, so it is not reused. In this paper, a discriminative classifier is added to study the intrinsic distinguishable information of visual features, and it is applied to the dual generation module to synthesize more distinctive feature representations according to the corresponding semantic attributes of categories.

Early works [31, 32] associated seen and unseen classes by directly learning attribute classifiers. However, most recent works either learn a compatibility function between the image feature and class embedding spaces [7, 11, 16, 17, 21] or learn unseen classes, which are the mixture of visible classes [33–35]. For example, SYNC [33, 36, 37] try to predict the labels of unseen classes by learning linear classifiers. Wang et al. [38] proposed to combine the knowledge graph with graph convolutional network [39] and semantic embeddings. Rohrbach et al. [40] and Ye and Guo [9] project image features to the semantic embedding space followed by label propagation. Verma and Rai [41] treat unknown labels of unseen class images as latent variables and apply expectation-maximization (EM). All the abovementioned models are nongenerative and suffer from the problems of hubness as well as domain-shifting, but our proposed method uses a dual generative model to transform ZSL or GZSL into traditional supervised learning by generating fake visual features of unseen classes, which is considered to alleviate the problems of embedding methods.

In recent years, generative models have been widely used. Generative adversarial network [26] was originally proposed as an image synthesis method based on a particular image data distribution [42] and has achieved the state-of-the-art results. Generative adversarial network [26, 42, 43] is composed of a generator that synthesizes fake data distribution and a discriminator that distinguishes fake data from real data. However, GANs are suffering from the problems of unstable training and mode collapse [44, 45]. In order to alleviate these problems and improve the quality of synthesized features, many researches have put forward their own methods. Arjovsky et al. [44] proposed WGAN to optimize GAN on an approximate Wasserstein distance by enforcing 1-Lipschitz smoothness. Although WGAN has obtained better theoretical performance than the original GAN, it still has the problems of disappearance and explosion gradient due to weight clipping to enforce the 1-Lipschitz constraint on the discriminator, and then, Gulrajani et al. [45] proposed an improved version of WGAN which is called WGAN-GP enforcing the Lipschitz constraint [3] through gradient penalty. Therefore, our method draws lessons from the idea of the improved

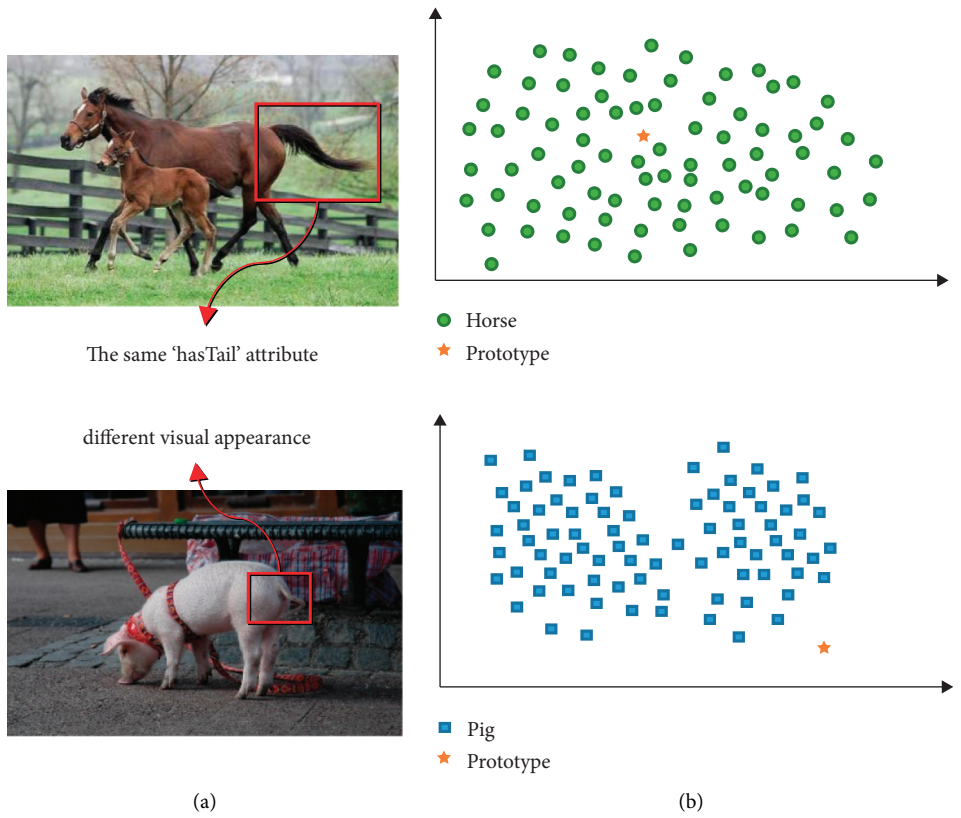

Figure 3: An illustration of the domain shift problem in zero-shot learning image classification. As we can see from the picture, both horses and pigs have tail attributes, but the visual characteristics of their tails are far apart. It is difficult to correctly identify pigs if the model is trained by horses. (a) Visual space. (b) Attribute space.

WGAN. Different from the existing works that directly generate image itself, our proposed model chooses to generate visuals features instead, which can be directly used to train a discriminative classifier for zero-shot learning.

Further, Zhu et al. [46] proposed an interesting application of GANs named CycleGAN that translates an image from one domain to another domain and then back to the original domain to form a closed loop. Schonfeld et al. [47] proposed an approach where cross and distribution alignment losses are introduced for aligning the visual features and corresponding embeddings in a shared latent space, by using two variational auto encoders [48]. The work of [25] is similar to our model, which introduces a f-VAEGAN framework that combines a VAE and a GAN by sharing the decoder of VAE and generator of GAN for feature synthesis. Xian et al. [8] used a conditional Wasserstein GAN [44] along with a seen category classifier to learn the generator for unseen class feature synthesis. Our proposed model combines the idea of VAEGAN of [25] and the seen classes classifier of [8] to encourage the generator to synthesize more discriminative features, which will improve the performance of zero-shot learning and generalized zero-shot learning to a certain extent.

The abovementioned generative methods of zero-shot learning and generalized zero-shot learning almost ignore the inherent distinguishability of visual feature representations between categories, which is actually very important to classification. Therefore, we apply the key discriminative information of visual feature representations to the proposed dual generation framework, which promotes the synthesized visual feature representations generated by the learned generator to be more easily distinguished from each other. In this paper, we also analyze the role of the additional classifier with different structures in the transmission of discriminative information.

3. Proposed Model

In this section, we first formally define the zero-shot learning generalized zero-shot learning problems, give an overview of our proposed dual generative model with using the discriminative information of visual feature representation by an additional classifier, and then introduce each component of our model in detail.

3.1. ZSL and GZSL Problem Formulation. In this paper, we study both the conventional and generalized zero-shot learning. Specifically, let the source dataset be defined as $S = \{v, y, s_s | v \in v_s, y \in \gamma_s, s_s \in A\}$, where S stands for the training data of seen classes, $v = R^{d_v}$ is the image's visual feature produced by a pretrained neural network which is usually ResNet101 trained on ImageNet1K, v_s is the set of visual features from seen classes, y is the label of image visual

feature v, γ_s is the set of labels for seen classes, and $s_s$is the semantic embedding for the class y. Similarly, we can define the test set, i.e., the target dataset as $T = \{v, y, s_u | v \in v_u, y \in \gamma_u, s_u \in A\}$ where the v_u represents the set of image features from unseen classes, γ_u represents the set of labels for unseen classes, and that $\gamma_u \cap \gamma_s = \varnothing$. The tasks in ZSL and GZSL are to learn the classifiers f_{zsl}: $v \longrightarrow \gamma_u$ and f_{gzsl}: $v \longrightarrow \gamma_u \cup \gamma_s$, respectively.

3.2. Model Overview. The overall framework of our proposed framework is illustrated in Figure 4. There are four main components in our model, i.e., an encoder, a generator/decoder, a discriminator, and a pretrained classifier, in which the encoder, the generator/encoder, and the discriminator form a dual generative framework, i.e., VAE-GAN. Our proposed method is based on the recently introduced f-VAE-GAN [25] that combines the advantages of the VAE [48] and GAN [26] which is the same as our proposed method and has achieved impressive results for ZSL classification. Referring to the idea of [25], we add an extra classifier which is the utilization of discriminative information to classify the generated visual features of the seen classes, in which the classifier is pretrained on seen classes. We believe that the additional classifier loss can make the generator learn to synthesize more discriminative visual features which is helpful. The core component of our model is the dual generative framework whose role is to generate various visual features conditioned on certain class semantic embedding. In this paper, we make full use of the inherent discriminative information of visual feature representations and apply this inherent feature to the dual generation module to encourage the generator to synthesize visual feature representations that are easier to be classified based on the corresponding category semantic attributes. In the following, we will introduce the main components dual generative network, the additional classifier, and their loss functions of the proposed model in detail.

3.3. Dual Generative Framework. In this work, we propose a dual generative framework to synthesize visual feature representations of unseen classes stably and efficiently. The dual generative network combines the strengths of improved WGAN and conditional VAE, which can deal with the mode collapse and unstable training problems well.

As we can see from Figure 4, the conditional VAE network is composed of a latent noise encoder $p(z|v, s)$ and a visual feature representation decoder $p(v|z, s)$, and the conditional VAE is proposed as a generative method that maps a random noise vector $z = R^{d_v}$ drawn from $p(z|v, s)$to a data point v in the data distribution conditioning on the semantic embeddings. We train conditional VAE by minimizing the following loss function L_{CVAE}:

$$L_{\mathrm{CVAE}} = \mathrm{KL}(p(z|v, s) \| p(z|s)) - E(\log p(v|z, s)), \quad (1)$$

where $\mathrm{KL}(p(z|v, s)||p(z|s))$ represents the L_{KL}, i.e., the Kullback–Leibler divergence between $p(z|v, s)$and $p(z|s)$, the conditional distribution $p(z|v, s)$ is modeled as $E(v, s)$,$p(z|v, s)$ is equal to $G(z, s)$, and $p(z|s)$ is treated as a unit Gaussian distribution.

As shown in Figure 4, the improved WGAN is composed of a generator G and a discriminator D. We aim to learn a generator$G$: $z \times c \longrightarrow v$ conditioned on semantic embeddings. The generator takes class embedding $s \in A$ and random Gaussian noise $z = R^{d_v}$as inputs and then outputs a fake visual feature $\tilde{v}$ of the class y. The loss function of our improved WGAN is

$$L_{\mathrm{WGAN}} = E[D(v, s_s)] - E[D(\tilde{v}, s)] - \lambda E\left[\left(\left\|\nabla_{\hat{v}} D(\hat{v}, s)\right\| - 1\right)^2\right], \quad (2)$$

where $\tilde{v} = G(z, s_s)$, $\hat{v} = \alpha v + (1 - \alpha)\tilde{v}$, with $\alpha \sim U(0, 1)$, and λ is the penalty coefficient, initialized to 10. Different from the pure GAN, the discriminative network of WGAN is defined as D: $v \times c \longrightarrow R$which eliminates the sigmoid layer and outputs a real value. The first two terms of Equation (2) are considered as Wasserstein distance, and the third term is the gradient penalty to enforce the gradient of D to have unit norm along the straight line between real and generated visual feature pairs. We also calculate the value of the gradient penalty term in each epoch of training to adjust the super-parameter λ.

Once the dual generative model learns to generate visual features of seen classes, conditioned on the seen class semantic embeddings s_s, it can also generate $\tilde{v}_u$ of any unseen category γ_u through its class semantic embedding s_u. So, the zero-shot learning and generalized zero-shot learning problems can be transformed into traditional supervised learning.

3.4. Additional Classifier for Discriminative Information. In order to ensure that the visual features generated by improved WGAN are well suited for training a discriminative classifier, we added a classifier C to make use of the discriminative information of visual feature representations, as shown in Figure 4, which is pretrained on the real features of seen classes to encourage the generator to generate distinctive features. For this purpose, module C uses the negative log likelihood to minimize the classification loss over the generated features in the following formulation:

$$L_{\mathrm{CLS}} = -E_{\tilde{v} \sim p_{\tilde{v}}}[\log P(y|\tilde{v}; \theta)], \quad (3)$$

where $\tilde{v} = G(z, s)$, y is the class label of $\tilde{v}$, and $P(y|\tilde{v}; \theta)$ denotes the probability of $\tilde{v}$ being predicted with its true class label y. The conditional probability is computed by a linear softmax classifier parameterized by θ. The classification loss can be regarded as a regularization that enforces the generator to construct discriminative features. In the next section, we carry out experiments to analyze the performance of different classifiers for zero-shot learning and generalized zero-shot learning.

In summary, our proposed model optimizes the following objective function:

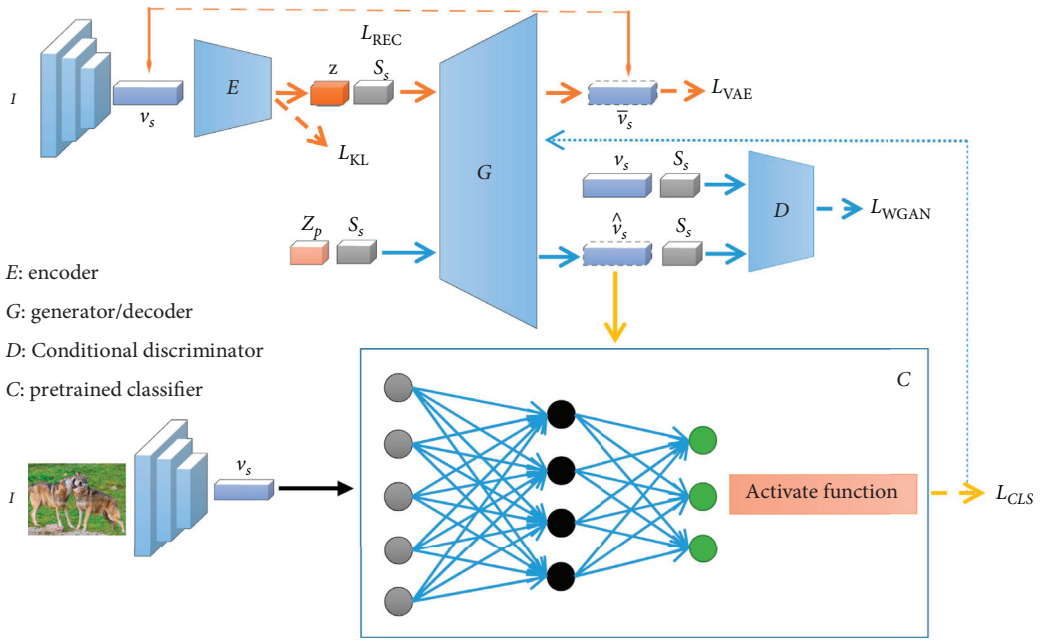

Figure 4: An overview of our proposed architecture, in which the upper part is a dual generation framework and the lower part is an additional classifier using discriminative information. Given the image samples I selected from seen classes, visual features v_s are extracted from the Resnet101 which is pretrained on ImageNet1K and input to the netE (encoder), along with the corresponding semantic embeddings s_s. The latent noise vector z output from netE is then input together with semantic embeddings s_s to the netG (generator) that synthesizes fake visual features $\bar{v}_s$. The netD (conditional discriminator) learns to distinguish real features v_s from synthesized $\bar{v}_s$. Both netE and netG together constitute the so-called conditional VAE, which is training by L_{KL} (KL divergence) and L_{BCE} (binary cross-entropy loss). Similarly, both netG and netD are trained using L_{WGAN}. The additional classifier is a multilayer fully-connected neural network, and we also discuss the influence of different classifier structures in the following.

$$\min_{G,E} \max_{D} L_{CVAE} + \gamma L_{WGAN} + \alpha L_{CLS}. \tag{4}$$

As shown in Figure 5, once the model has been trained, in order to predict the label of unseen classes, we can first generate pseudovisual features for each unseen class using the learned generator. Then, we construct a new dataset by combining these pseudovisual features with the real features of the seen classes for GZSL. After that, we can train any classifier based on this new dataset containing the visual features of the seen classes and unseen classes. Therefore, the GZSL task is transformed into a supervised learning problem. Here, we use a self-learning classifier to fine-tune the accuracy as in [24].

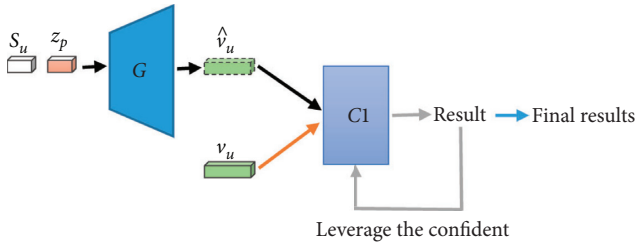

Figure 5: The test process of our method for ZSL: firstly, we use the learned generator to synthesize the visual features of unseen categories conditioned on semantic embeddings; then, we train the classifier by utilizing these synthesized visual features; finally, the real unseen samples are used for testing. The test part is divided into two steps, the first step is rough classification, and then the second step is to fine-tune the classifier by using the confident classification results in the first step.

4. Experiments

In this section, we have conducted a lot of experiments on six public benchmark datasets for both ZSL and GZSL. The detailed information of the experimental setup is provided in the respective chapters, and in order to make better use of the discriminative information, we discuss the influences of classifiers with different structures by conducting comparative experiments and comprehensively analyze the corresponding experimental results.

4.1. Datasets and Settings. We compare our proposed model with several baselines on six widely used datasets, i.e., Oxford Flowers (FLO) [49], Animals with Attributes 2 (AWA2) [14], Caltech-UCSD-Birds (CUB) [50], SUN Attribute (SUN) [51], and APascal-a Yahoo (APY). Among these datasets, APY contains 32 categories from both PASCAL VOC 2008 and YahooL that contain 15339 images. AWA2 is a coarse-grained and medium-size dataset which contains 30,475 images, 50 classes, and 85 attributes. CUB, FLO, and SUN are medium scale but fine-grained datasets, in which SUB contains 11788 images from 200 different types of birds annotated with 312 attributes. FLO dataset contains 8189 images from 102 different types of flowers without attribute annotations. However, we use the fine-

grained visual descriptions collected by [27]. SUN contains 14340 images from 717 scenes annotated with 102 attributes. Statistics of the datasets are presented in Table 1.

For real visual features, we extract 2048-dim top-layer pooling units of the ResNet101 [56] from the entire image. We do not do any image preprocessing such as cropping or use any other data augmentation techniques. ResNet101 is pretrained on ImageNet1K and not fine-tuned. For pseudovisual features, we generate 2048-dim features using our model. For the class semantic embeddings, we use per-class attributes for AWA (85-dim), CUB (312-dim) and SUN (102-dim), APY (64-dim). Furthermore, for dataset FLO, we extract 1024-dim character-based features from fine-grained visual descriptions by CNN-RNN [57].

At test time, in the ZSL setting, the goal is to correctly classify unseen class label, i.e., γ_u, and in the GZSL setting, the search space includes both seen and unseen classes, i.e., $\gamma_s \cup \gamma_u$. We use the unified evaluation protocol in [58]. In the ZSL setting, we first calculate the average accuracy of each category independently and then sum the average accuracy of all categories and divide by the total number of categories to get average per-class top-1 accuracy ($T1$). As for the GZSL setting, we compute the average per-class top-1 accuracy on seen classes γ_s denoted as s and the average per-class top-1 accuracy on unseen classes γ_u denoted as u; after that we calculate their harmonic mean as the final measure, i.e., $H = 2 * (s * u)/(s + u)$.

4.2. Implementation Details. In our proposed model, the encoder, the generator, and the discriminator are all implemented as multilayer perceptron (MLP). Through experiments, we find that when the dimensions of semantic embeddings s and Gaussian random noise $z \sim N(0, 1)$ are the same, the performance of zero-shot learning is the best. Therefore, we set the dimension of Gaussian random noise as the dimension of semantic embeddings of each dataset. The latent vector z and semantic embeddings s are concatenated and feed into the generator. Similarly, the discriminators take input as the concatenation of image features and class embeddings. In which, the discriminator, the encoder, and the generator are all two-layer fully-connected (FC) networks with 4096 hidden units. In addition to the output layer of G, other components use LeakyReLU as a nonlinear activation function. While for G, sigmoid activation is used to apply BCE loss. Through experiments, we prove that when this extra classifier is a single-layer perceptron, it is better to use the discriminative information by visual feature representations. The model is trained using the Adam optimizer with learning rate of 0.0001. Following the suggestion of WGAN paper [44], we update the generator once every 5 discriminator iterations. Hyperparameters α and γ are initialized to 1 and 10, respectively, and then tuned by cross-validation.

4.3. Comparing with State-of-the-Art Methods. We compare our approach with ALE [6], f-WGAN [8], SE-GZSL [52], Sycle-WGAN [22], LisGAN [24], f-VAEGAN [25], TCN [53], DVBE [55], and SAE [45] for both ZSL and GZSL, and two more approaches, CADA-VAE [54] and DVBE [55] are compared for GZSL. The above methods are either representative ones or the state-of-the-art ones published in the past few years. Following previous work [24, 25], we report the average per-class top-1 accuracy. Specifically, for ZSL, we report the top-1 accuracy of unseen samples by only searching the unseen label space. However, for the GZSL, we report the accuracy on both seen classes and unseen classes with the same settings in [58]. Some of the results reported in this paper are also cited from [5].

Table 2 reports the results of ZSL. In these experiments, the categories of test samples are only searched from γ_u . It can be seen that the classification accuracies obtained on AWA1, APY, FLO, SUN, and CUB are 71.4%, 44.9%, 73.6%, 65.1%, and 62.6%, respectively. Our proposed framework has improved the state-of-the-art performance on AWA1, APY, FLO, SUN, and CUB datasets by 0.3%, 1.8%, 3.3%, 0.4%, and 1.6%. As for AWA2, we achieve the best of previous works. From Table 2, we can also observe that the generation-based methods, e.g., LisGAN, f-CLSWGAN, and ours, generally have better results than embedding ones, e.g., ALE. The GAN method transforms ZSL into supervision problem by generating visual features of unseen classes, while the embedding methods use indirect way to deal with unseen classes. This also proves the validity of the generative model in ZSL problem. Generally speaking, our method produces one of the best performances compared to the existing methods on five of six datasets.

Table 3 summarizes the results of GZSL. From Table 3, we can observe that our proposed model has better performance than existing methods, which is similar to the conclusion to Table 2. Our method stably predicts seen and unseen classes. Although some previous methods, such as ALE, performed well in identifying unseen samples in ZSL settings, their performance in GZSL decreased significantly. When the number of unseen classes becomes larger, ZSL models always tend to be confused, resulting in performance degradation. This phenomenon is especially obvious when the number of unseen classes is much larger than that of seen classes. Moreover, in real life, the amount of seen classes that can get manual annotations is definitely far less than that of unseen classes. Therefore, the applicability of these ZSL methods in practical application is limited and GZSL is the development trend in line with the reality.

We use harmonic mean which is considered more stable than arithmetic and geometric mean to measure the mean value between the accuracy of seen and unseen classes. From the reported results from Table 3, we can find that our method is more stable than the existing methods. Our proposed method avoids the unbalanced and extreme results between $sacc_s$ and u. As far as harmonic mean H is concerned, we achieved up to 0.3%, 0.2%, 3.1%, 0.8%, and 1.1% improvements on AWA2, APY, FLO, SUN, and CUB, respectively. The average is 1.1% over the five. Although our model did not perform the best on AWA1, its performance is almost equal to the previous artistic level. It can be seen from the results that our method reduces the precision difference between known classes and unknown classes to a certain extent, which verified the effective generalization ability of our method.

Table 1: Statistics of datasets.

Dataset	att/stc	Seen classes (train + val)	Unseen classes	Images (train + val)	Images (test unseen/seen)
APY	64	15 + 5	12	5932	7924/1483
AWA1	85	27 + 13	10	19832	5685/4958
AWA2	85	27 + 13	10	23527	7913/5882
CUB	312	100 + 50	50	7057	2967/1764
SUN	102	580 + 65	72	10320	1440/2580
FLO	1024	62 + 20	20	5631	1403/1155

Table 2: Results of ZSL on six classification benchmarks. ZSL measuring per-class average top-1 accuracy (T1) on γ_u. The "-" means that there are no relevant results in the reference, while the underlined results are reproduced according to the description of references.

Method	AWA1	AWA2	APY	FLO	SUN	CUB
ALE [6]	59.9	—	—	48.5	58.1	54.9
f-WGAN [8]	68.2	—	—	67.2	60.8	57.3
SE-GZSL [52]	69.5	69.2	—	—	63.4	59.6
Sycle-WGAN [22]	66.8	—	—	70.3	59.9	58.6
LisGAN [24]	70.6	—	43.1	69.6	61.7	58.8
f-VAEGAN [25]	71.1	70.5	40.4	67.7	64.7	61.0
TCN [53]	70.3	71.2	38.9	—	61.5	59.5
Ours	71.4	71.2	44.9	73.6	65.1	62.6

Considering the fact that both f-WGAN and f-CLSWGAN leverage GANs to synthesize unseen visual features, the performance improvement of our method can be attributed to two aspects. One is that we introduce a classifier trained on seen classes to guarantee that the generated features of each class can be distinguished from each other, which is considered as the usage of the discriminative information. The other is our classifier self-learning mechanism at test time, which is able to leverage the confident results to fine-tune itself. In general, the results verify that it is beneficial to leverage the additional classifier to train VAEGAN. The correct classification of generated unseen visual features guarantee that each synthesized sample features is highly related with its category and is more distinguishable.

4.4. Discussion of the Additional Classifier. Here, we analyze the influence of the additional loss of classifiers with different structures on the performance of zero-short learning and generalized zero-shot learning. The experimental results on datasets SUN and CUB are shown in Table 4.

As we can see from Table 4, the effect of single-layer perceptron is the best among all tested classifiers, except for the accuracy of the ZSL of the SUN. The output layer of all classifiers uses sigmoid as the activation function to calculate the classification loss, thus constraining the dual generation network to synthesize the visual feature representation which is easy to classify. By comparing the experimental results from lines 2 to 4 and lines 3 to 7 in Table 4, we found that using ReLu as an activation function for the hidden layer worked best. At the same time, from the data of the last three rows and the top three rows in Table 4, it can be seen that the hidden layer uses 1024 units better than 512 for both ZSL and GZSL. Through experiments, we found that using single-layer neural network as an additional classifier to understand the discrimination information can not only get the best results, but also reduce the running time time.

4.5. Analysis of Synthetic Image Features. In order to provide an intuitive evaluation on our proposed model, we visualize the visual features of some synthetic image visual features and the corresponding real image visual features of unseen classes. The results are shown in Figure 6. For convenience, we chose 10 unseen categories of AWA2 dataset for visualization. First of all, we get the semantic embeddings and the real image features of the selected categories. Secondly, we input these semantic embeddings and Gaussian random noise into the learned generator to obtain the synthetic image features. Finally, we use t-SNE [30] to reduce the dimension of synthetic and real visual features from 2048 to 2 and plot the obtained feature data into scatter for visualization.

From the visualization of real feature samples in Figure 6(a), it can be seen that some categories overlap to a large extent, such as seals, walruses, blue whales, and dolphins. It is reasonable for them to overlap, because blue whales, dolphins, seals, and walruses are similar in biology and look very similar visually. The visualization of synthetic image features is shown in Figure 6(b). By comparing 6(a) and 6(b), we can clearly find that for most categories, such as seals and dolphins, the synthetic image features are very close to real samples, and some of them even overlap with real samples well, such as horses, sheep, and giraffes. One failure is rat, and we can see that the synthesized features are far from the real features. Another disadvantage is that there is almost no confusion between the categories of synthetic samples, which is contrary to the actual situation. However, the finally

Table 3: Results of GZSL on six classification benchmarks respectively. GZSL measuring the harmonic mean H of the per-class top-1 accuracy u on γ_u and the per-class top-1 accuracy s on γ_u. The "—" means that there are no relevant results in the reference, while the underlined results are reproduced according to the description of references.

Method	AWA1			AWA2			APY			FLO			SUN			CUB		
	u	s	H	u	s	H	u	s	H	u	s	H	u	s	H	u	s	H
ALE [6]	16.8	76.1	27.5	—	—	—	—	—	—	13.3	61.6	21.9	21.8	33.1	26.3	23.7	62.8	34.4
f-WGAN [8]	57.9	61.4	59.6	—	—	—	—	—	—	59.0	73.8	65.6	42.6	36.6	39.4	43.7	57.7	49.7
SE-GZSL [52]	58.3	67.8	61.5	58.3	68.1	62.8	—	—	—	—	—	—	40.9	30.5	34.9	41.5	53.3	46.7
Sycle-WGAN [22]	59.6	63.4	59.8	—	—	—	—	—	—	61.6	69.2	65.2	47.2	33.8	39.4	47.9	59.3	53.0
LisGAN [24]	52.6	76.3	62.3	—	—	—	34.3	68.2	45.7	57.7	83.8	68.3	42.9	37.8	40.2	46.5	57.9	51.6
f-VAEGAN [25]	57.6	70.6	63.5	55.2	73.6	63.1	30.3	58.6	39.9	56.8	74.9	64.6	45.1	38.0	41.3	48.4	60.1	53.6
TCN [53]	49.4	76.5	60.0	61.2	65.8	63.4	24.1	64.0	35.1	—	—	—	31.2	37.3	34.0	52.6	52.0	52.3
CADA-VAE [54]	72.8	57.3	64.1	75.0	55.8	63.9							36.7	47.2	40.6	53.5	51.6	52.4
DVBE [55]	—	—	—	63.6	70.8	67.0	32.6	58.3	41.8	—	—	—	45.0	37.2	40.7	53.2	60.2	56.5
Ours	58.7	70.3	64.0	60.1	76.4	67.3	36.5	61.7	45.9	62.6	83.0	71.4	48.3	37.4	42.1	53.8	61.9	57.6

Table 4: The results of different classifiers on SUN and CUB. The single-layer structure is what we use for our proposed model. The two layers mean that a latent layer is added to the single-layer structure, the _relu/_lrelu/_sigmoid indicates the activation function followed by the hidden layer, and _1024/_512 indicates the number of neurons in the added hidden layer.

	SUN				CUB			
	ZSL	GZSL			ZSL	GZSL		
	$T1$	s	u	H	$T1$	s	u	H
Single-layer (used)	65.1	37.4	48.3	42.1	62.6	61.9	53.8	57.6
two_layers_1024_relu	65.8	37.8	47.4	42.1	61.8	62.4	47.3	53.8
two_layers_1024_lrelu	65.1	37.3	48.1	41.6	61.3	60.4	47.5	53.2
two_layers_1024_softmax	65.1	38.2	46.1	41.8	61.3	61.7	47.5	53.7
two_layers_512_relu	65.3	37.6	45.6	41.2	61.4	59.0	48.3	53.1
two_layers_512_lrelu	64.5	38.0	45.6	41.5	61.1	62.3	46.0	52.9
two_layers_512_ softmax	64.7	37.3	46.1	41.2	61.2	57.5	49.2	53.0

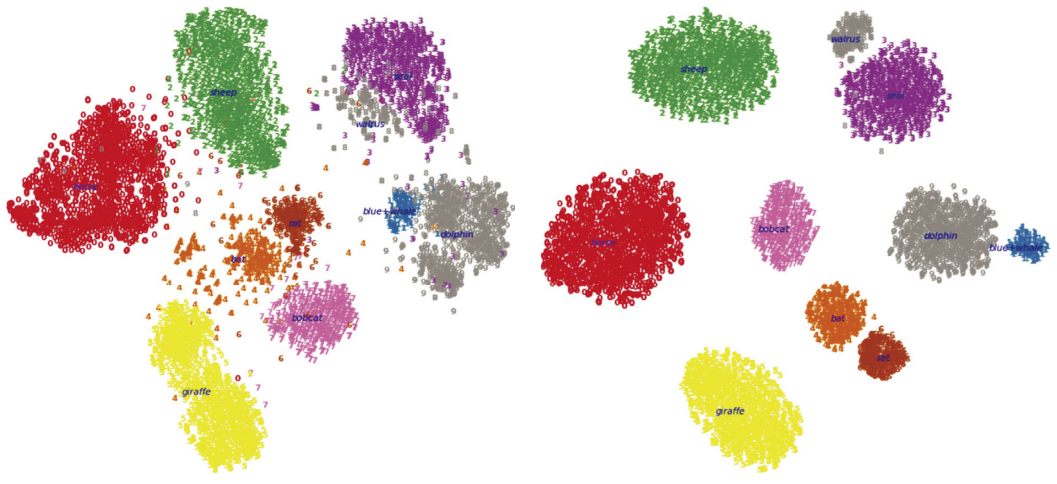

(a) (b)

Figure 6: . SNE visualization of real (a) and synthetic (b) image features for unseen classes in AWA2 datasets.

trained softmax classifier can well predict the labels of most categories of test images.

5. Conclusion

In this paper, we discuss the generalized zero-shot learning task and propose a model called DGDI, a dual generative framework that combines the advantages of conditional VAE and improved WGAN to obtain a more robust generative model with the using of discriminative information by adding a classification loss. We make full use of the discriminative information of visual feature representation between categories to further improve our dual generative module by adding a softmax classifier pretrained on the seen classes to encourage the generator to learn the discriminative information. The experimental results on six datasets clearly

show the effectiveness of our proposed framework; our method has achieved good performance on almost all datasets, which fully proves the importance of the discriminative information between the visual feature representations of categories. It is a meaningful problem to improve the precision and generalization ability of zero-shot learning, and we will further study it.

Data Availability

The datasets used in this study can be downloaded from http://datasets.d2.mpi-inf.mpg.de/xian/xlsa17.zip.

Conflicts of Interest

The authors declare that they have no conflicts of interest.

Acknowledgments

This work was supported in part by the National Key R&D Program of China under Grant no. 2019YFA0706200, the National Major Research Program of China under Grant no. 2018AAA0102002, and the National Natural Science Foundation of China (NSFC) under Grant nos. 61976076 and 61632007.

References

[1] T. Dong and T. Huang, "Neural cryptography based on complex-valued neural network," *IEEE Transactions on Neural Networks and Learning Systems*, vol. 31, no. 11, pp. 4999–5004, 2020.

[2] T. Dong and L. Xia, "Spatial temporal dynamic of a coupled reaction-diffusion neural network with time delay," *Cognitive Computation*, vol. 11, no. 2, pp. 212–226, 2019.

[3] T. Dong, X. Bu, and W. Hu, "Distributed differentially private average consensus for multi-agent networks by additive functional Laplace noise," *Journal of the Franklin Institute*, vol. 62, pp. 50–64, 2020.

[4] M. Wang, W. Fu, X. He, S. Hao, and X. Wu, "A survey on large-scale machine learning," *IEEE Transactions on Knowledge and Data Engineering*, vol. 1, 1 page.

[5] O. Russakovsky, J. Deng, H. Su et al., "ImageNet large scale visual recognition challenge," *International Journal of Computer Vision*, vol. 115, no. 3, pp. 211–252, 2015.

[6] Z. Akata, F. Perronnin, Z. Harchaoui, and C. Schmid, "Label embedding for image classification," *TPAMI-IEEE Transactions on Pattern Analysis and Machine Intelligence*, vol. 38, no. 7, 2016.

[7] B. Romera-Paredes and P. H. Torr, "An embarrassingly simple approach to zero-shot learning," in *Proceedings of the 32nd International Conference on Machine Learning*, Lille, France, July 2015.

[8] Y. Xian, T. Lorenz, B. Schiele, and Z. Akata, "Feature generating networks for zero-shot learning," 2018, https://arxiv.org/abs/1712.00981.

[9] M. Ye and Y. Guo, "Zero-shot classification with discriminative semantic representation learning," in *Proceedings of the 2017 IEEE Conference on Computer Vision and Pattern Recognition (CVPR)*, Honolulu, HI, USA, July 2017.

[10] J. He, R. Hong, X. Liu, M. Xu, Z.-J. Zha, and M. Wang, "Memory-augmented relation network for few-shot learning," in *Proceedings of the 28th ACM International Conference on Multimedia*, pp. 1236–1244, Association for Computing Machinery, New York, NY, USA, October 2020.

[11] Z. Akata, F. Perronnin, Z. Harchaoui, and C. Schmid, "Label embedding for attribute-based classification," in *Proceedings of the IEEE Conference on Computer Vision and Pattern Recognition*, pp. 819–826, Portland, OR, USA, June 2013.

[12] C. H. Lampert, H. Nickisch, and S. Harmeling, "Learning to detect unseen object classes by between-class attribute transfer," in *Proceedings of the IEEE Conference on Computer Vision and Pattern Recognition-CVPR 2009*, pp. 951–958, IEEE, Miami, FL, USA, June 2009.

[13] W.-L. Chao, S. Changpinyo, B. Gong, and F. Sha, "An empirical study and analysis of generalized zero-shot learning for object recognition in the wild," 2016, https://arxiv.org/abs/1605.04253.

[14] Y. Xian, C. H. Lampert, B. Schiele, and Z. Akata, "Zero-shot learning-a comprehensive evaluation of the good, the bad and the ugly," 2018, https://arxiv.org/abs/1707.00600.

[15] Z. Akata, S. Reed, D. Walter, H. Lee, and B. Schiele, "Evaluation of output embeddings for fine-grained image classification," in *Proceedings of the IEEE Conference on Computer Vision and Pattern Recognition*, pp. 2927–2936, Boston, MA, USA, June 2015.

[16] A. Frome, G. S. Corrado, J. Shlens et al., "A deep visual-semantic embedding model," in *Proceedings of the NIPS-26th International Conference on Neural Information Processing Systems*, Red Hook; NY, USA, December 2013.

[17] E. Kodirov, T. Xiang, and S. Gong, "Semantic autoencoder for zero-shot learning," in *Proceedings of the CVPR-Conference on Computer Vision and Pattern Recognition*, Honolulu, HI, USA, July 2017.

[18] Y. Xian, Z. Akata, G. Sharma, Q. Nguyen, M. Hein, and B. Schiele, "Latent embeddings for zero-shot classification," 2016, https://arxiv.org/abs/1603.08895.

[19] G. Dinu, A. Lazaridou, and M. Baroni, "Improving zero-shot learning by mitigating the hubness problem," 2014, https://arxiv.org/abs/1412.6568.

[20] Y. Shigeto, I. Suzuki, K. Hara, M. Shimbo, and Y. Matsumoto, "Ridge regression, hubness, and zero-shot learning," in *Proceedings of the Joint European Conference on Machine Learning and Knowledge Discovery in Databases*, pp. 135–151, Springer, Berlin, Germany, September 2015.

[21] L. Zhang, T. Xiang, and S. Gong, "Learning a deep embedding model for zero-shot learning," 2017, https://arxiv.org/abs/1611.05088.

[22] R. Felix, I. Reid, and G. Carneiro, "Multi-modal cycle-consistent generalized zero-shot learning," in *Proceedings of the ECCV-European Conference on Computer Vision*, Munich, Germany, September 2018.

[23] He Huang, C. Wang, S. Yu Philip, and C.-D. Wang, "Generative dual adversarial network for generalized zero-shot learning," in *Proceedings of the CVPR-Conference on Computer Vision and Pattern Recognition*, Salt Lake, UT, USA, June 2019.

[24] J. Li, M. Jing, Ke Lu, Z. Ding, L. Zhu, and Zi Huang, "Leveraging the invariant side of generative zero-shot learning," in *Proceedings of the CVPR-Conference on Computer Vision and Pattern Recognition*, Salt Lake, UT, USA, September 2019.

[25] Y. Xian, S. Sharma, Bernt Schiele, and Z. Akata, "f-vaegan-d2: a feature generating framework for any-shot learning," in *Proceedings of the IEEE/CVF Conference on Computer Vision and Pattern Recognition (CVPR)*, Salt Lake, UT, USA, June 2019.

[26] I. Goodfellow, J. Pouget-Abadie, M. Mirza et al., "Generative adversarial nets," in *Proceedings of the NIPS-International Conference on Neural Information Processing Systems*, Washington; DC, USA, December 2014.

[27] T. Mikolov, I. Sutskever, K. Chen, G. S. Corrado, and J. Dean, "Distributed representations of words and phrases and their compositionality," in *Proceedings of the NIPS-Neural Information Processing Systems*, Lake Tahoe, NV, USA, December 2013.

[28] M. Arjovsky and L. Bottou, "Towards principled methods for training generative adversarial networks," 2017, https://arxiv.org/abs/1701.04862.

[29] T. Dong and Q. Zhang, "Stability and oscillation analysis of a gene regulatory network with multiple time delays and diffusion rate," *IEEE Transactions on NanoBioscience*, vol. 19, no. 2, pp. 285–298, 2020.

[30] L. v. d. Maaten and G. Hinton, "Visualizing data using t-sne," *Journal of Machine Learning Research*, vol. 9, pp. 2579–2605, 2008.

[31] D. Jayaraman and K. Grauman, "Zero-shot recognition with unreliable attributes," in *Proceedings of the NIPS International Conference on Neural Information Processing Systems*, Washington; DC, USA, December 2014.

[32] C. Lampert, H. Nickisch, and S. Harmeling, "Attributebased classification for zero-shot visual object categorization," *IEEE Transactions on Pattern Analysis and Machine Intelligence*, vol. 36, no. 3, 2013.

[33] S. Changpinyo, W.-L. Chao, B. Gong, and F. Sha, "Synthesized classifiers for zero-shot learning," 2016, https://arxiv.org/abs/1603.00550.

[34] M. Norouzi, T. Mikolov, S. Bengio et al., "Zero-shot learning by convex combination of semantic embeddings," 2014, https://arxiv.org/abs/1312.5650.

[35] Z. Zhang and V. Saligrama, "Zero-shot learning via semantic similarity embedding," 2015, https://arxiv.org/abs/1509.04767.

[36] M. Elhoseiny, B. Saleh, and A. Elgammal, "Write a classifier: zero-shot learning using purely textual descriptions," in *Proceedings of the ICCV-International Conference on Computer Vision*, Sydney, Australia, December 2013.

[37] J. Lei Ba, K. Swersky, S. Fidler et al., "Predicting deep zeroshot convolutional neural networks using textual descriptions," in *Proceedings of the ICCV-2015 International Conference on Computer Vision*, Santiago, Chile, December 2015.

[38] X. Wang, Y. Ye, and A. Gupta, "Zero-shot recognition via semantic embeddings and knowledge graphs," 2018, https://arxiv.org/abs/1803.08035.

[39] T. N. Kipf and M. Welling, "Semi-supervised classification with graph convolutional networks," in *Proceedings of the ICLR-International Conference on Learning Representations*, Toulon, France, April 2017.

[40] M. Rohrbach, S. Ebert, and B. Schiele, "Transfer learning in a transductive setting," in *Proceedings of the NIPS-Neural Information Processing Systems*, Sierra Nevada, Spain, December 2013.

[41] V. K. Verma and P. Rai, "A simple exponential family framework for zero-shot learning," 2017, https://arxiv.org/abs/1707.08040.

[42] A. Radford, L. Metz, and S. Chintala, "Unsupervised representation learning with deep convolutional generative adversarial networks," 2016, https://arxiv.org/abs/1511.06434.

[43] M. Mirza and S. Osindero, "Conditional generative adversarial nets," 2014, https://arxiv.org/abs/1411.1784.

[44] M. Arjovsky, S. Chintala, and L. Bottou, "Wasserstein gan," 2017, https://arxiv.org/abs/1701.07875.

[45] I. Gulrajani, F. Ahmed, M. Arjovsky, V. Dumoulin, and A. Courville, "Improved training of wasserstein gans," 2017, https://arxiv.org/abs/1704.00028.

[46] J.-Y. Zhu, T. Park, P. Isola, and A. A. Efros, "Unpaired imageto-image translation using cycle-consistent adversarial networks," 2017, https://arxiv.org/abs/1703.10593.

[47] E. Schonfeld, S. Ebrahimi, S. Sinha, T. Darrell, and Z. Akata, "Generalized zero-and few-shot learning via aligned variational autoencoders," 2019, https://arxiv.org/abs/1812.01784.

[48] D. P. Kingma and M. Welling, "Auto-encoding variational bayes," in *Proceedings of the ICLR-International Conference on Learning Representations*, Banff, AB, Canada, April 2014.

[49] M.-E. Nilsback and A. Zisserman, "Automated flower classification over a large number of classes," in *Proceedings of the IEEE Conference on Computer Vision and Pattern Recognition*, Bhubaneswar, India, December 2008.

[50] P. Welinder, S. Branson, T. Mita et al., "Caltech-UCSD birds 200," Technical Report CNS-TR-2010-001, Caltech, Pasadena, CA, USA, 2010.

[51] G. Patterson and J. Hays, "Sun attribute database: discovering, annotating, and recognizing scene attributes," in *Proceedings of the 2012 IEEE Conference on Computer Vision and Pattern Recognition*, Providence, RI, USA, June 2012.

[52] V. Kumar Verma, G. Arora, A. Mishra, and P. Rai, "Generalized zero-shot learning via synthesized examples," in *Proceedings of the CVPR-Conference on Computer Vision and Pattern Recognition*, Salt Lake, UT, USA, June 2018.

[53] H. Jiang, R. Wang, S. Shan, and X. Chen, "Transferable contrastive network for generalized zero-shot learning," 2019, https://arxiv.org/abs/1908.05832.

[54] E. Schönfeld, S. Ebrahimi, S. Sinha, T. Darrell, and Z. Akata, "Generalized zero- and few-shot learning via aligned variational autoencoders," in *Proceedings of the 2019 IEEE/CVF Conference on Computer Vision and Pattern Recognition (CVPR)*, pp. 8239-8247, Long Beach, CA, USA, June 2019.

[55] S. Min, H. Yao, H. Xie, C. Wang, Z.-J. Zha, and Y. Zhang, "Domain-aware visual bias eliminating for generalized zero-shot learning," in *Proceedings of the 2020 IEEE/CVF Conference on Computer Vision and Pattern Recognition (CVPR)*, pp. 12661–12670, Seattle, WA, USA, September 2020.

[56] L. A. Hendricks, Z. Akata, M. Rohrbach, J. Donahue, B. Schiele, and T. Darrell, "Generating visual explanations," in *Proceedings of the European Conference on Computer Vision*, vol. 3–19, Springer, New York, NY, USA, August 2016.

[57] S. Reed, Z. Akata, H. Lee, and B. Schiele, "Learning deep representations of fine-grained visual descriptions," 2016, https://arxiv.org/abs/1605.05395.

[58] Y. Xian, B. Schiele, and Z. Akata, "Zero-shot learning - the good, the bad and the ugly," 2017, https://arxiv.org/abs/1703.04394.

Hindawi
Complexity
Volume 2021, Article ID 6667187, 16 pages
https://doi.org/10.1155/2021/6667187

Research Article

The Analysis of Opinion Evolution and Control Based on the Prisoner's Dilemma Game in Social Networks

Xianyong Li,[1] **Jian Zhu**,[2] **Yajun Du**,[1] **and Qian Zhang**[1]

[1]*School of Computer and Software Engineering, Xihua University, Chengdu 610039, China*
[2]*Department of Mathematics and Physics, Xinjiang Institute of Engineering, Urumqi 830023, China*

Correspondence should be addressed to Xianyong Li; lixy@mail.xhu.edu.cn

Received 24 November 2020; Revised 13 December 2020; Accepted 18 January 2021; Published 30 January 2021

Academic Editor: Chenquan Gan

In a social network, a user is greatly influenced by their neighbors' opinions, and the user's opinion updating can be regarded as the prisoner's dilemma game. In view of such considerations, this paper proposes an opinion evolution and control model based on the prisoner's dilemma game and gives the corresponding opinion evolution and control algorithm. Under different initial positive opinion proportions, different opinion control levels, and the same control threshold value and under different initial positive opinion proportions, different opinion control levels, and different opinion control threshold values in a scale-free network, the experiments illustrate the opinion evolution trends and control strategies according to the measures of changing the opinion control levels and opinion control threshold values for network regulators. The experiments show that the lower the initial positive opinion proportion is and the smaller (resp., larger) the control opinion threshold value chosen by the network regulators is, the lower (resp., higher) the opinion control level is; the larger the initial positive opinion proportion is and the larger the control opinion threshold value chosen by the network regulators is, the lower the opinion control level is.

1. Introduction

In social networks, the process of public opinion propagation is essentially the process of each netizen propagating their opinions in their community. Based on infectious disease models, Daley and Kendall [1] proposed DK model, thought that there is nothing critical in the process of rumors propagation, and analyzed the influence of randomness and certainty on rumor propagation. Maki and Thomson [2] presented MK model and believed that the first disseminators are controlled to suppress the propagation of rumors. Ising [3] connected the positive and negative of the particle with the positive and negative of the view and put forward Ising model to describe opinion dynamics. Sznajd-Weron and Sznajd [4] further proposed Sznajd model. In their model, they thought that one person will imitate their behavior around people and attract more people to imitate. On the basis of Sznajd model, Deffuant et al. [5, 6] established continuous opinion evolution model, i.e., Deffuant model and Hegselmann–Krause (HK) model. Moreno et al. [7, 8] made the simulation experiment on MK model and found that the clustering coefficient of network greatly influences the rumor propagation in scale-free networks. They further proposed a rumor dynamic model and made simulation experiments on homogeneous and heterogeneous networks. Martins [9] considered that all agents have inherent continuous opinions and external discrete behaviors and presented the continuous opinions and discrete actions (CODA) model. DeGroot [10] considered that the individual opinion is updated by the weighted average of all its neighbors' opinions and proposed DeGroot model. Friedkin and Johnsen [11] introduced stubborn individuals, extended the DeGroot model, and proposed the Friedkin–Johnsen (FJ) model. In the FJ model, individual opinion is updated by the weighted average of the convex combination of all its neighbor nodes' opinions and its opinion of innate belief. Gong et al. [12] improved the FJ model, proposed a structural-hole-based approach to control public opinion, and analyzed the influence of ordinary users and structural hole users on opinion evolution. Evidently, these researches

mainly focused on the opinion evolution rules and the opinion dynamics environments to depict the public opinion evolution laws in social networks.

To understand the ubiquitous existence of cooperative phenomena in the process of opinion evolution, some scholars introduced the game theory into the process of the opinion evolution and propagation in social networks. Liu et al. [13] thought that opinion propagation process is just the process of different strategy choices and applied the game theory to opinion evolution models. Li et al. [14] studied the rumor propagation based on the evolutionary game and investigated the influences of the penalty coefficient and negative message risk factor on the opinion propagation. Hilbe et al. [15] studied the evolution of extortion in iterated prisoner's dilemma games and found that the extortion is not a stable outcome of evolution but can catalyze the emergence of cooperation. Xu et al. [16] studied the evolution of cooperation structured populations in the context of repeated games by unconditional cooperation, unconditional defection, and extortion strategies and found a nontrivial role of the population structure and the microscopic strategy dynamics in the evolution of cooperation. Nowak and May [17] first adopted the prisoner's dilemma model to study the cooperation evolution of group organizations in rule network and found that the persons with the same strategies are gradually concentrated in a denser group by the self-organization evolution. Tang et al. [18] studied the effects of average degree on cooperation-based prisoner's dilemma game in random networks, small-world networks, and scale-free networks.

To the best of our knowledge, few scholars studied that the opinion evolution and control based on the prisoner's dilemma game. This paper aims to establish the opinion evolution and control model and corresponding opinion evolution and control algorithm and finds the relationships among the initial positive opinion proportions, opinion control levels, and opinion control threshold values, providing a wide variety of control strategies for network regulators in social networks.

The remainder of this paper is organized as follows. Section 2 establishes the opinion evolution and control model and the corresponding algorithm based on prisoner's dilemma game in detail. Section 3 carefully makes some experiments under the different initial positive opinion proportions, different opinion control levels, and same or different opinion control threshold values in scale-free networks. Finally, Section 4 summarizes this paper and gives some future research directions.

2. Opinion Evolution and Control Based on the Prisoner's Dilemma Game

In a social network, users mainly propagate two different opinions: positive opinion and negative opinion. Considering that a user is greatly influenced by its neighbors' opinions and inspired by the prisoner's dilemma game [15], we take two arbitrary adjacent users as two players, and consider two strategies: positive opinion propagation and negative opinion propagation for them. When two users choose the positive opinion propagation (resp., negative opinion propagation), each player obtains the payoff R (resp., P). When two players choose different strategies, the player who chooses the cooperation strategy gains the payoff S, and the other player obtains the payoff T. In general, the relationship among the four payoffs is $T > R > P > S$ and $2R > T + S$. In particular, the donation game is a game where the player who chooses cooperation strategy pays a cost c to provide a benefit b for the other player with $0 < c < b$, resulting in the parameters $T = b, R = bc, P = 0$, and $S = c$. For simplicity, we set $b - c = 1$ in the following.

For two adjacent users u and v, let Pf_{uv} denote by the payoff of the user u from the user v, and let the values of negative, neutral, and positive opinions of u be denoted by $o_u = -1, 0, 1$, respectively. Because the users holding neutral opinions are not susceptible to or influenced by others, we only consider the users holding positive and negative opinions and their interaction. Then, we can obtain the payoff of user u from user v:

$$\begin{aligned} Pf_{uv} &= \frac{1}{4}(1+o_u)(1+o_v)(b-c) + \frac{1}{4}(1+o_u)(1-o_v)(-c) \\ &\quad + \frac{1}{4}(1-o_u)(1+o_v)b + \frac{1}{4}(1-o_u)(1-o_v)\times 0 \\ &= \frac{1}{2}[(1+o_v)b - (1+o_u)c], \end{aligned} \tag{1}$$

where $o_u, o_v \in \{-1, 1\}$.

Denote the set of all neighbors of user u by $N(u)$. Then the total payoff of user u, that is, from its all neighbors, denoted by PF_u, is the following:

$$\begin{aligned} PF_u &= \sum_{v\in N(u)} Pf_{uv} = \frac{1}{2}\sum_{v\in N(u)}[(1+o_v)b - (1+o_u)c] \\ &= \frac{1}{2}\left[\sum_{v\in N(u)}(1+o_v)b - (1+o_u)|N(u)|c\right]. \end{aligned} \tag{2}$$

Let St_u and $\deg_u$ stand for the strategy, i.e., positive opinion propagation or negative opinion propagation, and the number of the neighbors of user u, respectively. During the game, user u continues to update its strategy based on its neighbors' payoffs and its payoff. Then we assume that u randomly chooses a strategy from one of their neighbors, say v with the strategy St_v, as their updating strategy, and the updating probability can be defined as

$$Pr_{u\leftarrow v, v\in N(u)} = \frac{PF_v - PF_u}{\max\{\deg_u, \deg_v\}(b+c)}. \tag{3}$$

In a social network excluding the nodes of neutral opinions, let pp (resp., pn) denote the proportion of the users holding positive opinions (resp., negative opinions), simplified as positive (negative) opinion proportion in the following, at some time. As users continue to change their opinion propagation strategies, the values pp and pn vary

continuously. If the values pp > 0.5, pp = 0.5, and pp < 0.5 in the network, we call the network as positive, neutral, and negative opinion networks, respectively. For the neutral opinion network and negative opinion network, we need to employ some control strategies to change the networks into positive opinion networks.

When the proportion of the users holding positive opinions pp (resp., the proportion of the users holding negative opinions 1 − pp) reaches a control threshold value, denoted by $L \in [0, 1]$, the network regulators should adopt the control strategy, such as persuading users, providing some positive information to change some users' opinions, to reduce the proportion of negative opinions in the social network. For user u holding a negative opinion, we assume that the penalty variable $C(k)$ that represents opinion control level k for the payoff of u is

$$C(k) = \gamma * \overline{\deg} * k, \tag{4}$$

where γ is a parameter, $\overline{\deg}$ stands for the average degree of the network, and $k = 0, 1, 2, 3, 4, 5$. The higher the opinion control level, the greater the costs that the network regulators need. Obviously, when $k = 0$, $C(k) = 0$ implies that the user is not controlled by network regulators in the network. Then, we further get a new payoff with opinion control level k for user u, denoted by $PF_u(k)$ as follows:

$$PF_u(k) = PF_u - \gamma * \overline{\deg} * k, \tag{5}$$

where $k = 0, 1, 2, 3, 4, 5$. Obviously, when $k = 0$, we have $PF_u(0) = PF_u$. Similar to the former user's strategy updating principle, a user u randomly chooses the strategy of one of their neighbors, say v with the strategy St_v, as their updating strategy, and the updating probability is

$$Pr_{u \leftarrow v, v \in N(u)}(k) = \frac{PF_u(k) - PF_v(k)}{\max\{\deg_u \times \deg_v\}(b + c)}. \tag{6}$$

Now, we propose an opinion evolution and control algorithm based on prisoner's dilemma game (PDG-OEC algorithm) as follows (Algorithm 1).

For the network regulators, they can control opinion evolution trends in social networks by flexibly changing opinion control levels and opinion control threshold values based on the PDG-OEC algorithm.

3. Experiment

As the connections of nodes (nodes' degrees) in social networks obey power law distribution, we will adopt the scale-free network [19] to make simulation experiments on the proposed opinion evolution and control model and the PDG-OEC algorithm. To illustrate the effect of network topology on our model, we set the parameters of scale-free networks with 1000 nodes as follows. The number of the initial nodes is $m_0 = 20$; the number of newly added nodes in each time is $m = 1, 3, 5, 7, 9$, respectively. On the five scale-free networks, when the proportion of the initial positive opinion (initial proportion) is pp = 0.5, we obtain five opinion evolution trends as shown in Figure 1. By comparison, it is found that the positive opinion proportions are slowly descending to a stable state (even tend to zero) in all networks. The reason is that, under the opinion evolution model based on prisoner's dilemma game, if two adjacent users choose different strategies, then the user who chooses negative opinion propagation gains more payoff compared to another user, resulting in users tending to choose negative opinion propagation in the networks. In fact, compared to true information, rumors (false information) are more easier to propagate from one user to others and to be accepted by users to some extent. When $m = 5$, the positive opinion proportion in the corresponding network declines the slowest compared with three other networks. For our experiment purpose, the scale-free network with the parameters $m_0 = 20$ and $m = 5$ will be chosen. For the newly added nodes, their initial strategies are randomly chosen from positive opinion propagation and negative opinion propagation.

In the following experiments, we directly set $\gamma * \overline{\deg} = 2$, and then the opinion control level k is $C(k) = 2 * k$ ($k = 0, 1, 2, 3, 4, 5$), abbreviated as $C = 0, 2, 4, 6, 8, 10$.

Next, we analyze the opinion evolution trends in the scale-free network under the different initial proportions, opinion control levels, and opinion control threshold value $L = 0.5$ (see Figure 2). In Figure 2(a), when the initial proportion pp = 0.1, if $C = 2$, it has no effect on the trend of network opinions; if $C = 4, 6, 8$, the positive opinion proportions are increasing to a small extent and are controlled within the range of 0.1 to 0.2, respectively; if $C = 10$, the control effect is significant, and the positive opinion proportion continues to rise more than 0.5. It can be seen that, under the initial proportion pp = 0.1, the network regulators should adopt the opinion control level 5 to achieve positive opinion network. In Figure 2(b), when the initial proportion pp = 0.2, if $C = 2$, the positive opinion proportion is controlled about 0.15, a stable state; if $C = 4$, the positive opinion proportion increases continually in excess of 0.5; if $C = 6, 8, 10$, the positive opinion proportions go up to 1, keeping a stable state, respectively, and the larger C is, the faster it goes up. It can be seen that, under the initial proportion pp = 0.2, the network regulators should adopt the opinion control level 2 to achieve positive opinion network. In Figure 2(c), when the initial proportion pp = 0.3, if $C = 2$, the positive opinion proportion just exceeds 0.1, a stable state; if $C = 4$, the positive opinion proportion just exceeds 0.3, a stable state; if $C = 6, 8, 10$, the positive opinion proportions keep going up, respectively. After the 16^{th} time step, the larger C is, the faster it goes up. It can be seen that, under the initial proportion pp = 0.3, the network regulators should adopt the opinion control level 2 to achieve positive opinion network. In Figure 2(d), when the initial proportion pp = 0.4, if $C = 2$, the positive opinion proportion quickly reaches about 0.52, a stable state, at the 7^{th} time step; if $C = 4, 6, 8, 10$, the positive opinion proportions rapidly increase and then slowly go up to 1, a stable state, respectively. It can be seen that, under the initial proportion pp = 0.4, the network regulators should adopt the opinion control level 1 to achieve positive opinion network. In Figure 2(e), when the initial proportion pp = 0.5, if $C = 2$, the positive opinion proportion

Input: Social network $G = (V, E)$ excluding the nodes of neutral opinions, $o_u \in V(G)$, γ, L
Output: The final pp
(1) Calculate the average degree of the graph G: $\overline{\deg}$;
(2) Compute the total payoff $PF_u = (1/2)[\sum_{v \in N(u)}(1 + o_v)b - (1 + o_u)|N(u)|c]$ for each $u \in V(G)$;
(3) Update the strategy of the user u by randomly choosing a strategy of some $v \in N(u)$ with the probability $Pr_{u \leftarrow v, v \in N(u)} = ((PF_u - PF_v)/(\max\{\deg_u \times \deg_v\}(b + c)))$;
(4) Count the proportion of the users holding positive opinions: pp
(5) **while** $pp < L$ **do**
(6) Output the value pp
(7) **while** $pp \geq L$ **do**
(8) **for** $k = 1, 2, 3, 4, 5$ **do**
(9) Compute the payoff with opinion control level k for each $u \in V(G)$: $PF_u(k) = PF_u - \gamma * \overline{\deg} * k$;
(10) Update the strategy of user u by randomly choosing a strategy of some $v \in N(u)$ with the probability $Pr_{u \leftarrow v, v \in N(u)}(k) = ((PF_u(k) - PF_v(k))/(\max\{\deg_u, \deg_v\}(b + c)))$;
(11) **end for**
(12) Output the final pp under different opinion control level k, $k = 1, 2, 3, 4, 5$.

Algorithm 1: PDG-OEC algorithm.

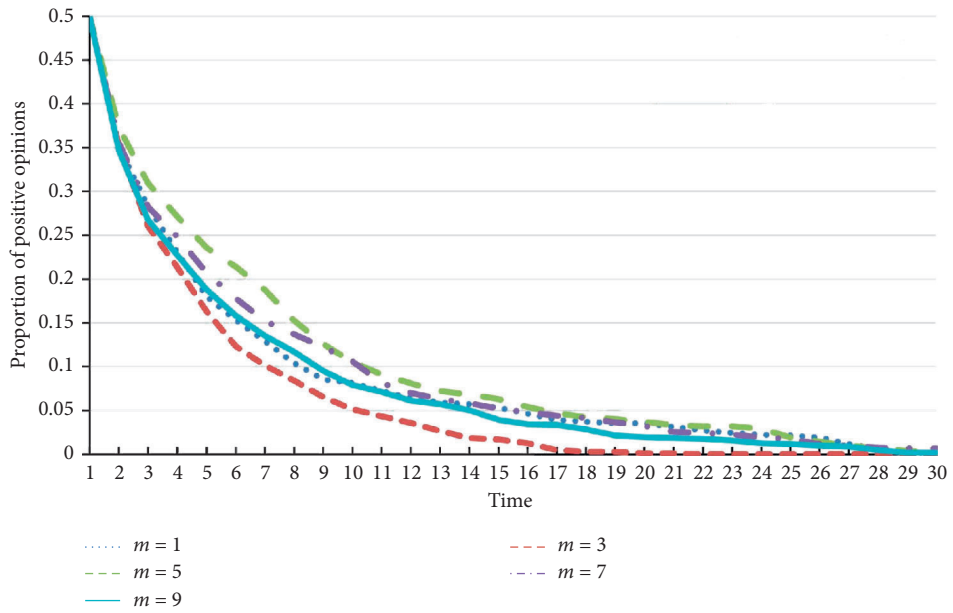

Figure 1: The opinion evolution trends for the initial proportion $pp = 0.5$ in scale-free networks with $m_0 = 20$ and $m = 1, 3, 5, 7$, and 9.

slowly decreases to 0.2, a stable state; if $C = 4, 6, 8, 10$, the larger C is, the faster the positive opinion proportion increases; finally, the positive opinion proportions are stable at 0.6 for $C = 4$ and at the range of 0.9 and 1 for $C = 6, 8, 10$. It can be seen that, under the initial proportion pp = 0.5, the network regulators should adopt the opinion control level 2 to achieve positive opinion network. By comparison of Figures 2(a)–2(e), under the control threshold value $L = 0.5$, if the positive opinion proportion $pp = 0.1$, the network regulators need to choose the opinion control level 5; if the initial proportion pp ≥ 0.2, they can choose opinion control level 2 ($C = 4$) to change the negative opinion network and neutral opinion network into positive opinion networks.

Now we discuss opinion evolution trends under different positive opinion proportions, opinion control threshold values, and opinion control levels in the scale-free network. For simplicity, in the following experiments, we only consider opinion control levels 1, 3, and 5 (i.e., $C = 2, 6, 10$), called low, medium, and high control levels, respectively.

For the initial proportion pp = 0.1, from Figure 3(a), it is shown that if the network regulators adopt the low control level ($C = 2$), while $L = 0.4, 0.3, 0.2, 0.1$, the positive opinion proportions add in small increments and then slowly go down below 0.1; meanwhile, when $L = 0.5$, the positive opinion proportion increases to about 0.15, a stable state. This implies that, under the initial proportion pp = 0.1, the network regulators using the low control level cannot change

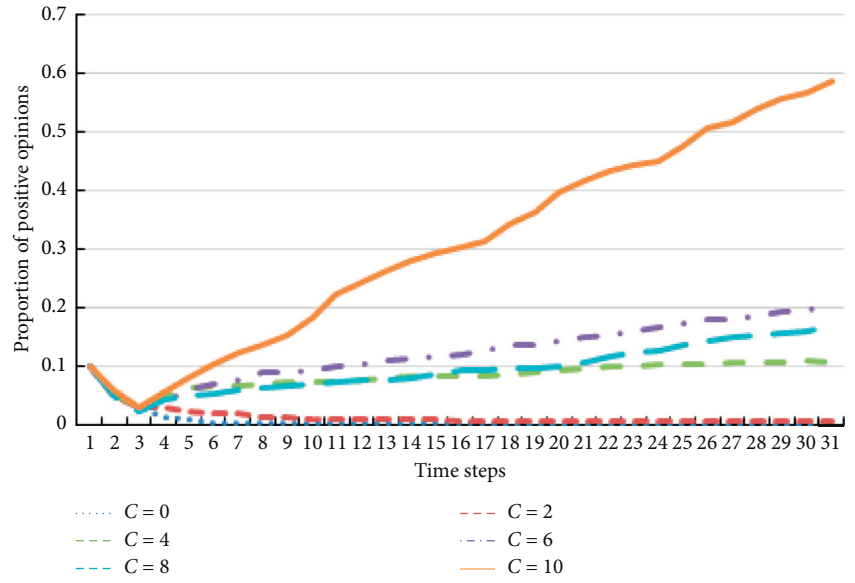

(a)

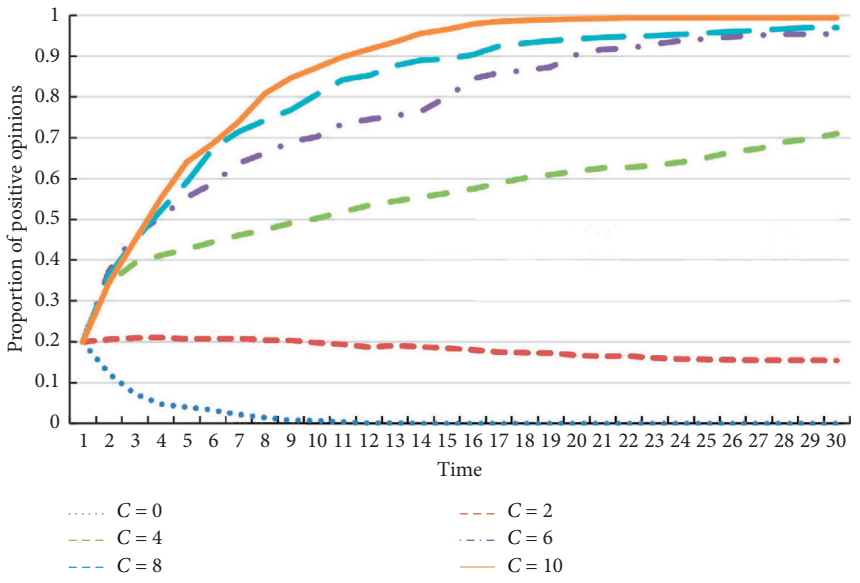

(b)

Figure 2: Continued.

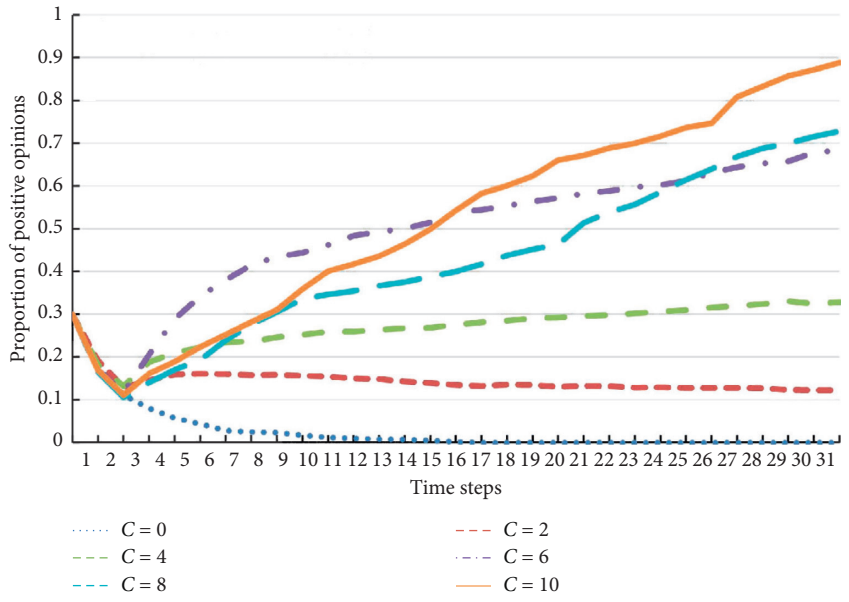

(c)

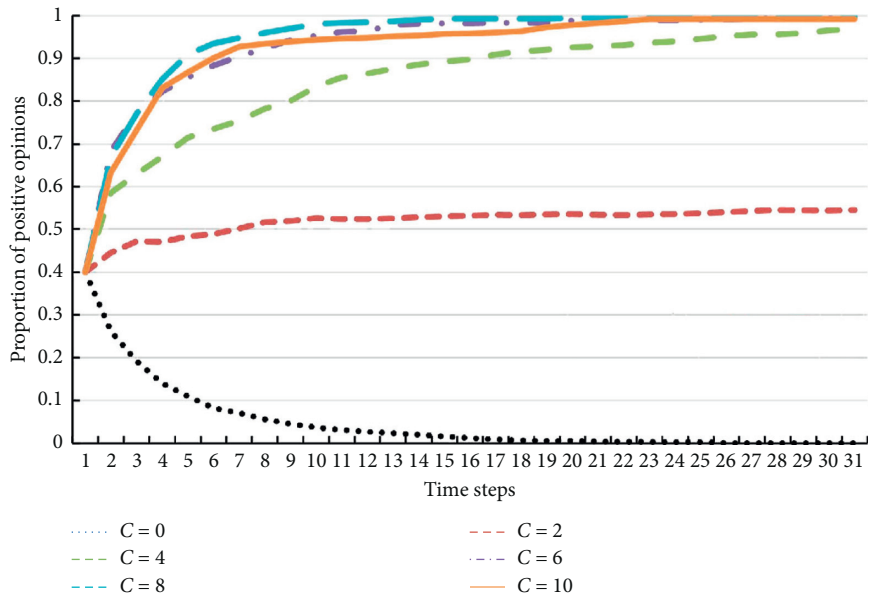

(d)

Figure 2: Continued.

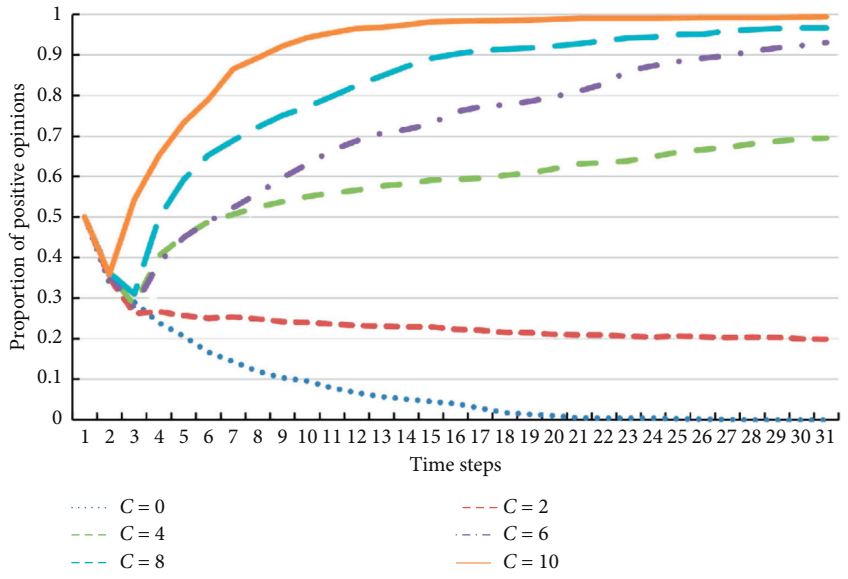

(e)

Figure 2: The evolution trends for the initial proportions pp = 0.1, 0.2, 0.3, 0.4, and 0.5, opinion control levels $k = 0, 1, 2, 3, 4$, and 5, and $L = 0.5$ in scale-free networks with $m_0 = 20$ and $m = 5$. (a) The initial proportion pp = 0.1, $C = 2$, 4, 6, 8, and 10, and $L = 0.5$. (b) The initial proportion pp = 0.2, $C = 2$, 4, 6, 8, and 10, and $L = 0.5$. (c) The initial proportion pp = 0.3, $C = 2$, 4, 6, 8, and 10, and $L = 0.5$. (d) The initial proportion pp = 0.4, $C = 2$, 4, 6, 8, and 10, and $L = 0.5$. (e) The initial proportion pp = 0.5, $C = 2$, 4, 6, 8, and 10, and $L = 0.5$.

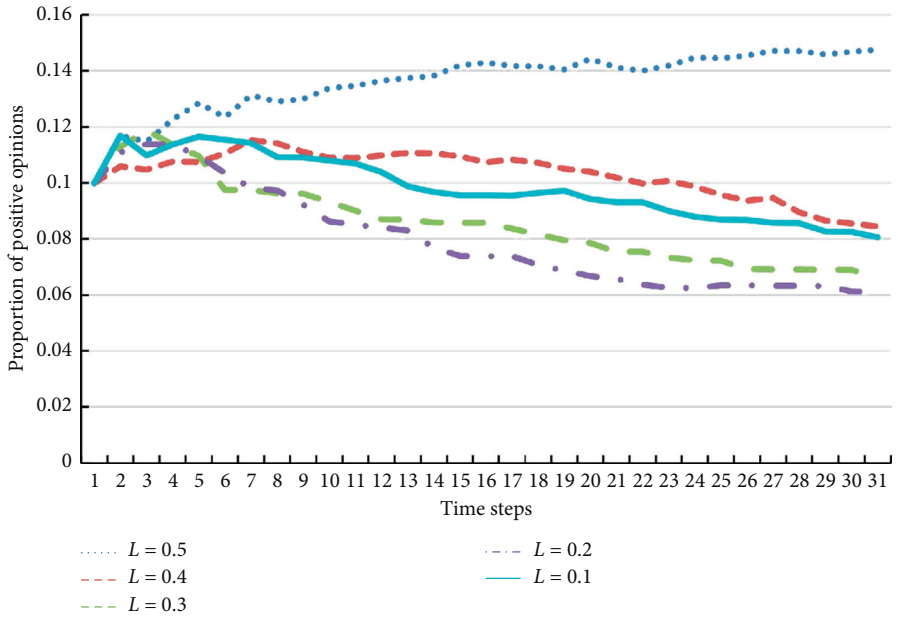

(a)

Figure 3: Continued.

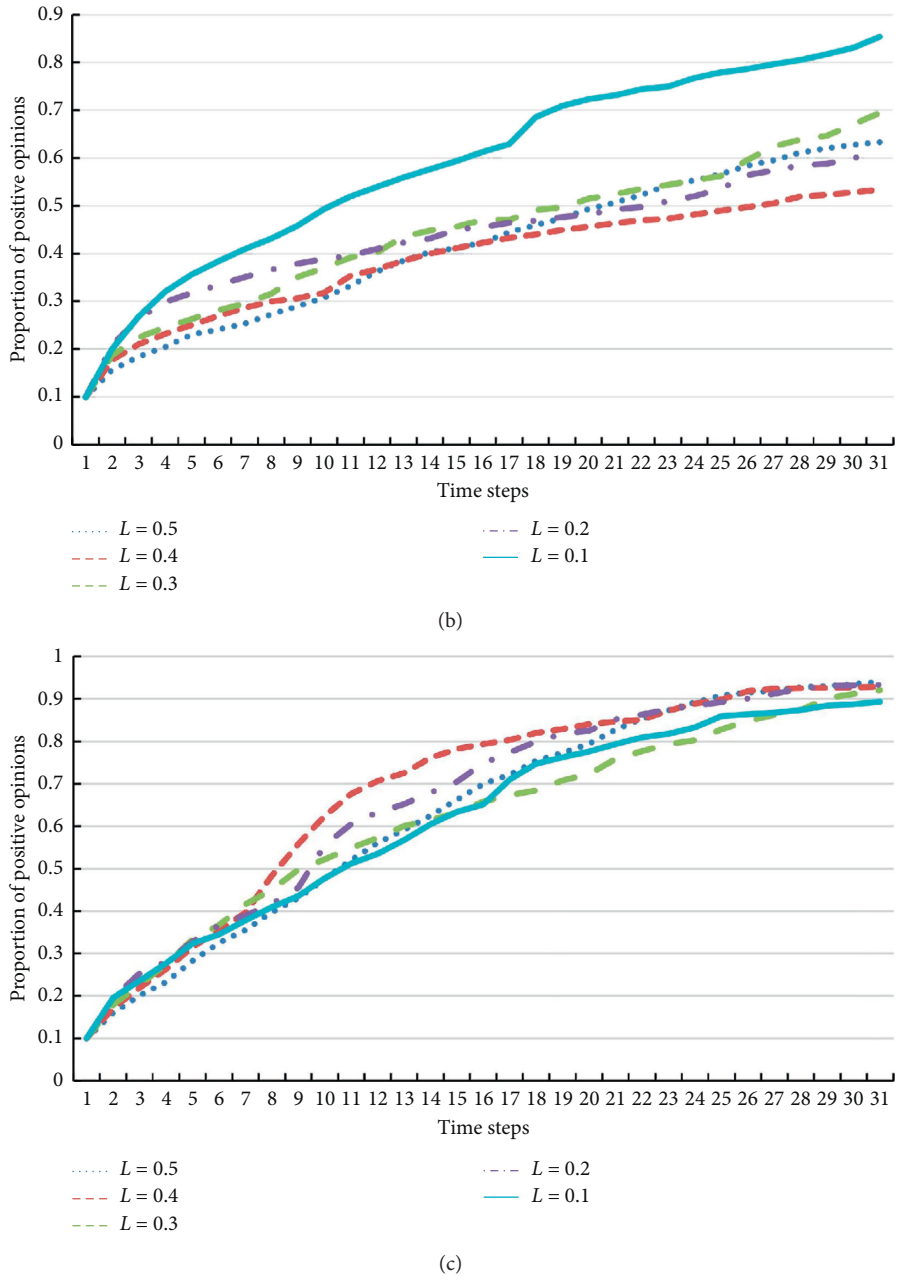

FIGURE 3: The evolution trends for the initial proportion pp = 0.1, opinion control levels $k = 1, 3,$ and 5, and $L = 0.5, 0.4, 0.3, 0.2,$ and 0.1 in scale-free networks with $m_0 = 20$ and $m = 5$. (a) The initial proportion $pp = 0.1$, $C = 2$, and $L = 0.5$, 0.4, 0.3, 0.2, and 0.1. (b) The initial proportion $pp = 0.1$, $C = 6$, and $L = 0.5$, 0.4, 0.3, 0.2, and 0.1. (c) The initial proportion $pp = 0.1$, $C = 10$, and $L = 0.5$, 0.4, 0.3, 0.2, and 0.1.

the network opinion trends whenever $L = 0.5, 0.4, 0.3, 0.2, 0.1$. From Figure 3(b), for the medium control level ($C = 6$) and $L = 0.5, 0.4, 0.3, 0.2, 0.1$, the positive opinion proportions all continuously increase over 0.5; in particular, for $L = 0.1$, the positive opinion proportion rises the fastest. It shows that, under the initial proportion pp = 0.1 and $C = 6$, the network regulators should select $L = 0.5$ to begin to control the network state, a low cost. From Figure 3(c), for the high control level ($C = 10$) and $L = 0.5, 0.4, 0.3, 0.2, 0.1$, the positive opinion proportions all rapidly go up over 0.5 and reach the final stable state value about 0.94; in particular, for $L = 0.4$, the positive opinion proportion rises to the stable state at the first speed. This presents that the network regulators should opt $L = 0.5$ to start to control the network state, a low cost, for $C = 10$. Combining the above analysis, it is concluded that if the initial proportion pp = 0.1, the network regulators should select medium control level and $L = 0.5$, which needs a low cost to change the negative opinion network into the positive opinion network.

For the initial proportion pp = 0.2, from Figure 4(a), it is shown that if the network regulators adopt the low control level ($C = 2$), while $L = 0.5$ and 0.2, the positive opinion proportions decline about 0.15, a stable state; meanwhile,

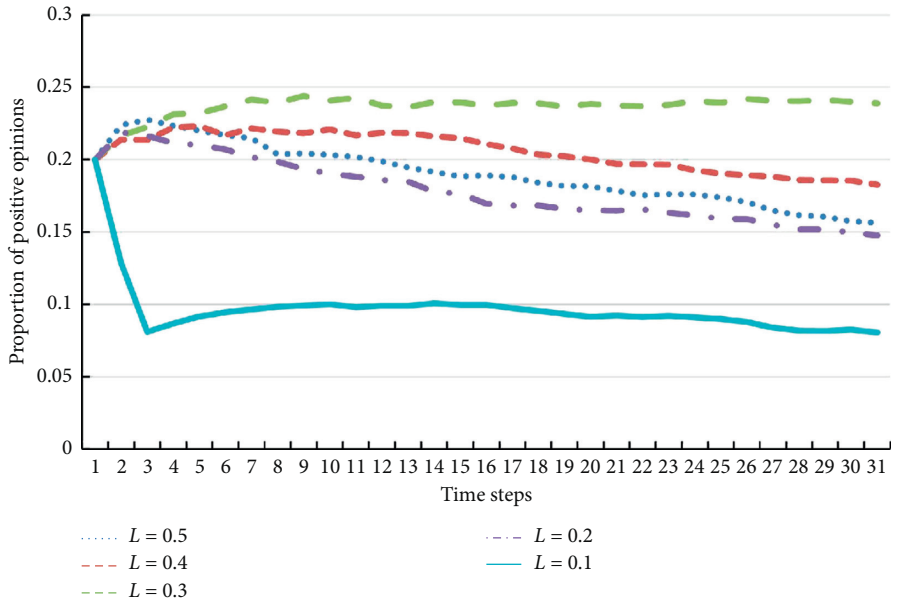

(a)

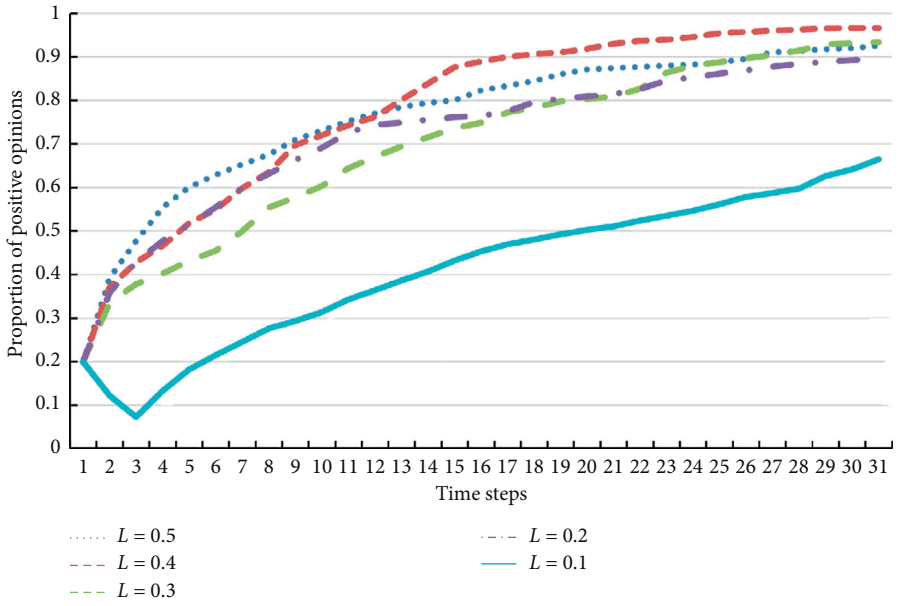

(b)

Figure 4: Continued.

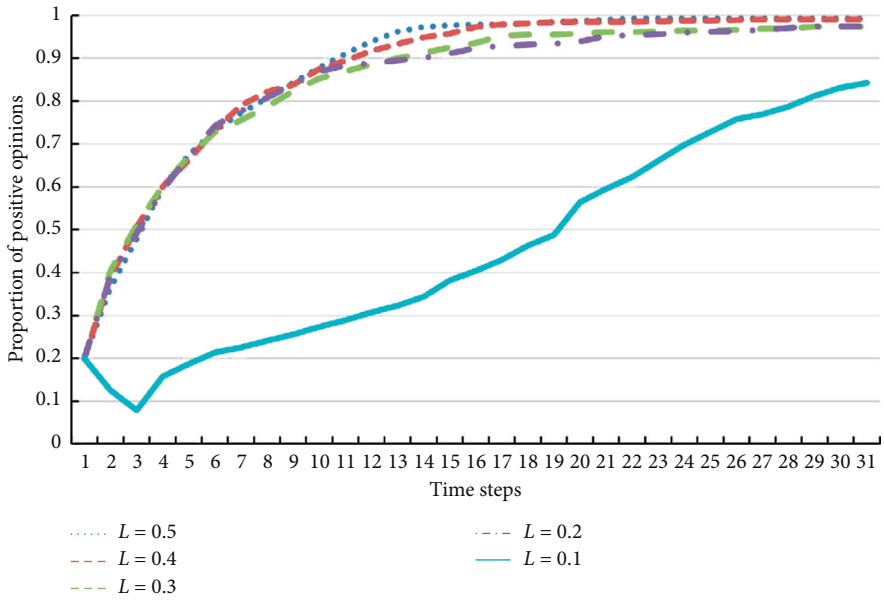

(c)

FIGURE 4: The evolution trends for the initial proportion pp = 0.2, opinion control levels $k = 1, 3,$ and 5, and $L = 0.5, 0.4, 0.3, 0.2,$ and 0.1 in scale-free networks with $m_0 = 20$ and $m = 5$. (a) The initial proportion $pp = 0.2$, $C = 2$, and $L = 0.5$, 0.4, 0.3, 0.2, and 0.1. (b) The initial proportion $pp = 0.2$, $C = 6$, and $L = 0.5$, 0.4, 0.3, 0.2, and 0.1. (c) The initial proportion $pp = 0.2$, $C = 10$, and $L = 0.5$, 0.4, 0.3, 0.2, and 0.1.

when $L = 0.4$, the positive opinion proportion presents small fluctuation and is finally stable at 0.2; when $L = 0.3$, the positive opinion proportion slowly rises to 0.24, a stable state; when $L = 0.1$, the positive opinion proportion slides to 0.04, a stable state. This implies that, under the initial proportion pp = 0.2, the network regulators using the low control level cannot change the network opinion trends into a positive opinion network whenever $L = 0.5, 0.4, 0.3, 0.2, 0.1$. From Figure 4(b), if the network regulators choose the medium control level ($C = 6$), while $L = 0.5, 0.4, 0.3,$ and 0.2, all positive opinion proportions constantly increase between 0.9 and 1 and, respectively, reach different stable states; when $L = 0.1$, the positive opinion proportion first rapidly declines and then rises almost linearly over 0.6, an unsteady state. In this case, the network regulators should select $L = 0.5$ to begin to control the network state, a low cost. From Figure 4(c), for the high control level ($C = 10$), while $L = 0.5, 0.4, 0.3, 0.2$, all positive opinion proportions increase at almost the same speed and run up to about 1, a stable state; when $L = 0.1$, the positive opinion proportion increases almost linearly at 0.75, a stable state. In this case, the network regulators should choose $L = 0.5$ to start the network control, changing the network into positive opinion network, a low cost. To sum up the analysis, it is concluded that if the initial proportion pp = 0.2, the network regulators should select medium control level and $L = 0.5$ to change the negative opinion network into the positive opinion network, a low cost.

For the initial proportion pp = 0.3, from Figure 5(a), if the network regulators choose the low control level ($C = 2$), while $L = 0.1$, the positive opinion proportion rapidly decreases to 0.09, a stable state; when $L = 0.2$, the positive opinion proportion rapidly descends to 0.2 and then slowly falls to 0.15, a stable state; when $L = 0.3$ and 0.4, the positive opinion proportions slowly go up to 0.35, a stable state; when $L = 0.5$, the positive opinion proportion slowly ascends to 0.41, a stable state. This implies that, under the initial proportion pp = 0.3, the network regulators using the low control level cannot change the network opinion trends into a positive opinion network whenever $L = 0.5, 0.4, 0.3, 0.2,$ and 0.1. From Figure 5(b), if the network regulators choose the medium control level ($C = 6$), while $L = 0.5, 0.4,$ and 0.3, the positive opinion proportions continuously increase over 0.5 and then reach the stable value 1 at almost the same time step; compared with the former three cases, while $L = 0.2$, the positive opinion proportion slowly goes up to 0.9, a stable state; when $L = 0.1$, the positive opinion proportion increases to 0.51 at the lowest speed, a stable state. It is concluded that, in this case, the network regulators should choose $L = 0.5$ to control the network opinion trends into a positive opinion network, a low cost. From Figure 5(c), if the network regulators choose the high control level ($C = 10$), while $L = 0.5$ and 0.4, the positive opinion proportions continuously increase over 0.5 and then reach the stable value 1 at almost the same time step; compared with the former two situations, while $L = 0.3, 0.2$, the positive opinion proportions go up to 0.94 at almost the same growth rate, a stable state; when $L = 0.1$, the positive opinion proportion slowly increases over 0.5 and does not reach a stable state. It concludes that, in this case, the network regulators should choose $L = 0.5$ to control the network opinion trends into a positive opinion network, a low cost. Combining the above analysis, it is concluded that if the initial proportion pp = 0.3, the network regulators should select medium control level and $L = 0.5$, which

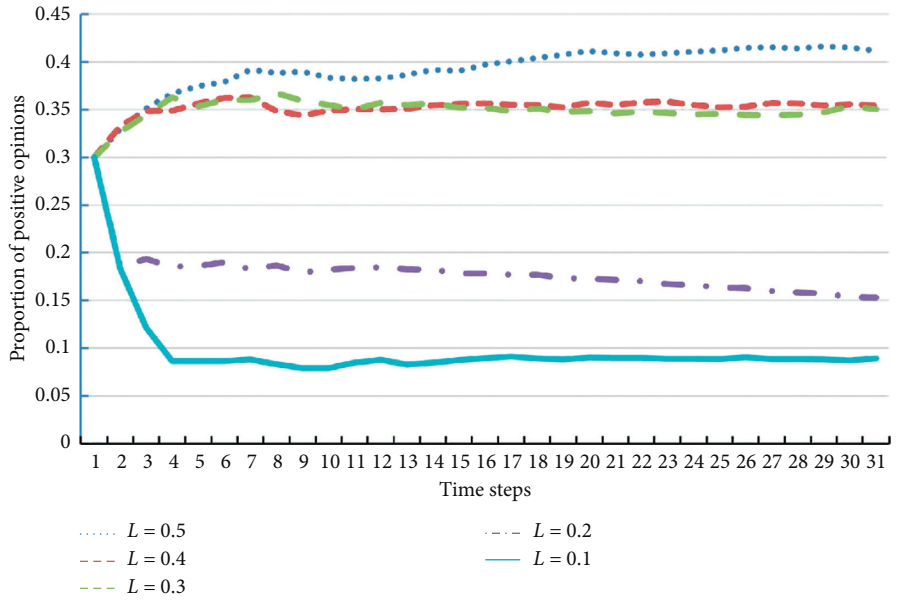

(a)

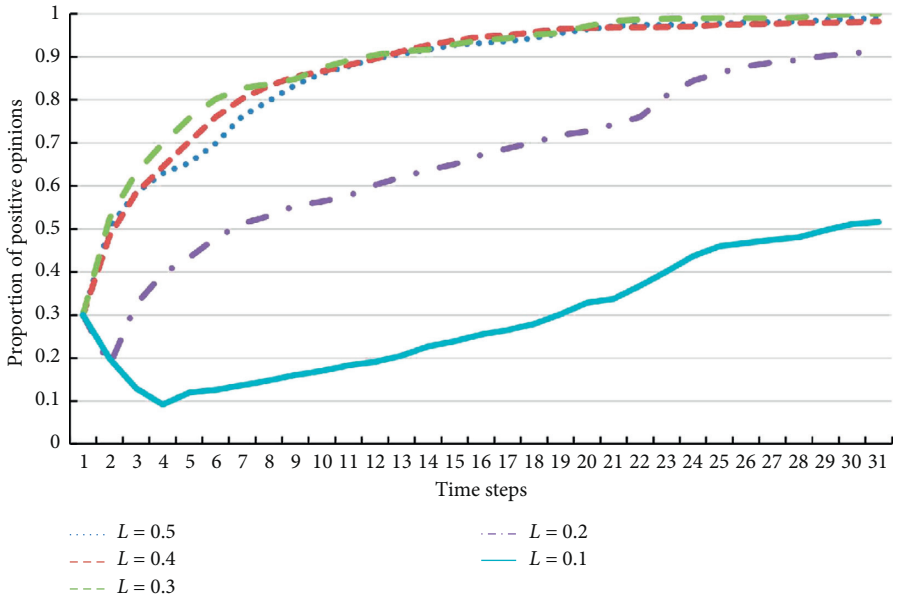

(b)

Figure 5: Continued.

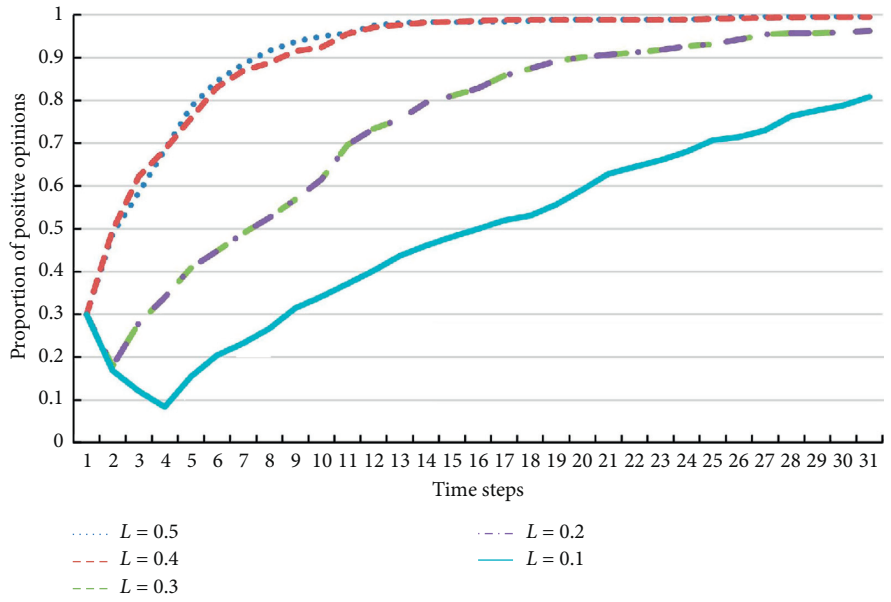

(c)

Figure 5: The evolution trends for the initial proportion pp = 0.3, opinion control levels $k = 1, 3,$ and 5, and $L = 0.5, 0.4, 0.3, 0.2,$ and 0.1 in scale-free networks with $m_0 = 20$ and $m = 5$. (a) The initial proportion $pp = 0.3$, $C = 2$, and $L = 0.5$, 0.4, 0.3, 0.2, and 0.1. (b) The initial proportion $pp = 0.3$, $C = 6$, and $L = 0.5$, 0.4, 0.3, 0.2, and 0.1. (c) The initial proportion $pp = 0.3$, $C = 10$, and $L = 0.5$, 0.4, 0.3, 0.2, and 0.1.

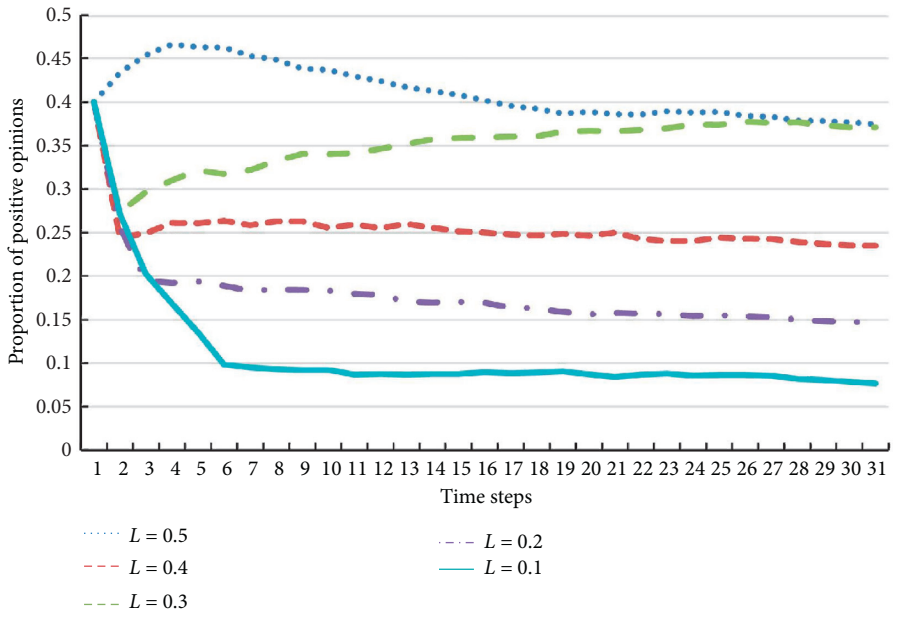

(a)

Figure 6: Continued.

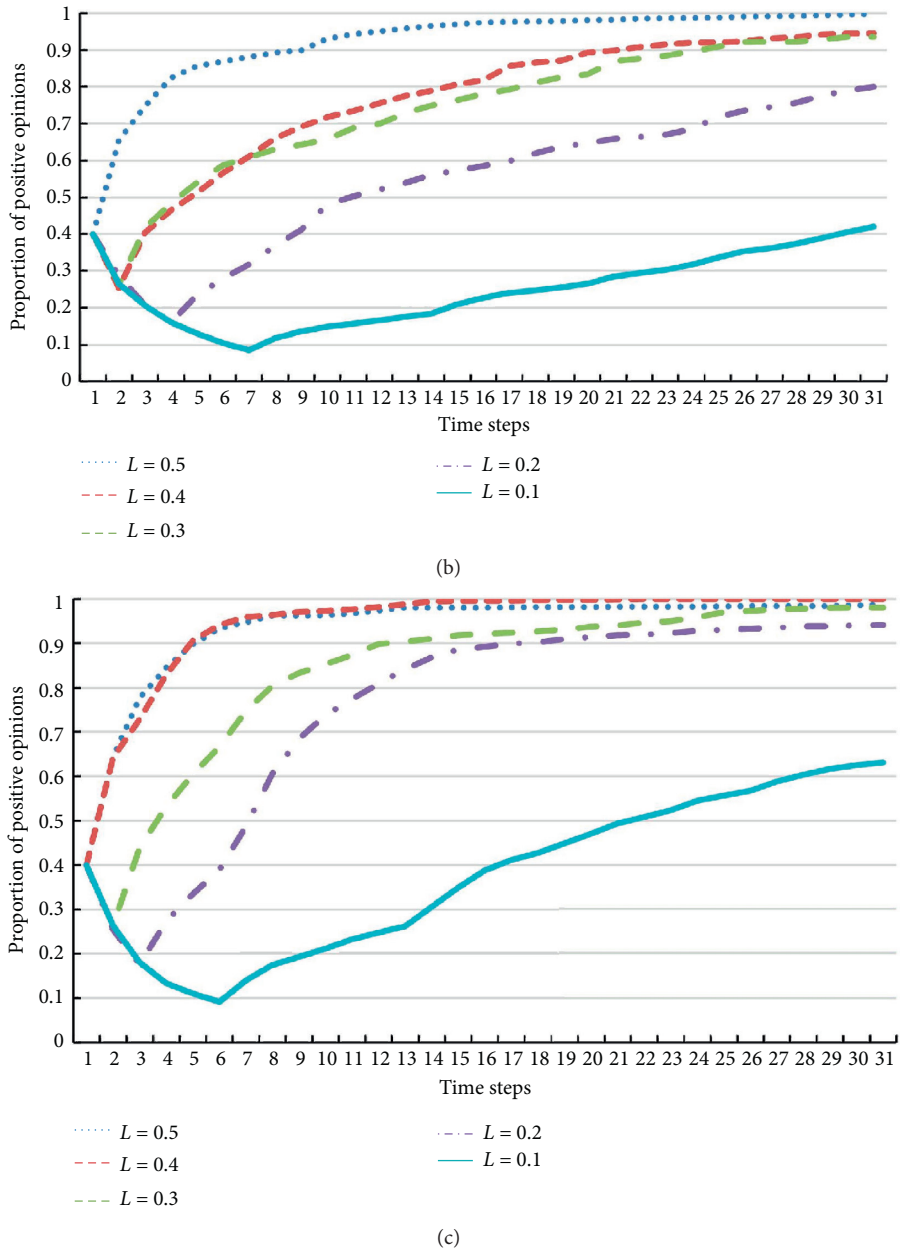

FIGURE 6: The evolution trends for the initial proportion pp = 0.4, opinion control levels $k = 1, 3,$ and 5, and $L = 0.5, 0.4, 0.3, 0.2,$ and 0.1 in scale-free networks with $m_0 = 20$ and $m = 5$. (a) The initial proportion $pp = 0.4$, $C = 2$, and $L = 0.5$, 0.4, 0.3, 0.2, and 0.1. (b) The initial proportion $pp = 0.4$, $C = 6$, and $L = 0.5$, 0.4, 0.3, 0.2, and 0.1. (c) The initial proportion $pp = 0.4$, $C = 10$, and $L = 0.5$, 0.4, 0.3, 0.2, and 0.1.

needs a low cost to change the negative opinion network into the positive opinion network.

For the initial proportion pp = 0.4, from Figure 6(a), if the network regulators choose the low control level ($C = 2$), while $L = 0.4, 0.2,$ and 0.1, the positive opinion proportions rapidly decrease and stabilize at 0.23, 0.15, and 0.08, respectively; when $L = 0.3$, the positive opinion proportion first rapidly descends and then slowly goes up to a stable value 0.37; when $L = 0.5$, the positive opinion proportion quickly goes up to 0.47 and then slowly decreases the stable value 0.37. This presents that, under this case, the network regulators cannot change the network opinion trends into a positive opinion network whenever $L = 0.5, 0.4, 0.3, 0.2,$ and 0.1. From Figure 6(b), if the network regulators choose the medium control level ($C = 6$), while $L = 0.5$, the positive opinion proportion quickly goes up to the stable value 1; when $L = 0.4$ and 0.3, the positive opinion proportions present a brief reduction and then rapidly increase to 0.95, a stable state; when $L = 0.2$ and 0.1, the positive opinion proportions first rapidly descend, then continuously go up more than 0.5 and 0.37, and finally do not reach the stable state. This shows that, under this case, the network regulators should choose $L = 0.5$ to change the network opinion trends into a positive opinion network, a low cost.

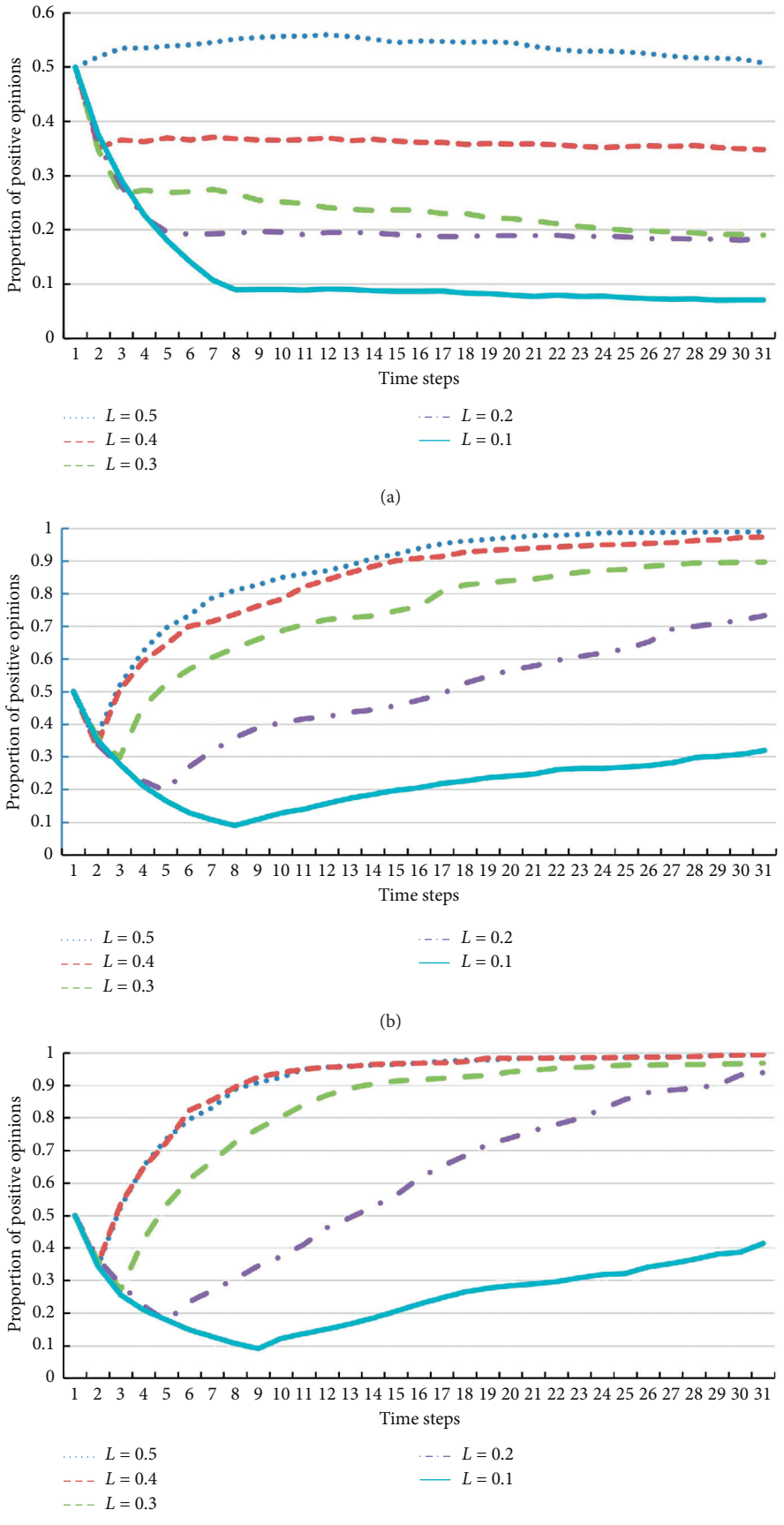

FIGURE 7: The evolution trends for the initial proportion pp = 0.5, opinion control levels $k = 1, 3,$ and 5, and $L = 0.5, 0.4, 0.3, 0.2,$ and 0.1 in scale-free networks with $m_0 = 20$ and $m = 5$. (a) The initial proportion $pp = 0.5$, $C = 2$, and $L = 0.5$, 0.4, 0.3, 0.2, and 0.1. (b) The initial proportion $pp = 0.5$, $C = 6$, and $L = 0.5$, 0.4, 0.3, 0.2, and 0.1. (c) The initial proportion $pp = 0.5$, $C = 10$, and $L = 0.5$, 0.4, 0.3, 0.2, and 0.1.

From Figure 6(c), if the network regulators choose the high control level ($C = 10$), while $L = 0.5$ and 0.4, the positive opinion proportions quickly go up to the stable value 1 at almost the same speed; when $L = 0.3, 0.2$, and 0.1, the positive opinion proportions present a brief reduction and then continuously increase to different stable values 0.98, 0.92, and 0.62, respectively. This shows that, under this case, the network regulators should choose $L = 0.5$ to change the network opinion trends into a positive opinion network, a low cost. To sum up the analysis, it is concluded that if the initial proportion pp = 0.4, the network regulators should select medium control level and $L = 0.5$, a low cost, to change the negative opinion network into the positive opinion network.

For the initial proportion pp = 0.5, from Figure 7(a), if the network regulators choose the low control level ($C = 2$), while $L = 0.5$, the positive opinion proportion slowly increases between 0.5 and 0.6 and then slowly decreases to 0.5, no stable state; when $L = 0.4, 0.3, 0.2$, and 0.1, the positive opinion proportions first rapidly descend and then slowly decrease to the stable values 0.35, 0.19, 0.19, and 0.08, respectively. This presents that, under this case, the network regulators cannot change the network opinion trend into a positive opinion network whenever $L = 0.5, 0.4, 0.3, 0.2$, and 0.1. From Figure 7(b), if the network regulators choose the medium control level ($C = 6$), while $L = 0.5, 0.4$, and 0.3, the positive opinion proportions quickly decrease and then continuously go up to the stable values 1, 0.98, and 0.8, respectively; when $L = 0.2, 0.1$, the positive opinion proportions present a brief rise and then continuously increase to more than 0.5. This shows that, under this case, the network regulators should choose $L = 0.5$ to change the network opinion trend into a positive opinion network, a low cost. From Figure 7(c), if the network regulators choose the high control level ($C = 10$), while $L = 0.5, 0.4, 0.3, 0.2$, and 0.1, the positive opinion proportions all first decrease and then continuously go up. Practically speaking, while $L = 0.5$ and 0.4, the positive opinion proportions rise to the stable value 1 at almost the same speed; when $L = 0.3$, the positive opinion proportion increases to the stable value 0.98; when $L = 0.2$, the positive opinion proportion goes up to more than 0.9 but does not reach a stable state; when $L = 0.1$, the positive opinion proportion presents a linear increase and eventually exceeds 0.5. This shows that, under this case, the network regulators should choose $L = 0.5$ to change the network opinion trends into a positive opinion network, a low cost. Combining with the analysis, if the initial proportion pp = 0.4, to reduce network control cost, the network regulators should choose medium control level and $L = 0.5$ to change the current opinion network into the positive opinion network.

According to the above experiments, it is concluded that, for the network, the lower the initial positive proportion is, the lower (higher) the opinion control level is, while the control opinion threshold value is chosen smaller (larger); the higher the initial positive proportion is, the lower the opinion control level is, while the control opinion threshold value is chosen larger.

4. Conclusion

As a user's neighbors impact the opinion of the user strongly and the process of users' opinion evolution can be considered the process of the prisoner's dilemma game, this paper proposes an opinion evolution and control model based on the prisoner's dilemma game and gives the corresponding opinion evolution and control algorithm, i.e., the PDG-OEC algorithm. For our purpose, based on the PDG-OEC algorithm, we first analyze the parameter selection of our experimental scale-free network. Then we make two types of simulation experiments in the scale-free networks. Under the different initial proportions, opinion control levels, and the same control threshold value, and under the different positive opinion proportions, opinion control levels, and opinion control threshold values in the scale-free network, the experiments show that if the initial positive proportion is lower, then the opinion control level needs to be lower (higher), while the control opinion threshold value is adopted smaller (larger); if the initial positive proportion is higher, then the opinion control level could be chosen lower, while the control opinion threshold value is chosen larger. The future work is finding more compatible game models to depict the opinion evolution and control in social networks and making some opinion evolution and control game models in the real social networks.

Data Availability

Data sharing is not applicable to this article as no datasets were generated.

Conflicts of Interest

All authors declare no conflicts of interest.

Authors' Contributions

The authors claim that the research was realized in collaboration with the same responsibility. All authors read and approved the last version of the manuscript.

Acknowledgments

This work was partially supported by the National Natural Science Foundation (nos. 61802316, 61872298, 61532009, and 61902324), Chunhui Plan Cooperation and Research Project, Ministry of Education of China (nos. Z2015109, Z2012030, and Z2015100), "Young Scholars Reserve Talents" program of Xihua University, Scientific Research Fund of Sichuan Provincial Education Department (nos. 15ZA0130 and 16ZA0157), Science and Technology Department of Sichuan Province (nos. 2017HH0083, 2018GZ0096, and 2019GFW115), the Natural Science Foundation of Xinjiang (NSFXJ) (no. 2019D01B10), Key Scientific Research Fund of Xihua University (no. z1422615), Open Research Subject of Key Laboratory of Security Insurance of Cyberspace, Sichuan Province (no. szjj2015-057), Open Research Subject of Key Laboratory of Grain and Oil Engineering and Food

Safety, Sichuan Province (no. szjj2016-023), and Outstanding Young Scholar Development Scheme, School of Computer and Software Engineering, Xihua University.

References

[1] D. J. Daley and D. G. Kendall, "Stochastic rumours," *IMA Journal of Applied Mathematics*, vol. 1, no. 1, pp. 42–55, 1965.

[2] D. J. Maki and M. Thomson, *Mathematical Models and Applications*, Prcntice-Hall, Englewood Cliff, NJ, USA, 1973.

[3] S. Galam and S. Moscovici, "Towards a theory of collective phenomena: consensus and attitude changes in groups," *European Journal of Social Psychology*, vol. 21, no. 1, pp. 49–74, 1991.

[4] K. Sznajd-Weron and J. Sznajd, "Opinion evolution in closed community," *International Journal of Modern Physics C*, vol. 11, no. 6, pp. 1157–1165, 2000.

[5] G. Deffuant, F. Amblard, and G. Weisbush, "How can extremism prevail? a study based on the relative agreement interaction model," *Journal of Artificial Societies and Social Simulation*, vol. 5, no. 4, pp. 49–74, 2002.

[6] R. Hegselmann and U. Krause, "Opinion dynamics and bounded confidence models, analysis and simulation," *Journal of Artificial Societies and Social Simulation*, vol. 5, no. 3, pp. 1–33, 2002.

[7] Y. Moreno, Y. Nekovee, and A. Vespignani, "Efficiency and reliability of epidemic data dissemination in complex networks," *Physical Review E*, vol. 69, no. 5, Article ID 055101, 2004.

[8] Y. Moreno, R. Pastor-Satorras, and A. Vespignani, "Epidemic outbreaks in complex heterogeneous networks," *The European Physical Journal B-Condensed Matter*, vol. 26, no. 4, pp. 521–529, 2001.

[9] A. C. R. Martins, "Continuous opinions and discrete actions in opinion dynamics problems," *International Journal of Modern Physics C*, vol. 19, no. 4, pp. 617–624, 2008.

[10] M. H. DeGroot, "Reaching a consensus," *Journal of the American Statistical Association*, vol. 69, no. 345, pp. 118–121, 1974.

[11] N. E. Friedkin and E. C. Johnsen, "Social influence and opinions," *Journal of Mathematical Sociology*, vol. 15, no. 3-4, pp. 193–206, 1990.

[12] C. Gong, Y. Du, X. Li et al., "Structural hole-based approach to control public opinion in a social network," *Engineering Applications of Artificial Intelligence*, vol. 93, Article ID 103690, 2020.

[13] B. F. Liu, L. Austin, and Y. Jin, "How publics respond to crisis communication strategies: the interplay of information form and source," *Public Relations Review*, vol. 37, no. 4, pp. 345–353, 2011.

[14] Q. Li, L. A. Braunstein, S. Havlin, and H. E. Stanley, "Strategy of competition between two groups based on an inflexible contrarian opinion model," *Physical Review E*, vol. 84, no. 2, Article ID 066101, 2011.

[15] C. Hilbe, M. A. Nowak, and K. Sigmund, "Evolution of extortion in iterated Prisoner's Dilemma games," *Proceedings of the National Academy of Sciences*, vol. 110, no. 17, pp. 6913–6918, 2013.

[16] X. Xu, Z. Rong, Z. X. Zhou, and C. K. Tse, "Extortion provides alternative routes to the evolution of cooperation in structured populations," *Physical Review E*, vol. 95, Article ID 052302, 2017.

[17] M. A. Nowak and R. M. May, "Evolutionary games and spatial chaos," *Nature*, vol. 359, no. 6398, pp. 826–829, 1992.

[18] C.-L. Tang, W.-X. Wang, X. Wu, and B.-H. Wang, "Effects of average degree on cooperation in networked evolutionary game," *The European Physical Journal B*, vol. 53, no. 3, pp. 411–415, 2006.

[19] A.-L. Barabási and R. Albert, "Emergence of scaling in random networks," *Science*, vol. 286, no. 5439, pp. 509–512, 1999.

Hindawi
Complexity
Volume 2021, Article ID 6654169, 7 pages
https://doi.org/10.1155/2021/6654169

WILEY | Hindawi

Research Article

Financial Risk Information Spreading on Metapopulation Networks

Min Lin[1] **and Li Duan**[2]

[1]*School of Economics and Management, Sichuan Normal University, Chengdu 610101, China*
[2]*Sichuan Academy of Social Sciences, Chengdu 610071, China*

Correspondence should be addressed to Li Duan; dllr7673@sina.com

Received 15 December 2020; Revised 6 January 2021; Accepted 18 January 2021; Published 29 January 2021

Academic Editor: Wei Wang

The financial risk information diffuses through various kinds of social networks, such as Twitter and Facebook. Individuals transmit the financial risk information which can migrate among different platforms or forums. In this paper, we propose a financial risk information spreading model on metapopulation networks. The subpopulation represents a platform or forum, and individuals migrate among them to transmit the information. We use a discrete-time Markov chain approach to describe the spreading dynamics' evolution and deduce the outbreak threshold point. We perform numerical simulation on artificial networks and discover that the financial risk information can be promoted once increasing the information transmission probability and active subpopulation fraction. The weight variance and migration probability cannot significantly affect the financial risk spreading size. The discrete-time Markov chain approach can reasonably predict the above phenomena.

1. Introduction

Many real-world systems in society, economy, and biological systems can be described as complex networks [1–3]. The nodes represent the element, and edges stand for the relationships among nodes. For instance, in financial network, the nodes stand for the financial institution, e.g., banks, and edges means the loan relationships among those financial institutions [4–6]. With such description framework, the dynamics of financial behavior, risk spreading can be mapped into studying the dynamics on financial networks [7–13]. Gai et al. [7] studied the risk contagion on directed financial networks and assumed that a bank's failure could trigger its lenders and further induce the cascading failures. Garas et al. [14] used a susceptible-infected-recovered (SIR) model to describe the economic crisis on the financial network and revealed that Belgium could initiate a global crisis.

In reality, the information about the financial risk is always accompanied by the financial risk [15]. That information widely spreads on various kinds of social platforms and forums, such as Twitter and Facebook. To describe the information spreading dynamics, some successful models have been proposed, such as the epidemic susceptible-infected-susceptible [16, 17], susceptible-infected-recovered [18, 19], Watts threshold model [20], and independent cascading [21]. Researchers have demonstrated that the network topologies markedly affect the spreading dynamics [22–28]. While spreading dynamics on networks with heterogeneous degree distribution, the strong heavy-tail may induce the outbreak threshold to disappear. When the information spreads on different platforms and forums, scholars are modeled as multiplex networks [29–33] or metapopulation networks [34–36]. Compared with spreading dynamics on single networks, multiplex networks can promote or suppress the spreading, which depends on the evolutionary mechanisms [37–39]. Recently, Gomez et al. [40] studied the phase diagram of the information spreading on metapopulation networks and revealed that mobility of individuals in large-size

subpopulations towards smaller ones suppress the spreading.

Real-data analysis has revealed that different platforms and forums usually have a different attitude on the same piece of information. Some exhibit enthusiasm in the information, while others demonstrate depression. To include this factor, Wang et al. [41] proposed an information-spreading model on heterogeneous multiplex networks and discussed the system's spreading size and critical points. There is still a mathematical model to describe the financial risk information-spreading dynamics on heterogeneous metapopulation networks to our vast knowledge. We, therefore, propose a model in Section 2. Then, we develop a discrete-time Markov chain approach to study the evolution of financial risk information spreading on metapopulation in Section 3. The numerical simulations of the spreading dynamics are performed in Section 4. Finally, we make conclusions in Section 5.

2. Model Descriptions

In this section, we propose information spreading model on metapopulation, which includes N subpopulation. In each subpopulation i, there are n_i aboriginal (nodes). An edge between two subpopulations represents a physical or cybernetic connection that exists. The edge's wight stands for the strength between the two subpopulations, which can be used to describe the interaction strength between different platforms or forums. In this paper, we build the interconnections among subpopulation according to a given degree distribution:

$$P(k) = \frac{\langle k\rangle^k}{k!}\exp(-\langle k\rangle), \tag{1}$$

where $\langle k\rangle$ is the average neighbor subpopulation. Assume the edge weight distribution

$$G(w) = \frac{1}{\sqrt{2\pi\sigma}}\exp\left(-\frac{(w-\langle w\rangle)^2}{2\sigma^2}\right), \tag{2}$$

where $\langle w\rangle$ is the average weight and σ is the standard variance. An illustration of the metapopulation is shown in Figure 1. Mathematically, the metapopulation's network topology can be described by using the weighted adjacency matrix W, in which $W_{ij} = 1$ means that subpopulation i and j are connected by an edge with strength W_{ij}. In reality, each subpopulation has its characters in spreading dynamics. To include this character, we classify the subpopulation into two types: active subpopulation ($\mathbb{AS}$) and depressing subpopulation ($\mathbb{DS}$). For the active subpopulation, the individuals actively participate and transmit the information. On the contrary, individuals in depressing subpopulation are less active in transmitting the information. To obtain a mathematical result, we assume a fraction α of ($\mathbb{AS}$) and $1-\alpha$ fraction of ($\mathbb{DS}$). At every time step, each individual will prefer to move to a neighboring subpopulation with probability p_d. The preference probability of an individual in subpopulation i moving to subpopulation j is as follows:

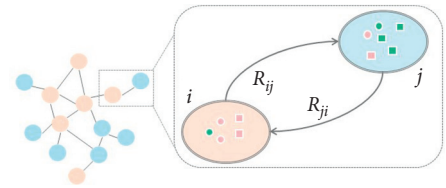

Figure 1: Illustration of financial risk information spreading on metapopulation network. Orange and blue circles represent the depressing subpopulation ($\mathbb{DS}$) and active subpopulation ($\mathbb{AS}$), respectively. Green and blue circles stand for the unaware and aware individuals. The directed edges R_{ij} means the preference travelling probability from subpopulation i to j.

$$R_{ij} = \frac{W_{ij}}{\sum_{l=1}^{N} W_{il}}. \tag{3}$$

At the end of each time step, each travelling individual returns to his/her place of residence.

To describe the financial risk information spreading dynamics, we adopt an unaware-aware-unaware (UAU) model [42, 43]. The unaware individual means that an individual does not know the financial risk information and maybe obtain the financial risk information in the following steps. An aware individual who stands for himself/herself has obtained the information and is willing to share it with others in the same subpopulation. The financial risk information spreading dynamics evolves as follows. Initially, we randomly select ϱn_i individuals as the seeds of the spreading, i.e., set those ϱn_i individuals in the aware state. At every time step, we perform the following two processes sequentially. (i) Each individual in each subpopulation moves with probability p_d, and his/her determination selection probability is determined according to equation (3). This migration can be regarded as an individual move from one forum (or communication group) to another. Individuals in the same subpopulation are sharing financial risk information. In ($\mathbb{AS}$), e.g., subpopulation i, each active individual will randomly contact $\tilde{k}$ individuals and try to transmit the financial risk information to each unaware individuals of the $\tilde{k}$ individuals with probability λ. For the unaware individual, he/she becomes aware if he/she receives at least one piece of financial risk information from neighbors successfully. The contagion process in the depressing subpopulation (DS) is similar to that in the AS. The only difference is that an unaware individual becoming aware should receive at least θ pieces of information from aware neighbors successfully. (ii) The travelling individuals return to his/her residence, and each aware individual becomes unaware with probability μ. The spreading dynamics evolve until the system reaches a dynamic steady state.

3. Theoretical Analysis

Inspired by [40, 44, 45], we develop a discrete-time Markov chain approach to study the evolution of financial risk information spreading on metapopulation. In theory, we assume that the infection probability of unaware node is independent, that is to say, there are no dynamical

correlations. Denote $\rho_i(t)$ $(i = 1, \ldots, N)$ as the fraction of active individuals in subpopulation i at time t. The evolution of $\rho_i(t)$ can be expressed as

$$\rho_i(t+1) = (1-\mu)\rho_i(t) + \big(1-\rho_i(t)\big)\Theta_i(t). \tag{4}$$

On the right-hand side of equation (4), the first expression represents the fraction of active individuals who do not recover. The second expression stands for the probability that the unaware individuals become aware. The expression $\Theta_i(t)$ means an unaware individual in subpopulation i is infected by active individuals.

Once the expression of $\Theta_i(t)$ is obtained, we know the evolution of $\rho_i(t)$. In the following, we solve the expression of $\Theta_i(t)$. An unaware individual b_i in subpopulation i becoming aware has two situations. (i) If individual b_i does not travel to neighboring subpopulation, he/she will be infected at time t in his own aboriginal subpopulation i with probability:

$$P_i(t) = \alpha P_i^1(t) + (1-\alpha)P_i^2(t). \tag{5}$$

The first expression on the right hand of equation (5) stands for the contagion probability when subpopulation i is $\mathbb{AS}$. The second expression represents the contagion probability when the subpopulation i is $(\mathbb{DS})$. When the subpopulation i is $(\mathbb{AS})$, the contagion probability is

$$P_i^1(t) = 1 - (1-\lambda)^{x_i(t)\widetilde{k}}, \tag{6}$$

where $x_i(t)$ stands for the fraction of active individuals in subpopulation i after the migration, and the expression of $x_i(t)$ is

$$\begin{aligned} x_i(t) &= \frac{\sum_{j=1}^{N} n_{j\longrightarrow i}\rho_j(t)}{\sum_{j=1}^{N} n_{j\longrightarrow i}} \\ &= \frac{\sum_{j=1}^{N} n_{j\longrightarrow i}\rho_j(t)}{n_i^{\text{eff}}}, \end{aligned} \tag{7}$$

where $n_i^{\text{eff}} = \sum_j n_{j\longrightarrow i}$ is the number of effective individuals in subpopulation i after migration. The term $n_{j\longrightarrow i}$ represents the number of individuals travelling from subpopulation j to subpopulation i and can be expressed as

$$n_{j\longrightarrow i} = \delta_{ij}(1-p_d)n_i + p_d\frac{W_{ji}}{\sum_{l=1}^{N} W_{jl}}n_j, \tag{8}$$

where $\delta_{ij} = 1$ when $i = j$; otherwise, $\delta_{ij} = 0$. In equation (8), the first second term stands for the number of individuals that do not travel to neighboring subpopulation, and the second term represents the number of individuals in which individuals in neighbors' subpopulation travelling to subpopulation i. (ii) If individual b_i travels to neighboring subpopulation and is infected at his/her determination, the contagion probability is $p_d\sum_{j=1}^{N} h_{i\longrightarrow j}P_j(t)$. Combining the above stated two situations, we obtain the expression of $\Theta_i(t)$ as

$$\Theta_i(t) = (1-p_d)P_i(t) + p_d\sum_{j=1}^{N}\frac{W_{ij}}{\sum_{l=1}^{N} W_{il}}P_j(t). \tag{9}$$

The above equations describe the financial risk information spreading dynamics on metapopulation. Iterating equation (4) from an initial value of $\rho_i(t)$, we obtain the dynamical steady state of $\rho_i(t \longrightarrow \infty)$. When the number of subpopulation is large, numerically solving the equations is hard, and we may use the dimensionality reduction approach. For the sake of simplicity, we denote $\rho_i(t \longrightarrow \infty)$ as ρ_i^*. The average fraction of individuals in the active state in the steady state is as

$$\langle\rho\rangle = \frac{1}{N}\sum_{i=1}^{N}\rho_i^*. \tag{10}$$

The values of $\langle\rho\rangle$ can be regarded as the order parameter of the system in statistical physics. That is to say, the global financial risk information outbreaks, i.e., $\langle\rho\rangle > 0$, when the information transmission probability λ is above a critical value λ_c. Otherwise, only a vanishingly small fraction of individuals is in the active state, i.e., $\langle\rho\rangle = 0$. In the following, we solve the expression of λ_c. In the steady state, we know $\rho_i(t+1) = \rho_i(t) = \rho_i^*$; therefore, equation (4) can be rewritten as

$$\mu\rho_i^* = \big(1-\rho_i^*\big)\left[(1-p_d)P_i + p_d\sum_{j=1}^{N}\frac{W_{ij}}{\sum_{l=1}^{N} W_{il}}P_j\right], \tag{11}$$

where

$$\begin{aligned} P_i &= \alpha P_i^1 + (1-\alpha)P_i^2 \\ &= \alpha\left(1-(1-\lambda)^{x_i\widetilde{k}}\right) + (1-\alpha) \\ &\quad\cdot\left[1-\left(\sum_{m=0}^{\theta-1}(1-\lambda)^{x_i\widetilde{k}-m}\lambda^m\binom{x_i\widetilde{k}}{m}\right)\right]. \end{aligned} \tag{12}$$

Near the critical value λ_c, the information spreading size is very small, i.e., $\rho_i^* \ll 1$; thus, we neglect the high orders of ρ_i^*. In addition, we assume that λ is small enough and obtain $(1-\lambda)^n \simeq 1-n\lambda$. Linearizing equation (12), we have $P_i \simeq \alpha x_i k\lambda$. Using this term, we further obtain

$$\Theta_i \simeq (1-p_d)\alpha x_i\widetilde{k}\lambda + p_d\sum_{j=1}^{N} R_{ij}\alpha x_j\widetilde{k}\lambda. \tag{13}$$

Inserting equations (7) and (8) into the above equation, we have

$$\begin{aligned} \Theta_i \simeq{}& (1-p_d)\alpha k\lambda\frac{(1-p_d)n_i\varepsilon_i^* + p_d\sum_{j=1}^{N} R_{ji}n_j\varepsilon_j^*}{(1-p_d)n_i + p_d\sum_{j=1}^{N} R_{ji}n_j} \\ &+ p_d\alpha k\lambda\sum_{j=1}^{N} R_{ij}\frac{(1-p_d)n_j\varepsilon_j^* + p_d\sum_{l=1}^{N} R_{lj}n_l\varepsilon_l^*}{(1-p_d)n_j + p_d\sum_{l=1}^{N} R_{lj}n_l}. \end{aligned} \tag{14}$$

During the computing process, we used the relation $\sum_{j=1}^{N}\delta_{ij}\varepsilon_j^* = \varepsilon_i^*$. We further obtain

$$\Theta \simeq (1-p_d)\alpha k\lambda\left(\mathbb{M}^1+\mathbb{M}^2R^T\mathbb{H}\right)\varepsilon^* + p_d\alpha k\lambda R\left(\mathbb{M}^1+\mathbb{M}^2R^T\mathbb{H}\right)\varepsilon^* = \alpha k\lambda\left(\mathbb{M}^1+\mathbb{M}^2R^T\mathbb{H}\right)\varepsilon^*. \tag{15}$$

An element of matrix $\mathbb{M}^1$ is

$$\mathbb{M}^1_{ij} = \begin{cases} 0, & i \neq j, \\ \dfrac{(1-p_d)n_i}{(1-p_d)n_i + p_d\sum_{l=1}^{N} R_{li}n_l}, & i = j. \end{cases} \tag{16}$$

The element of matrix $\mathbb{M}^2$ is

$$\mathbb{M}^2_{ij} = \begin{cases} 0, & i \neq j, \\ \dfrac{p_d n_i}{(1-p_d)n_i + p_d\sum_{l=1}^{N} h_{l\longrightarrow i}n_l}, & i = j. \end{cases} \tag{17}$$

The element of matrix $\mathbb{H}$ is

$$\mathbb{H}_{ij} = \begin{cases} 0, & i \neq j, \\ n_i, & i = j. \end{cases} \tag{18}$$

Denoting $\mathbb{M} = \alpha k(\mathbb{M}^1 + \mathbb{M}^2R^T\mathbb{H})$, we have

$$\frac{\mu}{\lambda}\varepsilon^* = \mathbb{M}\varepsilon^*. \tag{19}$$

The global financial risk information outbreak condition is

$$\lambda_c = \frac{\mu}{\Lambda_{\max}(\mathbb{M})}, \tag{20}$$

where $\Lambda_{\max}(\mathbb{M})$ is the largest eigenvalue of matrix $\mathbb{M}$. Numerically, solving equation (20), we obtain the value of λ_c.

4. Numerical Results' Analysis

To systemically investigate the financial risk information spreading dynamics on metapopulation networks, we perform extensive numerical simulations. We generate $N = 50$ subpopulation. For each subpopulation i, we set $n_i = 100$ number of residents. We randomly connect the 50 subpopulations with a given probability of $u = 0.3$. As a result, the average connection of a subpopulation is $\langle k\rangle = 15$. The edge weight distribution is $G(w)$ with average weight $\langle w\rangle = 10$. For the $\mathbb{DS}$, we set the $\theta = 3$. That is to say, an unaware individual in a $\mathbb{DS}$ becoming aware must receive three pieces of information successfully at a given time step. Through extensive numerical simulations, we found that other values of θ do not affect the results qualitatively. We perform numerical simulations at least 200 times when the system reaches a steady state for a given parameter set. We found that the spreading dynamics reached a steady state after 500 time steps through performing extensive numerical simulations. Mathematically, we verify that the system reaches a steady state when

$$\delta\rho = |\widehat{\rho}(t+1) - \widehat{\rho}(t)|, \tag{21}$$

is small than $\varepsilon = 10^{-5}$, where $\widehat{\rho}(t) = \sum_{t'=t-100}^{t}\rho(t\prime)$.

In Figure 2, we investigate the effects of four key parameters on the financial risk information spreading on metapopulation networks. We first discuss the impact of information transmission probability. As shown in Figures 2(a) and 2(b), we present the average fraction $\langle\rho\rangle$ of individuals in the aware state as a function of information transmission probability λ. We reveal that increasing the values of λ is beneficial for information spreading, i.e., $\langle\rho\rangle$ with λ. When $\lambda \leq \lambda_c$, which can be obtained by numerically solving equation (20), there are no individuals who received the financial risk information, that is, $\langle\rho\rangle = 0$. When $\lambda > \lambda_c$, we find that $\langle\rho\rangle$ is a finite value, which indicates the global financial risk information outbreak. This phenomenon demonstrates that we can contain the financial risk information spreading by reducing the information transmission probability.

We now discuss the effects of the second key parameter, fraction of $\mathbb{AD}$, on the spreading dynamics. As shown in Figure 2(a), we find that increasing the fraction of $\mathbb{AD}$ promotes the information spreading. That is to say, $\langle\rho\rangle$ increases with α. For large values of α, there are more $\mathbb{AD}$. Therefore, more unaware individuals becoming aware only need to receive one piece of information from others. As a result, the global financial risk information spreading dynamics is promoted.

The third key parameter is the variance of the weight distribution. In Figure 1, we set $\sigma^2 = 0$, 4, and 9 for different values of α and p_d. We reveal that the variance does not markedly affect the financial risk information spreading size and outbreak threshold. This phenomenon indicates that the varying connection strength among subpopulations cannot significantly affect the spreading of financial risk. Lastly, we revealed that the travelling probability does not significantly affect the spreading dynamics. Our proposed discrete-time Markov chain approach can predict the above phenomena.

Finally, we study the financial risk information spreading size as a function of travelling probability p_d and information transmission probability λ in detail in Figure 3. For small values of α, i.e., a few subpopulations are $\mathbb{AS}$, the financial risk information cannot globally outbreak for any values of p_d and λ, as shown in Figures 3(a) and 3(b). With

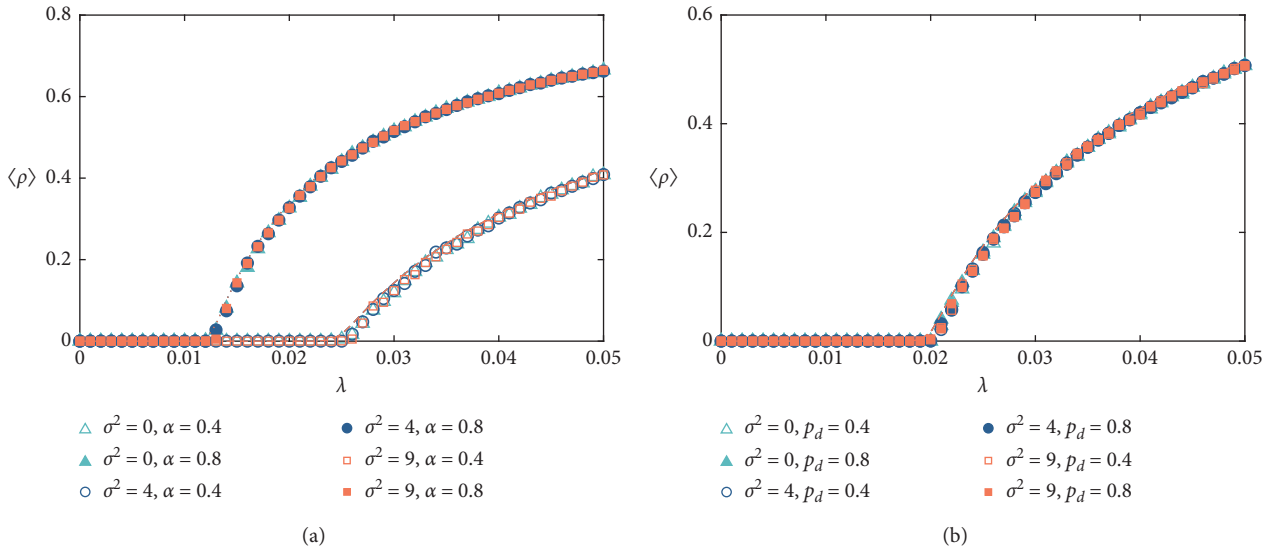

FIGURE 2: Financial risk information spreading on metapopulation networks. (a) The fraction of individuals in the active state $\langle\rho\rangle$ versus information transmission probability λ with travelling probability $p_d = 0.5$. (b) $\langle\rho\rangle$ versus λ with $\alpha = 0.5$. The average weight is set to be $\langle w\rangle = 10$ and recovery probability $\mu = 0.2$. The lines stand for the theoretical analysis and symbols represent the numerical simulation results.

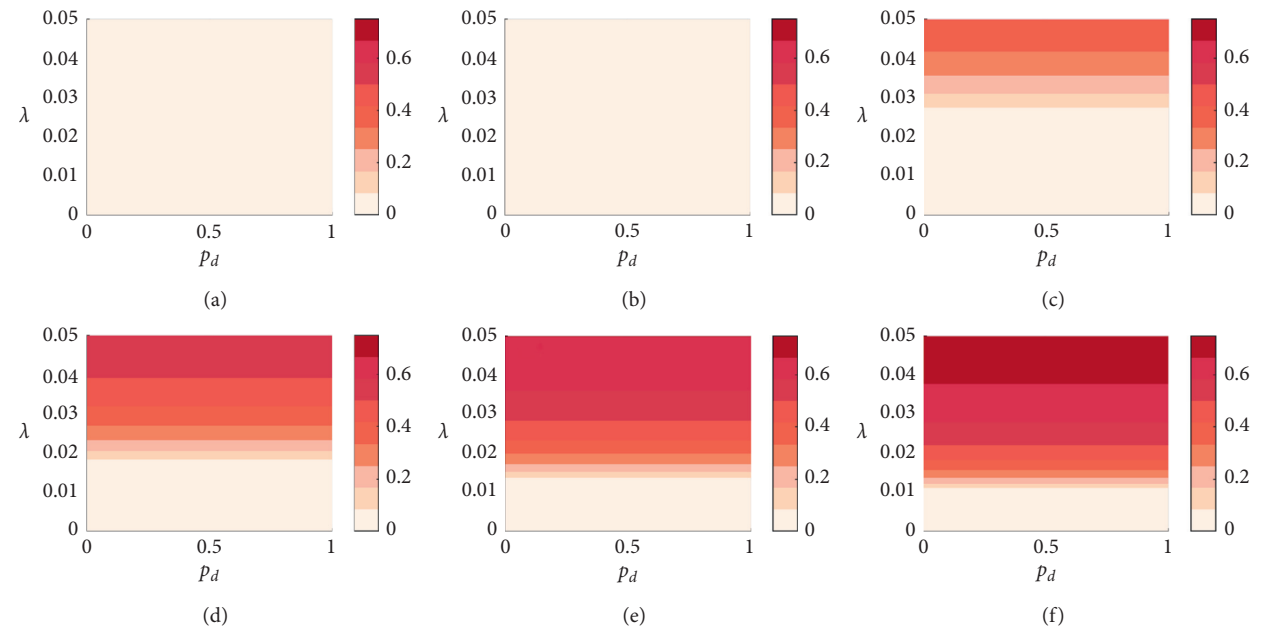

FIGURE 3: The financial risk information spreading on metapopulation on (p_d, λ) plane. The financial risk information spreading size $\langle\rho\rangle$ as a function of travelling probability p_d and information transmission probability λ with $\alpha = 0$ (a), $\alpha = 0.2$ (b), $\alpha = 0.4$ (c), $\alpha = 0.6$ (d), $\alpha = 0.8$ (e), and $\alpha = 1$ (f). Different colors represent the values of $\langle\rho\rangle$.

the increase of α, the global financial risk information outbreak becomes possible when $\lambda > \lambda_c$. In Figures 3(c)–3(f), we find that $\langle\rho\rangle$ does not vary with p_d.

5. Conclusions

In this paper, we investigated the financial risk information spreading on social networks. To describe the different social platforms and forums in the spreading dynamics, we adopt the metapopulation network, in which a forum is a subpopulation and mixed randomly. At every time step, each individual may travel from one subpopulation to another. We used a discrete-time Markov chain approach to describe the dynamical process and critical point. Our theory can reasonably predict numerical simulations. We noted that the financial risk information spreading size depends on the

information transmission probability, a fraction of active subpopulation, and independent on the variance of the weight distribution and travelling probability. Our results may shed some light on studying the financial risk information spreading dynamics and contain the financial risk. On the one hand, our model and theoretical approach maybe used to study other dynamics on metapopulation networks. On the other hand, to contain the financial risk information spreading, we can reduce the information transmission probability. For more realistical situations, the fraction of DS is not simply following a binomial distribution. Therefore, other forms of distribution need further studies.

Data Availability

The data that support the findings of this study are available from the corresponding author upon request.

Conflicts of Interest

The authors declare that they have no conflicts of interest.

Acknowledgments

This work was partially supported by Sichuan Science and Technology Program (no. 2020JDR0200) and National Social Science Foundation of China Western Project (no. 18XJY001).

References

[1] R. Albert and A.-L. Barabási, "Statistical mechanics of complex networks," *Reviews of Modern Physics*, vol. 74, no. 1, p. 47, 2002.

[2] M. Newman, *Networks*, Oxford University Press, Oxford, UK, 2018.

[3] S. N. Dorogovtsev and J. F. F. Mendes, "Evolution of networks," *Advances in Physics*, vol. 51, no. 4, p. 1079, 2002.

[4] A. G. Haldane and R. M. May, "Systemic risk in banking ecosystems," *Nature*, vol. 469, no. 7330, p. 351, 2011.

[5] A. G. Haldane, *Fragile Stabilität–Stabile Fragilität*, pp. 243–278, Springer, Berlin, Germany, 2013.

[6] P. Barucca, M. Bardoscia, F. Caccioli et al., "Network valuation in financial systems," *Mathematical Finance*, vol. 30, no. 4, pp. 1181–1204, 2020.

[7] P. Gai and S. Kapadia, "Contagion in financial networks," *Proceedings of the Royal Society A: Mathematical, Physical and Engineering Sciences*, vol. 466, no. 2120, p. 2401, 2010.

[8] Z. Wang, X. Gao, H. An, R. Tang, and Q. Sun, "Identifying influential energy stocks based on spillover network," *International Review of Financial Analysis*, vol. 68, pp. 101–277, 2020.

[9] F. Linardi, C. Diks, M. Van Der Leij, and I. Lazier, "Dynamic interbank network analysis using latent space models," *Journal of Economic Dynamics and Control*, vol. 112, Article ID 103792, 2020.

[10] M. Elliott, B. Golub, and M. O. Jackson, "Financial networks and contagion," *American Economic Review*, vol. 104, no. 10, p. 3115, 2014.

[11] R. Cont, A. Moussa, and E. B. e Santos, "Network structure and systemic risk in banking systems," *SSRN Electronic Journal*, 2010.

[12] S. Khanna and B. Hemenway Falk, *Jacobs Levy Equity Management Center for Quantitative Financial Research Paper*, University Of Pennsylvania, Philadelphia, PA 19104, USA, 2020.

[13] R. Doyle, "Transparency in language generation: levels of automation," 2020, https://arxiv.org/abs/2006.06295.

[14] A. Garas, P. Argyrakis, C. Rozenblat, M. Tomassini, and S. Havlin, "Worldwide spreading of economic crisis," *New Journal of Physics*, vol. 12, no. 11, p. 113043, 2010.

[15] Z.-K. Zhang, C. Liu, X.-X. Zhan, X. Lu, C.-X. Zhang, and Y.-C. Zhang, "Dynamics of information diffusion and its applications on complex networks," *Physics Reports*, vol. 651, p. 1, 2016.

[16] R. Pastor-Satorras and A. Vespignani, "Epidemic dynamics and endemic states in complex networks," *Physical Review E*, vol. 63, Article ID 066117, 2001.

[17] R. Pastor-Satorras and A. Vespignani, "Immunization of complex networks," *Physical Review E*, vol. 65, Article ID 035108, 2002.

[18] Y. Moreno, R. Pastor-Satorras, and A. Vespignani, "When individual behaviour matters: homogeneous and network models in epidemiology," *The European Physical Journal B*, vol. 26, no. 4, p. 521, 2002.

[19] W. Wang, M. Tang, H.-F. Zhang, H. Gao, Y. Do, and Z.-H. Liu, "Epidemic spreading on complex networks with general degree and weight distributions," *Physical Review E*, vol. 90, Article ID 042803, 2014.

[20] D. J. Watts, "A simple model of global cascades on random networks," *Proceedings of the National Academy of Sciences*, vol. 99, no. 9, pp. 57–66, 2002.

[21] W. Chen, Y. Wang, and S. Yang in *Proceedings of the 15th ACM SIGKDD International Conference on Knowledge Discovery and Data Mining*, pp. 199–208, June 2009.

[22] C. Castellano, S. Fortunato, and V. Loreto, "Statistical physics of social dynamics," *Reviews of Modern Physics*, vol. 81, no. 2, p. 591, 2009.

[23] C. Castellano and R. Pastor-Satorras, "Thresholds for epidemic spreading in networks," *Physical Review Letters*, vol. 105, Article ID 218701, 2010.

[24] W. Wang, M. Tang, H. E. Stanley, and L. A. Braunstein, "Unification of theoretical approaches for epidemic spreading on complex networks," *Reports on Progress in Physics*, vol. 80, no. 80, p. 36603, 2017.

[25] M. Boguná, R. Pastor-Satorras, and A. Vespignani, "Absence of epidemic threshold in scale-free networks with degree correlations," *Physical Review Letters*, vol. 90, Article ID 028701, 2003.

[26] W. Wang, Q.-H. Liu, J. Liang, Y. Hu, and T. Zhou, "Coevolution spreading in complex networks," *Physics Reports*, vol. 820, p. 1, 2019.

[27] M. Starnini, J. P. Gleeson, and M. Boguñá, "Equivalence between non-markovian and markovian dynamics in epidemic spreading processes," *Physical Review Letters*, vol. 118, Article ID 128301, 2017.

[28] D.-W. Huang, L.-X. Yang, X. Yang, Y. Y. Tang, and J. Bi, "Discrete dynamics in nature and society 2020," *Discrete Dynamics in Nature and Society (DDNS)*, 2020.

[29] M. Kivelä, A. Arenas, M. Barthelemy, J. P. Gleeson, Y. Moreno, and M. A. Porter, "Multilayer networks," *Journal of Complex Networks*, vol. 2, no. 3, p. 203, 2014.

[30] M. De Domenico, V. Nicosia, A. Arenas, and V. Latora, "Structural reducibility of multilayer networks," *Nature Communications*, vol. 6, p. 1, 2015.

[31] S. Boccaletti, G. Bianconi, R. Criado et al., "The structure and dynamics of multilayer networks," *Physics Reports*, vol. 544, no. 1, p. 1, 2014.
[32] M. De Domenico, A. Solé-Ribalta, E. Cozzo et al., "Mathematical formulation of multilayer networks," *Physical Review X*, vol. 3, Article ID 041022, 2013.
[33] K.-M. Lee, B. Min, and K.-I. Goh, "Towards real-world complexity: an introduction to multiplex networks," *The European Physical Journal B*, vol. 88, p. 48, 2015.
[34] V. Colizza, R. Pastor-Satorras, and A. Vespignani, "Reaction-diffusion processes and metapopulation models in heterogeneous networks," *Nature Physics*, vol. 3, no. 4, p. 276, 2007.
[35] L. Wang and X. Li, "Spatial epidemiology of networked metapopulation: an overview," *Chinese Science Bulletin*, vol. 59, no. 28, p. 3511, 2014.
[36] S.-Y. Liu, A. Baronchelli, and N. Perra, "Contagion dynamics in time-varying metapopulation networks," *Physical Review E*, vol. 87, Article ID 032805, 2013.
[37] B. Min, S.-H. Gwak, N. Lee, and K.-I. Goh, "Layer-switching cost and optimality in information spreading on multiplex networks," *Scientific Reports*, vol. 6, Article ID 21392, 2016.
[38] Z. Wang, C. Xia, Z. Chen, and G. Chen, *Institute of Electrical and Electronics Engineers Transactions on Cybernetics*, 2020.
[39] H. Liang'an, H. Guo, Y. Cheng, and X. Xie, "A new model for supply chain risk propagation considering herd mentality and risk preference under warning information on multiplex networks," *Physica A: Statistical Mechanics and Its Applications*, vol. 545, Article ID 123506, 2020.
[40] J. Gómez-Gardeñes, D. Soriano-Paños, and A. Arenas, "Critical regimes driven by recurrent mobility patterns of reaction-diffusion processes in networks," *Nature Physics*, vol. 14, no. 4, p. 391, 2018.
[41] W. Wang, X.-L. Chen, and L.-F. Zhong, "Social contagions with heterogeneous credibility," *Physica A: Statistical Mechanics and Its Applications*, vol. 503, p. 604, 2018.
[42] C. Granell, S. Gómez, and A. Arenas, "Dynamical interplay between awareness and epidemic spreading in multiplex networks," *Physical Review Letters*, vol. 111, Article ID 128701, 2013.
[43] E. H. Xu, W. Wang, C. Xu, M. Tang, Y. Do, and P. Hui, "Suppressed epidemics in multirelational networks," *Physical Review E*, vol. 92, Article ID 022812, 2015.
[44] S. Gómez, A. Arenas, J. Borge-Holthoefer, S. Meloni, and Y. Moreno, "Discrete-time Markov chain approach to contact-based disease spreading in complex networks," *EPL (Europhysics Letters)*, vol. 89, no. 3, p. 38009, 2010.
[45] W. Wang, Y. Ma, T. Wu, Y. Dai, X. Chen, and L. A. Braunstein, "Containing misinformation spreading in temporal social networks," *Chaos: An Interdisciplinary Journal of Nonlinear Science*, vol. 29, no. 12, pp. 123–131, 2019.

Hindawi
Complexity
Volume 2021, Article ID 3467485, 16 pages
https://doi.org/10.1155/2021/3467485

Research Article

Development of a Complex Network-Based Integrated Multilayer Urban Growth and Optimisation Model for an Efficient Urban Traffic Network

Rui Ding[1,2,3] **Yilin Zhang,**[1,2,3] **Ting Zhang**[1,2,3] **and Can Ma**[1,2,3]

[1]*School of Big Data Application and Economics (Guiyang College of Big Data Finance), Guizhou University of Finance and Economics, Guiyang 550025, China*
[2]*Guizhou Key Laboratory of Big Data Statistical Analysis, Guizhou University of Finance and Economics, Guiyang 550025, China*
[3]*Key Laboratory of Green Fintech, Guizhou University of Finance and Economics, Guiyang 550025, China*

Correspondence should be addressed to Ting Zhang; 269493818@qq.com

Received 7 June 2020; Revised 3 December 2020; Accepted 6 January 2021; Published 23 January 2021

Academic Editor: Jiaojiao Jiang

Previous research studies of traffic networks are mainly based on planar networks and less considered the influence of multilayer networks, which illustrate and represent different appropriate urban traffic modes. Development of rail and road networks is inseparable from the development of a prosperous urban area; thus, research on multilayer networks has scientific potential and fulfils a real need. In this paper, a framework of complex network based integrated multilayer urban growth and optimisation model (CNIMUGOM) is proposed, to analyse the complex relationships between the traffic network structure, the population growth, and the urban land-use. The innovation of this paper is the combination of the traffic complex multilayer networks and the "Four Step Model" (which stands for trip generation, trip distribution, model split, and traffic assignment steps). With the multiobjective, multilayer network coevolution and optimisation model, a more efficient traffic network layout was generated based on different land-use, population density, and travel speed scenarios. Then, this paper has proved that the proposed CNIMUGOM can save the traffic network construction investment, reduce the travel cost, make the urban traffic network more efficient, and decrease the total traffic flow amount. This research has connected the recent complex multilayer network related study and traditional urban economic model based study. The findings of the study afford to improve the current land-use and traffic integrated models and can provide traffic network planning suggestions for urban agglomeration development.

1. Introduction

Many developing countries still face rapid urbanisation process, with numerous scholars focusing on the prompt urban traffic network growth and coevolution process [1–3]. To measure the growth and coevolution process of an urban traffic network, research concentrated on two aspects: the first is modelling and simulation, and the second is its natural course [4–6]. The study of the coevolution process can clearly analyse the interrelationships between urban land-use and traffic networks [7, 8]. Focusing on the coevolution model of the 19th and 20th century in London, the group of Levinson and Xie found that population distribution and network density are positively correlated. They validated a simulation model to fit the empirical evidence better and noted that evolution is an iterative process of interaction, investment, and divestment. Moreover, they illustrated how surface traffic networks could grow and decline spontaneously over time, providing further evidence for the property of self-organisation [5, 9–11]. Similarly, a new dynamic model based on the logistic equation, which captures the dynamic characteristics of the coevolution process between the street surface and urban traffic structure, was developed [12]. After that, the coevolution of urban traffic growth grounded in the case of Beijing is described [13], and a coevolution model is suggested with stability analysis and numerical simulation. In another way, Rui [14] used the multiagent based model to discuss the complex traffic network growth and land-use coevolution

process, and centrality indices from different aspects were thoroughly analysed with the study of Stockholm. Recently, Li et al. [15] proposed an optimal urban expressway system model, which considered the interaction equilibrium of transportation and land-use.

Although those previous investigations are essential and necessary for further research of urban traffic network and land-use, they all treat networks as purely planar. Some of them considered the network growth and variation, but none of them considered the influence of multilayer networks, which is the cause of attention to multilayer networks related analysis.

Development of rail and street networks is inseparable from the development of a prosperous urban area; thus, research on multilayer networks has scientific potential and fulfils a real need. To bridge the gap of the multilayer network representation of real-world networks, Kurant and Thiran [16] first proposed a general multilayer model that facilitated the description and analysis of multilayer networks. The authors examined three transportation networks and found that a small error on a multilayer network could cause cascading failures. They also investigated the relationships between degree, betweenness, and real loads and found that, as opposed to the commonly acknowledged view, the correlations in their dataset between the three factors were not that apparent. More recently, multilayer networks earned more attention, as traffic dynamics in two-layer complex networks were considered by Ma et al. [17], and Albert et al. [18] introduced a standardised model to simulate the elements navigating those networks and analysed congestion in multilayer transportation networks. Furthermore, the ratio of speeds of coupling different modes, network accessibility, mobility, and behaviour of different layers were considered [18–23]. These researches bring a new broad of perspective, investigating the aspects of multilayer networks to consider the interrelationship and cooperation of different traffic layers and modes [22, 23].

With the novel study of multilayer networks, the relationships between the urban traffic networks and land-use of surrounding areas might be discussed. With the analysis of some new indicators, their complex relationships become measurable. This fills the research gap of recent urban traffic network structure based studies; with the study of network coevolution process, the complex dynamics growth process can be partly studied. The influence of multilayer networks can be also measured, which connect the growth of upper-layer and lower-layer network and the accessibility change of surrounding areas related to urban land-use [24]. Based on these works, in this paper, the framework of complex network based integrated multilayer urban growth and optimisation model (CNIMUGOM) will be proposed first. Considering the traffic network structure, with the population growth rate rp and its affection of urban land-use model (the change of accessibility of employment A_i^E and population A_i^P), and the coupling features of multilayer networks, the study identifies issues regarding the "Four Step Model" (FSM). For the travel demand model, the number of trips generated O_i and attracted D_i; the number of trips from traffic zone i to zone j, T_{ij}; the generalised travel cost t_{ij}; the travel time on the link a, t_a; and the traffic flow f_a will be calculated. For the street investment model and traffic network growth model, the collected revenue of this link R_a, the measurement of multilayer network structure status NS_i, the overall spending function S_a, and the general investment I^{k+1} of iteration $k+1$ will be calculated in Matlab. With the multiobjective, multilayer network coevolution and optimisation model, the more efficient network layout can be generated based on some different land-use (different population density) scenarios. Based on the traffic network and urban land-use coevolution process, the proposed CNIMUGOM can save the traffic network construction investment, reduce the travel cost, and make the urban traffic network more efficient. Based on the simulation, the proposed network can increase network efficiency and decrease the total traffic flow amount.

2. Methodology

This study refers to the general urban transportation system as a multilayer network. The upper-layer network represents the public rail network, which may include rapid transit, LRT, monorail, MRT, and subway. Here, this study does not distinguish between rail transit modes. The lower-layer network represents urban street and road networks.

2.1. Single-Layer Network Representation Method. This method is used by many scholars, and related studies of different cities were widely accepted [25–28]. According to the primal approach, the single-layer network representation method, as shown in Figure 1, the black lines on the right act as streets or roads, the nodes represent the street intersections, and the grey spots are buildings.

With this method, the different undirected or directed networks can be used to represent the urban transportation networks:

$$G = \langle V, E, W \rangle, \tag{1}$$

where V is the set of nodes, N is the number of nodes when

$$V = \{v_i | i \in I \equiv \{1, 2, \ldots, N\}\}, \tag{2}$$

E is the unordered pairs or edges of elements of V and is denoted by e_{ij},

$$E = \left\{e_{ij} = \left(v_i, v_j\right) | i, j \in I\right\}, \tag{3}$$

and W is the weight of each edge; in some functions, it can be denoted as w, and the weight can be treated as the length of the edge or lanes.

The number of edges is denoted as M. The adjacency matrix of networks is

$$A = \left[a_{ij}\right]_{n \times n}, \tag{4}$$

representing the connection between nodes v_i and v_j, which is defined as

$$a_{ij} = \begin{cases} 1, & \left(v_i, v_j\right) \in V, \\ 0, & \left(v_i, v_j\right) \notin V, \end{cases} \tag{5}$$

where $a_{ii} = 0$ to remove any self-connections. In addition, $A = [a_{ij}]_{n \times n}$ is symmetrical and nonnegative.

(a) (b)

Figure 1: The single-layer network representation method.

We define D as the network diameter, with

$$D = \max\{S_{ij}\}, \quad 1 \le D \le (N-1). \tag{6}$$

Here, S_{ij} is the sum of edge numbers between node pair i and j.

The degree centrality was proposed by Freeman [29]; the function is

$$\mathrm{DC}(v_i) = \frac{k_i}{N-1}. \tag{7}$$

The number of link incidents on a node can reflect the importance of the node v_i in relation to spatial geography, which indicates that a node with more neighbours is more important in a network.

The closeness centrality was proposed by Marchiori and Latora [30]; the function is

$$C_{\text{closeness}}(v_i) = \frac{1}{D_{ij}} = \frac{N-1}{\sum_{i \ne j} d_{ij}}. \tag{8}$$

It is denoted as the reciprocal of the average distance between each node pair $D_{ij} = (\sum_{i \ne j} d_{ij}/N-1)$. This index means that if a node is closer to the other remaining nodes, it is more important in the network; it describes the relative location of a node.

The betweenness centrality was proposed by Freeman [29]; the function is

$$\mathrm{BC}(v_i) = \frac{\sum_{i \ne s \ne t \in V} \left(d^i_{\min,\mathrm{st}}/d_{\min,\mathrm{st}}\right)}{(N-1)(N-2)}. \tag{9}$$

It is defined as the total number of shortest paths between two separate nodes $d_{\min,\mathrm{st}}$ and passing through node v_i; it reflects the load on node v_i and can be alternately understood as the controllability of the node. On this basis, centrality can be clarified as

$$C_{\text{betweenness}}(v_i) = \sum_{i \ne s \ne t \in V} \frac{d^i_{\min,\mathrm{st}}}{d_{\min,\mathrm{st}}}, \tag{10}$$

and the normalisation of betweenness $\mathrm{BC}(v_i)$ is described as the function shows, where $(N-1)(N-2)$ is the maximum possible value.

The average shortest path length was proposed by Albert and Barabási [31]; the function is

$$\mathrm{APL} = \frac{1}{N(N-1)} \sum_{i \ne j} d^{ij}_{\min}. \tag{11}$$

It is defined as the average number of steps along the shortest paths for all possible pairs of network nodes.

The network efficiency $E(G)$ was proposed by [32]; the function is

$$E(G) = \frac{1}{N(N-1)} \sum_{i \ne j} \frac{1}{d^{ij}_{\min}}. \tag{12}$$

It shows the average efficiency of transit flow or information between nodes in the network.

2.2. Multilayer Network Representation Method. Gu et al. [33] used this method to study airline networks and rail networks. The formula of the undirected multilayer network (see Figure 2) can be represented as

$$G = G^U, G^L, \tag{13}$$

as the set of different layers; here, the superscript U is used to define the upper-layer network and superscript L to set the lower-layer [33, 34].

The connected network can be used to represent the rail network and urban street network as

$$\begin{aligned} G^U &= V^U, E^U, W^U, \\ G^L &= V^L, E^L, W^L. \end{aligned} \tag{14}$$

The weight is denoted by W in the function [35]. Red nodes represent rail stations, and blue nodes represent street intersections; solid lines represent their connections, and dotted lines represent cross links (cooperative relationship) between different layers. The rail network station is connecting with the nearest street network intersection and its weight is equal to 1 [23]. To simplify the transfer process, when measuring the accessibility, this study sets the transfer time between the two layers to 3 minutes [36]. The multimodal transportation and relations between the vehicle-based network and the pedestrian network can be gained from the multilayer network.

The multilayer network model of urban traffic networks; the upper-layer represents rail network topology, and the

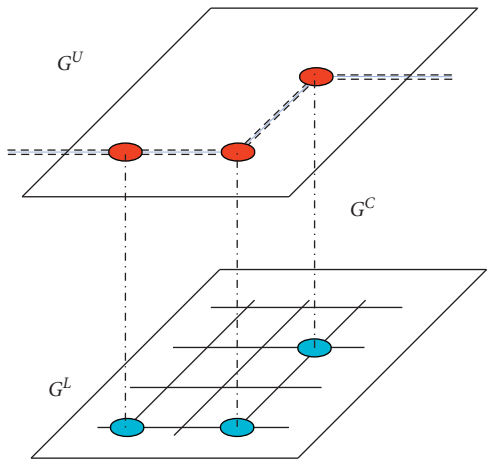

Figure 2: The multilayer network representation method.

lower-layer represents the street network topology or OD zones.

In this definition, V is the set of the street network topology, and N is the node number of lower-layer when

$$V = \{V_i | i \in I \equiv \{1, 2, \ldots, N\}\}, \tag{15}$$

and E represents the unordered pairs of edges and elements of V and is denoted by e_{ij}

$$E = \left\{e_{ij} = \left(v_i, v_j\right) | i, j \in I\right\}. \tag{16}$$

Similarly, the definition of the multilayer network is

$$\begin{aligned} N^{\text{multi}} &= N^U + N^L, \\ V^{\text{multi}} &= V^U + V^L, \\ E^{\text{multi}} &= E^U + E^L + E^C. \end{aligned} \tag{17}$$

The adjacency matrix of networks $\text{adj} = [a_{ij}]_{n \times n}$ is symmetrical and nonnegative, representing the connection between zones i and j, where

$$a_{ij} = \begin{cases} d_{ij} \times W, & \left(v_i, v_j\right) \in E, \\ 0, & \left(v_i, v_j\right) \notin E, \end{cases} \tag{18}$$

where d_{ij} is the Euclidean distance. Define $a_{ii} = 0$ to theoretically remove any self-connections to exclude the impact of the network element itself. Then, the adjacency matrix of multilayer networks is

$$\text{adj}^{\text{multi}} = \begin{bmatrix} \text{adj}^U_{N^U \times N^U} & \text{adj}^C_{N^U \times N^L} \\ \text{adj}^C_{N^L \times N^U} & \text{adj}^L_{N^L \times N^L} \end{bmatrix}. \tag{19}$$

2.3. Analysing the Coevolution Process of Multilayer Network

2.3.1. The Inner Connections of Multilayer Networks. For a big city, building all of these traffic links as railways is a waste of money and less effective, and only constructing streets without any massive rapid transit will cause a heavy traffic jam. The specific structure of the traffic multilayer networks is the result of the combination of natural and historical conditions, location characteristics, economic development and conditions, urban space layout, and even traffic customers. The network structures determine the relationships of different layers; they are highly related but have apparent differences. One of them is the complementary element of another, using their advantages to make up for the deficiency of others. The structural change of one layer will cause the change of another layer. Their combination completes the urban traffic networks functions

The traffic distribution is more focused on the choice of routes between origin-destination OD zones. It is an iterated process which compares the trips assigned with the link capacity to find an equilibrium status and show the number of travellers on each route and link in a given transportation network. The classic User Equilibrium (UE) is widely approved and used to describe the user's route behaviour. Once the users believe that they find the smallest impedance (perceptual impedance), they will not change their routes, although the routes are not the smallest route and the impedance may not be the smallest route impedance. Thus, an equilibrium is reached. Related functions will be provided in later sections.

With the population movement and growth, the growth of upper-layer and lower-layer networks is determined; considering the UE problem, we use the Frank–Wolfe BPR method and set the travel cost on the congested links as infinite. The Frank–Wolfe algorithm is "an iterative first-order optimisation algorithm for constrained convex optimisation" [37, 38], which is widely used to deal with the traffic equilibrium problem such as UE. After that, the network structure data, the cost of each link, the OD demand data, and the capacity of each link are obtained; then, we initialise the optimisation aims, construct the impedance function, and find the initial impedance. Then, we use the All or Nothing Assignment technique [39] to assign the traffic flow and update the data, and finally the optimal function value converging to 5% of estimation error range can be obtained. This technique is widely used and well accepted by many traffic network researchers [38, 40–42].

2.3.2. The Coevolution Relationships between Traffic Multilayer Network and Urban Land-Use. Many related types of research have discussed their connections and inner relationships [43, 44]. Because the traffic capacity and travel speed are different, the impacts of network structure change to land-use typically can be measured by the accessibility [45, 46]. The spatial connection means that urban land-use growth is characterised by continuity in a planar space [47], and then it is meaningful for the measurement of the population diffusion and urban growth process. Urban land-use change process also has a positive correlation with the variation of the population [48].

Their coevolution relationships can be simply represented in Figure 3, in which the traffic generation and attraction are determined by the urban land-use spatial distribution; with the increase of population density, land-use intensity, and sprawl or generation of new land-use

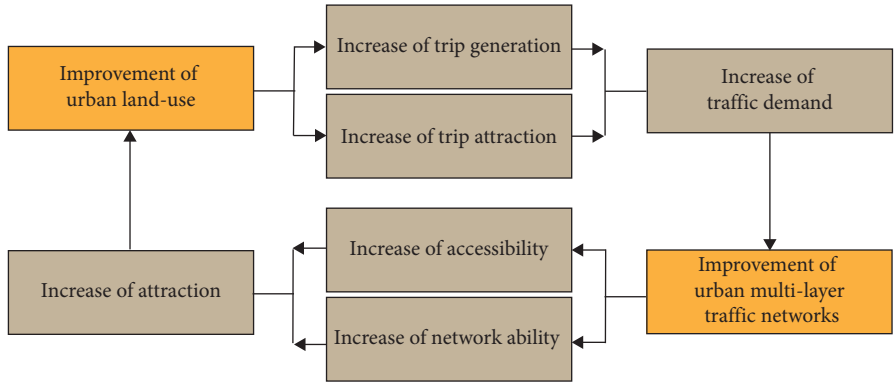

Figure 3: The simple coevolution relationships between traffic multilayer network and urban land-use.

parcels, traffic demand is increasing with different scales, which naturally needs more traffic infrastructures to satisfy it. In turn, the increase of the investment of multilayer traffic networks, which make the traffic networks grow densely, increases the accessibility of land parcels; as more streets pass the area, people can easily access this previously less developed area. The abilities of networks can also be improved, as the investment is always used to increase the capacities and the topological network functions of each layer. Based on the location theory and the scarcity of urban land resources, the attraction of these land parcels connected with traffic networks will increase. Then, more people are attracted, and the coevolution process emerges. Here, the land-use coevolution model is developed to reflect the relationship of accessibility with population growth and movement, and traffic network growth. Other factors, such as house price and related policies, are excluded to keep this relationship succinct and clear. Hence, the land-use model is highly simplified, mainly focused on the accessibility, and represented as the distribution of population and employment.

To represent the competition characteristic of neighbourhood interactions, the land-use coevolution model also includes both centrifugal and centripetal forces [49, 50]. Assume that people always want to live near to the location of jobs to save travel cost, but far away from other people such as potential contestants. However, on the other hand, employment wants to be accessible both to other businesses (to save cargo transportation cost) and to people (who are the suppliers of labour and customers). Both of them want to live with a higher traffic network structure service grade. Related functions will be provided in Section 3.

3. The CNIMUGOM

3.1. The Framework of CNIMUGOM. The content of the model is suggested, as shown in Figure 4, and different blocks stand for different models, with the relationships between those models illustrated as arrows. The most famous models are the travel demand model, street investment model, traffic network growth model, population growth model, urban land-use growth model, and network optimisation model.

3.2. Traffic Demand Model. The demographic, socioeconomic, land-use, and online hailing data were incorporated to reveal the root causing that influence traffic demand [51–53]. When considering the traffic network growth, an important part that must be focused on is that this kind of growth is always constrained and stimulated by traffic demand. Based on the initial traffic network data, the classic "Four Step Model" (FSM) can be generated and used, considering the multilayer networks and the network coevolution process. The travel demand model in an initial network is predetermined by population and employment data and related to the topology of the multilayer network.

3.2.1. Trip Generation Model. A simple traffic generation model was given by Levinson and Zhu [49] and Xie and Levinson [54], where trip generation and trip attraction of different traffic zones were calculated; with respect to the population and employment and their natural carriers, households and companies, the simple linear relationships were proposed, and the assumption formula is

$$\begin{aligned} O_i &= \xi_0 + \xi_1 E_i + \xi_2 P_i, \\ D_i &= \psi_0 + \psi_1 E_i + \psi_2 P_i, \end{aligned} \tag{20}$$

where O_i and D_i stand for the number of trips generated and attracted; E and P stand for the amount of the employment and population of traffic zone i, respectively; and ξ_0, ξ_1, ξ_2, ψ_0, ψ_1, and ψ_2 are adjustable coefficients of this simple linear equation set, and their values are 0, 0.5, 1, 0, 1, and 0.5, respectively.

3.2.2. Trip Distribution Model. For the general distribution process, the mostly used doubly constrained trip distribution model is adopted, that is, a gravity-based model, to match both trip generation and attraction of locations based on a negative exponential function that assumes that the interactions of zones decrease with the travel time between them [50, 54]:

$$T_{ij} = \left(K_i K_j\right) O_i D_j e^{-\phi t_{ij}} = \frac{O_i D_j e^{-\phi t_{ij}}}{\left(\sum_i K_i O_i e^{-\phi t_{ij}} \times \sum_j K_j D_j e^{-\phi t_{ij}}\right)}, \tag{21}$$

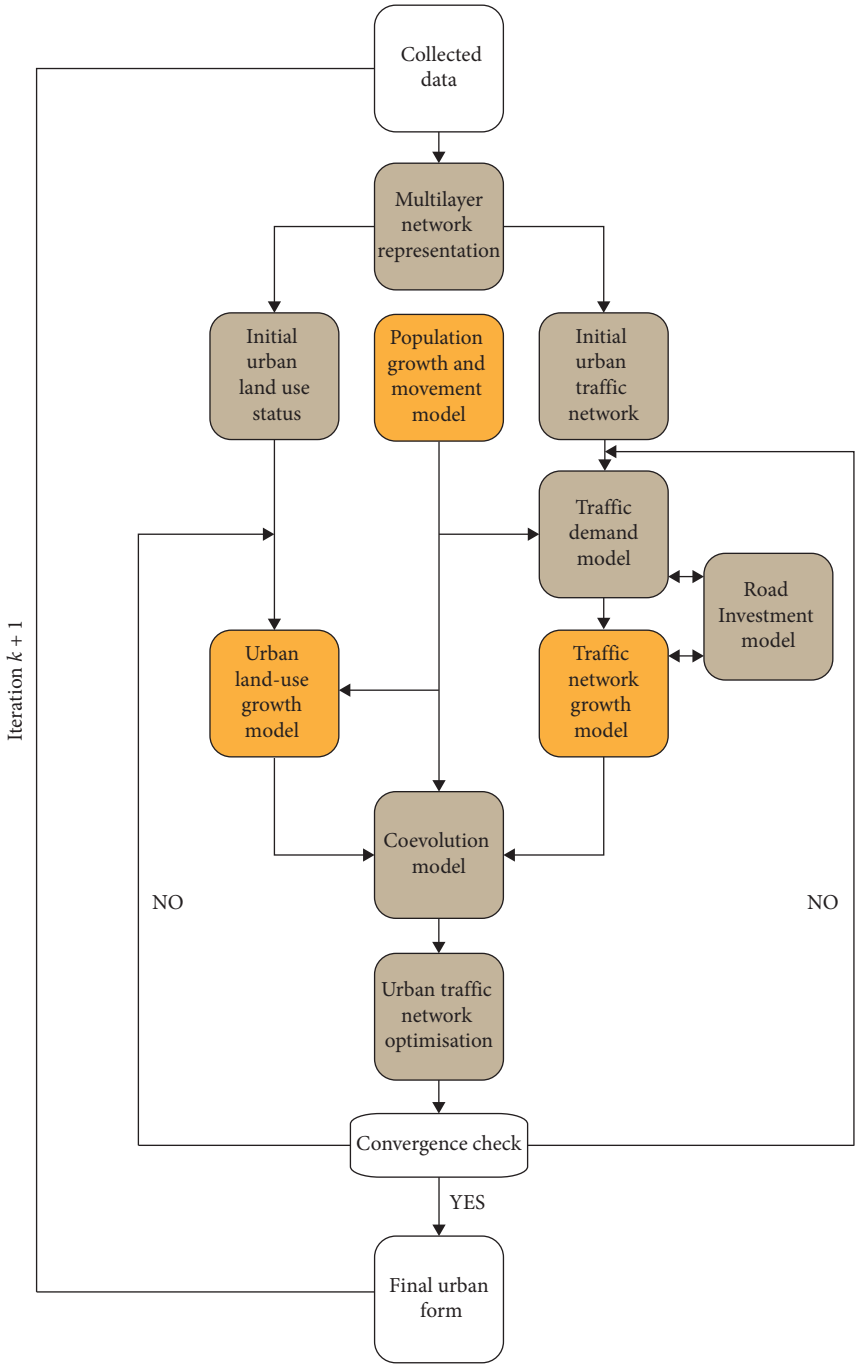

Figure 4: The framework of CNIMUGOM.

where T_{ij} is the number of trips from zone i to zone j, and its table can be gained as the OD matrix; O_i is the number of trips attracted in zone i; D_j is the number of trips attracted by zone j; and t_{ij} is the travel cost. $(K_iK_j) = (1/(\sum_i K_i O_i e^{-\phi t_{ij}} \times \sum_j K_j D_j e^{-\phi t_{ij}}))$ are the balancing coefficients which were precalibrated [55, 56].

3.2.3. Measurement of the Network Structure Related to Generalised Travel Cost. The generalised travel cost as normal travel cost t_{ij} is measured by travel time, a generalised concept considering the congested travel cost, zonal accessibility, and so forth from zone i to zone j and considering the intrazonal and interzonal costs. Hence, the equation can be written as

$$t_{ij} = \begin{cases} \sum_a \left(\delta_{i,j}^a, t_a\right) + t_{m,i} + t_{m,j}, & \text{for } i \neq j, \\ t_{m,i}, & \text{for } i = j, \end{cases} \tag{22}$$

where $\sum_a (\delta_{i,j}^a, t_a)$ is the interzonal travel time which is the summation of travel costs along the shortest path between i and j, and t_a represents the generalised travel time that vehicle spends on the link a; if this link exactly belongs to the

shortest path between zone i and zone j, $\delta^a_{i,j} = 1$; otherwise, $\delta^a_{i,j} = 0$. The $t_{m,i}$ embodies the generalised intrazonal travel time in zone i; this is a simplified measure method also for the convenient calculation. Sometimes, the intrazonal costs are neglected for convenient calculation, but they will be counted especially when the zone has higher land-use intensity and density; they capture a variety of costs incurred on trips associated with land-use and traffic network structure differences.

The travel time on the link a is measured as t_a; normally, it can be calculated as the ratio between the street length l_a and the speed v_a; however, it is always constrained by the traffic flow f_a and the collected revenue of this link R_a:

$$t_a = \frac{l_a}{v_a} + \frac{R_a/\eta}{f_a}. \tag{23}$$

Here, η is the balance parameter, which represents the average value of time.

The BPR function is used to reflect the relationship of the free flow time v^f_a and congested speed v^c_a on link a, C_a is the link capacity, and α_{BPR} and β_{BPR} are correction factors equal to 0.15 and 4, respectively:

$$v^c_a = \frac{v^f_a}{\left[1 + \alpha_{\mathrm{BPR}}\left(f_a/C_a\right)^{\beta_{\mathrm{BPR}}}\right]}. \tag{24}$$

For example, in a zone with higher land-use intensity and density, maybe the jobs provided and population amount are much more than the average level; thus, the travel cost will increase correspondingly considering the traffic congestion levels, longer elevator wait time in skyscrapers, and greater difficulty of finding parking. On the other hand, influenced by the traffic network structure, within most of the situations (without considering Braess's paradox), with higher traffic network structure service level, it will alleviate the traffic congestion and increase the accessibility, and usually the cost will be reduced. Based on these assumptions it can be measured as

$$t_{m,i} = \chi t^0_m \frac{\left[1 + \left(G_i/\overline{G}\right)^2\right]}{\left[1 + \left(\mathrm{NS}_i/\overline{\mathrm{NS}}\right)^2\right]}, \tag{25}$$

where t^0_m is a specified base intrazonal travel cost for all zones, χ is a changeable parameter to balance the impact of network structure, and $\chi = 1$. G_i is the number of activities (the employment and population) in zone i; the function is $G_i = E_i + P_i$, connecting with the trip generation model. $\overline{G}$ is the average number of activities for all zones. NS_i is the measurement of network structure status; generally for a zone with higher traffic infrastructure level, the time used to pass this zone will lower; hence, considering those fundamental traffic network indicators and MCA indicators, this study chooses the node degree centrality DC, the betweenness $C_{\mathrm{betweenness}}$, and the closeness centrality $C_{\mathrm{closeness}}$ as related indicators because of the previous analysis, and the function is

$$\mathrm{NS}_i = \varepsilon_{\mathrm{DC}}\mathrm{DC} + \varepsilon_{\mathrm{BC}}C_{\mathrm{betweenness}} + \varepsilon_{\mathrm{CC}}C_{\mathrm{closeness}}, \tag{26}$$

where $\varepsilon_{\mathrm{DC}}$, $\varepsilon_{\mathrm{BC}}$, and $\varepsilon_{\mathrm{CC}}$ are parameters equal to 1000, 1, and 10000, respectively, and $\overline{\mathrm{NS}}$ is the average status of network structure for all zones.

3.2.4. Mode Choice in a Multilayer Network. In this research, mode choice is used to connect the travel demand with multilayer networks. Over this process, the trips between a given origin and destination are split into trips using transit and automobile for simplicity. The most frequently used function is Binary Logit Model [57], also called "econometric formulation," which merely refers a log ratio of the possibility of choosing a mode (Po_i) to the possibility of not choosing this mode $(1 - Po_i)$, and the function is

$$\log\left(\frac{Po_i}{1 - Po_i}\right) = v(x_i) = \beta_0 + \beta_1\left(c_A - c_R\right) + \beta_2\left(t_A - t_R\right) + \beta_3 I_c + \beta_4 N_t, \tag{27}$$

where $\beta_{0,1,2,3,4}$ are related parameters, c_A and c_R are the travel costs of using the mode of street and rail transit (the measurement of c_A only considers the situation of travel using the street system, but c_R considers using street and rail systems and the cooperation parts), t_A and t_R are the travel times for using the mode of street and rail transit, I_c stands for income, and N_t is the number of travellers. This function has deterministic meaning; that is, when faced with the same options, they will always make the same choices. Hereby considering the multilayer relationship, a function set is proposed; related parameters refer to the basic multilayer network indicators, combined with the BPR function and the real traffic loads on the link a. This function set is

$$\begin{aligned} c_A &= (w_s\tau_s)l_a \sum f_a, \\ c_R &= (w_s\tau_s)l_a \sum f_a + (w_c\tau_c)l_c + (w_r\tau_r)l_r \sum f_r, \\ t_A &= \frac{l_a}{v^f_a\left[1 + \alpha\left(f_a/C_a\right)^\beta\right]} + \frac{R_a/\eta}{f_a}, \\ t_R &= \frac{l_r}{v_r} + \frac{R_r/\eta}{f_r}, \end{aligned} \tag{28}$$

where l_a and l_r are the length of automobile and train transit routes, v_r is the average speed of rail transit, f_r is the rail traffic flow, and R_r is the collected revenue of this rail link. The part $((R_r/\eta)/f_r)$ also means the transfer and wait time cost; for a higher investment rail line, the transfer and wait time are usually smaller.

3.2.5. Traffic Assignment Model. Here, User Equilibrium (UE) model is chosen; this model is proposed by Sheffi [42] and has been well recognised and validated by the traffic researchers; here, it will not be discussed further, and these conditions can be referred to in Sheffi [42].

$$\begin{aligned} &\max E(G), \\ &\min \quad C_{\text{system}} = \sum x_a t_A \\ &\text{S.T.} \quad \begin{cases} l_a,\ x_a \geq 0, \\ \sum (f_a)_{ij} = T_{ij},\ \forall i, j. \end{cases} \end{aligned} \tag{29}$$

Then, the lower-level function is shown as

$$\begin{aligned} &\min Z(x) = \sum_a \int_0^{x_a} t_a(x_a)\mathrm{d}x \sum_p f_p^{i,j} = q_{ij},\ \forall i, j, \\ &x_a = \sum_i \sum_j \sum_p \delta_{a,p}^{i,j} f_p^{i,j},\ \forall a, \\ &\text{S.T.} \quad f_a^{i,j} \geq 0,\ \forall p, i, j, \\ &x_a \geq 0,\ a \in S_{\text{link}}. \end{aligned} \tag{30}$$

Here, x_a is the equilibrium flows of link a, t_a is travel time, and the function is purposed to get the lowest travel costs. The p is the path, $f_p^{i,j}$ is the traffic flow of OD pair i and j, q_{ij} is the trips between i and j, $\delta_{i,j}^a$ is a definitional constraint, and S_{link} is the set of links in the network.

3.3. Link Investment Model for Multilayer Network. The network growth process from the network structure parts is discussed previously, but in fact, this process is constrained by the investment inputs too. As mentioned before, this study is mainly considering a close network system; here, this study also treats the growth process as autonomous investment process. The link investment models are following the definition of Levinson et al. [49] and Xie and Levinson [11], where they describe the economic decisions of individual links autonomously; that is, the price for using the street during a given period, which users should pay for this autonomous agent, is dependent on the general traffic flow and the total length of these links. After a period, all the revenues are used to improve the network structure and link capacity. In each period, it is assumed that the collected revenues of toll from links by a general toll rate $\iota 1 = 0.1$, and this is an iteration process:

$$R_a^{k+1} = \iota 1 \cdot l_a^k \cdot \left(f_{a-}^k + f_{a+}^k\right) = \iota 1 \cdot l_a^k \cdot \left(2 f_a^k\right), \tag{31}$$

where if the study treats the network as a directed graph, and the total traffic flow in a given period k can be given as f_{a-}^k and f_{a+}^k, or for an undirected graph as $2f_a^k$, then the connection between the collected revenues and the travel time on the link a can be discussed; that is, t_a is determined by the R_a^{k-1}. l_a^k is the link length of iteration k.

On the other hand, the maintenance cost function is based on the toll function; considering the link capacity C_a^k and average speed v_a^k, $\iota 2 = 0.0001$, for an ordinary street or rail line, the capacities in two directions are normally equal to each other, and the overall spending function S_a is

$$S_a^{k+1} = \iota 2 \cdot l_a^k \left(f_{a-}^k + f_{a+}^k\right) C_a^k v_a^k = \iota 2 \cdot l_a^k \left(2 f_a^k\right) C_a^k v_a^k. \tag{32}$$

The function of this profit part is

$$P^k = \sum R_a^k - \sum S_a^k = I^{k+1}. \tag{33}$$

Here, it is assumed that P^k is the profit of iteration k, also equal to the general investment I^{k+1} of iteration $k+1$, then connect with the network growth models and network optimisation models in the next sections.

The investment model considers the general revenues and expenditure of the system. Here, as per these previously proposed models, if the gathered revenue exceeds the maintenance cost, the profit part will be spent at the end of a time period without saving it for the future, with all being used for the capacity increase of each line, with the function

$$C_a^{k+1} = C_a^k \left(\frac{R_a^k}{S_a^k}\right)^{\rho}, \tag{34}$$

where $\rho = 0.1$. The free flow speed of new links with new capacity can be measured by a log-linear relationship calibrated by Zhang and Levinson [58] as $v_a^f = -30.6 + 9.8 \times \ln(C_a)$.

3.4. The Population Growth Model. The coevolution model has illustrated some basic points of the population movements and their impacts; they will be further discussed here. When dealing with the urban expansion process, especially the land-use change process and the evolution of the urban street network, the population is treated as the most frequently considered mechanism and has the most significant consequence [59]. Typically, the population evolution model includes two parts: the population movement and the natural increase. The natural increase of population will change the amount of the total population, whereas the population movement will change the population distribution [60].

For simplicity, it can be assumed that the natural increase rate of the population is a constant, and then a simple exponential function can be limitedly used, as follows:

$$\frac{dP\,op^{k+1}}{\mathrm{d}t} = \mathrm{rp} * \mathrm{Pop}^k, \tag{35}$$

where $(dP\,op^{k+1}/\mathrm{d}t)$ is the population increment of iteration $k+1$, Pop^k is the population amount of iteration k, and rp is the increase rate, as rp = 0.015 per iteration [61].

3.5. Urban Land-Use Change Model. For the evolution models, inspired by the research of Levinson et al. [49] and Xie and Levinson [11], accessibility A was used to reflect the desirability of a land parcel by calculating the accessibility of opportunities and activities [62], showing that smaller opportunities provide diminishing influences, also called gravity-based measurement, assuming that it fits a negative exponential cost function:

$$A_i = \sum_{j=1}^{J} D_j e^{-\vartheta c_{ij}}, \tag{36}$$

where A_i is the accessibility of node i to all opportunities D_j in node j if the total number of traffic analysis nodes is J. The ϑ is the travel cost sensitivity parameter ($\vartheta = 0.048$) to the node which also indicates how the accessibility of a node declines with the increase of travel time, and c_{ij} is the travel cost from i to j.

The only factors which affect location choice of households and companies are accessibility and population density. Then, for the accessibility of employment and population in a land parcel, the function can be expanded as

$$A_i^E = \sum_{j=1}^{J} E_j e^{-\vartheta c_{ij}},$$
$$A_i^P = \sum_{j=1}^{J} P_j e^{-\vartheta c_{ij}}, \tag{37}$$

where A_i^E is the accessibility to employment from node i while A_i^P is the accessibility to population. In the multilayer model, $c_{ij} = c_A + c_R$; hence, the accessibility considered different travel modes. This potential measure method has its specific practical advantage; that is, it can be easily calculated by the existing land-use and transport data.

3.6. Network Structure, Land-Use, and Population Coevolution Model. The desirability function sets are developed to illustrate the dynamics of employment accessibility and population accessibility based on independent decisions concerning their locations and network structure service grade NS_i. For the people desirability, the parameters $\lambda_1, \lambda_2, \lambda_3$ are all equal to 1:

$$U_{i,P} = A_i^{E\lambda_1} A_i^{P\lambda_2} NS_i^{\lambda_3}, \tag{38}$$

and, for the dynamics of employment desirability, $\lambda_4, \lambda_5, \lambda_6$ are equal to 0.9, −0.9 and 0.9, respectively:

$$U_{i,E} = A_i^{E\lambda_4} A_i^{P\lambda_5} NS_i^{\lambda_6}, \tag{39}$$

where, for the independent decisions made by people, the competition between employment accessibility and population accessibility acted as centrifugal forces. Conversely, for the independent decisions made by businesses, the employment accessibility and population accessibility both strengthen the employment desirability and serve as centripetal forces. $\lambda_1, \ldots, \lambda_6$ are the related parameters, and these relationships between parameters were discussed in Xie and Levinson [10] as follows: "... accessibility to jobs did show a statistically significant positive effect on home sale values, while accessibility to resident workers did show a statistically significant negative effect ..." (p.164).

The increase in employment and population in zone i is proportional to the single node's desirability difference quantity; here, $\overline{U_P^k}$ and $\overline{U_E^k}$ are the average desirability at iteration k, considering the natural increase rate r, and $\lambda_7 = \lambda_8 = 1$; then, we have the function

$$\Delta P = P_i^{k+1} - P_i^k = \lambda_7 \frac{\left(U_{i,P}^k - \overline{U_P^k}\right) P_i^k}{\overline{U_P^k}} + rP^k,$$
$$\Delta E = E_i^{k+1} - E_i^k = \lambda_8 \frac{\left(U_{i,E}^k - \overline{U_E^k}\right) E_i^k}{\overline{U_E^k}} + rE^k. \tag{40}$$

3.7. The Multilayer Network Growth Process. The multilayer network coevolution process is combined with the coevolution model. The design purpose of the rail network is to serve more people and increase convenience. Hence, the first objective is to maximise the total population covered. The second objective is to minimise the total travel costs—or to obtain a better network structure. For the upper-layer, a new node is randomly selected from these lower-layer nodes which have the highest population, and a new scale-free network is generated. For the lower-layer, a random number of new nodes (less than 10) will be added in, and a new scale-free network is generated. The network user will choose to use the rail networks for saving travel cost, and then, based on the limited capacity of rail networks, it has the upgraded distribution of traffic flow. Based on this, the population will be redistributed.

4. Solution Process and Related Simulation Scenarios

To solve the model, this section proposed a solution process given here, and the related simulation scenarios are discussed.

4.1. Solution Process. Here is the solution process by steps:

Step 1. Set the initial amount of population and employment (different land-use situations) and the travel speeds, and distribute them in a square area with 100 km of side length and 100 nodes. Here, the random network is used to discuss the growth model, and the population is equal to the employment.

Step 2. Based on the functions of traffic demand model, at each step, it can have the initial OD matrix and the initial travel costs, and the traffic flows can be measured based on the traffic assignment model by User Equilibrium (UE) model and Frank–Wolfe algorithm and converge to 5% of estimation error range.

Step 3. The collected revenues and overall expenditure can be calculated by the traffic flows. Generally, consider the spending of the total profit for the network growth, and the multilayer network growth process introduced here. With the growth of multilayer networks, the network growth will be based on them with optimised APL, D, and travel cost. After the network growth and considering these flows on the rail networks, the free flow speed of new links, and link capacity, traffic flows on different links

including upper-layers can be updated, and an equilibrium status can be reached again.

Step 4. Considering the change of population growth and network structures, land-use accessibility and desirability are changed, which causes the redistribution of population and employment, and then the OD matrix and traffic flows change. Then, with the new distribution of population and employment, the new travel speeds and network structure can be obtained; return to Step 1.

4.2. Related Simulation Scenarios. As per Step 3 and the initial status of the simulated city proposed, some scenarios will be considered here as in Table 1. For simplicity, here, we merely tested the model with the regular network not growing, and then more focus was given to the multilayer network growth-related models. Here, this study considers 8 different simulation scenarios; for example, RRR stands for the initial population and employment, travel speeds are randomly distributed (see Figure 5), and so on. As the relationship between land-use and population density could be modelled well [48], the discussion of different land-use scenarios can turn to the discussion of the distribution of population and employment.

5. Simulation and Validation

In the same way as the simulated city, suppose that a square urban area with length equal to 10×10^4 meters has an initial number of nodes (randomly and regularly distributed when the network is not growing to test the proposed model, and randomly distributed when the network is growing) ($n = 100$), with an initial population of 500 thousand, and the natural increase rate of population is 1.5% per iteration. Then, the model validation part is proposed at the end of this section.

5.1. When the Network Is Not Growing. The total profits are used for the capacity increase of each line, which means that although the network is not growing, the capacities are improving. Because the network structure is not changed, it cannot measure the change of APL, D, EG, and so on; hence, the study will more focus on the total travel times which not only show how easily one citizen can arrive one area but also describe the traffic status of the whole network. With the initial traffic flows on each street, the total travel time cost through these congested streets is also shown in Figure 6. With iteration, we can see that this time cost of different simulation scenarios decreases sharply until reaching a stable state (Figure 7) (results come from 10 times of simulation), which means that the street capacity is optimised during the population redistribution process. No matter what kind of simulation scenarios the network initially chose, at last, they have similar trends. The population is redistributed following the network travel cost change, and some areas with higher population also emerge because of the change of street capacity and travel speed.

Here, the red lines are the travel times of each street, and the width stands for their values. The black lines are the traffic flows on these streets. Here is the performance of the random network and regular network in 6 iterations.

5.2. When the Network Is Growing. With the growth of networks, based on a random network shown in Figure 8, in line with previous researches, the change trends of APL and D can be obtained. Considering these different scenarios, we can see that, with the increase of multilayer networks, the APL and D are ultimately decreased. With the growth of the rail network, it is clear that more traffic flows are attracted by the rail network, and after a few steps, the traffic flow becomes more evenly distributed.

APL decreased from more than 5.9×103 to around 4×103, a decrease of about 32% (see Figure 9), and D decreased from 15×104 to 8×104, a decrease of about 46% (see Figure 10). With the network growth process, the increase of network efficiency (Figure 11) by around 27% to 44% can be seen, with the URU having the lowest change rate and RUU having the highest change rate, which means that, with the multilayer network growth model, the proposed network structure became optimised. The total traffic flow is optimised by around 30% of decrease (Figure 12) by the process of redistribution of population and employment and land-use change, which reduce the movement between two nodes and make the population and employment reach the balance in an area, and intrazonal movement increases. Obviously, the total travel cost is also decreased; this also means the improvement of network efficiency. Some nodes with higher population have emerged with their advanced traffic accessibility, and "new town" or "developing area" also emerged, as more and more new nodes are located in the right middle area.

5.3. Model Validation. The change of average travel speed ratio can influence the model choice and the growth of networks [23]. To validate the simulation results, another quantitative index is proposed here as beta, the average travel speed ratio between upper-layer and lower-layer networks, and the function is

$$\text{beta} = \frac{v_a^k}{v_r}, \quad \text{beta} \in (0, 1), \tag{41}$$

where v_a^k is the average travel speed of the street network and v_r is the average travel speed of the rail network. Here, we set the average travel speed of the rail network as a constant; then, as the value of beta increases from 0 to 1, this means that the average travel speed of the street network is increasing.

Here, to validate the model, we have run the CNIMUGOM 100 times with UUU simulation scenario with the same network and have the average value of the APL (see Figure 13) and traffic flow (see Figure 14) with different beta values. It is shown that, with the value of beta belonging to 0.2 to 0.3, the APL has the lowest value. While the situation changes a little bit when the traffic flow is considered,

Table 1: The simulation scenarios.

No.	The population distribution	The employment distribution	The limited street speeds
Proposed models	Randomly (R)/uniformly (U)	Randomly (R)/uniformly (U)	Randomly (R)/uniformly (U)
1	R	R	R
2	R	R	U
3	R	U	R
4	R	U	U
5	U	R	R
6	U	R	U
7	U	U	R
8	U	U	U

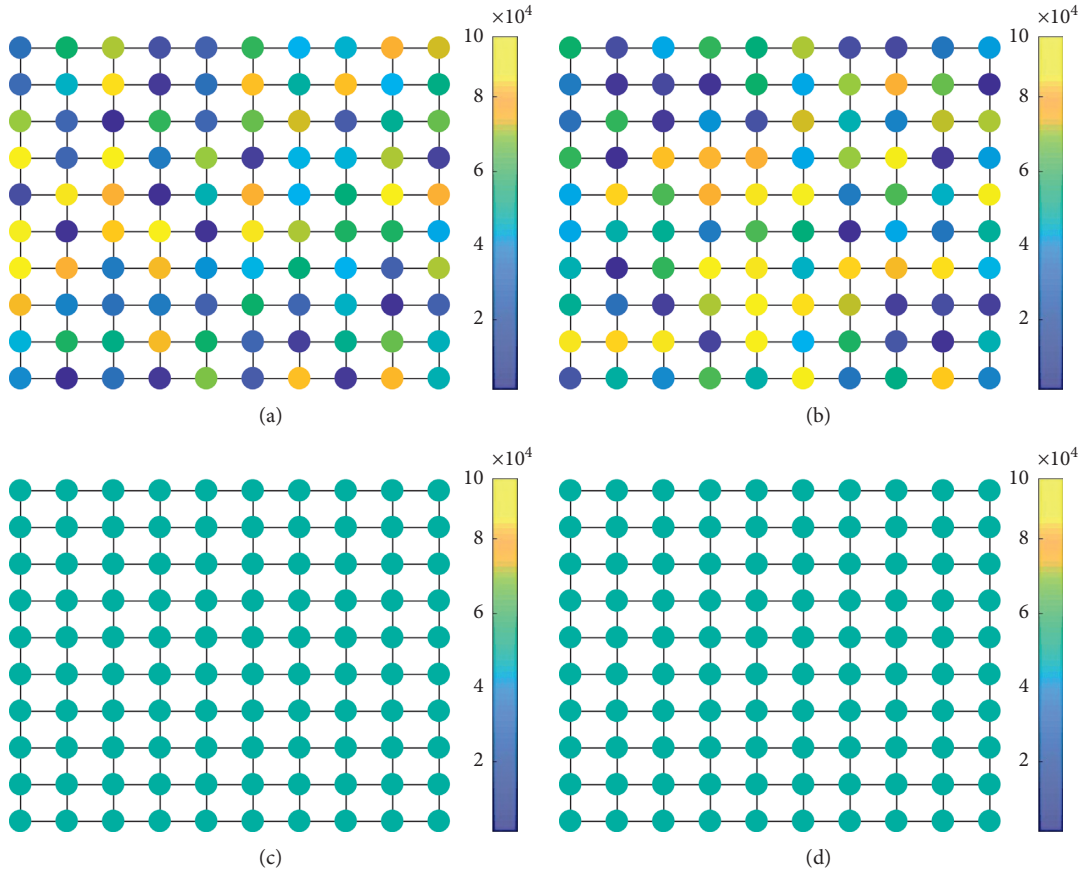

Figure 5: The initial distribution of population, employment, and travel speeds. Here, for each network, 100 nodes are plotted, and the black edges here stand for the travel speeds. (a) The population, employment, and travel speeds are randomly distributed. (b) The population and employment are randomly distributed, but the travel speeds are unified. (c) The population and employment are unified, but the travel speeds are randomly distributed. (d) All of them are uniformly distributed. The colour bar stands for the population amount, the colour of each node can stand for the population and employment amount, and the same is true for the multilayer network representation.

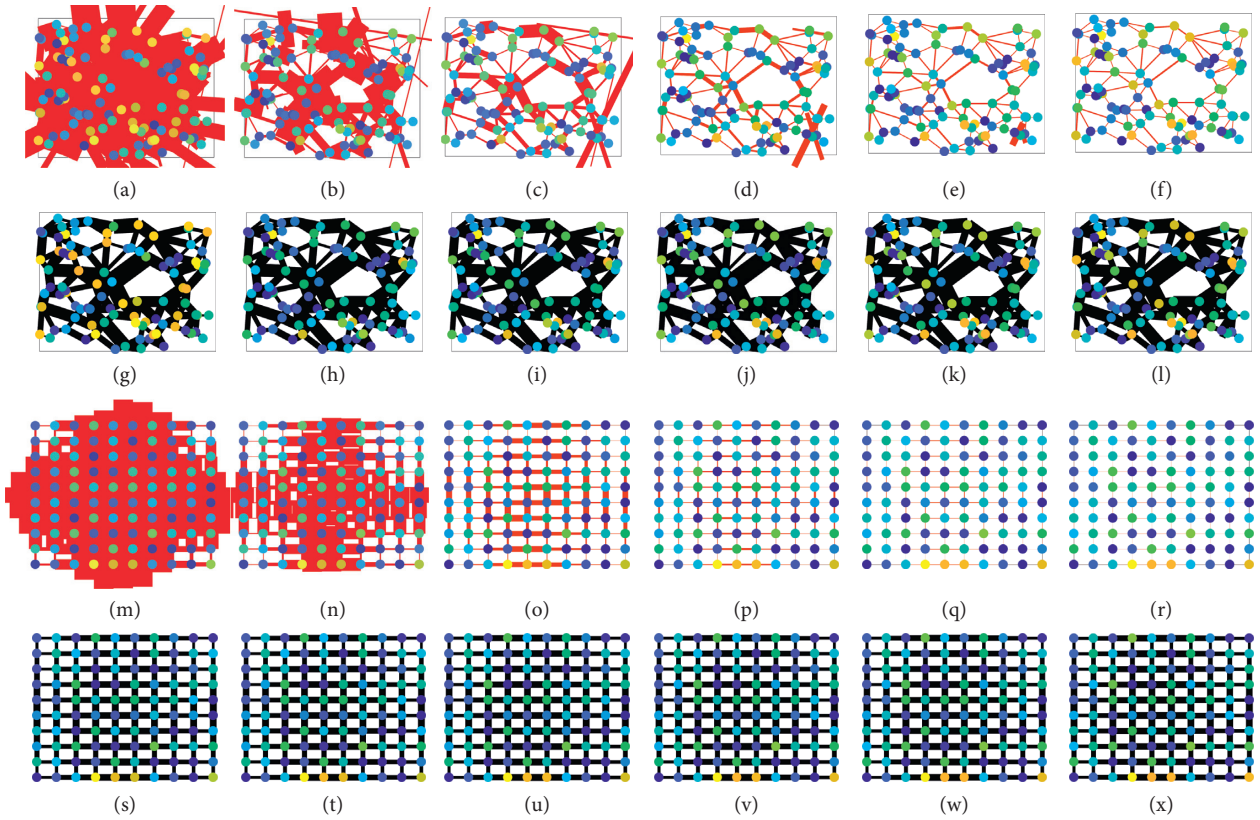

Figure 6: The optimisation of population distribution and travel times on the streets.

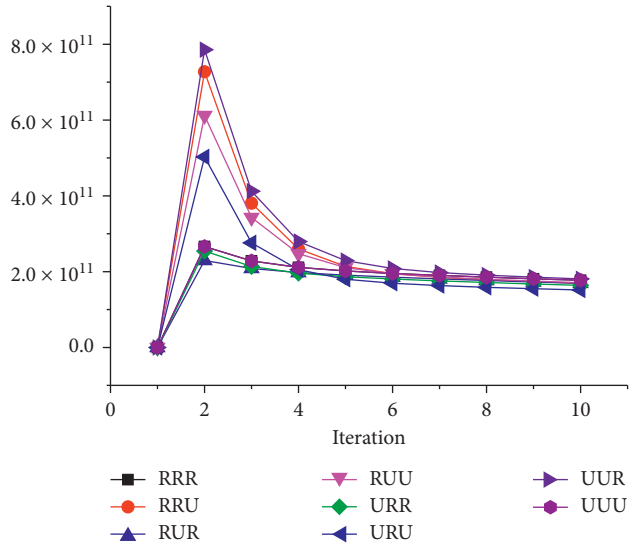

Figure 7: The total time cost of different simulation scenarios decreases sharply.

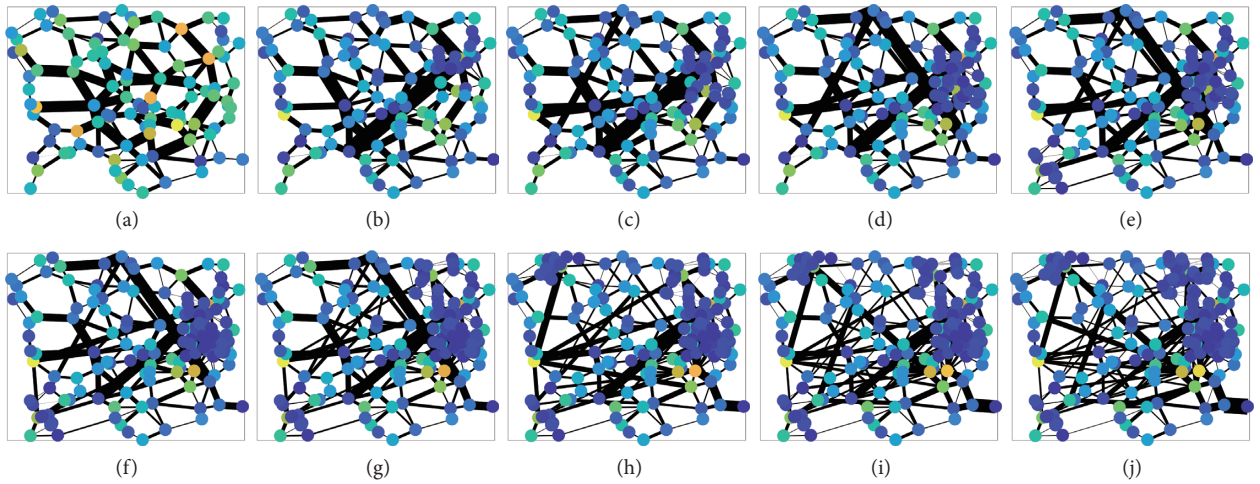

Figure 8: The growth of multilayer network and redistribution of population and traffic flow, increasing from the top left to bottom right with ten times of iterations.

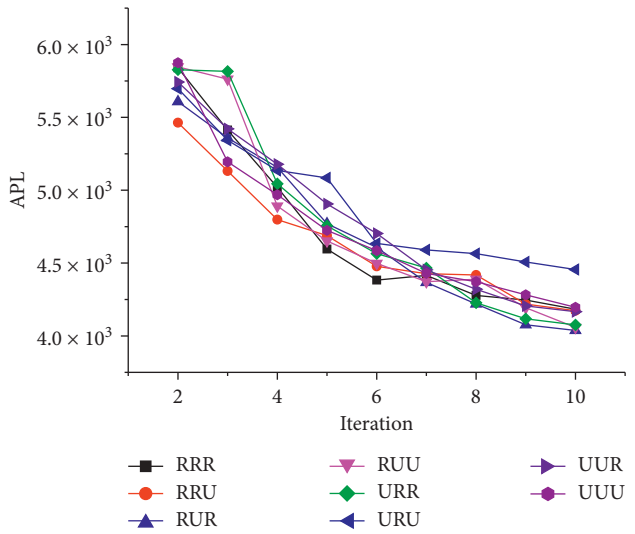

Figure 9: The change trends of APL of different simulation scenarios.

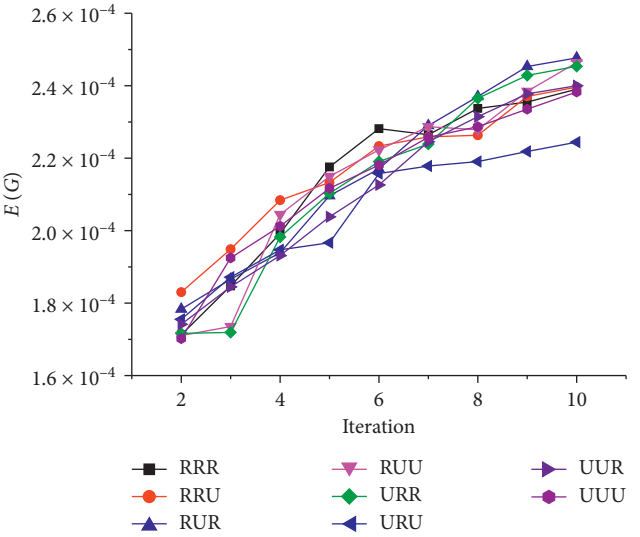

Figure 11: The change trends of network efficiency of different simulation scenarios.

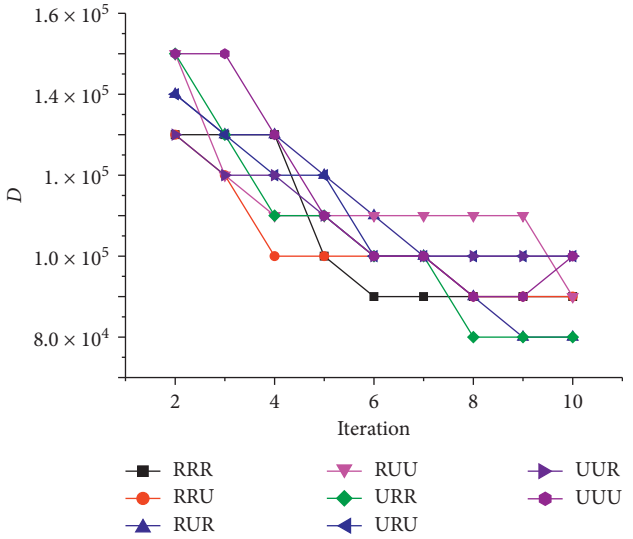

Figure 10: The change trends of D of different simulation scenarios.

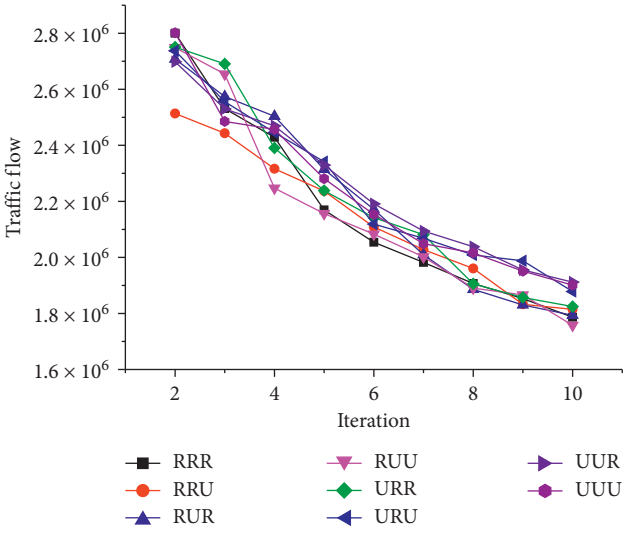

Figure 12: The change trends of traffic flow of different simulation scenarios.

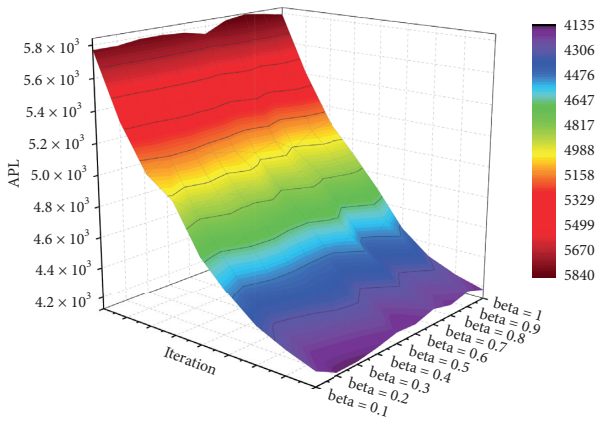

Figure 13: The change trends of APL with different beta values.

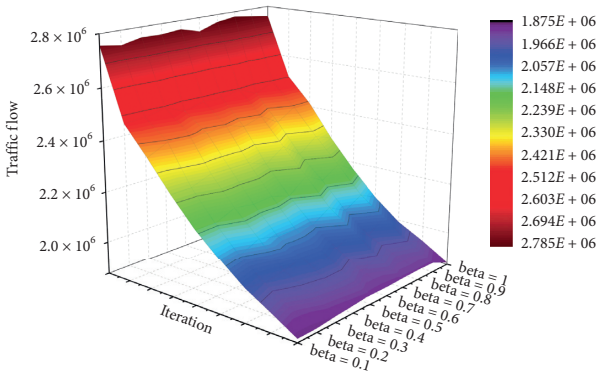

Figure 14: The change trends of traffic flow with different beta values.

showing that the traffic flow has the lowest value when the value of beta belongs to 0.1 to 0.2. Furthermore, the CNIMUGOM works pretty stably with different beta values and simulation scenarios.

6. Conclusion

Research about coevolution models and multilayer network models remains somewhat superficial; the combinations of coevolution models and multilayer network models with land-use applications are relatively rare. While research in this area is resolutely forward-looking and fulfils the requirements of mathematical ability, as with previous city models, it lacks a systematic and comprehensive economic description and combination with urban economic theory.

The proposed CNIMUGOM has expanded the traditional planar model to a multilayer network model, which can better fit the real situations. This research also considered the multilayer network coevolution process further and considered the self-organisation properties of networks. This model has proposed an efficient way to combine these different traffic modes, well considering the complex evolution and coevolution relationships between network structure, land-use, and population. CNIMUGOM can be used to optimise the APL and D, to make the network have smaller total traffic flow, and save the total travel cost; in other words, we can have a more efficient network structure. The inner relationships between submodels such as the travel demand model, street investment model, traffic network growth model, population growth model, urban land-use growth model, and network optimisation model were analysed and discussed.

The proposed CNIMUGOM has some superior properties compared to other models, as it is a universal model and can be used in many cities for their modelling optimal planning schemes and for the large-scale investments. However, some parts can be further improved. For example, the growth rate of the population is based on the exponential distribution for short-term analysis, which may not be very close to the real situation, and the logistic population growth model can be used for long-term analysis to adjust it. The study of economic models is still open and can be combined with big data; with the study of CNIMUGOM, the population distribution acquisition method of big data can be adopted; for example, the cellphone signalling data and GPS data can be used to represent the distribution of the urban population. Next, we proposed that all the revenues are used to improve the network structure and link capacity; however, in reality, the incomes can hardly be all used for the improvement of the networks. Thirdly, the redistribution of the population, for now, is relatively hard, which has to consider the place attachment for the population and the difficulty of its relocation, but from the experiences of Beijing, based on the public rental housing projects, it can be partly done. For now, the CNIMUGOM is based on the simulated city data; for a real city, the model can be easily applied with road network data, GPS data, and population data.

Data Availability

The simulated data used to support the findings of this study are included within the article, and related codes are available from the corresponding author upon request.

Disclosure

This paper is modified and expanded based on Section 4.4 of Rui Ding's doctoral dissertation.

Conflicts of Interest

The authors declare that they have no conflicts of interest.

Acknowledgments

This study was funded by National Natural Science Foundation of China (No. 72001053) and Science and Technology Planning Project of Guizhou Province of China (No. Qian ke he ji chu [2020]1Y283). Universiti Putra Malaysia is hereby acknowledged.

References

[1] S. Abdullahi, B. Pradhan, and A. A. Al-Sharif, *Introduction to Urban Growth and Expansion Spatial Modeling and Assessment of Urban Form*, Springer, Berlin, Germany, 2017.

[2] M. Barthélemy and A. Flammini, "Co-evolution of density and topology in a simple model of city formation," *Networks and Spatial Economics*, vol. 9, no. 3, pp. 401–425, 2009.

[3] J. Wu, R. Li, R. Ding, T. Li, and H. Sun, "City expansion model based on population diffusion and road growth," *Applied Mathematical Modelling*, vol. 43, pp. 1–14, 2017.

[4] R. Ding, N. Ujang, H. Bin Hamid, and J. Wu, "Complex network theory applied to the growth of kuala lumpur's public urban rail transit network," *PLoS One*, vol. 10, no. 10, Article ID e0139961, 2015.

[5] F. Xie and D. Levinson, "Modeling the growth of transportation networks: a comprehensive review," *Networks and Spatial Economics*, vol. 9, no. 3, pp. 291–307, 2009.

[6] D. Yamins, S. Rasmussen, and D. Fogel, "Growing urban roads," *Networks and Spatial Economics*, vol. 3, no. 1, pp. 69–85, 2003.

[7] R. Ding, "The complex network theory-based urban land-use and transport interaction studies," *Complexity*, vol. 201914 pages, 2019.

[8] R. Ding, N. Ujang, H. B. Hamid et al., "Application of complex networks theory in urban traffic network researches," *Networks and Spatial Economics*, vol. 19, pp. 1–37, 2019.

[9] D. Levinson, "Density and dispersion: the co-development of land use and rail in London," *Journal of Economic Geography*, vol. 8, Article ID lbm038, 2007.

[10] F. Xie and D. Levinson, "Measuring the structure of road networks," *Geographical Analysis*, vol. 39, no. 3, pp. 336–356, 2007.

[11] F. Xie and D. Levinson, "Topological evolution of surface transportation networks," *Computers, Environment and Urban Systems*, vol. 33, no. 3, pp. 211–223, 2009.

[12] J. Wu, M. Xu, and Z. Gao, "Coevolution dynamics model of road surface and urban traffic structure," *Nonlinear Dynamics*, vol. 73, no. 3, pp. 1327–1334, 2013.

[13] J. Wu, M. Xu, and Z. Gao, "Modeling the coevolution of road expansion and urban traffic growth," *Advances in Complex Systems*, vol. 17, no. 1, Article ID 1450005, 2014.

[14] Y. Rui, *Urban growth modeling based on land-use changes and road network expansion*, , Ph.D. thesis, Stockholm, Sweden, 2013.

[15] T. Li, H. Sun, J. Wu, Z. Gao, Y.-E. Ge, and R. Ding, "Optimal urban expressway system in a transportation and land use interaction equilibrium framework," *Transportmetrica A: Transport Science*, vol. 15, no. 2, pp. 1247–1277, 2019.

[16] M. Kurant and P. Thiran, "Layered complex networks," *Physical Review Letters*, vol. 96, no. 13, Article ID 138701, 2006.

[17] J. Ma, W. Han, Q. Guo, and Z. Wang, "Traffic dynamics on two-layer complex networks with limited delivering capacity," *Physica A: Statistical Mechanics and Its Applications*, vol. 456, pp. 281–287, 2016.

[18] S.-R. Albert, G. Sergio, and A. Alex, "Congestion induced by the structure of multiplex networks," *Physical Review Letters*, vol. 116, no. 10, Article ID 108701, 2016.

[19] A. Aleta, S. Meloni, and Y. Moreno, "A multilayer perspective for the analysis of urban transportation systems," *Nature*, vol. 7, 2016.

[20] R. Ding, N. Ujang, H. B. Hamid, M. S. A. Manan, R. Li, and J. Wu, "Heuristic urban transportation network design method, a multilayer coevolution approach," *Physica A: Statistical Mechanics and Its Applications*, vol. 479, pp. 71–83, 2017.

[21] R. Gallotti, A. Bazzani, S. Rambaldi, and M. Barthelemy, "How transportation hierarchy shapes human mobility," 2015.

[22] R. G. Morris and M. Barthelemy, "Transport on coupled spatial networks," *Physical Review Letters*, vol. 109, no. 12, Article ID 128703, 2012.

[23] E. Strano, S. Shai, S. Dobson, and M. Barthelemy, "Multiplex networks in metropolitan areas: generic features and local effects," *Journal of The Royal Society Interface*, vol. 12, no. 111, Article ID 20150651, 2015.

[24] R. Ding, N. Ujang, H. B. Hamid et al., "Detecting the urban traffic network structure dynamics through the growth and analysis of multi-layer networks," *Physica A: Statistical Mechanics and Its Applications*, vol. 503, pp. 800–817, 2018.

[25] P. Crucitti, V. Latora, and S. Porta, "Centrality in networks of urban streets," *Chaos: An Interdisciplinary Journal of Nonlinear Science*, vol. 16, no. 1, Article ID 15113, 2006.

[26] B. Jiang and C. Claramunt, "Topological analysis of urban street networks," *Environment and Planning B: Planning and Design*, vol. 31, no. 1, pp. 151–162, 2004.

[27] V. Latora and M. Marchiori, "Is the Boston subway a small-world network?" *Physica A: Statistical Mechanics and Its Applications*, vol. 314, no. 1–4, pp. 109–113, 2002.

[28] M. Newman, A.-L. Barabasi, and D. J. Watts, *The Structure and Dynamics of Networks*, Princeton University Press, Princeton, NJ, USA, 2011.

[29] L. C. Freeman, "A set of measures of centrality based on betweenness," *Sociometry*, vol. 40, no. 1, pp. 35–41, 1977.

[30] M. Marchiori and V. Latora, "Harmony in the small-world," *Physica A: Statistical Mechanics and its Applications*, vol. 285, no. 3, pp. 539–546, 2000.

[31] R. Albert and A.-L. Barabási, "Statistical mechanics of complex networks," *Reviews of Modern Physics*, vol. 74, no. 1, p. 47, 2002.

[32] V. Latora and M. Marchiori, "Efficient behavior of small-world networks," *Physical Review Letters*, vol. 87, no. 19, Article ID 198701, 2001.

[33] C.-G. Gu, S.-R. Zou, X.-L. Xu et al., "Onset of cooperation between layered networks," *Physical Review E*, vol. 84, no. 2, Article ID 26101, 2011.

[34] H. Sun, Z. Gao, and J. Wu, "A bi-level programming model and solution algorithm for the location of logistics distribution centers," *Applied Mathematical Modelling*, vol. 32, no. 4, pp. 610–616, 2008.

[35] S. Boccaletti, V. Latora, Y. Moreno, M. Chavez, and D. Hwang, "Complex networks: structure and dynamics," *Physics Reports*, vol. 424, no. 4, pp. 175–308, 2006.

[36] H. Xiaoyan, Z. Shuang, and C. Xiaoshu, "Spatial-temporal evolution of Guangzhou subway accessibility and its effects on the accessibility of public transportation services," *Progress in Geography*, vol. 33, no. 8, pp. 1078–1089, 2014.

[37] M. Frank and P. Wolfe, "An algorithm for quadratic programming," *Naval Research Logistics Quarterly*, vol. 3, no. 1, pp. 95–110, 1956.

[38] M. Jaggi, "Revisiting frank-wolfe: projection-free sparse convex optimization," in *Proceedings of the 30th International Conference on Machine Learning*, Atlanta, GA, USA, 2013.

[39] C. F. Daganzo and Y. Sheffi, "On stochastic models of traffic assignment," *Transportation Science*, vol. 11, no. 3, pp. 253–274, 1977.

[40] M. Fukushima, "A modified frank-wolfe algorithm for solving the traffic assignment problem," *Transportation Research Part B: Methodological*, vol. 18, no. 2, pp. 169–177, 1984.
[41] L. J. LeBlanc, R. V. Helgason, and D. E. Boyce, "Improved efficiency of the frank-wolfe algorithm for convex network programs," *Transportation Science*, vol. 19, no. 4, pp. 445–462, 1985.
[42] Y. Sheffi, *Urban Transportation Networks*, Prentice-Hall, Englewood Cliffs, NJ, USA, 1985.
[43] G. Giuliano, "Land use impacts of transportation investments," *The Geography of Urban Transportation*, pp. 237–273, Guilford Publications, New York, NY, USA, 2004.
[44] M. Wegener, "Overview of land use transport models," *Handbook of Transport Geography and Spatial Systems*, vol. 5, pp. 127–146, 2004.
[45] J. Gutiérrez, A. Monzón, and J. M. Piñero, "Accessibility, network efficiency, and transport infrastructure planning," *Environment and Planning A: Economy and Space*, vol. 30, no. 8, pp. 1337–1350, 1998.
[46] L. C. Molin Zhao and F. Li, "Railway network evaluation based on complex network analysis," *Advances in Applied Mathematics*, vol. 5, no. 3, pp. 560–566, 2016.
[47] L. Li, Y. Sato, and H. Zhu, "Simulating spatial urban expansion based on a physical process," *Landscape and Urban Planning*, vol. 64, no. 1, pp. 67–76, 2003.
[48] F. Li, S. Zhang, K. Bu, J. Yang, Q. Wang, and L. Chang, "The relationships between land use change and demographic dynamics in western Jilin province," *Journal of Geographical Sciences*, vol. 25, no. 5, pp. 617–636, 2015.
[49] F. Levinson Xie and S. Zhu, "The co-evolution of land use and road networks," *Transportation and Traffic Theory*, pp. 839–859, 2007.
[50] T. Li, J. Wu, H. Sun, and Z. Gao, "Integrated co-evolution model of land use and traffic network design," *Networks and Spatial Economics*, vol. 16, no. 2, pp. 579–603, 2015.
[51] D. Sun, K. Zhang, and S. Shen, "Analyzing spatiotemporal traffic line source emissions based on massive didi online car-hailing service data," *Transportation Research Part D: Transport and Environment*, vol. 62, pp. 699–714, 2018.
[52] J. Sun and X. Ding, "Spatiotemporal evolution of ridesourcing markets under the new restriction policy: a case study in Shanghai," *Transportation Research Part A Policy and Practice*, vol. 130, no. 227, p. 239, 2019.
[53] K. Zhang, D. J. Sun, S. Shen, and Y. Zhu, "Analyzing spatiotemporal congestion pattern on urban roads based on taxi GPS data," *Journal of Transport & Land Use*, vol. 10, no. 1, pp. 675–694, 2017.
[54] F. Xie and D. Levinson, *Evolving Transportation Networks*, Springer Science & Business Media, New York, NY, USA, 2011.
[55] M. Batty and S. Mackie, "The calibration of gravity, entropy, and related models of spatial interaction," *Environment and Planning A: Economy and Space*, vol. 4, no. 2, pp. 205–233, 1972.
[56] X. Xie, "Calibration method and comparison of gravity model," *Commun Stand*, vol. 8, pp. 17–20, 2008.
[57] J. De Dios Ortuzar and L. G. Willumsen, *Modelling Transport*, Wiley, Hoboken, NJ, USA, 1994.
[58] L. Zhang and D. Levinson, "Road pricing with autonomous links," *Transportation Research Record: Journal of the Transportation Research Board*, vol. 1932, no. 1, pp. 147–155, 2005.
[59] F. Zhao, J. Wu, H. Sun, Z. Gao, and R. Liu, "Population-driven urban road evolution dynamic model," *Networks and Spatial Economics*, vol. 16, no. 4, pp. 997–1018, 2015.
[60] F. Wang, "Urban population distribution with various road networks: a simulation approach," *Environment and Planning B: Planning and Design*, vol. 25, no. 2, pp. 265–278, 1998.
[61] W. Lutz, W. Sanderson, and S. Scherbov, "The coming acceleration of global population ageing," *Nature*, vol. 451, no. 7179, pp. 716–719, 2008.
[62] K. T. Geurs and B. Van Wee, "Accessibility evaluation of land-use and transport strategies: review and research directions," *Journal of Transport Geography*, vol. 12, no. 2, pp. 127–140, 2004.

Hindawi
Complexity
Volume 2021, Article ID 6630811, 10 pages
https://doi.org/10.1155/2021/6630811

Research Article

Exploring Coevolution of Emotional Contagion and Behavior for Microblog Sentiment Analysis: A Deep Learning Architecture

Qi Zhang,[1] Zufan Zhang ,[1] Maobin Yang,[1] and Lianxiang Zhu[2]

[1]*School of Communication and Information Engineering, Chongqing University of Posts and Telecommunications, Chongqing 400065, China*
[2]*School of Computer Science, Xi'an Shiyou University, Xi'an 710065, China*

Correspondence should be addressed to Zufan Zhang; zhangzf@cqupt.edu.cn

Received 19 November 2020; Revised 25 December 2020; Accepted 5 January 2021; Published 22 January 2021

Academic Editor: Luxing Yang

This paper aims to explore coevolution of emotional contagion and behavior for microblog sentiment analysis. Accordingly, a deep learning architecture (denoted as MSA-UITC) is proposed for the target microblog. Firstly, the coevolution of emotional contagion and behavior is described by the tie strength between microblogs, that is, with the spread of emotional contagion, user behavior such as emotional expression will be affected. Then, based on user interaction and the correlation with target microblog, the Hawkes process is adopted to quantify the tie strength between microblogs so as to build the corresponding weighted network. Secondly, in the weighted network, the Deepwalk algorithm is used to build the sequence representation of microblogs which are similar to the target microblog. Next, a CNN-BiLSTM-Attention network (the convolutional neural network and bidirectional long short-term memory network with a multihead attention mechanism) is designed to analyze the sentiment analysis of target and similar microblogs. Finally, the experimental results on two real Twitter datasets demonstrate that the proposed MSA-UITC has advanced performance compared with the existing state-of-the-art methods.

1. Introduction

Information diffusion is a widely concerned research topic, which involves the study of epidemic transmission in biology [1], computer virus propagation over complex networks [2, 3], and other topics [4, 5]. Social networks are one of the important carriers of information spreading [6, 7]; users often express their opinions and emotions on social media and even imitate the expressions, sounds, and gestures of others, which is called emotional contagion [8]. Under the contagion, emotions can be infected and spread from one person to another [9]. Therefore, emotions have become an important driving factor for information spreading on social networks. Furthermore, the emotional contagion on social networks is rarely independent of the propagation of behavior or information, and they are coevolving with strong interactions [10]. With the explosive growth of information on social media, microblogging has become a source of public opinions and emotions on various public topics. Consequently, it is necessary to analyze the sentiment of microblogging data. For example, microblog sentiment analysis can help enterprises accurately obtain the feedback information of customers on products [11, 12], thereby improving product quality according to the feedback information and developing more efficient product promotion plans. Moreover, the government can make quick response to public events through public opinion supervision and realize emotional guidance for netizens. In addition, microblog sentiment analysis plays an important role in many other fields [13, 14].

The most commonly studied methods of microblog sentiment analysis are lexicon-based methods, machine learning-based methods, and deep learning-based methods. The lexicon-based methods use the weight algorithm to analyze sentiment [15, 16] and are relatively simple in classifying sentiment polarity, but their performance is limited by the construction of emotional lexicon and the quality of judgment rules. For this issue, many researchers

have applied machine learning for microblog sentiment analysis [17, 18]. Unfortunately, the performance of machine learning-based methods depends on the quality of the annotated datasets. For automatic feature extraction, deep learning-based methods have been widely developed [19, 20]. However, microblog texts are relatively short with irregular grammar and rich data noise, which aggravates the validity problem of useful data. Therefore, these methods that only rely on independent microblogging data have their own disadvantages.

In fact, the work [21] claimed that there is a coevolutionary relationship between emotional contagion and user behavior. In other words, with the contagion and the spread of emotions, user behavior such as emotional expression will be affected. When the user browses information, the user's emotions are easily affected, so the content posted by the user will show the influence. Leskovec et al. [22] pointed out that users tend to make friends with similar people and will constantly adjust their behaviors to keep pace with their friends [23, 24]. Based on these theories, Miller et al. [25] found that the sentiment of microblog messages is influenced by the connected messages and spreads in the network formed by following the behavior between users. Besides, the results in [26] indicated that, under the emotional contagion, happy behaviors spread dynamically on social media. The above research results show that the propagation of behavior and information on social media is interdependent [27], and the closer the tie between users, the stronger of emotional contagion, and the sentiments of posts are become more similar. Therefore, the coevolutionary phenomenon on social media can be used to improve the insufficiency of the abovementioned methods that only rely on independent microblogging data.

Some researchers have considered the coevolutionary phenomenon to analyze the sentiment of microblogging data. Hu et al. [28] used sentiment consistency (i.e., the messages posted by the same user tend to have the same sentiment polarity) and emotional contagion to construct the tie for analyzing the sentiment of noisy and short tweets. On this basis, other studies have considered more influential factors to describe the tie strength between microblogs. For instance, the work [29] considered the similarity of users' personal information and the frequency of interaction, and the work [30] added the similarity of texts. These methods extract influencing factors that involved all topics when calculating the tie strength, but fail to consider that the tie strength between users will have significant differences under different topics.

For this problem, Zou et al. [31] considered the topic context as an influential factor of tie strength and Liu et al. [32] divided the datasets by topic category. Furthermore, the authors [33] proposed the subjective and objective factors that affect users' emotional changes to simulate the emotional contagion between users in the rumor propagation process on microblogging. The above research studies comprehensively consider the factors that influence the tie strength on social media, thereby obtaining the sentiment correlation between microblogs. However, these studies all empirically set the weight of each influencing factor when calculating the tie strength, which has a certain impact on the accuracy of the tie strength. In addition, most of the above methods adopt the least square method to classify sentiment polarity, which is not suitable for the high-dimensional and unlabeled data. With the successful application of deep learning in the field of natural language processing, in 2019, Zhao et al. [34] proposed to combine deep learning and the tie strength between microblogs to analyze microblog sentiment, and the results show that its performance is better than that of the least square method, but this method simply applies the traditional neural network architecture. Up to now, to our best knowledge, there is no other related follow-up work.

Inspired by the pioneering work [34], this paper proposes a deep learning architecture (denoted as MSA-UITC) to explore coevolution of emotional contagion and behavior for microblog sentiment analysis. Specifically, the coevolution of emotional contagion and behavior is described by the tie strength between microblogs, which is calculated by the Hawkes process. Besides, the Deepwalk algorithm is used to find the similar microblogs of the target microblog. Moreover, a CNN-BiLSTM-Attention network (the convolutional neural network and bidirectional long short-term memory network with a multihead attention mechanism) is designed to extract semantic features of microblog texts. Finally, the experimental results on two real datasets show that the proposed MSA-UITC can improve the accuracy of sentiment analysis.

The rest of this paper is organized as follows. Section 2 describes the proposed MSA-UITC in detail. The experimental results are described in Section 3. Finally, the conclusions are provided in Section 4.

2. The Proposed MSA-UITC

2.1. A Framework Overview. Figure 1 illustrates the overview of the proposed MSA-UITC for microblog sentiment analysis. It mainly consists of three parts: constructing the tie strength-based weighted network, building the sequence representation of similar microblogs, and CNN-BiLSTM-Attention network. Firstly, apply the Hawkes process to calculate the strength of tie based on user interaction and the correlation to the target microblog and construct the weighted network based on the tie strength. Secondly, utilize the Deepwalk algorithm to get the sequence representation of similar microblogs. Finally, use CNN-BiLSTM-Attention network to extract the joint features of target and similar microblogs for sentiment prediction. Now, let us elaborate on these processes.

2.2. Constructing the Tie Strength-Based Weighted Network. On social media, there is an interactive behavior between users, namely, the following relationship, which is similar to the friend relationship in real life. According to the emotional contagion theory, users are more susceptible to the sentiment of their friends (i.e., the two microblog texts posted by two users with the following relationship have similar sentiment [28]). Additionally, on the same topic, the

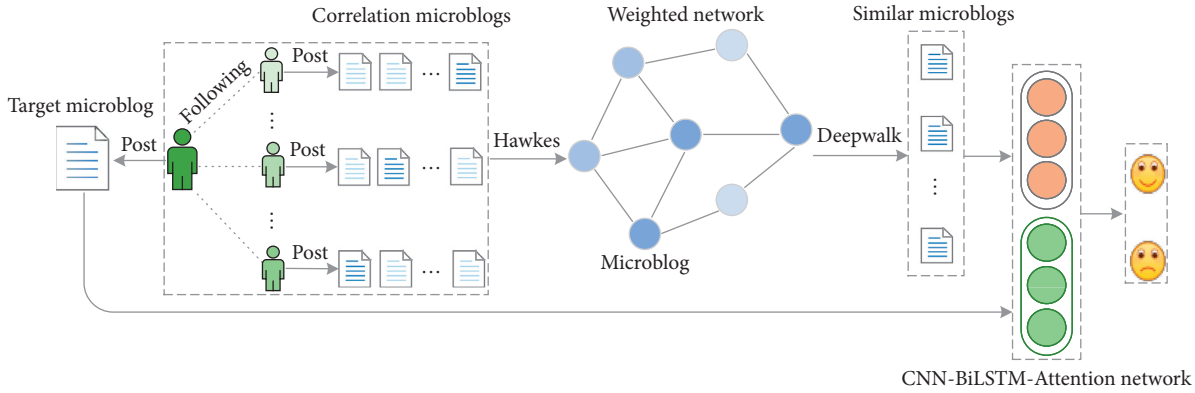

Figure 1: Overview of the proposed MSA-UITC.

closer the correlation between microblogs, the stronger the tie strength. Therefore, two factors that influence the tie strength between microblogs are considered. One is the following relationship between users, and the other is the correlation between microblogs.

To describe the correlation between microblogs, the Term Frequency-Inverse Document Frequency (TF-IDF) method [35] is adopted. Let the vector $\mathbf{T}_{u_i} = (t(w_1), t(w_2), \ldots, t(w_k), \ldots, t(w_n))$ denote the microblog text posted by user u_i, where w_k represents the kth word in this microblog text and $t(w_k)$ denotes the weight of w_k. Then, $t(w_k)$ can be calculated as follows:

$$t(w_k) = \mathrm{TF}_{u_i}(w_k) \times \mathrm{IDF}_{u_i}(w_k), \tag{1}$$

$$\mathrm{TF}_{u_i}(w_k) = \frac{f_{u_i}^{w_k}}{n_{u_i}}, \tag{2}$$

$$\mathrm{IDF}_{u_i}(w_k) = \log\left(\frac{M}{N_{w_k} + \rho}\right), \tag{3}$$

where $f_{u_i}^{w_k}$ represents the frequency of word w_k in the microblog text posted by user u_i, n_{u_i} represents the total number of words in the microblog text posted by user u_i, M is the total number of microblog texts in datasets, and N_{w_k} denotes the number of microblog texts containing word w_k in datasets.

To keep the denominator from 0, set ρ equal to 1. According to equations (1)–(3), the vectors $\mathbf{T}_{u_i}$ and $\mathbf{T}_{u_j}$ of the microblog texts that are posted by users u_i and u_j can be obtained. The correlation between $\mathbf{T}_{u_i}$ and $\mathbf{T}_{u_j}$ can be calculated by cosine similarity:

$$\mathrm{sim}_{\mathrm{text}}(u_i, u_j) = \cos\left(\mathbf{T}_{u_i}, \mathbf{T}_{u_j}\right) = \frac{\mathbf{T}_{u_i} \cdot \mathbf{T}_{u_j}}{\left|\mathbf{T}_{u_i}\right|\left|\mathbf{T}_{u_j}\right|}, \tag{4}$$

where $\cdot$ denotes the vector multiplication and $|\mathbf{T}|$ means the modulus.

Next, the tie strength is calculated by the Hawkes process, which is usually used to predict the impact on the current event based on the correlation between events. Therefore, the Hawkes process has been widely used in video popularity prediction [36] and disease prediction [37]. According to the definition of the Hawkes process in [38], the tie strength $z(i, j)$ can be expressed as follows:

$$P\left(z(i,j) \,\middle|\, \sum_{n=1}^{t} \mathbf{y}^n(i,j)\right) = \mu + \sum_{n=1}^{t}\sum_{m=1}^{2} \alpha_m \exp\left(-\beta_m (t-n)\right), \tag{5}$$

where $\mathbf{y}^n(i,j) = \{y_1^n(i,j), y_2^n(i,j)\}$, $y_1^n(i,j)$ and $y_2^n(i,j)$, respectively, represent the following relationship between users u_i and u_j and the correlation strength between microblog texts in time period $n = \{1, 2, \ldots, t\}$, μ is a constant number of the basic strength, α_m denotes the weight of the mth influencing factor, and β_m is the time adjustment factor of the mth influencing factor. The maximum likelihood estimation is used to calculate the parameters in the Hawkes process. Finally, the tie strength between users u_i and u_j can be calculated by equation (5).

For constructing the tie strength-based weighted network, let $\mathbf{A} \in \mathbb{R}^{c \times d}$ represent the microblog-user correlation matrix, and the matrix element $a_{ij} = 1$ mean that the ith microblog is posted by the jth user. Let $\mathbf{F} \in \mathbb{R}^{d \times d}$ represent the tie strength matrix between user u_i and u_j, and the element $f_{ij} = z(i, j)$. Let matrix $\mathbf{S} \in \mathbb{R}^{c \times c}$ denote the tie strength between microblogs. According to the above definition, the tie strength matrix between microblogs can be expressed as $\mathbf{S} = \mathbf{AFA}^T$. An example of calculating the tie strength matrix $\mathbf{S}$ between microblogs is shown in Figure 2.

As the graph can easily capture the tie strength between nodes, this paper transforms the tie strength matrix $\mathbf{S}$ into an undirected weight network $G = (V, E)$, where $V = \{v_1, v_2, \ldots, v_i\}$ represents the set of nodes and each node v_i in V is associated with a microblog text, E represents the set of edges, and the element e_{ij} represents the weight of each edge and $e_{ij} = s_{ij}$. Based on the above description, the weighted network $G = (V, E)$ is constructed.

2.3. Building the Sequence Representation of Similar Microblogs. To find the microblog texts that are more similar to the target microblog according to the edge weigth of G, the Deepwalk algorithm [39] that combines the Random Walk algorithm and Skip-Gram algorithm is adopted in this paper, which is the first network embedding

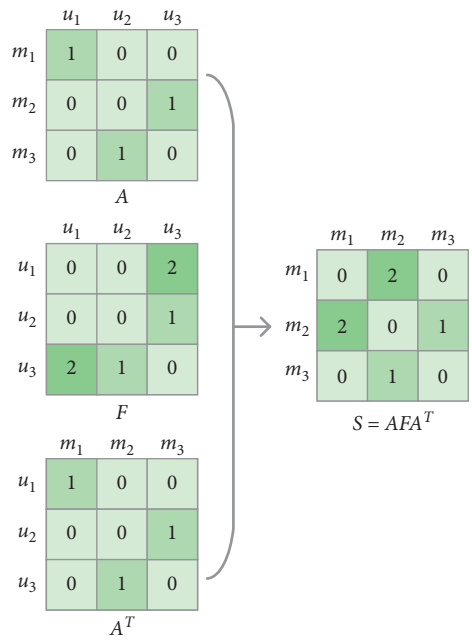

Figure 2: An example of calculating the tie strength matrix between microblogs.

method for learning low-dimensional latent representation of nodes in a network.

The main implementation process of Deepwalk algorithm is as follows. Firstly, randomly select a node v_i from the weighted network G as the starting node of random walk. Next, take walk sampling from the neighbor nodes until the maximum step size n is reached. Since the sampling probability of a node is related to the weight of the connected edges, the Random Walk algorithm gets a set of node $D = \{d_1, d_2, \ldots, d_i, \ldots, d_n\}$ based on the weight of edge. Specifically, $\{d_{i-K}, \ldots, d_{i+K}\}$ is defined as the set of contextual node which is related to each target node d_i and K represents the window size. Finally, use the objective function of Skip-Gram algorithm to predict the contextual node for each target node d_i. The expression of the objective function is

$$F = \frac{1}{n} \sum_{1 \le i \le n} \sum_{\substack{-K \le j \le K \\ K \ne 0}} \log p\left(d_{i+j} | d_i\right), \tag{6}$$

where

$$p\left(d_j \mid d_i\right) = \frac{\exp\left(\mathbf{o}_{d_i}\left(d_j\right)\right)}{\sum_{d_k \in S} \exp\left(\mathbf{o}\left(d_k\right)\right)}, \tag{7}$$

where $\mathbf{o}_{d_i}$ represents the N-dimensional vector space and can be expressed as follows:

$$\mathbf{o}_{d_i} = \mathbf{X}_{d_i} \mathbf{O}^T, \tag{8}$$

where $\mathbf{O} \in \mathbb{R}^{N \times l}$ denotes a matrix, $\mathbf{X}_{d_i} \in \mathbb{R}^{1 \times l}$ is the vector representation of node d_i, and l represents the embedded dimension.

The vector representation of nodes $\mathbf{X}_{d_i}$ can be obtained by maximizing the objective function F, and the vector representation matrix $\mathbf{X} \in \mathbb{R}^{N \times l}$ of all nodes in network G can be obtained. Thus, a representation matrix of all the similar microblog texts is obtained according to the Deepwalk algorithm.

2.4. CNN-BiLSTM-Attention Network. After obtaining the representation of similar microblogs, this paper designs the CNN-BiLSTM-Attention network to predict the sentiment polarity of target and similar microblogs. As shown in Figure 3, the sentiment analysis process can be divided into two branches. The left branch is used to extract semantic features of the target microblog, and the right branch is used to extract semantic features of the microblogs that are similar to the target microblog. The feature extraction process of the two branches will be introduced separately below.

Firstly, let us introduce the left branch of CNN-BiLSTM-Attention network. This paper uses CNN-BiLSTM with multihead attention mechanism to capture the high-level context information of the target microblog. For extracting the semantic features, the word embedding method is used to generate the vector representation of words. As microblog texts are short with irregular grammar, N dimensional pretraining word embedding [40] is used in this paper.

Assume that the sentence $\mathbf{s} = (w_1, w_2, \ldots, w_m)$ contains m words. Then, map each word into vector representation by word embedding which is denoted as $\mathbf{v} = (\mathbf{v}(w_1), \mathbf{v}(w_2), \ldots, \mathbf{v}(w_m))$, $\mathbf{v} \in \mathbb{R}^{m \times N}$, $\mathbf{v}(w_i) \in \mathbb{R}^N$. Thus, all the sentences are converted into vectors representation as the input of the neural network. Figure 4 shows the process of CNN extracting sentence features. Specifically, a vector representation sequence $(\mathbf{v}(w_1), \mathbf{v}(w_2), \ldots, \mathbf{v}(w_m))$ of sentence is generated by word embedding. Then, local features are generated through the convolutional layer. To extract multiple features, three different size filters are used for feature extraction, and the filter window size is set to $r = 1, 2, 3$. The output of the convolutional layer is

$$\hat{\mathbf{o}}_c = f\left(\mathbf{W}_c \mathbf{v}_{i:\, i+r-1} + \mathbf{b}_c\right), \tag{9}$$

where $\mathbf{W}_c \in \mathbb{R}^{N \times r}$ represents the weight matrix, $\mathbf{v}_{i:\, i+r-1}$ represents $(\mathbf{v}(w_i), \mathbf{v}(w_{i+1}), \ldots, \mathbf{v}(w_{i+r-1}))$, $\mathbf{b}_c$ is the bias vector, and f is a nonlinear function. So, the set of local features $\hat{\mathbf{O}} = (\hat{\mathbf{o}}_1, \hat{\mathbf{o}}_2, \ldots, \hat{\mathbf{o}}_{m-r+1})$ is obtained by the convolutional layer. To further obtain features that contain important information, the feature maps $\hat{\mathbf{O}}$ generated by the three filters are sent to the max pooling layer:

$$\mathbf{p} = \max\left(\hat{\mathbf{O}}\right), \tag{10}$$

and then connect the output.

Since the BiLSTM network is fused by forward and backward LSTM, the information features in the preceding and the following can be captured. To obtain the context-dependent information between sentences, BiLSTM is employed to capture contextual semantic information. The

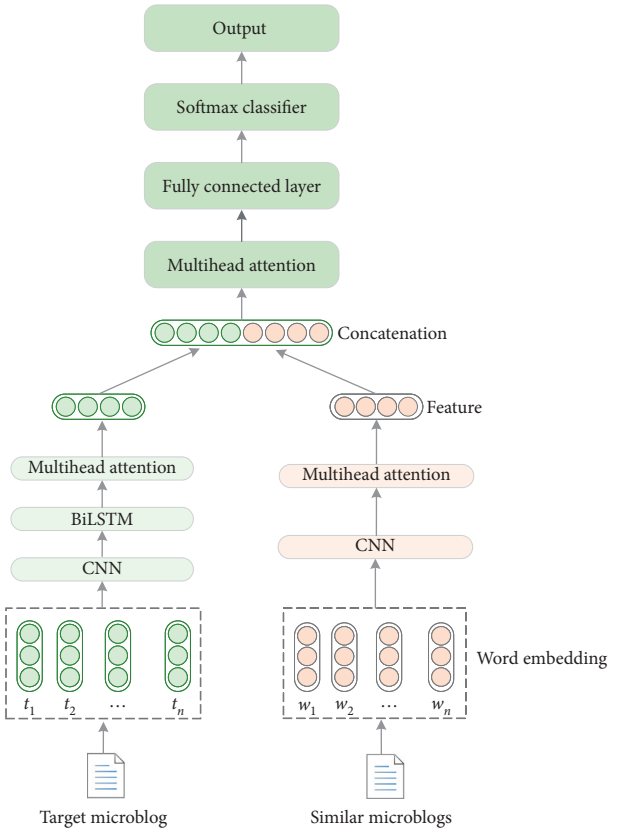

Figure 3: The sentiment analysis process of CNN-BiLSTM-Attention network.

input of BiLSTM is a connection of the pooling layer output vector that is denoted as $\mathbf{x}_i = (\mathbf{p}_1, \mathbf{p}_2, \ldots, \mathbf{p}_i)$. Figure 5 demonstrates the internal structure of BiLSTM to learn contextual semantic information. The internal information of BiLSTM is updated as follows:

$$\begin{aligned}
\mathbf{i}_t &= \sigma\left(\mathbf{W}_i\mathbf{x}_i + \mathbf{U}_i\mathbf{h}_{t-1} + \mathbf{b}_i\right),\\
\mathbf{f}_t &= \sigma\left(\mathbf{W}_f\mathbf{x}_i + \mathbf{U}_f\mathbf{h}_{t-1} + \mathbf{b}_f\right),\\
\mathbf{o}_t &= \sigma\left(\mathbf{W}_o\mathbf{x}_i + \mathbf{U}_o\mathbf{h}_{t-1} + \mathbf{b}_o\right),\\
\mathbf{C}_t &= \mathbf{f}_t * \mathbf{C}_{t-1} + \mathbf{i}_t * \tanh\left(\mathbf{W}_c\mathbf{x}_i + \mathbf{U}_c\mathbf{h}_{t-1} + \mathbf{b}_c\right),\\
\mathbf{h}_t &= \mathbf{o}_t * \tanh\left(\mathbf{C}_t\right),\\
\mathbf{H}_t &= \mathbf{h}_t^f + \mathbf{h}_t^b,
\end{aligned} \tag{11}$$

where $*$ means the elementwise multiplication, $\mathbf{x}_i$ denotes the input, $\sigma(x)$ is the activation function, $\mathbf{i}_t$, $\mathbf{f}_t$, and $\mathbf{o}_t$ represent input gate, forget gate, and output gate of LSTM, respectively, $\mathbf{C}_t$ stands for the memory unit of LSTM, $\mathbf{h}_t$, $\mathbf{h}_t^f$, and $\mathbf{h}_t^b$ represent the hidden state of LSTM, the hidden state of forward LSTM, and the hidden state of backward LSTM, respectively, $\mathbf{W}$ and $\mathbf{U}$ are weight matrices, $\mathbf{b}_i$, $\mathbf{b}_f$, $\mathbf{b}_o$, and $\mathbf{b}_c$ are bias vectors, and $\mathbf{H}_t$ means the output of the BiLSTM hidden state.

Next, the attention mechanism is used to assign different weights to the output features of BiLSTM. This paper uses the multihead attention mechanism that is composed of a series of self-attention models and is proposed in [41]. The

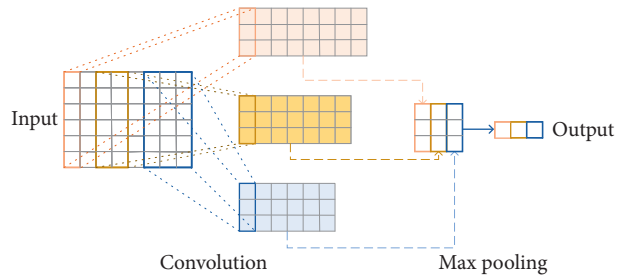

Figure 4: The process of CNN extracting sentence features.

expression for the self-attention mechanism is shown as follows:

$$\text{self} - \text{attention}\left(\mathbf{Q}, \mathbf{K}, \mathbf{V}\right) = \text{softmax}\left(\frac{\mathbf{Q}\mathbf{K}^T}{\sqrt{d_k}}\right)\mathbf{V}, \tag{12}$$

where $\mathbf{Q}, \mathbf{K}$, and $\mathbf{V}$ represent the query vector, key vector, and value vector, respectively, and they are the mapping vectors of self-attention function, and d_k denotes the dimension of $\mathbf{K}$. Then, the multihead attention mechanism can be expressed as follows:

$$\text{multi} - \text{head}\left(\mathbf{Q}, \mathbf{K}, \mathbf{V}\right) = \text{concat}\left(h_1, h_2, \ldots, h_c\right)\mathbf{W}, \tag{13}$$

where

$$h_i = \text{self} - \text{attention}\left(\mathbf{Q}\mathbf{W}_i^q, \mathbf{K}\mathbf{W}_i^k, \mathbf{V}\mathbf{W}_i^v\right), \tag{14}$$

where $\mathbf{W}$, $\mathbf{W}_i^q$, $\mathbf{W}_i^k$, and $\mathbf{W}_i^v$ represent the weight matrices for the linear layer. The structure of multihead attention mechanism is shown in Figure 6.

Now, let us introduce the right branch to learn the features of similar microblogs. According to the above introduction, the sequence representation of similar microblogs is generated by the Deepwalk algorithm. All similar microblogs are regarded as sentences, and their processing is similar to the target microblog. Specifically, the vector representation of words is generated by using the same word embedding method as the left branch. As the sentence order does not provide contextual dependency, here only CNN and multihead attention mechanism are used to extract the semantic features of each sentence, which are the same as the left branch.

After extracting the features from two branches, the joint features are generated by concatenating these two branch features. To further obtain the important features associated with sentiment expression, this paper uses the multihead attention mechanism after these two branches. Then, the joint features are fed into the fully connected layer to predict the sentiment polarity, and the softmax function is used to learn the probability of each sentiment polarity. This paper adopts the cross-entropy loss as the loss function in the training process, and the expression of objective function is

$$\text{loss} = \sum_{m \in T}\sum_{i=1}^{N} p_i^g(m)\log p_i(m), \tag{15}$$

where T is the training set, m is the microblog texts in the training set, N is the number of sentiment polarity

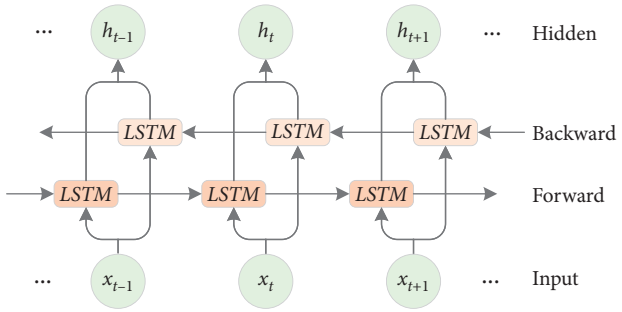

Figure 5: The structure of BiLSTM network.

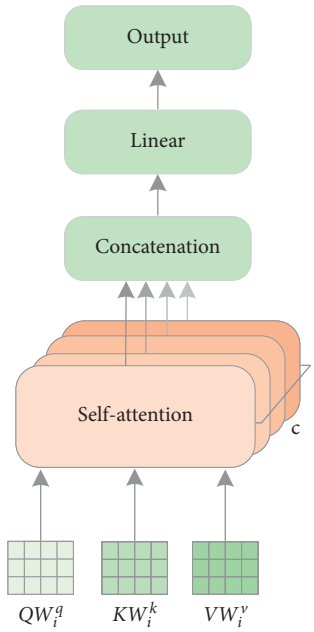

Figure 6: The structure of multihead attention mechanism.

categories, $p_i^g(m)$ means whether the sentiment polarity of the text m belongs to the category $i \in N$, and $p_i(m)$ represents the probability that the sentiment polarity of the predicted microblog m is i. This paper optimizes the network by minimizing the loss function and uses the back propagation algorithm to train the network.

3. Experiments

In the previous section, the proposed MSA-UITC has been introduced in detail. To further verify its validity, this section will conduct some experiments. Firstly, this section will introduce experimental settings. Then, the datasets and evaluation metrics will be described. Finally, the performance analysis including the comparison with other methods will be implemented.

3.1. Experimental Settings. In the experiments, the parameters of Deepwalk algorithm are set as follows: the maximum step size $n = 30$ and the window size $K = 2$. For the CNN-BiLSTM-Attention network, the pretrained word embedding dimension is set to $N = 200$, the training epoch is set to 50, the batch size is set to 64, the number of CNN filters and BiLSTM hidden units are both set to 128, and the number of self-attention mechanism is set to $c = 8$. Furthermore, this paper uses dropout operation before the fully connected layer, and the dropout rate is set to 0.5.

3.2. Datasets. All experiments are conducted on two real-word Twitter datasets: Obama-McCain Debate (OMD) [42] and Health Care Reform (HCR) [43]. OMD and HCR datasets include tweets and manual sentiment polarity labels:

(1) OMD: this dataset includes 3269 tweets and content is about the presidential debate between Barack Obama and John McCain in 2008. Tweets are annotated by at least three Amazon Mechanical Turkers and the sentiment is labeled by four polarities: positive, negative, mixed, and irrelevant. In this paper, the majority voting score is used to represent the sentiment polarity of tweets and only keeps tweets with positive and negative polarities. To obtain the following relationship between users, this paper uses the complete follower graph that is crawled by [44] in 2009. In the experiments, the OMD dataset is divided into three topics by the keywords it contained, i.e., Obama (including keyword "Obama" without "McCain"), McCain (including keyword "McCain" without "Obama"), and debate (including "Obama" and "McCain" or none of them).

(2) HCR: this dataset contains 2516 tweets and the content includes the healthcare reform event in the United States in March 2010. The sentiment labels are manually annotated with five polarities: positive, negative, irrelevant, neutral, and unsure. Besides, this dataset divides tweets into 9 manually annotated topics, i.e., health care reform, Obama, Democrats, Tea Party, Stupak, Republicans, conservatives, liberals, and others [43]. The same as OMD, in the experiments, only retain tweets with positive and negative polarities and use the following relationship crawled by [44] in 2009.

In the experiments, randomly divide 80% of the dataset into a training set and 20% of the dataset into a test set. The detailed information of OMD and HCR datasets is shown in Table 1.

3.3. Evaluation Metrics. To compare the performance of microblog sentiment analysis methods, this paper uses four metrics: accuracy, precision, recall, and $F1$score. Specifically, accuracy represents the probability of correctly predicted samples in the total predicted samples, precision is the probability of correctly predicted samples to be positive in the total number that predicted samples to be positive, recall denotes the probability of correctly predicted samples to be positive in the total positive samples, and $F1$score is the

Table 1: Statistics of OMD and HCR datasets.

Dataset	#Positive	#Negative	#Total	#User	#Topic
OMD	768	1295	2063	923	3
HCR	528	1340	1868	1085	9

harmonic average of precision and recall. The calculation formulas are shown as follows:

$$\begin{aligned} \text{accuracy} &= \frac{\text{TP} + \text{TN}}{\text{TP} + \text{FN} + \text{FP} + \text{TN}}, \\ \text{precision} &= \frac{\text{TP}}{\text{TP} + \text{FP}}, \\ \text{recall} &= \frac{\text{TP}}{\text{TP} + \text{FN}}, \\ F1\text{score} &= \frac{2 \times \text{precision} \times \text{recall}}{\text{precision} + \text{recall}}, \end{aligned} \tag{16}$$

where TP/FP denotes the TruePositive/FalsePositive and TN/FN represents the TrueNegative/FalseNegative.

3.4. Methodological Comparison and Analysis

3.4.1. Usefulness of the Tie and Attention Mechanism. Some comparative experiments are conducted to verify whether exploring the tie between microblogs and multihead attention mechanism can improve the accuracy of sentiment analysis.

To verify the effectiveness of the tie, Figures 7 and 8 show the comparison results of MSA-UITC and MSA architecture (the proposed microblog sentiment analysis architecture does not use the tie between microblogs) on OMD and HCR datasets, respectively. From them, one can conclude that MSA-UITC with the tie performs best both in accuracy, precision, recall, and $F1$score for microblog sentiment analysis, implying the usefulness of the tie. On the OMD dataset, the result shows that MSA-UITC outperforms MSA and obtains improvement of 3.72% in accuracy and 3.33% in $F1$score. Besides, on the HCR dataset, MSA-UITC has also achieved improvement with 3.21% in accuracy and 2.22% in $F1$score. This is because MSA-UITC with the tie alleviates the sparse problem of microblog texts by constructing the sentiment connection between microblogs.

To verify the effectiveness of attention mechanism, Figures 9 and 10 display the comparative results on two datasets. Specifically, "text + concat attention" denotes that the architecture uses three attention mechanisms, "text attention" means that the architecture only uses attention mechanism in the feature extraction process of target microblog and similar microblogs, "concat attention" represents that the attention mechanism is only used in the concatenation layer, and "none attention" implies that the architecture does not use any attention mechanism. From the experimental results, one can conclude that the attention mechanism plays a significant role in improving the performance of the architecture on two datasets. This is because the text layer attention and the concatenation layer attention assign effective weights to the sentiment words that determine the sentiment polarity in the microblog text. On the OMD dataset, MSA-UITC is 2.27% and 1.32% higher in accuracy and $F1$score than the architecture without attention mechanism. On the HCR dataset, MSA-UITC has also achieved improvement with 2.41% in accuracy and 1.18% in $F1$score compared with the architecture without attention mechanism.

3.4.2. Comparison with State-of-the-Art Methods. The above comparative experiments validate the usefulness of the tie between microblogs and attention mechanism in the proposed architecture. To further confirm the superiority of MSA-UITC, some comparative experiments are performed with state-of-the-art methods. The details of these methods are as follows:

(1) SANT is a supervised method proposed in [28]. It uses sentiment consistency and emotional contagion to classify microblog sentiment.

(2) SMSC is proposed in [45]. It is a structured framework by combining content and social context for microblog sentiment analysis.

(3) SASS is proposed in [31]. It uses structure similarity and topic context for sentiment analysis.

(4) SRPNN is proposed in [34]. It is the first work to combine user trust network and deep learning network for sentiment classification.

Table 2 shows the comparison of accuracy on OMD and HCR datasets. Compared with the state-of-the-art methods, MSA-UITC performs best both on OMD and HCR datasets, which means that the proposed tie strength calculation method and CNN-BiLSTM-Attention network can improve the performance of microblog sentiment analysis. In detail, compared with the SANT method, the accuracy of our proposed architecture on the OMD dataset is improved by 3.45% Besides, the accuracy of our proposed architecture outperforms the SMSC method with an improvement of 1.77% and 0.99%, respectively, on OMD and HCR datasets. Compared with the SASS method, MSA-UITC also gets an accuracy improvement of 0.76% and 2.12%, respectively, on OMD and HCR datasets. The main reason is that our proposed architecture can effectively connect similar microblogs and improve the accuracy of sentiment analysis by the CNN-BiLSTM-Attention network.

To further verify the validity of the proposed deep neural network, our architecture compared with the SRPNN method adopts CNN and simplified LSTM network for capturing semantic features of texts. The accuracy comparison results show that our architecture obtains an improvement of 2.99% on the OMD dataset and 2.92% on the HCR dataset. This indicates that the BiLSTM network and multihead attention mechanism have achieved performance improvement by extracting contextual semantic information and assigning different weights for features.

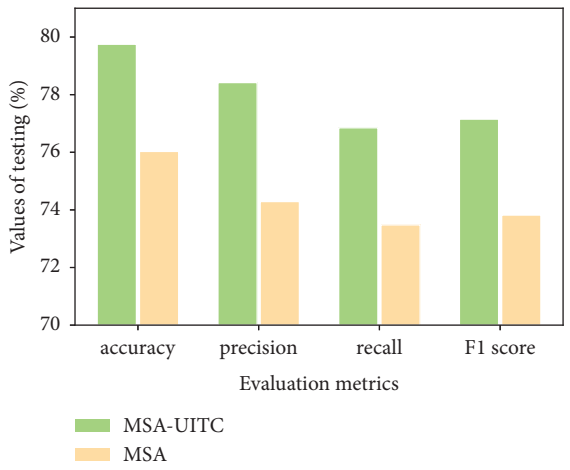

Figure 7: Performance comparison of MSA-UITC and MSA architecture on the OMD dataset.

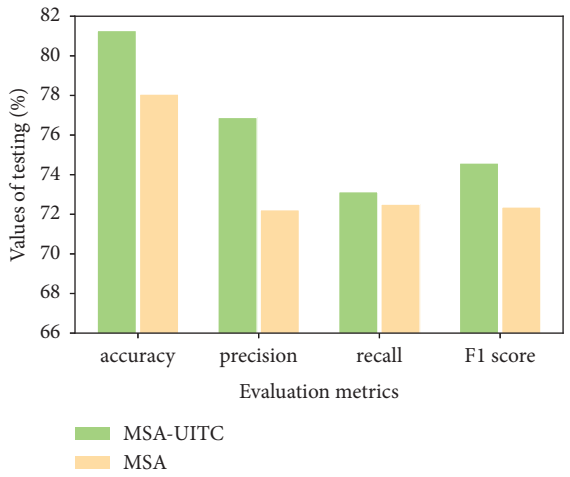

Figure 8: Performance comparison of MSA-UITC and MSA architecture on the HCR dataset.

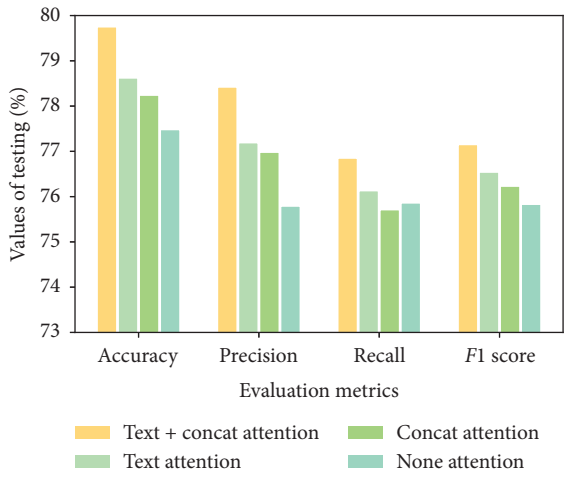

Figure 9: Performance comparison of attention mechanism on the OMD dataset.

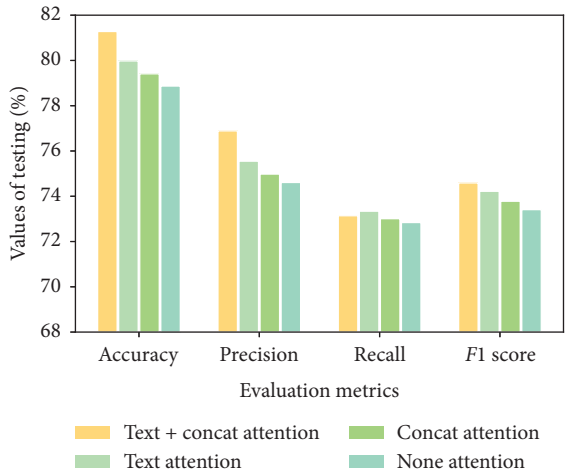

Figure 10: Performance comparison of attention mechanism on the HCR dataset.

Table 2: Accuracy comparison with state-of-the-art methods.

Method	OMD	HCR
SANT [28]	0.7630	—
SMSC [45]	0.7798	0.8029
SASS [31]	0.7899	0.7916
SRPNN [34]	0.7676	0.7836
MSA-UITC (ours)	0.7975	0.8128

4. Conclusions

In this paper, a deep learning architecture (denoted as MSA-UITC) has been developed to explore coevolution of emotional contagion and behavior for microblog sentiment analysis. Specifically, the proposed MSA-UITC considers the user interaction and microblog textes correlation as the influencing factors and uses the Hawkes process to calculate the tie strength. Besides, the Deepwalk algorithm is used to find the similar microblogs of the target microblog. Afterwards, a CNN-BiLSTM-Attention network is designed to improve the performance of sentiment analysis. Finally, some comparative experiments on two real Twitter datasets prove the superiority of the proposed architecture.

Although the proposed microblog sentiment analysis architecture has achieved competitive performance, there are some future works which can be continued. On the one hand, this architecture only classifies positive and negative labels about the tweets on the datasets, and it is necessary to expand the categories of sentiment labels. On the other hand, one can also continue to optimize the deep learning model to improve the performance of sentiment analysis, such as using an improved wording embedding model [46]. Additionally, this paper considers that user interaction and the correlation with target microblog are two factors influencing the tie strength between microblogs. However, the history of the target microblog also has the similar sentiment as the target microblog. Therefore, it is necessary to consider the history of the target microblog as a factor influencing the tie strength.

Data Availability

No data were used to support the findings of the study.

Conflicts of Interest

All authors declare no conflicts of interest.

Authors' Contributions

The authors claim that the research was realized in collaboration with the same responsibility. All authors read and approved the last version of the manuscript.

Acknowledgments

This work is supported by Natural Science Foundation of China (Grant Nos. 61702066 and 11747125), Major Project of Science and Technology Research Program of Chongqing Education Commission of China (Grant No. KJZDM201900601), Chongqing Research Program of Basic Research and Frontier Technology (Grant Nos. cstc2017jcyjAX0256 and cstc2018jcyjAX0154), Project Supported by Chongqing Municipal Key Laboratory of Institutions of Higher Education (Grant No. cqupt-mct-201901), Project Supported by Chongqing Key Laboratory of Mobile Communications Technology (Grant No. cqupt-mct-202002), Project Supported by Engineering Research Center of Mobile Communications, Ministry of Education (Grant No. cqupt-mct- 202006), Research Innovation Program for Postgraduate of Chongqing (Grant Nos. CYS17217 and CYS18238).

References

[1] S. Rajendran and P. Jayagopal, "Accessing covid19 epidemic outbreak in tamilnadu and the impact of lockdown through epidemiological models and dynamic systems," *Measurement*, vol. 169, Article ID 108432, 2021.

[2] C. Gan, Q. Feng, Q. Zhu, Z. Zhang, Y. Zhang, and Y. Xiang, "Analysis of computer virus propagation behaviors over complex networks: a case study of Oregon routing network," *Nonlinear Dynamics*, vol. 100, no. 2, pp. 1725–1740, 2020.

[3] C. Gan, Q. Feng, X. Zhang, Z. Zhang, and Q. Zhu, "Dynamical propagation model of malware for cloud computing security," *IEEE Access*, vol. 8, pp. 20325–20333, 2020.

[4] W. Wang, M. Tang, H. E. Stanley, and L. A. Braunstein, "Unification of theoretical approaches for epidemic spreading on complex networks," *Reports On Progress In Physics*, vol. 80, no. 3, Article ID 036603, 2017.

[5] W. Wang, Y. Ma, T. Wu, Y. Dai, X. Chen, and L. A. Braunstein, "Containing misinformation spreading in temporal social networks," *Chaos: An Interdisciplinary Journal of Nonlinear Science*, vol. 29, no. 12, p. 123131, 2019.

[6] Y. Yi, Z. Zhang, and C. Gan, "The effect of social tie on information diffusion in complex networks," *Physica A: Statistical Mechanics and Its Applications*, vol. 509, pp. 783–794, 2018.

[7] Y. Yi, Z. Zhang, L. T. Yang, C. Gan, X. Deng, and L. Yi, "Reemergence modeling of intelligent information diffusion in heterogeneous social networks: the dynamics perspective," *IEEE Transactions on Network Science and Engineering*, p. 1, 2020.

[8] E. Hatfield, J. T. Cacioppo, and R. L. Rapson, "Emotional contagion," *Current Directions in Psychological Science*, vol. 2, no. 3, pp. 96–100, 1993.

[9] K. J. P. Espinosa and A. M. J. Bernales, "Characterizing influence factors affecting emotion diffusion in facebook," in *Proceedings of the World Congress on Engineering and Computer Science*, vol. 2, pp. 797–802, San Francisco, CA, USA, 2014.

[10] W. Wang, Q.-H. Liu, J. Liang, Y. Hu, and T. Zhou, "Coevolution spreading in complex networks," *Physics Reports*, vol. 820, pp. 1–51, 2019.

[11] K. Dave, S. Lawrence, and D. M. Pennock, "Mining the peanut gallery: opinion extraction and semantic classification of product reviews," in *Proceedings of the 12th International Conference on World Wide Web*, pp. 519–528, Budapest, HU, USA, 2003.

[12] J. Yu, Y. An, T. Xu, J. Gao, M. Zhao, and M. Yu, "Product recommendation method based on sentiment analysis," in *Proceedings of the International Conference on Web Information Systems and Applications*, pp. 488–495, Springer, Qingdao, China, 2018.

[13] X. Zhao, Y. Zhang, W. Guo, and X. Yuan, "Jointly trained convolutional neural networks for online news emotion analysis," in *Proceedings of the International Conference on Web Information Systems and Applications*, pp. 170–181, Springer, 2018.

[14] A. B. Eliacik and N. Erdogan, "Influential user weighted sentiment analysis on topic based microblogging community," *Expert Systems with Applications*, vol. 92, pp. 403–418, 2018.

[15] M. Taboada, J. Brooke, M. Tofiloski, K. Voll, and M. Stede, "Lexicon-based methods for sentiment analysis," *Computational Linguistics*, vol. 37, no. 2, pp. 267–307, 2011.

[16] H. Saif, Y. He, M. Fernandez, and H. Alani, "Contextual semantics for sentiment analysis of twitter," *Information Processing & Management*, vol. 52, no. 1, pp. 5–19, 2016.

[17] A. Goel, J. Gautam, and S. Kumar, "Real time sentiment analysis of tweets using naive bayes," in *Proceedings of the in: 2016 2nd International Conference on Next Generation Computing Technologies (NGCT)*, pp. 257–261, IEEE, Dehradun, India, 2016.

[18] D. Torunoğlu, G. Telseren, Ö. Sağtürk, and M. C. Ganiz, "Wikipedia based semantic smoothing for twitter sentiment classification," in *Proceedings of the 2013 IEEE INISTA*, pp. 1–5, IEEE, Albena, Bulgaria, 2013.

[19] C. Gan, L. Wang, and Z. Zhang, "Multi-entity sentiment analysis using self-attention based hierarchical dilated convolutional neural network," *Future Generation Computer Systems*, vol. 112, pp. 116–125, 2020.

[20] C. Gan, L. Wang, Z. Zhang, and Z. Wang, "Sparse attention based separable dilated convolutional neural network for targeted sentiment analysis," *Knowledge-Based Systems*, vol. 188, pp. 1–10, 2020.

[21] S. Maghool, N. Maleki-Jirsaraei, and M. Cremonini, "The coevolution of contagion and behavior with increasing and decreasing awareness," *Plos One*, vol. 14, no. 12, Article ID e0225447, 2019.

[22] J. Leskovec, L. Backstrom, R. Kumar, and A. Tomkins, "Microscopic evolution of social networks," in *Proceedings of the 14th ACM SIGKDD International Conference on Knowledge Discovery and Data Mining*, pp. 462–470, New York, NY, USA, 2008.

[23] M. McPherson, L. Smith-Lovin, and J. M. Cook, "Birds of a feather: homophily in social networks," *Annual Review of Sociology*, vol. 27, no. 1, pp. 415–444, 2001.

[24] R. M. Bond, C. J. Fariss, J. J. Jones et al., "A 61-million-person experiment in social influence and political mobilization," *Nature*, vol. 489, no. 7415, pp. 295–298, 2012.

[25] M. Miller, C. Sathi, D. Wiesenthal, J. Leskovec, and C. Potts, "Sentiment flow through hyperlink networks," in *Proceedings of the International Conference on Weblogs and Social Media*, Barcelona, Spain, 2011.

[26] J. H. Fowler and N. A. Christakis, "Dynamic spread of happiness in a large social network: longitudinal analysis over 20 years in the framingham heart study," *Bmj*, vol. 337.

[27] L. Pan, D. Yang, W. Wang, S. Cai, T. Zhou, and Y.-C. Lai, "Phase diagrams of interacting spreading dynamics in complex networks," *Physical Review Research*, vol. 2, no. 2, Article ID 023233, 2020.

[28] X. Hu, L. Tang, J. Tang, and H. Liu, "Exploiting social relations for sentiment analysis in microblogging," in *Proceedings of the Sixth ACM International Conference on Web Search and Data Mining*, pp. 537–546, New York, NY, USA, 2013.

[29] X. Ruan, C. Mi, X. Lin, and Y. Lu, "Microblog sentiment analysis using user similarity and interaction-based social relations," in *Proceedings of the Pacific Asia Conference on Information Systems (PACIS)*, Association for Information Systems, Yokohama, Japan, 2017.

[30] T.-J. Lu, "Semi-supervised microblog sentiment analysis using social relation and text similarity," in *Proceedings of the 2015 International Conference on Big Data and Smart Computing*, pp. 194–201, BigComp IEEE, Langkawi, Malaysia, 2015.

[31] X. Zou, J. Yang, and J. Zhang, "Microblog sentiment analysis using social and topic context," *Plos One*, vol. 13, no. 2, Article ID e0191163, 2018.

[32] W. Liu and M. Zhang, "Semi-supervised sentiment classification method based on weibo social relationship," in *Proceedings of the International Conference on Web Information Systems and Applications*, pp. 480–491, Springer, Qingdao, China, 2019.

[33] R. Zeng and D. Zhu, "A model and simulation of the emotional contagion of netizens in the process of rumor refutation," *Scientific Reports*, vol. 9, no. 1, pp. 1–15, 2019.

[34] K. Zhao, Y. Zhang, Y. Zhang, C. Xing, and C. Li, "Learning from user social relation for document sentiment classification," in *Proceedings of the International Conference on Database Systems for Advanced Applications*, pp. 86–103, Springer, Chiang Mai, Thailand, 2019.

[35] G. A. Dalaorao, A. M. Sison, and R. P. Medina, "Integrating collocation as tf-idf enhancement to improve classification accuracy," in *Proceedings of the 2019 IEEE 13th International Conference on Telecommunication Systems, Services, and Applications (TSSA)*, pp. 282–285, IEEE, Bali, Indonesia, 2019.

[36] M.-A. Rizoiu, L. Xie, S. Sanner, M. Cebrian, H. Yu, and P. Van Hentenryck, "Expecting to be hip: hawkes intensity processes for social media popularity," in *Proceedings of the 26th International Conference on World Wide Web*, pp. 735–744, Perth, Australia, 2017.

[37] E. Choi, N. Du, R. Chen, L. Song, and J. Sun, "Constructing disease network and temporal progression model via context-sensitive hawkes process," in *Proceedings of the 2015 IEEE International Conference on Data Mining*, pp. 721–726, IEEE, Atlantic City, NJ, USA, 2015.

[38] F. Abergel and A. Jedidi, "Long-time behavior of a hawkes process--based limit order book," *SIAM Journal on Financial Mathematics*, vol. 6, no. 1, pp. 1026–1043, 2015.

[39] J. Xu, F. Huang, X. Zhang et al., "Sentiment analysis of social images via hierarchical deep fusion of content and links," *Applied Soft Computing*, vol. 80, pp. 387–399, 2019.

[40] J. Pennington, R. Socher, and C. D. Manning, "Glove: global vectors for word representation," in *Proceedings of the 2014 Conference on Empirical Methods in Natural Language Processing*, pp. 1532–1543, EMNLP), Doha, Qatar, 2014.

[41] A. Vaswani, N. Shazeer, N. Parmar et al., "Attention is all you need," in *Proceedings of the Advances in Neural Information Processing Systems*, pp. 5998–6008, Long Beach, CA, USA, 2017.

[42] D. A. Shamma, L. Kennedy, and E. F. Churchill, "Tweet the debates: understanding community annotation of uncollected sources," in *Proceedings of the First SIGMM Workshop on Social Media*, pp. 3–10, Beijing China, 2009.

[43] M. Speriosu, N. Sudan, S. Upadhyay, and J. Baldridge, "Twitter polarity classification with label propagation over lexical links and the follower graph," in *Proceedings of the First Workshop on Unsupervised Learning in NLP*, pp. 53–63, Edinburgh, Scotland, 2011.

[44] H. Kwak, C. Lee, H. Park, and S. Moon, "What is twitter, a social network or a news media?" in *Proceedings of the 19th International Conference on World Wide Web*, pp. 591–600, Raleigh, NC, USA, 2010.

[45] F. Wu, Y. Huang, and Y. Song, "Structured microblog sentiment classification via social context regularization," *Neurocomputing*, vol. 175, pp. 599–609, 2016.

[46] J. Liu, S. Zheng, G. Xu, and M. Lin, "Cross-domain sentiment aware word embeddings for review sentiment analysis," *International Journal of Machine Learning and Cybernetics*, pp. 1–12, 2020.

Hindawi
Complexity
Volume 2021, Article ID 6645113, 7 pages
https://doi.org/10.1155/2021/6645113

Research Article

Immunization of Cooperative Spreading Dynamics on Complex Networks

Jun Wang,[1] Shi-Min Cai ,[1,2,3] and Tao Zhou[1,2,3]

[1]*School of Computer Science and Engineering, University of Electronic Science and Technology of China, Chengdu 610054, China*
[2]*Institute of Fundamental and Frontier Sciences, University of Electronic Science and Technology of China, Chengdu 610054, China*
[3]*Big Data Research Center, University of Electronic Science and Technology of China, Chengdu 610054, China*

Correspondence should be addressed to Shi-Min Cai; shimin.cai81@gmail.com

Received 3 November 2020; Revised 14 December 2020; Accepted 6 January 2021; Published 18 January 2021

Academic Editor: Chenquan Gan

Cooperative spreading dynamics on complex networks is a hot topic in the field of network science. In this paper, we propose a strategy to immunize some nodes based on their degrees. The immunized nodes disable the synergistic effect of cooperative spreading dynamics. We also develop a generalized percolation theory to study the final state of the spreading dynamics. By using the Monte Carlo method, numerical simulations reveal that immunizing nodes with a large degree cannot always be beneficial for containing cooperative spreading. For small values of transmission probability, immunizing hubs can suppress the spreading, while the opposite situation happens for large values of transmission probability. Furthermore, numerical simulations show that immunizing hubs increase the cost of the system. Finally, all numerical simulations can be well predicted by the generalized percolation theory.

1. Introduction

Many real-world phenomena in social and biological systems (e.g., information diffusion and epidemic spreading) can be described as spreading dynamics on complex networks [1, 2]. Historically, according to the number of dynamics, the spread on complex networks experienced two periods. The first period is single spreading dynamics on complex networks, where there is only one dynamics on the network. Romualdo and Vespignani are the first to study the single spreading dynamics on complex networks with heterogeneous degree distribution [3, 4]. They revealed that the epidemic threshold vanishes if the heterogeneity of degree distribution is strong enough. The second period is coevolving spreading dynamics that more than one dynamics are evolving in the system [5, 6]. According to the interacting mechanisms between different spreading dynamics, we can divide into competing, asymmetric, and cooperative spreading dynamics.

The competing spreading dynamics is used to describe two competing hosts. For successively competing spreading dynamics of two epidemics, Newman [7] found that the second epidemic threshold is always larger than the first one. Brian and Newman Mark [8] further adopted a competing percolation theory to reveal the phase diagram of competing spreading dynamics of two epidemics and found that the faster spreading epidemic is dominant. Recently, more works focus on the competing spreading dynamics on overlay and multiplex networks [9–11].

The asymmetric spreading dynamics is widely used to describe the coevolving spreading of awareness and epidemic. It shows an asymmetric interaction, the dynamics a suppresses the dynamics b, while the dynamics b promotes the dynamics a. Granell et al. found that the diffusion of awareness significantly suppresses the epidemic spreading for reversible coevolving spreading [12, 13]. Wang et al. found that the interlayer degree correlation is beneficial for containing epidemic spreading, and there is an optimal

information diffusion rate to suppress the epidemic spreading [14, 15].

The cooperative spreading dynamics suggests that the dynamics a and b promote each other. A significant result revealed by Cai et al. is that the phase transition may be discontinuous if the cooperative strength is large enough [16]. Chen et al. further investigated the effects of network structures and dimensions on the phase diagram of cooperative spreading dynamics [17–19].

The immunization of spreading dynamics on complex networks is a hot topic. Some successful strategies have been proposed, such as targeted immunization, acquaintance immunization, and information spreading-based immunization [20–26]. To our best knowledge, there is still lack of systematic study on immunization of cooperative spreading dynamics on complex networks. In this paper, we propose an immunization strategy and use generalized percolation theory to study the final state of the two dynamics cooperatively spreading on scale-free (SF) random networks. The extensive numerical simulations are performed to verify the correctness and effectiveness of our proposed strategy.

2. Model Descriptions

This section introduces the immunization strategy for the cooperative spreading dynamics on complex networks. We consider a network with size N. Its degree distribution is $P(k)$. We construct the network by applying the uncorrelated configuration model [27]. To introduce the immunization strategy, we assign each node with an immunization probability. We suppose that the immunization probability of each node is affected by its surrounding environment. In the network, we consider the surrounding environment with the number of neighbors of the node. Denoting $W(k_i)$ as the probability of node i with degree k_i that does not be immunized, $W(k_i)$ can be expressed as

$$W(k_i) = \frac{k_i^{\alpha}}{\sum_j k_j^{\alpha}}, \quad -\infty < \alpha < +\infty, \tag{1}$$

where α is a hyperparameter. For $\alpha = 0$, every node is immunized with the same probability. When $\alpha \longrightarrow +\infty$, nodes with a small degree have a large immunization probability; the opposite situation happens when $\alpha \longrightarrow -\infty$. We select the fraction $1 - p$ of nodes in the network according to equation (1) and immunize them. If a node is immunized, the synergistic effect of two dynamics is disabled for the cooperative spreading dynamics on complex networks.

The epidemics (i.e., specific dynamics) a and b spread on the network following the susceptible-infected-recovered (SIR) model. At any time, each node can exist in one of the three states of each epidemic: susceptible (S), infected (I), and recovered (R). In the susceptible state, a node is susceptible and has not been infected. In the infected state, a node is infected by the epidemics $x \in \{a, b\}$ and can transmit the epidemics to its neighbors in the network. The recovered state indicates that a node has recovered from the epidemics and will not be infected again. For the coinfection epidemic spreading, the state of a node can be divided into nine types denoted as S_aS_b, S_aI_b, S_aR_b, I_aS_b, I_aI_b, I_aR_b, R_aS_b, R_aI_b, and R_aR_b.

In the process of the spreading of the two epidemics, we randomly select a seed node in the network for the epidemics a and b. For a node that does not be infected by any epidemic, it will be infected by the epidemic $a(b)$ with probability $1 - (1 - \lambda)^{k_a}$ (with probability $1 - (1 - \lambda)^{k_b}$), where λ is the infection probability of the epidemics a and b. The parameter $k_a(k_b)$ represents the number of infected neighbors in the network of the epidemic $a(b)$. If a node i is infected by one of the two epidemics, there are two situations. On the one hand, if node i does not be immunized, it will be infected by the other epidemic with probability $1 - (1 - \vartheta)^{k_x}$, where k_x is the number of infected nodes by the epidemic $x \in \{a, b\}$. To include the synergistic effect to the spreading dynamics, we assume $\vartheta > \lambda$. On the other hand, if node i is immunized, it will be infected by the other epidemic with probability $1 - (1 - \lambda)^{k_x}$. Each infected node recovers with probability γ. The cooperative spreading dynamics evolves until there are no nodes in the infected state.

In reality, immunizing a node usually costs some resources. In our model, we consider node i with degree k paying the immunizing cost as kc_1 when it is immunized. The c_1 is the cost unit. The recovery of infected nodes also needs some resources. If node i with degree k is infected by the epidemic $a(b)$, we consider that its recovery cost is $kc_a(kc_b)$, where $c_a(c_b)$ represents the cost unit. Moreover, if node i is not infected with any disease, it does not need to pay any recovery cost. Therefore, the overall cost of node i with degree k is

$$C_k = (I_c c_1 + I_a c_a + I_b c_b)k, \tag{2}$$

where $I_{a,b,c} \in \{0, 1\}$. I_c indicates whether node i is immunized. $I_a(I_b)$ indicates whether node i is infected by the epidemic $a(b)$. The mean cost of all nodes in the network is

$$C = \sum_k P(k) C_k. \tag{3}$$

3. Theoretical Analysis

Previous studies revealed that the final outbreak size of the SIR model could be mapped to solving the giant connection cluster (GCC) of bond percolation process [28–30]. To get the final outbreak size of the epidemics a and b simultaneously, we develop a generalized bond percolation theory inspired by Refs. [31, 32]. As we know, the generating function of a network with degree distribution $P(k)$ can be wrote as $G(x) = \sum_k P(k) x^k$. To get the GCC, we define $\mu_a(\mu_b)$ as the probability, that is, a randomly selected edge connecting to a node in the GCC infected by the epidemic a (b).

Next, we need to write down the self-consistent equation for μ_a and μ_b by considering whether a node is immunized. Firstly, we analyze diseases a and b separately. If node i is infected by the epidemic a with no coinfection, i.e., node i in the GCC of the epidemic a with no coinfection, the probability is $\nu_a(\lambda) = 1 - (1 - \lambda\mu_a)^{k-1}$. Contrarily, if node i is

infected by the epidemic a with coinfection, the probability is $\nu_a(\vartheta) = 1 - (1 - \vartheta\mu_a)^{k-1}$. For the epidemic b, we can get the same equations, $\nu_b(\lambda) = 1 - (1 - \lambda\mu_b)^{k-1}$ and $\nu_b(\vartheta) = 1 - (1 - \vartheta\mu_b)^{k-1}$. Then, we consider the synergistic effect of the epidemics a and b. If node i is in the GCC of the epidemic a, there are two situations. First, node i is only infected by the epidemic a with probability $\nu_a(\lambda)(1 - \lambda\mu_b)^k$. Second, node i is infected by the two epidemics. There are three subdivisions. (i) If node i is immunized with probability $1 - \ell_k$, there is no coinfection. It is infected by the two epidemics with probability $\nu_a(\lambda)[(1 - \lambda\mu_b)\nu_b(\lambda) + \lambda\mu_b]$. ℓ_k is the probability that node i with degree k does not be immunized. (ii) The node i is not immunized with probability ℓ_k, and there may be coinfection. If the coinfection happens in the epidemic a, in other words, node i is infected by the epidemic b first and then reinfected by the epidemic a; the probability is $\ell_k\nu_a(\vartheta)[(1 - \lambda\mu_b)\nu_b(\lambda) + \lambda\mu_b]s$. (iii) If the coinfection happens in disease b, the probability is $\ell_k\nu_a(\lambda)[(1 - \vartheta\mu_b)\nu_b(\vartheta) + \vartheta\mu_b](1 - s)$. The parameter s is the probability that node i is first infected by the epidemic b and reinfected by the epidemic a. That is, s is corrected to the transmission rate of the two epidemics. Considering the abovementioned situations, we have

$$\mu_a = \sum_k \frac{kP(k)}{\langle k\rangle}\left\{\begin{array}{l}(1-\ell_k)\nu_a(\lambda)\left[(1-\lambda\mu_b)\nu_b(\lambda)+\lambda\mu_b\right]+\nu_a(\lambda)(1-\lambda\mu_b)^k \\ +\ell_k\left[\begin{array}{l}\ell_k\nu_a(\vartheta)(1-\lambda\mu_b)\nu_b(\lambda)+\lambda\mu_b s+\ell_k\nu_a(\lambda)(1-\vartheta\mu_b)\nu_b(\vartheta) \\ +\vartheta\mu_a(1-s)\end{array}\right]\end{array}\right\}. \tag{4}$$

By using $G(x)$, we rewrite equation (4) as

$$\begin{aligned}\mu_a = {} & 1-(1-\ell_k s)G_1(1-\lambda\mu_a)+(1-\lambda\mu_b) \\ & \cdot\left[\ell_k(1-s)G_1(1-\lambda\mu_b)-\ell_k G_1\left((1-\lambda\mu_a)\cdot(1-\lambda\mu_b)\right)\right] \\ & -\ell_k s G_1(1-\vartheta\mu_a)-(1-\lambda\mu_b)G_1\left((1-\vartheta\mu_a)\right. \\ & \left.\cdot(1-\lambda\mu_b)\right)-\ell_k(1-s)(1-\vartheta\mu_b)G_1(1-\vartheta\mu_b) \\ & -G_1\left((1-\lambda\mu_a)\cdot(1-\vartheta\mu_b)\right),\end{aligned} \tag{5}$$

where $G_1(x) = (G'(x)/G'(1)) = (1/\langle k\rangle)\sum_k kP(k)x^{k-1}$ is the generating function for the excess degree distribution of the network. Similarity, we can get the μ_b as

$$\begin{aligned}\mu_b = {} & 1-(1-\ell_k+\ell_k s)G_1(1-\lambda\mu_b)+(1-\lambda\mu_a) \\ & \cdot\left[\ell_k s G_1(1-\lambda\mu_a)-\ell_k G_1\left((1-\lambda\mu_a)\cdot(1-\lambda\mu_b)\right)\right] \\ & -\ell_k s(1-\vartheta\mu_a)G_1(1-\vartheta\mu_b)-G_1\left((1-\vartheta\mu_a)\right. \\ & \left.\cdot(1-\lambda\mu_b)\right)-\ell_k(1-s)G_1(1-\vartheta\mu_b) \\ & -(1-\lambda\mu_a)G_1\left((1-\lambda\mu_a)\cdot(1-\vartheta\mu_b)\right).\end{aligned} \tag{6}$$

Note that the value of ℓ_k is still unknown in equations (5) and (6). We will solve it inspired by Refs. [33, 34]. Defining $A_f(k)$ as the number of immunized nodes with degree k and $P_f(k)$ as the degree distribution in the residual network, in which all nodes are immunized, here, f is the current fraction of immunized nodes. We get

$$P_f(k) = \frac{A_f(k)}{fN}. \tag{7}$$

Once another node is assigned without immunization according to equation (1), $A_f(k)$ changes as

$$A_{(f-1/N)}(k) = A_f(k) - \frac{P_f(k)k^\alpha}{\langle k^\alpha(f)\rangle}, \tag{8}$$

where $\langle k^\alpha(f)\rangle = \sum_k P_f(k)k^\alpha$. In the limit $N \longrightarrow \infty$, equation (8) can be presented in terms of derivative of $A_p(k)$ with respect to p,

$$\frac{\mathrm{d}A_f(k)}{\mathrm{d}f} \approx N\frac{P_f(k)k^\alpha}{\langle k^\alpha(f)\rangle}. \tag{9}$$

Differentiating equation (7) with respect to $\mathrm{d}A_f(k)/\mathrm{d}f \approx N(P_f(k)k^\alpha/\langle k^\alpha(f)\rangle)$ and using equation (9), we obtain

$$-f\frac{\mathrm{d}P_f(k)}{\mathrm{d}p} = P_f(k) - \frac{P_f(k)k^\alpha}{\langle k^\alpha(f)\rangle}. \tag{10}$$

Define $H_\alpha(g) = \sum_k P(k)g^{k^\alpha}$, and let $g = H_\alpha^{-1}(f)$. We find by direct differentiation that

$$P_f(k) = P(k)H_\alpha(g)g^{k^\alpha} = \frac{1}{f}P(k)g^{k^\alpha}, \tag{11}$$

$$\langle k^\alpha(f)\rangle = \frac{gH_\alpha'(g)}{H_\alpha(g)}. \tag{12}$$

We iterate these equations until $f = 1 - p$. By using equation (11), the probability ℓ_k is that a node with degree k without immunization is $\ell_k = 1 - P_f(k)$.

Inserting the value of ℓ_k into equations (5) and (6), we obtain the probabilities μ_a and μ_b. We can further get the coinfection outbreak size of two epidemics denoted as P_{ab}. If node i is in the GCC of the epidemics a and b simultaneously, it must be infected with the two epidemics. There are three possible situations. (i) $(1 - \ell_k)[(1 - \lambda\mu_a)\nu_a(\lambda) + \lambda\mu_a][(1 - \lambda\mu_b)\nu_b(\lambda) + \lambda\mu_b]$ means node i is immunized and infected by the epidemics a and b independently. (ii) $\ell_k s[(1 - \vartheta\mu_a)\nu_a(\vartheta) + \vartheta\mu_a][(1 - \lambda\mu_b)\nu_b(\lambda) + \lambda\mu_b]$ means node i without immunization, and first is infected by the epidemic b and reinfected by the epidemic a. (iii) $\ell_k(1 - s)[(1 - \lambda\mu_a)\nu_a(\lambda) + \lambda\mu_a][(1 - \vartheta\mu_b)\nu_b(\vartheta) + \vartheta\mu_b]$ means node i

without immunization, and first is infected by the epidemic a and reinfected by the epidemic b. We obtain

$$P_{ab} = \sum_k P(k) \left\{ \begin{array}{c} (1-\ell_k)[(1-\lambda\mu_a)\nu_a(\lambda)+\lambda\mu_a][(1-\lambda\mu_b)\nu_b(\lambda)+\lambda\mu_b] \\ +\ell_k \left[\begin{array}{c} [(1-\vartheta\mu_a)\nu_a(\vartheta)+\vartheta\mu_a][(1-\lambda\mu_b)\nu_b(\lambda)+\lambda\mu_b]s \\ +[(1-\lambda\mu_a)\nu_a(\lambda)+\lambda\mu_a][(1-\vartheta\mu_b)\nu_b(\vartheta)+\vartheta\mu_b](1-s) \end{array} \right] \end{array} \right\}. \tag{13}$$

By using $G(X)$, we can transform equation (13) into

$$\begin{aligned} P_{ab} = {} & 1-(1-\ell_k+\ell_k s)G_1(1-\lambda\mu_b)-(1-\ell_k s)G_1(1-\lambda\mu_a) \\ & ++(1-\ell_k)G_1((1-\lambda\mu_a)\cdot(1-\lambda\mu_b)) \\ & -\ell_k s[G_1 1-\vartheta\mu_a-G_1 1-\vartheta\mu_a\cdot 1-\lambda\mu_b]-\ell_k 1 \\ & -s[G_1 1-\vartheta\mu_b-G_1 1-\lambda\mu_a\cdot 1-\vartheta\mu_b]. \end{aligned} \tag{14}$$

When we get the nodes which infected with the epidemics a and b, we can get the mean cost of all nodes in the network as

$$C = \sum_k P(k)[(1-\ell_k)c_1 k + P_a(k)c_a k + P_b(k)c_b k], \tag{15}$$

where $P_a(k)$ is the probability that a node with degree k is infected with the epidemic a. Similarity, $P_b(k)$ is the probability for the epidemic b. Similar to equation (13), the $P_a(k)$ is

$$\begin{aligned} P_a(k) = {} & (1-\ell_k)[(1-\lambda\mu_a)\nu_a(\lambda)+\lambda\mu_a][(1-\lambda\mu_b)\nu_b(\lambda)+\lambda\mu_b] \\ & +\ell_k(1-\vartheta\mu_a)\nu_a(\vartheta)+\vartheta\mu_a(1-\lambda\mu_b)\nu_b(\lambda) \\ & +\lambda\mu_b s+(1-\lambda\mu_a)\nu_a(\lambda)+\lambda\mu_a(1-\vartheta\mu_b)\nu_b(\vartheta) \\ & +\vartheta\mu_b(1-s) \\ & +[(1-\lambda\mu_a)\nu_a(\lambda)+\lambda\mu_a](1-\lambda\mu_b)^k, \end{aligned} \tag{16}$$

and $P_b(k)$ is

$$\begin{aligned} P_b(k) = {} & (1-\ell_k)[(1-\lambda\mu_a)\nu_a(\lambda)+\lambda\mu_a] \\ & \cdot[(1-\lambda\mu_b)\nu_b(\lambda)+\lambda\mu_b] \\ & +\ell_k[[(1-\vartheta\mu_a)\nu_a(\vartheta)+\vartheta\mu_a][(1-\lambda\mu_b)\nu_b(\lambda)+\lambda\mu_b]s \\ & +[(1-\lambda\mu_a)\nu_a(\lambda)+\lambda\mu_a] \\ & \cdot[(1-\vartheta\mu_b)\nu_b(\vartheta)+\vartheta\mu_b](1-s)] \\ & +(1-\lambda\mu_b)\nu_b(\lambda)+\lambda\mu_b(1-\lambda\mu_a)^k. \end{aligned} \tag{17}$$

Considering all possible values of k, we obtain the probability of the fraction of nodes infected by the epidemics a and b as

$$P_a = \sum_k P(k)P_a(k), P_b = \sum_k P(k)P_b(k), \tag{18}$$

respectively.

Another important question is that when the two epidemics will globally outbreak? Taking the epidemic a as an example, in the bond percolation theory, equation (5) always has a trivial solution of $u_a = 0$. When there is a nontrivial solution, $\mu_a < 1$ indicates a global outbreaks. To determine the value of outbreak threshold λ_c, we rewrite equations (5) and (6) inspired by Ref. [35],

$$\begin{aligned} F_a(\mu_a,\mu_b) &= \mu_a - f_a(\mu_a,\mu_b) = 0, \\ F_b(\mu_a,\mu_b) &= \mu_b - f_b(\mu_A,\mu_B) = 0, \end{aligned} \tag{19}$$

respectively, where $f_a(\mu_a,\mu_b)$ and $f_b(\mu_a,\mu_b)$, respectively, represent the right hands of equations (5) and (6). At the point of outbreak threshold λ_c, the following condition

$$\frac{\partial f_a(\mu_a,\mu_b)}{\partial \mu_b}\frac{\partial f_b(\mu_a,\mu_b)}{\partial \mu_a}\Big|_{\lambda=\lambda_c} = 1, \tag{20}$$

is fulfilled. By numerically solving equation (20), we can obtain the outbreak threshold λ_c.

4. Results

In this section, we study the cooperative spreading dynamics of two epidemics on SF random networks. Specifically, we set the SF random network with power-law degree distribution $P(k) \sim k^{-\gamma_A}$, where γ_A represents the degree exponent. The smaller the γ_A, the stronger the heterogeneity of degree distribution will be. In our model, we set $c_1 = c_a = c_b = 1$ to include the immunization cost of a node and the recovery cost of an infected node, $s = 0.5$, by assuming an equal transmission rate of the epidemics a and b, and the recovery probability $\gamma = 1$. All numerical simulations are averaged over 100 times.

In Figure 1, we study the cooperate epidemic spreading on a SF random network with different p and α. We set $\vartheta = 0.99$ and $\gamma_A = 2.7$. When we fix $p = 0.5$, that is, fixing the number of unimmunized nodes, the outbreak threshold increases with the decreasing α. As the propagation probability λ increases, the propagation range increases. The reason is that when α is large, the synergy acts on the nodes with a large degree. These nodes are more likely to be infected preferentially, so that the epidemics will be more likely to break out under the coinfection. When the α is small, the synergy acts on the nodes with a small degree. At this time, the coinfection leads to a large outbreak size. When we fix $\alpha = 3$, $p = 0.2$ and $p = 0.5$ have the same outbreak threshold. Importantly, we find that immunizing large degree nodes suppresses the cooperate epidemic spreading when λ is

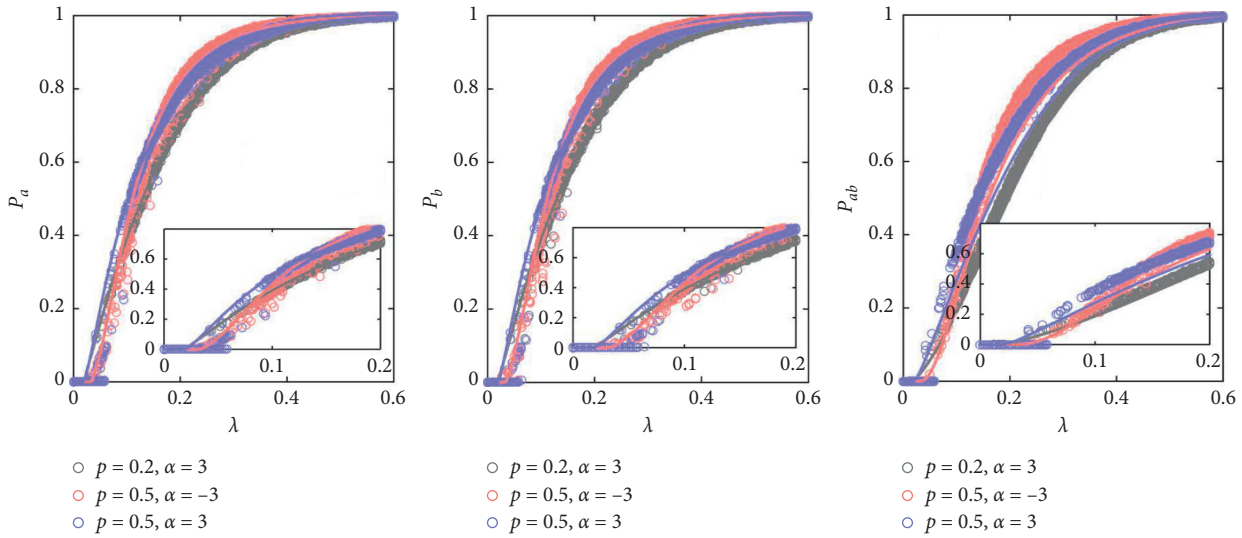

FIGURE 1: The coinfection outbreak size of the epidemic a (a), epidemic b (b), and two epidemics (c) versus the spreading probability λ with different p and α. The inset panels enlarge the results when λ is small. We set $\vartheta = 0.99$ and the SF random network with $N = 10^4$, $\langle k \rangle = 10$, and $\gamma_A = 2.7$.

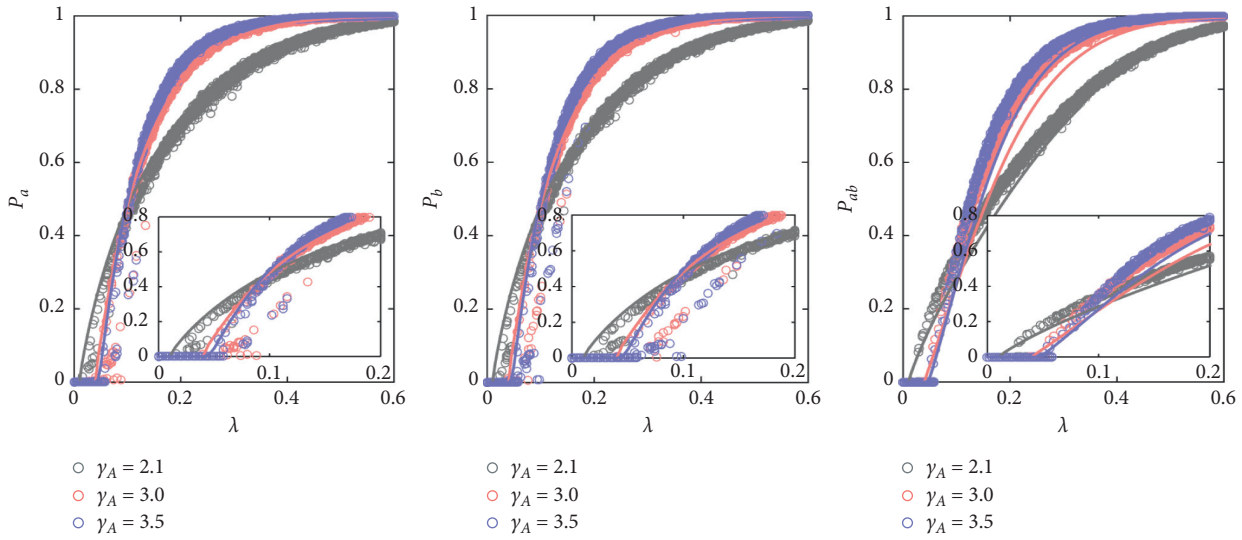

FIGURE 2: The coinfection outbreak size of the epidemic a (a), epidemic b (b), and two epidemics (c) versus the spreading probability λ with different γ_A. The inset panels enlarge the results when λ is small. We set $p = 0.5$, $\alpha = 3$, and $\vartheta = 0.99$. The other parameter of SF random network is set to be $N = 10^4$, $\langle k \rangle = 10$.

small, while promoting the spreading when λ is large. We explain the phenomenon as follows. The hubs are easy to be infected for any values of λ. If the epidemic a infects the hubs first, the epidemic b can hardly infect them when immunizing large degree nodes (e.g., $\alpha = -3$) and λ is small. As a result, the epidemic spreading size decreases. When λ is large, the epidemic b can infect the nodes with small degrees. As those small degree nodes have synergistic effect, the epidemic spreading is promoted.

We further investigate the effects of the heterogeneity of degree distribution on the epidemic spreading in Figure 2. We set $\vartheta = 0.99$, $p = 0.5$, and $\alpha = 3$. On the one hand, we find that strong heterogeneity of degree distribution decreases the global outbreak threshold of the epidemics because of the existence of some hubs. On the other hand, we find that P_a, P_b, and P_{ab} decrease with the decreasing γ_A when λ is small while increases with γ_A when λ is large.

Furthermore, we can see that the theoretical analysis well predicts the numerical simulation results in both Figures 1 and 2. Note that the values of P_a and P_b are approximately equal since the two SF networks have the same statistical characteristic. However, the values of $P_a b$ are smaller than those of P_a and P_b because a node infected by two epidemics is more difficult than that infected by only one of them.

Finally, we study the cost of cooperate epidemic spreading on SF random networks. In Figure 3, we present the effectiveness of p and α on the mean cost C of all nodes versus the spreading probability λ. When we fix $p = 0.5$ and

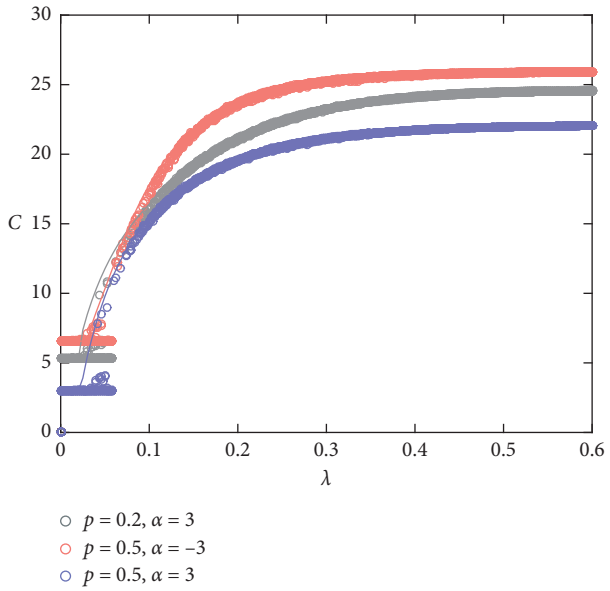

Figure 3: The mean cost C of all nodes versus the spreading probability λ with different p and α. We set $\vartheta = 0.99$ and the SF random network with $N = 10^4$, $\langle k \rangle = 10$, and $\gamma_A = 2.7$.

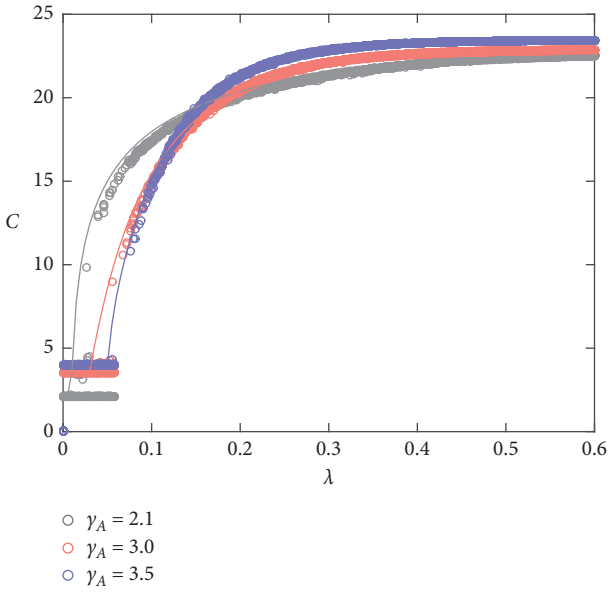

Figure 4: The mean cost C of all nodes versus the spreading probability λ with different degree distribution. We set $p = 0.5$, $\alpha = 3$, and $\vartheta = 0.99$. The other parameter of SF random network is set to be $N = 10^4$, $\langle k \rangle = 10$.

$c = 1$, the immunizing cost is large in $\alpha = -3$. In this case, the synergy acts on the nodes with small degree. The immunizing cost of large degree nodes is also large. But with the λ increase, the outbreak size increases and the recovery cost increases. When $\lambda \approx 0.06$, the mean cost of all nodes is almost the same. When we fix $\alpha = 3$, with p increase, the immunizing cost decreases. The recovery cost of $p = 0.5$ grows faster than the recovery cost of $p = 0.2$.

We further study the cost of cooperate epidemic spreading on SF random network with different degree distribution. As shown in Figure 4, we can see that with the γ_A increase, the immunizing cost increases. The mean cost of all nodes decreases with γ_A for small values of λ and increases with γ_A for large values of λ. In addition, we can see that the theoretical analysis well predicts the numerical simulation results in both Figures 3 and 4.

5. Conclusion

In conclusion, we studied the immunization of cooperative spreading dynamics on complex networks. In our model, we assumed that the immunization probability depends on the degree of nodes. Furthermore, the cost of immunization correlated with node degrees. Using a generalized percolation theory, we theoretically analyzed the final outbreak size and the cost of system. Compared with immunizing small degree nodes, we found that immunization nodes with large degrees suppress the spreading for small values of transmission probability, while the opposite situation happens for large values of transmission probability. For the cost of the system, we revealed that, immunizing hubs increase the cost of the system. Finally, we investigated the effects of degree heterogeneity on final spreading size and cost of the system. Our results shed some light on studying the cooperative spreading dynamics and may provide some clues for future researches.

Data Availability

Correspondence and requests for data should be addressed to S-M. C. (e-mail: shimin.cai81@gmail.com).

Conflicts of Interest

The authors declare that there are no conflicts of interest regarding the publication of this paper.

Acknowledgments

This work was partially supported by the National Natural Science Foundation of China (Grant nos. 11975071 and 61673086), the Science and Technology Department of Sichuan Province (Grant no. 2020YFS0007), the Chendu Science and Technology Agency (Grant no. 2020-YF05-00073-SN), and the Science Promotion Programme of UESTC, China (Grant no. Y03111023901014006).

References

[1] C. Claudio, F. Santo, and L. Vittorio, "Statistical physics of social dynamics," *Reviews of Modern Physics*, vol. 81, no. 2, p. 591, 2009.

[2] P.-S. Romualdo, C. Claudio, P. Van Mieghem, and V. Alessandro, "Epidemic processes in complex networks," *Reviews of Modern Physics*, vol. 87, no. 3, p. 925, 2015.

[3] P.-S. Romualdo and V. Alessandro, "Epidemic dynamics and endemic states in complex networks," *Physical Review E*, vol. 63, no. 6, 2001.

[4] P.-S. Romualdo and V. Alessandro, "Epidemic dynamics in finite size scale-free networks," *Physical Review E*, vol. 65, no. 3, 2002.

[5] W. Wang, L. Quan-Hui, J. Liang, Y. Hu, and T. Zhou, "Coevolution spreading in complex networks," *Physics Reports*, vol. 820, pp. 1–51, 2019.
[6] L. Pan, D. Yang, W. Wang, S. Cai, T. Zhou, and Y.-C. Lai, "Phase diagrams of interacting spreading dynamics in complex networks," *Physical Review Research*, vol. 2, no. 2, 2020.
[7] E. J. Newman Mark, "Threshold effects for two pathogens spreading on a network," *Physical Review Letters*, vol. 95, no. 10, Article ID 108701, 2005.
[8] K. Brian and E. J. Newman Mark, "Competing epidemics on complex networks," *Physical Review E*, vol. 84, no. 3, 2011.
[9] S. Funk and A. A. Jansen Vincent, "Interacting epidemics on overlay networks," *Physical Review E*, vol. 81, no. 3, 2010.
[10] J. Watkins Nicholas, N. Cameron, M. Preciado Victor, and J. Pappas George, "Optimal resource allocation for competing epidemics over arbitrary networks," in *Proceedings of the 2015 American Control Conference (ACC)*, pp. 1381–1386, IEEE, Chicago, IL, USA, 2015.
[11] B. Gao, Z. Deng, and D. Zhao, "Competing spreading processes and immunization in multiplex networks," *Chaos, Solitons & Fractals*, vol. 93, pp. 175–181, 2016.
[12] C. Granell, S. Gómez, and A. Arenas, "Dynamical interplay between awareness and epidemic spreading in multiplex networks," *Physical Review Letters*, vol. 111, no. 12, p. 128701, 2013.
[13] C. Granell, S. Gómez, and A. Arenas, "Competing spreading processes on multiplex networks: awareness and epidemics," *Physical Review E*, vol. 90, no. 1, 2014.
[14] W. Wang, M. Tang, H. Yang, Y. Do, Y.-C. Lai, and G.W. Lee, "Asymmetrically interacting spreading dynamics on complex layered networks," *Scientific Reports*, vol. 4, p. 5097, 2014.
[15] W. Wang, L. Quan-Hui, C. Shi-Min, M. Tang, A. Braunstein Lidia, and S. H. Eugene, "Suppressing disease spreading by using information diffusion on multiplex networks," *Scientific Reports*, vol. 6, 2016.
[16] W. Cai, L. Chen, F. Ghanbarnejad, and P. Grassberger, "Avalanche outbreaks emerging in cooperative contagions," *Nature Physics*, vol. 11, no. 11, pp. 936–940, 2015.
[17] Li Chen, "Persistent spatial patterns of interacting contagions," *Physical Review E*, vol. 99, no. 2, 2019.
[18] L. Chen, F. Ghanbarnejad, and D. Brockmann, "Fundamental properties of cooperative contagion processes," *New Journal of Physics*, vol. 19, no. 10, p. 103041, 2017.
[19] L. Chen, F. Ghanbarnejad, W. Cai, and P. Grassberger, "Outbreaks of coinfections: the critical role of cooperativity," *EPL (Europhysics Letters)*, vol. 104, no. 5, p. 50001, 2013.
[20] Z. Wang, C. T. Bauch, S. Bhattacharyya et al., "Statistical physics of vaccination," *Physics Reports*, vol. 664, pp. 1–113, 2016.
[21] P.-S. Romualdo and V. Alessandro, "Immunization of complex networks," *Physical Review E*, vol. 65, no. 3, 2002.
[22] R. Cohen, H. Shlomo, and D. Ben-Avraham, "Efficient immunization strategies for computer networks and populations," *Physical Review Letters*, vol. 91, no. 24, 2003.
[23] Y. Chen, G. Paul, H. Shlomo, L. Fredrik, and S. H. Eugene, "Finding a better immunization strategy," *Physical Review Letters*, vol. 101, no. 5, 2008.
[24] G.-G. Jesús, E. Pablo, and Y. Moreno, "Immunization of real complex communication networks," *The European Physical Journal B*, vol. 49, no. 2, pp. 259–264, 2006.
[25] Z. Liu, Y.-C. Lai, and N. Ye, "Propagation and immunization of infection on general networks with both homogeneous and heterogeneous components," *Physical Review E*, vol. 67, no. 3, 2003.
[26] C. Buono and L. A. Braunstein, "Immunization strategy for epidemic spreading on multilayer networks," *EPL (Europhysics Letters)*, vol. 109, no. 2, p. 26001, 2015.
[27] C. Michele, B. Marián, and P.-S. Romualdo, "Generation of uncorrelated random scale-free networks," *Physical Review E*, vol. 71, no. 2, 2005.
[28] E. J. Newman Mark, "Spread of epidemic disease on networks," *Physical Review E*, vol. 66, no. 1, 2002.
[29] C. Moore and M. E. J. Newman, "Epidemics and percolation in small-world networks," *Physical Review E*, vol. 61, no. 5, p. 5678, 2000.
[30] L. A. Meyers, M. E. J. Newman and B. Pourbohloul, Predicting epidemics on directed contact networks," *Journal of Theoretical Biology*, vol. 240, no. 3, pp. 400–418, 2006.
[31] W. Wang, Ze-X. Wang, and C. Shi-Min, "Critical phenomena of information spreading dynamics on networks with cliques," *Physical Review E*, vol. 98, no. 5, 2018.
[32] Z. Wang, M. Tang, S. Cai, Y. Liu, J. Zhou, and D. Han, "Self-awareness control effect of cooperative epidemics on complex networks," *Chaos: An Interdisciplinary Journal of Nonlinear Science*, vol. 29, no. 5, 2019.
[33] S. Jia, V. Buldyrev Sergey, A. Braunstein Lidia, H. Shlomo, and S. H. Eugene, "Structure of shells in complex networks," *Physical Review E*, vol. 80, no. 3, 2009.
[34] W. Wang, S. H. Eugene, and A. Braunstein Lidia, "Effects of time-delays in the dynamics of social contagions," *New Journal of Physics*, vol. 20, no. 1, 2018.
[35] T. Zhang, Y. Zhang, J. Ma, J. Chen, and X. Zhu, "Cooperate epidemic spreading on multiplex networks with heterogeneous population," *International Journal of Modern Physics C (IJMPC)*, vol. 31, no. 9, pp. 1–10, 2020.

Hindawi
Complexity
Volume 2021, Article ID 8862226, 10 pages
https://doi.org/10.1155/2021/8862226

Research Article

Public Opinion Communication Model under the Control of Official Information

Yuexia Zhang,[1,2,3] **Ziyang Chen**,[1] **and Lie Zou**[1]

[1]*School of Information and Communication Engineering, Beijing Information Science & Technology University, Beijing 100101, China*
[2]*Key Laboratory of Modern Measurement & Control Technology, Ministry of Education, Beijing Information Science & Technology University, Beijing 100101, China*
[3]*Beijing Key Laboratory of High Dynamic Navigation Technology, University of Beijing Information Science & Technology, Beijing 100101, China*

Correspondence should be addressed to Yuexia Zhang; zhangyuexia@bistu.edu.cn

Received 8 September 2020; Revised 8 October 2020; Accepted 24 December 2020; Published 7 January 2021

Academic Editor: Wei Wang

The rapid development of Internet technology has facilitated the dissemination of information that can threaten national security and public health, and effectively controlling the process of public opinion communication is an important topic in contemporary social network research. This paper establishes an official information-controlled public opinion propagation (OI-SEIR) model based on the delay, latency, and conversion of public opinion communication under the control of official information. According to the influence and importance of the network nodes, we theoretically derive the attitude conversion probability of the nodes, making the model more in line with the actual situation. Through actual cases, we analyzed the important influence of official information on the public opinion communication process and provided a theoretical basis for the government and relevant departments to supervise and correctly guide the public opinion network, which has certain practical significance.

1. Introduction

At present, China is in a critical period of economic development and transformation. Major emergencies occur frequently, and public opinion can be shaped by popular Internet platforms. Because of network characteristics such as many ways of formation, fast transmission speed, and wide diffusion range , when emergency occurs, public opinions spread rapidly online. Improper responses to these emergencies by the relevant departments can cause a public opinion crisis and can even affect social stability. Therefore, studying the impact of official information on public opinion communication is important for public opinion supervision and the maintenance of public safety.

Public opinion is formed in complex and interconnected networks [1] and can therefore be considered similar to other complex networks for research purposes [2–5]. The infectious disease model [6–9] is a common method of modeling complex networks, including public opinion networks. The infectious disease model is deployed as a mathematical model that simulates the information dissemination process through the public opinion network [10, 11], enabling detailed analyses of the information dissemination mechanism [12–14]. Therefore, this paper presents a public opinion communication model based on official information control based on a complex network.

2. Related Work

Current research on public opinion communication has mainly focused on improving public opinion communication models. The classical SIR [15] and SIS [16] infectious disease models established by Kermack and McKendrick were developed into the SEIR model by Zhao et al. [7] and continue to be widely used and improved based on actual conditions and background changes. In one study [17], the tuberculosis virus was divided into two types: tuberculosis and extrapulmonary tuberculosis, with the latter virus

considered not contagious and the former contagious. Another study [18] proposed a time lag consideration, taking the common cold and gonorrhea as examples and analyzing patient recovery at a certain moment in relation to the state of the current moment and the previous state. Several studies [19–21] have stratified the population by age largely because individuals of different ages often have different disease resistances, transmission abilities, and rehabilitation abilities. Bentaleb and Aminie proposed a multistrain SEIR epidemic model with bilinear and nonmonotonic incident functions [22]. Wu et al. proposed a nonlocalized diffusion SEIR model [23], and Liu et al. proposed a new SEIR rumor propagation model that included a hesitation mechanism [24]. Zhang and Cheng established the SETQR model and used the probability theorem to derive the information propagation law [25]. Thus, previous works have significantly improved the node types in the model and thereby more accurately simulated the public opinion communication process, which provides a reference for controlling the public opinion.

In addition, Wang et al. [26] introduced recent progress in the study of coevolution spreading dynamics, emphasizing the contributions from the perspectives of statistical mechanics and network science. The theoretical methods, critical phenomena, phase transitions, interacting mechanisms, and effects of network topology for four representative types of coevolution spreading mechanisms, including the coevolution of biological contagions, social contagions, epidemic-awareness, and epidemic-resources, are presented in detail. Zhang et al. [27] proposed the Media and Interpersonal Relationship-SEIR (MI-SEIR) model based on the SEIR model. The proposed model considers the impact of media transmission and interpersonal relationships on opinion propagation. Their MI-SEIR model divides the propagation nodes into three categories: support, neutral, and opposition. Wang et al. [28] introduced heterogeneous adoption threshold distribution into a non-Markovian spreading threshold model, in which an individual adopts a behavior only when the received cumulative pieces of behavioral information from neighbors exceed his adoption threshold. In order to understand the effects of heterogeneous adoption thresholds quantitatively, an edge-based compartmental theory is developed.

However, none of the above models considered the influence of an external interference mechanism on the public opinion propagation model. In order to solve this problem, Zhong and Sun [29] established a public opinion communication model with a control system under government intervention. However, this system assumed that rumors and official information are simultaneously published, which does not reflect the actual situation. Zhao and Cao [30] established an information diffusion model for the suppression of official information on unofficial information, in which the network nodes are divided into two categories: susceptible and infected. However, this model does not consider the knowledge of the public opinion and does not propagate the existence of information-like nodes for the time being. Zhang et al. [31] established a new model to support external control, but that model did not distinguish between official infected disseminators and false infected disseminators in the network. The model ignores the point that with the injection of official information, false information disseminators may be converted into official information disseminators. The above research results are basically consistent with some of the characteristics and laws of the process of public opinion dissemination, but all have their own shortcomings and deficiencies.

In order to solve the shortcomings of the above models, this paper establishes the OI-SEIR model to support the control of official information. The model focuses on the following three considerations. (1) *Time Delay*. False information and official information are often not released at the same time. After the false information is generated, the network public opinion is formed, causing adverse effects, before officials can publish the correct information in the network. Therefore, the official information is delayed compared with false information. (2) *Latency*. There are a large number of users in the public opinion network who receive the information but temporarily withhold from propagating it. These users can thus be considered latent nodes, which may more easily change state when the official information is injected, thereby supporting the dissemination of official information. (3) *Conversion*. The injection of official information can convert false information disseminators to official information disseminators. Thus, the OI-SEIR model divides the distributors of official information and false information and may be more suitable for practical situations.

3. SEIR Model

The SEIR model is shown in Figure 1. In the SEIR model, the node set is divided into four categories: S' (susceptible node), E' (exposed node), I' (infected node), and R' (recovered node). The susceptible node represents the initial user who has not yet received any message. The exposed node represents the user who receives a message but does not propagate it. The infected node represents the user who receives information and propagates the message. The recovered node represents the user who no longer transmits information or loses interest in the information she/he transmits. The conversion probability between each node is shown in Table 1. The transition probability between node states is in the interval, that is, $0 \le a', b', c', d', e' \le 1$.

Let the total number of nodes in the network be N, and the information propagation time is represented by t. The information propagation process in the SEIR model is described as follows.

When $t = 0$, false information is generated in the network. When $t \in (0, \infty)$, the susceptible nodes in the network first convert to exposed nodes with the probability of a', and then the exposed nodes convert to the infected node with the probability of c'. The susceptible node can also be directly converted to infected nodes with the probability of b'. Finally, the infected nodes can be converted into the recovered nodes with the probability of d', and the recovered nodes can be converted into the susceptible nodes with the probability of e'.

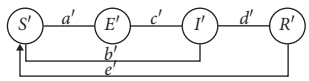

Figure 1: SEIR mode.

Table 1: Conversion probability.

Symbol	Meaning
$a\prime$	Probability that a susceptible node is converted into an exposed node
$b\prime$	Probability that a susceptible node is converted into a infected node
$c\prime$	Probability that an exposed node is converted into a infected node
$d\prime$	Probability that a infected node is converted into a recovered node
$e\prime$	Probability that a recovered node is converted into a susceptible node

At time t, the proportions of susceptible, exposed, infected, and recovered nodes in the network are $S\prime(t)$, $E'(t)$, $I'(t)$, and $R'(t)$, respectively. Since the total number of users in the network remains unchanged, the following equation can be obtained:

$$S'(t) + E'(t) + I'(t) + R'(t) = 1. \tag{1}$$

The differential form of the SEIR model is shown in the following equation:

$$\begin{cases} \dfrac{dS'}{dt} = -a'(t)S'(t)I'(t) - b'(t)S'(t)I'(t) + e'(t)R'(t), \\ \dfrac{dE'}{dt} = a'(t)S'(t)I'(t) - c'(t)E'(t), \\ \dfrac{dI'}{dt} = c'(t)E'(t) + b'(t)S'(t)I'(t) - d'(t)I'(t), \\ \dfrac{dR'}{dt} = d'(t)I'(t) - e'(t)R'(t), \quad t \in (0, +\infty]. \end{cases} \tag{2}$$

4. OI-SEIR Model

4.1. Network Description. Let the public opinion network be $G = (V, B, C, F, O)$, where V is the node set in the network, B is the edge set in the network, C is the set of node types, F stands for false information, and O stands for official information.

4.2. Node Division. In the OI-SEIR model, the node set is divided into five categories: S (susceptible node), E (exposed node), I_F (false infected node), I_O (official infected node), and R (recovered node), as shown in Table 2.

Table 2: Node status classification.

Status	Name	Meaning
S	Susceptible node	User who has not yet received any message
E	Exposed node	User who receives a message but does not propagate it
I_F	False infected node	User who receives false information and propagates the message
I_O	Official infected node	User who receives official information and propagates the message
R	Recovered node	User who no longer transmits information or loses interest in the information she/he transmits

4.3. Communication Mechanism. The OI-SEIR model contains an information dissemination layer and an official control layer, as shown in Figure 2. The information control layer includes the susceptible node S, the exposed node E, the false infected node I_F, and the recovered node R; the official control layer contains the official infected node I_O. The conversion probability between each node is shown in Table 3.

Let the total number of nodes in the network be N, $N = [1, \ldots, i, \ldots, j, \ldots, n, \ldots]$, and N will remain unchanged for the given network. The transition probability between node states is in the interval $[0, 1]$; that is, $0 \le a, b, c, d, e, \varepsilon, \eta, \theta \le 1$. The information propagation time is represented by t. At time $t \in (0, +\infty)$, the information propagation process in the OI-SEIR model is described as follows:

(1) $t = 0$: False information is generated in the network.

(2) $t \in (0, T)$: There is only false information in the network. The susceptible nodes in the network first convert to exposed nodes, and then the exposed nodes convert to the false infected node I_F, according to the respective probabilities. Susceptible nodes can also be directly converted to false infected nodes, false infected nodes can be converted into the recovered nodes, and recovered nodes can be converted into susceptible nodes, again following the respective probabilities.

(3) $t = T$: The false information spreads in the public opinion network for a period of time before government departments release official information to guide public opinion and avoid the further spread of false information. In this article, this time is denoted by T.

(4) $t \in (T, +\infty]$: The false information and the official information coexist in the network. The various types of network nodes begin to be converted to official infected nodes, according to the probabilities presented in Table 2. Among these, the probability of converting susceptible nodes to official infected nodes is called the direct immunization rate; the probability of converting exposed nodes to official infected nodes is called the latent immunization rate, and the probability of converting false infected nodes

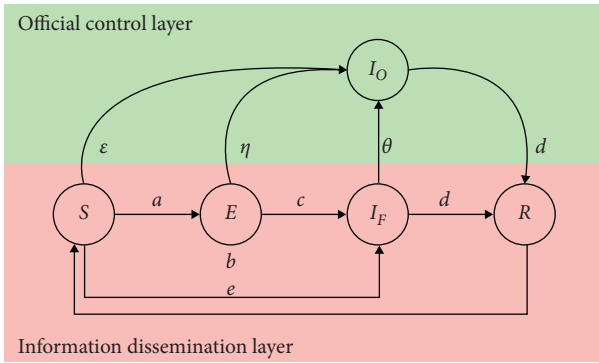

Figure 2: OI-SEIR model.

to official infected nodes is called the infection immunization rate. If the government successfully guides public opinion, only official infected nodes will be in the network over time, whereas if the government fails, only false infected nodes will persist.

At time t, the proportions of susceptible, exposed, false infected, official infected, and recovered nodes in the network are $S(t)$, $E(t)$, $I_F(t)$, $I_O(t)$, and $R(t)$, respectively. Because the total number of users in the network is assumed to remain unchanged,

$$S(t) + E(t) + I_F(t) + I_O(t) + R(t) = 1. \tag{3}$$

At $t = 0$, that is, at the initial moment of information dissemination, each node occupies the following proportions in the network:

$$\begin{cases} S(0) \approx 1, \\ E(0) = 0, \\ I_F(0) \approx 0, \\ I_O(0) \approx 0, \\ R(0) = 0. \end{cases} \tag{4}$$

The differential form of the OI-SEIR model is as follows:

$$\begin{cases} \dfrac{\mathrm{d}S}{\mathrm{d}t} = -[a(t) + b(t)]S(t)I_F(t) - \varepsilon(t-T)S(t-T)I_O(t-T) + e(t)R(t), \\ \dfrac{\mathrm{d}E}{\mathrm{d}t} = a(t)S(t)I_F(t) - c(t)E(t) - \eta(t-T)E(t-T)I_O(t-T), \\ \dfrac{\mathrm{d}I_F}{\mathrm{d}t} = c(t)E(t) + bS(t)I_F(t) - d(t)I_F(t) - \theta(t-T)I_F(t-T)I_O(t-T), \\ \dfrac{\mathrm{d}I_O}{\mathrm{d}t} = \varepsilon(t-T)S(t-T)I_O(t-T) + \eta(t-T)E(t-T)I_O(t-T) + \theta(t-T)I_F(t-T)I_O(t-T) - d(t-T)I_O(t-T), \\ \dfrac{\mathrm{d}R}{\mathrm{d}t} = d(t)I_F(t) + d(t-T)I_O(t-T) - e(t)R(t), \quad t \in (0, +\infty]. \end{cases} \tag{5}$$

The above analysis shows that the proportion of official infected nodes in the network is an important factor in evaluating the effect of official information on the control of public opinion communications. Because the number of official infected nodes is affected by the direct immunization rate ε, the latent immunization rate η, and the infection immunization rate θ, the remainder of this analysis focuses on these three types of immunization rate.

5. Immunization Rate Based on Attitude Value

5.1. Attitude Value. The node attitude value $a_p(t)$ indicates the degree to which the node recognizes the received official information at time t, and its value changes with time, as expressed by (4):

$$a_p(t+1) = a_p(t) + \gamma_{p \leftarrow q}(t). \tag{6}$$

Here, $a_p(t+1)$ represents the attitude value $a_p(t) \in [-1, 1]$ of the node at time $t+1$. When $a_p(t) = -1$, node i completely rejects the received information; when $a_p(t) = 1$, node i completely accepts the received information. $\gamma_{p \leftarrow q}$ represents the attitude influence between nodes, where the attitude value $\gamma_{p \leftarrow q}$ at a certain moment is affected by other nodes in the network at that moment.

$$\gamma_{p \leftarrow M}(t) = \frac{\sum M(t) \cdot a_M(t)}{p(t) + M(t)}. \tag{7}$$

Here, M is the set of node types that affect the attitude value of node p at time t, referred to as the impact set. The impact set M includes the false infected node I_F and the official infected node I_O, that is, $M \in (I_F, I_O)$. $a_M(t)$ indicates the attitude value of M at time t. $p(t)$ represents the proportion of the state of node p in the network at time t.

Table 3: Conversion probability.

Symbol	Meaning
a	Probability that a susceptible node S is converted into an exposed node E
b	Probability that a susceptible node S is converted into a false infected node I_F
c	Probability that an exposed node E is converted into a false infected node I_F
d	Probability that a false infected node I_F is converted into a recovered node R Probability that an official infected node I_O is converted into a recovered node R
e	Probability that a recovered node R is converted into a susceptible node S
ε	Probability that a susceptible node S is converted into an official infected node I_O
η	Probability that an exposed node E is converted into an official infected node I_O
θ	Probability that a false infected node I_F is converted into an official infected node I_O

5.2. Immunization Rate. With government intervention after the time delay T, various types of nodes in the public opinion network begin to switch to official infected nodes. Below, we define the direct immunization rate $\varepsilon(t)$, the latent immunization rate $\eta(t)$, and the infection immunization rate $\theta(t)$, respectively.

The direct immunization rate $\varepsilon(t)$ is as follows:

$$\varepsilon(t+1) = \varepsilon(t) \cdot \left[1 + \frac{a_S(t+1)+1}{2}\right]. \tag{8}$$

Combining (6)–(8),

$$\begin{cases} \varepsilon(t+1) = \varepsilon(t) \cdot \left\{1 + \frac{1}{2} \cdot \left[\left(a_S(t) + \frac{I_F(t) \cdot a_{I_F}(t) + I_O(t) \cdot a_{I_O}(t)}{I_F(t) + I_O(t) + S(t)}\right) + 1\right]\right\}, \\ t \in [0, +\infty). \end{cases} \tag{9}$$

The latent immunization rate $\eta(t)$ is as follows:

$$\eta(t+1) = \eta(t) \cdot \left[1 + \frac{a_E(t+1)+1}{2}\right]. \tag{10}$$

Combining (6), (7), and (10),

$$\begin{cases} \eta(t+1) = \eta(t) \cdot \left\{1 + \frac{1}{2} \cdot \left[\left(a_E(t) + \frac{I_F(t) \cdot a_{I_F}(t) + I_O(t) \cdot a_{I_O}(t)}{I_F(t) + I_O(t) + E(t)}\right) + 1\right]\right\}, \\ t \in [0, +\infty). \end{cases} \tag{11}$$

Infection immunization rate $\theta(t)$ is as follows:

$$\theta(t+1) = \theta(t) \cdot \left[1 + \frac{a_{I_F}(t+1)+1}{2}\right]. \tag{12}$$

Combining (6), (7), and (12),

$$\begin{cases} \theta(t+1) = \theta(t) \cdot \left\{1 + \frac{1}{2} \cdot \left[\left(a_{I_F}(t) + \frac{I_F(t) \cdot a_{I_F}(t) + I_O(t) \cdot a_{I_O}(t)}{I_F(t) + I_O(t)}\right) + 1\right]\right\}, \\ t \in [0, +\infty). \end{cases} \tag{13}$$

6. Simulation Verification and Analysis

A simulation was conducted to analyze the public opinion communication process under the control of official information. The case is introduced and analyzed as follows.

6.1. Case Introduction. The case of the alleged kidnapping of the female master of Peking University in the United States was taken as an example to study the control effect of official information on the public opinion communication process and the influence of different intervention points and intervention intensity on the control effect.

On June 12, 2017, many official Weibo accounts such as People's Daily, Headline News, CCTV News, and others released a microblog entry titled "Female master of Peking University lost in the United States and suspected of being kidnapped by 'fake police'." The release of this headline on Weibo quickly caused intense discussions among thousands of Weibo users, who expressed different attitudes toward this incident. On June 15, 2017, after a lapse of three days, many official Weibo accounts posted another microblog entry entitled "FBI categorizes this lost case as kidnapping." At this point, the various speculations of Weibo users gradually subsided under the control of official information, opening a new round of discussions based on verified information.

6.2. Control Effect of Official Information on Public Opinion Communication. To obtain the initial parameters for this case, the whole process of the public opinion propagation must be tracked in real time, and detailed statistical analyses must be conducted on the state changes of all users in the microblog client, which is highly complex. In order to reduce the complexity and still ensure the accuracy of the data, this study selected the official Weibo account of the People's Daily, which has a high number of Weibo fans and stimulates many fan interactions, which was the object of these statistical analyses. The initial node ratio and the conversion rate were self-set values, and the initial attitude value, initial immunization rate, and delay were statistical results obtained after using the professional crawler tool for data crawling.

First, the information dissemination process in the SEIR model is analyzed, that is, the process of public opinion dissemination under unofficial control. The initial parameter settings in the experiment are shown in Table 4, and the simulation results are shown in Figure 3, where the abscissa indicates the time of information propagation in days and the ordinates indicate the proportion (%) of various types in the network as predicted by the SEIR model. The blue solid line indicates the change in the proportion of susceptible nodes in the process of information dissemination. The yellow and green dotted lines indicate the changes in the proportion of exposed and infected nodes in the process of information dissemination, respectively. The red dotted line indicates the change in the proportion of recovered nodes in the process of information dissemination.

The following can be obtained from Figure 3:

(1) $t \in (0, 1)$

Table 4: Initial parameter setting of the SEIR model.

Initial node ratio				
$S'(0)$	$E'(0)$	$I'(0)$		$R'(0)$
0.96	0	0.04		0
Conversion rate				
a'	b'	c'	d'	e'
0.5	0.5	0.5	0.5	0.5

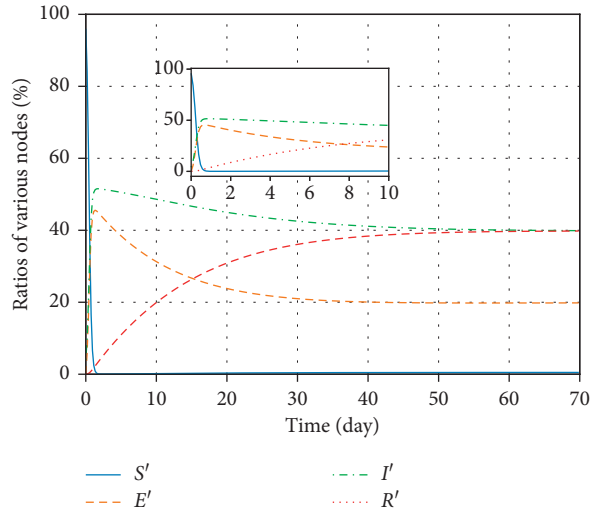

Figure 3: Public opinion communication map of the SEIR model.

The number of susceptible nodes in the network changes linearly and decreases rapidly, transforming into exposed nodes and infected nodes. Therefore, the number of information exposed nodes and infected nodes increases rapidly. At the same time, the number of recovered nodes increases slightly from 0.

(2) $t = 1$

The number of susceptible nodes is close to 0, and the number of exposed and infected nodes has reached the maximum, accounting for about 50% and 45% of the entire network, respectively. At the same time, the number of recovered nodes continues to increase. This shows that when public opinion just broke out, it spreads very fast.

(3) $t \in (1, 60)$

After $t = 1$, the number of susceptible nodes continues to decrease, until $t \approx 2$; the number of susceptible nodes is 0. At the same time, the number of exposed and infected nodes slowly decreases and eventually stabilizes. The proportions of exposed and infected nodes in the entire network are about 40% and 20%, respectively. When $t = 30$, the number of recovered nodes continues to increase and eventually stabilizes after $t = 60$. The number of recovered nodes in the entire network accounts for about 40%. The entire public opinion dissemination network stabilizes after $t = 60$.

Through the changes of the number of various nodes in the process of information dissemination, it can be seen that, in the absence of government interference, it took as long as 60 days to stabilize the distribution of the Internet public opinion on the case of a female student from Peking University who was abducted by "false police" in the United States, which means that people does not pay attention to the network incident and the online public opinion will basically be stable when the time of public opinion dissemination is long enough.

Then, the information dissemination process in the OI-SEIR model is analyzed, that is, the process of public opinion dissemination under official control. The initial parameter settings in the experiment are shown in Table 5. The simulation results are shown in Figure 4, where the abscissa indicates the time of information propagation in days and the ordinates indicate the proportion (%) of various types in the network as predicted by the OI-SEIR model. The blue solid line indicates the change in the proportion of susceptible nodes throughout the information dissemination process. The green and red dotted lines indicate the changes in the proportion of exposed and false infected nodes, respectively, and the curves with the green boxes and purple stars indicate the changes in the proportions of official infected nodes and recovered nodes, respectively.

The following can be obtained from Figure 4:

(1) $t \in (0, 1)$

The number of susceptible nodes decreases linearly and rapidly, while the number of exposed and false infected nodes increases linearly and rapidly. At the same time, the number of recovered nodes increases slightly.

(2) $t = 1$

The number of susceptible nodes is close to 0, while the number of exposed and false infected nodes has reached the maximum, accounting for about 50% and 45% of the entire network.

(3) $t \in (1, 3)$

The number of susceptible nodes continues to decrease, until $t = 2$, and the number of susceptible nodes is 0. The number of false infected nodes is almost stable. The number of exposed nodes is slowly decreasing. The number of recovered nodes continues to increase slightly.

Before the intervention of government information, comparing the SEIR model and the OI-SEIR model in the first three days after the outbreak of public opinion, the changing trend of each node in the two models is basically the same, which means that the trend of public opinion dissemination is basically the same, and the spread speed is very fast.

(4) $t \in (3, +\infty)$

When $t = 3$, with the injection of official information, the direction of public opinion changes. The number of susceptible nodes is 0. The number of false infected nodes drops rapidly. When $t \approx 5$, The number of false infected nodes is 0 and finally disappears in the network. Similarly, the number of exposed nodes drops rapidly. When $t \approx 4.5$, the number of exposed nodes is 0 and finally disappears in the network. The number of recovered nodes continues to increase linearly. However, compared with Figure 3, the number of information infected nodes slowly decreases and finally stabilizes after $t = 60$. When $t \in (3, 40)$, the number of exposed nodes slowly decreases, and after $t = 40$, it stabilizes. Comparing the SEIR model and the OI-SEIR model, it can be seen that 3 days after the outbreak of public opinion, due to government intervention, the number of susceptible, exposed, and false infected nodes in the OI-SEIR model decreases rapidly, while the number of recovered and official infected nodes increases rapidly, and the epidemic has quickly stabilized. Since the SEIR model has no government

Table 5: Initial parameter setting of the OI-SEIR model.

Initial node ratio				
$\eta(0)$	$\eta(0)$	θ	$\theta(0)$	$\theta'(0)$
0.95	0	0.04	0.01	0
Conversion rate				
θ	$\theta(0)$	$\theta(0)$	θ	$\varepsilon(0)$
0.5	0.5	0.5	0.5	0.5
Initial attitude value				
$a_S(T)$	$a_E(T)$		$a_{I_F}(T)$	
0.8	0.7		0.6	
Initial immunization rate			Delay	
$\varepsilon(0)$	$\eta(0)$	$\theta(0)$	T	
0.6	0.4	0.2	3	

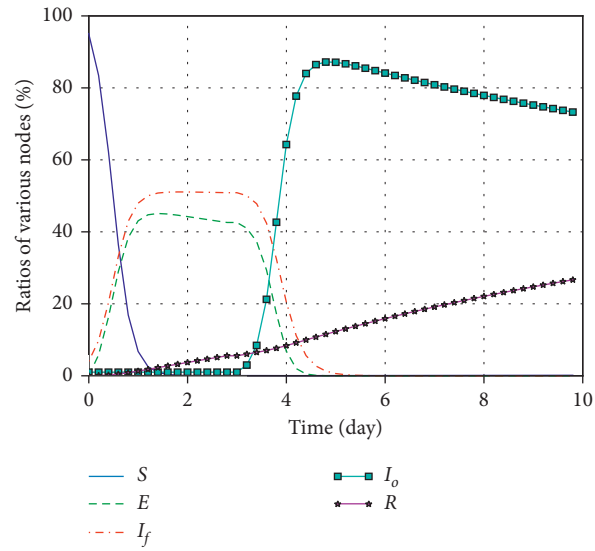

Figure 4: Public opinion communication map of the OI-SEIR model.

intervention, it will take a relatively long time to stabilize.

Based on the SEIR model and OI-SEIR model, it can be seen that it is very important and effective for the government and other relevant departments to control and guide the public opinion network. The injection of official information successfully changes the direction of the public opinion network and guides it to the right direction to avoid the further spread of false information.

6.3. Factors Influencing Official Information Control Effects

6.3.1. Effect of Delay T on the Control Effect of Official Information. The influence of the delay T on the control effect of the official information was analyzed by changing the delay T, as shown in Figure 5, where the axes and legend are the same as in Figure 4. Figure 5 shows that the delay T does not change the overall trend of diffusion through the public opinion network although the delay increases the time over which false information propagates in the network. Therefore, the smaller the delay T is, that is, the earlier the official information is injected into the public opinion network, the faster the false information disappears from the network and the faster the public opinion network is stabilized.

6.3.2. Effect of Direct Immunization Rate ε on the Control Effect of Official Information. The effect of the direct immunization rate ε on the control effect of official information was analyzed by changing the initial direct immunization rate $\varepsilon(0)$, as shown in Table 6. The simulation results are shown in Figure 6, where the axes and legend are the same as in Figure 4. Figure 6 shows that the initial direct immunization rate $\varepsilon(0)$ is reduced. After the delay T, the proportion of official infected nodes in the network shows a wave pattern where the peak value decreases with each cycle and eventually stabilizes. The proportion of false infected nodes in the network is gradually reduced but appears repeatedly until the final stabilization. Thus, the direct immunization rate $\varepsilon(0)$ has a significant influence on the guidance effect of the official information on the public opinion network. An insufficient initial direct immunization rate $\varepsilon(0)$ will greatly weaken the control effect of the official information, allowing the reappearance of false infected nodes in the network and reducing the guiding role of the official messages and prolonging the time for the release of public opinion.

6.3.3. Effect of Latent Immunization Rate η on the Control Effect of Official Information. The influence of the latent immunization rate η on the control effect of the official information was analyzed by changing the initial latent immunization rate $\eta(0)$, as shown in Table 7. The simulation results are shown in Figure 7, where the axes and legend are the same as in Figure 4. Figure 7 shows that reducing the initial latent immune rate $\eta(0)$ reduces the rate of decrease in latent nodes in the network but has little effect on the

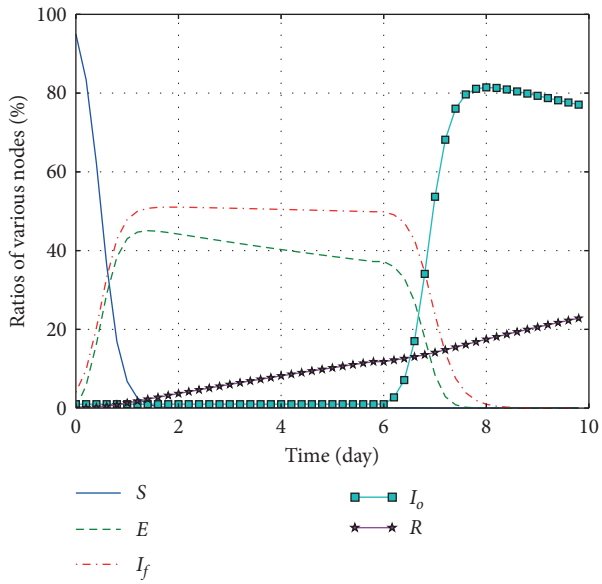

Figure 5: Effect of delay T on control effect.

Table 6: Initial direct immunization rate $\varepsilon(0)$.

Initial direct]immunization rate	Initial direct immunization rate after change
$\varepsilon(0)$	$\varepsilon\prime(0)$
0.6	0.001

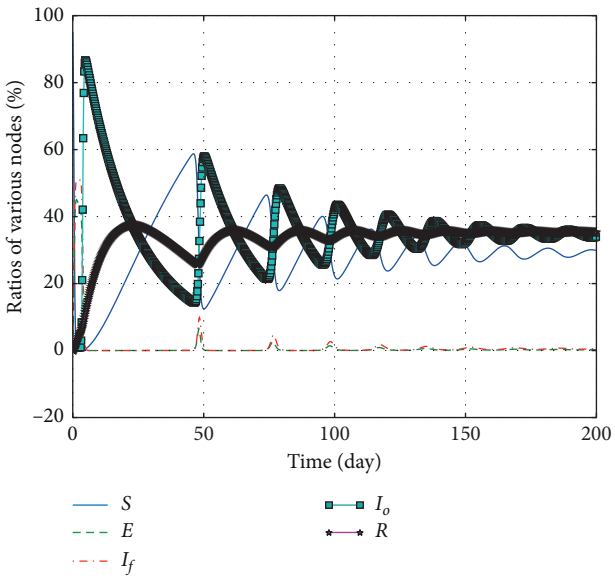

Figure 6: Effect of initial direct immunization rate on control effect.

Table 7: Initial latent immunization rate $\eta(0)$.

Initial latent immunization rate	Initial latent immunization rate after change
$\eta(0)$	$\eta\prime(0)$
0.4	0.001

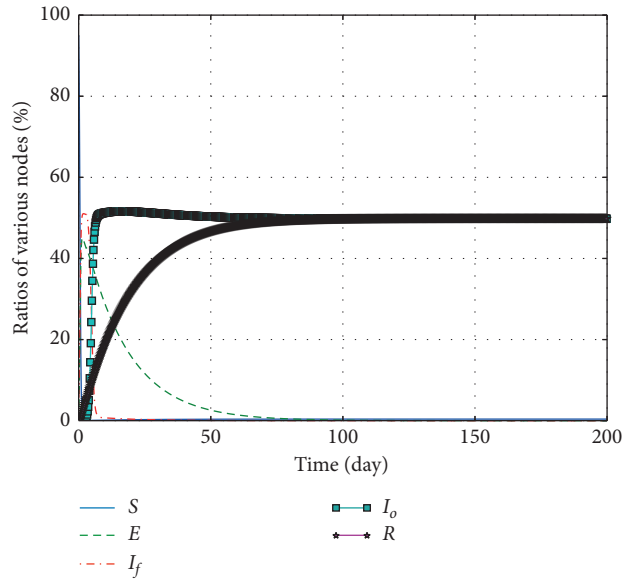

Figure 7: Effect of initial latent immunization rate on control effect.

Table 8: Initial infection immunization rate $\theta(0)$.

Initial infection immunization rate	Initial infection immunization rate after change
$\theta(0)$	$\theta\prime(0)$
0.2	0.001

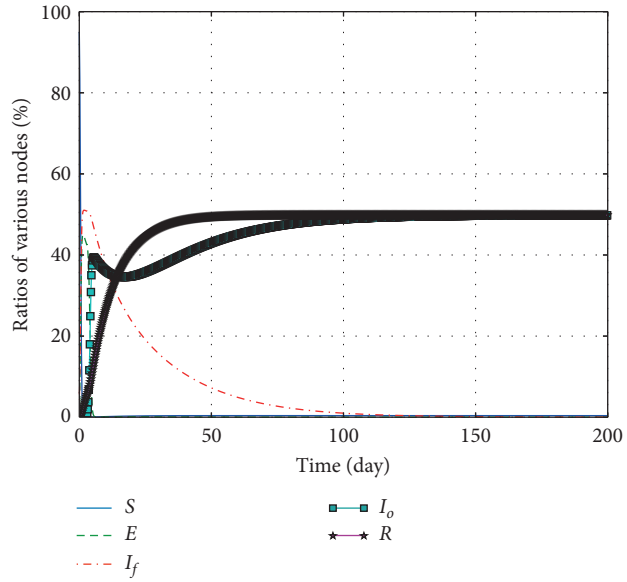

Figure 8: Effect of initial infection immunization rate on control effect.

speed at which false infected nodes disappear during information propagation. Therefore, the initial latent immunization rate $\eta(0)$ can increase the time required for the network to reach equilibrium and reduce the efficiency of information guidance.

6.3.4. Effect of Infection Immunization Rate θ on the Control Effect of Official Information. The influence of the infection immunization rate θ on the control effect of the official information was analyzed by changing the initial infection immunization rate $\theta(0)$, as shown in Table 8. The simulation results are shown in Figure 8, where the axes and legend are the same as in Figure 4. Figure 8 shows that reducing the initial infection immunity rate $\theta(0)$ seriously reduces the speed at which false infected nodes disappear during the information dissemination process. Thus, although the infection immunization rate does not cause false infected nodes to reappear in the network, the infection immunization rate increases the difficulty of guiding the information propagation direction. Therefore, the infection immunization rate θ has a significant influence on the guidance effect of the official information on the public opinion network, with a low initial direct immunization rate $\varepsilon(0)$ weakening the control effect and allowing false infected nodes to persist in the network for a longer period of time.

7. Conclusions

This paper proposed a model that considered the characteristics of time delay, latency, and conversion in the process of information dissemination, with official information inputs. The direct immunization rate, latent immunization rate, and infection immunization rate of the OI-SEIR model were derived according to the node attitude value. We selected a salient news topic on Weibo as a practical case to verify the proposed model by simulation. The simulation results showed the control effect of official information on public opinion transmission as predicted by the OI-SEIR model and demonstrated that the direct, latent, and infection immunization rates affect the guidance effect of official information, with the direct immunization rate having the greatest impact, followed by the infection immunization rate and then the latent immunization rate. The research work in this paper demonstrates the important role of official information in guiding public opinion, and the research on the effects of different types of immunization rates can elucidate information dissemination behavior in complex networks and improve the efficiency of information guidance.

Data Availability

No data were used to support this study.

Conflicts of Interest

The authors declare that they have no conflicts of interest regarding the publication of this paper.

Acknowledgments

This work was supported by the Sub Project of National Key Research and Development Plan in 2020 (grant no. 2020YFC1511704), National Natural Science Foundation of China (grant no. 61971048), Beijing Science and Technology Project (grant no. Z191100001419012), and Scientific research level improvement project to promote the colleges

connotation development of Beijing Information Science & Technology University in 2020 (no. 2020KYNH212).

References

[1] L. Zhang, T. Wang, Z. Jin, N. Su, C. Zhao, and Y. He, "The research on social networks public opinion propagation influence models and its controllability," *China Communications*, vol. 15, no. 7, pp. 98–110, 2018.

[2] J. Zhou, X. Yu, and J.-A. Lu, "Node importance in controlled complex networks," *IEEE Transactions on Circuits and Systems II: Express Briefs*, vol. 66, no. 3, pp. 437–441, 2019.

[3] C. J. Vega, E. N. Sanchez, and G. Chen, "Trajectory tracking on complex networks with non-identical chaotic nodes via inverse optimal pinning control," *IEEE Control Systems Letters*, vol. 2, no. 4, pp. 635–640, 2018.

[4] S. Das, S. Sharmin, and M. S. Rahman, "Generating proactive humanitarian aid networks with guided topology and small-world effect," 2017 IEEE Region 10 Humanitarian Technology Conference (R10-HTC). UET, Dhaka, Bangladesh," *IEEE Conferences*, vol. 2017, no. 1, pp. 682–685, 2017.

[5] W. Wang, M. Tang, H. E. Stanley et al., "Unification of theoretical approaches for epidemic spreading on complex networks," *Reports on Progress in Physics*, vol. 80, no. 3, Article ID 036603, 2017.

[6] C. Liu, Y. Q. Wang, L. X. Zhou et al., "Research on propagation model on complex networks," *Journal of Systems Science*, vol. 24, no. 2, pp. 81–86, 2016.

[7] J. L. Zhao, J. H. Cheng, and H. Y. Gao, "public opinion propagation model on social networks," in *Proceedings of the 2014 Seventh International Joint Conference on Computational Sciences and Optimization (CSO)*, pp. 325–328, IEEE, Beijing, China, July 2014.

[8] X. Z. Zhu, W. Wang, S. M. Cai et al., "Dynamics of social contagions with local trend imitation," *Scientific Reports*, vol. 8, no. 1, Article ID 7335, 2018.

[9] C. Xia, Z. Wang, C. Zheng et al., "A new coupled disease-awareness spreading model with mass media on multiplex networks," *Information Sciences*, vol. 471, pp. 185–200, 2019.

[10] W. Wang, M. Tang, H. Yang et al., "Asymmetrically interacting spreading dynamics on complex layered networks," *Scientific Reports*, vol. 4, no. 7502, 2014.

[11] W. Wang, Q. H. Liu, S. M. Cai et al., "Suppressing disease spreading by using information diffusion on multiplex networks," *Scientific Reports*, vol. 6, no. 1, Article ID 29259, 2016.

[12] M. H. Feyza and S. Sandip, "Analysis of opinion spread through migration and adoption in agent communities," *Lecture Notes in Comouter Science*, vol. 7455, pp. 153–167, 2012.

[13] W. Wang, Q. H. Liu, L. F. Zhong et al., "Predicting the epidemic threshold of the susceptible-infected-recovered model," *Scientific Reports*, vol. 6, no. 1, Article ID 24676, 2016.

[14] W. Wang, M. Tang, H. F. Zhang et al., "Epidemic spreading on complex networks with general degree and weight distributions," *Physical Review E*, vol. 90, no. 4, Article ID 042803, 2014.

[15] W. O. Kemack and A. G. McKendrick, "Contributions to the mathematical theory of epidemics," *Proceedings of the Royal Society of London*, vol. 115, no. 772, pp. 700–721, 1927.

[16] W. O. Kemack and A. G. McKendrick, "Contributions to the mathematical theory of epidemics-II. The problem of endemicity," *Bulletin of Mathematical Biology*, vol. 138, no. 834, pp. 55–83, 1932.

[17] J. P. Aparicio and C. Castillo-Chávez, "Mathematical modelling of tuberculosis epidemics," *Mathematical Biosciences and Engineering Mbe*, vol. 6, no. 2, pp. 209–237, 2009.

[18] K. L. Cooke and J. A. Yorke, "Some equations modelling growth processes and gonorrhea epidemics," *Mathematical Biosciences*, vol. 16, no. 1-2, pp. 75–101, 1973.

[19] R. Shrap and A. J. Lotka, "A problem in age distribution," *Philosophical Magazine*, vol. 21, pp. 435–438, 1911.

[20] A. J. Lotka, "The stability of the normal age distribution," *Proceedings of the National Academy of Sciences*, vol. 8, no. 11, pp. 339–345, 1922.

[21] B. Charlesworth, *Evolution in Age-Structured Populations*, Cambridge University Press, Cambridge, UK, 1994.

[22] D. Bentaleb and S. Amine, "Lyapunov function and global stability for a two-strain SEIR model with bilinear and non-monotone incidence," *International Journal Of Biomathematics*, vol. 12, no. 2, Article ID 195002, 2019.

[23] X. Wu, B. Tian, and R. Yuan, "Wave propagation in a diffusive SEIR epidemic model with nonlocal reaction and standard incidence rate," *Mathematical Methods in the Applied Sciences*, vol. 41, no. 17, pp. 8136–8160, 2018.

[24] X. D. Liu, T. Li, and M. Tian, "Rumor spreading of a SEIR model in complex social networks with hesitating mechanism," *Advances In Difference Equations*, vol. 2018, no. 1, 2018.

[25] Y. Zhang and Z. Chen, "SETQR propagation model for social networks," *IEEE Access*, vol. 7, no. 1, pp. 127533–127543, 2019.

[26] W. Wang, Q.-H. Liu, J. Liang, Y. Hu, and T. Zhou, "Co-evolution spreading in complex networks," *Physics Reports*, vol. 820, pp. 1–51, 2019.

[27] Y. X. Zhang, Y. X. Feng, and R. Q. Yang, "Network public opinion propagation model based on the influence of media and interpersonal communication," *International Journal of Modern Physics B*, vol. 33, no. 32, Article ID 1950393, 2019.

[28] W. Wang, Q. H. Liu, S. M. Cai et al., "Dynamics of social contagions with heterogeneous adoption thresholds: crossover phenomena in phase transition," *New Journal of Physics*, vol. 18, no. 1, Article ID 098701, 2016.

[29] D. S. Zhong and S. R. Sun, "Public opinion dissmination and control of serious emergencies: based on epidemic model," *Information Studies: Theory & Application*, vol. 41, no. 5, pp. 104–109, 2018.

[30] H. F. Zhao and X. Y. Cao, "The spread of official information in subway emergencies," *Systems Engineering*, vol. 34, no. 7, pp. 131–137, 2016.

[31] L. J. Zhang, T. Wang, Z. L. Jin et al., "The research on social networks public opinion propagation influence models and its controllability," *China Communications*, vol. 15, no. 7, pp. 98–110, 2018.

Hindawi
Complexity
Volume 2020, Article ID 6632956, 10 pages
https://doi.org/10.1155/2020/6632956

Research Article

Discovering Travel Spatiotemporal Pattern Based on Sequential Events Similarity

Juanjuan Chen,[1] **Liying Huang**,[2] **Chengliang Wang**,[2] **and Nijia Zheng**[1]

[1]*College of Computer and Information Science, Chongqing Normal University, Chongqing 401331, China*
[2]*College of Computer Science, Chongqing University, Chongqing 400044, China*

Correspondence should be addressed to Juanjuan Chen; 20131036@cqnu.edu.cn

Received 2 November 2020; Revised 23 November 2020; Accepted 13 December 2020; Published 29 December 2020

Academic Editor: Chenquan Gan

Travel route preferences can strongly interact with the events that happened in networked traveling, and this coevolving phenomena are essential in providing theoretical foundations for travel route recommendation and predicting collective behaviour in social systems. While most literature puts the focus on route recommendation of individual scenic spots instead of city travel, we propose a novel approach named City Travel Route Recommendation based on Sequential Events Similarity (CTRR-SES) by applying the coevolving spreading dynamics of the city tour networks and mine the travel spatiotemporal patterns in the networks. First, we present the Event Sequence Similarity Measurement Method based on modelling tourists' travel sequences. The method can help measure similarities in various city travel routes, which combine different scenic types, time slots, and relative locations. Second, by applying the user preference learning method based on scenic type, we learn from the user's city travel historical data and compute the personalized travel preference. Finally, we verify our algorithm by collecting data of 54 city travellers of their historical spatiotemporal routes in the ten most popular cities from Mafeng.com. CTRR-SES shows better performance in predicting the user's new city travel sequence fitting the user's individual preference.

1. Introduction

City tour has become popular in recent years as tourists may experience various food, culture, customs, and city views in this process while making use of commercial services like nice accommodation and inner-city transportation [1]. Unlike those traditional scenic spots, which are geographically isolated, a city tour combines civil resources, various facilities, and landscapes, and these form a city tour network with spatiotemporal multiplexity. Factors such as urban economy, society, and culture have an impact on the touring experience. They are coevolving through high relevance, so a city scenic spot has compound attributes of multiple labels. Furthermore, many ways of transport connect these city spots, which are geographically centered around the urban area. Thus, a city travel plan has the characteristics of personalization, flexibility, and evolving [2, 3], and the coevolving spreading dynamics of this network with multiscale structure is a great point of exploration that can apply to the city tour recommendation system. So far, the travel recommendations given by apps and OTAs are classical routes with scenic spots ranked by the number of visitors or preferences of most travellers. Thus, the recommendations are not suitable for every visitor because of a lack of personalization [4]. When modelling and solving the tour route planning problem, most papers investigate user preference and give travel route recommendations with a fixed start and endpoints [5], not taking the spatiotemporal travel sequence, length of stay, and ways of transport into consideration [6, 7].

Because of these problems mentioned above, this paper firstly defines the user travel sequence model and various elements involved in city tour travel planning, then based on this model, we present the travel sequence similarity measurement method. The method can help measure the similarities of various city travel sequences, which combine different scenic types, time slots, and relative locations. Secondly, clustering analysis is conducted based on the

historical travel database. By using the travel sequence similarity measurement method, we compute the baseline model of an individual visitor's personalized travel preference. Finally, we propose a novel approach named City Travel Route Recommendation based on Sequential Events Similarity (CTRR-SES). CTRR-SES helps recommend personal travel routes to a new destination for users. The recommendation routes are a better fit for the user's preference as they are calculated by the travel preference baseline model and from the historical travel sequence data of the user.

2. Research Background

Travel route recommendation system gives the user city travel routes that match user's preferences, satisfying the user's real needs and expectations. Exploiting historical data of users to make future prediction lives at the heart of building effective recommender systems [8]. For e-commerce, some personalized recommendation strategies can be designed to promote the diffusion of products [9]. However, city tourism is a new product of modern social arrangements as tourists spend time in pursuit of recreation, relaxation, and pleasure in cities. City tourism is featured by social media posts and marks of hot city attractions. Many types of research investigate tour preference by studying traveller's social media posts and tag data. Based on Geo-tagged photos, some research on the correlation of several Geo-tagged images with an actual number of visitors [10], some on traveller's spatiotemporal behaviour [11], some on travel route recommendation system algorithm [12], and some on city impressions and big events and their combined impact on travel decision [13]. However, those papers do not fully consider the features of new city tourists and their touring preference sequences. Hence, they are unable to explore the unique traits of city travellers.

Big data about travel knowledge is generated each day on the Internet and various platforms. Large amounts of structured or semistructured datasets are produced by visitors who share their travel experiences, skills, or feedback through communication technology and mobile appliances. Upon travel route recommendation algorithm studies, Sun et al. use Knowledge Graph to build a travel database by extracting traveling information from the content submitted by the users, to represent personalized touring routes [14]. Li et al. present a new approach for designing tourist routes for tourists visiting Gulangyu island by applying the Stated Preference method [15].

However, those papers only study the recommendations of scenic spots, while they do not analyze the sequential order of spots in visitors' historical touring routes. We believe the sequential order plays an important role in measuring tourist preference. For example, Sequence 1 represents user A who visits urban Chongqing city, given as Ciqikou-Hongyadong-Jiefangbei-Sichuan Fine Art Institute- Eling Park. The sequence of user B is given as Sichuan Fine Art Institute-Eling Park-Hongyadong-Jiefangbei-Ciqikou. If we consider scenic spots as the plain factor to impact the visitor's preference, then it is obvious to give both A and B the same recommendation of route sequence. However, users A and B visit those scenic spots in a different sequence, which indicates that user A prefers to spend daytime in spots tagged as shopping or fine food and night time for city sights, yet user B prefers to visit city sights in the day time and shop at night. We believe that travel route recommendations should include not only the user's preference for the scenic type but also the visiting sequence and time slot. Then the recommendation system may give users their personal travel routes matching their individual preferences.

This paper constructs the attraction of tourist city preference model based on the city attraction knowledge base and user's historical touring sequences. And a data mining algorithm is proposed to discover the city attraction label set. Traveller's historical touring events are analyzed to find clusters mostly reflecting traveller's preferences. By comparing the similarities of various travel event sequences, we aim to provide highly personalized travel recommendations that satisfy the traveller's real needs.

3. Preliminaries

Before the problem statement, we give the definitions of these concepts as follows.

Definition 1 (Attraction p). represents city places where visitors previously visited or are interested in visiting, and it could be a natural landscape, fork culture, historical landscape, civic landscape, or consuming place.

Definition 2 (Attraction labels **Profile**(**p**)). Given p as a city attraction, we define the labels of p as a sequence of $\text{Profile}(p) = \{p_{\text{id}}, p_{\text{name}}, p_{\text{type}}, p_{\text{position}}, p_{\text{score}}\}$.

Definition 3 (Travel history **r**). Given p as a city attraction, the travel history in p is given as a set of $\mathbf{r} = (\mathbf{p}, \mathbf{t_p^s}, \mathbf{t_p^e})$, in which t_p^s as the time arriving p and t_p^e as the leaving time.

Definition 4 (Touring sequence **L**). We define the touring sequence as a time-ordered sequence of a user visiting multiple city attractions, given as $L = \{r_1, r_2, \ldots, r_n\} = \{(p_1, t_{p_1}^s, t_{p_1}^e), (p_2, t_p \quad 2^s, t_{p_2}^e), \ldots, (p_n, t_{p_n}^s, t_{p_n}^e)\}$. where n represents the total number of attractions that have been visited. The time interval of visiting two adjacent attractions is no longer than a threshold value, denoted as $t_{p_{x+1}}^s - t_{p_x}^e < \varepsilon$. Considering the characteristics of city travel, we set a reasonable time interval threshold ε as 1 hour.

Based on the definitions above, we define our city travel route recommendation problem as follows. Given all users' historical touring sequences in the set $U = \{L_1, L_2, \ldots, L_n\}$, input the historical touring sequence set $U_{\text{user}A} = \{L_{A1}, L_{A2}, \ldots, L_{An}\}$ of user A, in which An denotes his/her total number of touring sequences. Then input city B. Our goal is to determine the best personalized city travel route recommendation for the user A from the travel sequence set of city B. The strategies are given as follows:

(1) Learning from the user's historical city tour sequences, identify the user's city travel preference model

(2) Based on all travel sequences in a given city and the user's city travel preference model, determine the best personalized city tour route recommendation for the user

4. Recommendation Algorithm

City tour recommendation is challenging to satisfy the visitor's preference and real needs when a tourist visits a new city. To meet this challenge, we propose a novel approach named City Travel Route Recommendation based on Sequential Events Similarity (CTRR-SES) by measuring the similarities of various city travel routes in a given city and learning from the user's historical city touring sequences.

4.1. Travel Route Recommendation Framework. There are three building blocks in our CTRR-SES, as indicated in Figure 1, which are Travel History/Sequences Construction, Scenic Type-based User Preferences Baseline Modelling, and Route Recommendation System. Travel History/Sequences Construction and User Preferences Baseline Model Learning are processed offline. By analyzing the user's open travel posts, we can obtain the user's historical city touring sequences. Then we may compute the baseline model from the travel history using clustering analysis. Route Recommendation is processed online. Firstly, CTRR-SES computes the feature vectors which represent user's travel characteristics from the city travel historical sequences and the preferences baseline model. Then it recommends the most similar touring sequence, which matches the user's personal preference from existing travel sequences.

4.2. Travel Knowledge Base and Touring Sequence Construction. Using data mining technology, we construct the travel knowledge base by obtaining big data from platforms like Baidu, Mafengwo, TripAdvisor, and Booking. Attraction information is comprised of attributes of Name, Geographic Position, Type and Rating, etc. Each attraction is also labelled with a category of one or many of the following, i.e., city park, garden, arboretum, natural landscape, architecture, church, temple, museum, college campus, historical sites, food and beverage, shopping site, amusement, art performance, etc. City tour transportation modes include Taxi, Bus, Subway, and Walk. Learning from the user's past space-time trajectory, travel sequences are generated by consecutively extracting data of geographic position, attraction label, visit duration, transportation mode, and time spent in transportation.

4.3. User Travel Preference Baseline Model Learning

4.3.1. Travel Sequence Similarity Measure. The travel sequence similarity measure is the measure by the proper algorithm of how much like multiple sequences are, which then derive similar clusters. In this paper, we present the travel sequence similarity measurement method using the Needleman–Wunsch (NW) algorithm. Moreover, we improve the traditional NW algorithm by integrating time information in the Score Function.

Definition 5 (Attraction touring history similarity **W**). Given p as a city attraction, $r_i = (p_i, t^s_{p_i}, t^e_{p_i})$ and $r_j = (p_j, t^s_{p_j}, t^e_{p_j})$ are two variables in the travel sequence **L**. Then the similarity formula between r_i and r_j is given as follows:

$$W(r_i, r_j) = \begin{cases} u_1 S_{\text{poi}} + u_2 S_{\text{time}}\left(p_i \text{ and } p_j \text{ belong to a class}\right), \\ d_1\left(p_i \text{ and } p_j \text{ do not belong to a class}\right), \\ d_2\left(p_i \text{ or } p_j \text{ aligns to a gap}\right). \end{cases} \tag{1}$$

S_{poi} indicates the similarity between two POIs, and S_{time} indicates the similarity between the time visiting the two spots. u_1 and u_2 are different weights put on S_{poi} and S_{time}, which can adjust the sensitivity of S_{poi} and S_{time}. $u_1 + u_2 = 1$; d_1 and d_2 are customized scores.

Definition 6 (Travel sequence similarity **S**). Given two travel sequences $L_1 = \{r_{11}, \ldots, r_{1n}\}$ and $L_2 = \{r_{21}, \ldots, p_{2m}\}$, the similarity score $S(i, j)$ of $L_i = \{r_{11}, \ldots, r_{1i}\}$ and $L_j = \{r_{21}, \ldots, r_{2j}\}$ $(L_i \subseteq L_1, L_j \subseteq L_2)$ is computed as follows:

$$S(i, j) = \max \begin{cases} S(i-1, j-1) + W(r_{1i}, r_{2j}), \\ S(i-1, j) + d_2, \\ S(i, j-1) + d_2, \end{cases} \quad (S(0, 0) = 0). \tag{2}$$

We can calculate the travel sequence similarity score matrix M. Normalization of data in the last row and column of the matrix generates the similarity scores of two travel sequences L_1 and L_2. The pseudocode of the algorithm is given in Algorithm 1.

TSSA uses the method of iteration to calculate the similarity of two sequences L_1 and L_2 by comparing each item in the sequences. Then the value of similarity is stored in the 2-dimensional matrix M. If the lengths of the two sequences are not equal, then add a space gap to make them equal. The first to 6th lines in the TSSA initializes the similarity matrix, and the 7th to 18th lines conduct similarity calculation and fill in the matrix. $M[i][j]$ represents the similarity of two corresponding items in L_1 and L_2, the value of which is determined by the values of $M[i-1][j]$, $M[i][j-1]$, and $M[i-1][j-1]$. Equation (2) is an iterative formula and gives three paths to calculate the values of $M[i][j]$, among which choosing the maximum value:

(1) Obtain from above in the vertical line of $M[i][j]$. Sequences L_1 and L_2 are compared, then suppose L_1' and L_2' are generated during the comparison. Reaching the cell of $M[i][j]$ from above is equivalent to adding the corresponding items in L_2 to L_2' and

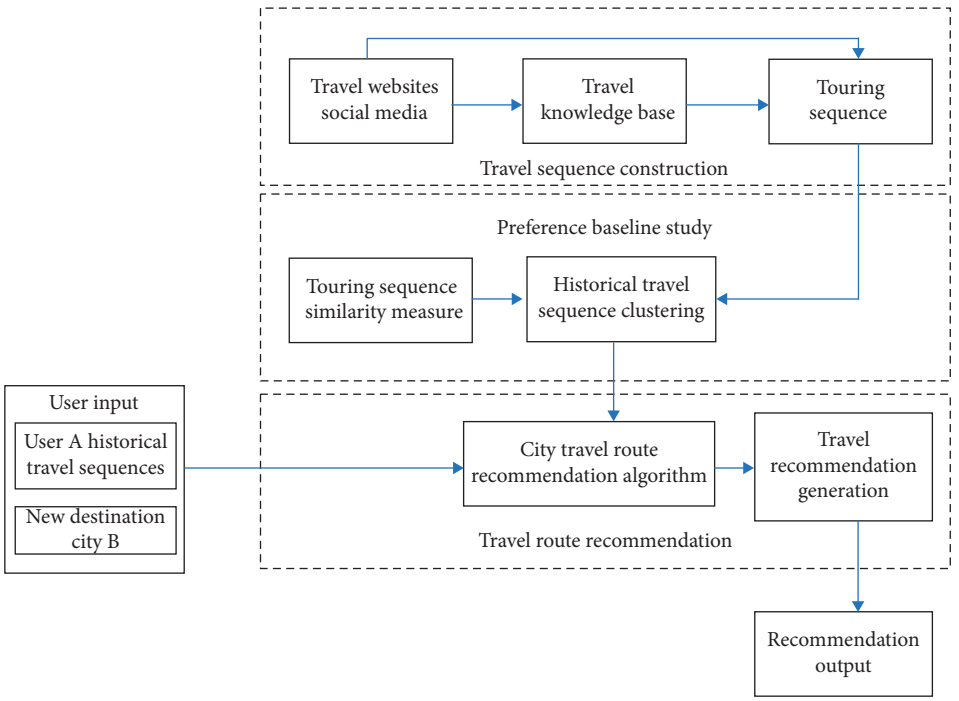

Figure 1: City travel route recommendation framework.

Input: Travel sequence L_1 and L_2
Output: Similarity of L_1 and L_2
Initialization: Set score matrix M to 0
(1) **for** $i \longleftarrow 0$ to $|L_1|$ **do**
(2) $M[i][0] \longleftarrow i * d_2$;
(3) **end for**
(4) **for** $j \longleftarrow 0$ to $|L_2|$ **do**
(5) $M[0][j] \longleftarrow j * d_2$;
(6) **end for**
(7) **for** $i \longleftarrow 1$ to $|L_1|$ **do**
(8) **for** $j \longleftarrow 1$ to $|L_2|$ **do**
(9) **if** Overlap $(L_1[i].p.\text{type}, L_2[j].p.\text{type})$ then, //Overlap (a, b) means the attraction type labels of POI a and POI b overlap
(10) $S_{\text{poi}} \longleftarrow$ **PSA** $(L_1[i].p, L_2[j].p)$;
(11) $S_{\text{time}} \longleftarrow$ **TSA** $(L_1[i].t, L_2[j].t)$;
(12) $\text{sim} \longleftarrow u * S_{\text{poi}} + (1-u) * S_{\text{time}}$;
(13) $M[i][j] \longleftarrow \max(M[i-1][j-1] + \text{sim}, M[i-1][j] + d_2, M[i][j-1] + d_2)$;
(14) **else**
(15) $M[i][j] \longleftarrow \max(M[i-1][j-1] + d_1, M[i-1][j] + d_2, M[i][j-1] + d_2)$;
(16) **end if**
(17) **end for**
(18) **end for**
(19) **return** $M[|L_1|-1][|L_2|-1]$;

Algorithm 1: Travel sequence similarity algorithm (TSSA).

adding a gap in L_1'. Therefore, the value of $M[i][j]$ is $M[i-1][j] + d_2$.

(2) Obtain from the left in the horizontal line of $M[i][j]$. Same as (1), reaching the cell of $M[i][j]$ from the left is equivalent to adding the corresponding items in L_1 to L_1' and adding a gap in L_2'. Thus, the value of $M[i][j]$ is $M[i][j-1] + d_2$.

(3) Obtain from the diagonal line of $M[i][j]$. By adding the corresponding items in L_1 to L_1' and adding the corresponding items in L_2 to L_2', we can calculate the

similarity value of $M[i-1][j-1] + W(L_1[i], L_2[j])$. When the ith POI label in L_1 is overlapped with the jth label in L_2, the calculation of $W(L_1[i], L_2[j])$ is written in the 10th to 12th line in the TSSA; otherwise, the value of $W(L_1[i], L_2[j])$ equals d_1.

The pseudocode of PSA (point similarity algorithm) in the 10th line and that of TSA (time similarity algorithm) in the 11th line are given in Algorithm 2 and Algorithm 3, respectively.

The first line in the algorithm calculates the intersection of scenic labels of two POIs. The second line measures the percent of an intersection of all labels added up and takes it as the similarity value of two POIs.

In the first line of the algorithm, we set half an hour as a single unit and then build the time axis based on it, and the time range spent in two POIs is indicated by two numeric sequences. In the second and third lines of the algorithm, the Longest Common Subsequence (LCS) algorithm is applied to find the longest subsequence present in both of the two numeric sequences. LCS can be solved using Dynamic Programming by dividing the original problem into some subproblems. The time similarity is the ratio of the length of the longest common subsequence to the length of the sequence.

4.3.2. Travel Sequences Clustering. The *K*-means algorithm is one of the most popular and widely used methods of clustering due to its simplicity, robustness, and speed. It is an iterative algorithm meaning that we repeat multiple steps making progress each time. Among many clustering algorithms, *K*-Means is also comparatively well known for its robustness as it is nonsensitive to noise and isolated points. *K*-means algorithm can deal with data sets of different types and discover clusters that are irrelevant with the input order of data. Thus, this paper adopts the *K*-Means algorithm for travel sequence clustering analysis.

(1) Clustering Algorithm Description. *K*-means algorithm partitions the dataset, which includes the number n data, into K number of clusters. Then the clusters are positioned as points, and all observations or data points are associated with the nearest cluster, computed, adjusted, and then the process starts overusing the new adjustments until the desired result is reached. The Travel Sequence Clustering Algorithm (TSCA) is given in Algorithm 4.

K clusters and a sequence containing K cluster centroids can be obtained by Algorithm 4. As each travel sequence reflects the traveller's preference, the base number will be great when adding those sequences altogether. Considering the meaning of centroids has great explaining value, so we set the sequence containing number K cluster centroids as the travel preference baseline model.

(2) Performance Evaluation of Sequence Clustering. Updated Sum of Squared Error (SSE) and Silhouette Coefficient (SC) is used in this paper to evaluate the performance of clustering.

Metric 1: SSE

SSE is a technique designed to find the sum of the squared error of sample points to centroids. Theoretically, the lower the SSE, then the better performance of clustering. This paper calculates the travel sequence similarity measure instead of a distance measure as the foundation of clustering. Therefore, the updated SSE is designed to find the sum of the similarity of sample points to centroids. Hence, the higher the updated SSE, theoretically, the better the performance of clustering.

Metric 2: SC

The Silhouette Coefficient is calculated using the mean intracluster distance $a(o)$ and the mean nearest cluster distance $b(o)$ for each sample o in D. To clarify, $b(o)$ is the distance between a sample and the nearest cluster that the sample is not part of. The calculation equation is given below:

$$SC(o) = \frac{b(o) - a(o)}{\max\{a(o), b(o)\}}. \tag{3}$$

The SC value ranges from −1 to 1, and 1 means the clusters are well apart from each other and clearly distinguished. Just the other way round, when the updated SC value is close to −1, the performance of clustering is better.

4.4. Travel Route Recommendation. Travel route recommendation requires the user to input his or her city travel historical sequences and a new destination city B. The user's travel preference is measured according to the relative distance between historical sequences and the preferences baseline sequence. We calculate the similarity between the city travel historical sequences and the preferences baseline model, and in the end compute the K-dimensional feature vectors which represent the user's travel preference, in which K represents the number of clustering. Therefore, we define user travel preference as follows.

Definition 7 (User travel preference **Userpre**). Given a user's travel history or sequence $L_1, \ldots, L_n$ (n is the number of travel sequences) and the preference referring sequence $L_{k1}, \ldots, L_{kk}$, the travel preference is indicated by a K-dimensional vector as follows:

$$\text{Userpre} = \left(\frac{\sum_{i=1}^{n} \text{TSSA}(L_i, L_{k1})}{n}, \ldots, \frac{\sum_{i=1}^{n} \text{TSSA}(L_i, L_{kk})}{n} \right). \tag{4}$$

In the same way, every travel history or sequence in city B can be indicated as a K-dimensional feature vector, in which we can find the vector that matches user A's travel preference with the highest similarity degree. This is to say, that is the travel recommendation presented to user A because the travel sequence represented by the feature vector satisfies the user's travel preference. As Cosine Similarity (equation (5)) is a commonly used approach, we use this metric to measure the similarity of feature vectors:

Input: POI information p_1 and p_2 of travel item r_1 and r_2
Output: POI similarity S_{poi} of r_1 and r_2
(1) count ⟵ Intersection (p_1.type, p_2.type);
//Intersection (a, b) means the number of intersections of label a and label b
(2) S_{poi} ⟵ count/(p1.type.size + p2.type.size − count);
(3) **return** S_{poi}

Algorithm 2: Point similarity algorithm (PSA).

Input: Time information t_1 and t_2 of travel item r_1 and r_2;
Output: Time similarity S_{time} of r_1 and r_2;
(1) Divide the time axis by half an hour, and number from 1, then t_1 and t_2 can be represented by digital sequence l_1 and l_2
(2) l = **LCS** (l_1, l_2) //Calculate the longest common subsequence of sequence l_1 and l_2
(3) S_{time} ⟵ $|l|/(|l_1| + |l_2| - |l|)$
(4) **return** S_{time}

Algorithm 3: Time similarity algorithm (TSA).

$$c(x, y) = \frac{\sum_{i=1}^{n} x_i y_i}{\sqrt{\sum_{i=1}^{n} x_i^2} \sqrt{\sum_{i=1}^{n} y_i^2}}. \quad (5)$$

The travel sequence recommendation algorithm is given in Algorithm 5.

In the first line of the algorithm, we use the TSCA for travel history clustering analysis of all users. The array newMedoids stores the sequence containing K cluster centroids (K as the number of clusters). In the second line to the seventh line in the algorithm, we calculate the user's travel preference, and the K-dimensional feature vector is stored in the one-dimensional array userpre. From the eighth to the twelfth line, every travel history or sequence in the user's destination city can be indicated as a K-dimensional feature vector, which is stored in the size $m * k$ 2-dimensional array cityseq (m as the total number of all historical sequences in the destination city). In the fourteenth to the nineteenth line, we use the Cosine Similarity function CosSim to find the feature vector in cityseq that match the user's travel preference vector with the highest similarity degree. The result is the travel recommendation presented to the user.

5. Experiment and Evaluation

There are various views on social network data based recommender systems by considering the usage of various recommendation algorithms. In our experiment, there are six steps to generate the dataset, as indicated in Figure 2. Web crawler collects travel spatiotemporal data from social media, travel agent websites, and navigation apps. We select 10 cities (Chongqing, Chengdu, Beijing, Shanghai, Xian, Hangzhou, Nanjing, Tianjin, Guangzhou, and Wuhan) and scenic spots in these cities to analyze the sample travellers' touring history sequences, as indicated in Figure 3. We further compare the scenic labels with those in the Tourist Attraction Knowledge Base (denoted as TAKB) using Natural Semantic Matching technology and manual filtering. In every city, 20 attractions are selected to form the city travel knowledge base. Finally, we split the travel sequence dataset as 70% of the data for training and 30% for testing the CTRR-SES algorithm. In the following experimental evaluation, we randomly select different users for testing.

To validate the CTRR-SES, the experiment was designed based on the collected touring data.

5.1. Accuracy and Validation of Travel Route Recommendation Algorithm

5.1.1. Impact of the Value of K on the Travel Preference Baseline Model. The value of K to perform the K-means clustering algorithm has a great impact on the experimental results. Thus, we run the fixed K value multiple times and use the updated SSE and the mean of SC to determine the optimal value. As indicated in Figure 4, when the K value is greater than 4, then the growth rate of SSE decreases. The increase of value K leads to the increase of the value of SC(o). Next, we set the degree of similarity as the recommendation accuracy rate. Feature vectors of the recommended route and that of the corresponding route in the testing dataset are computed using the similarity function when $K = 2, 3, 4, 5, 6$ (experimental results are shown in Figure 4). As the bars show, the recommendation accuracy rate is the highest when $K = 4$. Hence, in the following experiments, we set the value of $K = 4$ in this paper.

5.1.2. Length Comparison of Recommendation Sequence and Original Sequence. The sequence length of the original route in the testing dataset and that of the recommendation route

Input: travel sequences set TS = {L_1, L_2, . . ., L_n} and the number of clusters k
Output: travel sequence cluster set TC = {TC_1, TC_2, . . ., TC_k} and k center sequences set newMedoids = {L_1, L_2, . . ., L_K}
Initialization: oldMedoids ⟵ null, newMedoids ⟵ null;
(1) Select k sequences L_1, L_2, . . ., L_k from TS randomly as initial center sequences to oldMedoids;
(2) TC_i ⟵ L_i //Each center sequence corresponds to a cluster
(3) **while** (!isEqual (oldMedoids, newMedoids))
(4) Calculate the similarity of each sample sequence from TS to each center sequence from newMedoids and place the sample sequence in the cluster with the highest similarity to the center sequence;
(5) oldMedoids ⟵ newMedoids;
(6) Recalculate the center sequence of each cluster TC_i, sequences with the highest similarity from each sample sequence in the cluster, as newMedoids;
(7) **return** TC and newMedoids;

Algorithm 4: Travel sequence clustering algorithm (TSCA).

Input: Historical Travel sequences set HS = {L_{11}, L_{12}, . . ., L_{1n}} of user A, city a, historical travel sequences HSA = {L_{21}, L_{22}, . . ., L_{2m}} of city a, historical travel sequences HSAU of all users
Output: Travel recommendation sequences of city a for user A
(1) newMedoids = **TSCA** (HSAU) //Cluster historical travel sequences of all users
(2) **for** i ⟵ 1 to newMedoids.size **do**
(3) **for** j ⟵ 1 to n **do**
(4) userpre[i] ⟵ userpre[i] + **TSCA** (newMedoids[i], L_{1j});
(5) userpre[i] = userpre[i]/n;
(6) **end for**
(7) **end for**
(8) **for** t ⟵ 1 to m **do**
(9) **for** r ⟵ 1 to newMedoids.size **do**
(10) cityseq[t][r] = **TSSA** (newMedoids[r], L_{2t});
(11) **end for**
(12) **end for**
(13) sim ⟵ 0;
(14) **for** t ⟵ 1 to m **do**
(15) **if** sim < **CosSim** (userpre, cityseq[t]) **then**
(16) sim ⟵ **CosSim** (userpre, cityseq[t]);
(17) outputseq ⟵ L_{2t};
(18) **end if**
(19) **end for**
(20) **return** outputseq;

Algorithm 5: Travel sequence recommendation algorithm (TSRA).

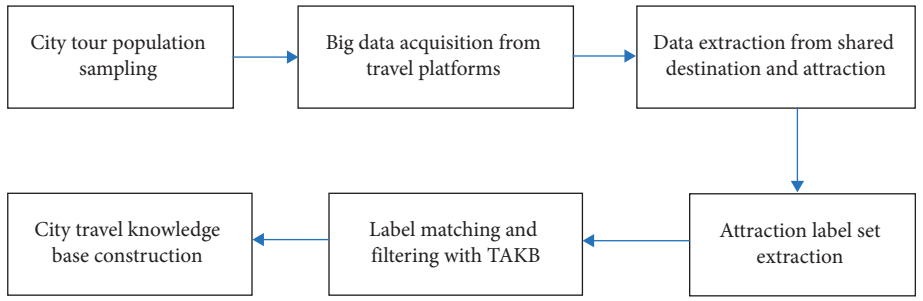

Figure 2: City travel knowledge data generating process.

are counted and compared, as shown in Figure 5. Compared with the sequence length of the real route, the experimental result of a small error proves that our algorithm is validated in its accuracy.

5.1.3. Hit Rate. The formula of hit rate is given:

$$\text{Hit rate} = \frac{2 * \left(\left|P_r \cap P_o\right|/P_r * \left(\left|P_r \cap P_o\right|/P_o\right)\right)}{\left(\left|P_r \cap P_o\right|/P_r\right) + \left(\left|P_r \cap P_o\right|/P_o\right)}. \quad (6)$$

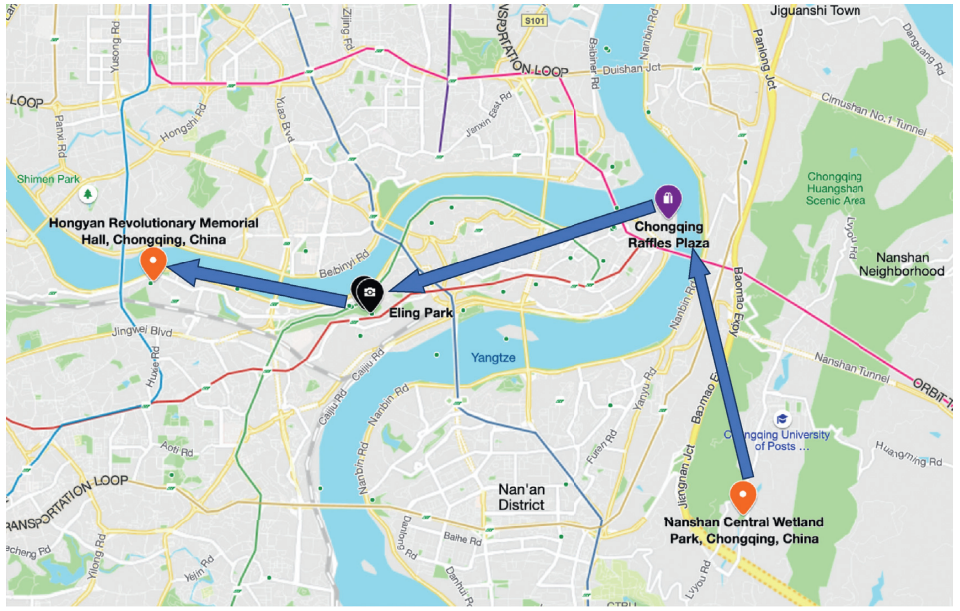

Figure 3: Example of city travel event sequence.

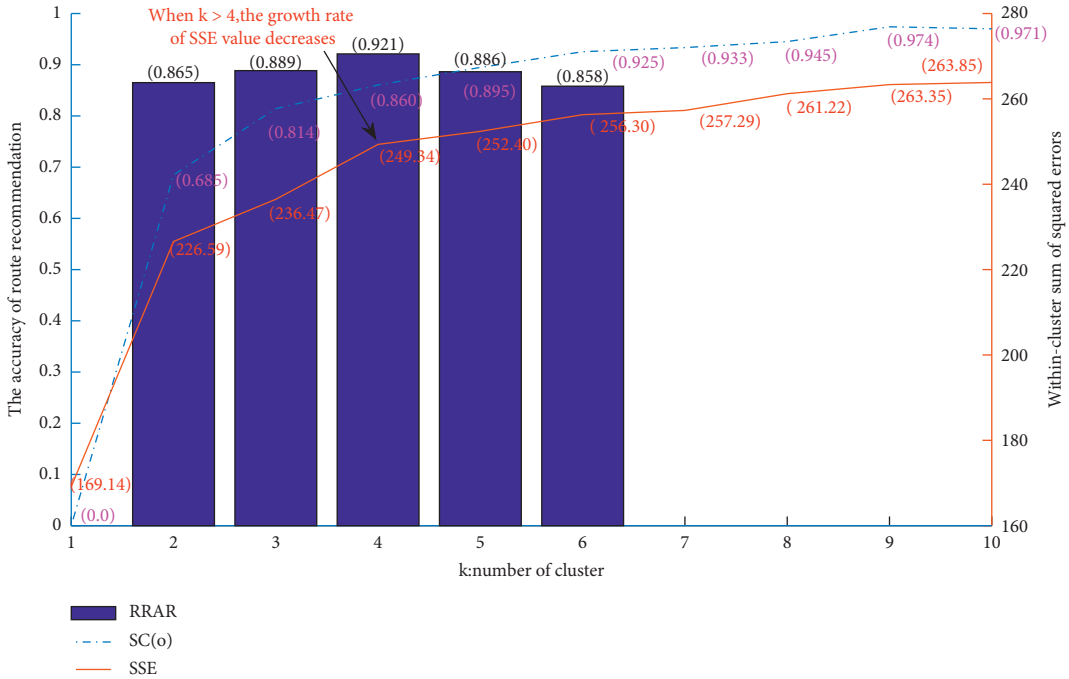

Figure 4: Evaluation index of clustering quality and accuracy with different K values.

In equation (6), P_r is the set of attractions in the recommended route, and P_o is the set of attractions in the user's travel historical sequence. The higher Hit Rate indicates better performance of recommendation by our algorithm. Then we calculate the accuracy of the route recommendation. The experimental hit rate result is 0.70, which further validates the CTRR-SES, proving that this algorithm will provide city travel route recommendation that effectively matches the user's preference.

5.2. Robustness of Travel Route Recommendation Algorithm. To test the robustness of the CTRR-SES, we design the following experiments, as shown in Table 1. Randomly change one or multiple sequences in the user's historical city touring sequence, and the experimental results are much like the original results detailed in Figure 6. Thus our algorithm has good performance in its robustness and stability.

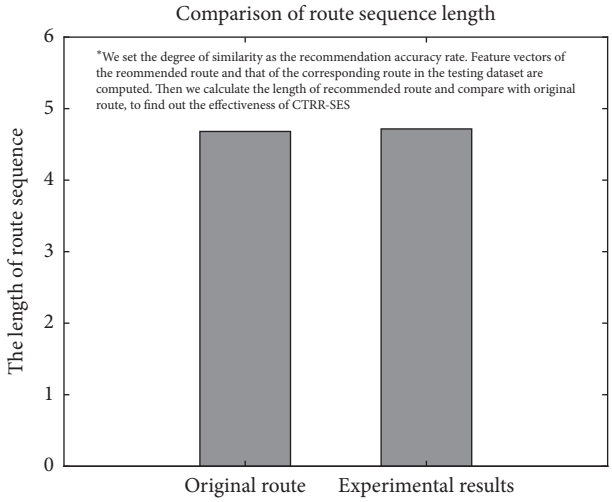

Figure 5: The length comparison of the original route with the recommendation route.

Table 1: Robustness tests.

Experiment no.	Result	Experimental design	Figure
1	The recommendation route accuracy rate is 92.1% after alteration and 99.8% of similarity degree with the original	Randomly change one item of one sequence in the user's historical city touring sequences	Figure 6
2	The recommendation route accuracy rate is 91.8% after alteration and 99.5% of similarity degree with the original recommendation route	Randomly change 50% items in one sequence in the user's historical city touring sequences	Figure 6
3	The recommendation route accuracy rate is 91.7% after alteration and 99.1% of similarity degree with the original recommendation route	Randomly change one item in each sequence of 50% sequences in the user's historical city touring sequences	Figure 6
4	The recommendation route accuracy rate is 91.5% after alteration and 98.8% of similarity degree with the original recommendation route	Randomly change 50% items in each sequence of 50% sequences in the user's historical city touring sequences	Figure 6

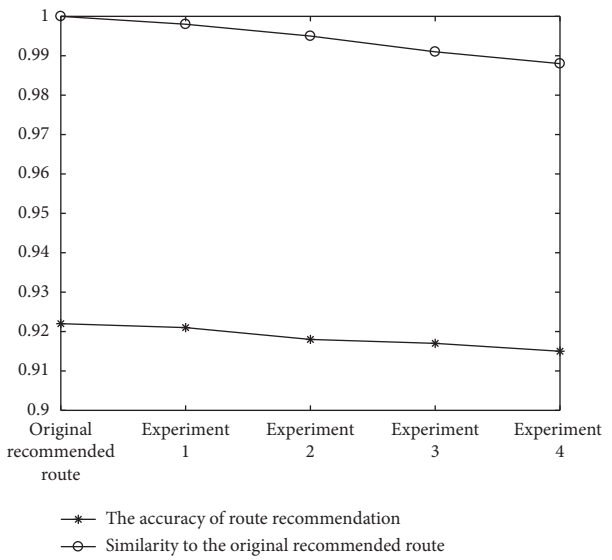

Figure 6: Comparative experiment of the original route with partial sequence alteration.

6. Conclusion

Existing travel recommendation studies seldom analyze user behavior with different granularities to calculate spatiotemporal sequence similarity. As a lack of full understanding of behavior events from multigranularity and multiperspective, those studies are not suitable for the growing need for in-depth city travel route recommendations. We adopt the coevolving spreading dynamics to the relevance of the traveling preferences and the events in the city tour networks and explore its application on the city tour recommendation system. Based on defining the user's touring sequence model, firstly, this paper presents the Event Sequence Similarity Measurement Method, which calculates the weighted mean of time, space, and activity similarity in certain granularity to measure spatiotemporal sequence similarity. Next, we design the CTRR-SES by applying the User Travel Preference Baseline Learning Model to study user's city travel historical data and compute personalized travel preferences. Finally, our algorithm is validated by a series of experiments of its effectiveness and feasibility, and CTRR-SES shows better performance in predicting the user's new city travel sequence fitting the user's individual preference. Our work provides reference and guidance to research the multigranularity spatiotemporal sequence similarity problem for city travel route recommendation. However, only 54 real cases are selected to evaluate the performance of the CTRR-SES algorithm, and we will include more experiments and datasets to validate the work in future research.

Data Availability

The travel historical data used to support the findings of this study have been deposited in the Mafengwo.com repository.

Conflicts of Interest

The authors declare that they have no conflicts of interest.

Acknowledgments

This work was supported by the National Natural Science Foundation of China under grant no. 61672115 and Project No. 2020CDCGJSJ040 supported by the Fundamental Research Funds for the Central Universities.

References

[1] Y. Zhu, Y. G. Zou, and L. Chen, "Analysis of spatial characteristics of urban tourism flow based on UGC data-taking Shanghai as an example," *Tourism Forum*, vol. 12, no. 4, pp. 33–41, 2019.

[2] L. Li and Y. Jing, *Android city tour guide system based on web service*, 2012.

[3] Y. Guo and H. Liu, "The embedding convergence of smart cities and tourism internet of things in China: an advance perspective," *Advances in Hospitality and Tourism Research*, vol. 2, no. 1, pp. 54–69, 2014.

[4] M. D. Aswale, "Survey on recommendation of personalized travel sequence," *Ijarcce*, vol. 6, no. 1, pp. 108–113, 2017.

[5] J. Huang, Y. Liu, Y. Chen, and C. Jia, "Dynamic recommendation of POI sequence responding to historical trajectory," *ISPRS International Journal of Geo-Information*, vol. 8, no. 10, p. 433, 2019.

[6] S. Jiang, X. Qian, T. Mei, and Y. Fu, "Personalized travel sequence recommendation on multi-source big social media," *IEEE Transactions on Big Data*, vol. 2, no. 1, pp. 43–56, 2016.

[7] W. Wörndl, A. Hefele, and D. Herzog, "Recommending a sequence of interesting places for tourist trips," *Information Technology & Tourism*, vol. 17, no. 1, pp. 31–54, 2017.

[8] L. Zheng, F. Z. Wei, C. T. Lu et al., "Gated spectral units: modelling co-evolving patterns for sequential recommendation," *SIGIR*, vol. 2019, pp. 1077–1080, 2019.

[9] W. Wang, Q. H. Liu, J. H. Liang et al., "Co-evolution spreading in complex networks," *Physics Report*, vol. 820, pp. 1–52, 2019.

[10] K. H. Lim, "Recommending tours and places-of-interest based on user interests from geo-tagged photos," 2015.

[11] T. Kurashima and T. Iwata, "Travel route recommendation using geotags in photo sharing sites," *CIKM*, vol. 10, pp. 579–588, 2010.

[12] H. Yin and C. Wang, "Trip mining and recommendation from Geo-tagged photos," 2012.

[13] M. Thenmozi and S. Harshitha, "A framework for tourist recommendation system exploiting geo-tagged photos," 2016.

[14] W. P. Sun, L. Chang, C. Z. Bin et al., "Travel route recommendation based on knowledge graph and frequent sequence mining," *Computer Science*, vol. 46, no. 2, pp. 56–61, 2019.

[15] Y. Li, J. H. Xie, and L. C. Yang, "The preference analysis for tourist choice of scenic spot: a stated preference approach," *Tourism Tribune*, vol. 33, no. 12, pp. 88–98, 2018.

Hindawi
Complexity
Volume 2020, Article ID 8861493, 12 pages
https://doi.org/10.1155/2020/8861493

Research Article

Effects of the Awareness-Driven Individual Resource Allocation on the Epidemic Dynamics

Xiaolong Chen,[1,2] **Ruijie Wang**,[3] **Dan Yang**,[4,5] **Jiajun Xian**,[4,5] **and Qing Li**[1,2]

[1]*School of Economic Information Engineering, Southwestern University of Finance and Economics, Chengdu 611130, China*
[2]*Financial Intelligence and Financial Engineering Key Laboratory of Sichuan Province, School of Economic Information Engineering, Chengdu 611130, China*
[3]*Aba Teachers University, Aba 623002, China*
[4]*Department of Computer Science, School of Engineering, Shantou University, Shantou 515063, China*
[5]*Key Laboratory of Intelligent Manufacturing Technology (Ministry of Education), Shantou University, Shantou 515063, China*

Correspondence should be addressed to Dan Yang; danyangsjhd@hotmail.com

Received 18 August 2020; Revised 7 September 2020; Accepted 27 September 2020; Published 14 October 2020

Academic Editor: Chenquan Gan

We investigate the effects of self-protection awareness on the spread of disease from the aspect of resource allocation behavior in populations. To this end, a resource-based epidemiological model and a self-awareness-based resource allocation model in complex networks are proposed, respectively. First of all, we study the coupled disease-awareness dynamics in complex networks with fixed degree heterogeneity. Through extensive Monte Carlo simulations, we find that overall the self-awareness inhibits the spread of disease. More importantly, the influence of the self-awareness on the spreading dynamics can be divided into three phases. In phase I, the self-awareness is relatively small and the outbreak of the epidemic can not be suppressed effectively. While, in phase II, the epidemic size is significantly reduced. Finally, in phase III, there is a sufficiently large value of self-awareness, the disease cannot outbreak anymore. Further, we study the impact of degree heterogeneity on the coupled disease-awareness dynamics and find that the network heterogeneity plays the role of "double-edged sword" in that it can either suppress or promote the epidemic spreading. Specifically, when the basic infection rate is relatively small, it promotes the spread of disease under the condition that there is a relatively small self-awareness. While, when the basic infection rate is relatively large, it inhibits the outbreak of epidemic at a relatively small self-awareness; in turn, it promotes the outbreak of epidemic at a relatively large self-awareness.

1. Introduction

From the Spanish Flu in Europe in the 1920s [1] to the SARS (Severe Acute Respiratory Syndrome) in 2003 [2] and the H1N1 flu outbreak in 2009 in the United States [3], the onset of each pandemic in the history always brought a tragic disaster to human beings. As of September 5, 2020, the ongoing COVID-19 outbreak has infected nearly 270 million people worldwide, and regrettably, more than 870,000 have lost their lives [4]. As a result, the mitigation and control of the spread of epidemics has always been a challenging subject for humans. During a pandemic, especially in the early stage of the epidemic, the individuals' self-protection awareness plays a vital role in the prevention and control of it [5]. The individuals can be well informed by the information about the status of the epidemic through social networking platforms and news media [6], which invokes the awareness of self-protection. Subsequently, the individuals will take protective measures, such as wearing masks, reducing public gathering, and washing hands, to avoid being infected.

In recent decades, a large body of literatures have highlighted the critical role that human responses playing in influencing the spread of disease [7–10]. Driven by the awareness of self-protection, the individuals will take a series of precautionary measures to avoid infection [11, 12], and it will, in turn, affect the course of the epidemic by reducing the

transmission of the disease. For example, due to the rapid response and the intensive control measures of both government and people in the early stages of the outbreak, the epidemic has been effectively controlled in China [13]. Consequently, the study of coupled dynamics of awareness and disease has been one of the most fruitful realms in various disciplines [5, 14, 15]. Typical representatives include the game theory in studying the vaccination behavior that the individuals decide whether to vaccinate or not based on an assessment of risks and benefits [16–18]. In addition to the application of game theory, the interplay between the awareness and epidemics in complex networks has attracted much attention in theoretical and empirical research [19–22]. The seminal work was the study of the spread of awareness in well-mixed populations and lattices and, in turn, its influence on the spread of disease by Funk et al. [7]. In addition to the well-mixed assumption, Wu et al. [23] explored, respectively, the impact of local, global, and contact awareness on epidemic spreading in networks with heterogeneous connections in populations. Moreover, based on the framework of multiplex networks, Granell et al. [24] investigated the coupled dynamics of the epidemic and awareness. Using a microscopic Markov chain approach and Monte Carlo simulations, they showed that the onset of the epidemics can be changed by the coupled dynamical process. Recently, Zhan et al. [25] studied the coupled dynamics of two different diseases and the corresponding information based on empirical analysis and theoretical modeling.

In addition to wearing masks, staying at home, etc., the behavior of resource donation in the individuals plays a vital role in disease control as the severe shortage of resources induced by the outbreak. For example, during the COVID-19 pandemic, both personal protective and medical equipment such as respirators, gloves, and face shields are in severe shortage all over the world [26]. Consequently, the research of optimal allocation of both public and individual resources in controlling the spread of the disease has been one of the hottest topics in the past years [27–30]. For example, Preciado et al. [31] investigated the optimal allocation of vaccination resources during an outbreak of the disease in complex networks and found the cost-optimal strategy of resource allocation. Nowzari et al. [27] developed an optimization framework to solve the problems of finding minimum resource cost required to eradicate the disease and the optimal strategy of resource allocation based on the analysis of the proposed epidemiological model. In terms of individual resources, Böttcher et al. [32] investigated the impact of the shortage of individual resources induced by the outbreak of epidemics. They showed that the epidemics can spiral out of control if the recovery cost is higher than a critical value. Inspired by the work of Ref. [32], the coupled dynamics of resource allocation and disease spreading on both single and multiplex networks has been widely researched in recent years [33–37]. In spite of a large body of literatures about the interplay between awareness (resource) and epidemics, there is a lack of research on the co-evolutionary mechanism among the three dynamical processes.

To investigate the effects of the awareness-driven resource support of individuals on the epidemic dynamics, we propose a novel resource-based susceptible-exposed-infected-recovered (r-SEIR) epidemiological model and a self-awareness-based resource allocation model, respectively, in this paper. In the models, the self-protection awareness of a susceptible node (abbreviated to self-awareness) is supposed to be composed of both local and global awareness measured by the number of infected neighbors and global infected nodes, and the resource allocation probability of each node is determined by its awareness. First of all, we study the coupled disease-awareness dynamics by incorporating the individual resource allocation in complex networks with fixed degree heterogeneity. Through extensive Monte Carlo simulations, we find that the self-awareness of the individuals can inhibit the spread of disease. Specifically, we find two critical values of the instinctive self-awareness that separate the parameter space into three phases. In phase I, when there is a relatively small self-awareness, the outbreak size of the epidemic increases abruptly with the basic infection rate, which implies that the epidemic can not be suppressed effectively. While, in phase II, the final fraction of infected nodes increases slowly with the basic infection rate, which indicates that the disease can be controlled to a certain extent. Finally, in phase III, when there is a sufficiently large value of the self-awareness, the disease is well controlled. Next, we continue studying the effects of degree heterogeneity on the coupled dynamics. Through Monte Carlo simulations, we find that there is "double-edged sword" effect of network heterogeneity on the coupled dynamics. Specifically, when the basic infection rate is relatively small, the network heterogeneity promotes the spread of disease under the condition that there is a relatively small value of self-awareness. While, when the basic infection rate is relatively large, it inhibits the outbreak of epidemic at a relatively small self-awareness; in turn, it promotes the outbreak of epidemic at a relatively large self-awareness. Our findings can be applied directly to guide people to maintain the right level of self-protection awareness and take rational behaviors during a pandemic. Moreover, the results in this paper will also provide a constructive viewpoint for policymakers of public health.

2. Model Description

2.1. Epidemic Model. To investigate the impact of awareness-driven individual resource allocation on the spread of the epidemic, we propose a resource-based susceptible-exposed-infected-recovered (r-SEIR) epidemiological model [38] in complex networks. The r-SEIR model is composed of the following four epidemiological compartments: susceptible (S), exposed (E), infected (I), and recovered (R). To facilitate the study of the dynamical processes, the individuals are represented by nodes in the network and an adjacency matrix $\mathbb{A}$ is introduced to store the information of network structure. If an edge between i and j exists, the matrix element $a_{ij} = 1$; otherwise, $a_{ij} = 0$. At each time step, the pathogen transmits from an I-state node to an S-state node at a basic infection rate β, if there is a contact between these two nodes and the S-state node does not take any protective measure. Those S-state nodes which get the pathogen will

turn to E-state immediately. In the real scenario, any individual who gets the information about the disease will have awareness for self-protection. We consider that, initially, all nodes in the network have the same level of instinctive self-awareness, which is denoted as α in the context. With the development of the epidemic, they can get the information about the status of the epidemic from local communities or global mass media [23], which will alter the awareness of each individual. Based on the description above, it is assumed that the self-awareness of a node i, which is denoted as α_i, is determined by both the number of I-state neighbors, denoted as $m_i(t)$, and the global confirmed cases, denoted as $I(t)$, in the complex network. Since the neighbor's infection of a node has a more intuitive effect on its self-awareness, a coefficient $\eta \in [0,1]$ is introduced as the weight of $I(t)$. Based on the above scheme, the self-awareness of node i at time t can be expressed as

$$\alpha_i(t) = 1 - (1-\alpha)^{m_i + \eta I(t) + 1}. \tag{1}$$

A S-state node with self-awareness $\alpha_i(t)$ at time t will take protective measures, such as wearing masks and washing hands, which will affect the transmission probability of the disease. Thus, the actual infection rate of i is

$$\beta_i = (1-\alpha_i)\beta. \tag{2}$$

A larger value of α_i means a smaller probability of being infected.

In addition, an exposed node becomes infected at rate δ at each time step. At the same time, each I-state node i will recover with a recovery rate μ_i, which is assumed to be dependent on the resources received from outside [34, 39]. Therefore, the recovery rate of node i is assumed to be proportional to its resource quantity $\omega_i(t)$ in this paper, and is defined as

$$\mu_i(t) = 1 - (1-\mu)^{\varepsilon\omega_i(t)+1}, \tag{3}$$

where the parameters μ and $\varepsilon \in [0,1]$ represent the basic recovery rate and the resource utilization rate, [40] respectively, since in real life, the phenomenon of resource waste is inevitable in medical and other service systems [41]. Besides, the fraction of susceptible, exposed, infected, and recovered nodes at time t is denoted by $s(t)$, $e(t)$, $i(t)$, and $r(t)$, respectively. Note that we also denoted the final infected density in the dynamical system as ρ, which satisfies $\rho \equiv r(\infty)$.

2.2. Self-Awareness-Based Resource Allocation Model. People aware of the disease would change the attitude and behavior of resource donation in suppressing the disease spreading and thus influences the epidemic dynamics. To investigate the impact of awareness-driven individual resource allocation, a resource allocation model is proposed. We assume that each healthy node can generate one unit resource at a time step. Subsequently, the healthy node will donate its resource to help the recovery of the I-state neighbors with probability $q_i(t)$, which is determined by the self-awareness $\alpha_i(t)$. Intuitively, for self-protection, the higher the level of self-awareness, the lower the probability of resource donation. Consequently, the resource donation probability $q_i(t)$ can be expressed as

$$q_i(t) = q_0(1-\alpha_i(t)), \tag{4}$$

where q_0 is the basic donation probability. Besides, it is assumed that the resources contributed by the healthy nodes will be allocated equally to their infected neighbors at each time step. Combining the donation probability q_i and the resource allocation scheme, the amount of resources that each healthy node i allocates to one of its I-state node j at time t is

$$\omega_{i\longrightarrow j}(t) = q_i(t)\frac{1}{m_i(t)}. \tag{5}$$

Based on equation (5), the resource quantity of each I-state node j can be expressed as

$$\begin{aligned}\omega_j(t) &= \sum_i a_{ij}h_i\omega_{i\longrightarrow j}(t)\\ &= \sum_i a_{ij}h_i\frac{q_i(t)}{m_i(t)},\end{aligned} \tag{6}$$

where h_i is introduced to represent the state of node i. When node i is in susceptible state, $h_i = 1$; otherwise, $h_i = 0$.

3. Simulation Results

In this section, we study systematically the effects of self-awareness on the spreading dynamics by incorporating the allocation of individual resources. First of all, we investigate the coupled awareness-disease dynamics on scale-free networks with fixed degree exponential, as many real-world networks have skewed degree distributions [42–44]. Then, we study the impact of network heterogeneity on the coupled dynamics through extensive Monte Carlo simulations.

In the simulations, we adopt the synchronous updating method [45] to mimic the processes of disease transmission and resource allocation on the complex networks. Specifically, the processes update as follows [45]: during a time interval $[t, t+\Delta t]$, each susceptible node is infected by one of its infected neighbors with probability $\beta_i\Delta(t)$ and subsequently, it changes to the exposed state. The actual infection rate β_i is expressed as [46]

$$\beta_i(t) = \lim_{\Delta t\longrightarrow 0}\frac{P\left(H^i_{t+\Delta t} = I \text{ infected by } j | H^i_t = S, H^j_t = I\right)}{\Delta t}, \tag{7}$$

where H^i_t is denoted as the state of node i at time t and $(H^i_{t+\Delta t} = I \text{ infected by } j)$ denotes that node i is infected by an I-state neighbor j [47]. At the same time, the E-state nodes becomes I-state ones with probability $\delta\Delta t$, and the I-state nodes change to R-state nodes with probability $\mu_i(t)\Delta t$, which is defined as

$$\mu_i(t) = \lim_{\Delta t\longrightarrow 0}\frac{P\left(H^i_{t+\Delta t} = R | H^i_t = I\right)}{\Delta t}. \tag{8}$$

The infection rate $\beta_i(t)$ and recovery rate $\mu_i(t)$ are determined by the number of infected neighbors $m_i(t)$, the global confirmed nodes $I(t)$, and the resource quantity $\omega_i(t)$ simultaneously.

The process of resource allocation evolves simultaneously with the spread of disease. In synchronous updating, the Δt is finite, and the infection and recovery probability of node i is $\beta_i = \beta_i \Delta t$, and $\mu_i = \mu_i \Delta t$. According to equations (7) and (8), the transition probability can be expressed as

$$\beta_i \Delta t = P\left(H_{t+\Delta t}^i = I \text{ infected by } j | H_t^i = S, H_t^j = I\right), \quad (9)$$

and the recovery probability can be written as

$$\mu_i \Delta t = P\left(H_{t+\Delta t}^i = R | H_t^i = I\right). \quad (10)$$

At the end of each time step, the state of all nodes in the network update synchronously. The processes terminate when there are no I-state and E-state nodes in the network.

3.1. Effects of Awareness-Driven Resource Allocation on the Spreading Dynamics. To study the coupled dynamics in complex networks, we use the uncorrelated configuration model (UCM) [48] to generate networks with power-law degree distributions $P(k) = \zeta k^{-\gamma}$, where the coefficient is $\zeta = 1/\sum_{k_{\min}}^{k_{\max}} k^{-\gamma}$, as many real-world networks have skewed degree distributions [43, 49]. The size of the network is set to $N = 10000$, and the average degree is $\langle k \rangle = 8$. To ensure that there is no degree correlation of the network, the maximum and minimum degrees are set to $k_{\max} = \sqrt{N}$ and $k_{\min} = 3$, respectively [50]. We focus on the case of $\gamma = 2.4$ in this section. To initiate a spreading process, a fraction $i(0) = 0.001$ of nodes is selected randomly as seeds and the remaining nodes are in susceptible state.

To numerically determine the size-dependent epidemic threshold β_c, we employ the variability measure [51], which has been demonstrated to be effective in identifying the epidemic threshold of SIR model [52]:

$$\Delta = \frac{\sqrt{\langle \rho^2 \rangle - \langle \rho \rangle^2}}{\langle \rho \rangle}, \quad (11)$$

where the operator $\langle \ldots \rangle$ represents the ensemble average over all realizations. We can identify the epidemic threshold β_c, at which the variability Δ exhibits a peak.

Figure 1(a) displays the final fraction of infected nodes ρ as a function of basic transmission rate β for different values of instinctive awareness α. Figure 1(b) shows the plots of variability measure Δ vs. β. The initial fraction of infected nodes is set to be $i(0) = 0.001$. We observe that the threshold β_c increases with the increase of α, see the peaks of Δ in Figure 1(b). In addition, when the basic infection rate is fixed, e.g., $\beta = 0.2$, the value of ρ decreases with the increase of α, as shown in Figure 1(a). The results suggest that the more self-protective people are during the outbreak of an epidemic, the more effectively the disease can be controlled.

Next, we study systematically the effects of self-awareness α and basic transmission rate β on the spreading dynamics by presenting the full phase diagram in parameter plane $(\alpha - \beta)$ in Figure 2(a). Colors in Figure 2(a) encode the value of ρ. The white circles connected by segments identify the epidemic thresholds β_c at different values of α, which are obtained by the method of variability measure presented in equation (11). We observe that the overall the epidemic threshold β_c increases monotonously with the increase of α. Besides, when α is relatively small (in phase I), the value of β_c increases slowly, and the final fraction of infected nodes ρ increases abruptly with β at a fixed value of α. And then, when the α grows larger (in phase II), the final infected density ρ increases slowly with β at a fixed α. Finally, when α is large enough (in phase III), the disease can not break out any more.

To identify the critical points of α, we calculate the change rate of β_c, which is defined as

$$\nu_r \equiv \frac{d\beta_c}{d\alpha} = \lim_{\Delta\alpha \longrightarrow 0} \frac{\beta_c(\alpha + \Delta\alpha) - \beta_c(\alpha)}{\Delta\alpha}, \quad (12)$$

where $\Delta\alpha$ is the increment in α and is set to be $\Delta\alpha = 0.01$. By performing extensive Monte Carlo simulations, we calculate the value of ν_r at each point of α, and identify the two critical points, namely, the first point $\alpha_c^I \approx 0.64$, at which the value of ν_r exceeds an threshold value that is preset to 0.1, and the second point α_c^{II}, at which ν_r reaches maximum value. Figure 2(b) shows the plot of ν_r as a function of α. We can observe that the parameter space is separated by the two critical values into three phases, which is in accordance with the three phases marked by phase I, phase II, and phase III in Figure 2(a), respectively.

The above results suggest that during the outbreak of an epidemic, as long as the populations maintain sufficient awareness of self-protection, say $\alpha > \alpha_c^{I}$, and take effective protective measures, such as conserving their resources to reduce waste of resources and reduce exposure, the disease can be suppressed effectively.

Next, we qualitatively explain the above conclusions by studying the time evolution of several important dynamical parameters at three typical values of α located in $\alpha < \alpha_c^{I}$, $\alpha_c^{I} \le \alpha < \alpha_c^{II}$ and $\alpha \ge \alpha_c^{II}$, respectively. Note that, in order to study the evolution of the dynamic parameters for nodes with large degrees and small degrees, respectively, we define the nodes with degrees larger than 30 as the hub nodes, and the remaining nodes as small-degree nodes. Subsequently, we define the average awareness, transmission rate, recovery rate, and probability of resource donation as $\langle \alpha_x \rangle$, $\langle \beta_x \rangle$, $\langle \mu_x \rangle$, and $\langle q_x \rangle$, respectively, where $x \in (h, s)$. For the hub nodes, $x = h$, and for the small-degree nodes, $x = s$.

First of all, we investigate the time evolution of the dynamical parameters in $\alpha < \alpha_c^{I}$, as shown in Figure 3. Without loss of generality, the instinctive self-awareness is set to be $\alpha = 0.1$. Figure 3(a) displays the evolution of the dynamic parameters for the hub nodes. We find that when $\alpha = 0.1$, nodes in the network have a relatively small instinctive self-awareness and a large probability of resource donation to support the recovery of the I-state nodes in the initial time. Therefore, we can learn from equation (3) that the recovery rate of the nodes is large. Consequently, it has a relatively small value of the effective infection rate β_e, which

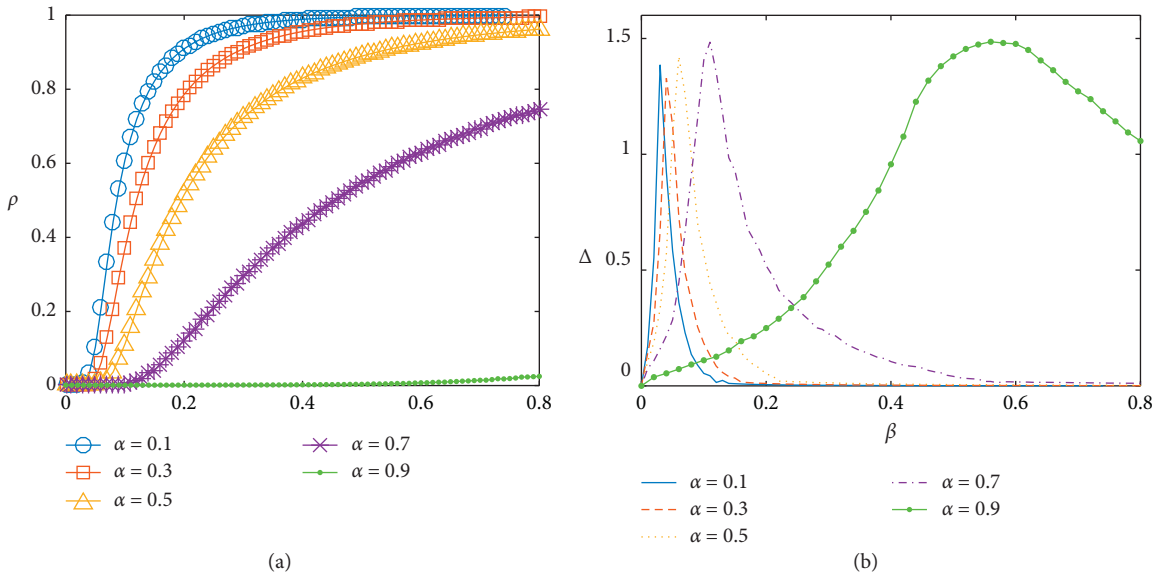

FIGURE 1: Effects of awareness-driven individual resource allocation on the spreading dynamics in scale-free networks. (a) The final infected density ρ as a function of basic transmission rate β for five typical values of instinctive self-awareness α. (b) Plots of variability measure Δ vs. β. The other parameters are set to be $\delta = 0.5$, $\eta = 0.001$, $\varepsilon = 0.6$, $\mu = 0.1$, and $q_0 = 0.8$, respectively. Data are obtained by averaging over $10^2 \times 10^2$ independent realizations on 10^2 networks.

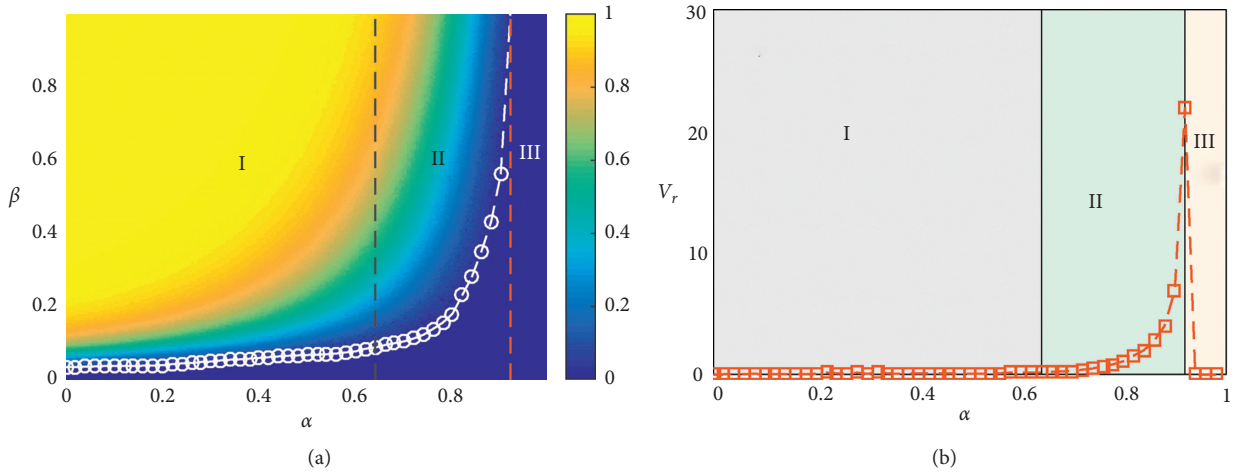

FIGURE 2: Dependence of ρ on parameters α and β. (a) The phase diagram in parameter plane $(\alpha - \beta)$. Colors-coded values ρ obtained from Monte Carlo simulations. The epidemic threshold β_c is represented by the white circles. Phases I, II, and III are separated by two critical values $\alpha_c^{\mathrm{I}} \approx 0.64$ and $\alpha_c^{\mathrm{II}} \approx 0.92$, which are marked by the black segment and red segment, respectively. (b) The change rate of the epidemic threshold v_r as a function of $v_r \alpha$. Phases I, II, and III are separated by α_c^{I} and α_c^{II}. The other parameters are set to be $\delta = 0.5$, $\eta = 0.001$, $\varepsilon = 0.6$, $\mu = 0.1$, and $q_0 = 0.8$, respectively.

is defined as $\beta_e = \beta/\mu$ [53]. Thus, we can observe from Figure 3(c) that the disease propagates slowly in the initial stage (about $t < 5$). The slow growth of the infected nodes leads to a weak awareness of the disease for the susceptible nodes. Thus, at the early stage, i.e., $t < 5$, there is a slow growth in the self-awareness and a slight decrease in the resource donation probability for all nodes in the network, as shown in Figures 3(a) and 3(b). Whereas, after the early stage, i.e., $t > 10$, there is a rapid increase in the exposed nodes $e(t)$ and infected nodes $i(t)$ (see Figure 3(c)). The surge in the number of infected nodes induces a rapid improvement of the self-awareness, which makes a rapid increase in $\langle \alpha_h \rangle$, as shown in Figure 3(a). However, the value of $\langle \alpha_s \rangle$ and $\langle q_s \rangle$ changes slowly, as shown in Figure 3(b). The above phenomena can be explained as follows: the propagation process of the epidemic exhibits hierarchical feature in the network [54], namely, the hubs are likely to be infected firstly, and then they transmits the disease to the intermediate nodes; finally, the small-degree nodes are infected. As a result, as more and more hub nodes become

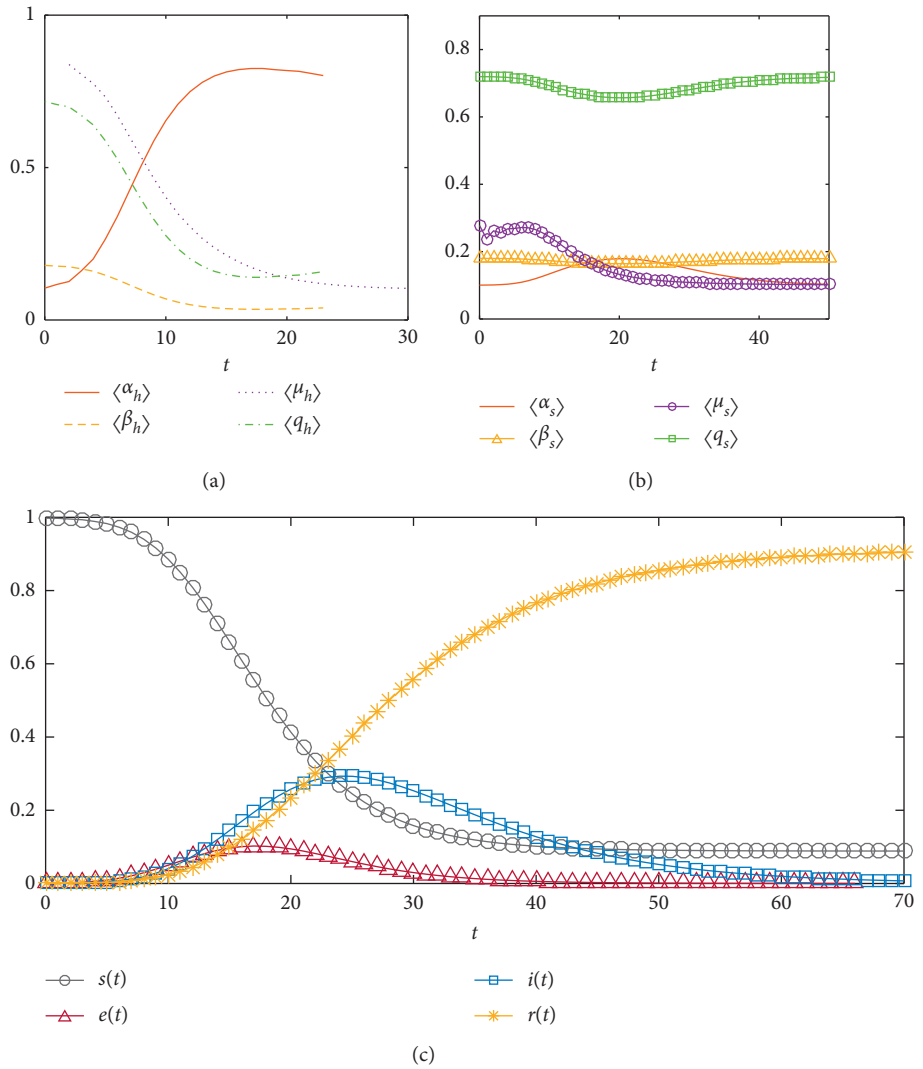

FIGURE 3: (a) Temporal evolution of average values of awareness $\langle \alpha_h \rangle$ (red line), transmission rate $\langle \beta_h \rangle$ (yellow segment), recovery rate $\langle \mu_h \rangle$ (purple dots), and probability of resource donation $\langle q_h \rangle$ for hub nodes. (b) The evolution of average values of awareness $\langle \alpha_s \rangle$ (red line), infection rate $\langle \beta_s \rangle$ (yellow triangles), recovery rate $\langle \mu_s \rangle$ (purple circles), and probability of resource donation $\langle q_s \rangle$ (green squares) for nodes with small degree. (c) The evolution of the fraction of the nodes in susceptible $s(t)$, exposed $e(t)$, infected $i(t)$, and recovered $r(t)$ states, respectively. The instinctive self-awareness is $\alpha = 0.1$, and the basic infection rate is $\beta = 0.2$. The other parameters are the same as those in Figure 2. The results of the simulations are obtained by averaging over $10^2 \times 10^2$ independent realizations on 10^2 networks.

infected, the disease transmits rapidly in a hub node-centered area, and the value of $e(t)$ and $i(t)$ increases rapidly. Consequently, there is an abrupt increase in $\langle \alpha_h \rangle$ and a rapid decrease in the resource donation probability $\langle q_h \rangle$ in this stage, which induces a decrease in both the transmission rate $\langle \beta_h \rangle$ and simultaneously, the recovery rate $\langle \mu_h \rangle$ as the shortage of treatment resources. We can observe that the effective infection rate β_e increases in this stage as the value of $\langle \beta_h \rangle$ drops more rapidly than $\langle \beta_h \rangle$. Consequently, the disease continues spreading in the network, and finally a large fraction of nodes are infected by the disease.

As for the small-degree nodes, as there are fewer connections with the outside, they have less information about the status of the epidemic and a lower self-protection awareness compared with the hub nodes in the early stage. Thus, the values of $\langle \alpha_s \rangle$ and $\langle q_s \rangle$ change slowly in this stage (Figure 3(b)). However, in the later stage, due to the protective measures adopted by hub nodes, the transmission of disease from hub nodes to small-degree nodes is basically blocked. Thus, there is a slight decrease in $\langle \alpha_s \rangle$ and a small increase in $\langle q_s \rangle$ in this stage.

Based on the above description, we can reasonably explain the phenomenon in phase I in Figure 2 that the disease increases abruptly in this phase.

Secondly, we study the time evolution of the dynamical parameters in $\alpha_c^{\mathrm{I}} \le \alpha < \alpha_c^{\mathrm{II}}$ in Figure 4. We find that, when $\alpha = 0.7$, nodes in the network have a larger instinctive self-awareness compared with the case of $\alpha = 0.1$. In this case, due to the hierarchical nature of disease transmission, a small number of global and local infected nodes (I_i and m_i) will lead to a high vigilance of the hub nodes. Therefore, the value of $\langle \alpha_h \rangle$ increases abruptly before time $t \approx 50$, as shown

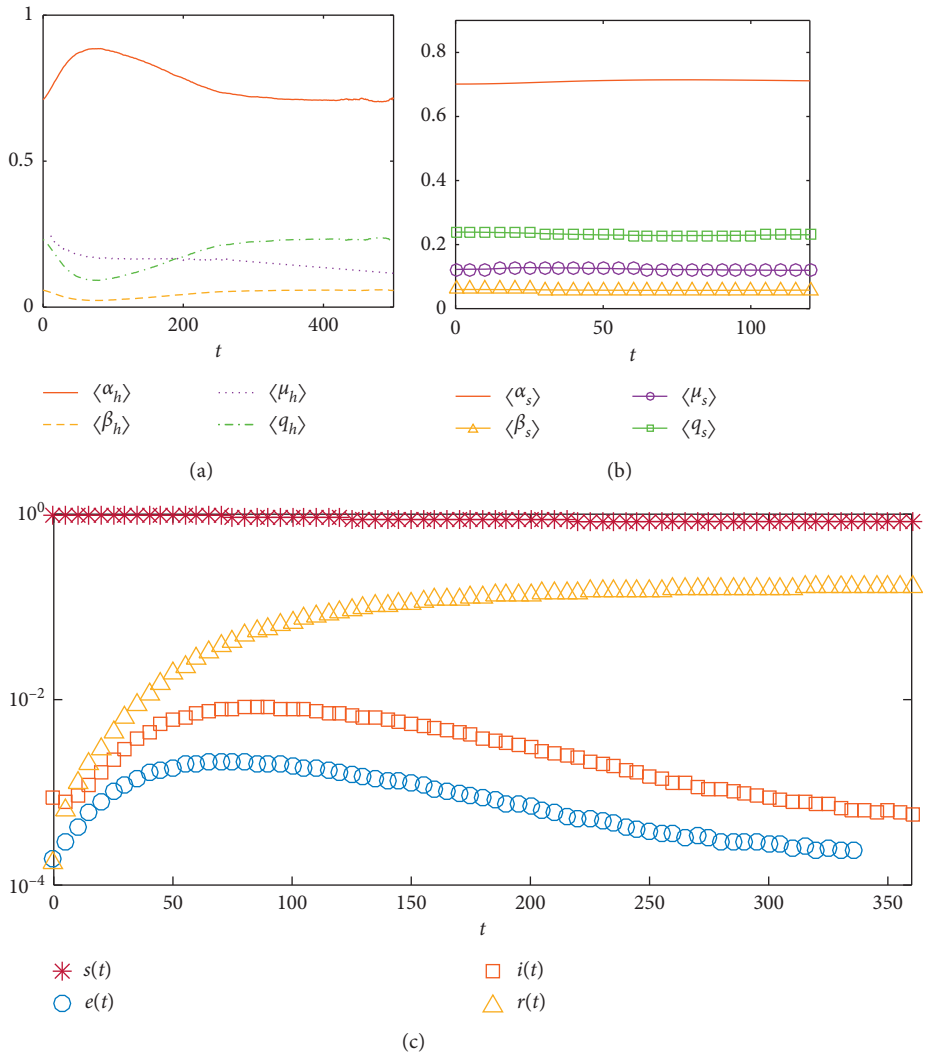

FIGURE 4: (a) Temporal evolution of the average values of awareness $\langle \alpha_h \rangle$ (red line), infection rate $\langle \beta_h \rangle$ (yellow segment), recovery rate $\langle \mu_h \rangle$ (purple dots), and probability of resource donation $\langle q_h \rangle$ for hub nodes. (b) The evolution of the average values of awareness $\langle \alpha_s \rangle$ (red line), infection rate $\langle \beta_s \rangle$ (yellow triangles), recovery rate $\langle \mu_s \rangle$ (purple circles), and probability of resource donation $\langle q_s \rangle$ (green squares) for nodes with small degree. (c) The evolution of fraction of the nodes in susceptible $s(t)$, exposed $e(t)$, infected $i(t)$, and recovered $r(t)$ state, respectively. The instinctive self-awareness is $\alpha = 0.7$ and the basic infection rate is $\beta = 0.2$.

in Figure 4(a), which leads to a rapid decrease of resource donation probability $\langle q_h \rangle$ and a reduction in the transmission rate $\langle \beta_h \rangle$. In this condition, the hub nodes are protected from been infected, which can also stop the reinfection of the hub nodes, as they can connect directly to each other or via a few small nodes [55, 56]. Further, the reduction of the resources will lead to a decrease in recovery rate $\langle \mu_h \rangle$, as shown in Figure 4(a). Besides, the effective infection rate β_e keeps a relatively small value in the initial stage, where the fraction of infected and exposed nodes $i(t)$ and $e(t)$ increases slowly. It indicates that the epidemic spreading is suppressed effectively compared with the case of $\alpha = 0.1$. After that, with the gradual recovery of the I-state nodes, there are fewer and fewer I-state neighbors around the hub nodes, which makes them gradually relax their vigilance against the disease and lead to the gradual decline of $\langle \alpha_h \rangle$. This phenomenon is fully consistent with the case that, in real scenarios, the slowdown in the epidemic spreading will lead to increased daily contact and economic recovery activities [57, 58]. As shown in Figure 4(a), the value of $\langle \alpha_h \rangle$ decreases after $t \approx 50$, which is accompanied by the increase of $\langle q_h \rangle$. The decrease of $\langle \alpha_h \rangle$ leads to a rise in the effective infection rate $\langle \beta_e \rangle$ (see the gap between $\langle \beta_h \rangle$ and $\langle \mu_h \rangle$), which will lead to a rise in the infected nodes, whereas the increase of infected nodes can immediately lead to the enhancement of self-protection awareness of hub nodes, as they have a high instinctive self-awareness, which in turn suppresses the spread of disease. Consequently, we can learn that there is a dynamic balance between the spread of disease and individuals' self-protection awareness after $t \approx 100$ (Figure 4(a)). Thus, there is a lower value of final infected density ρ compared to the case in phase I, and the disease can be suppressed to a certain extent.

Based on the above description, we can reasonably explain the reason why the disease increases slowly in phase II of Figure 2. Similarly, we can also explain the phenomena in phase III of Figure 2. Specifically, the hub nodes are very sensitive to the spread of disease as they all have a large value of instinctive self-awareness. Consequently, a small increase in the values of $m_i(t)$ and $I(t)$ will lead to the rapid increase in $\langle \alpha_h \rangle$ at the very early stage of spreading process. Therefore, the hub nodes are effectively protected from being infected and the disease is well suppressed at the beginning of the transmission process. Therefore, the disease will not breakout any more.

3.2. Effects of Network Heterogeneity on the Coupled Disease-Awareness Dynamics. In this section, we study the effects of network heterogeneity on the coupled dynamics of self-awareness and epidemic spreading. Since the network heterogeneity decreases with the increase of the power exponent γ [55], we construct the networks with different heterogeneity by changing the degree exponent based on the UCM model.

First of all, we study the value of ρ as a function of β in networks with different degree exponents. In Figure 5(a), the curves for the four typical values of γ are displayed. Interestingly, we find that the network heterogeneity plays the role of "double-edged sword" in that they can either suppress or promote the epidemic spreading. Specifically, we find that the curves of the infected density intersect at a fixed basic infection rate about $\beta^* \approx 0.13$ and dynamical processes are separated into two phases. In phase I, i.e., HTML transalation failed, the basic infection rate is small, the final infected density ρ increases with the increase of network heterogeneity at a fixed value of β, and the epidemic threshold β_c increases with γ. While, in phase II, i.e., $\beta > \beta^*$, the value of β is large, the value of ρ decreases with the increase of network heterogeneity. The results indicate that when the basic infection rate β is small, the network heterogeneity promotes disease spreading, which is consistent with the results in the classical epidemiological model [59]. While, when there is a large value of β, e.g., $\beta = 0.2$, it suppresses the outbreak of disease.

To illustrate the conclusions more clearly, we plot the value of ρ as a function of γ at two typical values of β in the two regions $\beta < \beta^*$ and $\beta > \beta^*$, respectively, in Figure 5(b). Without loss of generality, we select $\beta = 0.1$ in phase I and $\beta = 0.2$ in phase II, respectively. Through extensive simulations, we find that when $\beta = 0.1$, the value of ρ increases monotonously with γ; in contrast, it decreases with γ when $\beta = 0.2$.

Further, we study the relationship between the epidemic threshold β_c and the self-awareness α for different values of γ. Figure 6 displays the value of β_c as a function of α. We find that the value of β_c increases monotonously with the increase of α for each value of γ. Specially, the value of β_c increases abruptly when $\alpha > \alpha_c^{\mathrm{I}}$ defined in Figure 2. When α is fixed, the value of β_c increases γ.

We can use the same theory as in the previous section to qualitatively explain the "double-edged sword" phenomenon. Specifically, in a network with strong heterogeneity, the vast majority of nodes have small degrees and only a few nodes have a large number of connections. Due to the hierarchical character of the disease transmission, the disease is likely to spread rapidly in a hub node-centered area. Thus, when the basic infection rate β is large, e.g., $\beta = 0.2$, the number of infected nodes in the local area increases rapidly, which induces to a rapid increase in the self-awareness of the hub nodes $\langle \alpha_h \rangle$. Subsequently, the infection rate of the hub nodes $\langle \beta_h \rangle$ drops significantly, which reduces the infection between hub nodes and the small-degree nodes. Therefore, the stronger the network heterogeneity, the more the disease transmission can be suppressed. On the contrary, when the transmission rate is small, e.g., $\beta = 0.1$, this inhibition to disease transmission will disappear. In this case, the structural heterogeneity will promote the spread of the disease.

At last, to further investigate the "double-edged sword" effects of network heterogeneity on the coupling dynamics, we study the relationship between the final fraction of infected node ρ and self-awareness α on networks with different degree exponents when there is as relatively large basic infection rate, e.g., $\beta = 0.2$. Interestingly, once again, we find the "double-edged sword" effect of network heterogeneity on dynamic properties. As shown in Figure 7(a), the value of ρ decreases with α and the curves intersect at a critical value α^* that is equal to the first critical point in Figure 2. When $\alpha < \alpha^*$ (in phase I), the value of ρ increases with γ (see the curve for $\alpha = 0.5$ in Figure 7(b)), which indicates that the network heterogeneity inhibits the spread of disease. The above result is in accordance with that in phase II of Figure 5(a). On the contrary, when $\alpha > \alpha^*$, the value of ρ decreases with γ (see the curve for $\alpha = 0.7$ in Figure 7(b)), which indicates that the network heterogeneity promotes the spread of disease in this phase.

Next, we continue explaining the reason why the network heterogeneity promotes the spread of disease in phase II of Figure 7(a). Specifically, when $\alpha > \alpha^*$, there is a strong instinctive self-awareness for all nodes in networks. When there is strong degree heterogeneity of a network, e.g., $\gamma = 2.1$, the vast majority of nodes have small degrees and only a few nodes have a large number of connections. Due to the hierarchical character of the disease transmission, the disease is likely to spread rapidly in a hub node-centered area, which means that the value of $\langle \alpha_h \rangle$ increases abruptly in the early stage of an epidemic according to equation (1). Thus, there is a small value of $\langle \beta_h \rangle$. Consequently, the hubs are protected effectively in this condition. However, as the small-degree nodes that make up the vast majority of the network have few connections with other nodes, the number of their infected neighbors m_i is very small. Therefore, there is a relatively small value of $\langle \alpha_s \rangle$. Consequently, the infection rate $\langle \beta_s \rangle$ of the small-degree nodes is relatively large, which leads to a large probability to be infected for these nodes. On the contrary, in the network with a relatively homogeneous degree distribution, e.g., $\gamma = 4.0$, the proportion of nodes with large degree is larger than that of networks with strong degree heterogeneity. Thus, a larger proportion of nodes have a larger value of $\langle \alpha_h \rangle$ in these

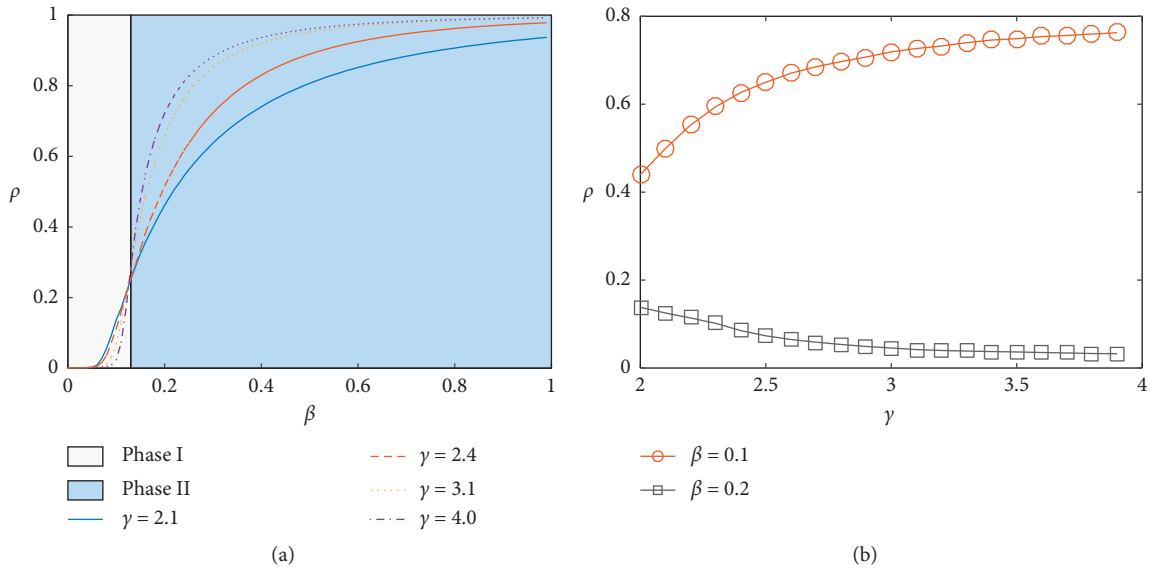

Figure 5: Effects of network heterogeneity on the coupled dynamics. (a) The final infected density ρ as a function of β when degree exponents $\gamma = 2.1$ (blue line), $\gamma = 2.4$ (red line segment), $\gamma = 3.1$ (yellow dots), and $\gamma = 4.0$ (purple dotted line), respectively. The two regions marked by phase I (filled by gray) and phase II (filled by sky blue) are separated by the critical value $\beta^* \approx 0.13$. (b) The value of ρ as a function of γ for $\beta = 0.1$ (red circles) and $\beta = 0.2$ (gray squares), respectively. The instinctive self-awareness is fixed as $\alpha = 0.5$. The other parameters are the same as those in Figure 1.

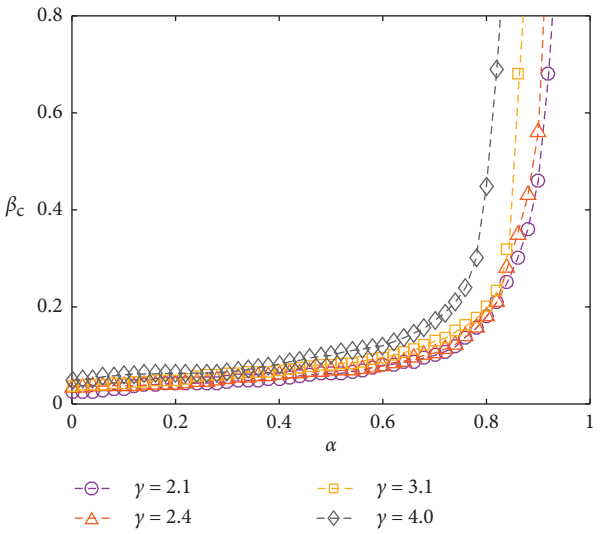

Figure 6: The relationship between the epidemic threshold β_c and the instinctive self-awareness α when the degree exponents are set at $\gamma = 2.1$ (purple circles), $\gamma = 2.4$ (red triangles), $\gamma = 3.1$ (yellow squares,) and $\gamma = 4.0$ (gray rhombuses), respectively. The other parameters are the same as those in Figure 1. Data are obtained by averaging over $10^2 \times 10^2$ independent realizations on 10^2 networks.

networks, and the disease can be suppressed under this condition.

4. Discussion

The self-protection awareness of the individuals can influence their behavior response to the epidemics, such as reducing contacts with others and large public gatherings. More importantly, it will also affect the behavior of individual resource allocation that is of critical importance in controlling the outbreak of an epidemic. To investigate the effects of the self-awareness-driven individual resource support on the epidemic dynamics, we have proposed a resource-based susceptible-exposed-infected-recovered (r-SEIR) epidemiological model and a self-awareness-based resource allocation model, respectively. In the models, the self-awareness of the individuals is assumed to come from both local communities and global mass media, which is measured by the number of infected neighbors and global infected nodes.

Firstly, we have studied the effects of the awareness-driven individual resource allocation on the spreading dynamics in sale-free networks with fixed degree exponent. Through extensive Monte Carlo simulations, we have found that the final infected density ρ decreases with the increase of the instinctive self-awareness α. More importantly, there are two critical values α_c^{I} and α_c^{II} that separate the parameter space into three phases. In phase I, i.e., $\alpha < \alpha_c^{\mathrm{I}}$, the final infected density ρ increases abruptly with the basic infection rate β, which implies that the disease can not be suppressed effectively. In phase II, i.e., $\alpha_c^{\mathrm{I}} \le \alpha < \alpha_c^{\mathrm{II}}$, the value of ρ grows gently with β, which means that the disease can be controlled to a certain extent. At last, in phase III, i.e., $\alpha \ge \alpha_c^{\mathrm{II}}$, the disease does not break out in the network and the value of ρ remains a very small value. Combining the study of the time evolution of dynamical parameters, we have qualitatively explained the corresponding phenomena. The results suggest that the disease can be effectively controlled as long as we maintain a proper level of self-protection awareness.

Next, we have investigated the effects of network heterogeneity on the coupled dynamics. Through extensive

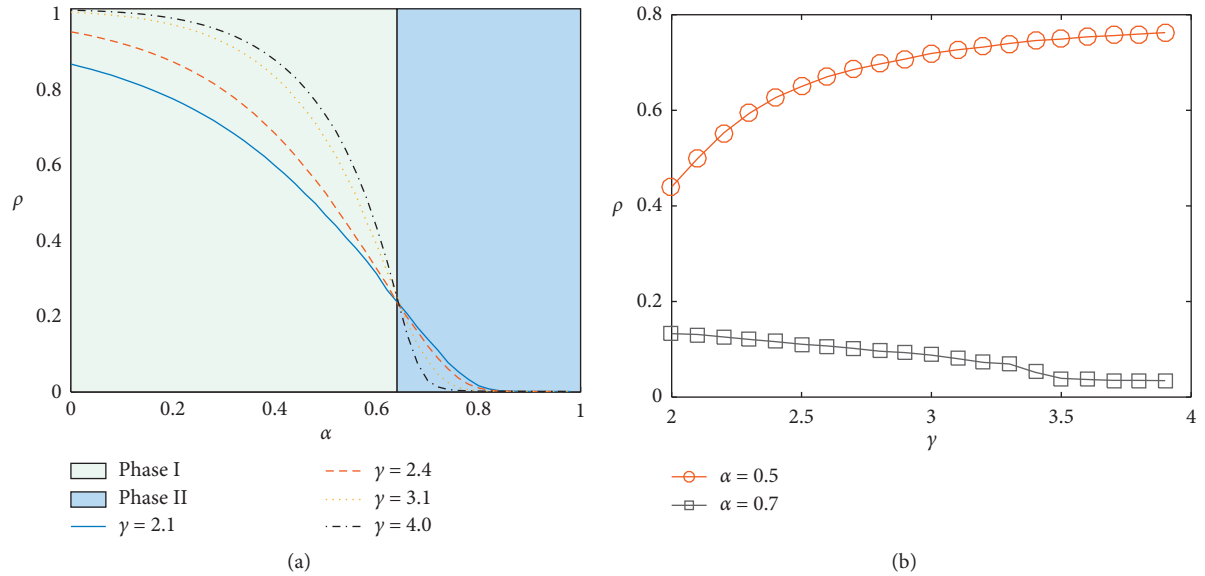

Figure 7: Effects of self-awareness and network structure on the spreading dynamics. (a) Plots of ρ vs. α when $\gamma = 2.1$ (blue line), $\gamma = 2.4$ (red line segment), $\gamma = 3.1$ (yellow dots), and $\gamma = 4.0$ (black dotted line), respectively. The two regions marked by phase I (filled by gray) and phase II (filled by sky blue) are separated by the critical value $\alpha^* \approx 0.64$. (b) The value of ρ as a function of γ when $\alpha = 0.5$ (red circles) and $\alpha = 0.7$ (black squares), respectively. The basic transmission rate is set at $\beta = 0.2$, and the other parameters are the same as those in Figure 1.

simulations, we have found that the network heterogeneity has "double-edged sword" effect on the coupling dynamics. Specifically, we have found that there is a critical value of basic infection rate β^*, when $\beta < \beta^*$, the network heterogeneity promotes the spread of disease. On the contrary, when $\beta > \beta^*$, the network heterogeneity inhibits the spread of disease. To further investigate "double-edged sword" effects of network heterogeneity on the coupling dynamics, we have studied the relationship between ρ and α on networks with different degree exponents when there is as relatively large basic infection rate. Through extensive simulations, we have found the instinctive self-awareness denoted as α^*, which is in accordance with α_c^{I}. When $\alpha < \alpha^*$, the network heterogeneity inhibits the spread of disease. On the contrary, when $\alpha > \alpha^*$, the network heterogeneity promotes the spread of disease.

Our findings make a substantial contribution to understanding the effects of people's awareness of self-protection on the spreading dynamics during a pandemic, which will be of practical significance in controlling the outbreak of infectious diseases, especially in the context of the COVID-19 pandemic. The results obtained in this paper can guide people to maintain the right self-awareness and behavior during an outbreak and also have a direct application in the development of strategies to suppress the spread of the disease.

Data Availability

The data used to support the findings of this study are available from the corresponding author upon request.

Conflicts of Interest

The authors declare that they have no conflicts of interest regarding this paper.

Acknowledgments

This work was supported by the Fundamental Research Funds for the Central Universities (nos. JBK190972, JBK171113, and JBK170505), National Natural Science Foundation of China (nos. 71671141 and 71873108), the 2020 school-level scientific research project of Aba Teachers University (no. ASA20-01), and the Financial Intelligence and Financial Engineering Key Lab of Sichuan Province.

References

[1] A. Trilla, G. Trilla, and C. Daer, "The 1918 "Spanish flu" in Spain," *Clinical Infectious Diseases*, vol. 47, no. 5, pp. 668–673, 2008.

[2] K. H. Chan, P. H. Li, S. Y. Tan, Q. Chang, and J. P. Xie, "Epidemiology and cause of severe acute respiratory syndrome (SARS) in guangdong, people's Republic of China, in february, 2003," *The Lancet*, vol. 362, no. 9393, pp. 1353–1358, 2003.

[3] M. P. Girard, J. S. Tam, O. M. Assossou, and M. P. Kieny, "The 2009 a (H1N1) influenza virus pandemic: a review," *Vaccine*, vol. 28, no. 31, pp. 4895–4902, 2010.

[4] WHO, *Coronavirus Disease 2019 (Covid-19) Situation Report–209*, WHO, Geneva, Switzerland, 2020.

[5] Z. Wang, M. A. Andrews, Z.-X. Wu, L. Wang, and C. T. Bauch, "Coupled disease-behavior dynamics on complex networks: a review," *Physics of Life Reviews*, vol. 15, pp. 1–29, 2015.

[6] C. Liu and Z.-K. Zhang, "Information spreading on dynamic social networks," *Communications in Nonlinear Science and Numerical Simulation*, vol. 19, no. 4, pp. 896–904, 2014.

[7] S. Funk, E. Gilad, C. Watkins, and V. A. A. Jansen, "The spread of awareness and its impact on epidemic outbreaks," *Proceedings of the National Academy of Sciences*, vol. 106, no. 16, pp. 6872–6877, 2009.

[8] W. Wang, H. E. Stanley, and L. A. Braunstein, "Effects of time-delays in the dynamics of social contagions," *New Journal of Physics*, vol. 20, no. 1, Article ID 013034, 2018.

[9] J. J. Van Bavel, K. Baicker, P. S. Boggio et al., "Using social and behavioural science to support covid-19 pandemic response," *Nature Human Behaviour*, vol. 4, no. 5, pp. 460–471, 2020.

[10] H. Peng, W. Peng, D. Zhao, and W. Wang, "Impact of the heterogeneity of adoption thresholds on behavior spreading in complex networks," *Applied Mathematics and Computation*, vol. 386, Article ID 125504, 2020.

[11] R. Li, W. Wang, and Z. Di, "Effects of human dynamics on epidemic spreading in Côte d'Ivoire," *Physica A: Statistical Mechanics and Its Applications*, vol. 467, pp. 30–40, 2017.

[12] S. P. Adhikari, S. Meng, Y.-J. Wu et al., "Epidemiology, causes, clinical manifestation and diagnosis, prevention and control of coronavirus disease (covid-19) during the early outbreak period: a scoping review," *Infectious Diseases of Poverty*, vol. 9, no. 1, pp. 1–12, 2020.

[13] M. U. G. Kraemer, C.-H. Yang, B. Gutierrez et al., "The effect of human mobility and control measures on the covid-19 epidemic in China," *Science*, vol. 368, no. 6490, pp. 493–497, 2020.

[14] R. Li, P. Richmond, and B. M. Roehner, "Effect of population density on epidemics," *Physica A: Statistical Mechanics and Its Applications*, vol. 510, pp. 713–724, 2018.

[15] W. Wang, Q.-H. Liu, J. Liang, Y. Hu, and T. Zhou, "Co-evolution spreading in complex networks," *Physics Reports*, vol. 820, pp. 1–51, 2019.

[16] X.-T. Liu, Z.-X. Wu, and L. Zhang, "Impact of committed individuals on vaccination behavior," *Physical Review E*, vol. 86, no. 5, Article ID 051132, 2012.

[17] H.-F. Zhang, P.-P. Shu, Z. Wang, M. Tang, and M. Small, "Preferential imitation can invalidate targeted subsidy policies on seasonal-influenza diseases," *Applied Mathematics and Computation*, vol. 294, pp. 332–342, 2017.

[18] K. A. Kabir, K. Kuga, and J. Tanimoto, "The impact of information spreading on epidemic vaccination game dynamics in a heterogeneous complex network- a theoretical approach," *Chaos, Solitons & Fractals*, vol. 132, Article ID 109548, 2020.

[19] Q. Guo, Y. Lei, X. Jiang, Y. Ma, G. Huo, and Z. Zheng, "Epidemic spreading with activity-driven awareness diffusion on multiplex network," *Chaos: An Interdisciplinary Journal of Nonlinear Science*, vol. 26, no. 4, Article ID 043110, 2016.

[20] K. M. A. Kabir, K. Kuga, and J. Tanimoto, "Analysis of SIR epidemic model with information spreading of awareness," *Chaos, Solitons & Fractals*, vol. 119, pp. 118–125, 2019.

[21] P. Zhu, X. Wang, S. Li, Y. Guo, and Z. Wang, "Investigation of epidemic spreading process on multiplex networks by incorporating fatal properties," *Applied Mathematics and Computation*, vol. 359, pp. 512–524, 2019.

[22] Z. Wang, Q. Guo, S. Sun, and C. Xia, "The impact of awareness diffusion on sir-like epidemics in multiplex networks," *Applied Mathematics and Computation*, vol. 349, pp. 134–147, 2019.

[23] Q. Wu, X. Fu, M. Small, and X.-J. Xu, "The impact of awareness on epidemic spreading in networks," *Chaos: An Interdisciplinary Journal of Nonlinear Science*, vol. 22, no. 1, Article ID 013101, 2012.

[24] C. Granell, S. Gómez, and A. Arenas, "Dynamical interplay between awareness and epidemic spreading in multiplex networks," *Physical Review Letters*, vol. 111, no. 12, Article ID 128701, 2013.

[25] X.-X. Zhan, C. Liu, G. Zhou et al., "Coupling dynamics of epidemic spreading and information diffusion on complex networks," *Applied Mathematics and Computation*, vol. 332, pp. 437–448, 2018.

[26] M. L. Ranney, V. Griffeth, and A. K. Jha, "Critical supply shortages - the need for ventilators and personal protective equipment during the covid-19 pandemic," *New England Journal of Medicine*, vol. 382, no. 18, p. e41, 2020.

[27] C. Nowzari, V. M. Preciado, and G. J. Pappas, "Optimal resource allocation for control of networked epidemic models," *IEEE Transactions on Control of Network Systems*, vol. 4, no. 2, pp. 159–169, 2015.

[28] A. Y. Lokhov and D. Saad, "Optimal deployment of resources for maximizing impact in spreading processes," *Proceedings of the National Academy of Sciences*, vol. 114, no. 39, pp. E8138–E8146, 2017.

[29] H. Chen, G. Li, H. Zhang, and Z. Hou, "Optimal allocation of resources for suppressing epidemic spreading on networks," *Physical Review E*, vol. 96, no. 1, Article ID 012321, 2017.

[30] S. Li, D. Zhao, X. Wu, Z. Tian, A. Li, and Z. Wang, "Functional immunization of networks based on message passing," *Applied Mathematics and Computation*, vol. 366, Article ID 124728, 2020.

[31] V. M. Preciado, M. Zargham, C. Enyioha, A. Jadbabaie, and G. Pappas, "Optimal vaccine allocation to control epidemic outbreaks in arbitrary networks," in *Proceedings of the 52nd IEEE Conference on Decision and Control*, pp. 7486–7491, IEEE, Florence, Italy, December 2013.

[32] L. Böttcher, O. Woolley-Meza, N. A. Araújo, H. J. Herrmann, and D. Helbing, "Disease-induced resource constraints can trigger explosive epidemics," *Scientific Reports*, vol. 5, Article ID 16571, 2015.

[33] X. Chen, W. Wang, S. Cai, H. E. Stanley, and L. A. Braunstein, "Optimal resource diffusion for suppressing disease spreading in multiplex networks," *Journal of Statistical Mechanics: Theory and Experiment*, vol. 2018, no. 5, Article ID 053501, 2018.

[34] X. Chen, R. Wang, M. Tang, S. Cai, H. E. Stanley, and L. A. Braunstein, "Suppressing epidemic spreading in multiplex networks with social-support," *New Journal of Physics*, vol. 20, no. 1, Article ID 013007, 2018.

[35] L. Long, K. Zhong, and W. Wang, "Malicious viruses spreading on complex networks with heterogeneous recovery rate," *Physica A: Statistical Mechanics and Its Applications*, vol. 509, pp. 746–753, 2018.

[36] J. Jiang, J. Liang, and T. Zhou, "Modeling of epidemic spreading on multilayer networks in uncertain environments," *Journal of Statistical Mechanics: Theory and Experiment*, vol. 2019, no. 10, Article ID 103404, 2019.

[37] X. Chen, Q. Liu, R. Wang, Q. Li, and W. Wang, "Self-awareness-based resource allocation strategy for containment of epidemic spreading," *Complexity*, vol. 2020, Article ID 3256415, 12 pages, 2020.

[38] T. Zhou, Q. Liu, Z. Yang et al., "Preliminary prediction of the basic reproduction number of the Wuhan novel coronavirus 2019-nCoV," *Journal of Evidence-Based Medicine*, vol. 13, no. 1, pp. 3–7, 2020.

[39] L. Wang, J. Wang, H. Zhao et al., "Modelling and assessing the effects of medical resources on transmission of novel coronavirus (covid-19) in Wuhan, China," *Mathematical Biosciences and Engineering*, vol. 17, no. 4, pp. 2936–2949, 2020.

[40] A. S. Mackie, L. Pilote, R. Ionescu-Ittu, E. Rahme, and A. J. Marelli, "Health care resource utilization in adults with congenital heart disease," *The American Journal of Cardiology*, vol. 99, no. 6, pp. 839–843, 2007.

[41] M. Gul and A. F. Guneri, "A computer simulation model to reduce patient length of stay and to improve resource

utilization rate in an emergency department service system," *International Journal of Industrial Engineering*, vol. 19, no. 5, pp. 221–231, 2012.

[42] M. Girvan and M. E. J. Newman, "Community structure in social and biological networks," *Proceedings of the National Academy of Sciences*, vol. 99, no. 12, pp. 7821–7826, 2002.

[43] M. Small, Y. Li, T. Stemler, and K. Judd, "Growing optimal scale-free networks via likelihood," *Physical Review E*, vol. 91, no. 4, Article ID 042801, 2015.

[44] R. Li, L. Dong, J. Zhang et al., "Simple spatial scaling rules behind complex cities," *Nature Communications*, vol. 8, no. 1, pp. 1–7, 2017.

[45] B. Schönfisch and A. de Roos, "Synchronous and asynchronous updating in cellular automata," *BioSystems*, vol. 51, no. 3, pp. 123–143, 1999.

[46] P. G. Fennell, S. Melnik, and J. P. Gleeson, "Limitations of discrete-time approaches to continuous-time contagion dynamics," *Physical Review E*, vol. 94, no. 5, Article ID 052125, 2016.

[47] S.-M. Cai, X.-H. Chen, X.-J. Ye, and M. Tang, "Precisely identifying the epidemic thresholds in real networks via asynchronous updating," *Applied Mathematics and Computation*, vol. 361, pp. 377–388, 2019.

[48] M. Catanzaro, M. Boguñá, and R. Pastor-Satorras, "Generation of uncorrelated random scale-free networks," *Physical Review E*, vol. 71, no. 2, Article ID 027103, 2005.

[49] P. Holme and B. J. Kim, "Growing scale-free networks with tunable clustering," *Physical Review E*, vol. 65, no. 2, Article ID 026107, 2002.

[50] M. Boguná, R. Pastor-Satorras, and A. Vespignani, "Cut-offs and finite size effects in scale-free networks," *The European Physical Journal B-Condensed Matter and Complex Systems*, vol. 38, no. 2, pp. 205–209, 2004.

[51] P. Shu, W. Wang, M. Tang, and Y. Do, "Numerical identification of epidemic thresholds for susceptible-infected-recovered model on finite-size networks, Chaos," *An Interdisciplinary Journal of Nonlinear Science*, vol. 25, no. 6, Article ID 063104, 2015.

[52] P. Crepey, F. P. Alvarez, and M. Barthélemy, "Epidemic variability in complex networks," *Physical Review E*, vol. 73, no. 4, Article ID 046131, 2006.

[53] R. Pastor-Satorras, C. Castellano, P. Van Mieghem, and A. Vespignani, "Epidemic processes in complex networks," *Reviews of Modern Physics*, vol. 87, no. 3, p. 925, 2015.

[54] M. Barthélemy, A. Barrat, R. Pastor-Satorras, and A. Vespignani, "Velocity and hierarchical spread of epidemic outbreaks in scale-free networks," *Physical Review Letters*, vol. 92, no. 17, Article ID 178701, 2004.

[55] M. Newman, *Networks: An Introduction*, Oxford University Press, Oxford, UK, 2010.

[56] S. C. Ferreira, R. S. Sander, and R. Pastor-Satorras, "Collective versus hub activation of epidemic phases on networks," *Physical Review E*, vol. 93, no. 3, Article ID 032314, 2016.

[57] C. M. O'Connor, A. A. Anoushiravani, M. R. DiCaprio, W. L. Healy, and R. Iorio, "Economic recovery after the covid-19 pandemic: resuming elective orthopedic surgery and total joint arthroplasty," *The Journal of Arthroplasty*, vol. 35, no. 7, pp. S32–S36, 2020.

[58] G. Bonaccorsi, F. Pierri, M. Cinelli et al., "Economic and social consequences of human mobility restrictions under covid-19," *Proceedings of the National Academy of Sciences*, vol. 117, no. 27, pp. 15530–15535, 2020.

[59] R. Pastor-Satorras and A. Vespignani, "Epidemic spreading in scale-free networks," *Physical Review Letters*, vol. 86, no. 14, p. 3200, 2001.